

DISS. ETH NO. 25913

Metal Centres in Pulsed Dipolar Spectroscopy
– From Methodology to Application –

A thesis submitted to attain the degree of
DOCTOR OF SCIENCES of ETH ZURICH
(Dr. sc. ETH Zurich)

presented by

KATHARINA KELLER

MSc ETH Interdisciplinary Science

born on 03.10.1989

citizen of Germany

accepted on the recommendation of

Prof. Dr. Gunnar Jeschke, examiner
Prof. Dr. Matthias Ernst, co-examiner
Dr. Maxim Yulikov, co-examiner

2019

*'Equipped with his five senses, man explores the universe around him and calls the adventure
Science.'*

Edwin Powell Hubble

In *The Nature of Science, and Other Lectures* (1954), 6.

*'Je suis de ceux qui pensent que la science est d'une grande beauté. Un scientifique dans son
laboratoire est non seulement un technicien : il est aussi un enfant placé devant des phénomènes
naturels qui l'impressionnent comme des contes de fées.'*

Marie Curie

Quoted in *Madame Curie*, Ève Curie, éd. Gallimard, 1938

*'Das schönste Glück des denkenden Menschen ist, das Erforschliche erforscht zu haben und das
Unerforschliche zu verehren.'*

Johann Wolfgang von Goethe

Maximen und Reflexionen. Aphorismen und Aufzeichnungen. Nach den Handschriften des Goethe- und
Schiller-Archivs. Hrsg.: Max Hecker. Weimar: Verlag der Goethe-Gesellschaft, 1907

Abstract

Knowledge of structure does not imply understanding of function of biological systems, but understanding of function is hardly possible without having some knowledge about the structure. Likewise, mechanistic models that rely on a dynamic view, i.e. structural transitions, are crucial for the design of biomimetic systems or for a rational approach to pharmacological intervention. In this framework, it is important to obtain structural data on biological systems with increasing size as well as complexity and to understand how well such data constrain these systems as well as models.

In that respect, pulsed dipolar spectroscopy has become a valuable tool in structural biology for the measurement of distance distributions in the nanometre range without the need of long-range order within the biological samples, i.e. crystallization, irrespective of the size of the system. This is particularly important to access functional states. In the past few years new insight into protein function has been obtained by hybrid structural models that incorporate restraints from pulsed dipolar spectroscopy in combination with site-directed spin labelling cooperatively with restraints from other techniques.

The work realized within this thesis pushes for increased sensitivity and reliable data analysis of pulse dipolar spectroscopy data at low hardware requirements. It contributes towards extending the arsenal of spectroscopically orthogonal spin probes that are important for site-directed spin labelling strategies, which in turn are crucial for applying Electron Paramagnetic Resonance (EPR) to heterologous complexes of biomacromolecules.

In that context, the thesis embarked on a study of several metal ions (Gd(III), Mn(II), Cu(II), Fe(III), Co(II)) with respect to their suitability in pulsed dipolar spectroscopy. Complexes of Cu(II), Mn(II) as well as Gd(III) were found to be most promising, with the optimal choice depending on the problem at hand. The EPR properties, i.e. lineshape or electronic relaxation, of Mn(II) and Gd(III) are strongly influenced by the zero-field splitting (ZFS) interaction that in turn influences the performance of distance measurements on such compounds. Hence, the reliability of extracting broadly distributed ZFS parameters was studied for a variety of Gd(III) complexes and two different models present in literature. These ZFS data allowed for the development of a superposition model to predict the magnitude of the ZFS based on knowledge of Gd(III)-complex's structure. This superposition model may be useful for designing new Gd(III) labels prior to synthesis efforts.

Currently, the major technique for obtaining distance distributions between spin pairs is the double electron electron resonance (DEER) experiment, in combination with nitroxide-based spin labelling. The reliability of this approach and the resulting distance distributions may be compromised by orientation selection effects in orthogonal labelling strategies, in which one of the two nitroxides is replaced by a metal ion that typically exhibits much more strongly anisotropically-broadened EPR lines. Further, if both labels are metal ions low modulation depths are observed in conventional DEER experiments consequently limiting sensitivity. In addition,

level mixing for high-spin pairs with insufficient difference in the resonance offset between the observed and pumped transitions may induce distortions to the distance distribution.

To some extent, these complications can be addressed by the relaxation induced dipolar modulation enhancement (RIDME) experiment without the need for technically demanding EPR spectrometers. Relaxation-induced spin flips have virtual infinite bandwidth and spins distributed over the whole spectrum contribute to the dipolar signal. Therefore, the average resonance frequency difference in spin pairs contributing to the modulation is much larger than the dipole-dipole coupling, which reduces distortions from level mixing. This also leads to reduced orientation selection compared to spin inversion induced by a pump pulse that only covers a small fraction of the EPR spectrum. Before commencing this thesis, RIDME at high field had shown potential for improving modulation depth as well as resolution of the distance distribution for Gd(III)-Gd(III) pairs. The technique had also been shown to provide information on metalloproteins with native paramagnetic metal ions. However, broad application of the RIDME technique in the framework of spin-labelled biomolecules is hindered by some difficulties: (i) for high-spin species, multiples of the dipolar frequency contribute to the dipolar signal, (ii) the technique is highly sensitive to nuclear modulation artefacts, (iii) no simple analytical expressions exist for intermolecular background decay and the signal decays faster than in the DEER experiment. Therefore the separation of the intermolecular background decay from the intramolecular modulation is more challenging, in particular for broad distance distributions, and the accessible distance range might be restricted.

In this respect, the thesis commenced a thorough study of several aspects that influence data analysis, such as background correction, nuclear modulations and contributions of higher harmonics. An approach - based on a modified kernel in Tikhonov regularization - was implemented that can provide the anticipated distance distributions for high-spin RIDME data if the relative contributions of the different higher harmonics are known. For either high-spin metal centre, Mn(II) or Gd(III), a significant gain in modulation depth could be confirmed and the harmonic overtone coefficients occurred to be relatively stable for spin-spin distances > 3 nm, different pulse sequence parameters as well as measurement temperature, ligand environment and in spin-labelled proteins compared to model compounds. By processing simulated data sets under the assumptions of too large or too small content of harmonics in the data, it was found how distance distributions are influenced by errors in estimating this content and that a mismatch of about 20% appears to be within the uncertainties due to other approximations for Gd(III)-Gd(III) measurements in biomolecules. Some deviations were observed for short spin-spin distances as well as for shifting the detection position away from the maximum of the Gd(III) spectrum or towards the low-field part of the Mn(II) spectrum. These deviations shall be investigated in more detail in follow-up studies appended with newly - to be synthesised - model compounds in the short distance range.

It was shown in previous work on Gd(III)-Gd(III) DEER measurements that using ultra-wideband (UWB) excitation over a range of 2.5 GHz, polarization can be transferred from satellite transitions to the central observer transition and thereby increase sensitivity. Within this thesis, it was demonstrated that similar schemes can be used to enhance the sensitivity in Gd(III)-Gd(III) as well as Mn(II)-Mn(II) RIDME measurements. In addition, such pre-polarization schemes were found to be promising to reduce the intensity of artefact peaks by enhancing only echoes excited by all pulses in the RIDME sequence.

Further, a new approach for suppression of nuclear modulation artefacts in RIDME was introduced. The approach avoids losses in signal-to-noise ratio that are present in the previously established approaches. Interesting trends were recognized in the experimental intermolecular RIDME background decay that are in agreement with approximate analytical equations computed under the assumption of instantaneous jumps of the non-resonant spins following an approach by Hu and Hartman. The observed proton-driven spectral diffusion processes in the RIDME background decay may allow designing new RIDME-based experimental schemes to characterize soft matter and biomacromolecules through the determination of the local proton distribution in the vicinity of the spin-labelled site.

A comparison of RIDME and UWB-DEER measurements on molecular Cu(II)-rulers revealed that both techniques perform similarly depending on the available hardware. For both experimental schemes, a much larger modulation depth and thus higher sensitivity was obtained in comparison to a conventional DEER setup. Notably, the RIDME technique reduces orientation selectivity from the inverted species and appears to be beneficial for situations with limited power over a broad range. Such situations are currently still often encountered at high field, where nuclear modulations in RIDME experiments are conveniently suppressed.

Eventually, paramagnetic metal-ion substitution of Mg(II) by Mn(II) was found to provide valuable means to follow metal binding in nucleotide binding domains of ATP-fuelled proteins as well as for accessing geometric assemblies through measurement of spin-spin distances. It was demonstrated how such data can be combined with solid-state NMR data in order to obtain deeper structural insight.

Zusammenfassung

Kenntnis der Struktur bedingt nicht ein Verständnis der Funktion biologischer Systeme, jedoch ist ein Verständnis der Funktion schwer möglich ohne eine gewisse Vorstellung von der Struktur. In ähnlicher Weise beruhen mechanistische Modelle, die für die Beschreibung biomimetischer Systeme oder für die Entwicklung pharmazeutischer Interventionen essentiell sind, auf Einsicht in dynamische Prozesse, wie z.B. strukturelle Übergänge. Aus diesem Grund ist es wichtig, Information über die Anordnung von biologischen Systemen mit steigender Grösse und Komplexität zu erhalten und zu verstehen, wie gut solche Information diese Systeme als auch Modelle beschreibt.

Die gepulste dipolare Spektroskopie hat sich zu einer wertvollen Methode in der Strukturbiologie entwickelt, um Abstandverteilungen im Nanometerbereich zu messen, ohne dass eine hochgeordnete Packung der Moleküle, wie zum Beispiel in der Kristallografie, notwendig ist. Zudem ist die EPR nicht durch die Grösse der Systeme limitiert. Dies ist besonders wichtig, um funktionelle Zustände zu charakterisieren. In den letzten Jahren konnten neue Erkenntnisse über die Funktion von Proteinen durch erste Hybridmodelle erlangt werden. Diese Modelle beruhen auf einer Kombination von Informationen, die durch verschiedene, komplementäre Techniken erhalten werden. Einen Baustein bilden hierbei Abstandsverteilungen, die aus der gepulsten dipolaren Spektroskopie, in Kombination mit gezielter Markierung verschiedener Positionen im Zielprotein, resultieren.

Diese Dissertation hat zum Ziel, die Empfindlichkeit sowie die Genauigkeit der Analyse von Daten aus der gepulsten dipolaren Spektroskopie zu verbessern, mit Augenmerk auf Situationen, in denen die technischen Möglichkeiten begrenzt sind. Die Arbeit trägt zudem dazu bei, die Auswahl an Spinsonden, die ausschlaggebend für die Anwendungen der gepulsten dipolaren Spektroskopie sind, zu erweitern.

In diesem Zusammenhang wurden zahlreiche Metallionen (Gd(III), Mn(II), Cu(II), Fe(II), Co(II)) in Bezug auf ihre Zweckmässigkeit in der gepulsten dipolaren Spektroskopie untersucht. Dabei zeigten Komplexe von Cu(II)-, Mn(II)- und Gd(III)-Ionen die vielversprechendsten Eigenschaften, jeweils abhängig von der zu untersuchenden Problematik. Eigenschaften der Elektronenspinresonanz (ESR) von Mn(II) und Gd(III), beispielsweise die Linienform oder elektronische Relaxation, sind abhängig von der Nullfeldaufspaltung, welche somit die Durchführung der Abstandsmessungen beeinflusst. Daher wurde die Zuverlässigkeit der Bestimmung von stark verteilten Nullfeldparametern für einige Gd(III) Komplexe untersucht. Diese Ergebnisse konnten auch zur Entwicklung eines Superpositionsmodells zur Vorhersage der Nullfeldparameter, basierend auf der Struktur der Gd(III) Komplexe genutzt, werden. Dieses Superpositionsmodell wiederum könnte nützlich sein, um neue Gd(III) Spinsonden zu entwickeln ohne die Komplexe vorher synthetisieren zu müssen.

Die momentan am häufigsten verwendete Methode zur Bestimmung von Abstandsverteilungen zwischen Spinpaaren ist das Doppel-Elektron-Elektron-Resonanz (DEER)-Experiment in Kombination mit Nitroxidradikalen als Spinsonden. Die Zuverlässigkeit dieser Methode und der

resultierenden Abstandsverteilungen kann durch orientierungs-abhängige Effekte in orthogonalen Spinpaaren, in denen ein Nitroxidradikal durch ein Metall mit deutlich breiterem EPR-Spektrum ersetzt wurde, kompensiert werden. In dem Fall, dass beide Spinsonden durch Metalle ersetzt werden wird die Modulationstiefe durch die breiten Spektren im konventionellen DEER-Experiment sehr klein, was folglich die Empfindlichkeit limitiert. Zudem kann die Überlappung von Energieniveaus in Hochspin-Paaren bei einer zu kleinen Resonanzverschiebung zwischen dem beobachteten und invertiertem Übergang zu einer Verzerrung der Abstandsverteilungen führen.

In einem gewissen Ausmass können diese Probleme mit dem Relaxations-Induziertem-Dipolare-Modulations-Erhöhung (RIDME) Experiment adressiert werden, wobei ohne technisch anspruchsvoll zu realisierende Spektrometer gearbeitet werden kann. Relaxations-induzierte Spinflips haben virtuell unendliche Bandbreite und Spins innerhalb des gesamten Spektrum können zum dipolaren Signal beitragen. Dadurch ist die durchschnittlichen Resonanzfrequenz der Spinpaare, die zur Modulation beitragen, viel grösser als die Dipol-Dipol Wechselwirkung, welches zur Reduktion der Verzerrung der Abstandsverteilungen führt. Zudem ist die Orientierungsabhängigkeit der Spininversion reduziert im Vergleich zu einer Spininversion, die durch einen Puls hervorgerufen wird, da dieser meist nur einen kleinen Bereich des Spektrums abdecken kann. Vor Beginn dieser Dissertation wurde bereits gezeigt, dass RIDME, gemessen bei hohen Feldern, das Potential hat, die Modulationstiefe und Auflösung der Abstandsverteilungen von Gd(III)-Gd(III) Spinpaaren zu erhöhen und die Technik konnte Informationen für Metalloproteine mit nativen, paramagnetischen Metallionen beitragen. Allerdings ist die Anwendung von RIDME für spinmarkierte Proteine auf Grund einiger Schwierigkeiten noch nicht weit verbreitet: (i) für Hochspin Systeme tragen Vielfache der dipolaren Frequenz zum Signal bei, (ii) die Technik ist sehr empfindlich auf Artefakte durch Kernfrequenz-Modulationen, (iii) es gibt keine einfache analytische Beschreibung des intermolekularen Hintergrundzerfalls und der Hintergrund zerfällt schneller als im DEER-Experiment. Dies führt zu Problemen bei der Separation des Hintergrunds von der intramolekularen Modulation, insbesondere für breite Abstandsverteilungen, und könnte somit den messbaren Abstandsbereich reduzieren.

Diesbezüglich wurde in dieser Doktorarbeit eine gründliche Studie einiger Aspekte, die die Datenanalyse betreffen durchgeführt. So wurden die Hintergrundkorrektur, Kernfrequenz-Modulationen und der Einfluss höherer harmonischer Obertöne, untersucht. Dazu wurde eine Methode, die auf einer modifizierten Kernelfunktion in der Tikhonov-Regularisierung beruht, eingeführt. Dieser Ansatz erlaubt es, die erwarteten Abstandsverteilungen zu erhalten, vorausgesetzt, dass die relativen Beiträge der harmonischen Obertöne bekannt sind. Für beide Metallionen, Mn(II) und Gd(III), wurde ein signifikanter Gewinn an Modulationstiefe bestätigt und die harmonischen Obertöne waren relativ stabil für Abstände > 3 nm, verschiedene Pulssequenzparameter sowie Messtemperaturen, Ligandenumgebungen und für spinmarkierte Proteinen im Vergleich zu Modellverbindungen. Durch Untersuchung simulierter Datensätze unter der Annahme zu grosser oder zu kleiner Beiträge der harmonischen Obertöne zu den Daten, konnte ermittelt werden, wie die Abstandsverteilung beeinflusst wird und dass eine Diskrepanz von etwa 20% im Rahmen der momentanen Unsicherheit, durch andere Faktoren bedingt, von Gd(III)-Gd(III) Abstandsmessungen in Biomolekülen ist. Abweichungen wurden für kürzere Spin-Spin Abstände, sowie gegenüber dem Maximum des Gd(III) Spektrums verschobene Detektionspositionen oder im niedrigen Feldbereich des Mn(II)-Spektrums beobachtet. Diese Abweichungen sollen in Folgestudien, die auf neuen - noch zu synthetisierenden - Modellsystemen beruhen sollen, untersucht werden.

Es wurde in früheren Arbeiten zu Gd(III)-Gd(III) DEER-Messungen gezeigt, dass Breitbandanregung über einen Bereich von 2.5 GHz Polarisation von den äußeren zu dem zentralen, beobachteten Übergang transferieren und dadurch die Empfindlichkeit der Messungen erhöhen kann. In dieser Doktorarbeit konnte gezeigt werden, dass ähnliche Strategien dazu verwendet werden können, um die Empfindlichkeit in Mn(II)-Mn(II) sowie Gd(III)-Gd(III) RIDME-Messungen zu erhöhen. Zusätzlich könnten solche Polarisierungssequenzen dazu genutzt werden, um Störsignale zu reduzieren, indem selektiv nur Echoamplituden die durch alle Pulse der RIDME Sequenz erzeugt werden, verstärkt werden.

Zudem wurde ein neuer Ansatz zur Unterdrückung von Kernfrequenz-Modulationen in RIDME eingeführt. Dieser Ansatz vermeidet eine Reduzierung des Signal-zu-Rausch-Verhältnisses, welches in den vorherig etablierten Methoden auftritt. Interessante Tendenzen konnten in experimentellen Daten zum Hintergrundzerfall in RIDME beobachtet werden, die mit analytischen Näherungsformeln übereinstimmen. Die Gleichungen wurden, einem Ansatz von Hu und Hartman folgend, berechnet unter Annahme von spontanen Spinflips der nicht-resonanten Spins. Der beobachtete, protonengetriebene spektrale Diffusionsprozess in RIDME-Hintergrundmessungen könnte erlauben, neue RIDME-basierte Experimente zu entwickeln, die eine Charakterisierung von weicher Materie und von Biomolekülen durch die Bestimmung lokaler Protonenverteilungen in der Nähe der Spinsonde, ermöglichen.

Ein Vergleich von Breitband-DEER und RIDME-Messungen an molekularen Cu(II) Stäbchen zeigte, dass beide Techniken abhängig von der Spektrometerausstattung ähnlich gute Ergebnisse liefern. Für beide Methoden wurde eine erhöhte Modulationstiefe und dadurch höhere Sensitivität im Vergleich zu einem konventionellen DEER-Experiment festgestellt. Insbesondere reduziert die RIDME-Technik Orientierungsabhängigkeiten und erscheint vorteilhaft in Situationen wo nur wenig Leistung über eine grosse Bandbreite zur Verfügung steht. Solche Bedingungen werden momentan vor allem noch bei hohen Feldern vorgefunden, bei denen Kernfrequenz-Modulationen vorteilhafterweise unterdrückt sind.

Schließlich konnte noch gezeigt werden, dass eine paramagnetische Metallsubstitution von Mg(II) zu Mn(II) eine gut geeignete Methodik ist, um die Bindung des Metalls an Nukleotid-Bindungsdomänen von ATP-angetriebenen Proteinen zu verfolgen sowie geometrische Strukturen durch die Messung von Spin-Spin Abständen zu untersuchen. Es wurde gezeigt, wie solche Daten mit paramagnetischer NMR kombiniert werden können, um tiefere Einblicke in die Struktur zu erhalten.

Acknowledgement

'If I have seen further it is by standing on the shoulders of Giants.'

Isaac Newton *

A lot of people have supported, stimulated and motivated me during my PhD. I would like to thank everyone who has made this thesis possible.

First, I would like to thank Gunnar Jeschke for the opportunity to discover the fascinating world of pulse EPR in his group. Many thanks for your continuous support and valuable advice. Your always open door and mind ensured a wonderful atmosphere in the group that provided the basis for an enjoyable and productive scientific life.

Likewise, I want to thank my direct supervisor Maxim Yulikov who introduced me to the RIDME experiment and supported me during the realization of this thesis. Thank you for always having an open-door for answering my questions, the many fruitful discussion, valuable comments and sharing your expertise.

I am grateful to Matthias Ernst for accepting to be my co-examiner. Thank you very much for working through all the pages of this thesis.

The work presented in this thesis would not have been possible without my numerous collaborators. I'm much obliged to Adelheid Godt and her group, in particular Mian Qi, Henrik Hintz, Julia Wegner, Vanessa Koch, Tobias Zwafing, Xuemei Yao and Miriam Hülsman who provided all the model compounds that build the basis for the method development presented here. Thank you very much for all your work and contributions.

Thank you Anton Savitsky, Anna Nalepa and Micheal Zalebera for welcoming me in Mühlheim, where I could make my first RIDME measurements and all your contributions to our joint projects. I appreciate the collaboration with Jessica A. Clayton, Songi Han and Mark Sherwin from University of Santa Barabra. Thank you for the fruitful discussions and your contributions to our joint project.

I am also very grateful for the fascinating project on paramagnetic metal ion substitution in ATP-fuelled proteins. Thank you Thomas Wiegand for bringing this project in our group, Riccardo Cadalbert and Denis Lacabanne for preparing all the samples and all of you as well as Anja Böckmann, Beat Meier, Laurent Terradot and Lauriane Lecoq for valuable comments and discussions.

*Letter to Robert Hooke (5 Feb 1675-6). In H. W. Turnbull (ed.), *The Correspondence of Isaac Newton*, 1, 1661-1675 (1959), Vol. 1, 416.

Thank you Inés García Rubio for welcoming me in Zaragoza, where I could make the experience to introduce somebody else to the RIDME techniques and explore the Spanish live.

A big thank you to all current and former members of the Jeschke group, be it for valuable comments, inspiring discussions, awesome group activities from jumping down canyons to pleasant after-work drinks ('Noch Eins zur Sicherheit') and most importantly the enjoyable and collaborative working atmosphere as well as friendship. It was a pleasure to work with you.

In particular, I want to mention the projects of internal collaboration: Thank you Daniel Klose for introducing me to the world of DFT, Yevhen Polyhach for all your contributions to unravel exchange couplings in PDS data, Christoph Gmeiner for providing me with the spin-labelled proteins samples.

Irina Ritsch for being my partner in crime when it comes to making RIDME measurements more reliable as well as Frauke Breitgoff when it comes to figuring out how to best measure Cu–Cu distances.

Thank you Valerie Mertens for your great contributions during your Bachelor's thesis.

Thank you Frauke Breitgoff and Andrin Doll for introducing me to the world of AWGs and shaped pulses.

I also want to thank all my fellow office mates for the great atmosphere in F238 as well as many useful chats from Matlab scripting to 'how to best run a marathon – JustRunIt': Anton Ashuiev, Andrin Doll, Christoph Gmeiner, Luis Fábregas Ibáñez, Vidmantas Kalendra and Janne Soetbeer.

A big shout-out to Kristina Comiotto for your help with all thinkable administrative concerns as well as René Tschaggelar and Oliver Oberhänsli for all your technical support. All of you always have an open door for all kinds of questions and make our lives as PhD students so much easier.

I would like to thank Claudia Hilty, Veronika Sieger and Christine Siegrist our administrative ladies as well as all members of the electronic, mechanical and chemistry workshops for being the best and most friendly staff an institute could wish for.

I would like to thank all 'magnetic memories' for sharing your expertise in the other resonance method, delicious lunch-break BBQs and fun events. In particular, Fabi and Schnozl - also for the latex template used in this thesis. Thank you Jasmine for motivating me to run across Käferberg and all your encouragement. Thank you to CP, David, Jojo, Lukas, Sebi and Erik for answering my chemistry questions and being such a great group during our studies. With some of you from the first day at ETH onwards.

No less, I want to thank all my friends - nearby and far - for your support and company during my life. I think of many great times and activities not only in the places we lived together - Starnberg, Zurich, Sydney, Hamburg, Oxford - but also on weekend trips or longer travels abroad. I also think of the many committees and groups I had the chance to be involved in – from VCS, VAC, Challenge, EquipSent to Student Riding. I am extremely grateful for your friendship and the unforgettable times we have spent together and am looking forward to the ones to come.

An extraordinary 'Thank you' goes to my family: my parents Jutta and Karl as well as my brother Martin for providing me with 'roots and wings'. You have been a constant source of love, advice, encouragement and strength during all of these years.

And last, but not least, thank you Jannick for your love and being my partner in life. You always supported, encouraged and listened to me, whenever I needed it. I'm very grateful for the time we spend together and I'm excited for the adventures to come.

Contents

Abstract	v
Zusammenfassung	ix
Acknowledgement	xiii
Abbreviations & Symbols	xxiii
1. Introduction	1
2. Theory	5
2.1. Spin Hamiltonian	5
2.1.1. Electron Zeeman Interaction	6
2.1.2. Nuclear Zeeman Interaction	7
2.1.3. Hyperfine Interaction	7
2.1.4. Nuclear Quadrupole Interaction	9
2.1.5. Zero-Field Splitting	9
2.1.6. Weakly Coupled Spins	10
2.2. Spin dynamics	12
2.3. Relaxation	13
2.4. EPR methods	15
2.4.1. Continuous Wave EPR	16
2.4.2. Pulsed EPR techniques	16
2.5. Pulse Sequences	17
2.5.1. Echo-detected EPR	17
2.5.2. Two-pulse ESEEM	18
2.5.3. Three-pulse ESEEM experiment	19
2.5.4. Inversion recovery	19
2.5.5. Distance measurements	20
3. Metal Complexes for Pulsed Dipolar Spectroscopy	23
3.1. Introduction	24
3.2. Experimental	26
3.3. Cu(II)-complexes	27
3.4. Co(II)- and Fe(III)-complexes	29
3.5. Mn(II)- and Gd(III)-complexes	31
3.6. Comparison of different complexes for pulsed dipolar spectroscopy	35

3.7. Conclusions	38
4. Quantitative analysis of zero-field splitting parameter distributions in Gd(III) complexes	41
4.1. Introduction	42
4.2. Theoretical background	44
4.2.1. Model 1 (<i>Benmelouka et al.</i>)	46
4.2.2. Models 2 and 3 (<i>Raitsimring et al.</i>)	47
4.3. Experimental and computational details	48
4.3.1. Synthesis of the Gd(III) complexes	48
4.3.2. Sample preparation	48
4.3.3. Q-, W- and G-band EPR measurements	49
4.3.4. Numerical simulations	50
4.4. Results and analysis	51
4.4.1. Model 1	52
4.4.2. Models 2 and 3	54
4.5. Superposition model for the ZFS tensor of Gd(III) complexes	62
4.5.1. Gd complex geometries for the superposition model	64
4.5.2. Mean ZFS parameters with fixed donor atom position (Model A)	64
4.5.3. Distribution of ZFS parameters from the superposition model (Model B)	65
4.5.4. Predictions	68
4.6. Discussion	70
4.7. Conclusions	72
5. Intermolecular background decay in RIDME experiments	75
5.1. Introduction	76
5.2. Theoretical Background	77
5.3. Experimental and analysis details	84
5.3.1. Sample preparation	84
5.3.2. EPR measurements	85
5.3.3. Data analysis	85
5.4. Results and Discussion	86
5.4.1. Transverse and longitudinal relaxation in Gd-PyMTA	86
5.4.2. Stimulated echo decays of Gd-PyMTA	88
5.4.3. Intermolecular background decay in refocused RIDME experiments with Gd-PyMTA	88
5.4.4. RIDME background decays of a Gd(III) spin-labelled protein sample	94
5.4.5. General discussion	96
5.5. Conclusions	99
6. Electron Spin Echo Envelope Modulation in RIDME experiments	101
6.1. Introduction	102
6.2. Averaging of ESEEM contributions	102
6.3. Presence of strong ESEEM oscillations	107
6.4. Conclusions	110

7. Distance measurements in Cu(II)-Cu(II) spin pairs	111
7.1. Introduction	111
7.2. Experimental	116
7.2.1. Sample preparation	116
7.2.2. EPR measurements	116
7.2.3. Data analysis	118
7.3. Results and Discussion	118
7.3.1. Characterization of Cu-PyMTA for dipolar spectroscopy	118
7.3.2. Shaped pulses	120
7.3.3. DEER experiments with wideband pulses	123
7.3.4. RIDME experiments	129
7.3.5. Orientation selection in DEER and RIDME	133
7.3.6. Advantages and disadvantages of DEER and RIDME	136
7.4. Conclusions	138
8. Computing Distance Distributions from Dipolar Evolution Data with Overtones: RIDME Spectroscopy with Gd(III)-Based Spin Labels	141
8.1. Introduction	142
8.2. Theoretical background	144
8.3. Experimental details	149
8.4. Results and discussion	151
8.4.1. Analysis of simulated RIDME data	151
8.4.2. Analysis of experimental RIDME data for a series of Gd rulers.	157
8.5. Conclusions	166
9. Towards high-spin RIDME in structural biology	169
9.1. Introduction	170
9.2. Experimental	171
9.3. Choice of experimental parameters	173
9.4. Sensitivity enhancement by pre-polarization	177
9.5. Calibration of overtone coefficients for Mn(II)	179
9.6. Stability of overtone coefficients	181
9.6.1. Nuclear spin bath	181
9.6.2. Ligand field	182
9.7. RIDME on proteins	191
9.8. Conclusions	193
10. EPR Spectroscopy of Mn²⁺-Substituted ATP-Fuelled Protein Engines	197
10.1. Introduction	197
10.2. Monitoring metal binding	198
10.3. Information on geometric assemblies	200
10.4. Conclusions	203
11. Conclusions & Outlook	205
Bibliography	209

A. Supplementary Information to Chapter 4	233
A.1. Characterization of ZFS tensor eigenvalue distributions by anisotropy and axiallyity	233
A.2. Q-band EDEPR spectra of R-(Gd-PyMTA) (4ab)	234
A.3. Further details of the numerical simulations	234
A.3.1. Orientation averaging	234
A.3.2. Range and number of magnetic field points	235
A.3.3. Regular grid vs. Monte Carlo sampling of the ZFS parameter distributions	235
A.3.4. Line broadening	239
A.3.5. Flip angle correction for Q-/W-band simulations	240
A.4. Parameters used for simulations with Model 1	241
A.5. Simulation parameters used for generation of rmsd error maps for Models 2 and 3	241
A.6. Procedure for determining best-fit ZFS parameter values and associated error bars from rmsd error maps (Models 2 and 3)	242
A.7. Parameters used for final simulations with best fit ZFS parameter values	244
A.8. Model 1 - additional results	244
A.9. Model 2 - additional results with central peak excluded from analysis	246
A.10. Model 3 - rmsd error maps with central peak excluded from analysis	249
A.11. Model 3 - $P(+D)/P(-D)$ parameter error estimation	250
A.12. Models 2 and 3 - fit results using the full EPR spectra	251
A.13. Models 2 and 3 - minimum rmsd errors of the D and σ_D parameter contour plots	251
A.14. Influence of D and σ_D on the EPR line shape and Model 3 fits obtained by visual inspection	257
A.15. Comparison of $P(D)$ and $P(D/E)$ distributions for Models 1 and 3	261
A.16. Calculated absolute ZFS magnitude and ZFS axiallyity for Model 1 and 3	262
B. Supplementary Information to Chapter 5	263
B.1. Synthesis of Cu-PyMTA	263
B.2. Examples of the fitting procedure	263
B.3. Influence of the detection position in RIDME background decays	265
B.4. Additional Figures to Section 5.4.3	265
B.5. Background decay in Cu-/Mn-PyMTA complexes	266
B.6. Background decay in spin-labelled protein mutant RRM34 Q388C	268
B.7. Relation of relaxation times to trace settings	269
C. Supplementary Information to Chapter 6	271
C.1. Averaging of the mixing block T_{mix}	271
C.2. Analytical calculations for a $S = 1/2$ and $I = 1/2$ spin system	271
C.3. Experimental settings	282
C.4. Three-pulse ESEEM measurements for Mn-PyMTA and Mn-DOTA	283
C.5. Interference of nuclear and dipolar frequencies	284
C.6. Extraction of harmonic overtones in the presence of ESEEM contributions	284
D. Supplementary Information to Chapter 7	287
D.1. Lineshape analysis of Cu-PyMTA	287
D.2. Longitudinal relaxation across the Cu-PyMTA ruler spectrum	288
D.3. Influence of pulse parameters on RIDME data	288

D.4. Additional analysis with respect to orientation selection	288
D.5. Sensitivity in RIDME and DEER experiments	292
D.6. Echoes from shaped pulses for the Cu-PyMTA mono-complex	294
D.7. Pulse optimization for echoes from shaped pulses of different shapes	294
D.8. DEER experiments with the observer pulses positioned at the maximum of the Cu(II) spectrum	295
D.8.1. Primary DEER data for experiments with shaped pump pulse	296
D.8.2. Pulse setups for DEER experiments	296
E. Supplementary Information to Chapter 8	299
E.1. Overtone Analysis	299
E.2. Experimental set-up and measurement conditions	302
E.3. Extraction of overtone coefficients for broad distance distributions	303
E.4. Filtering the artefact due to echo-crossing for long distances	305
E.5. Extraction of distance distributions for short distances (Gd-ruler $\mathbf{1}_1$)	306
E.6. Calibration of overtone coefficients for a series of Gd-rulers	310
F. Supplementary Information to Chapter 9	319
F.1. Simulated distance distributions and protein sequence	319
F.2. Relaxation measurements for Mn-based rulers	320
F.3. Optimization of pre-polarization pulses	321
F.4. Calibration of overtone coefficients for Mn(II)	322
F.4.1. Field dependence in Mn-PyMTA based RIDME measurements	327
F.5. RIDME in protonated solvent	328
F.6. Influence of ligand field	332
F.6.1. PymiMTA-based rulers	332
F.6.2. DOTA based rulers	335
F.6.3. TAHA-ruler	342
F.7. RIDME on proteins	344
F.8. Two-point optimization curves	346
G. Supplementary Information to Chapter 10	353
G.1. Materials and Methods	353
G.1.1. Samples for CW-EPR	353
G.1.2. Samples for pulsed EPR experiments	354
G.1.3. Experimental details	355
G.2. Detailed description of determination of the fraction of bound Mn^{2+} by EPR relaxation measurements	358
G.3. Additional discussion of the DEER distance measurements	358
Publications and Conference contributions	365
Curriculum Vitae	367

Abbreviations & Symbols

List of Abbreviations

ADP	Adenosine DiPhosphate
AMP-PNP	Adenylyl-imidodiphosphate
ATP	Adenosine TriPhosphate
AWG	Arbitrary Waveform Generator
CFI	Crystal Field Interaction
CIDME	Chirp-Induced Dipolar Modulation Enhancement
CW	Continuous wave
DEER	Double Electron-Electron Resonance
DFT	Density Functional Theory
DNP	Dynamic Nuclear Polarization
DQC	Double Quantum Coherence
ED	Echo Detected
ENDOR	Electron Nuclear DOuble Resonance
EPR	Electron Paramagnetic Resonance
ESD	Electron-Electron Spectral Diffusion
ESEEM	Electron Spin Echo Envelope Modulation
EZ	Electron Zeeman
FID	Free Induction Decay
FT	Fourier transform
FWHM	Full Width at Half Maximum
HF	HyperFine Interaction
HS	Hyperbolic Secant
NBD	Nucleotide-Binding Domain
NMR	Nuclear Magnetic Resonance
NOE	Nuclear Overhauser Effect
NQ	Nuclear Quadrupole Interaction
NSD	Nuclear-Electron Spectral Diffusion
mw	microwave
PDS	Pulsed Dipolar Spectroscopy
PE	Primary Echo
PTB	Polypyrimidine Tract-Binding protein

PRE	Paramagnetic Relaxation Enhancement
RBD	RNA Binding Domain
rf	radio frequency
RIDME	Relaxation-Induced Dipolar Modulation Enhancement
rmsd	root mean square deviation
RRM	RNA Recognition Motif
RSE	Refocussed Stimulated Echo
RVE	Refocussed Virtual Echo
SDSL	Site-Directed Spin Labelling
SIFTER	Single-Frequency TEchnique for Refocusing
SNR	Signal-to-Noise Ratio
SQ	Single Quantum
UWB	Ultra-WideBand
ZFS	Zero-Field Splitting

List of Symbols

A_k	hyperfine tensor
A	secular hyperfine coupling constant
a_{iso}	isotropic hyperfine coupling
\vec{B}_0	static magnetic field vector
B_0	static magnetic field
\vec{B}_1	mw field vector
B_1	mw field
B	pseudo-secular hyperfine coupling constant
B_i	specified field position i
B_{max}	field position of highest intensity in the EPR spectrum
$B(t)$	intermolecular background function
D	zero-field splitting tensor
D	dipole-dipole coupling tensor
D	axial second-order zero-field splitting parameter
d	distance
d	background dimensionality (stretching exponent)
d_i	interpulse delay i
d_k	single-atom zero-field splitting contributions
d_0	zero-time of pulsed dipolar spectroscopy time traces
e	elementary charge
E	rhombic second-order ZFS parameter
E_i	energy level i
E_k	ensemble of spin pairs k
$E(f)$	Inversion efficiency
f_0	centre of resonator mode
$F(t)$	background-corrected form factor in time domain
$F(\nu)$	background-corrected form factor in time frequency domain (dipolar spectrum)
g	g -tensor
g_e	g factor of the free electron
g_n	nuclear g factor
g_{eff}	effective g factor
\hat{H}	spin Hamiltonian operator
h	Planck constant
\hbar	reduced Planck constant: $h/2\pi$
\hat{H}_0	static spin Hamiltonian operator
\hat{H}_{dd}	dipole-dipole interaction Hamiltonian operator
\hat{H}_{ex}	exchange coupling Hamiltonian operator
\hat{H}_{EZ}	electron Zeeman Hamiltonian operator

\hat{H}_{HF}	hyperfine interaction Hamiltonian operator
\hat{H}_{NZ}	nuclear Zeeman Hamiltonian operator
\hat{H}_{NQ}	nuclear quadruple interaction Hamiltonian operator
\hat{H}_{ZFS}	zero-field splitting Hamiltonian operator
I	nuclear spin quantum number
\hat{I}_k	nuclear spin operator
$I(f)$	spectral intensity
J	exchange coupling constant
J	spin quantum number (total angular momentum)
k	ESEEM modulation depth parameter
k	characteristic decay rate
k_{B}	Boltzmann constant
K_d	equilibrium dissociation constant
$K(t, r)$	kernel function
$K_{\text{mod}}(t, r)$	modified kernel function to account for higher frequency overtones
L	orbital angular momentum quantum number
M_o	monochromatic observer pulse
M_p	monochromatic pump pulse
M	macroscopic magnetization
M_{eq}	equilibrium magnetization
M_{xy}	transverse magnetization components
M_z	longitudinal magnetization components
m_I	nuclear spin magnetic quantum number
m_S	electron spin magnetic quantum number
n_{H}	Hilbert space dimension
$n_{1,\text{M}}$	noise level on normalized time-domain traces
$n_{1,\text{FT}}$	noise level on normalized frequency-domain traces
\hat{O}_k^q	Hermitian operators
\mathbf{P}	nuclear quadruple tensor
p_m	probability of odd number of spin flips
P_1	fraction of primary dipolar frequency ω_{dd}
P_2	fraction of first harmonic overtone frequency $2\omega_{\text{dd}}$
P_3	fraction of second harmonic overtone frequency $3\omega_{\text{dd}}$
$P_{1,\text{sim}}$	simulated fraction of primary dipolar frequency ω_{dd}
$P_{2,\text{sim}}$	simulated fraction of first harmonic overtone frequency $2\omega_{\text{dd}}$
$P_{3,\text{sim}}$	simulated fraction of second harmonic overtone frequency $3\omega_{\text{dd}}$
$P(D)$	distribution of second-order ZFS parameter D
$P(E)$	distribution of second-order ZFS parameter E
$P_{\text{B}}(k)$	probability of Poisson distribution
$P(r)$	distance distribution

$p(r)$	distance distribution, Chapter 8
$p_{\text{id}}(r)$	true distance distribution, Chapter 8
$p_{\text{app}}(r)$	apparent distance distribution, Chapter 8
q	particle charge
q_m	probability of even number of spin flips
Q_{crit}	critical adiabaticity
Q	quality factor of resonator
\vec{r}	inter-spin distance
\hat{S}	electron spin operator
S	electron spin quantum number
S'	effective electron spin quantum number
\hat{S}^+, \hat{S}^-	ladder operators, raising and lowering operator
S_o	shaped observer pulse
S_p	shaped pump pulse
$S(t)$	detected primary pulsed dipolar spectroscopy data
t	time
t_p	pulse length
t_{inv}	inversion pulse length
T_1	longitudinal relaxation time
$T_{1,e}$	longitudinal relaxation time of electron spin
T_2	transverse relaxation time
T_m	phase memory time
$T_{m,e}$	phase memory time of electron spin
$T_{m,\text{outer}}$	phase memory time of satellite transitions
T_{mix}	mixing time
T	Temperature
T	first interpulse delay in inversion recovery sequence
T_{dd}	dipolar oscillation period, Chapter 7
T_k	anisotropic part of hyperfine tensor
W	flip rate, Chapter 5
Z	systems partition function
α	flip angle
α	spin state $ m_s = +1/2\rangle$
α, β, γ	Euler angles
β	spin state $ m_s = -1/2\rangle$
$\hat{\Gamma}$	relaxation superoperator
Δ	unsigned anisotropy for ZFS parameters
δ	deviation from simulated fraction
Δf_{res}	resonator bandwidth
Δf_{obs}	bandwidth of observer pulses

Δf_{pump}	bandwidth of pump pulses
Δf	bandwidth of pulses
Δm_S	change of electron spin magnetic quantum number
Δm_I	change of nuclear spin magnetic quantum number
η	sensitivity estimate
η	asymmetry parameter of nuclear quadrupole interaction
θ	angle between the static magnetic field and the spin-spin vector
θ	polar angle
$\vec{\mu}$	magnetic moment
μ_0	permeability of vacuum
μ_B	Bohr magneton
μ_n	nuclear magneton
λ	modulation depth
λ	event rate in Poisson distribution
ν	frequency $\omega/2\pi$
ν_{mw}	microwave frequency
ν_{obs}	observer frequency
ν_{pump}	pump frequency
$\nu_1(f)$	resonator profile
ν_1	nutation frequency of microwave pulse
ξ	axiality for ZFS parameters
$\xi(\theta)$	geometry factor
σ_D	width of Gaussian distribution of axial second-order ZFS parameter D
σ_E	width of Gaussian distribution of rhombic second-order ZFS parameter E
$\hat{\sigma}$	spin density operator
$\hat{\sigma}_0$	initial spin density operator
$\hat{\sigma}_{\text{eq}}$	spin density operator at thermal equilibrium
τ	free evolution period
τ	scaling factor
τ_c	rotational correlation time
ϕ_{BS}	Bloch-Siegert phase shift
ϕ	phase angle
ϕ	azimuth angle
ψ_i	eigenfunction in the given Hilbert space
ω_0	transition frequency
ω_α	nuclear angular frequency in electron spin manifold α
ω_β	nuclear angular frequency in electron spin manifold β
ω_{dd}	dipole-dipole coupling between two electron spins (dipolar frequency)
ω_I	nuclear Larmor frequency
ω_{mw}	microwave angular frequency

ω_S	electron Larmor frequency
ω_+, ω_-	sum and difference of the signed nuclear angular frequencies in the α and β manifold of the electron spin
Ω_S	resonance offset $\omega_S - \omega_{mw}$
$\mathbb{1}$	unit matrix
<i>A spin</i>	observed spin in A–B spin pair
<i>B spin</i>	non-resonant spin in A–B spin pair
<i>chirp</i>	linear frequency-swept pulse
<i>shaped pulse</i>	amplitude-modulated frequency-swept pulse

Introduction

Electron Paramagnetic Resonance (EPR) is based on the study of unpaired electrons. It is a sensitive spectroscopic method to extract information on the geometric and electronic structure, the dynamics and the spatial distribution of paramagnetic species. However, electron pairing is usually energetically favourable and thus only a small fraction of known chemical or biochemical compounds contains native paramagnetic centres or can be put in paramagnetic states to exhibit an intrinsic EPR signal.¹ Examples are studies of chemical reactivity in transition metal catalysis,²⁻⁴ electron transfer reactions,^{5;6} metalloproteins⁷⁻¹¹ or defects in solid-state materials as in semiconductors¹² or polymers.¹³⁻¹⁵ On the other hand, chemically stable paramagnetic species can be attached to sites of interest by so called site-directed spin labeling (SDSL) under a wide range of conditions¹⁶⁻¹⁸ and such sites can be accessed subsequently. The magnetic moment for electrons is much larger than for nuclei, inducing a larger Boltzmann spin polarization. Thus, as compared to nuclear magnetic resonance (NMR), in EPR spectroscopy the detected photons have larger energies and stem from a larger fraction of unpaired spins at a given magnetic field and sample temperature. In favourable cases, in continuous wave experiments, EPR is able to detect about 10^{10} spins or concentrations down to 10 nM in aqueous solution, while the best pulse EPR spectrometers can detect spin concentrations down to the micromolar range and a total number of spins in the subnanomole range ($\approx 10^{12} - 10^{13}$ spins). EPR studies can address the properties of electronic configuration for a single unpaired electron or a configuration of several unpaired electrons within one paramagnetic centre or cluster of a few strongly coupled spin centres. In this case, the information on the electronic configuration can be obtained by determining the parameters of the electron Zeeman (EZ) interaction, namely the g -tensor, and the zero-field splitting (ZFS) interaction. Electron-nuclear interactions are another source of information on the intrinsic electronic and geometric structure and on the local surrounding of the paramagnetic species. In this type of EPR investigations, the electron-nuclear hyperfine interactions, nuclear Zeeman and nuclear quadrupole interactions are analysed. As most of the above interactions are anisotropic, the detection of their time average, e.g. in solution, can also provide direct information about the dynamics of the paramagnetic centres under study.^{10;19} Weak magnetic dipole-dipole interactions can be studied in pairs of paramagnetic centres and allow for extraction of intramolecular distance distributions, for instance, in biomacromolecules. Herein, EPR is particularly valuable to access such distance distributions in systems without long-range order, i.e. cannot be crystallized, irrespective of the size of the system. The obtained restraints in the nanometre range can be combined with measures from complementary techniques to generate hybrid structural models.

At present, the most reliable way of extracting distances using EPR is the combination of SDSL utilizing nitroxide-based spin labels with the so-called Double Electron-Electron Resonance (DEER), also referred to as Pulsed Electron-Electron Double Resonance (PELDOR), experiment.^{16–18;20–23} Nitroxides are well suited, as they are relatively small, sterically not demanding molecules with rather short linkers and the labelling chemistry is well established. Furthermore, nitroxides are sensitive to environmental parameters, such as molecular motion on time scales between 10 ps and 1 ms, polarity, proticity, water or oxygen accessibility. Examples are the identification of secondary structure elements through nitroxide side chain mobility together with its solvent-accessibility or the detection of conformational changes in the range of μs -ms by time resolved EPR.^{16–18} Their EPR line shapes are relatively narrow, so that conventional microwave pulses can excite a sizeable fraction of all spins. The work presented in this thesis investigates several aspects of such distance measurements in combination with paramagnetic metal tags instead of nitroxides. Note that several interactions usually exceed the excitation bandwidth of the strongest microwave pulses in EPR experiments and one often lacks the ability to excite the full spectrum, especially for paramagnetic metal centres.

Hence, why should we bother about using metal centres as spin probes, which typically exhibit much broader EPR spectra, are moreover relatively large and bulky and are for the currently designed experiments less sensitive to their environment? There exist several answers to this question. First, some metal centres are chemically more stable than nitroxides and thus EPR experiments can be performed under reducing conditions, e.g. in in-cell experiments.^{24;25} Second, a valuable strategy in EPR, orthogonal spin-labelling, is based on using at least two different types of spins, which allows for spectroscopic selection of individual distances in multi-spin systems.^{26–28} Third, intrinsically occurring metal centres in materials or metalloproteins, as well as the possibility of substituting diamagnetic metal ions by paramagnetic ones, motivate the development of EPR techniques. A highly interesting example for a wide variety of systems is the substitution of Mg^{2+} by Mn^{2+} , since ATP: Mg^{2+} binding and hydrolysis, as used in ATP-fuelled motors, is a very widespread mechanism in living systems. As a consequence of all these considerations, the choice of spin probe depends on the problem at hand. Thus, this thesis aims towards extending the arsenal of paramagnetic metal-based spin probes and related EPR experiments with increased sensitivity at low hardware requirements.

To this end, - after Chapter 2 has introduced the theory and experimental schemes of the presented EPR studies - Chapter 3 describes the characterization of a series of chelator moieties and the transition metal centres: iron, cobalt, copper, manganese as well as the lanthanide ion gadolinium with respect to their potential use as spin tags in pulsed dipolar spectroscopy. In particular the focus is on low-spin Cu(II) and the high-spin Kramers ions Gd(III) and Mn(II). For all three metal centres, pulsed EPR experiments can be performed in glassy frozen solutions at temperatures up to at least 30 K. Copper is increasingly used as spin label^{29–31} and plays a variety of roles in nature.^{32–37} It has a $3d^9$ electron configuration with $S = 1/2$ and thus doublet ground state. The anisotropy of the g - and A -tensor spreads the EPR spectrum over several hundreds of Gauss, further broadening at higher fields. The electron group spin of the Kramers ions and half-filled f and d shells, respectively, results in a weak contribution of the orbital momentum to the total momentum causing a weak ZFS. The half-integer spin systems have a narrow central $m_s = -1/2 \leftrightarrow m_s = 1/2$ transition and are very convenient for high-field/high-frequency applications, since this central transition narrows with increasing magnetic field strength.²⁸ Additionally, because the half-filled d or f shell leads to an isotropic g -value

and isotropic metal hyperfine couplings, longitudinal and transverse magnetic relaxation of the metal ions Gd(III) and Mn(II) are slow compared to many other high-spin paramagnetic metal centres. The high-spin metal ions are strongly influenced by the zero-field splitting interaction (ZFS), which lifts the degeneracy between spin states even in the absence of a magnetic field. Thus, Chapter 4 focusses on the description and reliability of the extraction of ZFS parameters for a set of six Gd³⁺ complexes.

After having analysed intrinsic properties of the paramagnetic chelates, the following chapters focus on PDS experiments involving spin probes with broad EPR spectra. A promising experiment with virtual infinite bandwidth for spin inversion is the Relaxation-Induced Dipolar Modulation Enhancement (RIDME) experiment. Chapters 5 and 6 describe two important aspects of the RIDME sequence that hinder widespread application of the technique to spin-labelled biomolecules: the intermolecular background decay and nuclear modulation contributions, respectively. Chapter 7 presents the work resulting from a joint project with Frauke Breitgoff, in which the capabilities of the RIDME and DEER experiment were explored for a low-spin Cu(II) molecular ruler. The chapter concludes with a comparison of the two techniques. Chapters 8 and 9 then focus on methodological aspects of applying the RIDME technique to the high-spin Kramers ions Mn(II) and Gd(III). First, in Chapter 8, the extraction of distance distributions in the presence of harmonic overtones is presented for the case of molecular Gd(III) rulers. It is followed by a discussion of the choice of experimental conditions, sensitivity enhancement by pre-polarization schemes and stability of the harmonic overtones with type of metal centre, spin bath and metal environment in Chapter 9. The chapter concludes with the application of the RIDME technique to recombinant proteins. Finally, Chapter 10 demonstrates what insights can be obtained by the substitution of diamagnetic Mg(II) by paramagnetic Mn(II) in ATP-fuelled proteins using EPR spectroscopy. Last, Chapter 11 concludes the thesis.

Theory

The theoretical background of electron paramagnetic resonance (EPR) is well established and presented in several textbooks as for example Refs.^{19;38;39}. This chapter is reduced to the theoretical basis needed to describe the properties of the investigated metal spin systems and EPR experiments used within this thesis. This includes a description of the magnetic interactions by the spin Hamiltonian, their time evolution and basic aspects of relaxation. The last part of this chapter introduces experimental aspects of EPR and pulse sequences relevant to this thesis.

2.1. Spin Hamiltonian

The interactions between magnetic moments of electron and nuclear spins as well as an external magnetic field are described by the system's spin Hamiltonian. The energy levels of the spin system E_i can be obtained by solving the time-independent Schrödinger equation,

$$\hbar\hat{H}_0|\psi_i\rangle = E_i|\psi_i\rangle, \quad (2.1)$$

with the eigenfunctions ψ_i of the given Hilbert space. EPR can not directly access the magnitude of these energy levels. By applying microwave (mw) and radio frequency (rf) radiation, EPR experiments probe the transition energies ΔE between different levels.

In absence of mw or rf radiation the spin Hamiltonian \hat{H}_0 can contain the following terms

$$\hat{H}_0 = \hat{H}_{EZ} + \hat{H}_{NZ} + \hat{H}_{HF} + \hat{H}_{NQ} + \hat{H}_{ZFS} + \hat{H}_{ex} + \hat{H}_{dd}. \quad (2.2)$$

The electron (\hat{H}_{EZ}) and nuclear (\hat{H}_{NZ}) Zeeman terms depend linearly on the external magnetic field. The hyperfine term \hat{H}_{HF} results from coupling between electron and nuclear spins. Electric field gradients in nuclear spins with $I > 1/2$ induce nuclear quadrupole interactions \hat{H}_{NQ} . Strong electron-electron couplings in spin systems with spin quantum number $S > 1/2$ induce a zero-field splitting (ZFS) \hat{H}_{ZFS} that lifts the $2S + 1$ fold degeneracy of the ground state. Weak couplings between electron and/or nuclear spins are observed as exchange \hat{H}_{ex} and dipole-dipole interaction \hat{H}_{dd} . Figure 2.1 illustrates typical strengths of the magnetic interactions and measurement bands relevant to this thesis.

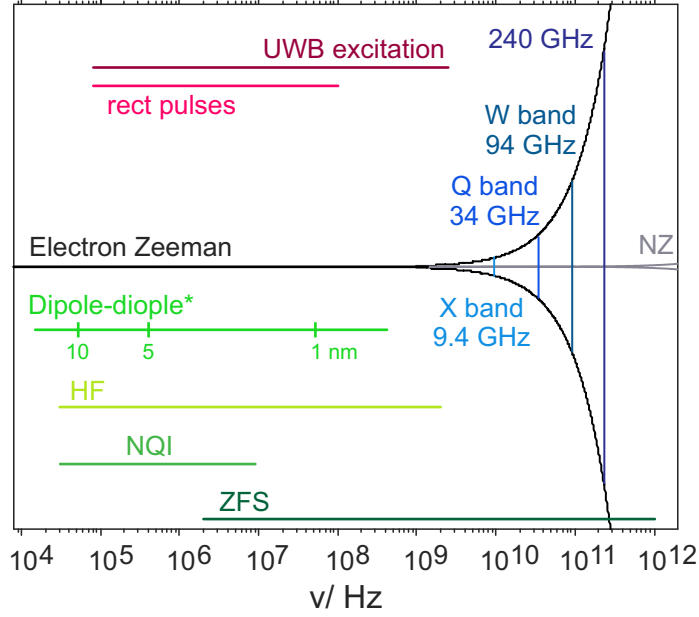


Figure 2.1. Typical magnitude of interactions and microwave frequency bands. The electron and proton nuclear Zeeman interaction are given in black and grey, respectively. *For weakly coupled electron spins. Adapted from Ref. ¹⁹.

2.1.1. Electron Zeeman Interaction

The electron Zeeman term results from the interaction of the electron spin with the external magnetic field. It is given as

$$\hat{H}_0 = \frac{\mu_B}{\hbar} \vec{B}_0^T \mathbf{g} \hat{S}, \quad (2.3)$$

where μ_B is the Bohr magneton ($\mu_B = 9.27400899(37)10^{-24} JT^{-1}$), \vec{B}_0^T the transpose of the external magnetic field vector, \mathbf{g} the g -tensor and \hat{S} the electron spin operator.

The g -tensor \mathbf{g} is characterized by six independent quantities, e.g. three principal values g_x , g_y , g_z and three Euler angles α , β , γ . The Euler angles describe the orientation of the principal axes in the molecular coordinate system (molecular frame). In cubic symmetry $g_x = g_y = g_z$, for axial symmetry $g_x = g_y = g_{\perp}$ and $g_z = g_{\parallel}$ and for orthorhombic symmetry $g_x \neq g_y \neq g_z$. Molecular tumbling in solution leads to the observation of an average value $g_{iso} = \frac{1}{3}(g_x + g_y + g_z)$.

The anisotropy of the g -tensor leads to an effective g -value g_{eff} at a given orientation (azimuthal angle ϕ , polar angle θ) of the magnetic field ($\vec{B}_0 = B_0[\sin(\theta) \cos(\phi), \sin(\theta) \sin(\phi), \cos(\theta)]$) with the principal axes system (PAS)

$$g_{\text{eff}} = \sqrt{g_x^2 \sin^2 \theta \cos^2 \phi + g_y^2 \sin^2 \theta \sin^2 \phi + g_z^2 \cos^2 \theta}. \quad (2.4)$$

In the absence of spin-orbit coupling and for a quenched orbital angular momentum ($L = 0$), the g -tensor is a scalar with $g = g_e = 2.0023$ of the free electron.⁴⁰ The deviation of the principal g -values from g_e and the orientation-dependence of the electronic Zeeman term arises from admixed angular momenta due to interactions between the ground and excited states. They are usually treated by perturbation theory.¹⁹ In the LS-coupling regime, the resultant angular momentum is associated with the quantum number J with $J = L + S$ and the g -value,³⁸ sometimes called Landé factor

$$g_J = \frac{J(J+1)(g_L + g_S) + L(L+1) - S(S+1)(g_L - g_S)}{2J(J+1)} \quad (2.5)$$

which can be reduced to the Landé form for $g_L = 1$ and $g_S = 2$:

$$g_J = \frac{3}{2} - \frac{L(L+1) - S(S+1)}{2(J+1)} \quad (2.6)$$

Being related to spin-orbit coupling, the g -value shift with respect to g_e increases with the atomic number, so that heavier atoms such as transition metal ions or lanthanide ions may cover a wide range of g -values. The observed g -values further depend on the coordinated ligands and can be used to provide information on the symmetry of a paramagnetic centre.¹⁹

2.1.2. Nuclear Zeeman Interaction

The nuclear Zeeman interaction describes the coupling of the nuclear spin \hat{I} to the external field in analogy to the electron Zeeman term (Equation (2.3))

$$\hat{H}_0 = -\frac{\mu_n}{\hbar} \vec{B}_0^T g_n \hat{I} = \omega_I \hat{I}. \quad (2.7)$$

The term $\frac{\mu_n}{\hbar} \vec{B}_0^T g_n$ is defined as nuclear Larmor frequency ω_I , describing the angular precession frequency of the nuclear spin around the external magnetic field. g_n the nuclear g -value is an intrinsic properties of each nucleus. The nuclear Bohr magneton μ_n ($\mu_n = 5.05078317(20)10^{-27} JT^{-1}$) is three orders of magnitude smaller than the electron Bohr magneton. Consequently, the nuclear Zeeman interaction is about three orders of magnitude smaller than the electron Zeeman interaction as visualized in Figure 2.1. This gives rise to an m_I -dependent shift of the spin energy levels and based on the EPR selection rules ($\Delta m_s = \pm 1$, $\Delta m_I = 0$) does not contribute to the EPR transition frequencies in first order. The nuclear Zeeman interaction becomes relevant for calculations of EPR transition probabilities if its magnitude is comparable to the anisotropic hyperfine interaction.

2.1.3. Hyperfine Interaction

Coupling between electron and nuclear spins with $I \neq 0$ induces a hyperfine splitting of the energy levels independent of the strength of the external magnetic field. The Hamiltonian for the hyperfine interaction can be expressed as

$$\hat{H}_{HF} = \sum_k \hat{S}^T \mathbf{A}_k \hat{I}_k, \quad (2.8)$$

in which the index k runs over all nuclei with $I_k > 0$, and \mathbf{A}_k is the corresponding hyperfine tensor. The hyperfine tensor is composed of isotropic Fermi contact interaction as well as anisotropic through-space dipole-dipole coupling of the magnetic moments.

$$\mathbf{A}_k = a_{iso} \mathbb{1} + \frac{g\mathbf{T}_k}{g_e}, \quad (2.9)$$

The isotropic Fermi contact interaction results from the non-zero probability of finding the electron and nuclear spin in the same position:

$$a_{iso} = \frac{2}{3} \frac{\mu_0}{\hbar} g_e \mu_B g_N \mu_N |\psi_0(0)|^2. \quad (2.10)$$

The ground state electronic wave function $|\psi_0(0)|^2$ gives the probability of finding the electron at the position of the nucleus. Based on orbital symmetry, this probability is only non-zero for electrons in orbitals with s character. The non-spherical symmetry of electrons in p -, d - and f -orbitals, leads to a dipole-dipole coupling between the electron and the nuclear magnetic moments. This anisotropic hyperfine coupling \mathbf{T} depends on the distance r between the nucleus and the unpaired electron. The tensor elements T_{ij} are given by

$$T_{ij} = \frac{\mu_0}{4\pi\hbar} g_e \mu_B g_n \mu_N \langle \psi_0 | \frac{3r_i r_j - \delta_{ij} r^2}{r^5} | \psi_0 \rangle. \quad (2.11)$$

In the framework of the point-dipole approximation, expression (2.11) can be simplified to:

$$\mathbf{T}_{\mathbf{k}} = \frac{\mu_0}{4\pi\hbar} g_e \mu_B g_n \mu_N \sum_{j \neq \mathbf{k}} \rho_j \frac{3\vec{n}_j \vec{n}_j^T - \mathbb{1}}{R_j^3}, \quad (2.12)$$

running over all centres with significant spin density ρ_j . R_j are the distances between the nuclei and centres of spin density under consideration and \vec{n}_j the unit vectors connecting the considered nucleus to the spin density centre.

Compared to the electron Zeeman interaction (see Figure 2.1), the hyperfine interaction is only a weak perturbation for the electron spin at magnetic fields above 0.1 T.⁴¹ On the contrary, for nuclear spins the hyperfine interaction can be on the same order as the nuclear Zeeman interaction and the nuclear spin eigenstates are mixed by the hyperfine field. The hyperfine spin Hamiltonian is then given as

$$\hat{H}_{HF} \approx A_{xz} \hat{I}_x \hat{S}_z + A_{yz} \hat{I}_y \hat{S}_z + A_{zz} \hat{I}_z \hat{S}_z. \quad (2.13)$$

In such cases, the magnetization axis of the nuclear spin is tilted with respect to the external magnetic field and forbidden electron-nuclear transitions can be excited by microwave pulses. Interference between the allowed and forbidden transition then results in a modulation of the electron spin echo with the nuclear frequency and - depending on the experiment - combinations thereof. These oscillations are referred to as Electron Spin Echo Envelope Modulation (ESEEM). In consequence of the field-independence of the hyperfine coupling, the effect vanishes at larger field, when the nuclear Zeeman interaction exceeds the hyperfine splitting by far. The echo modulation also disappears if the external magnetic field is oriented along one of the principal axes of the hyperfine tensor or the hyperfine interaction is isotropic, which is observed in liquid solution when the anisotropy is averaged through molecular tumbling. A detailed analysis can be found, for example, in Ref.¹⁹.

Hyperfine interactions can be measured by double resonance techniques, such as Electron Nuclear Double Resonance (ENDOR) spectroscopy or ESEEM-based experiments, often giving complementary information. In electron spin-spin distance measurements, ESEEM may contribute unwanted oscillations to the dipolar evolution data. Their contribution to the RIDME signal will be discussed in Chapter 6.

2.1.4. Nuclear Quadrupole Interaction

The non-spherical charge distribution for nuclei with $I > 1/2$ interacts with an electric field gradient, caused by nearby electrons and nuclei.¹⁹ The corresponding Hamiltonian is given by

$$\hat{H}_{NQ} = \hat{I}^T \mathbf{P} \hat{I}, \quad (2.14)$$

with the nuclear quadrupole tensor \mathbf{P} . In the principal axis system Equation (2.14) can be rewritten as

$$\begin{aligned} \hat{H}_{NQ} &= P_x I_x^2 + P_y I_y^2 + P_z I_z^2 \\ &= \frac{e^2 q Q}{4I(2I-1)\hbar} [(3I_z^2 - I(I+1)^2) + \eta(I_x^2 - I_y^2)]. \end{aligned} \quad (2.15)$$

Q represents the nuclear electrical quadrupole moment, eq is the electric field gradient and $\eta = (P_x - P_y)/P_z$ the asymmetry parameter. By convention $|P_z| \geq |P_y| \geq |P_x|$ and $0 \leq \eta \leq 1$. For the systems and experiments considered in this thesis, nuclear quadrupole interactions can be neglected.

2.1.5. Zero-Field Splitting

Strongly coupled spins are best described by a group spin $S > 1/2$. In such systems, the combined action of the spin-orbit coupling induced by the ligand field and the electron-electron dipole coupling results in a loss of spherical symmetry of the occupied orbitals, which lifts the $(2S+1)$ -fold degeneracy of the ground state. This zero-field splitting \hat{H}_{ZFS} is formally analogous to the nuclear quadrupole interaction (Equation (2.14)) and can be described by

$$\hat{H}_{ZFS} = \hat{S}^T \mathbf{D} \hat{S}, \quad (2.16)$$

where \mathbf{D} is the traceless zero-field splitting tensor. Note that according to first principles, the ZFS tensor also contains an isotropic contact term, which is typically neglected in the spin Hamiltonian, since it shifts all energy levels by an equal amount, without any observable effect on the EPR spectra. In the principal axis system of the \mathbf{D} tensor Equation (2.16) can be rewritten as

$$\begin{aligned} \hat{H}_{ZFS} &= D_x S_x^2 + D_y S_y^2 + D_z S_z^2 \\ &= D[S_z^2 - \frac{1}{3}S(S+1)] + E(S_x^2 - S_y^2) \end{aligned} \quad (2.17)$$

with $D = 3D_z/2$ and $E = (D_x - D_y)/2$. D_z is defined as the principal value with the largest magnitude. For cubic symmetry $D = E = 0$. In axial symmetry $D \neq 0$ and $E = 0$, while in rhombic symmetry $D \neq E \neq 0$. At frequencies of X-band and lower, the ZFS interaction is often dominant for $S > 1/2$ systems.¹⁹

For spin systems with $S > 3/2$ higher order terms may have to be considered. They can be described by the extended Stevens operators, a complete set of higher-order operators. The spin Hamiltonian is then given as

$$\hat{H}_{ZFS} = \sum_{k=2,4,6} \sum_{q=-k}^k B_k^q \hat{O}_k^q(S), \quad (2.18)$$

with the Hermitian operators $\hat{O}_k^q(S)$ and real coefficients B_k^q . A list of the spin operators is given by Abragam and Bleaney.³⁸

For integer spin in non-axial symmetry, all energy levels are split to first order by ZFS at zero field. ZFS can be much larger than the electron Zeeman interaction and available microwave frequency as illustrated in Figure 2.1. In such cases, no transition energies between neighbouring energy levels can be excited and the investigated system appears 'EPR silent', unless very high fields or frequencies are available. According to Kramers theorem⁴² for half-integer spin S , there are $\pm m_S$ pairs of levels that are degenerate in zero field, so that such pairs are always observable in EPR. The extraction of ZFS parameters from the EPR lineshape will be discussed in Chapter 4 for Gd(III) complexes in frozen glassy solutions.

2.1.6. Weakly Coupled Spins

While strongly coupled spins are described by a group spin, two weakly coupled spins are usually best characterized by their individual spins S_1 and S_2 . The electron-electron coupling is considered to be weak as long as $\hat{H}_{ee} \ll \hat{H}_{EZ}$. Electron-electron interactions consist of an exchange contribution and the dipole-dipole coupling.

Exchange Interaction

If the orbitals of two spins overlap significantly then the two electrons can exchange with each other and the Heisenberg exchange coupling term (Equation (2.19)) becomes relevant:

$$\hat{H}_{ex} = J \hat{S}_1^T \hat{S}_2. \quad (2.19)$$

The exchange coupling constant J decreases exponentially with increasing distance r between the two spins. Additionally it depends on the conductivity of the intervening medium or a conjugated bond network between them.¹⁹ $J > 0$ is defined as anti-ferromagnetic coupling and corresponds to a bonding orbital overlap, whereas $J < 0$ corresponds to ferromagnetic coupling and an anti-bonding orbital overlap.

For spin-spin distance measurements it can be typically neglected for distances larger than 1.5 nm. For conjugated systems or if the unpaired electrons are strongly delocalized, it may be still relevant at larger distances.¹³

Dipole-Dipole Interaction

Large g -anisotropy or strong ZFS can result in non-parallel magnetic moments with respect to the external magnetic field as illustrated in Figure 2.2. The interaction energy for two spins in random orientation with respect to the magnetic field is given by

$$E = -\frac{\mu_0}{4\pi} \mu_1 \mu_2 \frac{1}{r^3} (\cos \theta_1 \cos \theta_2 - \sin \theta_1 \sin \theta_2 \cos \phi). \quad (2.20)$$

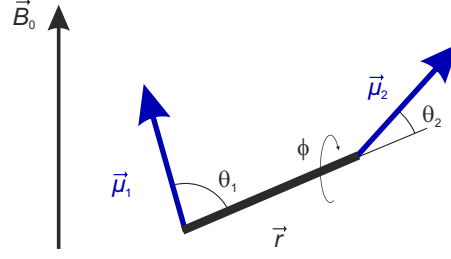


Figure 2.2. Coupling of two magnetic moments depending on their orientation in an external magnetic field. Adapted from Ref. ⁴³.

The spin Hamiltonian \hat{H}_{dd} of the through-space dipole-dipole interaction between two electron spins with g -values g_1 , g_2 and spin-spin distance r is given as

$$\hat{H}_{dd} = \hat{S}_1^T \mathbf{D} \hat{S}_2 = \frac{1}{r^3} \frac{\mu_0}{4\pi\hbar} g_1 g_2 \mu_B^2 [\hat{S}_1 \hat{S}_2 - \frac{3}{r^2} (\hat{S}_1 \vec{r})(\hat{S}_2 \vec{r})]. \quad (2.21)$$

In cases, where the magnetic moments are parallel to each other as well as to the external magnetic field, $\theta = \theta_1 = \theta_2$, the dipole-dipole Hamiltonian takes the form

$$\hat{H}_{dip} = \frac{1}{r^3} \frac{\mu_0}{4\pi\hbar} g_1 g_2 \mu_B^2 [\hat{A} + \hat{B} + \hat{C} + \hat{D} + \hat{E} + \hat{F}], \quad (2.22)$$

with \hat{S}_i and \hat{I}_i operators corresponding to the spin's eigenframe and the dipolar alphabet:

$$\hat{A} = \hat{S}_z \hat{I}_z (1 - 3 \cos^2 \theta), \quad (2.23)$$

$$\hat{B} = -\frac{1}{4} [\hat{S}^+ \hat{I}^- + \hat{S}^- \hat{I}^+] (1 - 3 \cos^2 \theta), \quad (2.24)$$

$$\hat{C} = -\frac{3}{2} [\hat{S}^+ \hat{I}_z + \hat{S}_z \hat{I}^+] \sin \theta \cos \theta e^{-i\phi}, \quad (2.25)$$

$$\hat{D} = -\frac{3}{2} [\hat{S}^- \hat{I}_z + \hat{S}_z \hat{I}^-] \sin \theta \cos \theta e^{i\phi}, \quad (2.26)$$

$$\hat{E} = -\frac{3}{4} [\hat{S}^+ \hat{I}^+ \hat{S}_z \hat{I}^+] \sin^2 \theta e^{-2i\phi}, \quad (2.27)$$

$$\hat{F} = -\frac{3}{4} [\hat{S}^- \hat{I}^- \hat{S}_z \hat{I}^-] \sin^2 \theta e^{2i\phi}. \quad (2.28)$$

The involved transitions for the different terms of the dipolar alphabet are illustrated in Figure 2.3.

Typically, EPR experiments are performed in mw bands in which the electron Zeeman interaction is much larger than the dipole-dipole coupling, such that the non-secular terms $\hat{C} - \hat{F}$ can be dropped. The pseudo-secular \hat{B} term can only be dropped if the difference between the energy levels $|\beta_A \alpha_B\rangle$ and $|\alpha_A \beta_B\rangle$ is much larger than the dipole-dipole interaction. A notable exception is the case of short distances between two high-spin Gd(III) centres,⁴⁴ which will be discussed in Chapter 8.

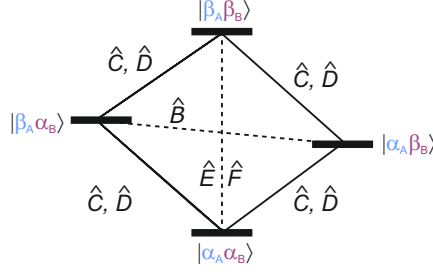


Figure 2.3. Transitions involved in the dipole-dipole interaction for two like spins $S = 1/2$.

Thus in the secular approximation, the dipole-dipole coupling is given as

$$d(\theta) = \omega_{dd}(1 - 3 \cos^2 \theta), \quad (2.29)$$

with the eigenvalues of the dipole-dipole tensor ω_{dd} ($-\omega_{dd}$, $-\omega_{dd}$, $2\omega_{dd}$)

$$\omega_{dd} = \frac{1}{r^3} \frac{\mu_0}{4\pi\hbar} g_1 g_2 \mu_B^2. \quad (2.30)$$

The nature of the dipolar-coupling is entirely anisotropic, so that molecular tumbling averages it to zero in solution and the couplings need to be extracted in the solid state.

2.2. Spin dynamics

The experimentally observable magnetization is composed of an ensemble of spins. In the external magnetic field, the individual spins can be either parallel (α state) or anti-parallel (β state) to the direction of the static magnetic field. For an isolated spin $S = 1/2$, the quantum mechanical state of that ensemble is represented by a superposition of α and β states. For systems of m coupled spins j and spin quantum number $S_j \geq 1/2$ with Hilbert space dimension $n_H = \prod_{j=1}^m (2S_j + 1)$, it is often described by the so-called density operator¹⁹

$$\hat{\sigma}(t) = \sum_{i=1}^n p_i |\psi_i\rangle \langle \psi_i| = \sum_{kl} \overline{c_l^* c_k} |l\rangle \langle k|, \quad (2.31)$$

where $|\psi_i\rangle = \sum_{k=1}^{n_H} c_k^{(i)} |k\rangle$ is the wave function of each subensemble i of spins in the same state (*pure state*) with basis states $|k\rangle$ and coefficients c_k in the given Hilbert space. p_i is the probability of each subensemble with $\sum_{i=1}^n p_i = 1$.

The elements σ_{kl} describe the coherences between states $|k\rangle$ and $|l\rangle$. For $k = l$, σ_{kk} quantifies the population of state k . In equilibrium, the density operator is given by the Boltzmann distribution

$$\hat{\sigma}_{\text{eq}} = \frac{1}{Z} \exp(-\hbar \hat{H}_0 / k_B T), \quad (2.32)$$

with system partition function $Z = \text{tr}\{\exp(-\hbar \hat{H}_0 / k_B T)\}$. In the high-field approximation ($\hat{H}_0 \approx \omega_S S_z$) and high-temperature approximation ($\hbar \omega_S \ll k_B T$), which apply in the majority of experimental situations described in this thesis, we find

$$\hat{\sigma}_{\text{eq}} \approx \mathbb{1} - \frac{\hbar \omega_S}{k_B T} S_z. \quad (2.33)$$

The detected macroscopic magnetization is proportional to the expectation values of the quantum-mechanical observables $\langle \hat{S}_x \rangle$, $\langle \hat{S}_y \rangle$, $\langle \hat{S}_z \rangle$. Commonly, it is detected perpendicular to the magnetic field direction and obtained by $\langle \hat{S}_y \rangle = \text{tr}\{\hat{\sigma}(t)\hat{S}_y\}$. It depends on the initial population difference between the states of a multi-level system, which is typically small, e.g. for a electron Larmor frequency ω_S of 10 GHz about one spin in a thousand spins contributes to the signal, and thus limits the sensitivity of EPR experiments.

The time evolution of spin systems can be described by the Liouville-van-Neumann equation considering the density operator $\hat{\sigma}$ and relevant spin Hamiltonian $\hat{H}(t)$

$$\frac{d}{dt}\hat{\sigma}(t) = -i[\hat{H}(t), \hat{\sigma}(t)]. \quad (2.34)$$

For larger spin systems this approach can become cumbersome and it is convenient to describe the time evolution in the product operator formalism.⁴⁵ The approach decomposes $\hat{\sigma}(t)$ into a linear combination of orthogonal basis operators and the evolution of the spin systems can be calculated according to¹⁹

$$\hat{\sigma}_{\text{initial}} \xrightarrow{\phi_1 \hat{B}_1} \xrightarrow{\phi_2 \hat{B}_2} \dots \xrightarrow{\phi_n \hat{B}_n} \hat{\sigma}_{\text{final}}, \quad (2.35)$$

using the evolution of product operators \hat{A} and \hat{B} as well as rotation angle ϕ .

$$\hat{A} \xrightarrow{\phi \hat{B}} \hat{A} \cos(\phi) - i[\hat{B}, \hat{A}] \sin(\phi). \quad (2.36)$$

ϕ can be the flip angle of a pulse or the interactions in the Hamiltonian during time t with amplitude ω , so that $\phi = \omega t$. This approach is utilized in Chapter 6 to describe the hyperfine contributions to the RIDME echo. Note that Equation (2.36) is a simplified form of the so-called Baker-Hausdorff formula, which appears due to the specific commutator rules of the spin operators for spins $S_i = 1/2$.¹⁹

2.3. Relaxation

Relaxation of coherence and polarization can provide a variety of information due to its dependence on the electronic structure and dynamics of the paramagnetic centre, but also restricts the resolution of EPR experiments. This section is reduced to a qualitative discussion of relaxation. A more detailed description of relaxation theory can be found in textbooks, for instance in Ref.^{19;38;39;46}.

Placed in an external magnetic field, the magnetization for an ensemble of electron spins aligns with the field direction according to the equilibration of spin populations. In this equilibrium state no ensemble magnetization is present in the transverse plane. When disturbed, e.g. by a mw pulse, the magnetization will return to its equilibrium by numerous single-spin relaxation events. These stochastic processes are typically separated into longitudinal (or spin-lattice) and transverse (or spin-spin) relaxation. The longitudinal relaxation drives the magnetization build-up along the direction of the external magnetic field by exchange of energy with the environment, while mutual interaction of the magnetic dipoles, referred to as local fields, causes the loss of electron spin phase coherence in the spin ensemble and thus the decay of transverse magnetization.

Both, transverse and longitudinal relaxation processes may depend on the orientation of the molecule with respect to the direction of the static field due to anisotropy of motions and of interactions in the Hamiltonian.¹⁹ The dependence of the spectral density function on the relative strength of the interactions present can induce a field/frequency and for high-spin systems a transition dependence of relaxation.^{39;47}

Relaxation processes were first described by Bloch in his classical vector model description of magnetization. In the rotating frame ($\omega = \omega_0$), the Bloch-equations describe an exponential decay of the transverse magnetization M_{xy} with rate $1/T_2$ and an exponential build-up of the longitudinal magnetization M_z with rate $1/T_1$ as illustrated in Figure 2.4.

$$\begin{aligned} M_{xy} &= M_{xy}(0) \cdot \exp(-t/T_2), \\ M_z &= M_{\text{eq}} + (M_z(0) - M_{\text{eq}}) \cdot \exp(-t/T_1), \end{aligned} \quad (2.37)$$

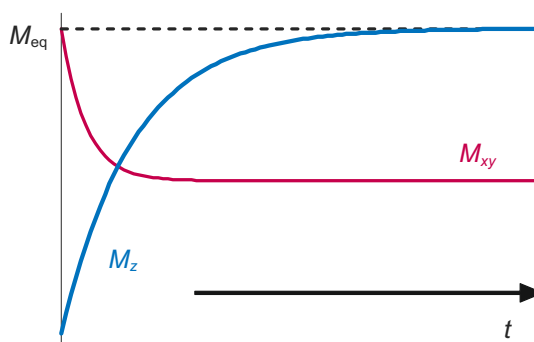


Figure 2.4. Illustration of transverse and longitudinal relaxation.

However, in reality the Bloch equations are not sufficient to describe relaxation data, because in many cases several processes contribute to the decay of magnetization. In such situations, the observed relaxation rates are the sums of the individual rates for these parallel processes, which are not always mono-exponential. Decay of transverse magnetization is then commonly described by the so-called spin echo dephasing time or phase memory time T_m .

Longitudinal relaxation requires the exchange of energy between the spin system and the environment, historically called lattice, and is accompanied by a flip of the spin's magnetization direction. Thermal motion is typically described by phonons (energy quanta of lattice vibrations) in crystalline solids or local modes in glasses that absorb or emit the spin transition energy. The main mechanisms contributing are the direct process, in which there is an exact energy match of the spin transition and the phonon energy, as well as the two-phonon Raman and Orbach processes. At measurement temperatures above 4 K and moderate fields, the phonon density is maximal at much larger energies than the spin transitions and thus the direct process is typically not very efficient and two-phonon processes are required.¹⁹ In the Raman processes the spin-system absorbs a higher energy phonon and re-emits a phonon with the energy difference. This corresponds to a transition to a virtual excited state. The Orbach processes is a resonant two-phonon process that involves excitation to an actual energy level and decay into the equilibrium state. Localized lattice-modes can further contribute to spin-lattice relaxation.³⁹ Determining the exact nature of the relaxation mechanism in the studied metal centres is beyond the scope of this thesis. However, it will be important, that in both Orbach as well as Raman processes higher-order spin flips by

up to four units of the spin projection operator can be present in a single relaxation event. This is based on S^2 terms in the spin-orbit coupling operator,⁴⁸ which has to be considered for each of the two phonons involved in the relaxation event.

There are many processes that contribute to a loss of electron spin phase coherence. They include the near energy-conserving flip-flop terms in electron-electron spin pairs (spin-spin relaxation) as well as pairs of unlike spins (also called cross relaxation).^{39;49} These relaxation processes become efficient if the coupling between both spins is on the same order of magnitude as the difference in their respective resonance frequencies.¹⁹ Half as effective, a spin flip caused by longitudinal relaxation, destroys the phase correlation between the affected spin and the other spins (known as lifetime broadening). Third, fluctuations in the hyperfine field at the observed electron spins occur by spin-lattice and more dominantly spin-spin interactions in the nuclear spin bath. These fluctuations are particularly strong in the case of protons due to their large gyromagnetic ratio and, thus, solvent deuteration helps to prolong phase memory times.⁵⁰ Methyl group rotation in the solvent or within the paramagnetic centre causes further dephasing. Processes, that transfer magnetization to other parts of the spectrum, where it can no longer be detected, are called spectral diffusion. They contribute to the transverse relaxation of the excited spins (called A-spins). The magnetization transfer is caused by longitudinal or spin-spin relaxation of non-resonant B spins that change the local field at the site of the A spins. At the same time transferred equilibrium magnetization from non-excited B spins to the detection window manifests itself as a relaxation process. Similarly, temporal fluctuations of spin Hamiltonian parameters by molecular motion or librations on the time scale of the EPR experiment lead to a distribution of local fields and spectral diffusion occurs.^{19;39}

In addition, local field changes can be introduced by mw pulses that excite only one spin of a dipolar coupled A-B spin pair. This is referred to as instantaneous diffusion. It is reduced by low spin concentrations and application of small angle pulses.^{19;39} A distribution of resonance offsets within the different spin packets and inhomogeneities of the applied external field induce a loss of coherence between the different spin packets and causes the overall field magnetization to defocus. Such interactions can, in principle, be refocussed by application of a π pulse. Moreover, multiple refocusing may prolong phase memory times by decoupling of spin bath interactions.^{51–55}

Spin dynamics including relaxation can be described by the master equation

$$\frac{d}{dt}\hat{\sigma}(t) = -i[\hat{H}(t), \hat{\sigma}(t)] - \hat{\Gamma}(\hat{\sigma}(t) - \hat{\sigma}_{\text{eq}}), \quad (2.38)$$

within Wangsness-Bloch-Redfield theory.^{56;57} $\hat{\Gamma}$ is the relaxation superoperator, which contains the decay rates across individual elements of the density matrix. It introduces the coupling of the components deviating from equilibrium $\hat{\sigma}_{\text{eq}}$. For details see for instance Ref.⁴⁶.

2.4. EPR methods

In the presence of a static magnetic field \vec{B}_0 , the Zeeman interaction splits the energy levels of the electron spins and the previously randomly oriented magnetic moments align parallel or anti-parallel to the magnetic field vector. Electromagnetic radiation in the microwave range ν with the energy $E = h\nu$ can induce transitions between different states if the resonance condition is fulfilled as illustrated in Figure 2.5. The splitting of the energy levels is determined by the spin system's static Hamiltonian (Equation (2.2)) as well as the strength and orientation of the

external magnetic field. The energy levels are populated according to the Boltzmann distribution $\frac{p_i}{p_j} \propto \exp -\frac{E_j - E_i}{k_B T}$, with k_B being the Boltzmann constant and T the temperature. The resulting spectra can be measured by sweeping the microwave radiation or the external magnetic field. For technical reasons usually the external field is swept, while the sample is exposed to a constant microwave frequency ν , either continuously irradiated or applied as short pulses.

2.4.1. Continuous Wave EPR

The first EPR experiment was performed in 1944 by Zavoisky in Kazan.⁵⁸ It measured the absorption of copper salts with low-power CW irradiation. Absorption of the incident microwave irradiation occurs, when the resonance condition is met. This is observed as detuning of a critically coupled resonator in which the sample is placed. The detuning of the resonator leads to a reflection of mw power, which is measured via diode detection.

In field-swept CW EPR, for a better signal-to-noise ratio, the magnetic field amplitude is typically modulated with a frequency of 100 kHz and the oscillating component of the diode voltage is measured as a function of the magnetic field via a lock-in amplifier. The amplitude of the modulated signal is proportional to the slope of the absorption line and thus the derivative spectrum is measured as shown in Figure 2.5.

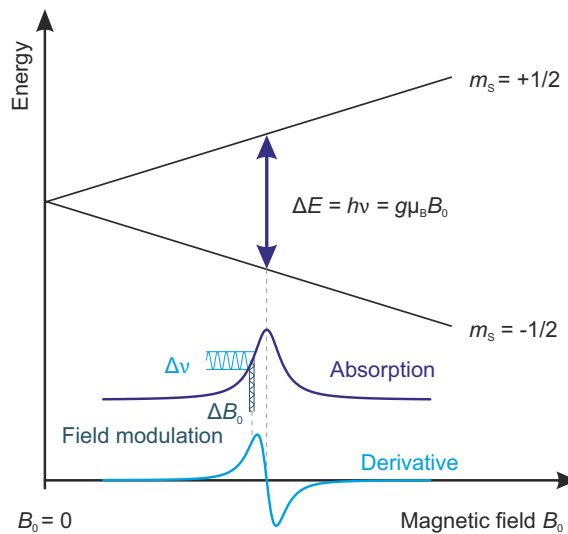


Figure 2.5. Illustration of CW signal generation for a $S = 1/2$ system.

The shape of the resulting EPR spectrum depends on the system's spin Hamiltonian. Thus, the analysis of the EPR lineshape allows identifying the paramagnetic species and to extract the spin Hamiltonian parameters. There exist several software packages to simulate such lineshapes and within this thesis the *Easyspin* package⁵⁹ was used.

2.4.2. Pulsed EPR techniques

Pulsed EPR techniques can lead to additional resolution by separating the various interactions contributing to the CW EPR spectrum. The constant microwave radiation is replaced by a sequence of short microwave pulses with duration in the order of nanoseconds. A single high-power mw pulse excites a large frequency range simultaneously at a constant magnetic field B_0 . The excitation bandwidth determines the fraction of excited species within the spectrum.

Pulses can be described in a semi-classical vector model, in which the macroscopic magnetization M is the vector sum of all magnetic moments in a given sample volume. In an external magnetic field B_0 (by convention aligned along the z -axis) the magnetic moments precess out-of-phase around the field axis with the Larmor frequency ω_0 , resulting in net magnetization along the z -axis. Perturbation of the magnetic field by a microwave pulse of frequency ω_{mw} with a B_1 field perpendicular to static field B_0 induces a nutation of magnetization around the resulting field. The flip angle is determined by the amplitude and length of the pulse. The most simple experiment consists of a $\pi/2$ pulse perpendicular to \vec{B}_0 , e.g. along the x -axis. The pulse rotates the magnetization into the x - y plane. After the pulse, the magnetization vector relaxes back towards equilibrium along the static magnetic field B_0 with frequency offset $\omega_0 - \omega_{mw}$, which creates an oscillation of transverse components M_x and M_y . This oscillating signal can be detected. It is called free induction decay (FID).

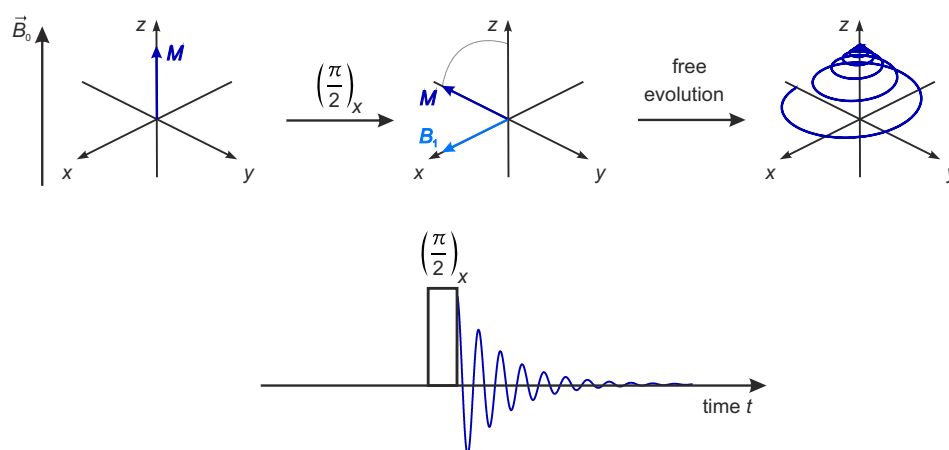


Figure 2.6. A $\pi/2$ microwave pulse rotates the equilibrium magnetization M into the x/y -plane during t_p . In the following free evolution period the magnetization relaxes back to its equilibrium.

Typically rectangular pulses with a sinc-like excitation profile in frequency domain were used in EPR. The excitation bandwidth is then given by the available amplitude and length of the mw pulse. In recent years, fast arbitrary waveform generators (AWG) became available, which led to the development of adiabatic, fast-passage ultra-wideband (UWB) pulses. Modulation of pulse frequency and amplitude allows for much better defined excitation profiles with a larger freedom in shape and frequency bandwidth of the applied pulses.^{60–65} As a result measurement sensitivity can be significantly improved and new experimental schemes have been developed. However, this thesis focussed on experimental schemes at low hardware requirements. Thus, if not stated differently monochromatic rectangular pulses were used.

2.5. Pulse Sequences

2.5.1. Echo-detected EPR

In EPR echo detection (ED) is typically preferred to free induction decay (FID) detection, as the FID often decays within the dead-time after the microwave pulse. The principle of echo generation is shown in Figure 2.7. A $\pi/2$ pulse flips the equilibrium magnetization into the x/y -plane. The transverse magnetization of the different spin-packets evolves during the free evolution period τ . Alongside transverse relaxation events (see Section 2.3), a distribution of resonance offsets

within the different spin packets and inhomogeneities of the applied external field induces a loss of coherence between the different spin packets, which causes the overall magnetization to defocus during time τ . A π pulse rotates the magnetization of the individual spin packets by 180° and the spins refocus after the same time τ . The refocused transverse magnetization gives rise to the electron spin echo. The absorption spectrum can be obtained by measuring the integrated echo intensity at different field positions and fixed microwave frequency.

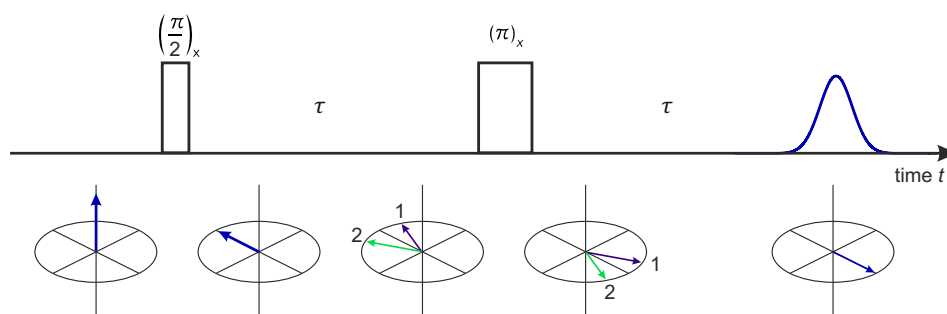


Figure 2.7. A $\pi/2$ microwave pulse rotates the equilibrium magnetization M into the x/y -plane. The magnetization then fans out during the first inter-pulse delay of length τ . The π pulse rotates the components of the magnetization vector around the x -axis and they begin to refocus and give an echo at a time τ after the second pulse.

In this thesis EDEPR spectra are used to identify spin species (Chapter 3), to extract spin Hamiltonian parameters (Chapter 4) and to choose the detection position for constant field experiments. In particular, if not stated differently experiments in this thesis were performed at the maximum of the corresponding EDEPR absorption spectrum.

2.5.2. Two-pulse ESEEM

The sequence of the two-pulse ESSEM experiment or Hahn-echo decay is shown in Figure 2.8. The loss of phase coherence due to field inhomogeneities and distribution of resonant offsets can mostly be refocused by applying a π refocussing pulse. However, pure relaxation events or spectral diffusion can not be refocussed. This leads to a decrease of echo intensity if the interpulse delay τ is increased as illustrated in Figure 2.8.

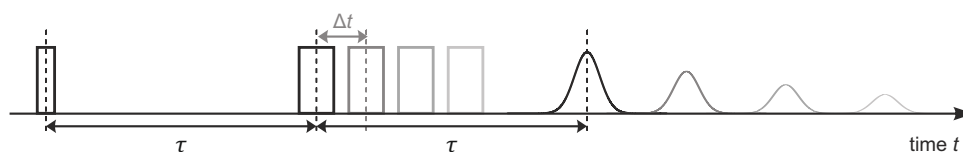


Figure 2.8. Hahn-echo decay sequence. The interpulse delay τ is incremented by Δt , which leads to a decreased echo intensity with the characteristic decay time T_m .

Measuring the echo intensity as a function of the interpulse delay τ reveals the characteristic decay of the magnetization with phase memory time T_m , which corresponds to the point where the echo-intensity is decayed to $1/e$ of its initial value. If nuclei with $I \neq 0$ are coupled to the electron spin by the hyperfine interaction, nuclear modulations, called Electron Spin Echo Envelope Modulation (ESEEM), can be observed on top of the echo decay as described in Section 2.1.3. After subtraction of the unmodulated decay, Fourier transform of the time trace results in a spectrum that contains the nuclear frequencies and combinations thereof (for details see for example Ref. ¹⁹).

In this thesis, the two-pulse ESEEM experiment is mainly used to extract phase memory times that give an estimate on the maximal detectable distance. Transverse relaxation traces of frozen glassy solutions studied in this thesis cannot be accurately fitted to mono-exponential functions. To extract the phase memory time T_m , Hahn echo decay traces were fitted to stretched exponential functions of the form $c \cdot \exp(-(t/T_m)^x)$. In some cases, data are poorly described by a single stretched exponential,⁵⁵ and are better described by a sum of stretched exponential functions of the form $c_1 \cdot \exp(-(t/T_{m,1})^{x_1}) + c_2 \cdot \exp(-(t/T_{m,2})^{x_2})$. If ESEEM oscillations occur, only the maxima of the oscillations were taken into account in the fitting routines. Constant offsets were removed prior to the fitting routine, which uses a nonlinear least-square fitting criterion (Nonlinear regression) implemented in MATLAB (The MathWorks Inc., Natick, MA, USA). Errors are extracted from the 95% confidence intervals of the fit using the statistics Toolbox.

2.5.3. Three-pulse ESEEM experiment

Hyperfine couplings can reveal valuable information about the spin centre environment and the degree of spin delocalization. If measured with the two-pulse ESEEM experiment described above, the modulations are sensitive to the decay of the transverse magnetization, which can be short and thus lead to broad lines upon Fourier transformation. An alternative experiment with higher resolution is the stimulated echo sequence or three-pulse ESEEM experiment, which is sensitive to the longer longitudinal relaxation time. A disadvantage of this experiment is a blind spot at nuclear frequencies with a period of $1/\tau$ (for details see for example Ref.¹⁹). The blind spot can be avoided by measuring the experiment for a set of τ values. On the other hand, the blind spot can be used to suppress certain nuclear frequencies which are not of interest to the current study.

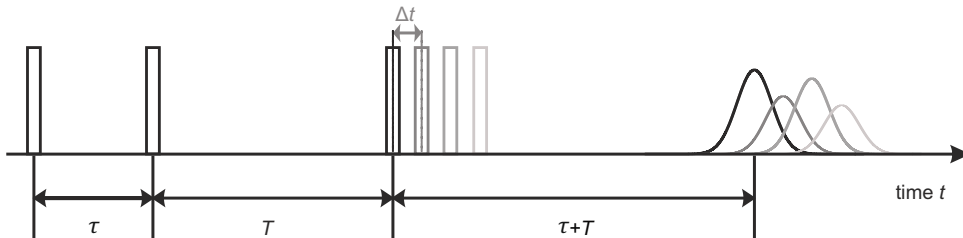


Figure 2.9. Stimulated-echo sequence to measure the ESEEM effect by incrementing the interpulse delay T at fixed τ -value.

In this thesis, three-pulse experiments are used to study the background decay of the stimulated echo as described in Chapter 5. Further, three-pulse ESEEM experiments have been used to identify nuclear frequencies occurring in RIDME experiments due to incomplete ESEEM averaging (see Chapter 6).

2.5.4. Inversion recovery

Besides other experimental schemes, longitudinal relaxation rates can be measured with the inversion recovery experiment. In this experiment the equilibrium magnetization is first inverted by a hard π pulse. The recovery to equilibrium is then followed using a soft $\pi/2 - \tau - \pi - \tau -$ echo detection scheme as shown in Figure 2.10. This scheme reduces spectral diffusion effects by probing only a small fraction in the centre of the inverted magnetization.

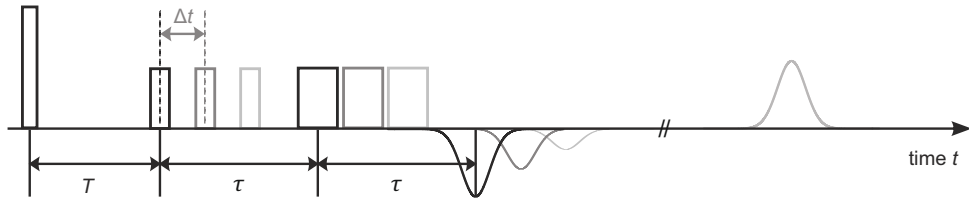


Figure 2.10. Inversion recovery sequence. The detection sequence ($\pi/2 - \tau - \pi - \tau - \text{echo}$) is moved apart from the inversion pulse with Δt to follow the build-up of magnetization to equilibrium.

In a homogeneous environment, the magnetization build-up should be mono-exponential. As for transverse relaxation traces, this situation is not encountered for the measurements presented in this thesis, which can be attributed to inhomogeneities of local environment and to the presence of several relaxation pathways.

Longitudinal relaxation times T_1 can be extracted from inverted and offset corrected inversion-recovery traces. The data are subsequently fitted by stretched exponential functions of the form $c \cdot \exp(-(t/T_1)^x)$ using a nonlinear least-square fitting criterion as implemented in MATLAB. Errors are extracted from the 95% confidence intervals of the fit using the statistics Toolbox.

2.5.5. Distance measurements

Over the last decades several methods have been developed to extract spin-spin distances from the dipole-dipole interaction. This thesis focuses on several aspects and methodological developments of the single-frequency Relaxation Induced Dipolar Modulation Enhancement (RIDME) experiment.^{66;67} To this end, the RIDME experiment is also compared to the commonly used Double Electron-Electron Resonance (DEER or PELDOR) experiment. The pulse sequences are shown in Figure 2.11.

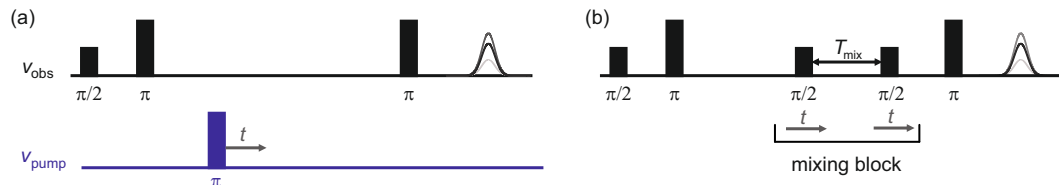


Figure 2.11. (a) DEER and (b) RIDME sequences.

Both experiments create electron coherence during the initial preparation period ($\pi/2 - \pi$ sequence). After the preparation period, a modulation to the local field at the position of the observed spin A is induced by inversion of a second spin B as illustrated in Figure 2.12(a) for the RIDME sequence. This causes a shift of the resonance frequency of the A spin. The change in local field is dependent on the inverse cube of the A-B distance as well as the strength of the J coupling. Thus, depending on the inversion efficiency λ of the coupled B spin, a fraction of the electron spin echo signal will oscillate with the sum of the dipolar frequency ω_{dd} and the exchange coupling constant J . This fraction λ is often called dipolar modulation depth. The time evolution of the A spin with changed frequency results in a phase gain of $\pm(\omega_{\text{dd}} + J)t$, which is then detected using a final refocusing pulse. The inversion time point is incremented in both sequences and the phase gain and thus the echo intensity will oscillate with the coupling frequency (Figure 2.12(c)). The dependency of the dipolar coupling constant on the angle between the spin-spin axis and the external magnetic field θ can lead to so-called orientational selectivity

effects if not all orientations are excited uniformly.⁶⁸ Considering the distance distribution $P(r)$ and a geometry factor $\xi(\theta)$, which accounts for the excited orientations in the signal evolution,⁶⁹ the signal caused by the A-B spin pair is given as

$$F(t) = \int \int P(r)\xi(\theta)\cos([\omega_{dd}(r_{AB}, \theta) + J]t)d\theta dr. \quad (2.39)$$

The signal $F(t)$ is typically called form factor.

Exchange couplings can be neglected within this thesis and are therefore omitted in the following description. However, if both coupling mechanisms are present it can be difficult to disentangle both interactions without further knowledge.^{13;70-72}

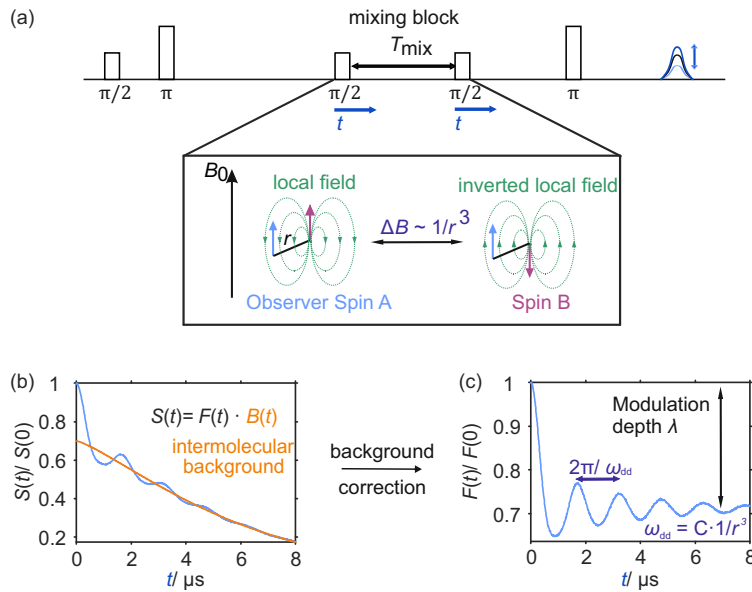


Figure 2.12. Illustration of the formation of the RIDME signal in the absence of exchange interaction. (a) RIDME sequence and schematic representation of the dipolar modulation build-up; (b) schematic raw data as well as background function and (c) schematic form factor.

An important difference between the two pulse sequences is the nature of the inversion of the B spins. In the DEER experiment B spins are inverted by a pump pulse at a second frequency and the inversion efficiency is thus determined by the bandwidth of the pump pulse. In the RIDME experiment the magnetization is stored in the direction of the external field in form of a polarization grating for a given mixing time T_{mix} . During T_{mix} longitudinal relaxation events lead to a stochastic inversion of B spins. In high-spin systems, inversion by relaxation can cause higher-order spin transitions $\Delta m_S \geq 2$, which lead to the observation of higher-frequency overtones in the dipolar evolution data.⁷³ After the mixing time, the magnetization is transferred back into the transverse plane, where it is eventually detected. The modulation depth is thus determined by the time allowed for stochastic, longitudinal spin flips. Assuming exponential longitudinal relaxation and the absence of correlated flip-flop processes in the A-B pairs, the modulation depth builds up according to the probability of an odd number of spin flips during the mixing block:⁷⁴

$$P_{\text{odd}} = \lambda_{\text{steady state}}(1 - \exp(-T_{\text{mix}}/T_{1,B})), \quad (2.40)$$

with the steady-state modulation depth $\lambda_{\text{steady state}} = 1 - 1/(2S + 1)$. The absence of the need for a second frequency in the RIDME experiment eases the requirement of broadband excitation as well as resonators and allows to choose the detection position freely within the spectrum.

The detected raw data are composed of the form factor $F(t)$ and the intermolecular background decay (Figure 2.12(b)), which needs to be removed prior to further data analysis. A drawback of the RIDME technique compared to the DEER experiment is the stronger background decay resulting from spectral diffusion during the mixing block. The details of the RIDME background will be discussed in Chapter 5.

In cases where all orientations can be excited uniformly, or be completely averaged over all orientations, Fourier transform after background correction yields a scaled Pake pattern as displayed in Figure 2.13(a), which is characterized by two maxima, split by $2\omega_{\text{dd}}$, and has a total width of $4\omega_{\text{dd}}$.

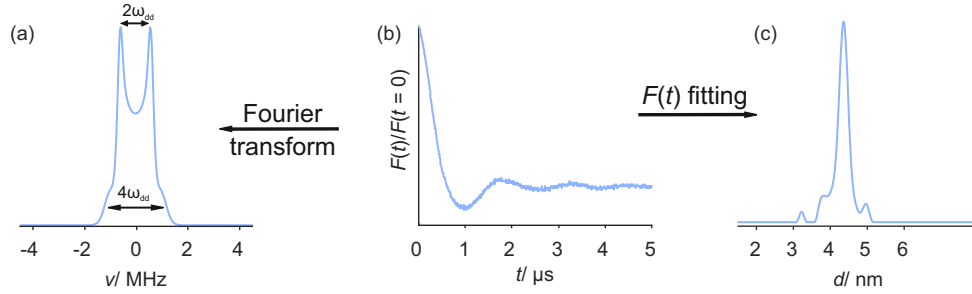


Figure 2.13. Extraction of distance information from dipolar evolution data. (a) Scaled Pake pattern obtain after Fourier transform of detected time-domain data (b) and (c) distance distribution resulting from Tikhonov regularization.

Distance distributions can be obtained by fitting a simulated form factor to experimental data and consequent inversion of equation

$$S(t, r) = \int_0^\infty K(t, r) \cdot P(r) dr, \quad (2.41)$$

with the kernel function $K(t, r) = \int_0^1 \cos[(3x^2 - 1)\omega_{\text{dd}}t] dx$. The ill-posed problem⁷⁵ is usually stabilized by Tikhonov regularization.^{76–78} Data analysis routines in the presence of higher harmonic overtones, i.e. in high-spin RIDME, have been developed during this thesis and are discussed in Chapter 8.

3

Metal Complexes for Pulsed Dipolar Spectroscopy

Spectroscopically orthogonal spin probes are important for selective excitation of a specific spin, e.g. to access distances between different pairs in three-spin systems, and open up perspectives for new experimental strategies in EPR studies of soft matter and biomacromolecules. The work presented in this chapter contributes towards extending the arsenal of such spectroscopically orthogonal spin probes by comparing a series of different metal-chelates with respect to their suitability for pulsed dipolar spectroscopy (PDS). Qualitative predictions are given for PDS-related characteristics, such as accessible distances, signal-to-noise ratio (SNR) or modulation depth at given measurement temperature and detection band.

Out of the tested metal ion/ligand combinations the complexes of Gd(III), Mn(II) and Cu(II) appeared to be most promising for application in PDS. The Co(II) and Fe(III) complexes studied herein were found unsuitable as resonant spins, yet, might be interesting as non-resonant spin probes in relaxation-based distance measurements. The spectroscopic properties of all studied complexes were sufficiently different to the most commonly used nitroxide-based spin probes, thus, allowing for spectroscopic selection schemes.

The synthesis of all complexes was performed in the group of Adelheid Godt (Bielefeld University) by Mian Qi, Henrik Hintz, Vanessa Koch, Xuemei Yao, Julia Wegner, Tobias Zwafing and Miriam Hülsman. Katharina Keller performed the EPR measurement with contributions from Gabriela Drabik and data analysis. The characterization of the compounds Mn-maleimide-DOTA, Mn-TAHA, Mn-PyMTA, and Mn-NO₃Py was published as part of Ref.⁷⁹.

3.1. Introduction

EPR spectroscopy is a valuable tool for the study of paramagnetic metal ion complexes and may provide information about the oxidation state, mode of coordination, geometry and type of ligand site.^{19;80} Using appropriate EPR techniques, binding of native paramagnetic metal centres to metalloproteins can be followed (see for example Chapter 10) and if not naturally occurring diamagnetic metal ions can often be substituted by paramagnetic ones. Further, stable chelates of paramagnetic metal ions can be introduced as spin probes by site-directed spin labelling schemes.^{16–18;23} Formation of thermodynamically and kinetically stable complexes with low dissociation rates can be achieved by using multi-dentate ligands,⁸¹ which allows applying EPR techniques in reducing environments, e.g. in-cell.^{24;25} In addition, the use of labels with different spectroscopic properties, e.g. metal centres and organic radicals, or high- and low-spin metal centres, allows for selective excitation of one spin tag or another which is used in orthogonal spin labelling schemes.^{26;82;83}

The spectroscopic properties of the paramagnetic metal chelates depend on the electronic configuration of the unpaired electrons in the open shell and their interaction with the neighbouring atoms. Complexes with open shells can be in low- or high-spin configurations depending on the interplay of the ligand field Δ_0 , the spin-orbit coupling and the pairing energy P of two electron spins.

Neglecting spin-orbit coupling contributions to the energy level splitting, in strong ligand fields ($\Delta_0 > P$) electron pairing is favourable resulting in low-spin complexes. In the opposite situation ($\Delta_0 < P$), occupation of higher energy levels is favoured yielding high-spin complexes in weak ligand fields.⁸⁰ Further, in high-spin systems the ligand-field interaction may exceed both the microwave frequency and the electron Zeeman interaction at a given magnetic field, and, consequently, if all energy levels become non-degenerate, none of the transitions is accessible to EPR techniques.¹⁹ However, for half-integer ions Kramers double-degeneracy of spin states remains in zero field,⁴² leading to transitions that are always observable in the presence of a static magnetic field. In cases where only transitions within each Kramer doublet can be excited, effective low-spin $S_{\text{eff}} = 1/2$ systems with different effective g -values are observed. If further, the energy level splitting caused by the ligand field exceeds the thermal energy $k_B T$ only the lowest Kramers doublet is populated and a single effective spin $S_{\text{eff}} = 1/2$ is found. To good approximation, the EPR properties of such ions can be described as an effective spin $S = 1/2$, however apparent g -anisotropy can be large due to strong spin-orbit coupling.^{84;85}

The pairing energy depends on the Coulomb repulsion and the energy difference of parallel and anti-parallel electron spin pairs due to the exchange interaction. The ligand field is influenced by several factors such as the metal ion electronic configuration, its oxidation number as well as the type, number and geometry of the ligands.⁸⁶ Overlap of the metal ion's and ligand's orbitals leads to the formation of molecular orbitals and delocalization of the electrons from the metal ion's open shell, which can induce hyperfine splitting of the energy levels or exchange coupling between neighbouring centres.

For the core-like $4f$ orbitals of lanthanide ions only a small fraction of the unpaired-electron density is transferred to the ligand, so that relatively weak ligand field interactions are observed.^{28;84} Thus, the magnetic moment of the $4f$ electrons may be regarded as being located in close proximity to the metal nucleus. In the important case of the Gd(III) ion, hyperfine couplings in isotopes with non-zero nuclear spin ($\sim 30\%$ natural abundance) are typically weak

($a/gJ\mu_B = 0.36$ mT for ^{155}Gd and 0.48 mT for ^{157}Gd ^{84;87}). For transition metal complexes with open d -shell, the metal-ligand orbitals interact stronger, resulting into significant hyperfine couplings to the surrounding nuclei (the so-called superhyperfine couplings) and large ligand field splittings, dependent on the coordination geometry.⁸⁸ Strong directional bonding, observed in some coordination polyhedra, may induce anisotropies in the EPR tensors as for example observed for Cu(II) complexes.

The coordination numbers differ between these two classes and also vary within each class, so that depending on the type of metal ion different ligands are expected to be optimal. For example, the coordination number of Gd(III) is usually 8 or 9, while it can be 4, 5 or 6 for Cu(II) complexes.^{88;89} Lanthanide ions are considered as hard Lewis acids binding preferentially to hard highly electronegative donors such as oxygen or fluoride with predominately ionic character, while transition metal ligand bonds have often more covalent character. The ionic radius of Gd(III) is larger than for most of the transition metal ions. A shrinkage of the ionic radius is typically observed upon gradual filling of the d - or f - shell. This needs to be taken into account when analysing spin-spin distances or in paramagnetic-metal ion substitution.

Important properties of lanthanide and transition metal ions studied in this chapter are summarized in Table 3.1.

	Lanthanide Ions	Transition Metal Ions
Metal Orbital	$4f$	$3d$
Ionic radii (Å)	1.06-0.85	0.75-0.6
Typ. Coordination numbers	6-9	4-6
Typ. Coordination Polyhedra	Triagonal prism Square antiprism Dodecahedron	Square planar Tetrahedron Octahedron
Bonding	Weak metal-ligand orbital interaction	Strong metal-ligand orbital interaction
Bond Direction	Little preference	Strongly oriented
Bond Strength	In order of electronegativity	Determined by orbital interaction
Solutions complexes	Ionic, rapid ligand exchange	Often covalent

Table 3.1. Comparison of $4f$ lanthanide and $3d$ transition metal ions. Adapted from Ref.⁸⁸.

For a given metal ion/ligand combination, key factors to consider for pulsed dipolar spectroscopy (PDS) are the spin state, the width of the EPR spectrum, the correlation between the position in the spectrum and the orientation of the g -tensor or zero-field splitting (ZFS) tensor (the so-called 'orientation selection'), as well as the electron spin relaxation times. These factors determine the spectroscopic selection, the maximal detectable distance, the signal-to-noise ratio (SNR) and in combination with the pulse bandwidth the fraction of excited species. The maximal detectable distance can be computed from the electron spin phase memory time, which is ultimately limited by the electron spin-spin relaxation and the electron spin's coupling to the environment, while the apparent phase memory time can be further shortened due to spectral diffusion processes. Solvent deuteration and spin dilution prolong the electron spin phase memory time.^{76;90;91} Dynamical decoupling sequences can also reduce the effect of spin diffusion and thus extend the detectable distance range.^{51;52;92} The longitudinal relaxation rate sets the lower limit for the repetition rate of pulse EPR experiments and thus influences the achievable SNR in a

given measurement time. Further, additional interactions such as the ZFS, may influence the spin-spin magnetic dipolar coupling regimes and complicate data analysis.⁴⁴ All these effects can lead to different optimal conditions in PDS experiments, depending on the distance of interest. In addition, the particular experimental scheme and available microwave technology can influence the choice of spin label.

In this work, a series of paramagnetic metal complexes with different central ions (Cu, Co, Fe, Mn, Gd) are investigated for their applicability in PDS. One aim of this project was to study the respective EPR properties for different metal ions in the same ligand. Thus, the presented ligands may not always be the most suitable ones for a particular type of metal centre. Detailed analysis of the coordination geometry as well as spin Hamiltonian parameters for the different complexes are outside the scope of this chapter and would deserve a dedicated study. Here qualitative predictions for PDS-related characteristics, such as accessible distances, SNR or modulation depth at selected measurement temperature and detection band are described. The latter parameters can be optimized for each particular type of metal centre as well as type of EPR experiment, but such an optimization is beyond the scope of this initial study. First, experimental results for the copper complexes are presented, followed by a discussion of cobalt and iron complexes. Third, experimental data for manganese and gadolinium are given.

3.2. Experimental

Synthesis. Figure 9.1 shows the structure of the studied ligands. The synthesis of the ligands PyDTTA, PCTA, PyMTA, TAHA, NO₃Pic, maleimido-DOTA is described in Refs.^{93–95}. Synthesis of the other ligands will be published elsewhere. The formation of the metal complexes was achieved by adding a solution of the respective salt for the metal ions Cu(II), Co(II), Fe(III), Mn(II) and Gd(III). Details can be found for Gd(III) in Ref.⁹⁵, for Mn(II) in Ref.⁹³, for Cu(II) in Chapter 5 and will follow elsewhere for Co(II) and Fe(III).

Sample preparation. For pulsed EPR measurements, stock solutions of the complexes were diluted in 1:1 (v:v) D₂O:glycerol-d₈ to 100 μM for the transition metal complexes and to 25 μM for the Gd(III)-compounds. Note that the different complexes were measured over a time range starting in March 2015 to June 2018 on different spectrometers and consequently different D₂O as well as different glycerol-d₈ stocks with potentially different degree of protonation were used in the sample preparation. This might have an influence on the transverse relaxation rates, so that a comparison of transverse relaxation times should be performed cautiously. For the CW experiments sample concentration between 200 μM and 1 mM in a 1:1 (v:v) H₂O:glycerol were probed.

EPR measurements. The pulsed characterization measurements were performed on a home-built high-power Q-band pulse EPR spectrometer⁹⁶ equipped with a rectangular cavity accommodating oversized 3 mm outer diameter cylindrical samples.^{97;98} A helium flow cryostat (ER 4118 CF, Oxford Instruments) was used to adjust the measurement temperature to 10 K.

The field sweeps were detected with a $\pi/2 - \tau - \pi - \tau$ - echo sequence as described in Chapter 2.5.1. Pulses were set to 12-24 or 16-32 ns at the maximum echo intensity (maximum of spectrum), depending on the available microwave power induced by the resonator. For the Gd(III)-complexes the power was set at maximum field by nutation experiments. The interpulse delay τ was set to 400 ns. In some cases of Co(II) and Fe(III), the interpulse delay was reduced to 200/ 300 ns to increase the signal-to-noise (SNR) ratio.

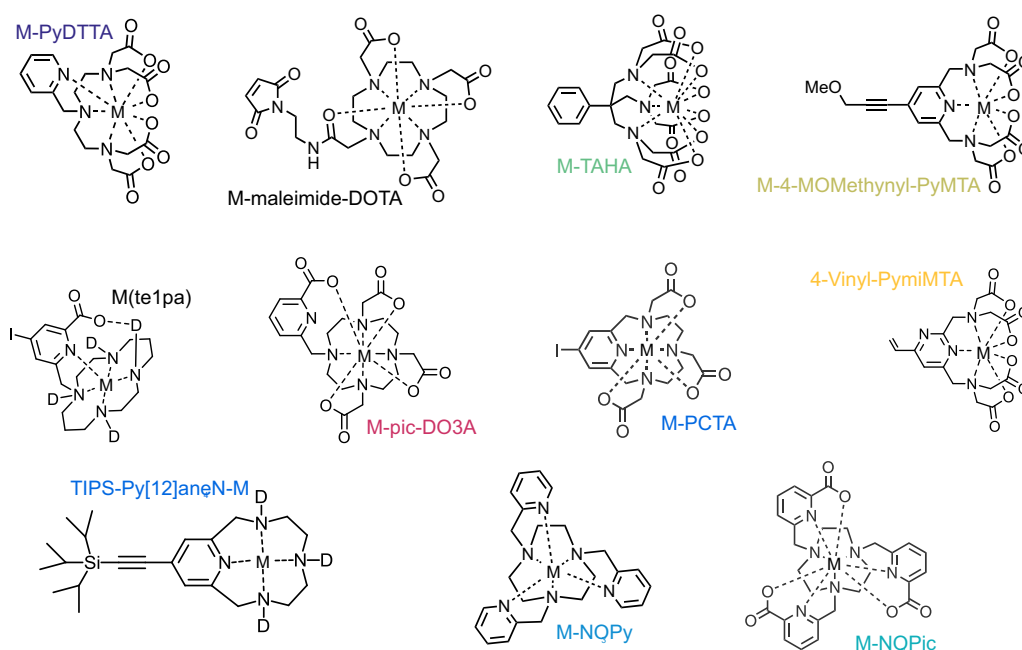


Figure 3.1. Ligands studied in this chapter. The dashed lines mark possible coordination sites. M = Cu, Fe, Co, Mn, Gd.

The same sequence was used to record Hahn echo decay curves by incrementing the initial interpulse delay τ (step size depending on decay rate). Longitudinal relaxation traces were measured using the inversion recovery sequence $\pi - T - \pi/2 - \tau - \pi - \tau - \text{echo}$ as described in Chapter 2.5.4. A soft detection sequence with $t_p = 54$ ns for the $\pi/2$ and $2t_p$ for the π pulse was used in combination with hard inversion pulses. The length of the inversion pulses t_{inv} was adjusted to 8 or 16 ns based on the available microwave power and τ was set to 400 ns (exception for some Fe, Co compounds). The delay T was incremented starting from 600 ns. Relaxation data were acquired at the high-field maximum of the corresponding field sweeps.

CW data were acquired in X band on a Bruker Elecsys E500 spectrometer equipped with a Bruker Elecsys Super High Sensitive probehead and nitrogen flow cryostat. CW derivative spectra (1400 mT field sweep) were acquired at 140 K, 100 kHz field modulation, 4 G modulation amplitude, and 0.2 mW microwave power (30 dB attenuation). The time constant was 40.96 ms and the conversion time 327.68 ms.

Extraction of relaxation times. The characteristic relaxations times T_m and T_1 were extracted from stretched exponential functions $c \cdot \exp[(-t/T_i)^x]$. The fitting procedure was performed as described in Chapter 2.5.2 and 2.5.4. Experimental uncertainties introduced by the dead time and pulse settings were found to be up to 8%, exceeding the fitting errors obtained from 95% confidence intervals. Deviations for different sample preparations due to difference in solvent deuteration level may still be larger in particular for phase memory times T_m .

3.3. Cu(II)-complexes

The EPR spectra of copper complexes exhibit characteristic features based on their electronic structure and common coordination geometries. The electron configuration of Cu(II) is $3d^9$ with a total electron spin quantum number $S = 1/2$. The ground state for Cu(II) in a variety of ligand

fields is essentially spin only and the orbital momentum is said to be 'quenched'⁸⁰ leading to relatively slow relaxation times, as compared to other paramagnetic metal ions. However, due to the presence of ligands, there is a weak admixture of states with non-zero orbital momentum to the ground state of Cu(II). This results in a deviation of the g -values from the free electron $g_e = 2.0023$ and in g -value anisotropy. The stable isotopes of copper (^{63}Cu , ^{65}Cu) have non-zero nuclear spin $I = 3/2$ inducing a hyperfine splitting to the energy levels. The quadrupole interaction is usually not resolved in the EPR spectra. Coordination of the copper nucleus to the surrounding ligands, with commonly axial or rhombic ligand fields, and symmetry breaking by the Jahn-Teller effect cause anisotropy in the g - and A -tensors. Binding to ligands with non-zero nuclear spin, e.g. nitrogen, evokes additional ligand superhyperfine structure, which is, however, not always resolved. A detailed description can be found for example in Ref.⁸⁰. For Cu(II) four-, five- and six-coordinate complexes are common. The favoured coordination number is six, although the consequences of ligand asymmetry or Jahn-Teller effects mean that usually one or two ligands are less strongly bound.⁸⁹

The EPR lineshapes of the studied Cu(II) complexes are found in Figure 3.2 showing commonly observed axial or rhombic symmetries of the g - and A -tensor. The ligand superhyperfine structures and the perpendicular (x/y -) components of the Cu(II) hyperfine tensor are not resolved. With respect to pulsed dipolar spectroscopy, it is immediately noticed that the spectral width is rather broad (> 100 mT in Q band) compared to the commonly used nitroxide (~ 10 mT), which reduces the EPR intensity at any chosen detection position for Cu(II). Because of the g -anisotropy the spectral width of any Cu(II) complex would further increase at higher fields/frequencies. In addition, the larger spectral width makes it impossible to excite the full spectrum (at Q-band frequencies and above), even with the currently available ultra-wideband (UWB) pulses. This can cause orientation selection effects in distance measurements.⁶⁸ Orientation selection makes the analysis of spin-spin distances more challenging, yet, can reveal additional information on the system of interest.⁹⁹ The many coordinating groups offered by most chelators exceed the coordination number of copper and different coordination geometries might be expected. This can be indeed observed by multi-component X-band CW spectra for some of the copper complexes (PyDTTA, TIPS, NO3Py, pic-DO3A) in Figure 3.2(b). These complexes would be problematic for orientation selection experiments due to a more difficult prediction of conformations. Also, presence of more than one conformation in the Cu(II) complex would complicate modelling of the spin-spin distance distributions in case such complexes are used as paramagnetic moieties of spin labels. Note also that some chelators, like Pic-DO3A or PyDTTA have eight or more potential ligand atoms, and could eventually accommodate two Cu(II) ions.¹⁰⁰ One would therefore expect that Cu(II) complexes with spectral features indicating more than one Cu(II) geometry are not well suited as spin labels.

The Hahn echo decays and inversion recovery data for these Cu(II) complexes are shown in Figure 3.3. Table 3.3 gives the corresponding relaxation times. If we consider PDS experiments, the maximal detectable trace length can be approximated to the delay time where 90% of the Hahn echo is decayed (black dashed line in Figure 3.3(a)). On this criterion, te1pa, NO₃Pic, PyDTTA, PyMTA and TAHA show the longest relaxation times (see also Table 3.3 in Section 3.6). For te1pa, time traces up to 120 μs would be feasible at this level of spin echo decay. This corresponds to one full oscillation of the dipolar coupling at distances of about 18 nm. Of the single component complexes, te1pa further outperforms TAHA by faster longitudinal relaxation (Figure 3.3(b)). Note, however, that for all complexes longitudinal relaxation is rather slow at 10

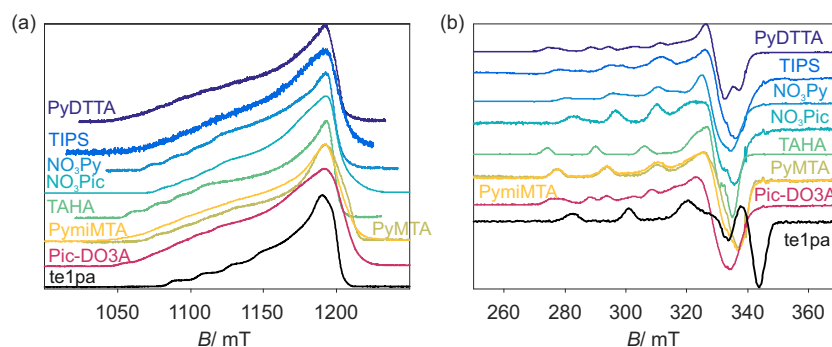


Figure 3.2. EPR lineshapes of Cu(II)-complexes. (a) Q band EDEPR absorption spectra at 10 K. (b) X band CW derivative spectra at 140 K.

K evoking slow repetition rates of the PDS experiments. Thus, higher measurement temperatures might be preferable for copper ions in PDS, whenever shorter transverse relaxation times can be tolerated. An optimization of measurement temperature is presented in Chapter 7 for Cu-PyMTA.

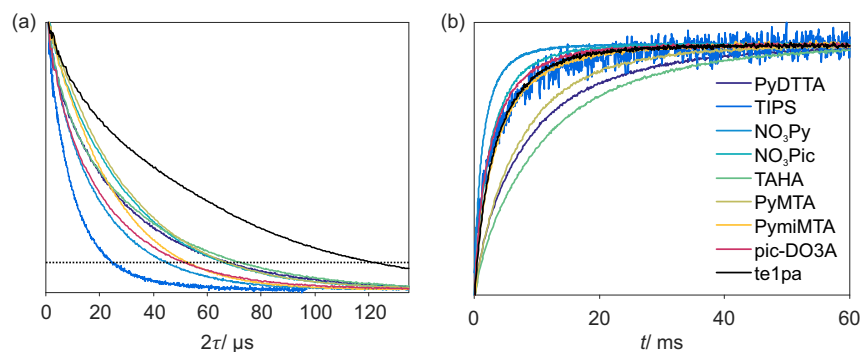


Figure 3.3. Relaxation behaviour of Cu(II)-complexes at 10 K in Q band. (a) Hahn-echo decay. The dashed black line marks the value, where the echo is decayed to 10% of its initial value. (b) Inversion recovery.

Knowledge of spin Hamiltonian parameters, as for example g values, can be important in distance analysis routines. They can be extracted from lineshape analysis or tailored pulse experiments and subsequent simulation. As mentioned earlier, this is beyond the scope of this chapter, but lineshape simulations are described in Chapter 7 for the Cu-PyMTA complex. Experimental data can further be supported by quantum mechanical calculations.

To summarize, in terms of electronic relaxation and orientation selectivity the te1pa-, PyMTA- and TAHA-complexes seem to be most promising with long T_m and just one conformation, as it is suggested by the CW EPR spectra. For the PyMTA-complex a large series of molecular rulers¹⁰¹ has been synthesized and linker chemistry has been established.¹⁰¹ Distance measurements between Cu-Cu spin pairs will be discussed in Chapter 7 at the example of a molecular ruler with PyMTA as coordinating ligand.

3.4. Co(II)- and Fe(III)-complexes

Cobalt and iron complexes can exist in low- and high-spin states depending on the oxidation state as well as on the interplay between spin-orbit coupling, electron-electron Coulomb interaction, and Pauli exchange - favouring the high-spin state - and ligand field interactions which usually favour the low-spin state. The differences in electronic structures for each spin state and coordination

geometry lead to distinct EPR lineshapes. Low-spin complexes are characterized by a smaller g dispersion around $g_e = 2.0023$ (e.g. low-spin Haemoglobin: $g = 1.8, 2.3, 2.6$ or planar low-spin Co(II): $g = 2.3, 2.3, 2$).⁸⁰ For the high-spin states one needs to differentiate half-integer (Kramers ions) from integer spin quantum numbers. For integer spin all levels are split to first order by the zero field interaction (ZFS). In high-spin metal complexes ZFS can be so large that the energy levels splittings exceed the photon energy at the EPR detection frequency and, thus, no EPR transitions can be observed. The paramagnetic metal ion complexes with integer spin are, thus, often 'EPR silent'. Such situations are encountered for Fe(II) and Co(III) ($3d^6$, $S=2$) unless the system is highly axial or very high frequency is available. Note that the low-spin states in these cases are diamagnetic ($S = 0$). For half-integer spins, according to Kramers theorem,⁴² there are at least two ($\pm m_s$) pairs of energy levels that are degenerate in zero field and the electron Zeeman interaction induces an observable EPR transitions. However, due to strong ZFS, transitions can often only be excited within each doublet and the spin system is best described using an effective spin $S' = 1/2$, which induces highly anisotropic g values for the different doublets, e.g. $g_{\parallel} = 2$ and $g_{\perp} = 6$ in iron complexes of axial symmetry.⁸⁰ Therefore, detection of the EPR lineshape can help to differentiate the spin states. A detailed description can be found for example in Refs.^{38;80;85}

Iron has only 2% natural abundance of the ^{57}Fe isotope with non-zero nuclear spin, so that typically hyperfine coupling is not observed. For cobalt, hyperfine couplings are present due to nuclear spin quantum number $I = 7/2$ (^{59}Co , 100% natural abundance). However, due to strains they are often not resolved in frozen glassy solutions.

The studied complexes of Co(II) and Fe(III) exhibit short transverse relaxation times in the order of one microsecond (data not shown), so that only very short time evolution traces can be measured. Further, the echo-detected (ED) EPR absorption spectra shown in Figure 3.4 are rather broad inducing low signal intensities. No EPR-silent complexes are observed. Some species show high-spin signatures, as for instance observed for Fe-TIPS or Fe-TAHA (see Figure 3.4). For the other compounds a high-spin state cannot be excluded from the pulsed EPR measurements at 10 K, because the low-field component can be suppressed due to fast transverse relaxation rates. To differentiate high-spin from low-spin compounds, low-temperature CW experiments can be performed. However, the fast transverse relaxation rates and low signal-to-noise ratio at 10 K make these complexes impractical as resonant spin in distance measurements and detailed analysis of the EPR lineshape is omitted here.

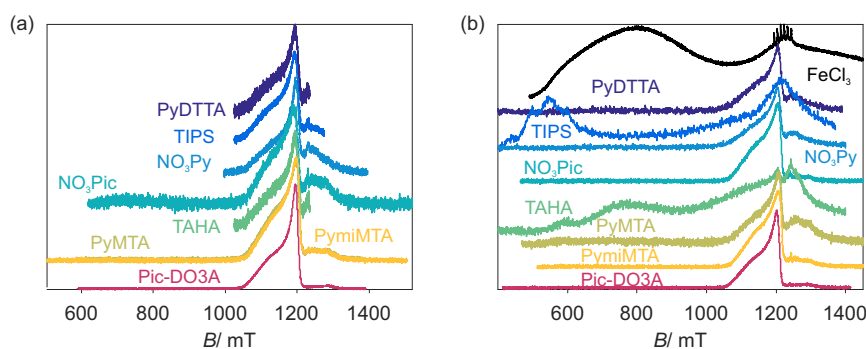


Figure 3.4. Q band EDEPR absorption spectra of (a) cobalt- and (b) iron-complexes at 10 K.

Efficient spin inversion is a requirement for non-resonant, dipolar coupled spins, that can be unlike the excited spins in orthogonal selection schemes. Experiments relying on a pumped spin for inversion, e.g. the DEER experiment, suffer from the broad spectra that implicate low inversion efficiencies with the currently available microwave technology. However, especially low-spin centres, which lead to the absence of higher harmonic overtones in RIDME experiments, might be interesting as a fast relaxing partner in orthogonal, relaxation based distance-measurements due to relatively short longitudinal relaxation times in the order of a few milliseconds (Figure 3.5) and relaxation rates are expected to increase at higher measurement temperatures. In situations where the RIDME technique is no longer feasible, i.e. a significant number of longitudinal spin flips occur during the transverse evolution period τ ($T_1 \ll \tau$), the longitudinal spin relaxation of the discussed Fe(III) and Co(II) complexes might even appear sufficiently fast for use in relaxation enhancement experiments,^{102–104} if at some higher temperature the conditions of the Redfield regime ($\tau_c \ll 1/\delta\omega$, with $\delta\omega$ being the maximum frequency change induced by the motion and τ_c the characteristic correlation time of the motion) could be reached.

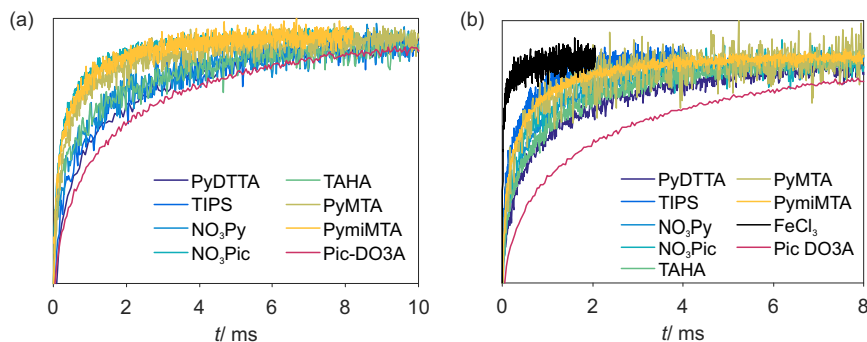


Figure 3.5. Q-band inversion recovery traces of (a) cobalt- and (b) iron-complexes at 10 K.

To conclude, the presented Fe(III) and Co(II) complexes are less suitable for PDS experiments, as compared to Cu(II) complexes. They could be potentially used as, e.g. an additional type of spin label to disentangle biomolecular interactions in complex systems, where several spectroscopically orthogonal spin label types are required. Yet, intrinsically occurring metal ions can be a valuable information source without the need of introduction of a labelling site and methodological developments presented here for other paramagnetic metal centres might be directly applicable to this situation. In consequence, this thesis focussed on Cu(II), Mn(II), and Gd(III) complexes.

3.5. Mn(II)- and Gd(III)-complexes

Mn(II) and Gd(III) are S-state Kramers ions with 5 and 7 electrons in the $3d$ and $4f$ shell, respectively. The half-filled shells make these systems special, as they correspond to an isotropic distribution of the unpaired electrons. These metal ion complexes form a ground multiplet with total angular momentum $L = 0$ and spin $S = 5/2$ for Mn(II) and $S = 7/2$ for Gd(III) and the contribution of the orbital angular momentum to the ground multiplet is weak. This results in the total momentum being approximately equal to the spin momentum ($J \approx S$). Concomitantly, negligible spin-orbit coupling is observed, leading to isotropic g -values close to g_e and relatively weak ZFS. The ZFS interaction lifts the degeneracy of the energy levels into pairwise degenerate levels at zero magnetic field according to Kramers theorem.⁴² The outer transitions are broadened by ZFS to first order in perturbation theory, while the central transition is only affected by

second order and higher. Second order effects scale with D^2/ω_0 , so that a narrowing of the central transition is observed in high-field/high-frequency applications.²⁸ The core-like f -orbitals of Gd(III) lead to little orbital overlap and only rather small hyperfine couplings of ~ 15 MHz are observed for the metal nuclear isotopes $I = 3/2$ with $\sim 30\%$ natural abundance (^{157}Gd , ^{159}Gd).¹⁰⁵ Contrary, the $3d$ -orbitals of isotopically pure ^{55}Mn exhibit a more covalent character and significant isotropic hyperfine couplings (~ 250 MHz) are usually observed and a splitting into six lines is induced by the nuclear spin $I = 5/2$.¹⁰⁶

Experimental Gd(III) data. The Gd(III) EDEPR absorption spectra (Figure 3.6) are characterized by a narrow central transition and a broad envelop caused by the broadening of the outer transitions by ZFS to first order. The zero-field splitting, and thus the appearance of the Gd(III) absorption spectra strongly depend on the type of ligand, being largest for the PyDTTA/PCTA ligands and smallest for the symmetric NO_3Pic ligand.

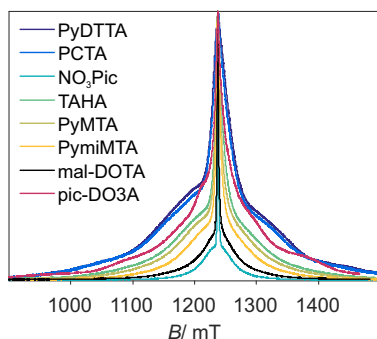


Figure 3.6. Q-band EDEPR absorption spectra of Gd(III) coordinated to different ligands at 10 K.

Figure 3.7 illustrates the effect of second-order perturbation by ZFS to the central transition for three different ZFS values (~ 0.5 GHz - 1.8 GHz) and different external fields (9.5 - 94 GHz). It can be observed that at high field/frequency (~ 94 GHz) the central transition is narrow compared to the broad resonance from the outer transitions, while at low frequencies/field (~ 9.5 GHz) the central transition may no longer be separated from the satellite transitions depending on the particular ZFS of each complex. A detailed analysis of the ZFS parameter distributions in Gd(III) complexes is presented in the succeeding Chapter 4.

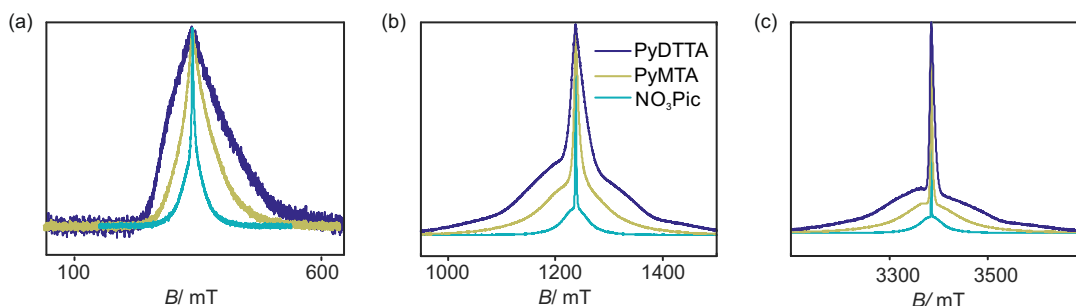


Figure 3.7. EDEPR absorption spectra of different Gd(III) chelates at 10 K in (a) X band (~ 9.5 GHz), (b) Q band (~ 34 GHz) and (c) W band (~ 94 GHz). The ZFS parameters D are given as 1830 ± 105 MHz for PyDTTA (purple), 1231 ± 60 MHz for PyMTA (light green) and 485 ± 20 MHz for NO_3Pic (cyan).

The Q-band transverse and longitudinal relaxation data for $25 \mu\text{M}$ spin concentration are shown in Figure 3.8. It can be observed that the Hahn echo decay is not mono-exponential and that the shape of the decay varies for the different ligands. On average an increase in ZFS

leads to a decrease of the characteristic decay time T_m . This would be in line with the proposed theory of transition dependent ZFS-driven transverse relaxation of Gd(III) complexes.⁴⁷ For the NO₃Pic-complex, potentially, dipolar evolution time traces up to 73 μ s can be measured, indicated by the time when the echo is decayed to 10% of its initial value (black dashed line in Figure 3.8). This corresponds to one full oscillation of the dipolar coupling at distances of about 15 nm. The longitudinal relaxation time does not seem to be strongly influenced by the chelator as shown in Figure 3.8. However, the complexes with smallest ZFS maleimido-DOTA and NO₃Pic show not only slowest transverse, but also slowest longitudinal relaxation rates. Tables of relaxation times are given in Section 3.6. Note that for Gd(III) transverse relaxation times are depending on the detection position (see Chapter 5 or Ref.⁴⁷).

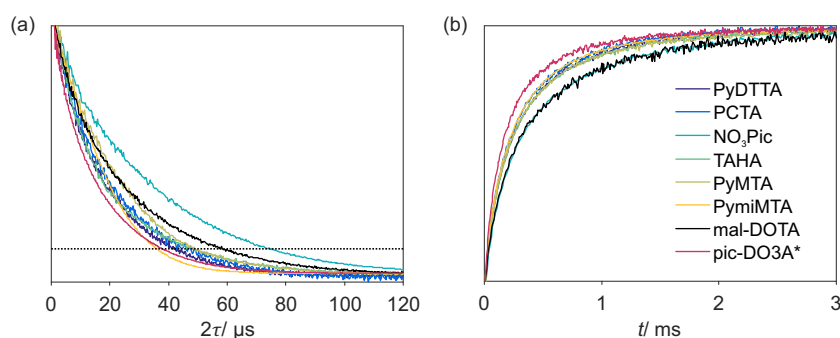


Figure 3.8. Relaxation behaviour of 25 μ M Gd(III)-complexes with different ligands at 10 K in Q band. (a) Hahn-echo decay. The dashed black line marks the value, where the echo is decayed to 10% of its initial value. (b) Inversion recovery. *Note: The concentration of the pic-DO3A complex is 100 μ M.

For the PyMTA complexes, we studied additionally a change in pH and linker group. Assuming that solvation of Gd(III) complexes depends on pH, processes that depend on surrounding solvent molecules may be altered. A change in pH within the biologically relevant range does not have an influence on the spectral shape, as was earlier observed for Gd-DOTA.¹⁰⁷ Here, however, it could be observed that variation of pH from 2 to 12 causes some weak changes in the Gd(III) EPR lineshape, which is an indication of weak variations of the ZFS parameters. Relaxation times that depend on interactions with the environment are also slightly affected by pH. For more acidic solvents a slight decrease of T_m and T_1 is observed as seen in the relaxation curves in Figure 3.9. The observed change is larger for transverse relaxation.

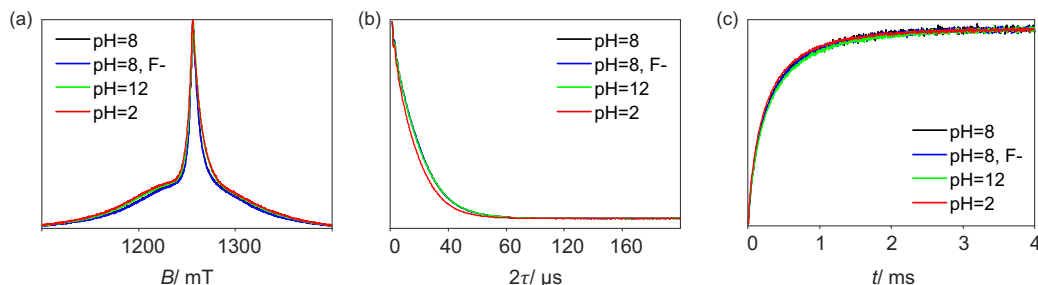


Figure 3.9. Influence of pH on Gd-PyMTA at 10 K in Q band. (a) EDEPR absorption spectra, (b) Hahn echo decay and (c) inversion recovery.

Adding a linker or changes in the linker groups are required for the use of paramagnetic chelates in site-directed spin labelling. Exchanging the MOMethynyl-group with an iodide results in somewhat faster transverse as well as longitudinal relaxation of the Gd-PyMTA-complex. The

absorption spectra are independent of the substitute (Figure 3.10), indicating that the ZFS is mostly influenced by the directly coordinated ligands.

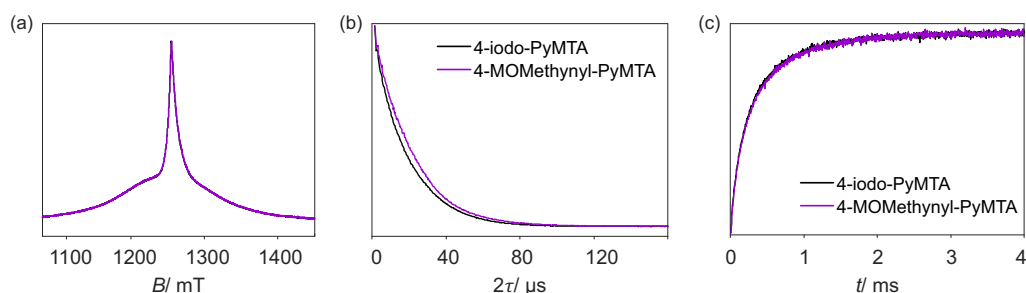


Figure 3.10. Influence of substitutes on Gd-PyMTA at 10 K in Q band. (a) EDEPR absorption spectra, (b) Hahn echo decay and (c) inversion recovery.

Experimental Mn(II) data. Figure 3.12 shows the EDEPR spectra, transverse and longitudinal relaxation for the studied series of Mn(II) complexes. Similar to the Gd(III) complexes, the strength of the ZFS interaction depends on the ligand environment. The isotropic hyperfine coupling splits the central transition into six lines, which is, however, not resolved for all complexes. Small changes in the ligand structure (see Figure 3.11), as for example the substitution of an carboxylate ligand by an α -picolinic in DO3A compared to DOTA, cause deviations of the ZFS as revealed by the changing width of the Mn(II) EPR spectrum.

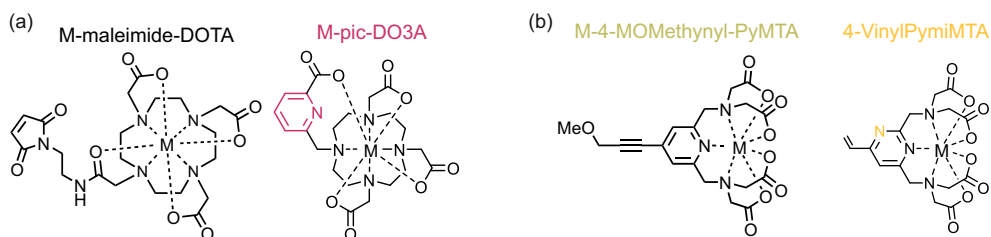


Figure 3.11. Schematic illustration of structure variations in similar ligands. (a) Maleimide-DOTA and pic-DO3A; (b) PyMTA and PymiMTA.

Transverse relaxation is slowest for the DOTA-type complexes and decreasing with increasing ZFS as described earlier for a subset of this complexes in Ref.⁹³. For the maleimide-DOTA complexes the echo decays to about 10% at 70 μ s, so that potentially distances up to 15 nm can be measured in Q band. The characteristic decay times T_m (see Table 3.3) are on the same order as for the Gd(III) complexes. Longitudinal relaxation is about 1.2-3 fold slower than in Gd(III), but still in the sub-millisecond range, which allows for convenient experimental conditions and relatively fast repetition rates at 10 K.

A more detailed study of the Mn(II) relaxation rates at different measurement temperatures, detection bands as well as spin concentration was published for the complexes Mn-maleimide-DOTA, Mn-TAHA, Mn-PyMTA, and Mn-NO₃Py in Ref.⁹³. An important finding for the later discussion and comparison to the Gd(III) complexes is that the transverse as well as longitudinal relaxation did not change significantly between 50 and 100 μ M spin concentration for the Mn-maleimide-DOTA complex, indicating that electron-electron interactions are no longer the main contribution in this concentration range. This allows a qualitative discussion of the differences in relaxation of Gd(III) and Mn(II) even though the different metal ion complexes were not measured at the same spin concentration.

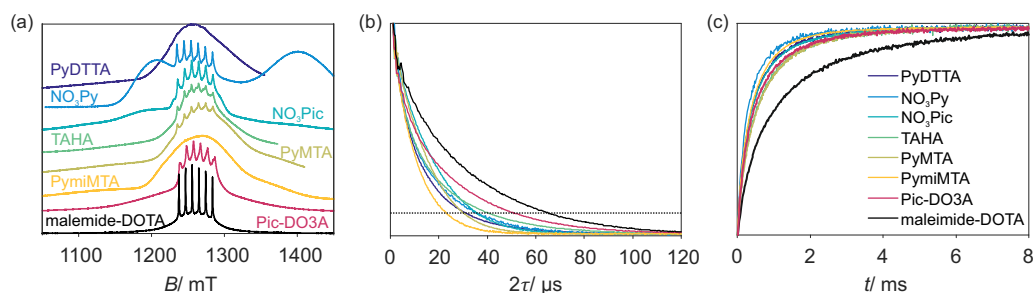


Figure 3.12. (a) EDEPR absorption spectra, (b) Hahn echo decay and (c) inversion recovery of different Mn(II)-complexes studied at 10K in Q band. The dashed black line marks the value, where the echo is decayed to 10% of its initial value.

Echo reduction in Gd(III) and Mn(II). The reduction of the refocused echo upon application of a pump pulse due to the combined action of the Bloch-Siegert^{108;109} and ZFS-dependent mechanisms is known to be particularly strong in orthogonal measurement schemes of nitroxide - high-spin metal centre pairs in Q band.^{110;111} Table 3.2 lists the amplitude of the refocused echo with applied pump pulse with respect to its initial value in absence of the pump pulse. The values were obtained using 12 ns rectangular pump pulses, which were set at an offset of 300 MHz from the observer pulse. The power of the pump pulse, optimized on the metal ions, was increased by 12 dB to mimic for the smaller transition moment of nitroxides. Echo reduction is smaller for Gd(III) in the same ligand and for complexes with larger ZFS, which is an advantage for DEER measurements.

Complex	Mn(II)	Gd(III)
NO3Pic	-	10 (1)
Maleimido-DOTA	-	30 (1)
PyMTA	38 (3)	49 (2)
PyDTTA	32 (2)	53 (3)
TAHA	39 (2)	61 (1)
PCTA	-	66 (1)

Table 3.2. Remaining echo intensity after application of a pump pulse in %. The brackets give the deviation between three measurements.

In summary, the presented Mn(II)- and Gd(III)-complexes are suitable for pulsed dipolar spectroscopy. Relaxation times are of the same order of magnitude for both central ions and complexes with weak ZFS exhibit slower relaxation times, yet, are more prone to echo-reduction. A comparison with respect to different aspects of pulsed dipolar spectroscopy is presented in the next section.

3.6. Comparison of different complexes for pulsed dipolar spectroscopy

Comparison of relaxation times. Although not studied in this chapter, an important point to consider when discussing relaxation data, is that they depend strongly on the measurement temperature, spin concentration and may vary with the detection position within the EPR spectrum. However, a detailed study of the relaxation behaviour depending on microwave band, detection positions as well as measurement temperature would deserve a detailed study for each metal centre, which is beyond the scope of this chapter. In this comparative project for the

different metal ions, the measurement temperature was always set to 10 K and detection was performed at the field position of maximal intensity. It is clear that these are not the optimal conditions for all spin centres, but we think that it does allow us to compare qualitative aspects for different metal centres important in PDS.

The transverse relaxation times of the studied Co(II) and Fe(III) complexes are rather short on the timescale of distance measurements, while relaxation properties of all studied Cu(II), Mn(II) or Gd(III) complexes are sufficient for detecting at least one full period of dipolar oscillation up to 10 nm in pulse EPR experiments. The characteristic relaxation times are given in Table 3.3 and 3.4 for transverse and longitudinal relaxation, respectively. Experimental uncertainty margins (up to 8%), introduced by the dead time and pulse sequence settings, were found to exceed the deviations caused by the fitting routines, while in particular for phase memory times larger errors may be introduced by the solvent deuteration level. Nevertheless, it can be noticed that for the same ligand the relaxation times are longer for Cu(II) than for Mn(II) or Gd(III). A comparison of transverse magnetization for Mn(II) and Gd(III) reveals that for these two metal ions it depends on the type of ligand.

ligand	Cu(II)	Mn(II)	Gd(III)
PyDTTA	25.8 (67.8) {0.86}	9.1 (27.8) {0.75}	17.2 (40.3) {0.98}
NO ₃ Py	16.6 (43.3) {0.87}	9.7 (31.0) {0.73}	-
NO ₃ Pic	28.5 (66.0) {0.99}	16.8 (36.1) {1.09}	32.0 (73.7) {1.00}
TAHA	26.3 (71.2) {0.84}	10.8 (35.9) {0.69}	15.3 (42.7) {0.81}
PyMTA	30.3 (67.0) {1.05}	14.7 (30.5) {1.15}	22.6 (48.9) {1.08}
PymiMTA	24.6 (52.6) {1.10}	9.6 (22.3) {0.99}	19.5 (36.3) {1.35}
pic-DO3A	18.4 (50.3) {0.83}	16.5(49.4) {0.76}	14.2 (36.2) {0.89}
te1pa	55.0 (127) {1.00}	-	-
m-DOTA	-	26.4 (65.9) {0.91}	21.9 (55.8) {0.91}

Table 3.3. Characteristic phase memory relaxation times T_m in μs extracted from a fit of the primary data (Q band, 10 K) by stretched exponential functions of the form $c \cdot \exp(-(t/T_m)^x)$. The time for which the echo amplitude is decayed to 10% of its initial value is given in brackets. Curly brackets give the stretching exponent. Experimental uncertainties (up to 8%) were found to exceed the errors introduced by the fitting routine. In addition, larger errors may be caused by differences in the solvent's deuteration level.

It is also clear that for detection of particularly long distances, the Cu-te1pa would perform best out of all studied complexes. At 10 K and Q band dipolar evolution traces up to 120 μs seem feasible, which would translate into a distance of about 18 nm for one full period of dipolar oscillation. However, longitudinal relaxation times for the Cu(II) complexes are several milliseconds, which leads to slow repetition rates in the experiments and is a disadvantage of using Cu(II) at 10 K. An increase in measurement temperature will accelerate T_1 , but also T_m , so that transverse relaxation of Cu(II) may become comparable to Mn(II) and Gd(III) ions at higher measurement temperatures. For Mn(II) and Gd(III), longitudinal relaxation is sufficiently fast at 10 K, being a factor 1.2-3 faster in Gd(III) than Mn(II) in Q band. Out of these complexes Mn-maleimide-DOTA and Gd-NO₃Pic perform best in terms of transverse relaxation with the 10% echo intensity being reached after about 70 μs , corresponding to one full period of dipolar oscillation at 15 nm. These complexes exhibit smallest ZFS out of the studied compounds and due to the longest relaxation times they are most suitable for measurements of long spin-spin distances. On the other hand, if we consider determining short distances, the complexes with weak ZFS may cause difficulties due to a stronger impact of level crossing on the dipolar signal as was observed in DEER experiments with Gd(III) and Mn(II).^{44;112} In such a situation, complexes

which stronger ZFS are beneficial. The decrease of transverse relaxation should not be problematic in this case as for shorter distances much shorter dipolar evolution traces are sufficient. Note that the level-crossing problem appears to be much weaker in case of the RIDME experiment,^{113;114} chirped DEER experiment¹¹⁵ or the CIDME experiment.¹¹⁶ For metal-metal RIDME experiments additionally the ratio of T_1/T_m is of interest. If $T_1 \sim T_m$, a significant number of spontaneous longitudinal spin flips occur during the transverse evolution periods, which will reduce the RIDME modulation depth and change the background decay properties. Further, coherences that are not transferred to polarization at the beginning of the RIDME mixing block, may survive and induce additional unwanted echoes during detection evoking extended phase cycling schemes. Both effects should be avoided and metal-metal RIDME experiments should be performed at higher T_1/T_m ratios between three and ten.⁹³ The difference in temperature dependence of transverse and longitudinal relaxation may allow for optimization of this ratio.

ligand	Cu(II)	Mn(II)	Gd(III)
PyDTTA	8.3 {0.73}	0.93 {0.67}	0.26 {0.66}
NO3Py	1.3 {0.66}	0.24 {0.62}	-
NO3Pic	2.6 {0.74}	0.38 {0.64}	0.32 {0.61}
TAHA	11 {0.80}	0.50 {0.67}	0.26 {0.65}
PyMTA	7.3 {0.81}	0.54 {0.69}	0.25 {0.63}
PymiMTA	3.6 {0.71}	0.37 {0.69}	0.23 {0.64}
pic-DO3A	2.6 {0.67}	0.42 {0.62}	0.18 {0.62}
te1pa	3.4 {0.73}	-	-
m-DOTA	-	0.99 {0.62}	0.34 {0.60}

Table 3.4. Characteristic longitudinal relaxation times T_1 in ms extracted from a fit of the primary data (Q band, 10 K) by stretched exponential functions of the form $c \cdot \exp(-(t/T_1)^x)$. The stretching exponent x is given in curly brackets. Experimental uncertainties (up to 8%) were found to exceed the errors introduced by the fitting routine.

EPR lineshape. The narrow central line of the high-spin complexes Gd(III) and Mn(II) in Q band and above lead to a high signal intensity of the central transition, which is further improved in complexes with weaker ZFS. The signal intensity is reduced in Mn(II) compared to Gd(III) by the splitting of the central transition into six lines due to the isotropic hyperfine coupling. Consequently, Mn(II) and Gd(III) are particularly advantageous at high fields/frequencies where the g -anisotropy of the Cu(II)-complexes further broadens the spectra. Depending on the particular strength of ZFS, this advantage might be lost at low fields/frequencies of X band or below.

Another consideration connected to the EPR line is the presence of orientation selection. If it should be avoided, Mn(II) or Gd(III) are beneficial as the broadly distributed ZFS parameters in frozen glassy solution lead to the absence of orientation selection effects.^{26;28} On the other hand if it is of interest, rigidly attached Cu(II) tags would provide more information, as parallel and perpendicular orientations can be selectively excited.

All metal centres have in common that the EPR lines are very broad, as compared to nearly any organic radicals, in particular nitroxides, leading to low inversion efficiency with rectangular pulses. The modulation depth can be improved by broadband pump pulses using arbitrary waveform generator (AWG)-technology. In Cu-Cu Q-band UWB-DEER measurements modulation depths of about 30% can be reached as shown in Chapter 7. For Gd(III) a maximum of approximately 20% has been reached in Q band.¹¹⁵ The modulation depth can be further

increased by using longitudinal relaxation for spin inversion as detailed in Chapters 7-9.

Low-spin versus high-spin systems. The theoretical description of spin dynamics and analysis of dipolar evolution data (in the absence of orientation selection) appears much easier for low-spin $S = 1/2$ systems. In high-spin systems additional effects, such as distortions for the ZFS interaction or higher frequency overtones need to be considered. On the other hand, high-spin systems allow for sensitivity enhancement by pre-polarization schemes.¹¹⁷ In addition the larger transition moment of $S > 1/2$ systems allows for excitation with shorter pulses at given power or with lower power at given pulse length, which is particularly important at high fields.

Spin delocalization. The degree of electron spin delocalization over the surrounding nuclei was not directly studied in the course of this chapter, but should be considered when choosing a metal tag as a label for distance determination.⁹⁹ Importantly, the determination of distance distributions from measured dipolar frequencies is not as straightforward in cases of large spin delocalization and requires knowledge of the full spin density distribution.^{76:118;119}

Delocalization is expected to be low in Gd(III), due to the nature of the $4f$ orbitals and a recent study on several Gd(III) chelate complexes revealed an almost exclusive localization of the spin density on the Gd(III) ion.¹²⁰ The authors concluded that the spin density distribution over the nuclei of the ligands can be ignored in the analysis of distance measurements. Similar observations were made for the complexes Mn-maleimide-DOTA and Mn-4-MOMethynyl-PyMTA studied in this chapter.⁹³ ^1H and ^{14}N ENDOR experiments showed negligible proton hyperfine couplings (< 0.2 MHz) and thus negligible spin density on the ligand protons. In combination with small isotropic ^{14}N hyperfine coupling values of 2 MHz, which correspond to a spin density of only about 0.11% on each nitrogen atom, a high spin localization on the Mn(II) ion can be concluded. For Cu(II), spin delocalization has been observed in conjugated systems¹²¹ and should be avoided through the choice of the linker chemistry.²⁷

3.7. Conclusions

The selection of a particular complex for pulsed dipolar spectroscopy depends on several factors and should be considered individually for each particular type of experiment. What is the 'best' spin tag may also depend on the spin-spin distances or on geometric considerations. The optimal measurement conditions, e.g. measurement temperature or detection band, vary for the different complexes and can be optimized for each metal (see for example Chapter 7 for Cu(II)). Factors that should be considered for optimal SNR at a given spin-spin distance (i.e. for a given fixed length of the time trace to be detected) are thermal spin polarization, relative signal intensity at the detection position, longitudinal and transverse relaxation times, and, for metal-metal RIDME experiments, also the ratio of T_m/T_1 .

Furthermore, when selecting a spin tag, electron spin delocalization, its chemical stability, as well as labelling reactivity should be taken into account. These factors were not yet studied for the presented complexes. It is important to note that not all complexes presented in this chapter have linkers ready to attach to a site of interest. Modifying these compounds might induce changes in the ligand field and relaxation properties, however, general trends should remain.

In conclusion, out of the tested metal ion/ligand combinations the complexes of Gd(III), Mn(II) and Cu(II) are most suitable for pulsed dipolar measurements. The Co(II) and Fe(III)

complexes studied herein are found not to be suitable as resonant spins. However, in particular potential low-spin complexes might be an interesting fast relaxing partner in relaxation-based distance measurements due to the absence of harmonic overtones in the RIDME experiment. Cu(II)-based spin labels are an interesting low-spin ($S = 1/2$) system especially at moderate field strength up to Q band. At high-fields, the high-spin centres Gd(III) and Mn(II) appear to exhibit better properties. The spectroscopic properties of these metal ion complexes are sufficiently different to the most commonly used nitroxide-based spin probes allowing for spectroscopic selection schemes.

Quantitative analysis of zero-field splitting parameter distributions in Gd(III) complexes

The magnetic properties of paramagnetic species with spin $S > 1/2$ are parametrized by the electron Zeeman as well as the zero-field splitting (ZFS) terms. The latter one lifts the degeneracy between spin states even in the absence of a magnetic field. In the previous chapter, the ZFS interaction was found to influence EPR properties that are relevant to the performance of distance measurements in Mn(II) and Gd(III) complexes. Thus, reliable extraction of broadly distributed ZFS parameters is important for characterizing such spin systems and is addressed in this chapter. Mean values and distributions of the ZFS parameters D and E for six Gd(III) complexes ($S = 7/2$) are determined and the accuracy of such determination is discussed. EPR spectra of the Gd(III) complexes were recorded in glassy frozen solutions at 10 K or below at Q-band (~ 34 GHz), W-band (~ 94 GHz) and G-band (240 GHz) frequencies, and simulated with two widely used models for the form of the distributions of the second-order ZFS parameters D and E . It was found that the form of the distribution of the ZFS parameter D is bimodal, consisting roughly of two Gaussians centred at D and $-D$ with unequal amplitudes and width σ_D . The extracted values of D (σ_D) for the six complexes are, in MHz: Gd-NO₃Pic, 485 ± 20 (155 ± 37); Gd-DOTA/Gd-maleimide-DOTA, -714 ± 43 (328 ± 99); iodo-(Gd-PyMTA)/MOMethynyl-(Gd-PyMTA), 1213 ± 60 (418 ± 141); Gd-TAHA, 1361 ± 69 (457 ± 178); iodo-Gd-PCCTA-[12], 1861 ± 135 (467 ± 292); and Gd-PyDTTA, 1830 ± 105 (390 ± 242). The extracted $P(D)$ distributions are related to the structure of the individual Gd(III) complexes by fitting them to a model that superposes the contribution to the D tensor from each coordinating atom of the ligand. Using this model, the D , σ_D , and E values are predicted for several additional Gd(III) complexes that were not measured in this work. The results of this chapter may be useful as benchmarks for quantum chemical calculations of ZFS parameters, and point the way to designing Gd(III) complexes for particular applications and estimating their magnetic properties *a priori*.

This chapter is reproduced from Ref.⁹⁵ with permission from the PCCP Owner Societies and edited for consistency: 'J. A. Clayton, K. Keller, M. Qi, J. Wegner, V. Koch, H. Hintz, A. Godt, S. Han, G. Jeschke, M. S. Sherwin, M. Yulikov, Quantitative analysis of zero-field splitting parameter distributions in Gd(III) complexes, Phys. Chem. Chem. Phys., 20 (2018) 10470–10492' where J.A. Clayton and K. Keller contributed equally. M. Qi, J. Wegner, V. Koch and H. Hintz synthesized the Gd(III) complexes under the supervision of A. Godt. K. Keller performed the EPR measurements in Q and W band, worked on the convergence criteria for all models, and performed calculations relating to Model 1. J. A. Clayton performed the 240 GHz

EPR measurements and the rmsd calculations relating to Models 2 and 3. G. Jeschke performed the analysis with the superposition models.

4.1. Introduction

Complexes of trivalent gadolinium have been the focus of numerous electron paramagnetic resonance (EPR) studies over the last decade. The EPR parameters and relaxation properties of Gd(III) complexes are conducive to their exploitation as spin labels in most standard pulsed and continuous wave (CW) EPR experiments. Due to the differing chemical and spectroscopic properties of Gd(III) complexes as compared to nitroxide radicals, some of which are favorable for biological applications, Gd(III) complexes have attracted growing attention for use in site-directed spin labeling (SDSL), as substitutes or partners for the conventional nitroxide-based spin labels.^{26;28;122} Furthermore, Gd(III) ions can be substituted by Dy(III), Tm(III), Tb(III) or Eu(III) ions while keeping the same ligand structure. This offers the possibility to obtain data through pseudo-contact shift (PCS) NMR spectroscopy and luminescence microscopy^{123–127} that are complementary to those obtained with Gd(III)-based EPR spectroscopy.

Gd(III) is a high-spin paramagnetic ion with seven unpaired electrons in the open $4f$ shell, forming a ground multiplet with the total spin of $S = 7/2$. Due to the half-filled $4f$ shell, Gd(III) has a very weak contribution of the orbital angular momentum to the ground multiplet; therefore, the total momentum is approximately equal to the spin momentum ($J \approx S$). The large energy gap between the ground multiplet and the higher energy multiplets is the reason for the slow magnetic relaxation of Gd(III) complexes, as compared to other lanthanide ions. The eight energy levels of the ground Gd(III) multiplet are pairwise degenerate at zero magnetic field according to Kramers' theorem. In the presence of a static magnetic field, there are seven allowed EPR transitions, corresponding to the change of the spin projection onto the magnetic field axis between the upper and the lower energy level of $\Delta m_S = 1$.^{38;128}

For Gd(III) complexes, the lineshapes of individual EPR transitions are dominated by the angle-dependent zero-field splitting (ZFS) term in the spin Hamiltonian, which is due to the interaction of the Gd(III) ion with the ligand (often referred to as crystal field interaction, or CFI), as well as some relativistic corrections and configuration interaction terms arising from the two-electron spin-orbit coupling operators.¹²⁹ Due to the angular dependency of the ZFS, there can arise cases of energy level crossings or resonant conditions, where a single microwave frequency corresponds to two different EPR transitions with or without a level in common. Accordingly, several spectroscopic effects observed for Gd(III) complexes are connected to the mean values and distributions of the ZFS parameters.

In particular, the following effects can be influenced by the details of the distributions of ZFS parameters: distortions of the Gd(III)-Gd(III) distance distributions measured by the DEER experiment at short distance ranges;^{44;113;114;130} population transfer in the Gd(III)-Gd(III) DEER experiment;¹¹⁷ the effect of the reduction of the Gd(III)-nitroxide DEER echo intensity;^{104;110} the width and shape of the central Gd(III) transition, which is relevant for CW EPR-based distance measurements at high fields;¹³¹ the absence of orientation selection for Gd(III) in the DEER experiment;¹³² the transition-dependent transverse relaxation of Gd(III) complexes.⁴⁷

An understanding of these spectroscopic effects requires determination of the ZFS parameters of the Gd(III) complex(es) in use. The current state of quantum chemistry calculations does not allow for the prediction of the ZFS parameters of Gd(III) complexes with a precision sufficient

for EPR applications.¹³³ Computation of ZFS parameters is further complicated by the broad distributions of the ZFS parameters D and E , as typically observed for Gd(III) complexes in glassy frozen solutions. Determination of these parameters through fitting of the EPR spectra is currently the most accurate way of obtaining their spectroscopic information. In this respect, both the quality of the EPR data and the reliability of the fitting procedure are of crucial importance for accurate determination of the distributions of ZFS parameters. Carefully analysed ZFS data, with realistic error bars, would also be required as benchmarks for further developments in quantum chemical calculations, should such developments follow up in the future. The major developments in this direction were done in studies focused on the relaxivities of Gd(III) complexes for magnetic resonance imaging (MRI) applications.^{134;135} These studies used two different models for the distributions of the ZFS parameters, which were based on Gaussian distributions for D and either Gaussian or polynomial distributions for E .

This project has two primary goals. First, we discuss important considerations for choosing models to fit the measured EPR data to extract accurate ZFS parameter values. We do this by using models for the distributions of ZFS parameters as found in the literature to a set of multi-frequency EPR lineshape data. We discuss which features of the EPR spectra and detection frequencies are most useful in determining particular features of the ZFS parameter distribution. In doing so, we offer a realistic estimate of the stability of fits for the ZFS parameter values using simple models for their distributions, and compute typical error bars for the extracted ZFS parameter values. The second goal of this project is to discuss possible correlations between the molecular structures of Gd(III) complexes and their experimentally determined ZFS parameter distributions, which are tested with the aid of the superposition model of pairwise Gd-ligand atom contributions.^{129;134} We propose that the magnitude of the ZFS is correlated with the geometrical arrangement and the type of the donor atoms, i.e., the atoms of the ligands that are in direct contact with the Gd(III) ion. We provide predictions for Gd(III) complexes that were not included in this experimental study which could be verified or falsified in the future, potentially opening an opportunity for an on-paper design of Gd(III) complexes with desired spectral characteristics.

The chapter is organized as follows. First, we present the theoretical framework in which the ZFS parameters are defined, and describe models most commonly used in the literature for the distribution of the ZFS parameters D and E . Next, we describe the six very stable Gd(III) complexes that were chosen to be included in this study. These differ from each other with respect to the number of donor atoms of the ligands, the complex symmetry, and the conformational flexibility of the ligand. We also describe the experimental measurements of Gd(III) spectra in Q (~ 34 GHz), W (~ 94 GHz), and G band (240 GHz), and numeric simulation of Gd(III) EPR spectra including broad distributions for the ZFS parameters in the order of up to two GHz. Procedures for extracting values of the ZFS parameters from experimental measurements and numerical simulations are carefully described. The experimental values for the ZFS parameters D and E are then compared to values predicted by a superposition model for the Gd(III) complexes, whose crystal structures are known, and correlations between the structures of the Gd(III) complexes and the magnitudes and distributions of ZFS parameters are discussed. Finally, we present a general discussion of our findings, a direct comparison of the three models used to describe the distributions of ZFS parameters, simulation and fitting procedures for accurate determination of ZFS parameters, an estimation of the stability of such fits, and typical errors associated with the determined ZFS parameter values.

4.2. Theoretical background

Two out of six stable isotopes of Gd (^{155}Gd and ^{157}Gd) have nuclear spin $I = 3/2$, and together account for about 30% of the total natural abundance. The nuclear gyromagnetic ratios for these isotopes are about 25 times smaller than for ^1H , resulting in a very weak hyperfine interaction between the electron spin and the nuclear spin which is typically ignored in EPR simulations. The other four stable isotopes of Gd (^{154}Gd , ^{156}Gd , ^{158}Gd and ^{160}Gd) have zero nuclear spin. The main contributions to the spin Hamiltonian of an isolated Gd(III) centre are then the electron Zeeman (EZ) interaction and the zero-field splitting (ZFS) interaction. The general form of this spin Hamiltonian in frequency units can be written as follows:

$$\hat{H} = \frac{\mu_{\text{B}}}{h} \left(\vec{B} \cdot \mathbf{g} \cdot \hat{S} \right) + \sum_{k,q} B_k^q \hat{O}_k^q \quad (4.1)$$

In Equation (4.1), μ_{B} stands for the Bohr magneton, h for Planck's constant, \vec{B} for the static magnetic field, \mathbf{g} for the \mathbf{g} -tensor, \hat{S} for the total spin vector operator, \hat{O}_k^q for spin operator equivalents for the corresponding spherical harmonics, and B_k^q for the numeric coefficients for each of the spherical harmonics operators using the extended Stevens operator notation. In the EPR spectral simulations performed in this work, we assume an isotropic \mathbf{g} -tensor that is described by a single g -value of $g = 1.992$. Due to time-reversal symmetry, in the above sum only operators with even rank are allowed non-zero coefficients. For the total spin $S = 7/2$ of the Gd(III) ion, only operators of the rank 2, 4, and 6 are allowed.

In principle, all of the coefficients B_k^q can be determined from EPR data. Such studies were reported for Gd(III)-doped single crystals, where the angular dependencies of EPR transitions could be precisely determined. It was found in these studies that the ZFS parameters were nearly identical among all detected Gd(III) centres within each particular single crystal.^{38;136} In these cases, fitting a rather large number of ZFS coefficients from Equation (4.1) to angle-resolved EPR data produced a reliable output. However, in all reported cases of Gd(III) complexes in frozen glassy solutions, the EPR spectra reveal rather broad distributions of the ZFS parameters.^{26;28;137} In frozen glassy samples, where orientations are isotropically distributed and ZFS parameters broadly distributed, one does not have access to the detailed angle-resolved information provided by EPR spectra of a crystalline sample. Rather, all spin Hamiltonian parameters need to be determined from a single EPR spectrum or from a series of EPR spectra measured at different microwave frequencies. In this case, one cannot expect a stable fit if all of the higher-order operators in the spin Hamiltonian are included.^{134;137}

The modelling of EPR spectra for frozen glassy solutions of Gd(III) complexes is therefore performed under the simplification that only terms quadratic in total electron spin operators are left in the spin Hamiltonian. The commonly used form of the ZFS term in the spin Hamiltonian is given by

$$\begin{aligned} \hat{H}_{ZFS} &= D \cdot \left(\hat{S}_z^2 - \frac{1}{3} S(S+1) \right) + E \cdot \left(\hat{S}_x^2 - \hat{S}_y^2 \right) \\ &= 2D/3 \cdot \hat{S}_z^2 + (-D/3 + E) \cdot \hat{S}_x^2 + (-D/3 - E) \cdot \hat{S}_y^2 \end{aligned} \quad (4.2)$$

where the coefficients D and E are the axial and rhombic ZFS parameters, respectively. We shall focus on this simplified form of the ZFS interaction term for Gd(III) complexes in the following

analysis. This approximation appears to be physically reasonable, as it has been validated on a number of examples of Gd(III) complexes in frozen glassy solutions. For glassy samples, fitted distributions of ZFS parameters typically show a very small fraction of complexes with nearly axial symmetry ($E \approx 0$) and an even smaller fraction of high symmetry cases with $D \approx 0$ and $E \approx 0$, which would be the species for which higher-rank ZFS terms (e.g. 4th and 6th order ZFS terms) become significant.¹³⁴ Given the small fraction of such species in the full ensemble of Gd(III) complexes in frozen glassy solutions, the (D, E) approximation of the ZFS interaction is reasonably accurate.

If the eigenvalues of the ZFS tensor in its eigenframe are given as D_x , D_y and D_z , then the coefficients D and E in Equation (4.2) are defined as $D = \frac{3}{2}D_z$ and $E = \frac{1}{2}(D_x - D_y)$. It follows that

$$D_x = -D/3 + E; D_y = -D/3 - E; D_z = 2D/3. \quad (4.3)$$

By convention, the absolute value of D_y value should lie between the absolute values of D_x and D_z . In other words, the relation

$$|D_x| \leq |D_y| \leq |D_z| \quad (4.4)$$

must hold true.¹³⁸ By this convention, D and E must have the same sign and $|E| \leq |D/3|$. While, generally speaking, the ZFS tensor is not traceless, in the spin Hamiltonian the constant offset is usually removed, since it does not affect the EPR spectra. Thus, for the purpose of lineshape simulations, the ZFS tensor can be assumed traceless, and thus $D_x + D_y + D_z = 0$.

In order to determine the ZFS parameters of a particular Gd(III) complex one needs to fit two distributions, $P(D)$ and $P(E)$, to the measured EPR spectra. As a result of the above definitions, it is convenient to fit for the distribution $P(E/D)$ instead of fitting for $P(E)$ directly, since $P(E/D)$ always assumes the same range of values $0 \leq E/D \leq 1/3$ according to the above convention.

ZFS distributions in Gd(III) chelate complexes are rather broad. It is thus feasible to assume essentially uncorrelated distributions for the eigenvalues of the ZFS tensor. Correlations between D and E values would then only appear due to the above mentioned convention, and the distributions of D and E/D could be assumed to be uncorrelated. It is worth mentioning that similar EPR works were done for other S-state ions, like Fe(III) or Mn(II), and different variants of data analysis, including model-free 1D and 2D fits, correlated or uncorrelated D , E , or E/D distributions, were tested.^{139–145} In this respect, however, one has to keep in mind that for iron and manganese the d orbitals are less compact as compared to the f orbitals of Gd(III). This leads to a stronger covalent character of the metal-ligand interactions in the d element complexes, which also affects strength, distribution widths and correlations of the ZFS parameters. The results of the cited publications, thus, have only restricted relevance to the study presented here.

For the Gd(III) case, fitting many-parameter distributions for D and E (or E/D) is not practical, since such fit would be unstable and likely produce multiple solutions of comparable quality. Since the relatively featureless EPR spectra of Gd(III) complexes suggest broad ranges of ZFS parameters, simple models for the form of the distributions of D and E (or E/D) are often assumed to reduce the number of free parameters in the fit. This problem was tackled in two different ways in the reports of Raitsimring *et al.*¹³⁴ and Benmelouka *et al.*¹³⁵. The models for the ZFS parameter distributions proposed in these works are briefly summarized next. Their

relation to the superposition model for realistic coordination geometries will be discussed in Section 4.5.

4.2.1. Model 1 (*Benmelouka et al.*)

The simplest model for the distributions of D and E in the ZFS term of the spin Hamiltonian (Equation (4.2)) was tested by Benmelouka *et al.*¹³⁵. The authors assumed that the distributions of D and E for Gd(III) complexes in frozen glassy solutions can be described by two uncorrelated Gaussian distributions (drawn schematically in Figure 4.1(a)), which we write here in the standard form:

$$\begin{aligned} P(D) &= \frac{1}{\sqrt{2\pi\sigma_D^2}} \cdot \exp\left(-\frac{(D - \langle D \rangle)^2}{2\sigma_D^2}\right) \\ P(E) &= \frac{1}{\sqrt{2\pi\sigma_E^2}} \cdot \exp\left(-\frac{(E - \langle E \rangle)^2}{2\sigma_E^2}\right) \end{aligned} \quad (4.5)$$

The authors reported reasonably good agreement between EPR spectra of Gd(III) complexes and their simulations with this model for spectra measured in G band, Q band, and X band.^{135;146} Since the D and E values are linear combinations of the eigenvalues of the ZFS tensor, this model essentially assumes Gaussian distributions for the D_x , D_y and D_z values. Note that if these distributions are broad, some combinations of D and E values are non-compliant with respect to the convention in Equation (4.4). Due to this conflict with the convention, the properly re-defined distributions for D and E appear bimodal (sketched in Figure 4.1(b)), as described in more detail in the Results section. Due to the conventional definition described above, in the vicinity of $E/D = 1/3$, small variations in the D_x , D_y and D_z values can shift the position of a point in the D and/or E distributions from the positive to the negative component of the distribution. The bimodality of such distributions is thus a consequence of the convention, rather than a matter of physical significance. In fact, it can be argued that the definitions of D and E combined with Equation (4.4) are not well suited for discussing broadly distributed ZFS parameters, as these definitions lead to a sign discontinuity in D when $|E| = 1/3$. Therefore, after rearranging the D_x , D_y and D_z values according to the convention, we additionally define an unsigned anisotropy Δ and an axiality ξ as

$$\Delta = |D_z| \quad (4.6)$$

and

$$\xi = 2\frac{D_y + D_z}{\Delta} . \quad (4.7)$$

Unlike $P(D)$, the distribution of $P(\Delta)$ has a physically meaningful mean value and standard deviation. The axiality ξ is zero for $E = 1/3$, where the assignment of D_y and D_z , and thus the sign of D_z is undefined, and has an absolute value of 1 for axial symmetry ($E = 0$). The axiality ξ is negative if D_z is negative and positive if D_z is positive. Appendix A.1 provides a more detailed explanation of the characterization of the ZFS parameter distribution by the anisotropy Δ and axiality ξ parameters.

4.2.2. Models 2 and 3 (*Raitsimring et al.*)

Another approach to model the broad distributions of ZFS parameters D and E was suggested by Raitsimring *et al.*^{134;137}. The ZFS parameter distributions were built under the approximation that the ZFS term can be represented as a linear combination of the ZFS contributions from the individual coordinating atoms of the ligand, where each of these donor atoms is assumed to be identical, and contributes an axial ($E = 0$) ZFS of magnitude D directed along the bond between the Gd(III) ion and the donor atom. This model was then incorporated into Monte Carlo simulations where the donor atoms were assumed to have randomly distributed positions on a spherical shell with the Gd(III) ion at its centre. To exclude ligand clashes, any two ligand-metal bonds were restricted to form an angle of at least 60 degrees. This Monte Carlo modelling led to bimodal $P(D)$ distributions, with the centres of the two approximately Gaussian modes of the distribution placed nearly symmetrically with respect to $D = 0$. This distribution was found to well describe EPR spectra for several Gd(III) complexes, even though they could not be physically described by a fully random distribution of ligands around the Gd(III) ion, due to the structures of the chelators. When applying this model to fit experimental EPR spectra, this distribution was simplified to a bimodal Gaussian distribution, in which the positive ($D > 0$) and negative ($D < 0$) modes of the $P(D)$ distribution are assumed to have equal amplitude and width. The distributions $P(E/D)$ were found to be slightly different for the positive and negative modes, but could be approximately described by a polynomial function of the form

$$P(E/D) \propto (E/D) - 2 \cdot (E/D)^2. \quad (4.8)$$

According to Equation (4.8), the maximum of the probability density function $P(E/D)$ corresponds to the value $E/D = 0.25$. At $E/D = 0$ (axially symmetric) the probability density is exactly zero and $P(E/D)$ builds up approximately linearly as E/D for $0 \leq E/D \ll 0.25$ (Figure 4.1(e)). For typical Gd(III) complexes with ligands that offer multiple donor atoms, this model is a rather phenomenological assumption, since not all clash-free arrangements of the donor atoms around Gd(III) ions are physically possible, due to intramolecular bonds. Nevertheless, simulations with this model were found by Raitsimring *et al.* to match well with experimental EPR spectra of a series of Gd(III) complexes.^{134;137}

In order to discuss the effect of the bimodality of the distribution of the ZFS parameter D , we shall consider two versions of the 'Raitsimring distribution'. In Model 2, we fix the relative weights of the positive and negative modes of the $P(D)$ distribution to be equal. In Model 3, we allow different relative weights (amplitudes) for the positive ($D > 0$) and negative ($D < 0$) Gaussian modes of the $P(D)$ distribution, denoted by $P(+D)/P(-D)$. This asymmetry in the bimodal $P(D)$ distribution was observed in the Monte Carlo simulations of Raitsimring *et al.*,¹³⁴ and was found in the present work to be necessary to account for the experimentally observed asymmetry of the Gd(III) EPR spectra at high fields. The $P(D)$ and $P(E/D)$ distributions defined by Models 2 and 3 are sketched in Figure 4.1(c-e).

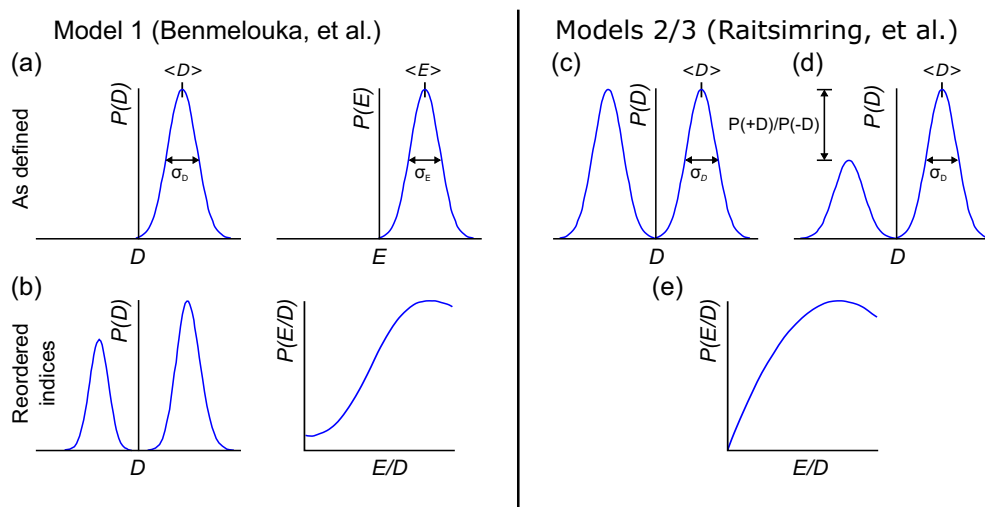


Figure 4.1. Graphical representation of the models used in this work for the distributions of the ZFS parameters D and E (or E/D). (a) Model 1 assumes that $P(D)$ and $P(E)$ are described by two uncorrelated Gaussian distributions. (b) Reshuffling of the indices to correct for the inconsistencies of Model 1 with the conventional definitions of the D and E parameters results in a bimodal Gaussian distribution. (c) Model 2 assumes $P(D)$ is a bimodal Gaussian distribution, where the positive ($D > 0$) and negative ($D < 0$) contributions have equal amplitude and width. (d) Model 3 adds an asymmetry parameter (denoted $P(+D)/P(-D)$) to Model 2, which allows the relative amplitudes of the positive and negative contributions to the $P(D)$ distribution to vary. (e) For Models 2 and 3, $P(E/D)$ follows a polynomial distribution given by $P(E/D) \propto (E/D) - 2 \cdot (E/D)^2$.

4.3. Experimental and computational details

4.3.1. Synthesis of the Gd(III) complexes

The series of the six Gd(III) complexes **1** - **7** (Figure 4.2) was chosen to be included in this work. Gd-DOTA (**2**) was obtained commercially from Macrocyclics and used without further purification. The synthesis details of the complexes Gd-NO₃Pic (**1**), Gd-maleimide-DOTA (**3**), iodo-(Gd-PyMTA) (**4a**), MOMethynyl-(Gd-PyMTA) (**4b**), Gd-TAHA (**5**), iodo-(Gd-PCTA-[12]) (**6**), and Gd-PyDTTA (**7**) are given in the Supporting Information 2 of the published article (Ref. ⁹⁵).

For the complexes iodo-(Gd-PyMTA) (**4a**) and MOMethynyl-(Gd-PyMTA) (**4b**), we assume that the substituents iodo and MOMethynyl do not have a strong influence on the ZFS parameter distributions. This assumption is supported by nearly identical Q-band (34 GHz) spectra (see Appendix A, Figure A.1).

4.3.2. Sample preparation

For Q- and W-band measurements, stock solutions of the Gd(III) complexes were diluted to a final concentration of 25 μM in 1:1 (v:v) D₂O/glycerol-d₈. Sample solutions were filled into 3 mm o.d. quartz capillaries for Q-band measurements and 0.5 mm i.d./0.9 mm o.d. quartz capillaries for W-band measurements and subsequently flash frozen in liquid nitrogen under ambient conditions. For 240 GHz measurements, stock solutions of the Gd(III) complexes were diluted to a final concentration of 300 μM in 0.4:0.6 (v:v) D₂O/glycerol-d₈. Sample solutions of 10 μL volume were loaded into a Teflon sample cup of ~ 3.5 mm i.d. and ~ 5 mm height and subsequently flash frozen in liquid nitrogen under ambient conditions.

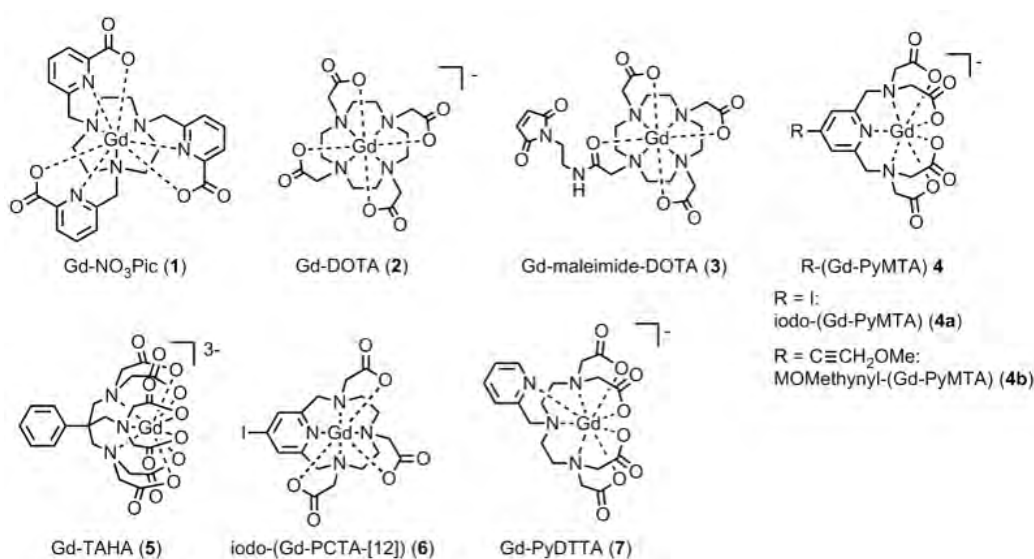


Figure 4.2. Structural formulae and naming of the Gd(III) complexes **1 - 7** which were studied in this work. Please note that in the case of Gd-TAHA (**5**) and Gd-PyDTTA (**7**) no crystal structures are available, and the dotted lines only indicate possible ligand atom-Gd(III) ion interaction.

4.3.3. Q-, W- and G-band EPR measurements

Q-band (~ 34 GHz) measurements were performed on a home-built high-power Q-band pulse EPR spectrometer⁹⁶ equipped with a rectangular cavity accommodating oversized 3 mm outer diameter cylindrical samples.^{97;98} W-band (~ 94 GHz) spectra were recorded on a Bruker Elexsy E680 X-/W-band spectrometer using a TE₀₁₁ resonator. The measurement temperature was stabilized by a Helium-flow cryostat (ER 4118 CF, Oxford Instruments) to 10 K. Echo-detected (ED) field-swept EPR spectra were acquired using the Hahn-echo pulse sequence $t_p - \tau - 2t_p - \tau$ with a pulse length t_p of 12 ns. The interpulse delay τ was set to 400 ns. The power to obtain $\pi/2 - \pi$ pulses of 12 - 24 ns was determined at the central transition of the Gd(III) spectrum by nutation experiments. Resulting Q-/W-band spectra had a constant field and baseline offset removed and were normalized to the maximum for comparison with the simulated spectra.

G-band (240 GHz) EPR measurements were carried out on a home-built spectrometer, as described elsewhere.^{147;148} A solid-state frequency-multiplied source (Virginia Diodes, Inc.) with CW power of ~ 50 mW at 240 GHz was used. Incident microwave power was adjusted as needed by voltage-controlled attenuation of the source and a pair of crossed wiregrid polarizers. The spectrometer operates in induction mode detection with a quasi-optical bridge, superheterodyne detection with a Schottky subharmonic mixer (Virginia Diodes, Inc.), and a home-built intermediate frequency (IF) stage operating at 10 GHz. The IF signal is mixed down to baseband for detection in quadrature with a pair of lock-in amplifiers (Stanford Research Instruments, Inc. SR830).

The Teflon sample cup was backed by a mirror and mounted within a modulation coil at the end of an overmoded waveguide (Thomas Keating Ltd.). No resonant cavity was used. This assembly was then loaded into a continuous flow cryostat (Janis Research Company) mounted in the room-temperature bore of the magnet. Measurements were carried out at a sample temperature of approximately 5 K. Sample temperature was monitored with a Cernox temperature sensor (Lakeshore Cryogenics Inc.), mounted at the end of the waveguide near the sample position.

Recorded sample temperatures for each measurement are given in Table A.5. EPR spectra at 240 GHz were acquired using a rapid passage technique, which is similar in practice to CW EPR but records an absorption lineshape rather than a derivative lineshape.^{135;149;150} Rapid passage EPR measurements were carried out with field modulation at 20 kHz with ~ 0.3 mT modulation amplitude. The main coil of the superconducting magnet (Oxford Instruments), which is sweepable from 0 - 12.5 T, was used to carry out measurements at a sweep rate of 0.1 T/min. Initial calibration experiments with Gd(III) complexes indicated that, given the range of experimental parameters available in this 240 GHz EPR spectrometer, the rapid passage regime could be entered by simply increasing the microwave power when the sample is held at 5 K. Once the microwave power was sufficiently high to achieve a passage regime, a further increase of the applied microwave power resulted only in a change in the SNR of the signal and the saturation of the central $| - 1/2 \rangle \leftrightarrow | + 1/2 \rangle$ transition. Changing the sweep rate of the magnetic field or the modulation frequency and amplitude was found to not affect the transition from the CW to the rapid passage regime for the range of values tested, and therefore these experimental parameters were set so as to optimize SNR. Linearity of the magnetic field over the sweep range was verified with independent measurements using a Mn:MgO field standard.^{151;152} The measured 240 GHz spectra have a constant baseline removed and were normalized to the envelope resulting from the outer EPR transitions for comparison with simulated spectra, as the relatively high powers and fast sweep rates necessary to collect data in the rapid passage regime were found to artificially broaden the very narrow central transition of Gd(III).

4.3.4. Numerical simulations

The EPR spectra of Gd(III) complexes were simulated in MATLAB (The MathWorks Inc., Natick, MA, USA) with home written scripts based on the EasySpin toolbox.⁵⁹ Absorption powder spectra were computed using full matrix diagonalization with the EasySpin function *pepper*. The spin system structure in EasySpin was defined as a single spin $S = 7/2$ with an isotropic g -value of 1.992. The strains for g , D , and E were set to zero in the EasySpin spin system structure. This was done because in the EasySpin package the EPR line broadening resulting from a strain on these parameters is computed using a linear approximation. This linear approximation is sufficiently accurate for small strains, but becomes imprecise for large ones where the strain is comparable to the mean values of D and E . Therefore, all calculations in this work were performed by generating the distributions $P(D)$ and $P(E)$ (or $P(E/D)$) according to one of the three models described in the previous section, computing an EPR spectrum for each pair (D, E) with the EasySpin function *pepper*, and summing these spectra with the weights $W(D, E)$ according to the probability products: $W(D, E) = P(D) \cdot P(E)$. Unless otherwise noted, additional line broadening parameters were set to zero in the simulations.

Orientation averaging was performed in 3 degree increments and a 10-fold interpolation of the orientation grid. The magnetic field range for simulation was chosen to well cover the experimental one, as the EasySpin function *pepper* forces the computed spectra to zero at its boundaries. The number of field points was set to 8000 to reach sufficient convergence. The simulation output was set to separate the subspectra computed for each transition of the $S = 7/2$ spin system. For the 240 GHz spectra, whose data were obtained by rapid passage measurements, the contributions of the individual transitions were summed as is to arrive at the final simulated spectra. For the spectra obtained from echo-detected field-swept EPR measurements (Q/W band),

the contributions of the individual transitions were summed with a weighting factor according to their effective flip angles (Appendix A.3.5).

Two different approaches to the sampling of the $P(D)$ and $P(E)$ ($P(E/D)$) distributions were investigated. First, the distributions of ZFS parameters were sampled using a regular grid of points. Second, a Monte-Carlo approach was used in which a large set of randomly distributed (D, E) pairs was generated and the overall EPR spectrum is computed as a linear combination of the EPR spectra for all of those pairs. It was found in the course of this work that the Monte-Carlo sampling of the $P(D)$ and $P(E)$ (or $P(E/D)$) distributions resulted in the optimal computation cost and avoided unphysical artefacts in the simulated spectra associated with oversampling in the vicinity of the $D = 0$ point of the $P(D)$ distribution. Note that both approaches require careful calibration of the number of random steps in the Monte Carlo scheme, or equivalently, of the step size in the regular grid, in order to reach convergence of the simulated EPR spectrum.

Extensive details of the numerical simulations, including convergence tests, can be found in Appendix A.3. For all simulations presented in the main body of the paper, the Monte-Carlo approach to sampling of the $P(D)$ and $P(E)$ (or $P(E/D)$) distributions was used.

4.4. Results and analysis

The simulated EPR powder spectra of Gd(III) complexes predominantly consist of seven allowed transitions $|m_S\rangle \leftrightarrow |m_S + 1\rangle$, broadened by the anisotropy of the ZFS interaction. According to Kramers' theorem, for a half-integer spin the levels $|\pm m_S\rangle$ are degenerate in zero magnetic field. For weak ZFS (as compared to the EZ interaction) the subspectrum of the central $|-1/2\rangle \leftrightarrow |1/2\rangle$ transition is much narrower than the other transitions of the Gd(III) complex, which primarily contribute to the broad envelope of the total lineshape.¹⁵³ This spectral feature results from the $|-1/2\rangle \leftrightarrow |1/2\rangle$ transition being broadened by ZFS to second (and higher) order of the perturbation series on the $hD/g\mu_B B$ parameter, while the other Gd(III) transitions are broadened to first order by ZFS. Due to this scaling of the width of the $|-1/2\rangle \leftrightarrow |1/2\rangle$ transition with the magnetic field strength, the relative width of this transition with respect to the full width of the Gd(III) EPR spectrum decreases with increasing detection field/frequency.

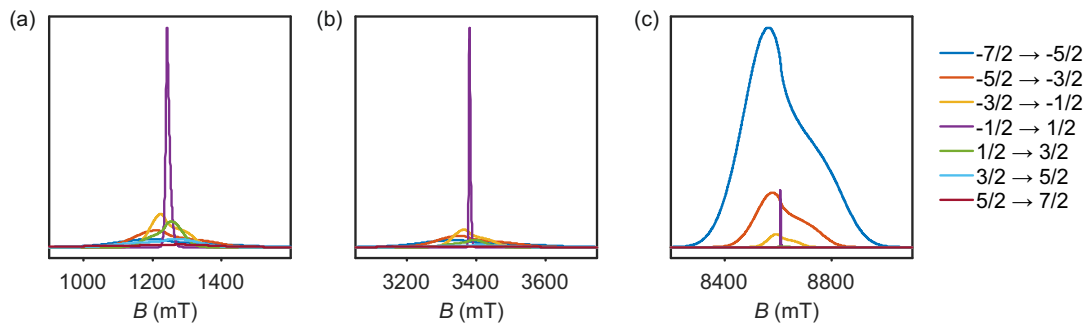


Figure 4.3. Resonance field distributions of allowed EPR transitions as a function of frequency and temperature for an unimodal $P(D)$ distribution with $\langle D \rangle = 1200$ MHz, $\sigma_D = 400$ MHz, and $P(E/D)$ as given in Equation (4.5). (a) Q band and 10 K, (b) W band and 10 K, (c) G band and 5K.

An illustration of this spectral feature is given in Figure 4.3. Note also that at high fields and low temperatures the relative integral intensities of the different Gd(III) subspectra are not equal. At 10 K, the narrow central transition dominates the spectra in Q band (~ 34 GHz) and W band (~ 94 GHz). The increasing relative contribution of the EZ interaction as compared to

ZFS in W band leads to a narrowing and higher relative peak amplitude of the central transition as compared to Q band. A predominant population of the lowest energy levels at 5 K and 240 GHz induces a change in the relative intensities of the different sublevels resulting in the broad envelope of the $|-7/2\rangle \leftrightarrow |-5/2\rangle$ transition subspectrum dominating the Gd(III) spectral shape. The lineshape of this outer transition is most asymmetric with respect to the position of the narrow peak of the central transition with a shift towards lower fields for positive D distributions and towards higher fields for negative D distributions. If both positive and negative modes are present in the $P(D)$ distribution, the remaining anisotropy of the EPR lineshape indicates a difference in the weights of these two modes (e.g. in Model 3).

4.4.1. Model 1

The multi-frequency set of EPR spectra for the six Gd(III) complexes were simulated with Model 1 using visual inspection to obtain an estimate of the parameter space, and so to evaluate the performance of the model. In these initial simulations for Model 1, the variables D , σ_D , E , σ_E , and a small convolutional line broadening term (*Sys.lwpp* in EasySpin) were taken as free parameters. The visually optimized EPR simulations for the complexes Gd-NO₃Pic (**1**) and Gd-PyDTTA (**7**) are shown in Figure 4.4. The analogous simulations for all other complexes are found in Appendix A.8.

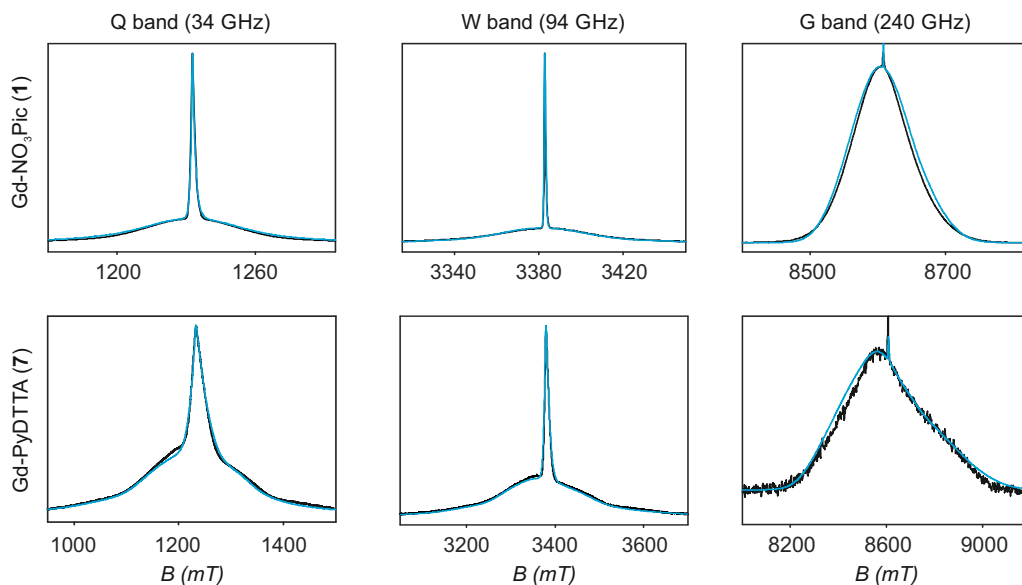


Figure 4.4. EPR spectra (black lines) and corresponding fits (light blue lines) obtained using Model 1 and the ZFS parameters given in Table 4.2 for the complexes Gd-NO₃Pic (**1**) and Gd-PyDTTA (**7**). Q band spectra at 10 K, W band spectra at 10 K, and G band spectra at approximately 5 K.

In the analysis using Model 1, it was found that in certain cases a conflict can arise in the definitions of the distributions $P(D)$ and $P(E)$ as a pair of uncorrelated Gaussian distributions (Equation (4.5)). It has been found in our results and in those reported by other authors^{90;134;135} that the widths (σ_D and σ_E) of the $P(D)$ and $P(E)$ distributions are typically smaller, but comparable to the average values $\langle D \rangle$ and $\langle E \rangle$. In this situation, two uncorrelated Gaussian distributions for $P(D)$ and $P(E)$ produce a large fraction of cases where either D and E have different signs, or where the signs of D and E are the same but the relation $|E| \leq |D/3|$ does not hold. In such cases, one can still formally write Equation (4.2) for any pair of values D

and E and compute the values D_x , D_y , and D_z according to Equation (4.3). However, in order to satisfy the conditions of Equation (4.4), one would have to reshuffle the indices (x, y, z) of the computed D_x , D_y and D_z values. After such an index rearrangement, the D and E values need to be newly computed. The resulting distributions of $P(D)$ and $P(E/D)$ after this index rearrangement are sketched in Figure 4.1(b). An example calculation carrying out this reordering of the $P(D)$ and $P(E)$ distributions is shown for Gd-NO₃Pic (**1**) and Gd-PyDTTA (**7**) in Figure 4.5, with the corresponding ZFS parameters given in Table 4.1. The corrected $P(D)$ and $P(E)$ distributions are both bimodal with different weights of the positive and negative components. The distribution of $P(E/D)$ fully covers the allowed range from 0 to 1/3, with a significant probability density at $E/D = 0$ for some of the Gd(III) complexes (e.g. for Gd-NO₃Pic (**1**) in Figure 4.5). The maximum of the probability distribution $P(E/D)$ appears in the vicinity of the value $\langle E \rangle / \langle D \rangle$. Overlaying the newly obtained D distribution by two Gaussians shows that the maxima are slightly asymmetric with respect to zero and shift towards larger values for the dominant component. Additionally, the widths of the two new Gaussian distributions are reduced compared to the width of the input distribution.

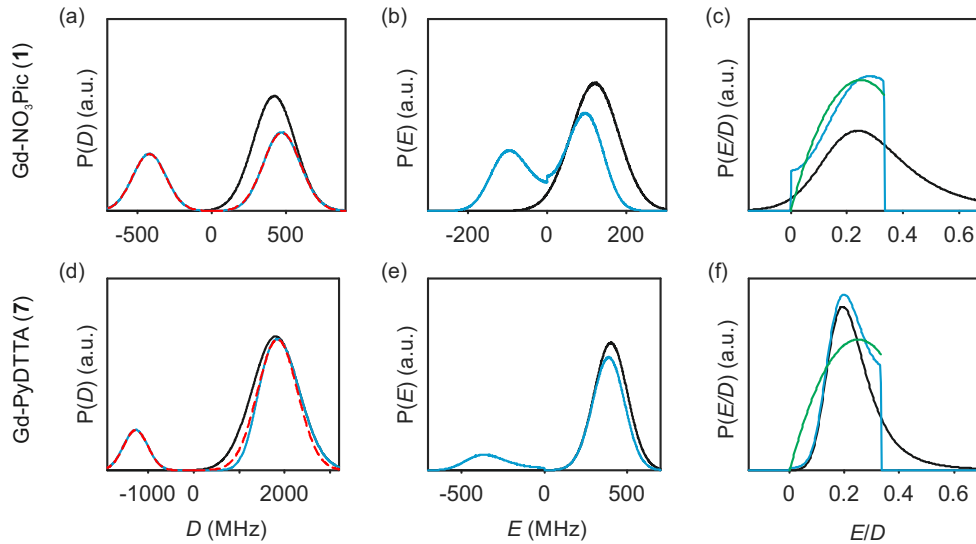


Figure 4.5. Distribution of ZFS parameters for Model 1 as defined in Equation (4.5) (black) and after rearranging of the indexes (x, y, z) of the computed D_x , D_y and D_z values (light blue) for the Gd(III) complexes Gd-NO₃Pic (**1**) and Gd-PyDTTA (**7**). Gaussian distributions are overlaid over the rearranged $P(D)$ distributions (red dashed lines). Distributions are scaled so that the area under the curves integrates to 1. (a, d) $P(D)$ distributions, (b, e) $P(E)$ distributions, and (c, f) $P(E/D)$ distributions. The green line shows $P(E/D)$ defined in Equation (4.8),¹³⁴ used in the simulations with Models 2 and 3 in this manuscript.

Complex	D_{init}	D_{pos}	D_{neg}	$\sigma_{D,\text{init}}$	$\sigma_{D,\text{pos}}$	$\sigma_{D,\text{neg}}$	$\frac{P(+D)}{P(-D)}$
Gd-NO ₃ Pic (1)	420	472	- 418	140	124	111	1.4
Gd-PyDTTA (7)	1800	1845	- 1275	514	439	271	3.3

Table 4.1. Change in $\langle D \rangle$ and σ_D upon reordering the ZFS parameters in Model 1 according to the conventional definition given by Equations (4.3) and (4.4) for Gd-NO₃Pic (**1**) and Gd-PyDTTA (**7**). Units are given in MHz.

Table 4.2 summarizes the ZFS parameter values for Model 1 determined by visual inspection before reordering of the indices. The values obtained after reordering of the indices are given for Gd-NO₃Pic (**1**) and Gd-PyDTTA (**7**) in Table 4.1, and for the remaining Gd(III) complexes in

Table A.6 of the Appendix A. For Model 1, we find that the width σ_D lies between 29-40 % of $\langle D \rangle$ and that $\langle E \rangle$ corresponds to approximately 25% of the value of $\langle D \rangle$ (Table 4.2). The width σ_E is 33-50% with respect to $\langle E \rangle$, which corresponds to the main fraction of the $P(E/D)$ distribution used in Models 2 and 3. For the Gd(III) complexes Gd-NO₃Pic (**1**), R-(Gd-PyMTA) (**4ab**), and Gd-TAHA (**5**), showing rather symmetric EPR spectra, the ratio of E/D is higher than for the complexes Gd-PyDTTA (**7**) and iodo-(Gd-PCTA-[12]) (**6**), which exhibit more asymmetric EPR spectra. Thus, for complexes with rather symmetric EPR spectra a shift of the maximum of the $P(E/D)$ distribution towards $E/D = 1/3$ is observed, while the maxima of the $P(E/D)$ distribution of asymmetric EPR spectra are shifted towards smaller values (see Figure 4.5(c, f)). This observation was discussed previously by Raitsimring *et al.*¹³⁴.

Comparing the corrected $P(D)$ and $P(E/D)$ distributions for Models 1 and 3 (see Appendix A, Figure A.25), we can make a few important notes. First, the corrected $P(D)$ distributions found for Model 1 can be rather closely approximated by the asymmetric bimodal $P(D)$ distribution of Model 3. Note that the widths of the two modes of the corrected $P(D)$ distribution for Model 1 are somewhat smaller than the initial width of the non-corrected single Gaussian distribution. This is important to keep in mind when comparing literature data for ZFS parameter values obtained with Model 1 to the analogous ZFS parameter values obtained with Model 3. Second, the corrected $P(E/D)$ distribution has a minimum probability density at $E/D = 0$ and a maximum probability density around $\langle E \rangle / \langle D \rangle = 0.25$, which is again similar to the $P(E/D)$ distribution in Model 3. However, the overall similarity of the $P(E/D)$ distributions for Models 1 and 3 is not as good as for the $P(D)$ distributions. The maximum of the $P(E/D)$ distribution of Model 1 is not at exactly $\langle E \rangle / \langle D \rangle = 0.25$ but rather deviates from this value by about 15% for the various Gd(III) complexes. Additionally, the probability density at $E/D = 0$ is zero in Model 3, but usually assumes a nonzero value in Model 1.

Models 1 and 3, while differently defined, both appeal to physical intuition. Model 1 appeals to the central limit theorem, which, however, requires the presence of a virtually unlimited number of different randomly distributed donor atom contributions to the $P(D)$ and $P(E)$ distributions in order to be strictly valid. Model 3 appeals to the near equality of ZFS contributions for all ligands and to the non-directional character of the bonds in the Gd(III) complex. Model 3 also includes flexibility to vary the relative weights of the positive and negative modes in the $P(D)$ distribution, while for Model 1 with a given set of D , E , σ_D , and σ_E , the relative weights of the positive and negative mode of the $P(D)$ distribution are fixed. After recognizing that Models 1 and 3 result in rather similar distributions of ZFS parameter values, with some additional flexibility available in Model 3, we turn to a more detailed analysis of the Gd(III) ZFS parameter distributions using Models 2 and 3.

4.4.2. Models 2 and 3

Model 3 was initially investigated by visual inspection to determine ZFS distribution parameters for each of the Gd(III) complexes. The results of this visual comparison of the experimental data with simulated EPR spectra for different (D, σ_D) pairs and $P(+D)/P(-D)$ ratios are given in Appendix A.11. It was observed that for rather broad ranges of the ZFS distribution parameters the correspondence between experimental and simulated data was quite good. In such a case, reporting a single best-fit set of values does not capture this range of possible variations of the ZFS distribution parameters. In order to assign error bars to the determined ZFS parameter values,

we monitored the rmsd between the experimentally determined and the simulated lineshapes over a wide range of ZFS parameter values as follows.

To formalize the determination of error bars on the determined ZFS parameters for Models 2 and 3, we generated a large library of simulated spectra for each measurement frequency and temperature. This library maps out a region of the parameter space spanning values of $D = 300 - 1950$ MHz and $\sigma_D = 50 - 600$ MHz in steps of 50 MHz, chosen so as to include the expected values of these parameters for the Gd(III) complexes studied here, as estimated from our initial investigations by visual inspection. In order to have a common library to query all Gd(III) complexes studied in this work, typical values for the measurement frequency (in Q and W band) and temperature (in G band) were used in place of the exact experimental values for each Gd(III) complex, as detailed in Appendix A (Table A.2). The small measurement-to-measurement deviations in frequency and temperature from these typical values were found to not significantly impact the lineshape of the simulated EPR spectra, and hence are not expected to alter the final determined ZFS parameter values. For this library of simulations, the contributions to the lineshape from each transition and from the positive and negative modes of the $P(D)$ distribution according to Models 2 and 3 were saved separately. In this way, the same library may be used for both Models 2 and 3, by either summing these contributions as is, or by adding a weighting term denoted $P(+D)/P(-D)$ which introduces an asymmetry in the $P(D)$ distribution for Model 3. Further details of the inputs used to generate the library of simulated spectra can be found in Appendix A.5.

Each lineshape in the library of simulated spectra was compared to the data at the corresponding frequency by scaling the amplitude of the simulation to best fit the baseline-corrected experimental data in a least-squares sense. The rmsd between each simulation and the experimentally obtained data was then computed according to

$$rmsd = \sqrt{\frac{1}{n} \sum_{i=1}^n (sim(i) - dat(i))^2} \quad (4.9)$$

where n is the number of points of the measured EPR lineshape.

For all three models, the contribution from complexes with very small ZFS (corresponding to the region of the $P(D)$ distribution near $D = 0$) is still sufficiently large to produce a sharp feature in the vicinity of the Gd(III) g -value position in the simulated EPR spectra. This results in the models predicting a sharper feature than is experimentally observed in the field range spanning the middle of the central peak of the Gd(III) EPR spectrum (see Appendix A.3.4). It is rather difficult to define precisely the field range where this distortion of the shape of the central peak is significant, since no clear 'kinks' are observed between the middle and the outer parts of the central transition. This overly sharp feature in the simulated spectra can be smeared out by introducing an intrinsic linewidth as a 'beautifying parameter' (see Appendix A.3.4). However, in the rmsd analysis with Models 2 and 3 we attempted to avoid introducing additional free parameters into the fit. As an alternative and straightforward approach, we completely excluded the region of the central transition of the EPR spectra from the fit. The parts of the spectra in the remaining field ranges to the left and to the right of the central peak region were then used to compute the rmsd error.

The dependence of the rmsd on the D and σ_D values input in the simulation can be visualized as rmsd error maps (e.g. shown for Model 2 and the Gd(III) complexes Gd-NO₃Pic (**1**) and

Gd-PyDTTA (**7**) in Figure 4.6), where the lines represent contours of constant rmsd and the asterisk denotes the value of D and σ_D with the minimum rmsd value on the 50 MHz grid of ZFS parameter values at the given EPR frequency. Each plotted contour line represents a doubling of the minimum rmsd value. rmsd error maps for all of the Gd(III) complexes fitted with Model 2 with the region about the central peak excluded are given in the Appendix A (Figure A.10).

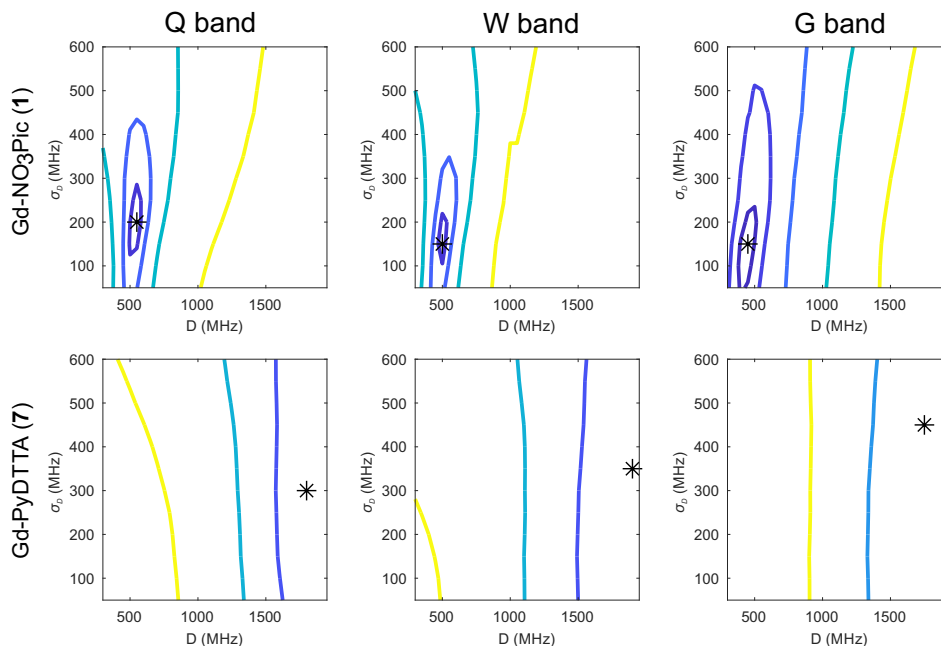


Figure 4.6. Contours of constant rmsd as a function of D and σ_D parameter values using Model 2 for the complexes Gd-NO₃Pic (**1**) and Gd-PyDTTA (**7**) in Q band and 10 K, W band and 10 K, and G band and 5 K. Simulated spectra were normalized to the experimental data using only the outer shoulders of the spectra. The asterisk denotes the set of parameter values available in the library of simulated spectra which has the minimum rmsd value for each measurement frequency. Each contour line represents a doubling of this minimum rmsd value.

It should be noted that in this work and in studies reported in the literature,^{134;135} one attempts to describe the ZFS interactions in an ensemble of Gd(III) complexes using a simplified model for the ZFS parameter distributions. While these simplified models seem to be reasonably accurate, as evidenced by the rather good fits to the experimental data, this does not necessarily mean that the given model accurately describes the physical system. Such an inadequacy is implied in the deviation of the best fit simulations exceeding the noise level of the experimental data. This means that the minimum rmsd between experimental and simulated EPR spectra will not approach zero even for EPR spectra with extremely high signal-to-noise ratio (SNR). Additionally, the D and σ_D values corresponding to the minimum rmsd value in the contour plots are not exactly identical for the three tested microwave bands, again indicating the approximate nature of these models. Therefore, while it is possible to characterize the precision of the determined ZFS parameter values within a model, it is not possible to ascertain the physical accuracy of these values in an absolute sense.

To obtain a conservative estimate for the precision of the determined ZFS parameter values, we look for the variations of ZFS parameters around the best fit values and take as an acceptable fit those values which result in an rmsd less than twice the minimum rmsd value. If the problem was linear and the rmsd dominated by noise, this choice would correspond to a 95% confidence interval. The first contour line about the minimum rmsd value gives the region where the rmsd

doubles, as shown in e.g. Figure 4.6, and this is consistently done for all other contour plots in this work. However, the 50 MHz grid of ZFS parameters available in the library of simulated EPR spectra is a somewhat coarse sampling of these parameter values, particularly for complexes with small ZFS. In order to interpolate the ZFS parameter values on this grid, we make the assumption that the contour bounding the region of twice the minimum rmsd value should be smooth given arbitrarily fine sampling of D and σ_D values. Therefore, we estimate this contour by fitting an ellipse, from which the best fit values of D and σ_D is taken to be given by the centre of an ellipse fit to this first contour line. The errors on the D and σ_D parameters are given by the lengths of the semi-minor and semi-major axes of the fitted ellipse. Taking a weighted average of the so-determined values for D and σ_D and their associated errors at each frequency (Appendix A.6) gives our final results with Model 2, as summarized in Table 4.2.

The contour plots show that the value of D is rather well constrained for Model 2, and thus its actual physical value most likely does not deviate from the best-fit value for Model 2 by more than 10%. By comparison, the σ_D value is less well constrained in the fits with Model 2. In particular, for iodo-(Gd-PCTA-[12]) (**6**) and Gd-PyDTTA (**7**), the contour plots suggest that the σ_D value can assume essentially any allowed value. For the Gd(III) complexes with weaker ZFS, Gd-NO₃Pic (**1**) and Gd-DOTA (**2**)/Gd-maleimide-DOTA (**3**), the σ_D value is somewhat better constrained by the fit. But even in the best case of Gd-NO₃Pic (**1**) in W band, the σ_D value varies by $\pm 30\%$ within the area encompassed by the contour curve bounding the region of twice the minimum rmsd (Figure A.10).

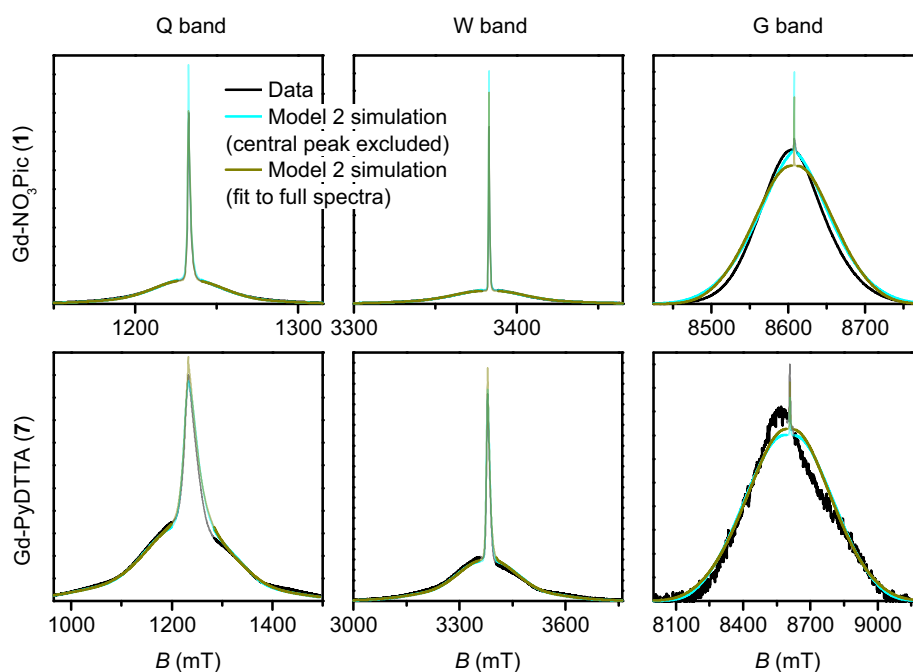


Figure 4.7. Simulations using the best-fit ZFS parameters for Model 2, with and without the region of the central transition included in the rmsd error map analyses, for the complexes Gd-NO₃Pic (**1**) and Gd-PyDTTA (**7**).

Two examples of the EPR spectra simulated at the three microwave bands using the determined best-fit ZFS parameters for Model 2 (Table 4.2) are shown in Figure 4.7 for the complexes Gd-NO₃Pic (**1**) and Gd-PyDTTA (**7**). Full results for all the other Gd(III) complexes can be found in the Appendix A.9. For EPR spectra in Q band and W band, Model 2 gives quite

reasonable fits of the experimental data, despite the fixed equal ratio between the positive and negative modes of the $P(D)$ distribution. Note that the position and width of the central peak is rather well reproduced by the simulation in Q band and W band, even though the region of this peak was excluded from the fit. However, the spectra measured in G band show strong deviations between the experimental data and their respective fits with Model 2.

Model 3 is similar to Model 2, but with an additional allowance for the optimization of the relative contributions from the positive and negative modes of the $P(D)$ distribution. The asymmetry of such a distribution can be defined by the ratio between the two amplitudes of the positive and negative modes of the $P(D)$ distribution, which we denote $P(+D)/P(-D)$. Note that $P(+D)/P(-D) < 1$ in Model 3 corresponds to $D < 0$ in Model 1 (case of Gd-DOTA, see Table 4.2), whereas $P(+D)/P(-D) > 1$ in Model 3 corresponds to $D > 0$ in Model 1 (all other complexes). The asymmetry $P(+D)/P(-D)$ was determined by fixing the mean of D to the closest available value in the library of simulations to that determined using Model 2 (Table 4.2) and then varying $P(+D)/P(-D)$ to find the best fit to the G-band data where the asymmetry in the EPR spectra is most prominent. We additionally attempted to determine $P(+D)/P(-D)$ using the Q-/W-band data, but these spectra were not sufficiently sensitive to variations in this parameter to assign a best-fit value. It is interesting to visualize the effect of this parameter with rmsd contour plots of varying $P(+D)/P(-D)$ and σ_D values, e.g. for Gd-NO₃Pic (**1**) and Gd-PyDTTA (**7**) in Figure 4.8. Contour plots are given for all of the Gd(III) complexes in the Appendix A (Figure A.13). In the following calculations with Model 3, we use the optimal $P(+D)/P(-D)$ values as determined by the σ_D and $P(+D)/P(-D)$ contour plots for consistency. Once the asymmetry parameter $P(+D)/P(-D)$ was determined via the minimum rmsd value in this error map, that value was fixed and the (D, σ_D) rmsd error maps were recomputed for the three microwave bands to find the best-fit values of these parameters.

It appeared that an error estimate by the parameter range bounded by a contour of twice the minimum rmsd may not be reasonable for the asymmetry parameter $P(+D)/P(-D)$ in Model 3. The most obvious effect of this parameter on the EPR spectra is to set the relative position of the broad component of the spectrum with respect to the sharp central peak corresponding to the $| -1/2 \rangle \rightarrow | 1/2 \rangle$ transition. This is because the width of this central peak is so narrow compared to the broad component of the 240 GHz EPR spectrum that it has a relatively small impact on the overall rmsd of the fit, though there is enough effect on the rmsd to assign a position of minimum rmsd in a contour plot of $P(+D)/P(-D)$ and σ_D (e.g. in Figure 4.8), as was done to determine the other parameter values for Models 2 and 3. It was found that the separation between the sharp central transition and the peak of the broad component of the 240 GHz EPR spectra varies approximately linearly with the determined $P(+D)/P(-D)$ values. This was used to estimate a typical deviation of 0.34 for the value of the $P(+D)/P(-D)$ parameter (Appendix A.11), though this varied for the different Gd(III) complexes. Practically, it was found to be difficult given the available data and models to assign an accurate ratio for the relative contributions of these two components of the $P(D)$ distribution.

The final best-fit ZFS values from Model 3 with the region about the central peak excluded from the analysis are presented in Table 4.2, and the corresponding simulated spectra presented with the full dataset in Figures 4.9 and 4.10. Including an asymmetry in the $P(D)$ distribution helped to slightly better constrain the range for the σ_D values, but did not significantly alter the best-fit for the D and σ_D values (Figure 4.11). For the Q-band and W-band spectra, the minimum rmsd of the (D, σ_D) contour plots was not significantly altered by the addition of the

Model	Complex	D (MHz)	σ_D (MHz)	$\frac{\sigma_D}{D}$	$\frac{P(+D)}{P(-D)}$	E (MHz)	σ_E (MHz)	$\frac{\sigma_E}{E}$	$\frac{E}{D}$	lwpp (mT)
1	Gd-NO ₃ Pic (1)	420	140	0.33	—	120	60	0.50	0.29	[0.5 0]
	Gd-DOTA (2)/ Gd-maleimide-DOTA (3)	-600	240	0.40	—	150	75	0.50	0.25	[1.0 0.1]
	R-(Gd-PyMTA) (4a,b)	1070	357	0.33	—	306	153	0.50	0.29	[0.8 0]
	Gd-TAHA (5)	1250	417	0.33	—	357	119	0.33	0.29	[0.6 0]
	iodo-(Gd-PCTA-[12]) (6)	1780	508	0.29	—	396	132	0.33	0.22	[1.0 0.1]
	Gd-PyDTTA (7)	1800	514	0.29	—	400	133	0.33	0.22	[2.0 0.1]
	Gd-NO ₃ Pic (1)	500 ± 19	169 ± 52	0.34	—	—	—	—	—	[0 0]
2	Gd-DOTA (2)/ Gd-maleimide-DOTA (3)	652 ± 44	409 ± 200	0.63	—	—	—	—	—	[0 0]
	R-(Gd-PyMTA) (4a,b)	1263 ± 112	350 ± 109	0.28	—	—	—	—	—	[0 0]
	Gd-TAHA (5)	1335 ± 75	408 ± 178	0.31	—	—	—	—	—	[0 0]
	iodo-(Gd-PCTA-[12]) (6)	1845 ± 194	400 ± 289	0.22	—	—	—	—	—	[0 0]
	Gd-PyDTTA (7)	1810 ± 173	367 ± 289	0.20	—	—	—	—	—	[0 0]
	Gd-NO ₃ Pic (1)	485 ± 20	155 ± 37	0.32	1.8	—	—	—	—	[0 0]
	Gd-DOTA (2)/ Gd-maleimide-DOTA (3)	714 ± 43	328 ± 99	0.46	0.3	—	—	—	—	[0 0]
3	R-(Gd-PyMTA) (4a,b)	1213 ± 60	418 ± 141	0.34	1.6	—	—	—	—	[0 0]
	Gd-TAHA (5)	1361 ± 69	457 ± 178	0.34	1.9	—	—	—	—	[0 0]
	iodo-(Gd-PCTA-[12]) (6)	1861 ± 135	467 ± 292	0.25	3.6	—	—	—	—	[0 0]
	Gd-PyDTTA (7)	1830 ± 105	390 ± 242	0.21	3.6	—	—	—	—	[0 0]
	Gd-NO ₃ Pic (1)	485 ± 20	155 ± 37	0.32	1.8	—	—	—	—	[0 0]

Table 4.2. Extracted D and E values using Model 1 including an additional Voigtian line broadening lwpp ([Gaussian Lorentzian]), extracted D and σ_D values using Model 2 with the region about the central peak excluded from analysis, and extracted D , σ_D , and $P(+D)/P(-D)$ values using Model 3 with the region about the central peak excluded from analysis. For the complexes Gd-DOTA (2)/Gd-maleimide-DOTA (3) fit by Model 3 we find $P(+D)/P(-D) < 1$, and thus assume a negative sign for the mean D value. Note that the values reported for Model 1 are the D and σ_D values before reordering of the indices (the corresponding values after reordering can be found in the Appendix A, Table). The bold font indicates the overall best-fit parameters from the three models which were used for calculations with the superposition model. Estimated errors on $P(+D)/P(-D)$ values are ± 0.34 . The corresponding values of mean absolute ZFS magnitude $|\overline{D}| = 3\Delta/2$ and mean ZFS axiality ξ can be found in the Appendix A, Table A.9.

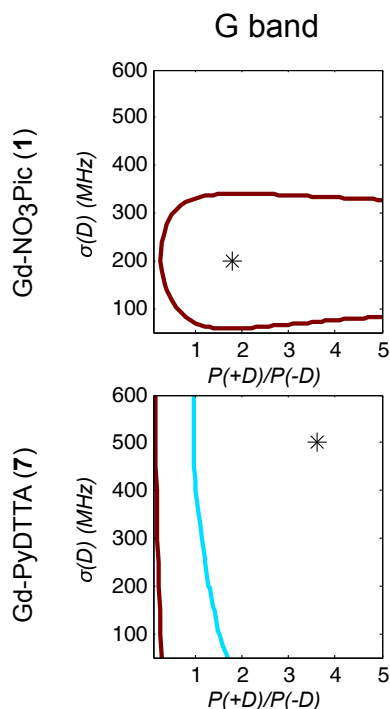


Figure 4.8. Contours of constant rmsd as a function of $P(+D)/P(-D)$ and σ_D parameter values using Model 3 and the complexes Gd-NO₃Pic (**1**) and Gd-PyDTTA (**7**) in G band and 5 K. The mean values of the ZFS parameter D were set to $D = 500$ MHz and $D = 1800$ MHz, respectively, corresponding to the closest D value available in the library of simulations to the D value as determined by Model 2 for these complexes (Table 4.2). The asterisk denotes the position of minimum rmsd.

asymmetry parameter. For the G-band data, which displays the greatest degree of asymmetry in the measured spectra, the minimal rmsd value in the contour plots decreased by more than a factor of two in some cases with the addition of the $P(+D)/P(-D)$ parameter in Model 3 compared to the fits using Model 2 (see Appendix A, Figure A.22).

We next investigated what changes would be induced by including the region of the central peak into the rmsd error map calculations. The rmsd contour plots, best-fit ZFS parameter values, and the corresponding best-fit spectra for Models 2 and 3 when including the full EPR spectra in the analysis are given in Appendix A.12. In general, the deviations in the lineshape in the region of the central peak lead to larger overall rmsd values as a result of the larger intensities in this portion of the spectra (Figure A.22). When the region of the central peak is included in the fit it dominates the rmsd for complexes with small ZFS. Even for complexes with large ZFS, the central transition still strongly affects the fit despite being broadened and thus displaying lower relative peak intensity. We additionally find that the range of D values within the doubled minimal rmsd curve is increased due to the large increase of the minimal rmsd value. This effect is clearly visible in the W-band data for Gd-NO₃Pic (**1**), Gd-maleimide-DOTA (**3**), and MOMethynyl-(Gd-PyMTA) (**4b**), and is much less pronounced for the complexes with larger ZFS.

For Gd(III) complexes with small D values, the central peak is fit well at the expense of an enhanced discrepancy between the simulated and experimental lineshapes of the shoulders of the Gd(III) spectrum (e.g. for Gd-NO₃Pic (**1**) in Figure 4.7). This results in an order of magnitude increase of the minimal rmsd values in the Q-/W-band fits when the full spectra are used, compared to when the region of the central transition is excluded (Figure A.22). This effect

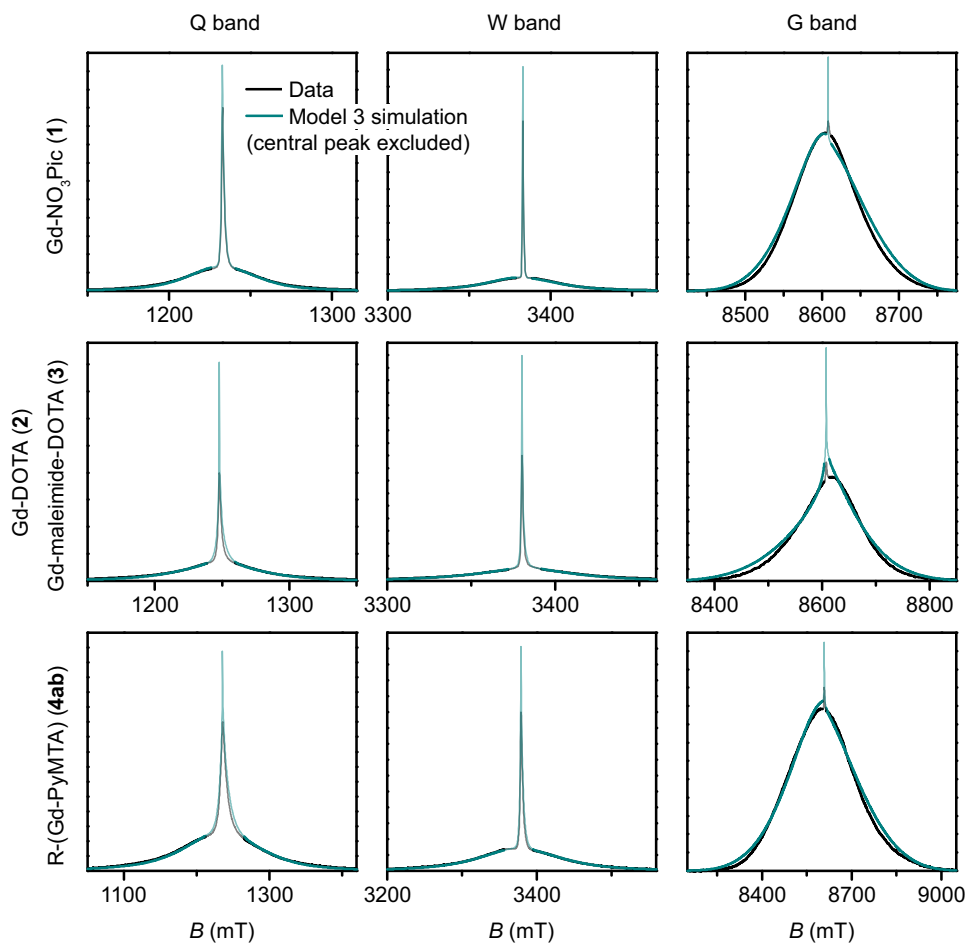


Figure 4.9. Measured EPR spectra in Q band, W band, and G band for the Gd(III) complexes Gd-NO₃Pic (1), Gd-DOTA (2) (G-band spectra)/Gd-maleimide-DOTA (3) (Q-/W-band spectra), and iodo-(Gd-PyMTA) (4a) (G-band spectra)/MOMethynyl-(Gd-PyMTA) (4b) (Q-/W-band spectra). Overlaid are simulations with Model 3 using the best-fit ZFS parameters presented in Table 4.2. The faded regions indicate the portion of the spectra about the central transition which was excluded from the rmsd error map calculations.

is less dramatic in the fits to the G-band data, where the central peak constitutes a much smaller fraction of the overall EPR spectrum. For the Gd(III) complexes with the largest D values, we still obtain minimal rmsd values that are about twice as large when the central transition is included, even in G band. Unfortunately, the relative strength of the artefact due to contributions in the simulated spectra from D values near $D = 0$ also changes with a change of ZFS distribution parameters. The rmsd contour plots computed with the central transition region included will also be affected by this change.

Despite these complications, the best-fit D and σ_D values for Models 2 and 3 did not change significantly upon inclusion of the region of the central transition (Figure 4.11). Furthermore, the best-fit D and σ_D values were found to be consistent across all three models tested. Note that for Model 1, uncorrected D and σ_D values show some deviation from the best-fit values determined by Models 2 and 3 (Figure 4.11), however if the corrected bimodal $P(D)$ distributions calculated for Model 1 are instead compared, then the mean D value and the width σ_D of the more intense component of the corrected distribution matches even better with the best fit D and σ_D values for the Models 2 and 3 (see Appendix A, Figure A.25 and Table A.6 for values). However, despite the observation that the inclusion of the region of the central transition does not largely affect the

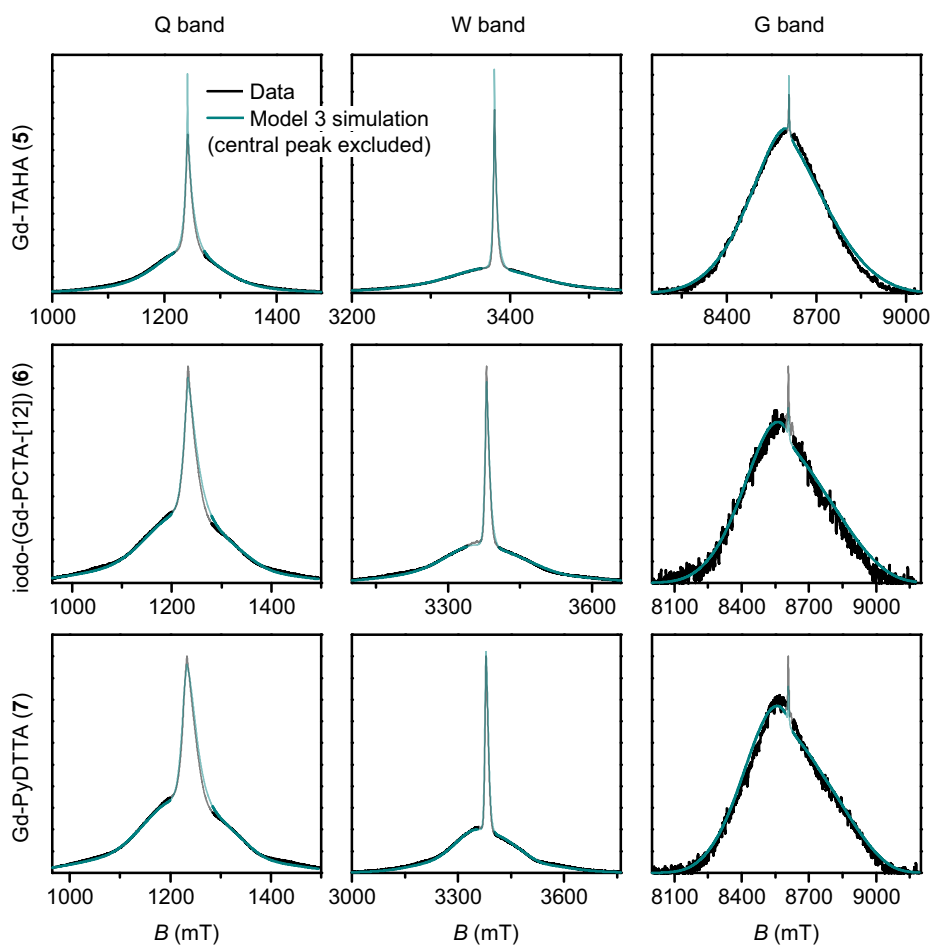


Figure 4.10. Measured EPR spectra in Q band, W band, and G band for the Gd(III) complexes Gd-TAHA (5), iodo-(Gd-PCTA-[12]) (6), and Gd-PyDTTA (7). Overlaid are simulations with Model 3 using the best-fit ZFS parameters presented in Table 4.2. The faded regions indicate the portion of the spectra about the central transition which was excluded from the rmsd error map calculations.

results of the fit, the interpretation of the rmsd becomes complicated. Therefore, we excluded the region of the central transition from the fit in our final comparison of the best-fit ZFS parameters determined with Models 1, 2 and 3, as given in Table 4.2. In the following section we use these ZFS values to optimize the parameters of the revised version of superposition model.

4.5. Superposition model for the ZFS tensor of Gd(III) complexes

In the superposition model, the zero-field splitting (ZFS) tensor is expressed as a sum of ligand-field contributions from individual nuclei in the coordination spheres of an s state ion¹²⁹. Here, we use the simplification for Gd(III) complexes in glassy frozen solution that was previously introduced by Raitsimring *et al.*,¹³⁴ where only the donor atoms of the ligand are considered and only the first order contribution to the ZFS Hamiltonian is computed. This contribution is

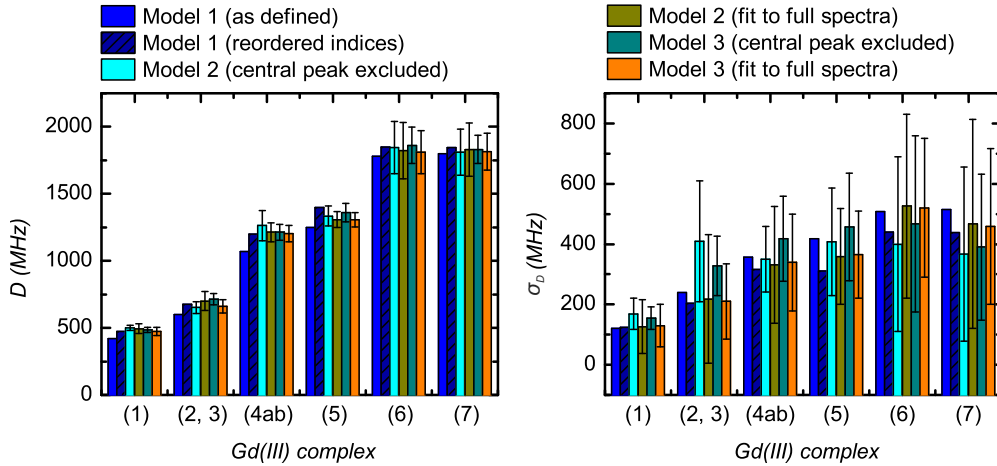


Figure 4.11. Comparison of the extracted values for the mean ($\langle D \rangle$) and width (σ_D) of the ZFS parameter D for the three models and each of the tested Gd(III) complexes. Structural formulae and naming for the Gd(III) complexes **1** - **7** are given in Figure 4.2. Model 1 was fit by visual inspection, and therefore error bars on the ZFS parameters D and σ_D were not computed. For Models 2 and 3, mean values and error bars for D and σ_D were computed by combining results from rmsd error maps which compare a library of simulated spectra to the data at the three measurement frequencies. Models 2 and 3 were fit with the region about the central transition excluded from analysis, and also with the full EPR spectra included in the analysis.

quadratic in the spin operators and can be parametrized by the magnitudes of D and E/D . We follow Raitsimring *et al.* in first building a ZFS tensor,

$$\mathbf{D} = \sum_k \left(\frac{r_{0,k}}{r_k} \right)^\tau \mathbf{R}(0, \theta_k, \phi_k) \begin{pmatrix} d_k & 0 & 0 \\ 0 & d_k & 0 \\ 0 & 0 & -2d_k \end{pmatrix} \mathbf{R}^T(0, \theta_k, \phi_k), \quad (4.10)$$

where $r_{0,k}$ is a reference donor atom-Gd(III) distance, r_k is the actual donor atom-Gd(III) distance, τ is a scaling exponent, $\mathbf{R}(0, \theta_k, \phi_k)$ is an Euler rotation matrix in $zy'z''$ notation and $\mathbf{R}^T(0, \theta_k, \phi_k)$ its transpose, and the d_k are single-atom ZFS contributions that are assumed to have axial symmetry with the unique axis being along the donor atom-Gd(III) vector. Accordingly, the parameters of θ_k , ϕ_k , and r_k are the spherical coordinates of the donor atom in the reference frame of the ZFS tensor \mathbf{D} .

In contrast to Raitsimring *et al.*, we rely on known coordination geometries from the crystal structures of lanthanide complexes available in the literature. We additionally allow for a distance dependence of the individual donor atom contributions as well as for atom-type dependent ZFS magnitudes d_k at atom-type dependent reference distances $r_{0,k}$. Specifically, we distinguish between the donor atoms oxygen with $r_O = 2.42$ Å and nitrogen with $r_N = 2.65$ Å. Our model thus has three fit parameters: the scaling exponent τ and the reference ZFS magnitudes d_O and d_N . Note that the choice of r_O and r_N , which were taken as typical donor atom-Gd(III) distances for these elements in the crystal structures referred to in Section 4.5.1, is not critical. For a given scaling exponent τ , changes in these reference distances merely result in a well-defined change in d_O and d_N . We have also tried to fit a model with only two parameters that does not distinguish between oxygen and nitrogen atoms, but the fits were significantly worse and gave an unphysical negative scaling exponent τ (data not shown). The parameters D and E of the zero-field splitting are obtained by diagonalization of the traceless symmetric tensor \mathbf{D} and ordering of the principal

values as described in Section 4.2. This simplest superposition Model A predicts only mean values for D and E , not their distributions.

4.5.1. Gd complex geometries for the superposition model

The required ligation polyhedra were taken from crystal structures obtained from the Cambridge Crystallographic Data Centre and converted to .xyz files using the Mercury software. Homewritten MATLAB scripts were used for further processing. Oxygen and nitrogen atoms closer than 3 Å to a lanthanide ion were considered as belonging to the first coordination shell. For the crystal structures of Gd-NO₃Pic,¹⁵⁴ of a Gd-DOTA-monoamide¹⁵⁵ which closely resembles Gd-maleimide-DOTA, and of a compound of the type Gd-PyMTA—spacer—Gd-PyMTA,¹⁵⁶ a full set of nine donor atoms was detected. For the latter two cases, one of these donor atoms came from water. The unit cell of the Gd-PyMTA—spacer—Gd-PyMTA crystals contains several Gd(III) centres that are not symmetry-related; the third Gd(III) centre in the CIF file was used. Those of the other centres that also feature nine directly ligated atoms gave similar results.

No structure was found for a lanthanide ion coordinated by PCTA-[12]. Instead, we used the structure of Ho(III) coordinated by a ligand that derives from formal substitution of the three carboxylate groups of PCTA-[12] with phosphonate groups.¹⁵⁷ The coordination polyhedron of this Ho(III) complex is assumed to be very similar to that of Gd-PCTA-[12], and thus also iodo-(Gd-PCTA-[12]). Although the crystals contain nine water molecules per two Ho(III) complexes, none of the water molecules are coordinated to the Ho(III) ion and the coordination number is only eight. The same coordination type is observed for Lu(III). We tried to place a water molecule as an additional ligand at a typical lanthanide-oxygen distance for such ligation (2.43 Å), but this led to a situation where the oxygen atom comes at least as close as 2.13 Å to another donor atom. Since no distance between two donor atoms shorter than 2.62 Å was found in any other complex, we assume that the lanthanide complexes of PCTA-[12] have low affinity for water as a ninth ligand.

No structures were found for a lanthanide complex with TAHA or PyDTTA as the ligand. Hence, Model A, which predicts only a mean D value and has three free parameters can be fit to experimentally determined mean D values for only four complexes. As a fit criterion, we used the mean square relative deviation $\sum_i (1 - |D_{\text{model},i}| / \bar{D}_{\text{exp},i})^2$ of the ZFS magnitude predicted by superposition Model A from the mean experimental ZFS magnitude determined by the fit with Model 3, as given by the ZFS parameter values in bold in Table 4.2.

4.5.2. Mean ZFS parameters with fixed donor atom position (Model A)

The best fit was obtained for $\tau = 1.102$, $d_N = 991.3$ MHz, and $d_O = 915.9$ MHz and is very good (Table 4.3). The mean D values of the Gd(III) complexes of NO₃Pic, maleimide-DOTA, and PyMTA are reproduced with three digit precision, whereas the prediction for iodo-PCTA-[12] is about 10% too low. The positive scaling coefficient τ is physically plausible, as are the similar reference values for the ZFS contributions by the coordinated N and O atoms. This result confirms that the ZFS is dominated by the symmetry of the first coordination shell.

Model A was further tested with structurally related complexes. For Gd-DOTA (**2**),¹⁵⁸ we find a D_{model} value of 666 MHz, which is similar to the value of 714 MHz, found by fitting experimental EPR spectra with Model 3 for Gd-maleimide-DOTA/Gd-DOTA. Likewise, similar values are obtained for Gd-DOTA complexes with the coordination geometry found for the

Ligand	\bar{D}_{exp} (MHz)	\bar{D}_{model} (MHz)
NO ₃ Pic	485	485
maleimide-DOTA	714	714
PyMTA	1213	1213
iodo-PCTA-[12]	1861	1684

Table 4.3. Experimentally determined magnitudes of the ZFS parameter D and magnitudes determined by a fit with a superposition model (Model A). The prediction for iodo-PCTA is based on a crystal structure of a similar complex where the three carboxylate groups are replaced by phosphonate groups.

DOTA complexes of other lanthanide(III) ions,¹⁵⁹ assuming that Gd(III) takes the position of the other lanthanide ion. For the geometry of Pr-DOTA, we find $D = 689$ MHz, $D = 688$ MHz for Nd-DOTA, $D = 679$ MHz for Dy-DOTA, but for the coordination geometry of Ce-DOTA a strongly different ZFS of $D = -301$ MHz was found.

4.5.3. Distribution of ZFS parameters from the superposition model (Model B)

In the superposition model, a distribution of the ZFS is caused by a spatial distribution of the donor atoms. Raitsimring *et al.*¹³⁴ allowed for a very wide distribution that may appear unrealistic given the sterical constraints of the ligands. Here we assume that the donor atom positions are distributed around the mean positions found in the crystal structures. In the simplest approximation, distributions of the individual atoms are independent of each other, and correspond to a Boltzmann equilibrium distribution in an isotropic three-dimensional harmonic potential. What we refer to as the superposition Model B then leads to an isotropic three-dimensional Gaussian distribution of the donor atom positions that can be characterized by a single parameter, the standard deviation σ_{xyz} of the atom positions along the x , y , and z coordinates. This distribution type corresponds to the Debye-Waller factor (B factor) used in crystal structure determination.

As a first step, we varied σ_{xyz} for the model of the maleimide-DOTA complex. The experimentally observed relative standard deviation σ_D/D of $\approx 33\%$ was matched at $\sigma_{xyz} \approx 0.1$ Å. For some of the crystal structures, σ_{xyz} can be estimated from Debye-Waller factors to be in the range of 0.15 - 0.25 Å at ambient temperature.^{159;160} It is not surprising that similar values are found in glassy frozen solutions, where they probably correspond to the thermal distribution at the glass transition temperature, but may also be influenced by strain in the glass.

Model B led, however, to a larger mean ZFS magnitude D than obtained with the same model parameters for $\sigma_{xyz} = 0$ (corresponding to Model A). This is expected, since the spatial distribution of the atom position on average causes more asymmetry of the ligand field. We corrected for this effect by reducing d_N and d_O by the same factor of 0.845. Model B with these reduced d_N and d_O inputs successfully reproduced D and σ_D/D for Gd-maleimide-DOTA and provided a mean value of 0.195 for E/D , which is in reasonable agreement with the experimental value of 0.25 obtained using Model 1. Furthermore, Model B still reproduced the trend in D among the four tested Gd(III) complexes for which there were both experimentally determined ZFS parameter values and crystal structures available (Table 4.4). However, the variation of the mean D value between the ligands was weaker than observed experimentally and the relative distribution width σ_D/D decreased more strongly with increasing D than was experimentally observed. In assessing this discrepancy, one needs to take into account the large uncertainty

in σ_D reported in Table 4.2. The discrepancy suggests, but does not prove, that Model B has difficulties in predicting σ_D .

Closer inspection of the structures with Debye-Waller factor information^{159;160} shows that the thermal ellipsoids of the donor atoms usually have a smaller extension along the lanthanide ion-donor atom bond than perpendicular to it. An attempt to fit a Model C with different Gaussian distributions σ_r and $\sigma_{\theta,\phi}$ for spherical coordinates r on the one hand and θ and ϕ on the other hand did not significantly improve the situation. For the final distribution model, we thus returned to the σ_{xyz} parametrization of Model B, but reduced σ_{xyz} to 0.05 Å in order to obtain a compromise between reproducing the mean values and distribution widths σ_D for the four tested Gd(III) complexes. We also tested $\sigma_{xyz} = 0.03$ Å and $\sigma_{xyz} = 0.07$ Å, but these choices provided worse agreement with experimental data when considering both D and σ_D/D . The results for Model B with $\sigma_{xyz} = 0.05$ Å are compared in Table 4.4 to the results obtained by fitting of experimental data by Models 1 and 3. The superposition model parameters used for this calculation were $d_N = 989$ MHz, $d_O = 943.5$ MHz, and $\tau = 0.100$.

The probability density distributions of the anisotropy Δ and axiality ξ predicted by superposition Model B are compared in Figure 4.12 to the corresponding distributions obtained by fitting of experimental data with Models 1 and 3. Good agreement of superposition Model B with Models 1 and 3 is observed for Gd-NO₃Pic. Model 3 mimics the asymmetry of the axiality distribution $P(\xi)$ by a different scaling of the $\xi < 0$ and $\xi > 0$ moieties that is implied by the bimodal distribution of $P(D)$ with Gaussian peaks for both positive and negative D values.

For Gd-DOTA (**2**), the superposition Model B predicts the mean value of anisotropy Δ and thus of $|D|$ quite well, but underestimates the standard distribution of anisotropy. More importantly, Model B predicts a wrong asymmetry of the axiality distribution $P(\xi)$. The asymmetry of $P(\xi)$ seen in Model 3 (green line in Figure 4.12(d)) with stronger contributions at $\xi < 0$ than at $\xi > 0$ and in Model 1, where $D = -600$ MHz was used as a simulation input, is at least qualitatively correct, as it is in line with the asymmetry of the low-temperature G-band spectrum. Surprisingly, this asymmetry is nicely predicted by Model B if the crystal structure of Ce-DOTA instead of the one of Gd-DOTA (**2**) is used (grey line). Since all donor atoms are farther away from the lanthanide ion in the Ce-DOTA structure, a too small mean value is predicted for Δ . Although it may be possible to find a coordination polyhedron that leads to very good agreement between Models 3 and B, we refrain from this, since an arrangement of nine donor atoms cannot be uniquely determined from the information content in these distributions and since Model 3 is not perfect either.

Note also that the predictions by Model B based on the crystal structures of Gd-DOTA (**2**)¹⁵⁸ and of the Gd-monoamide-DOTA¹⁵⁵ that resembles Gd-maleimide-DOTA (**3**) differ significantly from each other. This difference can be traced back to a lengthening of the dative bond between Gd(III) ion and the oxygen atom of the carboxamide group by about 0.2 Å compared to a bond between a Gd(III) ion and a carboxylate oxygen atom and a concomitant slight shortening of the opposite dative bond.

For Gd-PyMTA, Model B predicts the mean value of the anisotropy quite well, but underestimates the width of the distribution (Figure 4.12(e)). In particular, Model B with $\sigma_{xyz} = 0.05$ Å dramatically underestimates the width of the axiality distribution $P(\xi)$ (Figure 4.12(f)), which nicely agrees between Models 1 and 3. The deviation is significant, as the predicted distribution has significant contributions only from $\xi > 0$, which would cause a much stronger asymmetry of the low-temperature G-band spectrum than experimentally observed. This strongly suggests that

Ligand	$ D _{\text{exp},1}$	$ D _{\text{exp},3}$	$ D _{\text{sim},B}$	$(\sigma D)_{\text{exp},1}$	$(\sigma D)_{\text{exp},3}$	$(\sigma D)_{\text{sim},B}$	$\bar{\xi}_{\text{exp},1}$	$\bar{\xi}_{\text{exp},3}$	$\bar{\xi}_{\text{sim},B}$	$ \bar{\xi} _{\text{exp},1}$	$ \bar{\xi} _{\text{sim},B}$
NO ₃ Pic	452	485	510	122	155	158	0.103	0.114	0.044	0.398	0.381
DOTA ^a	635	717	699	208	320	172	0.181	-0.209	0.099	0.425	0.379
maleimide-DOTA ^a	635	717	724	208	320	174	0.181	-0.209	0.321	0.425	0.433
PyMTA	1152	1214	1257	312	417	210	0.102	0.092	0.617	0.398	0.620
iodo-PCCTA-[12] ^b	1811	1861	1637	469	467	213	0.279	0.226	0.242	0.373	0.287

Table 4.4. Comparison of the mean absolute ZFS magnitude $\overline{|D|} = 3\overline{\Delta}/2$, the standard deviation $\sigma|D|$ of the absolute ZFS magnitude, the mean ZFS axiality $\bar{\xi}$, and the mean absolute ZFS axiality $|\bar{\xi}|$ between fits to experimental data by Models 1 and 3 and simulations by superposition Model B. The mean absolute ZFS axiality for Model 3 is fixed by Equation (4.8) at $|\bar{\xi}| = 0.4$.

^aIn experiments, Gd-DOTA was used in Q and W band and Gd-maleimide-DOTA in G band.

^bThe prediction for iodo-(Gd-PCCTA-[12]) is based on a crystal structure of a Ho(III) complex with a ligand that derives from iodo-PCCTA-[12] by formal exchange of the carboxylate groups for phosphonate groups.

for Gd-PyMTA the coordination geometry is less well defined than by a variation of the donor atom positions with $\sigma_{xyz} = 0.05 \text{ \AA}$ with respect to their mean position in the crystal structure, as is assumed in Model B. This is plausible, since the position of the two coordinating water molecules is expected to vary more strongly in a frozen glassy solution. Note also that the crystal structure reported in¹⁵⁶ features one Gd(III) centre coordinated by only eight donor atoms. We tested this hypothesis by recomputing superposition Model B with $\sigma_{xyz} = 0.10 \text{ \AA}$ (orange curves). Indeed, both the width of $P(\Delta)$ and the width and position of the maximum of $P(\xi)$ are in much better agreement with the experimental results for this choice.

A similar trend as for Gd-PyMTA is observed for iodo-(Gd-PCTA-[12]) (**6**), albeit to a lesser extent (Figure 4.12(g, h)). In addition, the mean value of the anisotropy is slightly underestimated. In this case, a simulation with $\sigma_{xyz} = 0.10 \text{ \AA}$ and otherwise unchanged model parameters (orange lines in Figure 4.12(g, h)) led to a very good agreement between the distribution predicted by ZFS Models 3 and superposition Model B, considering that Model 3 can mimic the asymmetry only by different vertical scaling of the $\xi > 0$ and $\xi < 0$ branches.

4.5.4. Predictions

When the crystal structure of a Gd(III) complex or the corresponding complex with another lanthanide(III) ion is known, the superposition model can be used for the prediction of ZFS values (Table 4.5). The values predicted by Model B with $\sigma_{xyz} = 0.05 \text{ \AA}$ for an additional set of the seven Gd(III) complexes **8-14** shown in Figure 4.13 are mostly within the range of the values measured in this work, with the exception of Gd-HAM2 for which a larger ZFS is predicted than for iodo-(Gd-PCTA-[12]). Note that the uncertainties of the predictions for Gd-EDTA and Gd-HAM2 may be particularly large because water coordination geometry is likely to differ in the crystal and in aqueous solution when three free coordination sites are available. In both crystal structures, three water molecules are coordinated with Gd(III)-O distances between and 2.416 and 2.530 \AA (EDTA) and 2.319 and 2.384 \AA (HAM2). In solution, on average longer and more varied Gd(III)-O(H₂O) distances are to be expected, which would then lead to a larger mean ZFS magnitude. In both of these cases, one may also expect a larger standard deviation of the ZFS magnitude due to the larger variability of the donor atom coordinates for water ligands. We tested for this effect by repeating the computations for these two ligands with $\sigma_{xyz} = 0.10 \text{ \AA}$. For Gd-EDTA, this leads to an increase in $|\overline{D}|$ from 528 to 838 MHz and in $\sigma_{|D|}$ from 154 to 273 MHz. For Gd-HAM2, $|\overline{D}|$ increases only slightly from 2168 to 2276 MHz, while $\sigma_{|D|}$ more than doubles from 147 to 302 MHz. In general, one expects a larger effect on small $|\overline{D}|$ upon increasing σ_{xyz} , since a small $|\overline{D}|$ corresponds to a highly symmetric coordination polyhedron whose symmetry is rather sensitive to changes in the donor atom coordinates.

Ligand	EDTA	DOTAM	DTMA	DO4Py	DO3A	DTPA	HAM2
$ \overline{D} $ (MHz)	528	738	775	959	1109	1242	2168
$\sigma_{ D }$ (MHz)	154	176	177	182	176	193	147
$\overline{\xi}$	-0.088	0.360	0.185	0.340	0.340	-0.171	0.166
$ \overline{\xi} $	0.387	0.449	0.384	0.414	0.379	0.268	0.181
Reference	161	160	162	163	158	164	165

Table 4.5. ZFS distribution parameters predicted by the superposition Model B for the Gd(III) complexes **8-14** (Figure 4.13) and references for the crystal structures used.

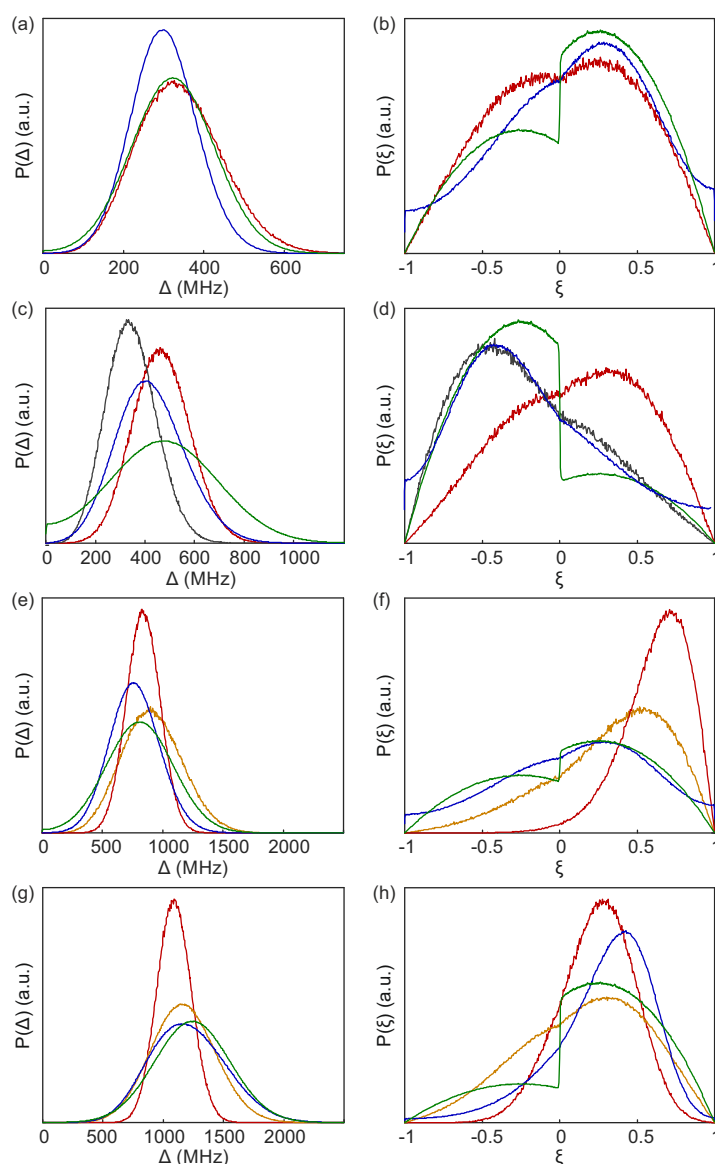


Figure 4.12. Comparison of distributions of anisotropy Δ (a, c, e, g) and axiality ξ (b, d, f, h) between fits to experimental data by Model 1 (blue) and Model 3 (green), as well as the prediction by superposition Model B with an isotropic standard deviation of atom positions $\sigma_{xyz} = 0.05$ Å (red). The orange curves are predictions by superposition Model B with an isotropic standard deviation of atom positions $\sigma_{xyz} = 0.10$ Å. (a, b) Gd-NO₃Pic (**1**). (c, d) Gd-DOTA (**2**). The grey curves are predictions by superposition Model B based on the crystal structure of the Ce(III)-DOTA. (e, f) Gd-PyMTA (**4**). (g, h) iodo-(Gd-PCTA-[12]) (**6**). The prediction for iodo-(Gd-PCTA[12]) is based on a crystal structure of the Ho(III) complex with a ligand that formally derives from PCTA-[12] by substitution of the carboxylate for phosphonate groups.

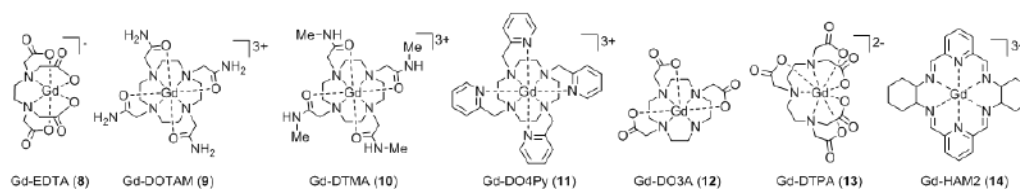


Figure 4.13. Structural formulae and naming of the Gd(III) complexes **8-14** considered for ZFS parameter value prediction with the superposition Model B.

4.6. Discussion

In this work, we determined the ZFS parameters D and E (or E/D) for a series of Gd(III) complexes by fitting three models for the ZFS parameter distributions to a set of multi-frequency EPR spectra acquired in Q band (34 GHz), W band (94 GHz), and G band (240 GHz). The determined ZFS parameter values D and σ_D were found to be comparable within error across all three tested models if for Model 1 the dominant components of D and σ_D after reordering of the indices were taken into account. We find that the model proposed by Raitsimring *et al.*, with the addition of an asymmetry parameter in the bimodal $P(D)$ distribution (here, Model 3), provides a good compromise between a small number of fit parameters and a good match between the simulated and experimental EPR spectra.

The combination of EPR data obtained at multiple frequencies greatly enhances the confidence of the determined ZFS parameter values, as each measurement frequency provides slightly different information due to the varying contributions of the different EPR transitions at the different measurement frequencies and temperatures. In particular, the high-field and low-temperature G-band (240 GHz) spectra, whose lineshape is dominated by the $|-7/2\rangle \rightarrow |-5/2\rangle$ transition, was found to be crucial in determining the asymmetry of the bimodal $P(D)$ distribution. However, inspection of the rmsd contour plots for Models 2 and 3 implies that a rough estimation of the ZFS parameters D and σ_D is possible with data at only a single measurement frequency in Q band or above. EPR spectra recorded in Q band and W band are rather insensitive to the asymmetry parameter $P(+D)/P(-D)$ of Model 3, and so the lineshape can be adequately described under the assumption that the bimodal D distribution is symmetric about zero (i.e. Model 2).

The three phenomenological models tested in this work (Models 1-3) appear to be reasonable approximations of the ZFS parameter distributions, but they do not perfectly reproduce the experimental EPR spectra of the Gd(III) complexes. The systematic deviations between the best-fit simulations and the experimental data resulting from approximations taken in the models limit the precision with which we can determine ZFS parameter values, forcing us to set relatively large error bars for the D and σ_D values. The largest deviations for all three models are observed in the vicinity of the sharp central peak of the Gd(III) spectrum, resulting from an oversampling of values near $D = 0$ in the simulations. Adding a small intrinsic linewidth to broaden the region of the central peak in the Gd(III) spectrum was found to improve the agreement between the simulated and experimental EPR spectra (Appendix A.3.4), perhaps by accounting for unresolved broadenings (i.e. hyperfine interactions, higher-order ZFS parameters, etc.) which are not included in the tested models and would be most visible as broadenings of the narrow central peak. However, it is difficult to introduce such a line broadening in a clear and systematic way into the global fits of multi-frequency EPR data and the physical interpretation of such a phenomenological parameter is ambiguous. For these reasons, it was found best to carry out normalization of the simulated spectra to the measured EPR data considering only the shoulders of the EPR spectra. This outer portion of the spectra is not sensitive to these extraneous broadening terms, while the height of the sharp central peak is highly sensitive to any additional broadening, and would thus bias an rmsd calculation if the spectra were normalized to the central peak.

The three tested models for the ZFS parameter distributions were found to produce simulated Gd(III) spectra that had small, but systematic, deviations from the measured EPR spectra resulting from approximations taken in the definition of the models. This necessitated the assignment of rather large error bars for the determined D and σ_D parameter values. In light of

this, it is difficult to argue why the rigorous analysis performed here is necessary in every case where only an estimation of the ZFS parameter values for a Gd(III) complex is desired. It is tempting to simplify the fitting of ZFS parameter distributions to the mathematically ill-defined fit-by-eye approach. This manual fitting approach was conducted here for Models 1 and 3 (Section 4.4.1, A.14) before the rigorous analysis was conducted, and was found to produce ZFS parameter values that fell - with one exception - within the conservatively defined error bars if for Model 1 the dominant component of D and σ_D after reordering of the indices were considered. The exception is the manually estimated D values for Gd-DOTA (**2**)/Gd-maleimide-DOTA (**3**) using Model 3, that lie within the error band of the rmsd analysis for the whole field range, but are out of the error band for the rmsd analysis excluding the central peak. Yet this method of fitting must be undertaken with caution, as the results are dependent on the physical intuition of the person performing the fit, and error bars cannot be assigned to the determined ZFS parameter values.

In this work we neglected a possible change of ZFS parameters between the measurement temperature of 5 K for G band and of 10 K for Q and W band. The best fit ZFS parameters vary between different microwave bands, indicating approximate character of the used ZFS models (Appendix A, Tables A.3 and A.4). This variation exists between each two bands, and its magnitude seems to be uncorrelated with the temperature difference. Variations of ZFS with temperature were observed, for instance, for Mn(II) impurities in magnetically dense iron-based metalloorganic crystals¹⁶⁶ or for a Manganese Superoxide Dismutase,¹⁶⁷ and were related to the sensitivity of zero-field interactions to metal-ligand distances and/or angular ligand positions. For the studied model compounds we presume that the ligand sphere stays approximately constant in the studied range. Note also that, in the cited works, the variation of ZFS over a range of 5 K in the low temperature regime would be too small compared to the accuracy of the presented ZFS determination and the widths of obtained ZFS parameter distributions.

Even given the conservative estimate of the accuracy of the D values for Gd(III) complexes determined in this work, the magnitude of the assigned error bars are still smaller than typical error bars from quantum chemical calculations of ZFS parameter values performed by standard computational approaches, which often fail to arrive at the correct sign or magnitude of the ZFS parameter values.¹⁶⁸ This is one of the primary motivations for attempting to construct a semi-phenomenological model for ZFS parameter value predictions. The superposition model developed in this work, using known crystal structures of Gd(III) complexes as inputs, was found to qualitatively reproduce the ZFS parameter distribution described by Model 3. Furthermore, by assuming variation in donor atom coordinates consistent with Debye-Waller factors in crystal structures, the superposition Model B was successful in roughly estimating the magnitudes of D , distribution σ_D and the trends in the experimentally determined values. However, the ZFS parameter values determined by the superposition model lie slightly outside of the assigned error bars for some of the Gd(III) complexes studied here. Reproducing the distribution widths of D and of the axiality ξ require that different Debye-Waller factors are assumed for different ligands. For the DOTA ligand, the superposition model wrongly predicts an excess of configurations with positive ZFS if the crystal structure of Gd-DOTA is used, whereas it correctly predicts an excess of configurations with negative ZFS if the crystal structure of Ce-DOTA is used. This indicates that, at least for highly symmetric coordination polyhedra, subtle differences in donor atom coordinates can cause strong changes in the ZFS parameter distribution. The accuracy of predictions by the superposition model is thus limited if there are differences of the

coordination polyhedra between crystal structures and solution. Furthermore, due to the relatively restricted set of input experimental data for calibration of the superposition model, it is currently difficult to estimate the strength of this model in predicting unknown ZFS parameter values for other Gd(III) complexes. Moreover, it was also observed in the above mentioned study on a Manganese Superoxide Dismutase,¹⁶⁷ that the superposition model of Newman and Urban¹²⁹ for six- and four-coordinate d^5 metal ions, does fail to predict the correct ZFS parameters in cases of high geometric asymmetry, so that some caution should be taken when applying superposition modelling. Given the importance of accurate knowledge of ZFS parameter values for optimal design of particular EPR experiments and interpretation of data, this calls for additional work in this area - both in experimentally measuring ZFS parameter values for additional Gd(III) complexes and developing semi-phenomenological models relating the structure of the Gd(III) complex to the magnitude of the ZFS which will allow for the design of tailored Gd(III) complexes.

Nevertheless, the work presented here, allows to give some general comments on the current state of ZFS analysis in Gd(III) complexes, and on the capability of the existing methods to relate spectroscopic parameters to the metal-ligand chemical bonding. The superposition model relates the widths of D and E distributions to variations in the metal complex structure. In the earlier work of Raitsimring and colleagues, reorientations of the ligands around the central Gd(III) ion, with constant interatomic distances, were assumed. In the present work, we rather approximate ligand position variations as isotropic narrow Gaussian distributions in a 3D space, according to the x-ray Debye-Waller factors, and allow different strength of ZFS contributions from oxygen and nitrogen atoms. Fitting of the superposition model to the set of experimental data suggests that nitrogen ligands have about 8% stronger contributions to ZFS than oxygen ligands. It appears that both Raitsimring's and our assumptions lead to very similar types of D and E distributions, which cannot be unambiguously discriminated even by the rigorous analysis of multi-frequency EPR data. Hence, it is difficult to say with confidence if ZFS distributions originate mainly from metal-ligand distance variations, from orientational distributions of the ligands around the metal ion, or from both these factors. The superposition model assumes that the same type of ligating atom (in our case, oxygen or nitrogen) gives the same distance-dependent contribution to the total ZFS. This is an approximation, which does not perfectly describe the presented experimental data, but it correctly catches the overall ZFS variation trend. Since currently accurate quantum chemical calculations for Gd(III) are not available, it would be difficult to relate the observed ZFS values to some deeper details of the chemical bonding at e.g. molecular orbital level. While some speculations on a case-by-case basis might still be possible, such speculations are beyond the scope of this work. It would be very helpful to generate a library of ZFS data on different Gd(III) centers, including Gd-EDTA and Gd-DOTAM as examples for small ZFS and scan this large experimental data set for such relations.

4.7. Conclusions

We made an extensive attempt to verify the accuracy of the determination of ZFS parameters and their distributions from multi-frequency EPR data. We discussed the relation between the two most commonly used models for the ZFS parameter distributions: (1) the model proposed by Benmelouka *et al.*,¹³⁵ which assumes that the distributions of D and E are described by uncorrelated Gaussian distributions, and (2) the model proposed by Raitsimring *et al.*, which takes the distribution of D to be a bimodal Gaussian distribution centred about $D = 0$

and the distribution of $P(E/D)$ to be described by the polynomial expression $P(E/D) \propto (E/D) - 2 \cdot (E/D)^2$. We additionally investigated a third model, in which we allowed for an asymmetry of the bimodal D distribution of Model 2. We found that the distribution described by Model 1 could lead to an inconsistency with the typical definitions of the ZFS parameter values D and E . This inconsistency can be easily corrected and the ZFS parameter distributions recomputed, resulting in distributions rather similar to those described by Model 3. We furthermore showed that the predicted D and σ_D values are consistent between the three models. The value of D is reasonably well constrained by fitting with these models, but the σ_D and asymmetry parameter $P(+D)/P(-D)$ are much less well constrained. The use of multi-frequency EPR data increased the confidence of the determination of ZFS parameters, with high-field low-temperature spectra being crucial for determination of the asymmetry parameter $P(+D)/P(-D)$ and the sign of D . In our opinion, the model proposed by Raitsimring *et al.*,¹³⁴ with the addition of an allowance for asymmetry of the bimodal D distribution, appears to provide the most adequate description of ZFS distributions for Gd(III) complexes in frozen glassy solutions.

Finally, we proposed an extension to the superposition model for the prediction of ZFS parameters, which allowed for reproduction of the trends in the strength of the ZFS for different Gd(III) complexes and rough estimation of the magnitude of D . This extended superposition model may be useful in estimating the strength of ZFS for Gd(III) complexes, e.g. based on optimized geometry calculations, which are typically more accurate than quantum chemical ZFS calculations. While this approach cannot be expected to predict exact ZFS parameters, it may provide a reasonable guideline for the selection of a Gd(III) complex with particular ZFS for experiments in which the strength of ZFS is important (e.g., Gd(III) complexes with weak, intermediate or strong ZFS), and, thus, help to design tailored Gd(III) complexes prior to any synthesis efforts.

MATLAB routines to extract ZFS parameters distributions from experimental data and for the prediction of ZFS parameters using the described superposition model are available from www.epr.ethz.ch/software.

5

Intermolecular background decay in RIDME experiments

After having examined important properties related to the performance of paramagnetic metal centres as spin probes in pulsed dipolar spectroscopy, the following chapters investigate several aspects of the Relaxation-Induced Dipolar Modulation Enhancement (RIDME) technique. RIDME allows for determination of distance distributions in pairs containing two paramagnetic metal centres, a paramagnetic metal centre and an organic radical, and, at some conditions, also in pairs of organic radicals. The strengths of the RIDME technique are its simple setup requirements, and the absence of bandwidth limitations for spin inversion which occurs through relaxation. A strong limitation of the RIDME technique is the background decay, which is often steeper than in the Double Electron Electron Resonance (DEER) experiment, and the absence of an appropriate theoretical description of the intermolecular background signal. In this chapter the latter problem is addressed and an analytical calculation of the RIDME background decay in the simple case of two types of randomly distributed spin centres each with total spin $S = 1/2$ is presented. The obtained equations allow explaining the key trends in RIDME experiments on frozen chelated metal ion solutions, and singly spin-labelled proteins. At low spin label concentrations, the RIDME background shape is determined by nuclear-driven spectral diffusion processes. This fact opens a new path for structural characterization of soft matter and biomacromolecules through the determination of the local distribution of protons in the vicinity of the spin-labelled site.

This chapter was submitted for publication as 'Katharina Keller, Mian Qi, Christoph Gmeiner, Irina Ritsch, Adelheid Godt, Gunnar Jeschke, Anton Savitsky, Maxim Yulikov: Intermolecular Background Decay in RIDME Experiments' and is under revision. C. Gmeiner prepared the spin-labelled protein sample. The PyMTA complexes of Cu(II), Gd(III) and Mn(II) were synthesized by M. Qi in the group of A. Godt. Experimental RIDME background measurements and corresponding fits were performed by K. Keller. M. Yulikov developed the theoretical description of the RIDME background.

5.1. Introduction

Pulse dipolar EPR spectroscopy (PDS) is a valuable tool in the studies of macromolecular structures and conformational changes therein.^{20;22;41;169} PDS techniques are designed to detect the magnetic dipolar interaction within pairs of paramagnetic species from which the spin-spin distances and distance distributions can be extracted. This approach finds application particularly in structural biology. The experiments are typically performed *in vitro* at low temperatures in frozen glassy buffer/cryoprotectant mixtures, but they can also be conducted in frozen cells,^{24;25;170;171} or *in vitro* at ambient temperatures^{172;173}

Site-directed spin labelling is used to attach paramagnetic moieties to specific sites in diamagnetic biomacromolecules.^{16–18;23} Different types of spin labels and matching PDS experiments are available. For organic radical-based spin labels, typically, the four-pulse double electron-electron resonance (DEER) technique,^{75;76;98;174} double-quantum coherence (DQC) technique^{175;176} or single-frequency technique for refocusing (SIFTER)¹⁷⁷ are applied.

In cases of spin labels with broad EPR spectra, as in the case of most of the metal ion-based spin labels, there are two main types of PDS techniques to consider:

(i) First, the DEER experiment can be performed with broad-band frequency-modulated pulses.^{60–62} This requires an experimental setup with an arbitrary waveform generator (AWG) and a broadband resonator, as well as a microwave bridge with a high power output. Such setups became only available over the last years. Yet, in quite a few cases the ratio between the EPR spectral width and bandwidth of broadband pulses is still unfavourable, so that the necessary frequency offset in two-frequency PDS experiments, such as DEER, is difficult to achieve.

(ii) Alternatively, a version of the RIDME experiment^{66;67} can be used. In this experiment, the inversion pulse is substituted by spin flips of the coupling partner due to the longitudinal relaxation process. This experiment has a virtually infinite 'pump bandwidth' and works irrespective of the resonance frequency offset between the two spins.

Over the last four years several studies were reported on RIDME with pairs of paramagnetic metal centres,^{73;79;93;113;178} or pairs of an organic radical and a paramagnetic metal centre.^{179–184} These works demonstrated an overall good performance of the RIDME technique for such systems. To properly analyse RIDME data in practically important cases, it is necessary to correctly discriminate between the so-called intramolecular form factor contribution, and the intermolecular background contribution. While this step is rather well understood for the DEER technique,^{169;185} no systematic RIDME background study has been reported so far. In this work we report on such a RIDME background analysis for frozen solutions of paramagnetic metal complexes.

The key contributions to the RIDME background decay come from electron-electron and electron-nuclear spectral diffusion processes. To analyse these processes, two main approaches have been described. The first one utilizes the 'many small steps' diffusion-like model of the evolution of the spin packet.¹⁸⁶ This approach leads to a version of the one-dimensional diffusion equation over the frequency coordinate. It is well suited, for instance, in hole-burning experiments, to describe transfer of non-equilibrium polarization through the EPR spectrum due to electron-electron flip-flops, which include the excited spins. This approach is, however, not suited to describe small changes of the local field due to changes of the directions of surrounding spins, in case that the detected spins do not flip. Furthermore, this description is not applicable to the electron-nuclear spectral diffusion process. The second approach, more appropriate for the RIDME background problem, assumes a number of instantaneous jumps of the B spins, which

can lead to a change of the A-spin precession frequency of any physically feasible magnitude. In the work of Klauder and Anderson¹⁸⁷ the main principles of such an approach have been defined and good results were obtained for short evolution times, where a homogeneous Markov process can be assumed. Later, Mims critically discussed the results of Klauder and Anderson and made calculations for the other limiting case of long evolution times with large average numbers of B-spin flips.¹⁸⁸ Following these works, Hu and Hartmann¹⁸⁹ described a generally applicable approach and performed general-case calculations for the free induction decay, as well as for the two- and three-pulse echo sequence.

The present chapter is organized as follows: First, in the Theoretical section, following the approach of Hu and Hartmann, an analytic equation for the spectral diffusion terms in the RIDME experiment is derived under the assumption of mono-exponential longitudinal relaxation of B spins for an $S = 1/2$ system. Then the main properties of the derived expressions are discussed as well as the consequences of non-mono-exponential longitudinal relaxation and the corrections that would appear for high-spin paramagnetic centres. After describing the experimental procedures, relaxation data and RIDME background measurements on complexes of the paramagnetic Gd(III) ions at different conditions are presented (RIDME background data for Mn(II), and Cu(II) are given in Appendix B.5). The experimental trends are compared with qualitative predictions of the simplified theoretical model. The chapter concludes by discussing the observed dependencies and relating them to practical aspects of RIDME measurements on spin-labelled macromolecules.

5.2. Theoretical Background

In Figure 5.1 the five-pulse version of the RIDME pulse sequence is shown, which was introduced by Milikisyants et al.⁶⁷ to circumvent the detection dead time of the original three pulse RIDME experiment.⁶⁶ The first pulse creates electron coherence on the on-resonant spins (A-spins) and the second pulse refocuses the transverse magnetization of the A-spins at the time $t = 2d_1$ forming a primary spin echo. The first $\pi/2$ pulse of the mixing block stores half of the electron coherence along the z -direction in form of a polarization grating. Spectral diffusion processes erase parts of the polarization grating during the mixing time T_{mix} . The second $\pi/2$ -pulse of the mixing block flips the stored magnetization back into the transverse plane, where it is then detected after a final refocusing π pulse.

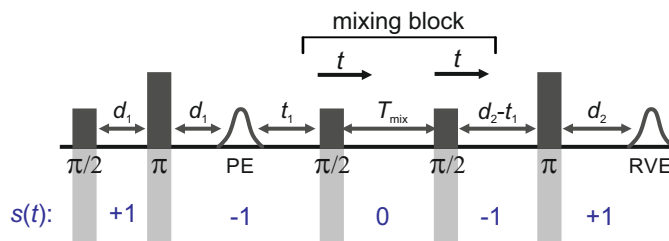


Figure 5.1. Illustration of the 5-pulse RIDME sequence and timings (d_1 , t_1 , T_{mix} , d_2). The mixing block is incremented by t . The position of the primary echo (PE) and refocused virtual echo (RVE) are indicated. The sign factor $s(t)$ describes phase accumulation during the experiment.

To derive an analytic expression for the RIDME background for $S_A = S_B = 1/2$ species we follow the approach of Hu and Hartmann¹⁸⁹ with some necessary adaptations. A qualitative discussion for the $S > 1/2$ case will follow after the derivation.

We consider a reference frame rotating with the Larmor frequency of the A-spins so that the time evolution of the spin-packet magnetization is described by the dipolar term in the spin Hamiltonian. Note that the Larmor frequencies of A and B spins are assumed to be sufficiently different for B spins not being excited by the pulses. This is a good approximation in the RIDME experiment, since it is mostly applied to systems where at least one spin type has broad EPR spectrum. In such a case the overlap of the resonance frequencies of A and B spins within the excitation bandwidth of the microwave pulses would have low probability, which can be neglected in the calculations. We can, thus, assume that B spins stay along the external field, so that for an isolated A-B spin pair we obtain for the RIDME signal:

$$f(t_1) = \exp \left[\int_0^{t_{\text{RVE}}} i \omega(t) dt \right]. \quad (5.1)$$

Here, the RIDME signal f is detected at the time t_{RVE} , at which the refocused virtual echo is formed. This signal f depends on time t_1 , at which the mixing block in the RIDME sequence starts. We abbreviate the delay time between the first $\pi/2$ and the first π pulse as d_1 , the duration of the RIDME mixing block as T_{mix} , and the time between the primary Hahn echo and the second π pulse as $T_{\text{mix}} + d_2$ (see Figure 5.1). With these abbreviations, the position of the refocused virtual echo equals $2d_1 + 2d_2 + T_{\text{mix}}$ after the first $\pi/2$ pulse. The dipolar frequency ω_{dd} in the A-B pair depends on the length r_{AB} of the spin-spin vector and angle θ_{AB} between this vector and the external magnetic field:

$$\omega_{dd}(r_{AB}, \theta_{AB}) = \frac{\mu_0 g_A g_B \beta_A \beta_B (1 - 3 \cos^2 \theta_{AB})}{4\pi \hbar r_{AB}^3} \frac{1}{2}. \quad (5.2)$$

The remaining symbols in this equation depict fundamental constants, such as vacuum permeability μ_0 , and g -values and electron or nuclear magnetons for A and B spins ($g_{A/B}$, $\beta_{A/B}$). To describe the time evolution in Equation (5.1), we introduce a sign factor $s(t)$ of phase accumulation, which is chosen as +1 right after the primary ($\pi/2$)-pulse. This factor changes its sign at every refocusing (π)-pulse, and is zero during the RIDME mixing block, where the magnetization is along z and does not accumulate phase. For the refocused virtual echo we have $s(t) = +1$ for $t < d_1$, $s(t) = -1$ for $d_1 < t < 2d_1 + t_1$, $s(t) = 0$ for $2d_1 + t_1 < t < 2d_1 + t_1 + T_{\text{mix}}$, $s(t) = -1$ for $2d_1 + t_1 + T_{\text{mix}} < t < 2d_1 + d_2 + T_{\text{mix}}$, and $s(t) = +1$ for $2d_1 + d_2 + T_{\text{mix}} < t < 2d_1 + 2d_2 + T_{\text{mix}}$. This is schematically shown in blue in Figure 5.1. The refocusing condition $\int_0^{t_{\text{RVE}}} s(t) dt = 0$ is fulfilled, meaning that phase accumulation due to both the resonance offset and the dipole-dipole coupling cancels. Furthermore, we have to analyse the case, where B-spins spontaneously flip at any time point t' during the transverse evolution of the A spin. This is described by an additional factor $h(t_1, t)$ which starts at the value +1 at the beginning of the time evolution and changes its sign each time, when the B spin flips. After these additions, Equation (5.1) changes to

$$f(t_1) = \exp \left[i \omega_{dd} \int_0^{t_{\text{RVE}}} s(\tau) h(t_1, \tau) d\tau \right]. \quad (5.3)$$

We need to consider only the contribution of ω_{dd} to ω , since B-spin flips affect only the sign of this contribution and we have already shown that $s(t)$ cancels all other contributions. The many-spin solution is obtained, if we multiply the contributions from all B spins:

$$\begin{aligned}
f_N(t_1) &= \prod_{k=1}^N \exp \left[i\omega_{dd}^{(k)} \int_0^{t_{\text{RVE}}} s(\tau) h_k(t_1, \tau) d\tau \right] \\
&= \exp \left[i \sum_{k=1}^N \omega_{dd}^{(k)} \int_0^{t_{\text{RVE}}} s(\tau) h_k(t_1, \tau) d\tau \right].
\end{aligned} \tag{5.4}$$

To describe the macroscopic ensemble, we have to average Equation (5.4) over all spatial positions of the B-spins (r and θ), as well as over all possible realizations of the $h(t)$ processes:

$$F(t_1) = \prod_k \left\langle \left\langle \exp \left[i\omega_{dd}^{(k)} (r_k, \theta_k) \int_0^{t_{\text{RVE}}} s(\tau) h_k(t_1, \tau) d\tau \right] \right\rangle \right\rangle_{h, r, \theta}. \tag{5.5}$$

Here we assumed that position and flip trajectory of each B spin are statistically independent on those of the other spins in the sample. Before averaging over the random $h(t)$ trajectories, we make the following simplifications. First, we assume that the average number of B-spin flips during the transverse evolution part of the refocused RIDME pulse sequence is small, so that only trajectories with one or zero B-spin flips in this interval are statistically relevant. This is equivalent to $T_{1,B} \gg T_{m,A}$, since the total time of A-spin phase acquisition cannot be much larger than the phase memory time $T_{m,A}$ of the A spins. This assumption does not apply to the mixing block time, where A spin magnetization relaxes with $T_{1,A}$ and where we allow for an arbitrary number of B-spin flips. In practice, one often works under conditions $T_{1,B} > 2 T_{m,A}$. Gd(III)-Gd(III) RIDME experiments can be performed at $T_m/T_1 = 1.2$ (this work) but this condition is not optimal for distance measurements. In the applications of dipolar spectroscopy, the length of the transverse evolution part of the RIDME experiment is rarely longer than $3 T_m$ and the average number of B-spin flips during this time is usually less than one. In this work we did measure somewhat longer traces to obtain the full shapes of the RIDME background decays. Such long measurements up to the times where background decayed nearly to zero are typically not relevant in distance measurements. Under the condition of, on average, less than one B-spin flip, according to the Poisson distribution law, with $\lambda = (2d_1 + 2d_2) / 2 T_{1,B}$ the probability for k flips of the B spin $P_B(k) = e^{-\lambda} \frac{\lambda^k}{k!}$ is getting small quickly for $\lambda < 1$ and $k > 1$. In fact, for $\lambda < 0.5$ all probabilities for $k = 3, 4, \dots$ can be neglected to a good approximation, and the cases with $k = 2$ can be considered as a 'weak perturbation'. For example, at $\lambda = 0.5$ we have $P_B(0) \approx 0.606$, $P_B(1) \approx 0.303$, $P_B(2) \approx 0.076$, and $P_B(3) \approx 0.013$. At $\lambda = 0.2$ we have $P_B(0) \approx 0.819$, $P_B(1) \approx 0.164$, $P_B(2) \approx 0.016$, and $P_B(3) \approx 0.001$.

Second, we assume for the moment that during the first Hahn echo block of duration $2d_1$, which is much shorter than $T_{1,B}$ in most cases, no B-spin flips occur. Thus, we only consider B-spin flips in the time period from the primary Hahn echo until the refocused virtual echo, which is used for detection of the RIDME signal. The consequence of including the first Hahn echo block into the calculations will be discussed at the end of this section.

Let us first discuss the mixing block of length T_{mix} . We can compress the mixing block into a single point on the time evolution diagram (see Figure 5.1), indicating that during this time $s(t) = 0$ and that no dipolar phase accumulation takes place. If the number of B spin flips of times during the mixing time T_{mix} is odd, this corresponds to the inversion of the sign of the dipolar frequency. The probability of an odd number of flips can be computed as:¹⁸⁹

$$p_m = e^{-WT_{\text{mix}}} \sum_{k=0}^{\infty} \left[W^{2k+1} \int_0^{T_{\text{mix}}} dt_1 \int_{t_1}^{T_{\text{mix}}} dt_2 \cdots \int_{t_{2k}}^{T_{\text{mix}}} dt_{2k+1} \right] = \frac{1}{2} (1 - e^{-2WT_{\text{mix}}}). \quad (5.6)$$

In Equation (5.6) the flip rate W has to be related to the longitudinal relaxation time as $T_{1,B} = 1/2W$. If the number of B-spin flips is even, then no sign change for the dipolar frequency happens. The probability of such an event equals to

$$q_m = e^{-WT_{\text{mix}}} \sum_{k=0}^{\infty} \left[W^{2k} \int_0^{T_{\text{mix}}} dt_1 \int_{t_1}^{T_{\text{mix}}} dt_2 \cdots \int_{t_{2k-1}}^{T_{\text{mix}}} dt_{2k} \right] = \frac{1}{2} (1 + e^{-2WT_{\text{mix}}}). \quad (5.7)$$

Additionally, let the probability be q that no B-spin flips happen during the transverse evolution time, and the probability be p that one B-spin flip happens during this time. We can approximately write that $p = \lambda/(1 + \lambda)$ and $q = 1/(1 + \lambda)$.

Thus, we need to consider four different cases. Case 1 corresponds to the situation when no B-spin flips occur during the transverse evolution of A spins, and an even number of B-spin flips occurs during the mixing time T_{mix} . The probability of this event is $P_1 = q \cdot q_m$. Case 2 corresponds to no B-spin flips during the transverse evolution of A spins, and an odd number of B-spin flips during the mixing time. The probability of this event is $P_2 = q \cdot p_m$. Case 3 has one B-spin flip during the transverse evolution time, and an even number of B-spin flips during the mixing block, with $P_3 = p \cdot q_m$, and, finally, case 4 has one B-spin flip during the transverse evolution and an odd number of B-spin flips during the mixing block, with the probability $P_4 = p \cdot p_m$.

We now compute the absolute values of the trajectory integrals of the form

$$I_l(t_1, t') = \left| \int_0^{2d_2} s(\tau) h_l(t_1, t', \tau) d\tau \right|, \quad (5.8)$$

with $l = 1, 2, 3, 4$, according to the four listed cases, and assuming that the random flip of the B spin (if it happens) takes place at the time t' . We obtain $I_1 = 0$, $I_2 = 2t_1$, $I_3 = 2t'$ for $t' < d_2$, and $I_3 = 2(2d_2 - t')$ for $d_2 < t' < 2d_2$. In case 4, we get for $t' < d_2$ the value $I_4 = 2|t_1 - t'|$, and for $t' > d_2$ we can write $I_4 = 2|t_1 + t' - 2d_2|$. Averaging over all equally probable times t' can be done according to the equation:

$$\bar{I}_l(t_1) = \frac{1}{2d_2} \int_0^{2d_2} I_l(t_1, t') dt'. \quad (5.9)$$

The integration, according to Equation (5.9), results in the following correspondences: $\bar{I}_1 = 0$, $\bar{I}_2 = 2t_1$, $\bar{I}_3 = d_2$, $\bar{I}_4 = d_2 (1 - 2t_1/d_2 + 2t_1^2/d_2^2)$. Let us now return to the derivation of the RIDME background function $F(t_1)$. We can assume that every B spin has the same homogeneous spatial probability distribution, and the same relative probabilities for the four different cases of the stochastic evolution $h_i(t)$. We can, thus, rewrite the function $F(t_1)$ for a large number N of B spins as a product of N single-pair space-time averages of an identical form:

$$F(t_1) = \left[\left\langle \left\langle \exp \left[i\omega_{dd} \int_0^{t_{\text{RVE}}} s(\tau) h(t_1, t', \tau) d\tau \right] \right\rangle \right\rangle_{h, r, \theta} \right]^N. \quad (5.10)$$

Due to the very large number of B spins considered, we can conclude that, according to the central limit theorem, the average number N_l of the A-B pairs evolving according to the case l would be equal to $N_l = P_l N$, and the fluctuations around these numbers will be statistically very small. We can thus rewrite Equation (5.10) in the form

$$F(t_1) = \prod_{l=1}^4 \left[\left\langle \left\langle \exp \left[i\omega_{dd}(r, \theta) \int_0^{t_{\text{RVE}}} s(\tau) h_l(t_1, t', \tau) d\tau \right] \right\rangle \right\rangle_{h, r, \theta} \right]^{N_l} = \prod_{l=1}^4 F_l(t_1). \quad (5.11)$$

Each individual term $F_l(t_1)$ can be rewritten as:

$$\begin{aligned} F_l(t_1) &= \left[\left\langle \left\langle \exp \left[i\omega_{dd}(r, \theta) \int_0^{t_{\text{RVE}}} s(t) h_l(t_1, t', \tau) d\tau \right] \right\rangle \right\rangle_{h, r, \theta} \right]^{N_l} \\ &= \left[1 - \left\langle \left\langle 1 - \exp \left[i\omega_{dd}(r, \theta) \int_0^{t_{\text{RVE}}} s(\tau) h_l(t_1, t', \tau) d\tau \right] \right\rangle \right\rangle_{h, r, \theta} \right]^{N_l}. \end{aligned} \quad (5.12)$$

In the original work,¹⁸⁹ Hu and Hartmann demonstrated that spatial averaging results into

$$F_l(t_1) = \left[1 - \frac{\mu_0}{4\pi} \frac{4\pi^2 g_A g_B \beta_A \beta_B}{9\sqrt{3}\hbar} \frac{1}{V} \left\langle \left| \int_0^{t_{\text{RVE}}} s(\tau) h_l(t_1, t', \tau) d\tau \right| \right\rangle_h \right]^{N_l}$$

Using our previously derived results for the time evolution averaging (Equation (5.9)), we can, thus, write for each case $F_l(t_1)$

$$F_l(t_1) = \left[1 - \frac{\mu_0}{4\pi} \frac{4\pi^2 g_A g_B \beta_A \beta_B}{9\sqrt{3}\hbar} \frac{1}{V} \bar{I}_l \right]^{N_l} = \left[1 - \Delta\omega_{1/2} \frac{P_l}{N_l} \bar{I}_l \right]^{N_l},$$

and, for large N_l , arrive at the formula

$$F_l(t_1) = \exp \left[-\Delta\omega_{1/2} P_l \bar{I}_l \right]. \quad (5.13)$$

Here we used the abbreviation

$$\Delta\omega_{1/2} = \frac{\mu_0}{4\pi} \frac{4\pi^2 g_A g_B \beta_A \beta_B}{9\sqrt{3}\hbar} \frac{N}{V} \quad (5.14)$$

for the average dipolar frequency between A and B spins, where the spin concentration N/V is proportional to the inverse cube of the average spin-spin distance r_{AB} . We note that in these equations that A and B spins might have different g -values (g_A and g_B) and might be characterized by different electron or nuclear magnetons β_A and β_B . The full equation for the RIDME background function is thus

$$F(t_1) = \exp \left[-\Delta\omega_{1/2} \sum_{l=1}^4 P_l \bar{I}_l \right]. \quad (5.15)$$

We can now write explicitly all exponential terms

$$-\frac{\ln F(t_1)}{\Delta\omega_{1/2}} = \frac{2T_{1,B} (1 - e^{-T_{\text{mix}}/T_{1,B}})}{2(2T_{1,B} + 2d_2)} 2t_1 + \frac{2d_2 (1 + e^{-T_{\text{mix}}/T_{1,B}})}{2(2T_{1,B} + 2d_2)} d_2 \quad (5.16)$$

$$+ \frac{2d_2 (1 - e^{-2T_{\text{mix}}/T_{1,B}})}{2(2T_{1,B} + 2d_2)} d_2 \left(1 - \frac{2t_1}{d_2} + \frac{2t_1^2}{d_2^2} \right). \quad (5.17)$$

They can be separated into terms, which depend on the time t_1 , where the mixing block starts,

$$-\frac{\ln F(t_1) - \ln F_0}{\Delta\omega_{1/2}} = \frac{1 - e^{-T_{\text{mix}}/T_{1,B}}}{T_{1,B} + d_2} ((T_{1,B} - d_2)t_1 + t_1^2), \quad (5.18)$$

and those, which do not vary with t_1 and correspond to a constant attenuation of the RVE,

$$-\frac{\ln F_0}{\Delta\omega_{1/2}} = \frac{d_2^2}{T_{1,B} + d_2}. \quad (5.19)$$

If we assume $d_2 \ll T_{1,B}$, then for the non-varying factor F_0 we arrive at the same equation as for the two-pulse echo decay in the original work of Hu and Hartmann: $F_0 = F_{2p}(d_2) = \exp(-\Delta\omega_{1/2} d_2^2 / T_{1,B})$.

We finally arrive at a compact representation of the RIDME background contribution due to spectral diffusion in the A-B spin system, which can be written as follows:

$$F(t_1) = F_0 \exp \left[-\Delta\omega_{1/2} (\alpha t_1 + \beta t_1^2) \right]. \quad (5.20)$$

The value $\Delta\omega_{1/2}$ is defined above, and the factors α and β are defined as

$$\alpha = \frac{T_{1,B} - d_2}{T_{1,B} + d_2} \cdot \left(1 - e^{-T_{\text{mix}}/T_{1,B}} \right), \quad (5.21)$$

$$\beta = \frac{1}{T_{1,B} + d_2} \cdot \left(1 - e^{-T_{\text{mix}}/T_{1,B}} \right). \quad (5.22)$$

If we consider the case of a DEER experiment in the presence of random flips of the B spins, the derivation of the background function $F(t)$ would be similar. However, the pump pulse in DEER is rather short in time and we can neglect any spontaneous B-spin flips during the pump pulse. The inversion probability of the pump pulse λ_p would in this case substitute the probability of the odd number of B-spin flips during the RIDME mixing block. If we substitute in the above equations p_m by λ_p and q_m by $1 - \lambda_p$, we, thus, obtain the equation for the background shape in the DEER case. This equation would, however, neglect the instantaneous diffusion due to the microwave pulses at the detection frequency. The combined action of the instantaneous and spectral diffusion was considered for the cases of some standard pulse sequences.¹⁹⁰ For the RIDME background signal, it is feasible to assume that spectral diffusion is the major factor.

Equations (5.20) - (5.22) allow us to discuss some general properties of the RIDME background function. First, both linear and quadratic terms in the exponent scale in the same way with increasing the ratio $T_{\text{mix}}/T_{1,B}$. When $T_{\text{mix}} \ll T_{1,B}$, the α and β coefficients are small, and depend

approximately linearly on T_{mix} . They monotonically grow with increasing T_{mix} and reach limiting values $\alpha_\infty = (T_{1,B} - d_2) / (T_{1,B} + d_2)$ and $\beta_\infty = 1 / (T_{1,B} + d_2)$, when $T_{\text{mix}} \gg T_{1,B}$. Second, the coefficients α and β depend in different ways on d_2 and $T_{1,B}$. When d_2 increases for given values of T_{mix} and $T_{1,B}$, both α and β decrease, and the relative magnitude of the linear term in the exponent gets weaker as compared to the quadratic term. As a consequence, changing the length of the measured RIDME trace affects the shape of the background function. As we will discuss in the following sections, this effect is, indeed, experimentally observed in regimes when T_1 and T_m times of the paramagnetic species differ by less than an order of magnitude. If we reduce $T_{1,B}$, e.g., by increasing the measurement temperature, with constant values of $T_{\text{mix}}/T_{1,B}$ and d_2 , the linear-term coefficient α decreases, while the quadratic-term coefficient β increases. Third, both the linear and the quadratic term in the exponent are proportional to the concentration of the paramagnetic species via the factor $\Delta\omega_{1/2}$. Fourth, the quadratic terms in the exponent appear only in case 4, when B-spin flips happen both during the mixing block and during the transverse evolution of the A spins. When $2d_2 \ll T_{1,B}$, the RIDME background decay in the present model turns almost perfectly exponential.

It is worth mentioning once again that these equations are rather accurate only up to the value $d_2 = T_{1,B}/2$. The apparent problem that the term $T_{1,B} - d_2$ gets negative at $d_2 > T_{1,B}$ is then of no concern, since this happens outside of the validity range. At such lengths of the RIDME experiment, more than a single B-spin flip needs to be considered during the transverse evolution of A spins, and, thus, the equations need to be modified. For the complexes studied in this work, at temperatures of 30 K and, for long traces, even sometimes at 20 K, our assumptions do not always hold (see Table B.2 in Appendix B).

The above calculations can be extended to the case of the full 5-pulse RIDME experiment, which would then include the dependency on the first interpulse delay of the primary echo block, d_1 . The derivation is lengthier than the one detailed here, due to more possible spin-flip pathways. However, the final result has the same form as Equations (5.19)-(5.22), namely,

$$-\frac{\ln F_{5p,0}}{\Delta\omega_{1/2}} = \frac{d_1^2 + d_2^2}{T_{1,B} + d_1 + d_2}, \quad (5.23)$$

$$F_{5p}(t_1) = F_{5p,0} \exp[-\Delta\omega_{1/2} (\alpha_{5p} t_1 + \beta_{5p} t_1^2)], \quad (5.24)$$

$$\alpha_{5p} = \frac{T_{1,B} - (d_2 - d_1)}{T_{1,B} + d_1 + d_2} \cdot \left(1 - e^{-T_{\text{mix}}/T_{1,B}}\right), \quad (5.25)$$

$$\beta_{5p} = \frac{1}{T_{1,B} + d_1 + d_2} \cdot \left(1 - e^{-T_{\text{mix}}/T_{1,B}}\right). \quad (5.26)$$

Importantly, the relative contribution of the mono-exponential versus the Gaussian decay is larger for longer d_1 at the same d_2 . Of course, since we assume zero or one B-spin flip during the transverse evolution time $2(d_1 + d_2)$, the ratio $(d_1 + d_2)/T_{1,B}$ must be small and, accordingly, the mentioned effect must be weak. If the value d_1 in Equations (5.25) and (5.26) increases with all other parameters being constant, then the coefficient α_{5p} stays unchanged, neglecting contributions which scale with the power law $(d_1/T_{1,B})^2$ or higher. At the same time, the coefficient β_{5p} decreases, thus, making the overall decay of the RIDME background function

slower. This is counter-intuitive, but results from compensation between the average phase acquisition in the d_1 and d_2 intervals.

Mono-exponential longitudinal relaxation of B spins is a rather strong simplification that we used here to derive the analytic equations. In practice, in frozen glassy solvent mixtures, one observes distributions of T_1 times, which are rather well described by stretched exponential decay functions. We, thus, can speculate that the real RIDME background shape will also be similar to a stretched exponential, and the stretching parameter will decrease when we change the experimental conditions in favour of the linear term, while it will increase, where we favour the quadratic term in Equations (5.20) and (5.24).

For the case of high-spin B species, such as Gd(III)^{73;113;114} or Mn(II)^{93;178;182} ions, the number of possible random trajectories for $h(t)$ would be yet larger, since at each B-spin flip the dipolar frequency might change by one, two, or more units of ω_{dd} . However, the combination of linear and quadratic terms in the exponent would stay on, and the qualitative trends with respect to the changes of the critical parameters T_{mix} , d_2 and $T_{1,B}$ would be the same.

Note that the derived equations also hold true, for instance, for the nuclear spin-induced spectral diffusion contribution to the RIDME background function. There could also be situations, when both electron and nuclear B spins play an important role in the RIDME background. In such cases, one also has to consider 'interference contributions' when the flip during the transverse evolution time is due to one type of B spins, while the flip during the mixing block is due to another B-spin type. In particular, for describing such contributions, one would need to treat the situation with two unequal $\Delta\omega_{1/2}$ values of the electron and the nuclear spin flip events, which can have similar strength since, for instance, the lower magnetic moment of the protons can be compensated by their large concentrations in H₂O-glycerol mixtures. Note further that the RIDME background equations would be also applicable to the case of pairs of paramagnetic centres 'slow spin'-'fast spin', with non-identical A and B spins, which might have relaxation times differing by orders of magnitude.

5.3. Experimental and analysis details

5.3.1. Sample preparation

The background decay behaviour was studied with Gd(III), Mn(II), and Cu(II) complexes formed with the ligand MOMethynyl-PyMTA as well as on a single mutant (Q388C) of the cysteine-free RNA recognition motifs 34 (RRM34) of the polypyrimidine tract binding protein labelled with Gd-DOTA. The syntheses of Gd-PyMTA and Mn-PyMTA are described in Refs.⁹³⁻⁹⁵. The synthesis of Cu-PyMTA is given in Appendix B. The compound solutions were filled into 0.5 mm i.d./0.9 mm o.d. quartz capillaries for W-band and 3 mm o.d. quartz capillaries for Q-band measurements, respectively. The samples were subsequently shock-frozen by immersion into liquid nitrogen before insertion into the precooled microwave cavity. For metal-ion-PyMTA stock solutions in D₂O were diluted to the final concentrations in the range of 25 to 500 μM , either with a 1:1 (v:v) D₂O/glycerol- d_8 or 1:1 (v:v) H₂O/glycerol mixture. Protein expression and purification is described in Ref.¹⁹¹. The RRM34 mutant Q388C was labelled with Gd-maleimide-DOTA according to Reference.¹⁹² 550 μM stock solutions in a low salt buffer (10 mM NaPO₄, 20 mM NaCl, pH = 6.5) were diluted 1:10 (v:v) in either D₂O or H₂O. Both solutions were then diluted 1:1 (v:v) in glycerol- d_8 .

5.3.2. EPR measurements

W-band EPR experiments were performed on a commercial Bruker Elexsys E680 X/W band spectrometer as well as on a modified Bruker Elexsys E680 W-band spectrometer,^{193–195} both operating at about 94 GHz. For the latter spectrometer, a home-built ENDOR cavity with a microwave frequency bandwidth of 130 MHz, was used.¹⁹³ The commercial spectrometer was equipped with a Bruker TE011 resonator. Q-band data were acquired at a Bruker Elexsys E580 Q band spectrometer equipped with a home-built cavity operating at about 34.5 GHz.^{97;98} A helium flow cryostat (ER 4118 CF, Oxford Instruments) was used to adjust the measurement temperature to 10, 20 or 30 K.

Echo-detected (ED) field-swept EPR spectra were acquired using a Hahn-echo pulse sequence $t_p - \tau - 2t_p - \tau$ with a pulse length t_p of 12 ns. The interpulse delay τ was set to 400 ns. The power to obtain the $\pi/2 - \pi$ pulses was set at the central transition of the Gd(III) spectrum by nutation experiments. Longitudinal relaxation measurements were performed using an inversion recovery sequence $t_{\text{inv}} - T - t_p - \tau - 2t_p$, in which the delay T was incremented starting from 1 μs . $t_{\text{inv}} = 12$ or 16 ns and $t_p = 60$ ns. Stimulated echo decays were recorded using $t_p - \tau - t_p - T - t_p - \tau$ for different τ values increment T and $t_p = 12$ ns. RIDME data were acquired using the refocused five pulse sequence shown in Figure 5.1 with $(\pi/2)$ - pulses being set to 12 ns and (π) -pulses to 24 ns. If not explicitly mentioned, the first interpulse delay was set to $d_1 = 400$ ns and the starting point of the mixing block was set to $t_{1,0} = -120$ ns (120 ns before the first Hahn echo), while d_2 was adjusted to the required trace length. The mixing time T_{mix} was varied to study its influence on the signal evolution, and it is specified in each case in the Results and Discussion section. To remove echo crossings and phase offsets, an eight-step phase cycle was used.⁶⁷ For Q-band measurements averaging of ESEEM contributions was performed.⁷⁹

5.3.3. Data analysis

Data were analyzed and processed with home-written MATLAB (The MathWorks Inc., Natick, MA, USA) scripts. In order to extract longitudinal relaxation times T_1 , inverted and offset corrected inversion-recovery traces were fitted by stretched exponential functions of the form $c \cdot \exp(-(t/T_1)^x)$ using a nonlinear least-square fitting criterion based on the function 'nlinfit' (Nonlinear regression) in MATLAB. Errors were extracted from the 95% confidence intervals of the fits using the function 'nlparci' (Nonlinear regression parameter confidence intervals). Hahn-echo decay traces were processed by removing a constant offset averaged over the last 20 data points. The data were then fitted by stretched exponential functions of the form $c \cdot \exp(-(t/T_m)^x)$. Errors were extracted from the 95% confidence intervals of the fits.

RIDME traces were fitted by a stretched exponential function (SE model) of the form $c \cdot \exp(-(kt)^{d/3})$, a sum of two stretched exponential functions (SSE model) of the form $c_a \cdot \exp(-(k_a t)^{d_a/3}) + c_b \cdot \exp(-(k_b t)^{d_b/3})$ or a product of two stretched exponential functions (PSE model) of the form $c \cdot \exp(-(k_a t)^{d_a/3}) \cdot \exp(-(k_b t)^{d_b/3})$. If not stated explicitly the SE model was used. Fits were performed with MATLAB scripts, based on the functions 'lsqcurvefit' (Nonlinear least-squares solver) and 'nlparci' (Nonlinear regression parameter confidence intervals) from the Optimization and Statistic Toolbox. Similar to the DEER experiment, k quantifies the density of spins or decay rate and d is the dimensionality of the fitted function or stretching exponent. $d = 3$ corresponds to a mono-exponential function and $d = 6$ corresponds to a Gaussian decay function. Errors were estimated from the 95% confidence of the fit. An additional uncertainty

was taken into account by varying the starting positions of the fit from 0 to about 200 ns after the zero time point as the region around the zero time point is in some cases distorted by an echo-crossing artefact. Note, however, that the MATLAB function mentioned above computes the confidence interval based on an approximate method, using the gradients at the best-fit point. This approach was found to provide good error estimates once the RIDME background trace was decaying to about 30-40% of the initial echo signal. For traces decaying only to about 60%, the errors were estimated manually (See Appendix B for details). The actual relative errors for d were about 10%. For traces decaying by only 10% of the initial value, the error was around 30%, depending in all these cases also on the particular signal-to-noise ratio, which was slightly varying between data sets. The corresponding relative errors for k were systematically smaller than for d . The inaccuracies allowed us only to discuss trends in d variations for the sample with 500 μM Gd-PyMTA concentration and for some of the data at 100 μM concentration. The much larger changes in k upon variation of temperature and concentration, ensured that all trends observed for k were exceeding the estimated error bars. More details can be found in the Results and Discussion section and in Appendix B.

5.4. Results and Discussion

5.4.1. Transverse and longitudinal relaxation in Gd-PyMTA

Figure 5.2 shows transverse and longitudinal relaxation traces measured for Gd-PyMTA in a frozen, glassy $\text{D}_2\text{O}/\text{glycerol-d}_8$ matrix in W band. We observed a strong temperature dependence of the Gd(III) electronic relaxation times T_1 and T_m in the investigated temperature range from 10 to 30 K. Transverse relaxation times increase approximately by a factor of two for each temperature decrease of 10 K (see Figure 5.2(a)). Longitudinal relaxation measurements (see Figure 5.2(d)) exhibit a yet steeper increase of T_1 with decreasing temperature. Longitudinal relaxation of the Gd-PyMTA centres is almost unaffected by a change in metal ion concentration from 25 to 500 μM (Figure 5.2(e)) and only slightly affected for different detection positions within the EPR spectrum of Gd(III) (see Figure 5.2(f)). In contrast, the transverse relaxation rate is significantly increased when the detection is moved away from the central peak in the Gd(III) spectrum (Figure 5.2(c)). This phenomenon is related to differences in transverse relaxation of the different Gd(III) electronic transitions, which was previously discussed by Raitsimring *et al.*,⁴⁷ and attributed to a ZFS-driven relaxation pathway. Here, however, we are most interested in the relaxation properties at the central peak of the Gd(III) spectrum, since this is the usual detection field position in the RIDME experiment. Field-dependent relaxation properties of high-spin metal centres are an interesting and important topic in itself, which deserves a dedicated study.

The characteristic transverse relaxation time of Gd(III) centres defines the upper limit of the detectable distance range in RIDME experiments. This might still be shortened if the RIDME background decay is too steep. The latter possibility is discussed in the following section. Here we conclude that transverse evolution for the Gd-PyMTA complex in a deuterated matrix and at low concentration (25 μM) allows detecting spin echoes after about 80 μs of transverse evolution, which corresponds to a distance of about 14 nm.⁵⁰ Note that in this work we used protonated PyMTA and the intramolecular interactions between the electron and the proton spins would still make an additional contribution to the electronic relaxation.⁵⁵

There is a clear concentration dependence of the shape of the transverse evolution decay for Gd-PyMTA. In a deuterated matrix, where the contribution by the electron-nuclear relaxation pathway is relatively weak, there is still a significant difference between the transverse relaxation curves measured at 100 μM and at 25 μM Gd-PyMTA concentration (Figure 5.2(b)). Interestingly, while the characteristic $1/e$ decay time does not change significantly between these two concentrations, the shape of the Hahn echo decay curve clearly changes from a more mono-exponential-like shape for the 25 μM sample to a more bell-like shape for the 100 μM sample. This is a clear indication that the main relaxation mechanisms, contributing to the Hahn echo decay, change within this concentration range. It is likely that at 25 μM Gd-PyMTA concentration nuclear-electron spectral diffusion (NSD) along with ZFS-driven processes dominate the transverse relaxation, while at a concentration of 100 μM electron-electron spectral diffusion (ESD) starts to play a significant role.

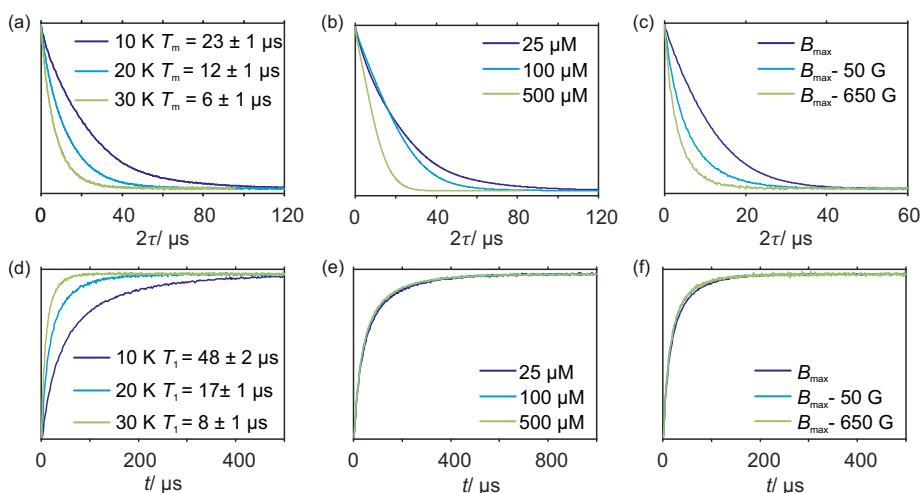


Figure 5.2. Transverse (a-c) and longitudinal (d-f) relaxation traces for Gd-PyMTA (1:1 (v:v) D_2O :glycerol- d_8 matrix) in W band. The $T_{(1/e)}$ times in the panels (a, d) report the times when the decay down to $1/e$ level of the initial value is reached. (a, d) Temperature dependence at 25 μM , detection at magnetic field position of maximum EPR signal intensity, B_{max} ; (b, e) concentration dependence at 20 K, detection at B_{max} ; (c, f) dependence of detection field position at 20 K, 100 μM .

Neither transverse nor longitudinal relaxation traces of Gd-PyMTA can be accurately fitted to mono-exponential functions. Most experimental data can be well approximated by stretched exponential functions. However, at some conditions the use of a sum of two stretched exponential functions resulted in a further improvement of the fit quality. A similar situation was observed earlier for nitroxide radicals and related to differences in intramolecular- and solvent-driven relaxation pathways.⁵⁵ In the present case, this finding might be attributed to the diversity of local surrounding in the glassy matrix, as well as to the presence of several relaxation pathways. We thus conclude that in frozen glassy solutions, the relaxation data need to be described by a distribution of T_m and T_1 times. Consequently, distributions of the mono-exponential and the Gaussian decay rates are expected in the spectral diffusion processes during the RIDME experiment. Therefore, stretched exponential shapes are expected for the RIDME background decay, being either of more mono-exponential or more Gaussian character depending on the weighting of the pre-factors α and β in Equation (5.24). Based on the strong change in transverse relaxation rate (Figure 5.2(b)), we assume that, at 500 μM Gd-PyMTA concentration, ESD processes dominate.

5.4.2. Stimulated echo decays of Gd-PyMTA

Compared to inversion recovery traces, stimulated echo decay is more sensitive to spectral diffusion and this sensitivity increases with an increase of the first interpulse delay τ due to a narrower spacing $1/\tau$ (on the angular frequency scale) of the polarization grating with increasing τ .

The W-band stimulated echo decay data for Gd-PyMTA in a deuterated water/glycerol frozen glassy matrix are presented in Figure 5.3. A single homogeneous Markovian process is predicted to produce a mono-exponential dependence on the second delay time T in stimulated echo experiments.¹⁸⁷ The experimental decay shapes are close to stretched-exponential functions and indicate that the assumption of a single homogeneous Markovian process is not sufficient for describing the data. If we consider electron-electron or electron-nuclear dipolar interactions, the width of the distribution of possible effective fields at the spatial point of an A spin is comparable to the strength of a single A-B spin coupling for several B spins which are in the nearest vicinity (among all B spins) of the A spin. Thus, a single B-spin flip might bring the resonance position of the A spin to the other side of the resonance frequency range, over which it can diffuse. Furthermore, the probability of frequency jumps in one or the other direction would correlate with the current resonance frequency of the A spin. For the A spins with effective field at the edges of this distribution and for the A spins with the effective field in the middle of the distribution the probabilities of corresponding spontaneous increase and decrease of the effective field would not be the same. This breaks Markov's assumption of the independence of the probability distribution on the pre-history of the stochastic process. Fortunately, the calculation routine used in this work allows avoiding this Markovian assumption, and thus is adequate for the description of the present case of spectral diffusion.

In absence of spectral diffusion, the stimulated echo decay still contains contributions from longitudinal relaxation of the electron spins, since the second delay time is varied during the experiment. From comparison of the data in the three lower panels of Figure 5.2 with the data of Figure 5.3, we conclude that the stimulated echo decay is faster than the longitudinal relaxation decay at all tested conditions. In line with the expectations, the characteristic decay time in the stimulated echo experiment gradually decreases with the increase of τ . The more pronounced change of characteristic decay time with τ for the sample containing 500 μM of Gd-PyMTA, as compared to the sample with the 25 μM concentration, can be attributed to either a higher rate of spectral diffusion or a larger average strength of dipolar interactions for the more concentrated sample. To remove the contributions from longitudinal relaxation, constant time measurements, sensitive to spectral diffusion, would be useful. This approach can be realized with the 5-pulse version of the RIDME experiment, where the total times of transverse and longitudinal relaxation are identical for all measurement points.

5.4.3. Intermolecular background decay in refocused RIDME experiments with Gd-PyMTA

Relations of the relaxation times of the Gd(III)-PyMTA complexes to the delay settings in the refocused RIDME experiment are given in Appendix B.7. Figure 5.4 shows the five-pulse RIDME background decay data for the Gd-PyMTA complex in frozen deuterated water/glycerol mixtures, as well as a comparison of the characteristic decay time between samples in protonated and deuterated solvents. Figure 5.4(a) shows the dependence of the RIDME background decay on the concentration of the Gd(III) centres. The RIDME experiment is very sensitive to spectral

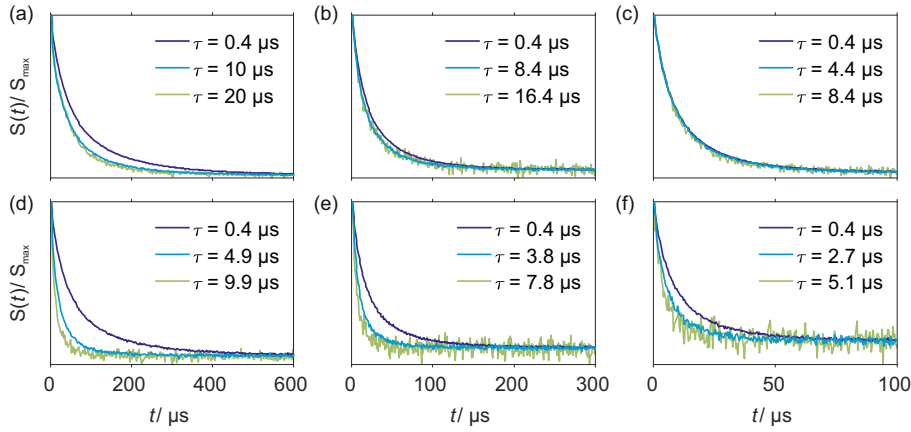


Figure 5.3. W-band stimulated echo decay of Gd-PyMTA for different interpulse delays τ at different temperatures. Two concentration regimes were probed in a deuterated water/glycerol frozen glassy matrix: (a-c) 25 μM sample, negligible electron-electron coupling and (d-f) 500 μM , significant electron-electron interactions. (a, d) 10 K; (b, e) 20 K; (c, f) 30 K.

diffusion driven mechanisms. Therefore, the changes in decay shape with spin concentration are more systematic than for the transverse relaxation traces in Figure 5.2. One can clearly recognize a further increase of the characteristic decay time with decreasing concentration even between the samples with 100 μM and 50 μM Gd-PyMTA concentration.

Figure 5.4(b) demonstrates the decrease of the characteristic decay time of the RIDME background trace with increasing mixing time, which well reproduces the trend predicted by Equations (5.21, 5.22) and (5.25, 5.26). Conceptually similar and, thus, leading to the same trend, is the decrease of the characteristic decay time with increasing measurement temperature, as shown in Figure 5.4(c). An increase in temperature induces shorter $T_{1,B}$ times, and thus the ratio $T_{\text{mix}}/T_{1,B}$ increases at constant mixing time.

Figure 5.4(d) compares the RIDME decay for a 25 μM Gd-PyMTA sample in protonated and deuterated water/glycerol. First, note a further increase of the characteristic decay time in the deuterated sample of 25 μM as compared to the 50 μM data in Figure 5.4(a). This shows that even at 50 μM electron spin concentration an electron-driven RIDME decay pathway plays an important role in deuterated solvent. Second, the comparison of the characteristic decay time reveals a drastic change if protons are replaced by deuterium. The coupling of the electron spin to the nuclear spin bath results in rapidly fluctuating environments at the electron spin site. These fluctuations, caused by nuclear spin diffusion, are much more efficient for proton than deuteron spins for two reasons: (i) a proton spin flip corresponds to a stronger field change at the electron due to the larger magnetic moment of the proton, (ii) proton spin flips occur more frequently, since nuclear spin diffusion results from the coupling between the nuclear spins, which is much stronger for protons than for deuterons. The comparison reveals that the performance of the RIDME technique can be drastically improved by matrix deuteration.

Equations (5.21, 5.22) and (5.25, 5.26) predict a slower RIDME background decay for longer delays d_1 and d_2 . This was, indeed, observed experimentally, as illustrated in Figure 5.5. Figures 5.5(a, b) demonstrate the trend of decelerated background decay with an increasing delay d_1 , while Figure 5.5(c) shows the effect for increasing the delay d_2 . Figure 5.5(d) demonstrates the effect for a simultaneous increase of d_1 and d_2 . Note that in some series shown in Figure 5.4, it was not possible to always keep the same delay time d_2 , e.g. for different Gd(III) concentrations

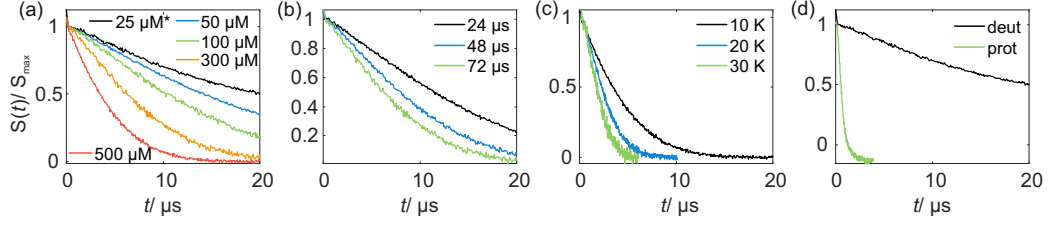


Figure 5.4. Experimental RIDME background decay of Gd-PyMTA samples in W band: (a) at 10 K, $T_{\text{mix}} = 72 \mu\text{s}^*$ and varying spin probe concentration in deuterated solvent; $^*25 \mu\text{M}$ sample has $T_{\text{mix}} = 96 \mu\text{s}$ (b) 300 μM spin probe concentration in deuterated solvent, at 10 K and varying T_{mix} ; (c) 500 μM spin probe concentration in deuterated solvent, $T_{\text{mix}} = 72 \mu\text{s}$ and varying measurement temperature; (d) 25 μM spin probe concentration in deuterated or protonated solvent, at 10 K and $T_{\text{mix}} = 96 \mu\text{s}$. Note that signals are scaled to maximum intensity excluding the zero-time artefact.

or mixing times. The changes in the RIDME background decay times with Gd(III) concentration, mixing time or temperature, shown in Figure 5.4 are, however, much larger than the changes with delay time variations in Figure 5.5, thus making our previous discussions of the trends still valid. For instance, in Figure 5.4(a) the change of the characteristic decay time between the 300 μM and the 500 μM samples is larger than 50%, and the length difference in the RIDME background decay traces is about 20%. To compare, a still smaller change of the characteristic decay time is obtained if the length of the RIDME trace is increased more than three times from 3.2 μs to 10.2 μs , with all other experimental parameters kept constant (Figure 5.5(c, d)).

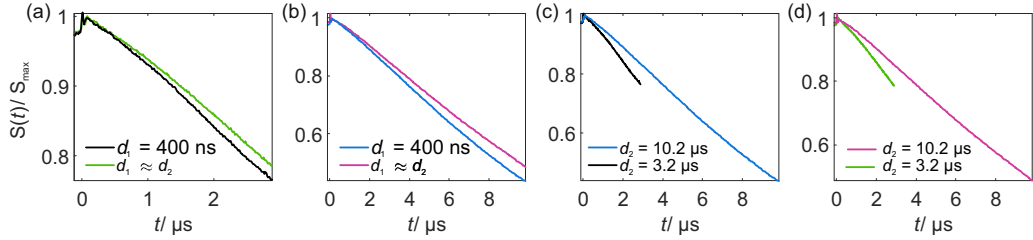


Figure 5.5. Experimental W-band RIDME background decays at 10 K for different interpulse delays ($T_{\text{mix}} = T_1$, 100 μM Gd-PyMTA, 1:1 (v:v) D_2O :glycerol- d_8). (a) $d_2 = 3.2 \mu\text{s}$, $d_1 = 400 \text{ ns}$ and $d_1 \approx d_2$; (b) $d_2 = 10.2 \mu\text{s}$, $d_1 = 400 \text{ ns}$ and $d_1 \approx d_2$; (c) $d_1 = 400 \text{ ns}$, $d_2 = 3.2$ and $d_2 = 10.2 \mu\text{s}$; (d) $d_1 \approx d_2$, $d_2 = 3.2$ and $d_2 = 10.2 \mu\text{s}$. Note that time traces are scaled to maximum intensity excluding the zero-time artefact.

As the pulse sequence settings strongly influence RIDME background decay, a systematic study of the influence of metal ion concentration (25, 100, 500 μM), measurement temperature (10, 20, 30 K) as well as mixing time was performed at four fixed pulse sequence settings. The trends obtained from fitting the refocused RIDME background decays with a single stretched exponential decay model to this set of data are illustrated in Figures 5.6, 5.7 and 5.8. Figure 5.6 shows the dependencies of the dimensionality parameter d and decay rate constant k on the normalized mixing time T_{mix}/T_1 for three Gd-PyMTA concentrations. The comparison in each panel is shown for one of the three temperatures: 10 K, 20 K or 30 K (left to right), and for one fixed set of delay times (d_1, d_2). Figure 5.7, in turn, shows analogous graphs, comparing in each panel data for the listed three temperatures, while keeping the same Gd-PyMTA concentration, and fixed set of delay times (d_1, d_2). Finally, Figure 5.8 compares data for the four different time delay sets (d_1, d_2), with each panel dedicated to one fixed concentration and one fixed temperature. Figure B.6 and B.7 show decay rates k with enlarge vertical axis to better visualize differences in addition to Figure 5.7 and 5.8, respectively.

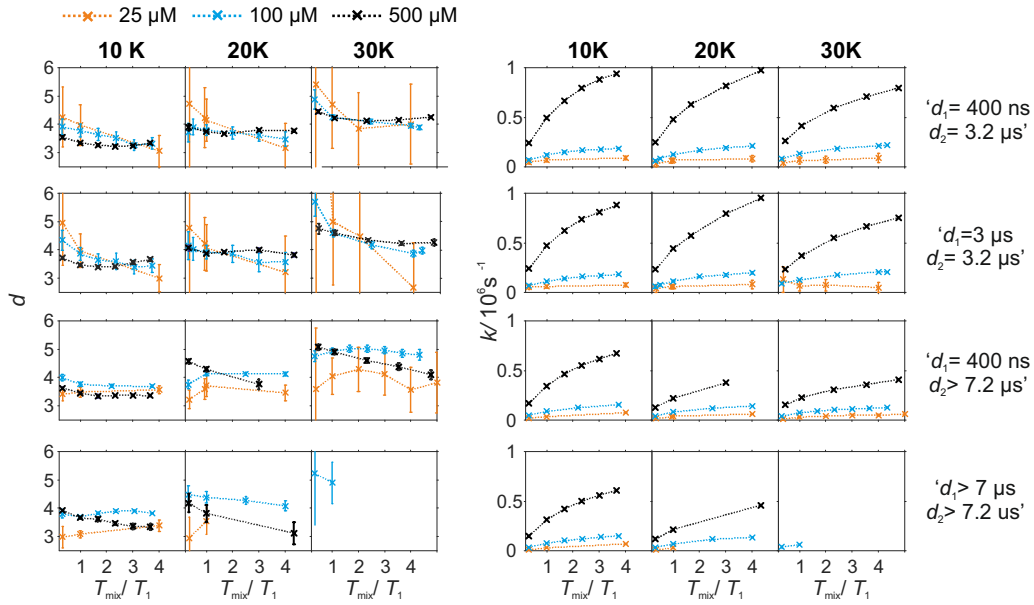


Figure 5.6. Comparison of the stretched exponent factor d and decay rate constant k versus the relative mixing time T_{mix}/T_1 obtained from the analysis of experimental W-band RIDME decays at given pulse sequence settings (top to bottom) and measurement temperatures (left to right). The Gd-PyMTA concentration ranges are colour encoded: orange $25 \mu\text{M}$, light blue $100 \mu\text{M}$, purple $500 \mu\text{M}$ in 1:1 (v:v) D_2O :glycerol- d_8 .

In general, for varying experimental conditions, accurate determination of the trends for the dimensionality parameter d was more difficult than for the decay constant k , because the relative changes in k were significantly larger. An accurate determination of d and k requires acquisition of RIDME traces, which are longer than the $1/k$ time (for a stretched exponential function this is equal to the $1/e$ time), and this was not always possible in the series of measurements with fixed sequence settings. Nevertheless, for short RIDME traces the product $k \cdot d$ can be determined rather accurately from the initial slope of the trace. Variations of the d parameter fall into the range between 3 and 6, corresponding to the expected range between mono-exponential and Gaussian decay. Slower decay of the RIDME traces at low Gd-PyMTA concentrations makes the determination of d values less accurate than for the highest tested Gd-PyMTA concentration. Similarly, at the same concentration the d values determined for shorter RIDME traces (shorter delay times d_2) are less accurate than for longer ones due to the shortened fitting range. Furthermore, at 30 K, where the relaxation times of Gd(III) centres are the shortest among tested conditions, signal-to-noise ratio is rather low. Thus, a higher inaccuracy of the fitted parameters is induced at 30 K as compared to those at 10 K and 20 K. The relative changes of k are much larger and, therefore, trends for the k parameter can be also caught from the measurements with short RIDME traces.

Equations (5.21, 5.22) and (5.25, 5.26) predict no change of the dimensionality parameter for varying mixing time. In the experiment, however, we deal with distributions of transverse and longitudinal relaxation times, and changes may result from a lower contribution of fast-relaxing species at long mixing times. For instance, in some panels, especially for high Gd-PyMTA concentrations and long transverse evolution delay times, there is a trend of decreasing d with increasing mixing time (see, for instance, in Figure 5.7 the d dependence on T_{mix}/T_1 in the two panels for $500 \mu\text{M}$ and long d_2 and long or short d_1). The scenario requires that the longitudinal relaxation time $T_{1,A}$ of A spins correlates with the longitudinal relaxation times $T_{1,B}$ of B spins

in the near vicinity of the given A spin. This might happen, e.g. if the sample contains regions with slightly better and slightly worse glass quality. In such a sample, if the relaxation time of the A spin is slower than the average value through the whole sample, then the B-spins around this A spin will also relax slower than average. The distribution of the relaxation times for such a sub-ensemble of B-spins would be narrower than the overall distribution, describing the entire sample. If such areas in the glass would not exist, then the distribution of relaxation times of B spins around any A spin would be the same.

Another contribution might stem from combined action of different types of B-spins (e.g. once nuclear spins and once electron spins) during the transverse evolution time and the mixing block. This can lead to interference effects of more Gaussian or more exponential-like RIDME background decay shape. The weighting of both contributions would in such cases depend on the length of the mixing time. One might speculate that such trends are sometimes present in the left set of panels in Figure 5.7.

A clear and systematic trend for the d parameter can be seen for the 500 μM Gd-PyMTA sample upon temperature variation (Figure 5.7). With the sample temperature increase the ratio $(d_1 + d_2)/T_{1,B}$ gets smaller, which enhances the relative contribution of the quadratic term, as compared to the linear term in Equations (5.21, 5.22) and (5.25, 5.26). This trend is still visible for the 100 μM sample. It is, however, absent or within precision of the performed background measurements for the 25 μM sample, where the nuclear spectral diffusion plays a key role in the shape of the RIDME background decay. Apparently, flip rates of nuclear spins are smaller than for Gd(III) electron spins, and also the nuclear spin flip rates change much slower with temperature in the given temperature range from 10 K to 30 K. Both these effects would lead to the reduction of the magnitude of the discussed change of d with temperature.

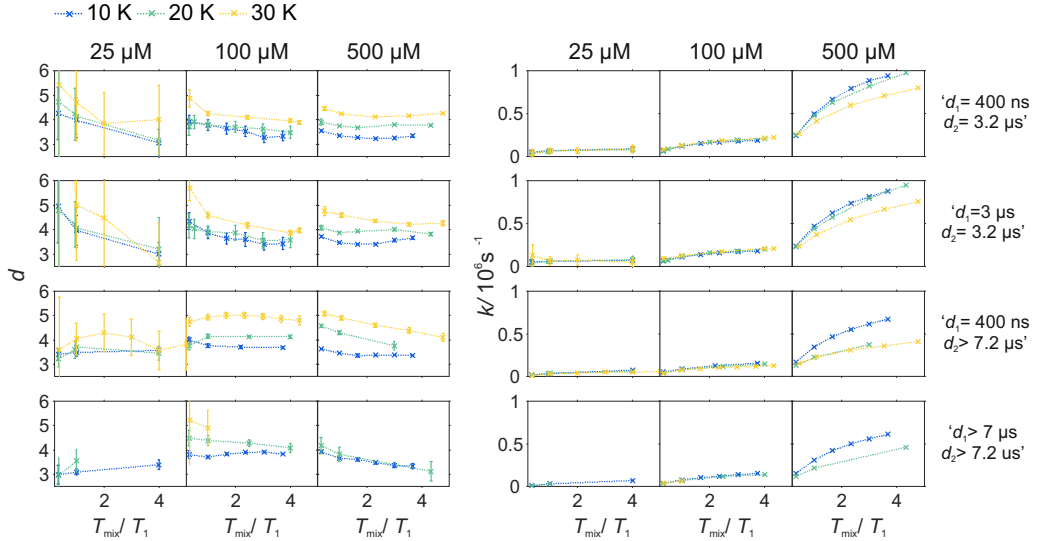


Figure 5.7. Comparison of the stretched exponent factor d and decay rate constant k versus the relative mixing time T_{mix}/T_1 obtained from the analysis of experimental W-band RIDME decays in deuterated solvent matrix at given pulse sequence settings (top to bottom) and spin concentration (left to right). The measurement temperature is colour encoded: blue 10 K, green 20 K, yellow 30 K.

Spectral diffusion contributions to the RIDME background shape increase at longer mixing times T_{mix} . This is also expressed in Equation (5.24). The characteristic decay rate k must increase upon increase of the ratio $T_{\text{mix}}/T_{1,B}$ as well as upon increase of the concentration of the

B spins, which is clearly visible in all three Figures (5.6), (5.7) and (5.8). The ratio $T_{\text{mix}}/T_{1,B}$ can be altered by either changing the mixing time, or, the longitudinal relaxation of the B spins. The latter can be achieved by increasing the sample temperature, which should lead to shorter $T_{1,B}$. In the studied temperature range (10 - 30 K), this only affects the cases of electron spin dominated mechanisms. For $T_{\text{mix}} \ll T_{1,B}$, k should monotonically increase, flattening to plateau for $T_{\text{mix}} \gg T_{1,B}$ as suggested by Equations (5.24) - (5.26). These findings are reproduced in the experiments (Figure 5.6) at higher electron spin concentrations. In cases of dominating nuclear-spin mechanisms (25 μM spin concentration), there seems to be a rather large $T_{1,\text{nuclei}}$ as we observe an almost linearly increasing k in the studied range of T_{mix} .

Note that, in Figures 5.6 - 5.8, we always normalize the mixing time to the electronic longitudinal relaxation time $T_{1,e}$. This partially compensates for the effect of changing temperature, so that, for instance, the dependencies of k on normalized mixing time for the 100 μM and 500 μM samples are nearly perfectly identical for 10 K and 20 K data. Deviations from this trend for the 500 μM sample at 30 K or for the longest sets of transverse delays might be partially due to filtering effects on the relaxation time distributions. Furthermore, at this temperature, the used transverse evolution times $d_1 > 7 \mu\text{s}$ or $d_2 > 7.2 \mu\text{s}$, are already in the regime in which they approach $T_{1,B}$. This alters the algebraic factors $((T_{1,B} - (d_2 - d_1))/(T_{1,B} + d_1 + d_2))$ and $1/(T_{1,B} + d_1 + d_2)$ in the equations for α and β and it can also lead to deviations from the derived theory due to the sufficiently high probability of more than one B-spin flip during the transverse evolution.

The change of the RIDME background decay coefficients upon changing the delays d_1 and d_2 , illustrated by comparison of the decay traces in Figure 5.5, can be seen as systematic trends in Figure 5.8. The clearest trend is visible for the 500 μM sample where any increase of either d_1 or d_2 leads to smaller k , which is predicted by the dependence of the factors α (Equations 5.21, 5.25) and β (Equations 5.22, 5.26) on d_1 and d_2 . In line with the derived equations, the change of the coefficients is stronger with d_2 than with d_1 . At lower temperatures the trend upon d_2 change becomes somewhat weaker due to the influence of the longitudinal relaxation times of the Gd(III) centres on the coefficients. Whereas this trend can still be recognized for the sample with 100 μM Gd-PyMTA concentration, it is invisibly weak for the 25 μM sample. As discussed above, due to lower accuracy of d determination, no systematic changes of the d parameter could be determined in the series of transverse delay times with the 25 μM sample.

For the 100 μM and 500 μM samples we observed that for longer dipolar evolution times d_2 the background dimensionality d weakly increases. This supports our theory: looking into Equations (5.21) - (5.22) it can be seen that α decreases with a factor of $(T_1 - d_2)$ faster than β , which favours a more Gaussian-like decay with higher dimensionality of the stretching exponent for longer delays d_2 .

The situation is more complex for a change in the d_1 value. The changes in d as well as k , predicted by theory, are much smaller with changing d_1 than changing d_2 . While with increasing d_1 , β is predicted to be decreasing (Equation 5.26), α at the same time is kept approximately constant (Equation 5.25). This means that a lower stretched exponent parameter d would be expected for longer d_1 evolution. In our experimental data, we observe that this parameter is, however, increasing. The effect is reduced at longer mixing times. The longer first interpulse delay allows for more spin flips during the transverse evolution, which might then in some way favour a Gaussian decay shape, yet a mono-exponential decay is favoured by the longer mixing block.

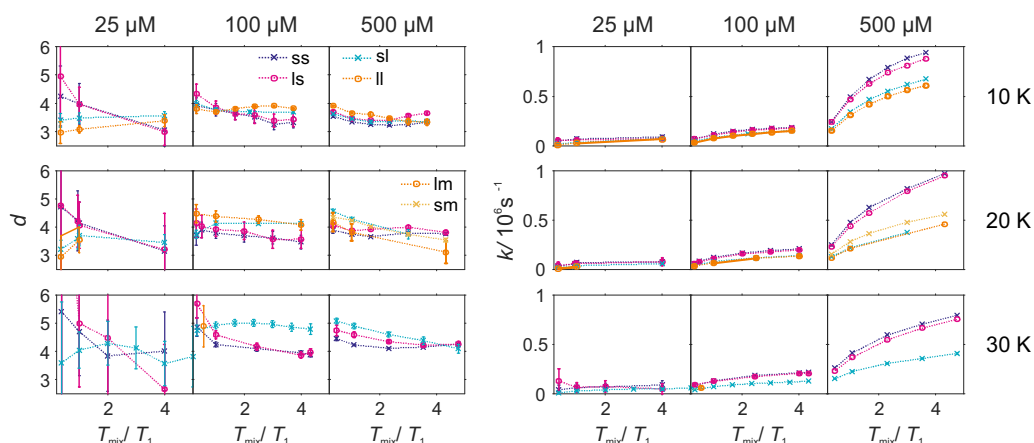


Figure 5.8. Comparison of the stretched exponent factor d and decay rate constant k versus the relative mixing time T_{mix}/T_1 obtained from the analysis of experimental W-band RIDME decays in deuterated solvent matrix at given measurement temperature (top to bottom) and spin concentration (left to right). The pulse sequence settings are colour encoded: purple line (ss): $d_1 = 0.4 \mu\text{s}$, $d_2 = 3.2 \mu\text{s}$; dark blue line (ls): $d_1 = 3 \mu\text{s}$, $d_2 = 3.2 \mu\text{s}$; light blue line (sl): $d_1 = 0.4 \mu\text{s}$, $d_2 = 10.2 \mu\text{s}$ and green line (ll): $d_1 = 10 \mu\text{s}$, $d_2 = 10.2 \mu\text{s}$. At 30 K, the long d_2 values was only set to $7.2 \mu\text{s}$ and correspondingly d_1 to $7 \mu\text{s}$. At 20 K the green line (lm) corresponds to $d_1 = 7 \mu\text{s}$, $d_2 = 7.2 \mu\text{s}$ and the yellow line (sm) to $d_1 = 0.4 \mu\text{s}$, $d_2 = 7.2 \mu\text{s}$. Cross marks correspond to a short interpulse delay d_1 of 400 ns; circles to a long d_1 on the order of d_2 .

Moving the detection position away from the central line of the Gd(III) spectrum leads to an accelerated RIDME background decay in a deuterated matrix by an increase of the decay rate k (see Appendix B, Figure B.4 and Figure B.5). It is accompanied by a shift of the background dimensionality to a more mono-exponential decay. However, the effect is only observed at short dipolar evolution delays $d_2 = 3.2 \mu\text{s} < T_{\text{m,Bouter}}$, where $T_{\text{m,Bouter}}$ stands for the phase memory time of Gd(III) centres at the spectral positions outside of the central peak. For longer delays ($d_2 > T_{\text{m,Bouter}}$) the effect becomes insignificant. We speculate that the increase of the decay rate is driven by a stronger contribution of ZFS-driven flip-flops at the outer transitions. At longer delays $d_2 > T_{\text{m,Bouter}}$, spins with a strong contribution to the transverse relaxation from the ZFS-driven pathway might be already decayed and thus filtered out.

5.4.4. RIDME background decays of a Gd(III) spin-labelled protein sample

In experiments with spin-labelled biomolecules it is sometimes difficult to prepare fully deuterated samples (including, both, deuterated solvent and deuterated biomolecule). An often more realistic scenario is that the spin-labelled protein stems from expression in protonated media, and is not deuterated, while the buffer solution is fully or partially deuterated. In this case the RIDME background decay may be dominated by the proton-driven NSD mechanism already at higher spin label concentrations. The spin label concentration threshold in such cases will depend on the overall average proton concentration in the sample.

In Figure 5.9 a set of RIDME background decays is presented for the two-domain construct RRM34 of PTBP1 spin labelled with the Gd(III)-DOTA at residue Q388C, where the native amino acid was substituted by a cysteine. The three upper panels show data for a partially deuterated solvent matrix ($\approx 50\%$ protons) composed of protonated water and deuterated glycerol, while the lower three panels present the data for an almost fully deuterated solvent matrix ($< 5\%$ protons).

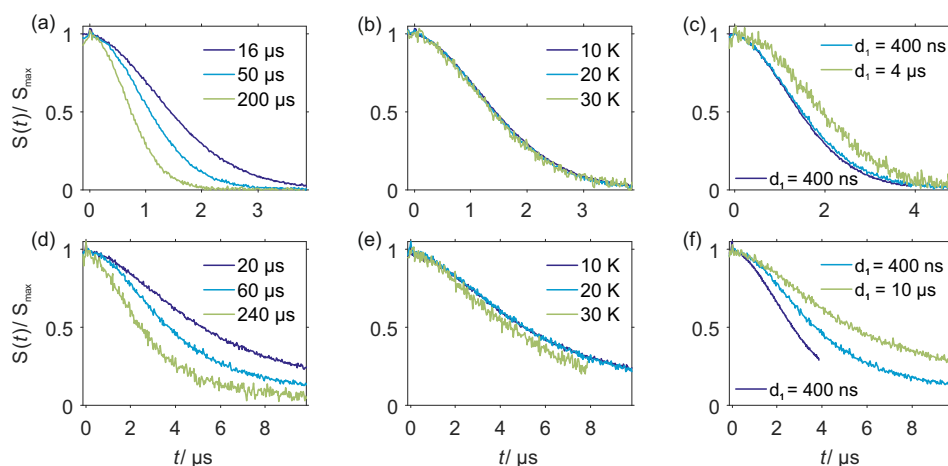


Figure 5.9. Experimental W-band RIDME background decays of RRM34 Q388C Gd(III)-DOTA ($\approx 30\mu\text{M}$). (a-c) in H_2O buffer:glycerol- d_8 ; (d-f) in D_2O buffer:glycerol- d_8 . (a, d) 10 K, varying T_{mix} , $d_1 = 400$ ns; (b) $T_{\text{mix}} = 16$ μs , $d_1 = 400$ ns, varying temperature; (e) $T_{\text{mix}} = 20$ μs , $d_1 = 400$ ns; (c) at 10 K, $T_{\text{mix}} = 16$ μs and varying pulse sequence settings: purple line: $d_1 = 400$ ns, $d_2 = 4.2$ μs ; blue line: $d_1 = 400$ ns, $d_2 = 5.2$ μs ; green line: $d_1 = 4.2$ μs , $d_2 = 5.2$ μs ; (f) at 10 K, $T_{\text{mix}} = 60$ μs and varying pulse sequence settings: purple line: $d_1 = 400$ ns, $d_2 = 4.2$ μs ; blue line: $d_1 = 400$ ns, $d_2 = 10.2$ μs ; green line: $d_1 = 10$ μs , $d_2 = 10.2$ μs . Note that time traces are scaled to maximum intensity excluding the zero-time artefact.

Comparing the data in Figure 5.9(a) and 5.9(d) reveals that deuteration of the buffer solution significantly increases the characteristic decay time of the RIDME background (by a factor of two to four) and, thus, facilitates measurements of longer spin-spin distances in RIDME experiments. Still, the characteristic decay times in these measurements are significantly shorter than for Gd-PyMTA in fully deuterated solvent mixture, which can be attributed to the protons in the protein and the remaining protons in the buffer solution. Importantly, for a fixed mixing time (Figures 5.9(b, e)) no temperature dependence of the RIDME decay shape was observed, except at 30 K in almost fully deuterated buffer solution. The exception most likely results from a shorter length of the trace at 30 K, which was enforced by a low sensitivity due to fast transverse relaxation at 30 K. Thus, we conclude that the proton flip rates relevant in the RIDME experiment are constant over the studied temperature range, at least between 10 K and 20 K. This suggests that at these temperatures and the studied concentration the spectral diffusion mechanism is driven by coupling of the electron spin to the surrounding bath, in which proton flips due to dipole-dipole couplings are temperature independent. These findings are also in line with the very strong change of the NSD contribution, once protons are substituted by deuterium nuclei.

It is important to note that at some conditions the RIDME background decay is not well fitted by a single stretched exponential function as shown in Figure 5.10(a). It follows from Equation (5.24) that the decay function is composed of a product of mono-exponential and Gaussian component. Taking into account the distribution of relaxation times, one could construct a test function which is a product of two stretched exponential functions, with the expectation that one of the two fitted d parameters will appear to be closer to three and the other one - closer to six. However, also fitting the protein RIDME data to a product of two stretched exponential functions does not improve fit quality, as presented in Figure 5.10(b). On the other hand, the trace can be fitted by a single stretched exponential function if the data trace is cut (Figure 5.10(c)) or by a sum of two stretched exponential functions (Figure 5.10(d)). This can be explained by the assumption that the spin label relaxes in different surroundings, depending on the conformation of the tether between the paramagnetic moiety and the protein backbone. One type of spin

label surrounding, corresponding to more compact tether conformations, would contain more protons from the protein and would be characterized by shorter phase memory times T_m . The local surroundings of the spin label with more stretched tether conformations would be more strongly influenced by the solvent deuterons, and would have longer T_m . Of course, here we talk about a distribution of surroundings and T_m times, rather than about two distinct well-defined spin label states. This is in line with a strong influence of the spatial arrangement and degree of protonation for phase memory times T_m described earlier for DEER experiments.⁵⁰ Local environmental effects on the spin-label phase memory relaxation time T_m of protonated proteins in deuterated solvents were also found to introduce a dependence on the distance distribution $P(r)$ on the length of the dipolar evolution period T .¹⁹⁶

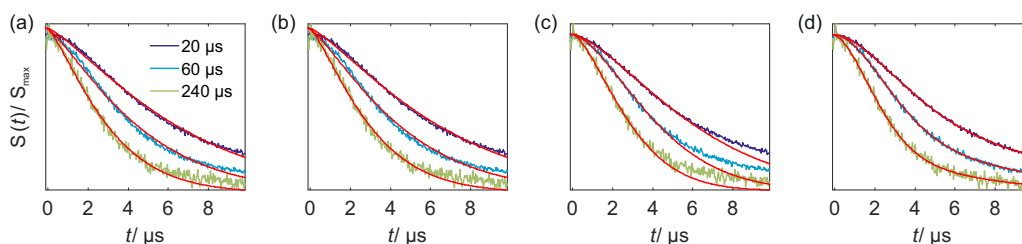


Figure 5.10. Comparison of fitting range and fitted model for W-band RIDME background decays at 10 K. Spin-labelled protein mutant RRM34 Q388C in D_2O buffer:glycerol-d8. (a) Stretched exponential function fit to full trace; (b) product of two stretched exponential function fit to full trace; (c) stretched exponential function fit to first part of the trace; (d) sum of two stretched exponential functions fit to full trace. Note time traces are scaled to maximum intensity excluding the zero-time artefact.

5.4.5. General discussion

The theoretical model, presented in this work, includes only one type of slowly flipping B spin with defined flip rate. The analysis of the experimental RIDME data on frozen solutions of Gd-PyMTA and peptide-bound Gd-DOTA reveals that this simple model is capable to describe the key trends in the shape of the RIDME background decays. Experimental features can be understood using the combination of the presented theoretical model and the assumption of distributed relaxation times for A and B spins. The model predicts a mixture of mono-exponential and Gaussian decay curves for the RIDME background. From analysis of experimental data we always obtained dimensionality parameters d between 3 (corresponding to mono-exponential decay) and 6 (corresponding to Gaussian decay). This is consistent with the theoretical prediction, provided we average the derived theoretical equations over a distribution of $T_{1,B}$ times. We see, however, in Figure 5.11 that a product of Gaussian and mono-exponential decay allows for a slight improvement of the fits for an almost fully decayed trace. Yet, in many cases the systematic study presented above did not allow to measure almost fully decayed traces, which makes analysis more ambiguous and often no significant difference in the fit quality could be observed (see Appendix B, Figures B.2, B.3) so that a single stretched exponential model was used for data analysis.

There are some weak trends in the d value, which seem to go above the estimated error bars, and for which some realistic speculations can be constructed based on the assumptions of distributed relaxation times, interference of spin flips of different types of spins and, eventually, distribution of the local glass quality throughout the EPR sample. The theoretical model presented here is also helpful in analyzing those scenarios. However, these effects are relatively weak as compared to the main trends for d and k .

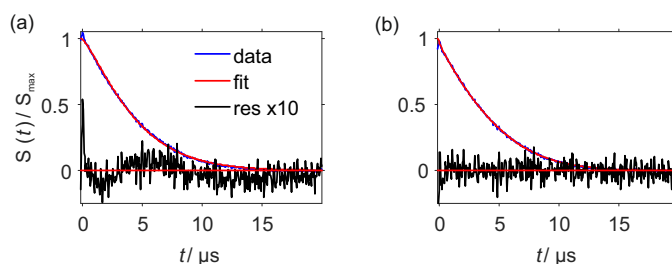


Figure 5.11. W-band RIDME background decay curve and corresponding fits for 500 μM Gd-PyMTA in 1:1 (v:v) D_2O :glycerol- d_8 at 10 K with $T_{\text{mix}} = 72 \mu\text{s}$: (a) single stretched exponential function; (b) product of two stretched exponential functions. Note measurement are scaled to maximum intensity excluding the zero-time artefact.

Importantly, since the overall derivation scheme will not change in the presence of multiple relaxation pathways, e.g. due to the multi-level high-spin centres or due to several types of B spins, the theoretical model also allows discussing general trends in those, more complicated cases. The trends in the shape of the RIDME background data with respect to variation of different parameters are summarized in Table 5.1. Note that we observe weak trends for the changes in the transverse delay settings and much stronger trends with changing mixing time, temperature or concentration. These magnitudes of change are fully consistent with the derived equations.

Parameter	d_{exp}	d_{theory}	k_{exp}	k_{theory}
Temperature \uparrow	\uparrow	\uparrow	\downarrow	\downarrow
25 μM	n.a.		\approx constant	
Spin concentration \uparrow	n.a.	constant	\uparrow	\uparrow
$T_{\text{mix}}/T_1 \uparrow$	slightly \downarrow	constant	\uparrow	\uparrow
$d_2 \uparrow$	\uparrow	\uparrow	\downarrow	\downarrow
25 μM	n.a.			
$d_1 \uparrow$	\uparrow^*	\downarrow	\downarrow	\downarrow

Table 5.1. General trends in the RIDME background decay on Gd-PyMTA in deuterated frozen solutions. Note that at 25 μM spin concentrations, general trends of d are not applicable (n.a.) due to the larger error bars. (*Effect relatively weak and reduced at longer mixing times. Most likely, accuracy issues are present here.)

By far less exhaustive background measurements on Cu(II) or Mn(II) compounds do support the findings for the d and k parameters described in this section (for details see Appendix B.5). The transverse relaxation data in combination with the RIDME background data for the 25 μM Gd-PyMTA-complex in deuterated solvent suggest that Gd(III)-Gd(III) RIDME experiments with dipolar evolution periods up to 50 μs should be feasible (see Figures 5.2(b) and 5.4(d)). This time corresponds to a decay of the Hahn echo to the 10% level, while extrapolated RIDME background decay data of 25 μM PyMTA at 16 μs mixing time decay to at most 0.4 for both, the RIDME decay fit with a single stretched exponential (SE) and the sum of two stretched exponential functions (SSE). This time corresponds to one full period of dipolar oscillation for a spin-spin distance of approximately 13.5 nm. This distance can be thus taken for now as a rough estimate of the upper detectable distances for Gd(III)-Gd(III) RIDME, until direct experimental evidence is provided. Note, however, that fitting the background shape for such long dipolar evolution times might become difficult due to several decay contributions stemming from different relaxation pathways if no clear oscillations can be observed. One might consider using reference background measurements in such demanding situations to improve the overall quality of the

background correction procedure. Note that if we compare the RIDME background shapes for the Gd(III) samples in fully protonated and fully deuterated solvent (Figure 5.4(d)), we find that the change of the characteristic decay time between protonated and deuterated solvent case exceeds the change in the gyromagnetic ratio expected from the ratios of protons and deuterons. This implies that the nature of the nuclear contribution to the RIDME background might be more complicated than just a series of single spin flips. This phenomenon deserves a dedicated study.

For RIDME measurements in orthogonal pairs consisting of one organic radical and one metal centre the typical situation would be that the RIDME background shape is mostly determined by the concentration and spatial distribution of the metal centres, because the longitudinal relaxation times of organic radicals are significantly longer than the ones of metal centres. The contribution from organic radicals might, however, become more significant if, for instance, their longitudinal relaxation rates are enhanced due to the presence of metal centres. In cases of unequal concentration of metal centres and organic radicals combined effects of longitudinal relaxation rates and spin concentrations have to be considered, in order to determine if contributions from any type of paramagnetic species would dominate in the RIDME background shape. Such situations might appear, for instance, in studies of weak interactions between differently spin-labelled biomolecules, where one type of biomolecules needs to be present in excess.

RIDME measurements in biological samples are characterized by the presence of non-homogeneous proton distributions around the spin labels due to the use of deuterated solvents. On the one hand, this complicates the analysis of the intramolecular label-to-label distance distributions, since they are affected by the differences in the proton surrounding for different spin label's tether conformations. On the other hand, the sensitivity of the RIDME background shape to the proton concentration can potentially be used as an auxiliary short- or middle-range constraint in biomolecular structure determination studies. It is difficult to define the actual sensitive distance range prior to a dedicated study. As a speculation we could propose that this should exceed the 'pure NMR' range of the Nuclear Overhauser Effect (NOE)-based constraints (i.e. $r < 1$ nm), and might appear to be comparable or even larger than the typical paramagnetic NMR distance range (between one and a few nanometres). Such a methodology, would, of course, first require detailed investigation of the proton-driven spectral diffusion mechanism, which appears to be more complicated than the electron-driven one. Such a study, which might be also relevant for low-temperature dynamic nuclear polarization (DNP), is currently underway in our lab.

Lastly, we would like to point out that some of the pathways considered here can be directly transferred to the case of a DEER experiment in pairs of non-equivalent A-B spins, with fast longitudinal relaxation of B spins. In such an experiment, when the length of the transverse evolution period starts to be comparable to the longitudinal relaxation time of B spins, the Gaussian decay contributions to the intermolecular DEER decay should appear in the same fashion as the quadratic term in Equation (5.24) appears due to a B spin flip during the transverse evolution time and one during the mixing block within one stochastic trajectory. Such contributions might be, for instance, present in Gd(III)-Gd(III) DEER, where non-monoexponential background is often observed.^{44;110}

5.5. Conclusions

In this work we provided a theoretical basis for describing the intermolecular RIDME background decay and discussed the most important practical aspects of intermolecular RIDME background measurements and their analysis. An important result of this work is the understanding that the RIDME background shape depends on all time delays in the RIDME pulse sequence and that RIDME traces measured with different trace lengths need to be compared with care. This is particularly important for reference background measurements for biological applications, where exactly the same delay settings as in the original measurement need to be used in order to obtain the correct background decay shape.

The applicability of the presented theoretical approach goes beyond the formal limitations of the simple A - B spin pair model analysed in detail here, since more complicated spectral diffusion mechanisms can be described in very similar ways and would result in analogous trends for the RIDME background shape. The particular case of proton-driven electron spectral diffusion appears to be very interesting for elucidation of some steps in polarization transfer from electron spins to the nuclear spin bath. Such an information would be valuable for improving low-temperature DNP techniques. Additionally, we propose that an understanding of the proton-driven spectral diffusion mechanism might help to construct a RIDME-based approach to study the local or mid-range surrounding of spin labels attached to biomolecules.

Electron Spin Echo Envelope Modulation in RIDME experiments

The presence of artefacts due to Electron Spin Echo Envelope Modulation (ESEEM) complicates the analysis of dipolar evolution data in Relaxation Induced Dipolar Modulation Enhancement (RIDME) experiments. Established strategies to avoid ESEEM artefacts cause losses in the signal-to-noise ratio. In this chapter a new approach for suppression of nuclear modulation artefacts in RIDME is introduced. First, it is demonstrated that averaging over two delay times in the refocused RIDME experiment allows for nearly quantitative removal of the ESEEM artefacts, resulting in potentially much better performance than the so far used methods. Analytical equations are given for the case of electron and nuclear spins $S = 1/2$ and $I = 1/2$, respectively. The presented analysis is also relevant for Double Electron Resonance (DEER) and Chirp-Induced Dipolar Modulation Enhancement (CIDME) techniques. The applicability of the ESEEM averaging approach is demonstrated on a Gd(III)-Gd(III) rigid ruler compound in deuterated frozen solution in Q band (35 GHz). The second part shows unpublished results for the performance of the developed average scheme in the presence of strong deuterium ESEEM in X band (9.5 GHz) and for Mn(II) compounds in Q band. In this case averaging does not allow for full suppression of the additional frequencies.

The results of the first part have been published in Ref. ⁷⁹: 'Katharina Keller, Andrin Doll, Mian Qi, Adelheid Godt, Gunnar Jeschke, Maxim Yulikov: Averaging of nuclear modulation artefacts in RIDME experiments', *J. Magn. Reson.*, 2016, 272, 108-113. The EPR experiments and product operator calculations were performed by K. Keller. The model compounds were synthesized by M. Qi in the group of A. Godt. K. Keller, A. Doll and M. Yulikov developed the averaging procedure.

6.1. Introduction

Site-specific distance measurements based on different types of pulse experiments in electron paramagnetic resonance (EPR) attract increasing interest in structural biology studies.^{16–18;20–22;41} Herein, we have already discussed that the Relaxation Induced Dipolar Modulation Enhancement (RIDME) technique is particularly valuable for spin-spin distances measurements involving metal centres with broad EPR spectra.^{66;67;73;113;179–182} Being a single frequency technique, RIDME imposes low requirements on the resonator profile and measurement setup, while at the same time offering virtual infinite bandwidth for the inverted spins. On the downside, RIDME time traces have typically faster decaying intermolecular background, as compared to DEER, which has been described in the previous Chapter 5. Importantly, and unfortunately for measurement of dipole-dipole interactions, the RIDME technique is even more prone than DEER to unwanted Electron Spin Echo Envelope Modulation (ESEEM) effects, which introduce hyperfine frequencies to the dipolar evolution traces and thus interfere with distance measurements. This problem is less important at W-band (~ 94 GHz) or yet higher measurement frequencies, since at those conditions ESEEM contributions are usually weak and can be neglected in the majority of cases. However, in X and Q band (~ 9.5 and ~ 35 GHz) the ESEEM contributions from protons or deuterons (in deuterated solvents or for deuterated biomolecules) make RIDME measurements significantly more difficult. The currently used approaches to avoid ESEEM artefacts at these measurement frequencies lead to a loss of signal-to-noise ratio (SNR), since they are either based on the use of very soft microwave pulses or require trace-by-trace division.^{67;179;180} The latter approach reduces signal-to-noise ratio by at least a factor of two, with a factor $\sqrt{2}$ coming from the requirement of measuring a reference trace that does not add to the dipolar modulation and another factor of $\sqrt{2}$ at the signal maximum and more at later time from dividing two noisy traces.

In this chapter, a new averaging approach is introduced in Section 6.2 that is conceptually analogous to the one used in DEER spectroscopy. The approach allows using hard broadband pulses in RIDME measurements and does not require division of the RIDME trace by a reference. Importantly, the ESEEM averaging does not produce any distortions in the dipolar evolution traces and does not significantly change the shape of the intermolecular background decay. Such an approach is of particular importance for measuring deuterated samples. Deuteration of the solvent and if possible the protein leads to much slower (flatter) intermolecular background decays in RIDME measurements and is recommended whenever possible to improve the quality of distance distribution curves. However, the amplitude of deuterium (^2D) ESEEM is typically large at X-band and Q-band measurements, which made sample deuteration not very popular in RIDME-based studies to date. This is also reflected in Section 6.3 of this chapter, which presents situations where the averaging scheme did not allow for full removal of ESEEM oscillations in the RIDME experiment, e.g. ^2D ESEEM in X band.

6.2. Averaging of ESEEM contributions

We demonstrate the approach on frozen solutions in D_2O /glycerol- d_8 of mono-Gd(III) compound Gd-PyMTA (Figure 6.1(c)) and the Gd-ruler (3.4 nm), a di-Gd(III) compound with a most probable Gd-Gd distance of about 3.4 nm and a very narrow distance distribution,¹⁹⁷ shown in Figure 6.1(d). The pulse sequence of the dead time free RIDME experiment⁶⁷ is shown in Figure

6.1(a) and the echo-detected (ED) EPR spectrum of the Gd-PyMTA complex is shown in Figure 6.1(b) with the RIDME detection position marked by an arrow. Detailed experimental settings and sample preparation descriptions can be found in Appendix C.

Considering the formation of the RIDME echo, it is convenient to distinguish between A spins, which are the spins excited by the microwave pulses, and B spins, which are all other spins, in particular those dipolar coupled to the A spins within the same molecule. Using this terminology, the evolution of non-equilibrium magnetization in the RIDME pulse sequence (Figure 6.1(a)) can be described as follows. First, transverse magnetization is created for the A spins by the $\pi/2$ pulse, it evolves for the time d_1 , gets refocused by the π pulse and forms a spin echo at the time point $2d_1$. Next, the A spin transverse magnetization starts to defocus again and at the time point $2d_1 + d_{12}$ half of it is transferred to the z -direction by the first $\pi/2$ pulse of the mixing block, thus forming a non-equilibrium polarization grid for A spins along the direction of the external magnetic field. This grid is stored for the mixing time T_{mix} , to allow for spontaneous flips of the B spins, resulting in a change of the dipole-dipole interaction, and thus shifting the resonance frequencies of the A spins. After that the second $\pi/2$ pulse of the mixing block transfers the A spins polarization back to the transverse plane. The resulting transverse magnetization evolves for the time $d_2 - d_{12}$, is refocused by the last π pulse and forms the RIDME echo at time d_2 after the last π pulse. The time d_{12} is incremented, and the amplitude of the RIDME echo is recorded as a function of d_{12} .

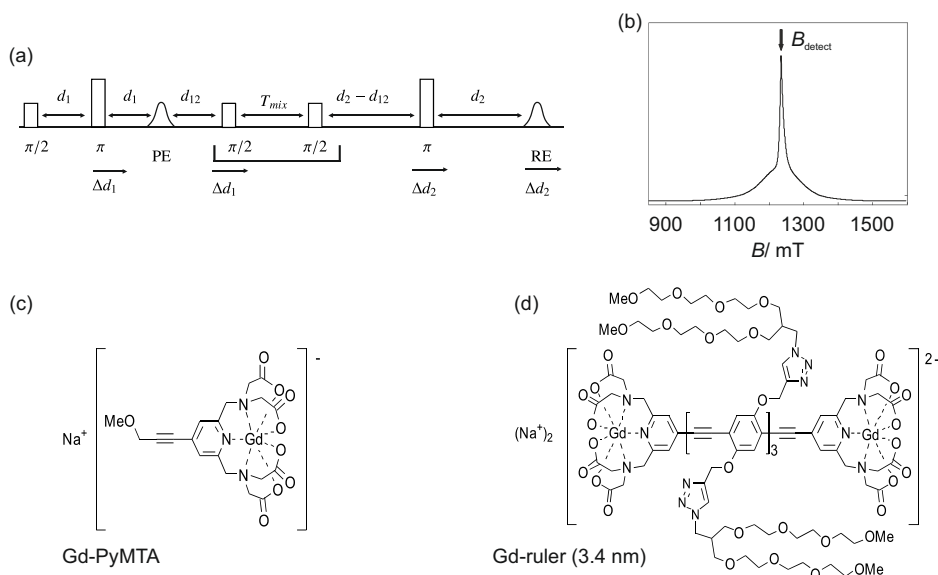


Figure 6.1. (a) RIDME pulse sequence, PE stands for the primary spin echo, and RE for the detected RIDME echo (refocused virtual echo in Ref. ⁶⁷), (b) EDEPR spectrum of the Gd-ruler (3.4 nm) at 34.5 GHz. The magnetic field position for detection of the RIDME sequence is marked by an arrow. (c), (d) Structural formulae of the studied model compounds.

The ESEEM effect appears as a modulation of the intensity of the electron spin echo due to the interaction of the electron spin with surrounding nuclei.¹⁹ In a real experiment, in addition to the just described ideal pathway, each microwave pulse in the RIDME pulse sequence transfers electron coherence or polarization to electron-nuclear or pure nuclear coherence and polarization. As a result, the RIDME echo has contributions that oscillate with the nuclear frequencies and combinations thereof when any delay time in the experiment is varied. An analytical computation of the propagation of coherence through the RIDME pulse sequence is provided in Appendix C.

This computation was performed for an effective spin $S = 1/2$, which implies that we neglect any level crossing effects of the $S = 7/2$ spin of Gd(III). As long as this approximation is valid, our analysis of ESEEM averaging should be rather general and applicable to any paramagnetic centre, including low-spin and high-spin metal centres.

There are two time points in the RIDME sequence where all contributions to the detected RIDME echo (refocused virtual echo in Ref.⁶⁷) assume a rather simple dependence on the electron spin operators. First, at the primary echo time point $2d_1$ all contributions that later form the RIDME echo refocus along the y -direction. The RIDME signal has, therefore, the well known two-pulse ESEEM formula as a pre-factor, which is shown analytically in Equation (C.5) in Appendix C. This two-pulse ESEEM contribution in the RIDME signal has identical phase for any position of the mixing block, and, in principle, does not affect the dipolar evolution signal. The first refocusing π -pulse in the refocussed RIDME sequence⁶⁷ only serves as a tool for avoiding temporal overlap of the mixing block with excitation pulses and the dipolar evolution time. Therefore the nuclear modulation contribution of this block can be fully removed by averaging the RIDME echo signal over a range of d_1 times. The second time point, important for the formation of the RIDME signal, is the time right after the first $\pi/2$ pulse of the mixing block (third pulse in the refocused RIDME pulse sequence in Figure 6.1(a)). At this point the part of the transverse magnetization that is later detected as RIDME echo is turned into z -direction, creating electron polarization, electron-nuclear two-spin order ($S_z I_z$), and nuclear coherence and polarization, while all terms that are proportional to the S_x and S_y operators in the (xy) plane would nearly completely decay during the mixing time, which should be thus set at least 2-3 times longer than the electron phase memory time $T_{m,e}$. The S_x and S_y terms are also suppressed by phase cycling. The polarization terms are constants of motion during the mixing time, while the phase of nuclear coherence evolves. All this terms are transferred back to the electron coherences by the second $\pi/2$ pulse of the mixing block, and participate in formation of the RIDME signal. Thus, there would be another factor in the RIDME signal that is essentially the same as the part of the three-pulse ESEEM formula that depends on the mixing time T_{mix} (see Equations (C.6) and (C.7) in Appendix C).¹⁹ At typical RIDME setup conditions, however, the mixing time is rather long and the terms that contain nuclear coherences, dephase or irreversibly decay over this period of time. Thus, in the majority of cases, the ESEEM oscillations during the mixing time do not affect the RIDME measurement and can be dropped in analytical computations. In the Appendix C these terms are still considered for the sake of completeness.

The remaining evolution periods from the primary echo until the beginning of the mixing block, from the end of the mixing block until the last, refocusing π pulse, and from this last pulse until the position of the RIDME echo, produce further oscillatory terms with the properties of the transverse evolution part of the three-pulse ESEEM experiment, additionally refocused, as well as the ones of another two-pulse ESEEM block. In the equations given in Appendix C one can recognize that the majority of the terms either depend on the time d_2 (time delay between the last π -pulse and the RIDME echo, see Figure 6.1(a)), or on the sum or difference of the time d_{12} (the time between the primary echo and the beginning of the mixing block, Figure 6.1(a)) and the time d_2 . All these terms are averaged out by varying the second static delay d_2 in the RIDME experiment. There are still two terms ($\cos(d_{12}\omega_\alpha) + \cos(d_{12}\omega_\beta)$ - Appendix C) left after such averaging that depend solely on the d_{12} time and are thus not averaged out. The overall pre-factor for these terms is $k/(8 - 6k)$ times smaller than the constant term, which is a rather

small number for most values of k . Here $k = \left(\frac{B\omega_I}{\omega_\alpha\omega_\beta}\right)^2$ is the modulation depth parameter, B the pseudo-secular hyperfine coupling, ω_I the nuclear Zeeman frequency and $\omega_\alpha, \omega_\beta$ the nuclear frequencies in the spin-manifolds α, β .¹⁹ If we consider the 'worst' cases with $k \sim 1$, which can appear in X band for ²D ESEEM, the remaining non-averaged ESEEM oscillations have an amplitude of about 50% of the total echo intensity. Such a situation is described in the next section. In Q band, where for deuterons the value of k is typically less than 0.1 these remaining ²D ESEEM contributions have an amplitude of about 1.3% or less and do not affect the dipolar measurements to a significant extent in most applications, except for cases with very low spin labelling efficiencies when the RIDME modulation depth decreases to a level of 1-2% of the total echo intensity. Note that at typical lengths of d_2 of RIDME traces of one to several microseconds, the ESEEM modulation depths are actually smaller than the mentioned maximum values, so that a stronger suppression of the ESEEM artefacts due to the d_2 averaging would be expected even in X band. Note that other nuclei may have stronger ESEEM contributions already in Q band.

Note further that the RIDME mixing block can be considered as a composite π -pulse. Such a π -pulse is, of course, applied at the same frequency as the detection pulses, but it produces ESEEM artefacts in a similar way as the pump pulse in the DEER experiment, which is applied at a different frequency but typically still slightly overlaps with the detection pulses in the frequency domain. This bandwidth overlap in DEER can be controlled by the pump-detection frequency offset and the pulse power settings. The main difference between the DEER pump and 'RIDME composite pulse' is thus the much stronger bandwidth overlap between the 'composite π -pulse' and the detection pulses of RIDME in comparison to the bandwidth overlap in DEER. This overlap makes ESEEM artefacts stronger in the RIDME case. The effect of spontaneous spin flips is analogous to the effect of a chirp pulse applied during the mixing block of the Chirp-Induced Dipolar Modulation Enhancement (CIDME) experiment.¹¹⁶ Our analytical treatment of the ESEEM averaging would thus be relevant also for DEER and CIDME measurements.

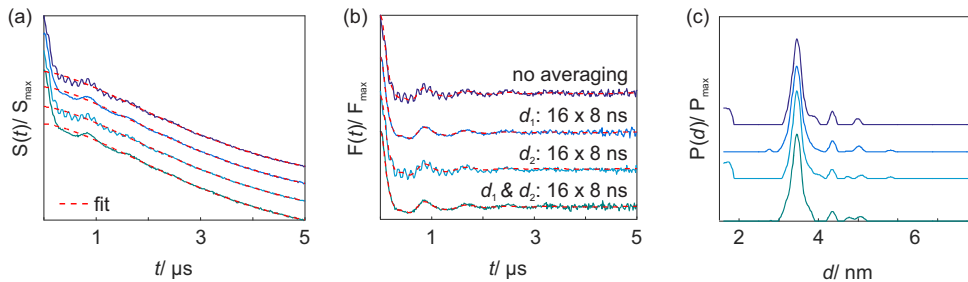


Figure 6.2. Q-band RIDME data for the Gd-ruler (3.4 nm) at 20 K showing different averaging schemes. (a) Primary data, (b) form factor and (c) distance distribution.

The performance of the ESEEM averaging scheme based on the above analysis has been investigated experimentally. Considering the structure of the compound (Figure 6.1), solvent, and chosen microwave frequency (35 GHz), mainly nuclear modulation from ²D nuclei of about 7.8 MHz (at 1200 mT) is expected and can be identified in the primary data in Figure 6.2 (top, purple line). The time steps and durations of the averaging period used in the following, thus, directly apply to the deuterium nuclear modulations in Q band, and should be adjusted accordingly for other nuclei and detection frequencies. Note also that in cases of ESEEM oscillations originating from two or more types of nuclei, more extended ESEEM averaging schemes might appear necessary.

The principle of the averaging scheme is sketched in Figure 6.1. It can be considered as two two-pulse ESEEM like blocks consisting of the characteristic $\pi/2 - \pi$ pulses and interpulse delay d_1 and d_2 , respectively. In this framework, both building blocks will introduce nuclear modulations in the primary data. To suppress the generated nuclear modulations, the RIDME traces are acquired for several d_1, d_2 pairs, starting from the initial values and increasing the delays in steps of Δd_1 and Δd_2 . Eventually all traces are summed up. Averaging of the first interpulse delay d_1 ($\Delta d_2 = 0$) already results in a drastic decrease of the deuteron ESEEM modulations (blue, second top line). Nevertheless, small ESEEM oscillations can be observed towards the end of the trace. These can be suppressed by averaging the second interpulse delay d_2 ($\Delta d_1 = 0$) (third top, cyan line), yet strong deuterium oscillations remain at the beginning of the traces. Averaging of both interpulse delays ($\Delta d_1 = \Delta d_2$) suppresses the deuterium ESEEM effect to a level below the noise if the averaging period exceeds 128 ns (bottom, green line). It should be noted that for very short mixing times $T_{\text{mix}} < T_m$ an additional oscillating term, dependent on T_{mix} plays a role as shown in Figure C.1 in Appendix C. This term, however, becomes unimportant at longer mixing times ($\sim 2T_m$) due to nuclear coherence decay.

Importantly, the averaging approach does not change the primary RIDME signal or the RIDME form factor. Tikhonov regularization thus results in alike distance distributions. Small differences are observed in the artefact peaks. Especially incomplete averaging of the fast oscillations in the beginning of the trace induces a short distance artefact, while incomplete averaging towards the end of the trace introduces some small changes in the long-range artefact level around 5 nm.

The mean signal intensity of the RIDME background traces is shown for Gd-PyMTA as a function of Δd_1 with $\Delta d_1 = \Delta d_2$ in Figure 6.3(a). It exhibits the typical cos-like amplitude oscillation of nuclear modulation,¹⁹ while the contribution of the unmodulated part remains constant with increasing interpulse delay (in practice, it slowly decays, mainly due to the spectral diffusion). As estimated from the ²D Larmor frequency, a full period of oscillation is approximately 128 ns. Figure 6.3(b) reveals that by averaging of the RIDME time traces by increasing d_1, d_2 pairs, only the unmodulated part of the signal decay remains, while its shape is not distorted. These experiments on a mono-gadolinium compound show no change in the RIDME background upon application of such ESEEM averaging procedures.

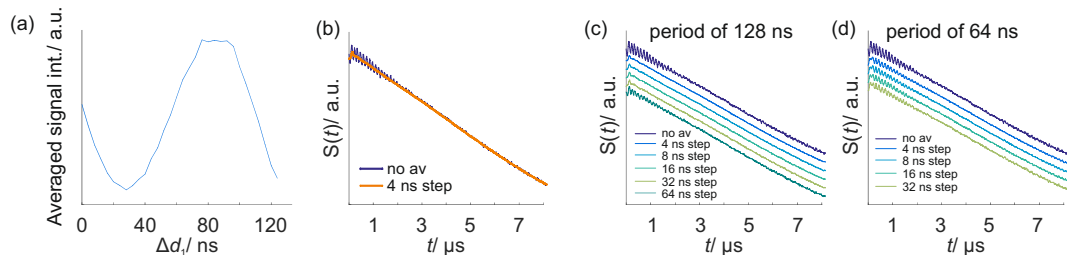


Figure 6.3. Q-Band RIDME data for Gd-PyMTA ligand acquired at 20K. (a) Mean intensity of the primary RIDME traces as a function of Δd_1 with $\Delta d_1 = \Delta d_2$. (b) Comparison of unprocessed primary data (purple) to a summation of all traces (orange). (c) Averaging of traces with increasing step size from top to bottom for a period of 128 ns. (d) Averaging of traces with increasing step size from top to bottom for a period of 64 ns.

Figure 6.3(c, d) shows the influence of averaging period and spacing $\Delta d_1, \Delta d_2$ on the quality of ESEEM artefact removal. It can be concluded that the averaging approach is rather insensitive to the applied step size up to the step of 32 ns corresponding to roughly a quarter of the total

oscillation period. On the other hand, at least one full period of nuclear modulation needs to be detected (Figure 6.3(c)). Averaging only half a period (64 ns) of the deuterium modulation (Figure 6.3(d)) results in a reduction of the ESEEM effect, but not in full suppression. Nevertheless, the level of reduction remains constant within a step size of 32 ns. Note that averaging with more steps does not reduce signal-to-noise ratio, since all traces contribute the full dipolar modulation. A larger number of steps merely increases the minimum duration of the experiment. Some signal loss occurs since the average d_1 and d_2 intervals are larger than would be required without nuclear modulation averaging. With a total averaging interval of 256 ns in deuterated samples this loss is moderate for the typical transverse relaxation times, where RIDME can be measured.

To summarize, we have demonstrated that introduction of an ESEEM averaging loop in the RIDME measurement protocol efficiently removes the electron-nuclear interaction artefacts in the studied model compound and allows obtaining pure dipolar time traces in Q band. Importantly, the averaging on two delay times (d_1 and d_2) as well as varying of the delay times by at least one full period of ESEEM oscillations is crucial for obtaining clean data. The proposed averaging procedure does not reveal any detectable changes in the RIDME form factor and background decay, thus leading to no influence on the distance analysis.

6.3. Presence of strong ESEEM oscillations

Let's first consider the same Gd-PyMTA mono complex, but for detection at X-band frequencies. Measurement details are given in Section C.3. Figure 6.4(a) presents a two-pulse ESEEM measurement for Gd-PyMTA that exhibits strong contributions from ^2D ESEEM with a frequency of ~ 2.3 MHz and modulation depth of about 40%. Such ESEEM contributions are then also pronounced in RIDME measurements on the Gd-PyMTA mono-complex with a modulation depth of $\sim 30\%$ (Figure 6.4(b)). Using different d_2 values and thus shifting the zero-time of the second two-pulse ESEEM block with respect to the first one in the RIDME sequence, clear interference effects of both ESEEM contributions can be observed. Some variations in ESEEM modulation depth are observed throughout the different data sets, however, there is no clear trend for smaller modulation depth at longer d_2 in the studied range up to $4 \mu\text{s}$. The variations might be caused by destructive or constructive interference of the ESEEM contributions of each two-pulse ESEEM block depending on the interplay of d_1 and d_2 .

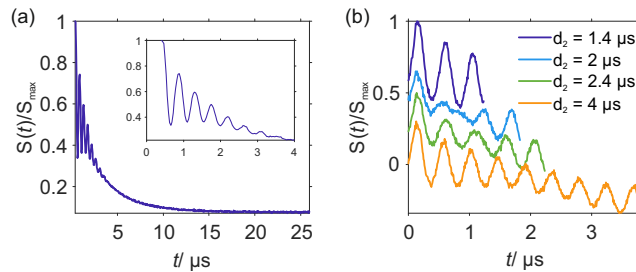


Figure 6.4. X-band measurements for Gd-PyMTA at 20 K. (a) Two-pulse ESEEM. The inset shows a zoom into the region from 0 to 4 μs . (b) RIDME traces for different d_2 values as colour coded. $T_{\text{mix}} = 16 \mu\text{s}$, $d_1 = 400$ ns.

Application of the developed averaging scheme over a period of 27×16 ns (432 ns $\sim 1/2.3$ MHz $^{-1}$), did reduce the modulation depth of the ESEEM contribution, but full suppression could not be achieved as shown in Figure 6.5. This is in agreement with the remaining contribution of

($\cos(d_{12}\omega_\alpha) + \cos(d_{12}\omega_\beta)$) with amplitude $k/(8-6k)$ as described in the previous section. Further, in addition to the oscillation with the nuclear frequency, the averaged signal intensity (Figure 6.5(a)) also decreases in intensity which may hamper averaging. Indeed, a better suppression is achieved for traces averaged over a 432 ns period after the first drop of signal intensity in Figure 6.5(b) ($\Delta d_1, d_2 > 176$ ns).

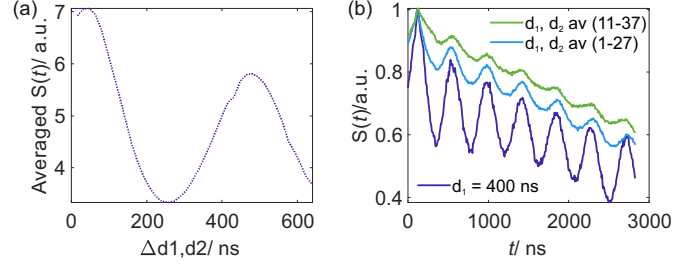


Figure 6.5. X-band RIDME data for Gd-PyMTA at 20 K, $T_{\text{mix}} = 16 \mu\text{s}$. (a) Averaged signal intensity versus the increment Δ of d_1 and d_2 . (b) RIDME traces for $d_1 = 400$ ns (purple), averaged over 432 ns from $d_1 = 400$ to 832 ns (1-27) (blue) and averaged over 432 ns from $d_1 = 576$ to 992 ns (11-37) (green).

To investigate if ^2D ESEEM can be suppressed in X band by other approaches, an averaging scheme based on division of two time traces was tested.^{67;179;180} Division of traces as shown in Figure 6.6 with short ($T_{\text{mix}} = 2 \mu\text{s}$) and long mixing time ($T_{\text{mix}} = 36 \mu\text{s}$) resulted in a somewhat better suppression than the averaging approach, yet remaining ESEEM contributions were still visible. These contributions may be caused by differences in nuclear coherence decay during the mixing block. Good suppression was achieved for division of two intermediate mixing times ($T_{\text{mix}} = 16$ and $36 \mu\text{s}$), but this will also lead to a reduction of the wanted spin-spin dipole coupling modulation depth as well as signal intensity. Division of time traces, detected at different temperatures are expected to give similar results.¹⁸⁰ Suppression by the application of soft pulses is not feasible for ^2D ESEEM in X band as a pulse bandwidth < 2 MHz would be required.

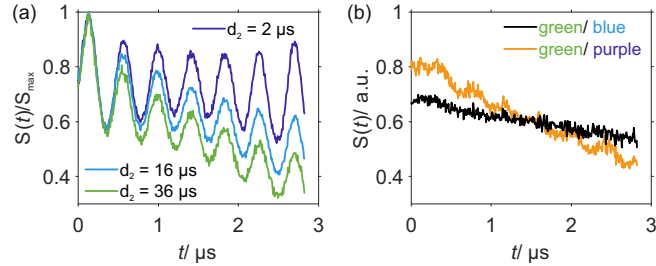


Figure 6.6. X-band RIDME for Gd-PyMTA at 20 K. (a) Different mixing times: $T_{\text{mix}} = 2 \mu\text{s}$ (purple), $16 \mu\text{s}$ (blue) and $36 \mu\text{s}$ (green). (b) Division of $T_{\text{mix}} = 36 \mu\text{s}$ RIDME trace by $T_{\text{mix}} = 2 \mu\text{s}$ (orange) and by $T_{\text{mix}} = 16 \mu\text{s}$ (black).

Note that in Q band and detection on nitroxides a significant reduction of weakly contributing ^2D ESEEM has been observed for long interpulse delays d_1 and such long d_1 values were proposed as alternative ESEEM removal scheme.¹⁹⁸ The data presented in Figure 6.4(b) indicate that at a d_2 value of $4 \mu\text{s}$, there is still significant contribution from ESEEM of the second two pulse ESEEM block observed as slight interference effects at $2 \mu\text{s}$. Therefore, it is expected that such an approach would require long d_1/d_2 values, which might not be feasible due to transverse relaxation. Yet, such an approach could be combined with the averaging scheme and then might result in sufficient suppression of the contributing nuclei, which needs however to be investigated experimentally.

In cases where the RIDME zero time corresponds to a maximum of the ESEEM modulation, it may become very difficult to differentiate dipolar from other modulation. Additional frequencies in the dipolar data cause artefact peaks in the distance distributions as shown in Figure 6.7(a-c) for a structural similar Mn-PyMTA ruler, in which Gd(III) has been replaced by Mn(II). In high-spin systems such peaks might be misinterpreted as harmonic overtones and disentangling ESEEM from harmonic overtone contributions is ambiguous as demonstrated for simulated data in Appendix C, Figure C.4 and C.5. In the case at hand RIDME background measurement on the Mn-PyMTA mono-complex (Figure 6.7(d-f)) and three-pulse ESEEM experiments (see Appendix C, Figure C.2) revealed the same oscillation, which could thus be identified as artefact peak possibly due to ESEEM with low oscillation frequency. Similarly for Mn-DOTA strong non-dipolar modulation was observed only in Q band that could not be suppressed by increasing the length of the first interpulse delay d_1 as shown in Figure 6.7. Note that in this case averaging was only performed for a period of 128 ns (\cong ^2D ESEEM). The additional modulation might result from ^{14}N nuclei, thus implementation of an additional averaging loop for the observed frequency of ~ 2.5 MHz (\cong 400 ns oscillations period) might reduce the observed contributions. In cases where no background sample is available, ESEEM frequencies may be identified by detecting RIDME traces at a set of different d_1 times, so that frequency contributions of different physical origin, i.e. dipolar and hyperfine, and thus different dependence of the zero time on the RIDME sequence timings, interfere destructively as exemplified for the Gd-PyMTA ruler in Appendix C, Figure C.3. Typically, a good indication for ESEEM are oscillations that increase towards the end of the RIDME trace (see for instance black or blue trace in Figure 6.7(e)) where the dipolar frequency is already decayed. Three-pulse ESEEM measurements may provide additional insight into the frequency contributions.

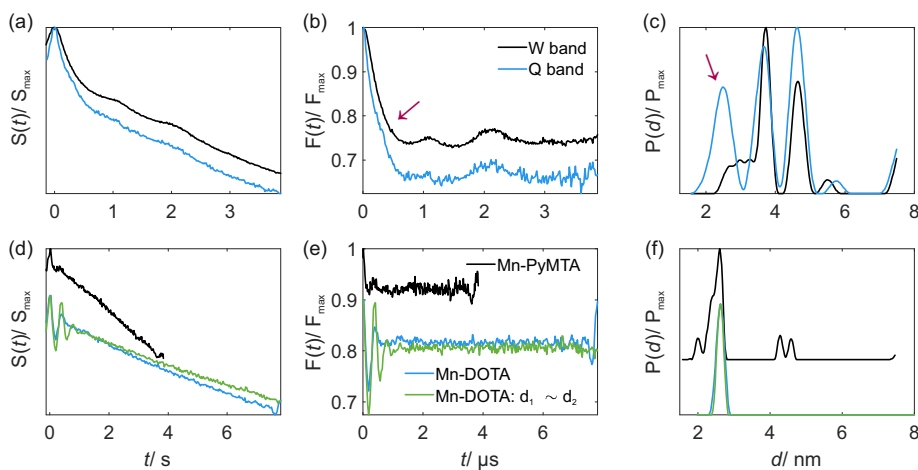


Figure 6.7. RIDME data on Mn(II) model compounds at 20 K. (a-c) Mn-PyMTA ruler with anticipated spin-spin distance of 4.7 nm in W band (black, $T_{\text{mix}} = 24 \mu\text{s}$) compared to Q band (blue, $T_{\text{mix}} = 20 \mu\text{s}$). The distance peak marked by the purple arrow is also observed for RIDME measurement on mono complexes. (d-f) Mn-PyMTA (black, $T_{\text{mix}} = 20 \mu\text{s}$) and Mn-DOTA (blue, green, $T_{\text{mix}} = 32 \mu\text{s}$) mono complexes in Q band, 20 K. (a, b) Primary data; (b, e) background-corrected form factors; the purple arrow indicates the kink where dominant modulation by a different, contaminating frequency changes to dominant dipole-dipole coupling. (c, f) Resulting distance distribution using Tikhonov regularization.

To summarize, in cases where the ESEEM modulation is strong, the developed averaging scheme is not sufficient to fully suppress its contribution. Division of time traces for different mixing times was found to work only for some experimental conditions and may therefore be ambiguous. Remaining ESEEM contributions induce additional peaks in the distance distribution,

thus making them difficult to interpret. This circumstance is particularly pronounced for high-spin centres, where in addition harmonic overtones are observed.

6.4. Conclusions

Averaging RIDME data on both time delay times, d_1 and d_2 , for at least one full period of the observed nuclear frequency allows to reduce ESEEM contributions. In cases where the modulation depth of the nuclear frequencies is low, i.e. ^2D ESEEM in Q band and above, sufficient suppression is obtained to observe undisturbed dipolar time traces. Important advantages of the described procedure are that no reference measurement is required and that microwave pulses of arbitrary bandwidth can be used. Therefore signal-to-noise ratio is generally improved as compared to the previously suggested ESEEM removal procedures.^{67;179;180} The approach is expected to work with a similar efficiency at any other relevant microwave band for comparable depths of ESEEM oscillations. However, due to the incomplete nuclear modulation averaging, the performance of the proposed approach performs worse for particularly strong ESEEM modulations, which are typical for low detection frequencies and for strongly coupled nuclei, e.g. ^2D ESEEM in X band. In such cases, combination with long d_1 and d_2 intervals may help to further reduce ESEEM peaks, however, at the cost of signal intensity.¹⁹⁸ For Mn(II) as paramagnetic centre strong modulation by an unassigned additional frequency was observed in Q band, which hampers interpretation of distance distributions.

The proposed ESEEM averaging procedure is expected to simplify the use of the RIDME technique for distance measurements in biomacromolecules. However, in particular at low microwave frequencies, the larger ESEEM contribution in the RIDME compared to the DEER experiment remains a disadvantage of the technique.

Distance measurements in Cu(II)-Cu(II) spin pairs

After having addressed the RIDME background decay as well as contributions from nuclear modulations to the RIDME signal, this chapter investigates and compares the performance of DEER and RIDME measurements for spin systems with broad EPR spectra, using the example of a low-spin molecular Cu(II) ruler. Distance determination by EPR based on measurements of dipolar coupling is technically challenging for such spin systems due to comparatively narrow microwave pulse excitation bandwidths. Large improvements in sensitivity could be achieved when substituting the monochromatic pump pulse by a frequency-swept one in DEER experiments with monochromatic observer pulses. This effect was especially strong in X band, where nearly the whole spectrum can be included in the experiment. The RIDME experiment is characterised by a compromise between signal intensity, modulation depth and background decay depending on the mixing time. A simple two-point optimization experiment was found to serve as good estimate to identify the mixing time of highest sensitivity. Using frequency-swept pulses in the observer sequences resulted in lower SNR in both the RIDME and the DEER experiment. Orientation selectivity was found to vary in both experiments with the detection position as well as with the settings of the pump pulse in DEER. In RIDME, orientation selection by relaxation anisotropy of the inverted spin appeared to be negligible as form factors remain relatively constant with varying mixing time. This reduces the overall observed orientation selection to the one given by the detection position. Field-averaged data from either method resulted in the same dipolar spectrum. It is shown that both methods have their advantages and disadvantages for given instrumental limitations and sample properties. Thus the choice of method depends on the situation at hand and it is discussed which parameters should be considered for optimization.

This chapter is prepared for publication as 'Frauke D. Breitgoff, Katharina Keller, Mian Qi, Daniel Klose, Maxim Yulikov, Adelheid Godt, Gunnar Jeschke: Distance measurements in Cu(II)-Cu(II) spin pairs', where F. D. Breitgoff and K. Keller contributed equally.

M. Qi synthesized the studied model compounds. K. Keller performed the characterization of the EPR lineshape and relaxation properties of Cu-PyMTA as well as RIDME measurements. F. D. Breitgoff performed experiments with shaped pulses and DEER experiments. Together, F. D. Breitgoff and K. Keller carried out RIDME measurements with shaped pulses.

7.1. Introduction

Knowledge of the structure of biological macromolecules is often crucial for understanding their function.^{199;200} However, structural information is often difficult to attain for such complex systems

and modelling usually relies on combining information obtained by different techniques.^{201;202} A variety of methods has been developed: Crystallisable parts of protein complexes can be characterized by X-ray crystallography²⁰³ and NMR techniques can yield short-range distance restraints for structure determination.^{204;205} Mass spectrometry (MS) can be used in combination with resolving ion size (ion mobility),^{206;207} dissociation properties (tandem mass spectrometry)²⁰⁸ or reactivity (for example H/D exchange)²⁰⁹ or as native MS.²¹⁰ Further methods include fluorescence spectroscopy, specifically Förster Resonance Energy Transfer (FRET)^{211;212}, and cryo-Electron Microscopy.^{213;214} Among these fields, Pulsed Dipolar Spectroscopy (PDS) by Electron Paramagnetic Resonance (EPR) represents a unique method as it can provide long-range distance distributions for systems with and without long-range order with an upper limit of 4-6 nm^{20;22;215} to 16 nm,²¹⁶ depending on the spin environment. Distance distribution information by PDS can provide a snapshot of the conformational ensemble or be used to solve structures,²¹⁷ e.g. by hybrid structural modelling.^{218;219}

PDS experiments determine the distance distribution between two spin centres in the sample. Often, these centres are engineered by site-directed spin labelling^{16–18;23} of the macromolecule. Naturally occurring metal centres, however, are also abundant.^{3;11;199} Such systems include metallo-enzymes pivotal to many processes of life such as haemoglobin.²²⁰ If the metal centre in its natural oxidation state and ligand field does not possess a spin, i.e. one or more unpaired electrons, it can often be substituted by a paramagnetic ion to allow for EPR and paramagnetic NMR measurements.^{166;221–223}

Furthermore, spin labels containing metal centres are the subject of ongoing method development.^{224–228} Due to their chemical inertness, redox stability and non-toxicity²⁰¹ they are promising candidates for in-cell experiments. In-cell Gd–Gd distance measurements have been demonstrated^{24;25} and show promise for longer spin-label lifetimes than possible in in-cell measurements between standardly used types of nitroxides^{171;229}. In addition, metal-based spin labels represent building blocks for the development of orthogonal labeling schemes which can be combined with spectroscopic selection in pulse EPR experiments.^{26;82;83}

EPR spectra – especially of metal ions but also from other spin centres – often span several GHz.³⁸ Broadening can be orientation dependent or could stem from distributions of particular spectroscopic parameters. Important examples are anisotropic electron Zeeman and hyperfine interactions, characterized by the g -tensor or hyperfine tensor anisotropies, as well as in high-spin systems the joint effect of g -tensor and zero-field splitting interaction caused by strong electron-electron interactions. The maximal achievable excitation bandwidth by monochromatic pulses in EPR is, with about one hundred MHz, rather narrow. Sensitive measurements of systems with broad spectra are therefore challenging and more prone to effects of orientation selectivity.

PDS techniques detect the difference in resonance frequency of an observed spin A for two different states of a dipolar coupled spin B.⁶⁸ Assuming only secular contributions, the dipolar coupling Hamiltonian in EPR is given by

$$\hat{H}_{\text{dd,sec.}} = \omega_{\text{dd}} \hat{S}_{\text{A},z} \hat{S}_{\text{B},z} \quad (7.1)$$

with $\hat{S}_{i,z}$ being the z -component of spin i and ω_{dd} the strength of the dipolar coupling described by Equation (7.2)²⁰

$$\omega_{\text{dd}}(r_{\text{AB}}, \theta) = \frac{\mu_0 \mu_{\text{B}}^2 g_{\text{A,eff}} g_{\text{B,eff}}}{4\pi \hbar r_{\text{AB}}^3} (1 - 3 \cos^2 \theta). \quad (7.2)$$

Here, μ_0 is the vacuum permeability, μ_B the Bohr magneton, $g_{A,\text{eff}}$ and $g_{B,\text{eff}}$ are the effective g -values of the A and B spins at the given field and frequency and \hbar is the reduced Planck's constant. The angular dependence of the dipolar coupling in EPR is parametrized by the angle θ between the spin-spin vector and the external magnetic field B_0 .⁶⁸ The effective g -values $g_{i,\text{eff}}$ result from the orientation of the individual spins A and B with respect to the external magnetic field B_0 according to Equation (7.3) for spin i in the Bleaney transformation¹⁹

$$g_{i,\text{eff}}(\theta_i, \phi_i) = \sqrt{g_{i,x}^2 \sin^2 \theta_i \cos^2 \phi_i + g_{i,y}^2 \sin^2 \theta_i \sin^2 \phi_i + g_{i,z}^2 \cos^2 \theta_i}. \quad (7.3)$$

Here $g_{i,x}$, $g_{i,y}$, and $g_{i,z}$ are the principal values of the g tensor of the spin i and the polar angles θ_i and ϕ_i determine the orientation of B_0 in the g_i -tensor eigenframe.

Experimentally, excitation of A and B spins in the PDS experiments can be performed in two conceptually different ways.^{230;231} 'Single-frequency' schemes that excite both, A and B spins, at the same time by all pulses can be separated from 'pump-probe' schemes that select specific fractions of the spectrum for an observed spin A and a pump spin B. The former group comprises solid-echo based experiments like SIFTER¹⁷⁷ (SINGLE Frequency Technique for Refocusing) and DQC^{175;176} (Double Quantum Coherence) experiments. They were so far predominantly applied to systems with relatively narrow spectra like trityl or nitroxides, although Cu(II)-Cu(II) DQC distance measurements have been conducted.^{232;233}

In contrast, excitation of all spins simultaneously is technically challenging for systems with broad spectra. For distance determination in such systems, pump-probe experiments, like Double Electron Electron Resonance (DEER),^{174;234} also called Pulsed Electron Double Resonance (PELDOR), or Relaxation Induced Dipolar Modulation Enhancement (RIDME)^{66;67} are more commonly applied. Both in DEER and in RIDME, a specific fraction of the spectrum is selected as A spin by the observer pulses. The two techniques differ in the way how the inversion of the B spin is performed. While in DEER inversion of B spins is achieved by a pump pulse at a second frequency, RIDME relies on stochastic relaxation events to flip the coupled B spin. In RIDME, in order for a significant number of B spin flips to occur during the measurement time, the phase-dispersed coherence on the A spin is stored in form of a polarization grating for a period T_{mix} called the mixing time. The most commonly used pulse sequences for DEER¹⁷⁴ and RIDME⁶⁷ are compared in Figure 7.1(a, b).

The timing of the pump pulse in DEER and the mixing block in RIDME, respectively, is varied to probe the difference in resonance frequency of the A spin for the two different states of the B spin. The difference frequency is detected as an oscillation of the observed echo with a distribution of frequencies $\omega_{dd}(r, \theta)$. In an ideal powder, all θ values are present weighted by $\sin \theta$. For a specific distance r , the distribution of ω_{dd} is described by a Pake pattern. In reality, different conformers can exhibit different spin-spin distances r , resulting in a distance distribution $P(r)$ for the ensemble instead of just a single distance. An ideal dipolar spectrum therefore is a superposition of Pake patterns with each Pake pattern weighted by the probability of the corresponding distance in $P(r)$.

If ω_{dd} is not detected for all θ values, or not with the correct weighting, the dipolar spectrum will deviate from a superposition of Pake patterns. This effect is called orientation selection and can be described by including a so-called geometry factor $\xi(\theta)$ in the calculation of the form factor $F(t)$ ^{68;69}

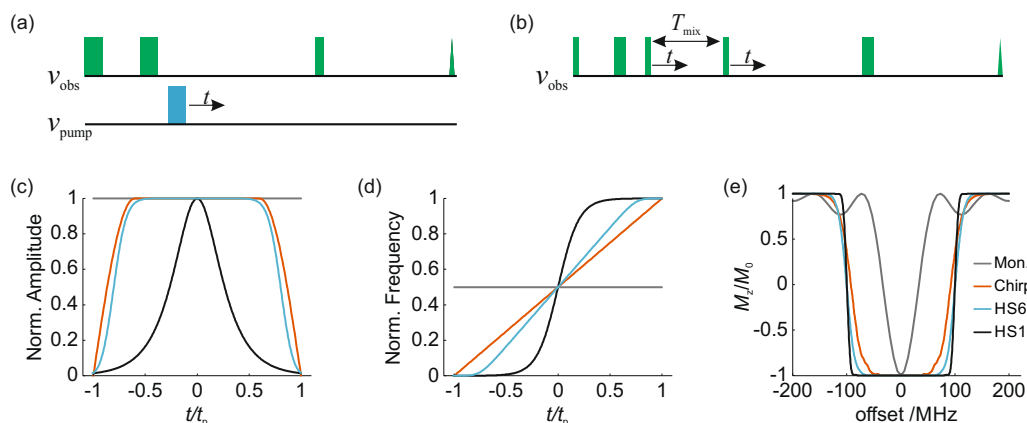


Figure 7.1. Pulse sequences for (a) four-pulse DEER¹⁷⁴ and (b) five-pulse RIDME⁶⁷. ν_{obs} indicates the observer frequency, ν_{pump} the frequency for the inversion pulse, t the time increment and T_{mix} the length of the mixing block. Pulse lengths in the DEER sequence correspond to the version of the experiment with shaped observer pulses. (c-e) Pulse shapes used for the experiments: monochromatic (grey), linear frequency sweep (*chirp*, orange), sech/tanh pulses of order 6 (blue) and 1 (black). (c) Amplitude modulation, (d) frequency modulation, (e) inversion profiles simulated with EasySpin.

$$F(t) = \int \int P(r) \xi(\theta) \cos(\omega_{dd}(r_{AB}, \theta)t) d\theta dr \quad (7.4)$$

Applications of Cu–Cu DEER in the past often exploited this effect in order to study the relative orientation of the two g -tensors.⁹⁹ Distance determination, however, was often complicated by orientation selection caused by the anisotropy of the Cu(II) spectra.^{235–242} The modulated part of the DEER trace, i.e. the form factor, is multiplied with a smooth decay due to distributed couplings to remote spins. This background contribution can be corrected for by fitting and subsequent division and usually does not interfere with distance distribution determination for sufficiently long DEER traces.⁷⁸

Applications of RIDME on nitroxide–Cu systems^{181;183} as well as Cu–Cu systems²³⁵ have been demonstrated. Provided that relaxation is uniform enough over the spectrum to avoid different relaxation of the various spin packets during T_{mix} one can assume complete orientation averaging for the B spins in RIDME experiments and only orientation selection by the observer pulses influences distance distribution determination from RIDME data.^{179;181;235;243;244} For spin $S = 1/2$ systems RIDME dipolar evolution data can be treated in the same way as data from DEER experiments, i.e. by taking into account only the primary dipolar frequency contributions.¹⁷⁹ Note that for high-spin systems with $S > 1/2$ harmonic overtones of the primary dipolar frequency are introduced⁷³ and need to be accounted for in data analysis routines.¹¹⁴ On the other hand, the intermolecular background is steeper and more curved in RIDME as compared to DEER experiments due to additional contributions from nuclear spin diffusion. Generally, the pump excitation bandwidth is larger in RIDME than in DEER which also enhances the intermolecular electron–electron background contribution alongside enhancing modulation depth. A detailed description of the RIDME background decay was presented in Chapter 5.

To increase the excitation bandwidth, pulses with frequency and amplitude modulation were recently introduced to EPR.^{63–65} Technically this was made possible by home-built implementation of recently developed Arbitrary Waveform Generators (AWG) into existing spectrometers^{60;245–247} or dedicated instruments.^{62;248;249} At first, such frequency-swept excitation was limited to X-band frequencies but soon was extended to Q band, followed by increasingly higher frequencies since.

Bandwidths up to 2.5 GHz for excitation and 0.8 GHz for detection have been demonstrated.⁶³ Recently, frequency-swept excitation has also been used with commercial spectrometers.²⁵⁰

During a frequency-swept pulse with sufficient field strength B_1 , the magnetization effectively stays locked to the effective field in the frame rotating with the instantaneous frequency $f(t)$.¹¹⁶ Performance of such an 'adiabatic' pulse can be described in terms of its smallest effective field strength ω_{eff} , i.e. upon passage of the transverse plane, in relation to its sweep rate.⁶³ This is summarized in the critical adiabaticity Q_{crit} of the pulse defined by Equation (7.5)

$$Q_{\text{crit}} = \frac{2\pi \cdot \nu_1^2 \cdot t_p}{\Delta f}, \quad (7.5)$$

where ν_1 defines the amplitude of the pulse, t_p the pulse length and Δf the pulse bandwidth. Pulse length requirements for achieving simultaneous refocusing for pulses with time-dispersed excitation have previously been generalized.²⁵¹

First implementations of frequency-swept pulses in EPR incremented the instantaneous frequency linearly with time, referred to as *chirp* pulses.⁶⁰ The frequency modulation is illustrated in Figure 7.1(d). To avoid excitation outside the intended band, the amplitude usually is apodized by a quarter sine (see Figure 7.1(c)). The resulting inversion profile in subfigure (e), simulated for a two-level system and $t_p = 200$ ns, achieves 100% inversion around the center of the nominal frequency band of 200 MHz while the frequency flanks lead to partial excitation over about 50 MHz. From NMR, pulses modulated by sech/tanh pulses, so-called hyperbolic secant or HS1 pulses, are known to provide very well defined inversion bands.^{53:252} The simulated inversion profile in Figure 7.1(e) indeed demonstrates a much higher selectivity for the HS1 pulse with 100% inversion efficiency over nearly the complete frequency band and very steep frequency flanks. At given maximum amplitude HS pulses of higher order h , i.e. HS h pulses, provide higher adiabaticity Q_{crit} ,²⁵³ at the expense of a somewhat less steep frequency flank. This is illustrated in Figure 7.1 for a HS1 and HS6 pulse: the amplitude of the HS6 pulse is higher over a larger fraction of the total pulse length t_p which results in a higher Q_{crit} . At the same time, steepness of the simulated frequency flanks of the HS1 pulse outperform the ones of the HS6 pulse in Figure 7.1(e). In other words, the order h of HS h pulses provides a parameter to tune the adiabaticity against the steepness of the frequency flank to optimize a given experimental setup.^{54:63} In the following, we use the expression *shaped pulse* for any pulse with amplitude and frequency modulation.

Application of an ultra-wideband (UWB) pump pulse, i.e. $\Delta f > 0.5$ GHz, in X-band DEER measurements has been shown to yield large increases in modulation depth and thus sensitivity for a nitroxide-Cu system.⁶⁰ Compensation for the instrument response function $\nu_1(f)$ was developed to allow for offset-independent adiabaticity and thus uniform excitation.⁶² Applications of UWB pulses at higher frequencies mainly focused on high-spin systems so far: large sensitivity gains for Gd-Gd DEER measurements were achieved by an UWB pump pulse^{115:254} and by pre-polarization of the observed central transition by magnetization transfer from $m_S > 1/2$ levels.¹¹⁷ Recently, shaped pulses were employed for RIDME measurements of a copper-nitroxide system.¹⁹⁸ Determination of Mn-Mn distances allowed for characterization of ATP-fuelled proteins by paramagnetic ion substitution of Mg(II).²²³

Even though compensation of the sweep rate of adiabatic pulses can allow for uniform excitation beyond the resonator bandwidth,⁶² adiabaticity of the pulses is ultimately limited by the resonator B_1 and resonator bandwidth Δf_{res} . Furthermore, broadband detection is attenuated

by the resonator $\nu_1(f)$ -profile. For these reasons, broadband resonators with high and uniform B_1 fields and large Δf_{res} are a field of ongoing development.^{255–258} High B_1 fields are of less concern for excitation of high-spin systems due to their larger transition moment. The recent design of a Q-band resonator based on a loop-gap structure allows for microwave field amplitudes ν_1 of 40 MHz for $S = 1/2$ over a range of nearly one GHz.²⁵⁷ This development set a promising starting point to study potential increases in sensitivity by shaped pulses for distance measurements of a spin $S = 1/2$ system with a broad spectrum.

In this study we set out to compare the performance of DEER and RIDME measurements of Cu–Cu systems. In particular, we explore the sensitivity gain by shaped pulses for both experiments. We first characterize relaxation parameters of the Cu-PyMTA ruler used throughout this work. The performance of different shaped pulses for the given spin system is studied first for two-pulse echoes in Section 7.3.2. In DEER measurements, application of shaped pulses for the pump band and the observer band is studied individually and in combination in the Section 7.3.3. In Section 7.3.4 delays in the RIDME experiments are first optimized before we discuss the application of shaped pulses. We proceed to compare orientation selection in UWB-DEER and RIDME for the geometrically constrained system studied here before we conclude the work with a summary of our findings for both methods.

7.2. Experimental

7.2.1. Sample preparation

The synthesis of the Cu-PyMTA complex and the stiff Cu-PyMTA ruler employed in this study have been described elsewhere.^{94;101;257} The structure of the stiff Cu-PyMTA ruler is shown in Figure 7.10(d). Stock solutions were diluted to final concentrations of 200 μM in a 1:1 (v:v) D_2O /glycerol- d_8 mixture. The sample solutions were filled into 1.6 mm or 3 mm o.d. quartz capillaries and subsequently shock-frozen by immersion into liquid nitrogen.

7.2.2. EPR measurements

CW X-band EPR spectra were detected using a Bruker Elexsys E500 spectrometer equipped with a Bruker Elexsys Super High Q probehead and a nitrogen flow cryostat. Measurements were performed at 140 K, 100 kHz field modulation, 140 mT field sweep width, 0.4 mT modulation amplitude, and 0.2 mW microwave power (30 dB attenuation). The time constant was 40.96 ms and the conversion time 327.68 ms.

Pulsed EPR experiments in Q band were acquired on two different spectrometers. A commercial Bruker Elexsys E580 spectrometer, which can be used with a homemade AWG extension to allow for broadband pulses at a second frequency band,⁶⁰ or a home-built spectrometer based on a Keysight Arbitrary Waveform Generator (AWG)⁶² with a high-power Q-band extension.²⁵⁹ Both spectrometers were equipped with TWT amplifiers with 200 W nominal power and either a home-built TE_{102} box cavity operating at about 34.5 GHz⁹⁷ allowing for 3 mm samples or a broadband resonator with a pent loop-gap design for 1.6 mm samples was used. In the latter one the coupler was set to provide the lowest possible Q -value.²⁵⁷ W-band EPR experiments were performed on a Bruker Elexsys E680 X-/W-Band spectrometer operating at roughly 94 GHz with a home-built W-band microwave bridge and 2 W solid-state amplifier. The spectrometer was equipped with a Bruker TE_{011} resonator. X-band pulse EPR measurements were performed on

the home-built AWG spectrometer⁶² with a commercial MS3 resonator (Bruker). A helium flow cryostat (ER 4118 CF, Oxford Instruments) was used to adjust and stabilize the measurement temperature.

Echo-detected field-swept EPR spectra were acquired using the Hahn-echo pulse sequence $\pi/2 - \tau - \pi - \tau$ with a pulse length t_p of 12 ns or 16 ns for the $\pi/2$ pulse. The length of the π -pulse was set to $2t_p$. The interpulse delay τ was set to 400 ns. Transverse relaxation was studied using the same pulse sequence, where the interpulse delay τ was incremented. Longitudinal relaxation measurements were performed using an inversion recovery sequence $\pi - T - \pi/2 - \tau - \pi - \tau$ with hard inversion by the first π -pulse of length 12 ns, and a soft detection scheme with pulse lengths of 60 ns for the $\pi/2$ and 120 ns for the π -pulse. τ was set to 400 ns. The delay T was incremented starting from 1 μ s.

RIDME data were acquired using the refocused five pulse RIDME experiment $\pi/2 - \tau_1 - \pi - (\tau_1 + t) - \pi/2 - T_{\text{mix}} - \pi/2 - (\tau_2 - t) - \pi - \tau_2$, illustrated in Figure 7.1. If not specified differently, $\pi/2$ -pulses were set to 12 ns and π -pulses to 24 ns. The interpulse delays were set to $\tau_1 = 400$ ns and $\tau_2 = 5$ or 6 μ s while t was incremented starting at -120 ns in steps of 16 ns. The mixing time is given by T_{mix} and set to values between 25 and 400 μ s. In the two-point optimization it was varied from 1 to 600 μ s in steps of 2 μ s to study its influence on the signal evolution. To remove echo crossings and phase offsets, an eight-step phase cycle was used.⁶⁷ Nuclear modulation averaging was performed according to Ref.⁷⁹. Unless otherwise specified, RIDME data were collected on the Bruker Elexsys E580 spectrometer equipped with a home-built TE₁₀₂ box cavity for oversized samples.⁹⁷

DEER measurements were performed with the dead-time free four-pulse version of the experiment¹⁷⁴ $\pi/2_{\text{obs}} - \tau_1 - \pi_{\text{obs}} - (\tau_1 + t) - \pi_{\text{pump}} - (\tau_2 - t) - \pi_{\text{obs}} - \tau_2$ where τ_1 was set to 550 ns, τ_2 to 5 μ s and t was varied in steps of 16 ns. Nuclear modulations were averaged by varying τ_1 in 8 steps of 16 ns. Unless otherwise specified, DEER measurements were performed on the home-built spectrometer using the broadband resonator with a pent loop-gap design.

The sweep rate of shaped pulses was compensated by the $\nu_1(f)$ profile of the resonator to achieve uniform excitation⁶² which was measured in each session. The non-linear amplification by the excitation chain was characterized as described previously⁶² and used for pulse compensation. Inversion efficiencies were measured as described in Ref.⁶² UWB pump pulses were employed at the full available amplitude. Shaped observer pulses had length ratios 2:1 for two-pulse echoes, 2:2:1 for refocused echoes and the DEER observer subsequence and 2:2:2:2:1 for the refocused virtual echoes detected in the RIDME sequence in order to cancel phase shifts.²⁵¹ The adiabaticity of the observer pulses was set by sweeping the amplitude of each pulse and selecting the amplitude for maximum echo intensity. The sweep range and direction was the same for all observer pulses, from low to high frequency. The observer frequency band was centred in the 1-2 GHz detection window of the digitizer and the local oscillator (LO)-frequency adjusted such that the pulses were located around the centre of the resonator at resonance frequency f_0 . Experiments with shaped observer pulses with a bandwidth of 0.5 to 0.9 GHz were evaluated by integration over 3 ns (six datapoints) of the echo transients. The frequency offset between observer and pump pulses is defined from pulse edge to pulse edge, where only the two inner (closest) pulse edges of observer and pump pulses are considered.

An optimization of the pump pulse parameters in DEER measurements was performed as described previously.⁶² The delay τ_2 was set to 2 μ s and two points were measured with $t = \tau_1$

and $t = \tau_1 + 1 \mu\text{s}$, respectively. For details regarding the setups for different DEER measurements, see Table D.3 in Appendix D.

All RIDME and DEER traces presented in the sensitivity comparison were recorded with the same measurement time of ca. 1.5 h at 20 K.

7.2.3. Data analysis

Relaxation times. Data were analyzed and processed with home-written MATLAB (The MathWorks Inc., Natick, MA, USA) scripts. Inversion recovery traces were offset-corrected, sign-inverted and subsequently fitted by stretched exponential functions of the form $c \cdot \exp(-(t/T_1)^\xi)$ using nonlinear least-squares fitting. Longitudinal relaxation times T_1 were extracted as fit parameters. Hahn echo decay traces were offset-corrected by removing a (weak) constant offset from the last 20 data points. The data were then fitted by stretched exponential functions of the form $c \cdot \exp(-(t/T_m)^x)$ using nonlinear least-squares fitting. Fitting errors were extracted from the 95% confidence intervals of the fit. However, we found that experimental uncertainties introduced by the dead time as well as pulse settings can cause larger variation of T_m up to 8%.

Processing of PDS data. RIDME and DEER data were processed with DeerAnalysis.⁷⁸ For background correction, the dimension of an exponential background decay was fit to the DEER and RIDME data. Note that this resulted in different background dimensionality for the two methods. Subsequently, the experimental trace was divided by the background fit and normalized. Dipolar spectra were obtained after background correction by Fourier Transform and normalised to their integral in DeerAnalysis.

Extraction of noise. Determination of noise levels as the root mean squared deviation (rmsd) between time or frequency domain fits and experimental data – as is often used as noise estimate – was disturbed by differences due to orientation selection for our data. Instead, noise levels were determined from the outer halves of the dipolar frequency spectrum. White noise of time-domain data is distributed equally over the (dipolar) frequency domain and in this case it is possible to extract the noise independently from the quality of the fit. In the data presented, a slight frequency dependence of the noise level is observed in frequency domain due to the time dependence of the noise in the primary data. The noise is thus not strictly white. However, using different fractions of the frequency domain data in the noise analysis did not influence the qualitative findings. Consequently, the noise level $n_{\text{I,FT}}$ was determined from the rmsd between the dipolar spectrum and the zero baseline in the outer halves of the frequency domain data. Because the dipolar spectra were normalized to their integral, the noise level extracted in this way is already inversely scaled by the modulation depth λ and the sensitivity η can be directly calculated as the inverse of $n_{\text{I,FT}}$. To estimate the noise level $n_{\text{I,M}}$ on the time domain traces, i.e. independent of the modulation depth, the rmsd between the moving average of 15 data points and the experimental traces was calculated. In this case, the sensitivity η_M corresponds to $\lambda/n_{\text{I,M}}$.

7.3. Results and Discussion

7.3.1. Characterization of Cu-PyMTA for dipolar spectroscopy

Relaxation rates are important parameters in PDS experiments. The transverse relaxation rate limits the maximal detectable trace length and thus the distances that can be extracted. In this respect a long phase memory time T_m is beneficial and T_m can be significantly prolonged by

solvent deuteration.⁵⁰ Equilibrium magnetization builds-up with the longitudinal relaxation rate due to spin-lattice interactions. It thereby sets an upper limit for the repetition rate of the EPR experiment. For a given measurement time, it thus also constrains the SNR. Further, in the case of RIDME experiments spontaneous spin flips of the B spins during the mixing block introduce the dipolar modulation to the RIDME signal. The smaller $T_{1,B}$, the higher the probability of a spin flip. However, if $T_1 \sim T_m$ a significant number of spontaneous flips of A spins will occur during the transverse evolution period reducing the modulation depth in dipolar spectroscopy. Further in the case of RIDME experiments, the electron coherences that are not transferred to polarization by the first $\pi/2$ pulse of the RIDME mixing block will further contribute additional, unwanted echoes to the RIDME signal evolution if $T_{\text{mix}} \leq T_m$. Accordingly, a ratio of T_1/T_m of about 5 was considered to be best suited for metal-metal RIDME experiments.⁹³ The temperature and field dependence of the relaxation rates makes these parameters factors to consider in the optimization of measurement conditions for a certain spin system. Figure 7.2 shows the extracted T_m and T_1 times for the Cu-PyMTA ruler in the range of 10 to 30 K. It can be seen that for decreasing temperatures ≤ 15 K, the T_1 times become significantly longer, which leads to an increase in measurement time due to long repetition rates at the same SNR. On the other hand, transverse relaxation increases more gradually. In the studied system at 20 K and in Q band, the signal intensity is decayed to 10% of its initial value at 18 μs , which serves as an estimate of the upper distance limit assuming the background decay can be neglected, e.g. in DEER at very low spin concentration. This corresponds to a full period of the dipolar coupling frequency for distances up to 10 nm. For temperatures ≥ 20 K, the T_1/T_m ratio is in a reasonable range for RIDME measurements. Thus, a measurement temperature of 20 K was chosen for all distance measurements as best compromise between long T_m , experimental repetition rate and T_1/T_m ratio.

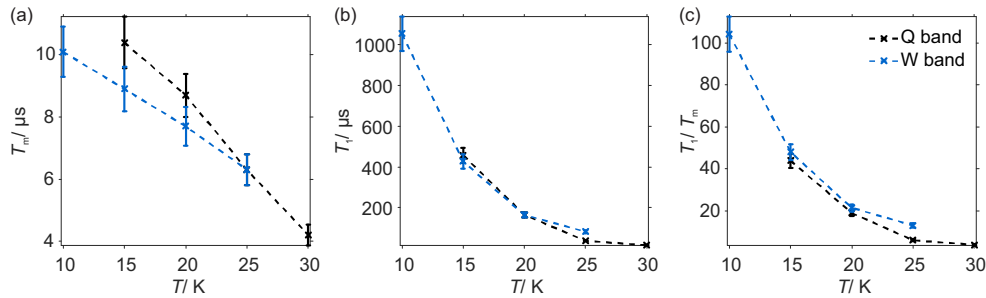


Figure 7.2. (a) Phase memory time T_m and (b) longitudinal relaxation time T_1 of the Cu-PyMTA ruler in Q and W band. (c) Division of longitudinal by transverse relaxation T_1/T_m . The relaxation times are estimated from fitting stretched exponential functions of the form $c \cdot \exp(-t/T_i)^x$.

The qualitative findings for the relaxation rates are the same in Q and W band. While the number of detectable spins decreases with increasing microwave frequency, the situation is more complex for concentration sensitivity and in pulse EPR experiments with limited bandwidth. Significant broadening of the Cu(II) spectrum occurs while the excitation bandwidth remains similar (between X and Q band) or even decreases (for W band) due to technical difficulties to provide and apply amplifier technology with similar output power in W band. This leads to a loss in SNR as only a smaller fraction of the spectrum can be excited. Thus, most of the experiments were performed at Q-band frequencies. In order to excite a larger fraction of the Cu(II) spectrum, the performance of DEER experiments using shaped pulses was also studied in X band.

7.3.2. Shaped pulses

Performance of shaped pulses

In Figure 7.3(a), the Q-band EPR spectrum of the Cu-PyMTA ruler is shown cast on a frequency axis. As is common for the EPR spectra of metal centers, the spectrum spans several GHz, in this case more than 4 GHz. In comparison, most commercial resonators exhibit a narrow mode $B_1(f)$ and the available resonator bandwidth Δf_{res} is usually below hundred MHz even at complete overcoupling. As mentioned in before, limitations in $\nu_1(f)$ and bandwidth Δf_{res} by the resonator ultimately restrict the adiabaticity of the pulses as well as broadband detection. The $\nu_1(f)$ profile (red) of a recently developed broadband resonator²⁵⁷ is overlaid onto the spectrum (black) in Figure 7.3(a). Fast nutation frequencies $\nu_1 > 40$ MHz, are available over a range of nearly one GHz. With

$$\frac{\nu_1 \cdot h}{g \cdot \mu_B} = B_1 \quad (7.6)$$

this corresponds to $B_1 > 1.43$ mT. Such high B_1 fields over such a large resonator bandwidth Δf_{res} are highly promising for measurements of spin 1/2 systems using shaped pulses and it was recently demonstrated²⁵⁷ that the gain in sensitivity for Cu–Cu DEER measurements using a HS6 pump pulse in such a resonator is larger than in a resonator with narrower bandwidth.⁹⁷

Inversion efficiencies $E = (M_0 - M_z)/2M_0$ measured on the Cu-PyMTA ruler for linear frequency sweeps (*chirps*) covering different frequency bandwidths Δf are shown in Figure 7.3(b). For all pulses, the frequency flanks are well defined and excitation in the specified frequency band is largely uniform. A slightly lower inversion efficiency is observed for a pulse bandwidth Δf of 900 MHz. This is expected, as according to Equation (7.5) the adiabaticity at a broader sweep range Δf is lower, see Table 7.1, which in turn decreases the inversion efficiency. However, the inversion efficiency does not exceed 70% in any case. This is well below the expected inversion efficiency which should be 100% for an ideal system and $Q_{\text{crit}} > 5$.

Pulse bandwidth Δf / GHz	0.9	0.7	0.6	0.5	0.3	0.2	0.1
Adiabaticity Q_{crit} for chirp pulses	2.4	4.1	5.2	7.1	14.7	23.6	49.5
Adiabaticity Q_{crit} for HS6 pulses	1.4	2.6	3.4	4.5	10.4	17.3	35.8

Table 7.1. Predicted adiabaticities of the shaped observer pulses used for the two-pulse echoes in Figure 7.3 (chirp pulses) and for HS pulses of order 6 at the same pulse bandwidth Δf .

We tested if this loss in inversion efficiency is caused by the dipolar coupling in the Cu-PyMTA ruler by performing the same experiments on the loaded ligand, i.e. the Cu-PyMTA mono-complex. The same frequency-dependent inversion profiles were obtained as shown in Figure D.8 in Appendix D. We currently do not fully understand what limits the inversion efficiency. Spin dynamics during adiabatic pulses differs from the one upon simultaneous excitation of all transitions by monochromatic pulses. The time-dependence of excitation can lead to coherence transfer effects if transitions with slightly different frequencies are passed consecutively.²⁵¹ This resulted for example in the observation of additional peaks in three-pulse ESEEM spectra that were dependent on the sweep direction.²⁶⁰ However, the maximal inversion achieved by monochromatic pulses is with less than 80% for this spin system also significantly below the expected level. This suggests that the loss in inversion efficiency for the Cu-PyMTA complex is not dominated by coherence transfer effects resulting from dipolar coupling. Instead it could be a consequence of the hyperfine coupling and excitation of forbidden transitions. Preliminary tests on E' -centres in

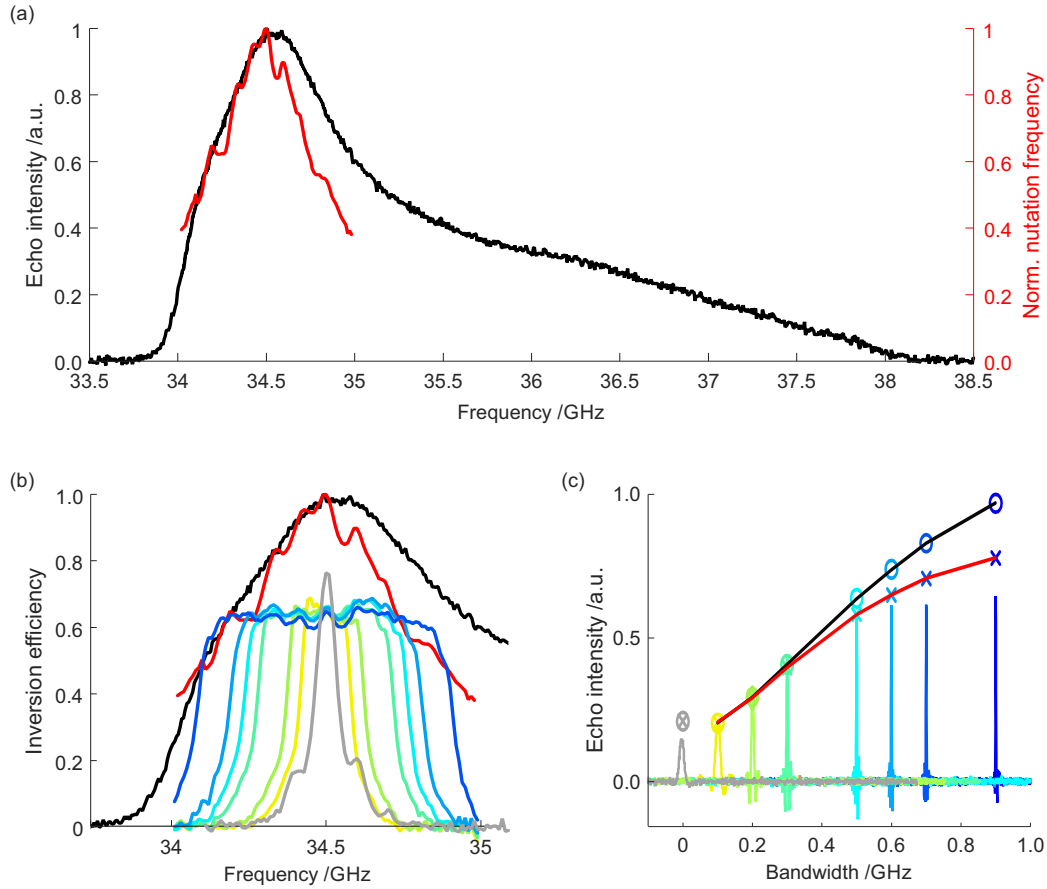


Figure 7.3. (a) Overlay of the resonator $\nu_1(f)$ -profile (red) of the broadband resonator on the echo-detected field sweep spectrum $I(f)$ (black). (b) Inversion efficiencies $E(f)$ for chirp pulses of different pulse bandwidth Δf (coloured lines) and of a monochromatic 12 ns pulse (grey), with $I(f)$ and $\nu_1(f)$ overlaid. (c) Echo transients for two-pulse chirp echoes, centred around 0 and shifted according to the pulse bandwidth Δf , with the same colour code as in (a) and (b). As expectation for the maximal echo intensity, we compare the normalized integrals $\int E(f) \cdot I(f) df$ (circles) and $\int E(f) \cdot I(f) \cdot \nu_1(f) df$ (shown as x). The predicted echo intensities were scaled so that the prediction for a two-pulse echo with 100 MHz chirps agrees with the experimentally observed echo intensity. Lines connecting the circles (black) and x-symbols (red) are guides for the eye.

γ -irradiated quartz glass, a system that does not exhibit hyperfine couplings, showed that 100% inversion can be achieved on our experimental setup. Note that for the Cu-PyMTA complex it might be possible to achieve higher inversion efficiencies if the sweep rates of the pulses are not compensated for the resonator $\nu_1(f)$ profile. However, this gain in peak inversion efficiency would be at the expense of inversion uniformity. Investigation of these effects is deferred to a dedicated study. Here, we proceeded to the comparison of methods based on the currently achievable performance.

To summarize, broadband pulses with well defined frequency bands and largely uniform inversion profiles are available in our experimental setup using the broadband resonator. However, the level of inversion is limited to 65-75% for the Cu-PyMTA complex due to reasons which have yet to be understood.

Shaped observer pulses

To test the performance of shaped pulses for the observer subsequences in DEER and RIDME experiments, we first considered the simpler case of a two-pulse echo. In Figure 7.3(c), echo transients resulting for 2-pulse echoes of chirp pulses of different Δf are shown with the same colour code as the pulse profiles in Figure 7.3(b). Simultaneous refocusing is achieved by adjusting pulse lengths to avoid phase dispersion.²⁵¹ Two observations can be made: (i) The broader the excited frequency range, the narrower is the observed echo in time domain. (ii) The peak echo intensity increases with an increased fraction of the spectrum being covered.

(i) A narrower echo is expected for simultaneous refocusing of a broader range of frequencies: before and after the exact time of refocusing, the different frequency contributions will lead to destructive interference. In a linear approximation, the shape of the echo transient is the Fourier Transform of the product of the excitation profile with the spectral lineshape. With increasing pulse bandwidth (range of frequencies), destructive interference takes place closer in time to the refocusing point. When comparing shaped pulses to monochromatic pulses, shortened two-pulse echoes were already observed for nitroxide samples^{62;261} as well as for X-band measurements of a hexaqua Cu(II) complex.⁶² Due to the narrower spectrum in both cases, the effect was less pronounced. Here, we observed a systematic shortening of the echo with increasing excitation bandwidth as it would be expected from theory. It follows, that the echo integration window has to be adjusted individually based on the excited frequency range for experiments with shaped observer pulses evaluated by echo integration.

(ii) For increasing the bandwidth Δf of the pulses, the peak echo intensity increases approximately linear with the bandwidth for $\Delta f < 0.5$ GHz before it saturates for broader pulse bandwidth Δf . The peak echo intensity corresponds to the number of excited spins which in turn corresponds to the integral over the product of the excitation efficiency profiles $E(f)$ of the pulses and the spectrum $I(f)$. We compared the integrals $\int E(f) \cdot I(f) df$ for each pulse bandwidth Δf to the maximal value of the averaged echo transient in Figure 7.3(c). The intensity value is of arbitrary unit. We thus had to choose a reference point for comparison of the predicted echo integrals and the maximal value of the echo transients. The predicted echo integral for two-pulse echo of a 100 MHz chirp was calculated from the pulse profile of such a pulse, shown in yellow in Figure 7.3(b), and used to determine a scaling factor. Note that this scaling factor only represents a rough estimate so that we can discuss trends but not absolute values. The predicted echo intensities follow the initial trend of increasing echo intensity for $\Delta f < 0.5$ GHz. However, the effect of saturation at broader Δf is not reproduced by the calculated echo intensities.

The frequency-dependence of the resonator attenuates the echo contributions with frequencies further away from the center of the resonator mode f_0 . Compensation of the sweep rate of the pulses should alleviate attenuation by the resonator for excitation, but not for detection. We tried to mimick this attenuation by including $\nu_1(f)$, which is proportional to the frequency dependence of detection efficiency, into the calculation as $\int E(f) \cdot I(f) \cdot \nu_1(f) df$. The echo intensities predicted with inclusion of $\nu_1(f)$ are marked by x-symbols in Figure 7.3(c) and connected by a red line as guide for the eye. For broad pulse bandwidth Δf , attenuation of the increase in peak echo intensity is observed albeit less strongly than in the experimental data. This suggests that also other effects contribute to the reduction in echo intensity for broad Δf . Some of these losses in echo intensity might result from instantaneous diffusion which is expected to increase if a larger fraction of the spectrum is excited. Interestingly, the predicted

echo intensities for the mono-Cu-PyMTA complex match the experimental ones better (see Figure D.8). This might indicate that some of the echo loss at higher Δf is due to coherence transfer to forbidden transitions, which was predicted theoretically for a system of two dipolar coupled spins.²⁵¹ However, as the scaling of the echo intensities is arbitrary, the agreement for the mono-Cu-PyMTA complex has to be interpreted with caution.

We further tested the influence of pulse length, pulse shape and compensation for the $\nu_1(f)$ profile of the resonator on the peak echo intensity, see Figures D.9 and D.10 in Appendix D. We found similar performance for HS6 pulses and chirps. For shaped pulses with different parameters, the optimal amplitudes were found to be different, as expected due to differences in adiabaticity. However, the maximal peak echo intensity was found to remain very similar provided a sufficient adiabaticity can be reached for the given pulse length and shape. We therefore conclude that the peak echo intensity is not limited due to these technical parameters.

Based on these experiments, we chose HS6 pulses for the observer part of the pulse sequence in the following DEER and RIDME measurements as they were found to provide robustly a high adiabaticity and still maintain a reasonable steepness of the frequency flanks and thus well defined excitation profiles. With HS6 pulses, the highest echo intensities were found for a pulse bandwidth Δf of 0.5 GHz.

Analogous results as in these optimizations regarding two-pulse echoes were obtained for the intensity of a refocused echo, which corresponds to the observer subsequence of the DEER experiment (data not shown).

7.3.3. DEER experiments with wideband pulses

Shaped pump pulses

Shaped pulses were employed as pump pulses in DEER measurements with monochromatic observer pulses. In order to find optimal parameters for the shaped pump pulse, a procedure adapted from Doll et al.⁶² was used: two points of the DEER trace $S(t)$ were recorded while pump pulse parameters were varied. The timings of the pump pulse corresponded to the maximal echo intensity of the DEER trace, i.e. the zero time, and to the first local minimum of the DEER trace, respectively. The difference between the two data points serves as sensitivity estimate because $S(0) - S(t) = S(t) \cdot \lambda$. Note that this two-point procedure can lead to distorted results for systems with strongly correlated geometry if the first local minimum is artificially lowered by orientation selection effects. However, the measurements presented here were detected at the maximum of the Cu(II) spectrum where many orientations contribute so that orientation selection effects are reduced.²⁴²

Optimization of the offset and pulse bandwidth Δf (frequency range) were carried out for different shapes and lengths of the pump pulse. In Figure 7.4, the results for a HS pump pulse of order 1 or 6 and length of 250 ns, as well as for a 100 ns-long HS6 pulse are shown to visualize two general trends that were observed:

(i) The optimal pulse bandwidth Δf is larger with increasing HS order and with increasing pulse length. The former effect is nicely illustrated by the difference in optimal Δf for the HS1 and HS6 pulse of the same length of 250 ns in Figure 7.4(a) and (c): 0.8 GHz and 1.2 GHz, respectively. The latter effect is observed when increasing the pulse length of a HS6 from 100 ns to 250 ns: the optimal Δf changes from 0.8 GHz to 1.2 GHz, cf. Figure 7.4(b) and (c). Both observations agree with expectations: A HS pulse of higher order has a higher adiabaticity.²⁶²

And a longer pulse can maintain a high adiabaticity Q_{crit} at higher Δf based on Equation (7.5). However, the length of the pump pulse in DEER is limited by the shortest distance r_{min} contributing to the distance distribution: the time-dependence of inversion by the shaped pump pulse can lead to an artificial broadening of the distance peaks if the length of the pump pulse t_p is $> \frac{T_{\text{dd}}}{4}$ where T_{dd} is the dipolar oscillation period.¹¹⁵ The pulse lengths 100 ns and 250 ns were chosen to model distance measurements of systems with a shortest distance contribution $r_{\text{min}} > 2.75$ nm and $r_{\text{min}} > 3.73$ nm, respectively.

From this optimization, we conclude that the modulation depth and thus sensitivity of DEER measurements with monochromatic observer and shaped pump pulses increases with Δf , HS order and length of the pump pulse, while the shortest distance to be detected limits the pump pulse length.

(ii) The optimal frequency offset between observer and pump pulse correlates with the steepness of the frequency flank of the pump pulse. A lower order of the HS pulse leads to a more defined frequency flank, see Figure 7.1(e). Similarly, an increased pulse length helps defining the frequency flank better. A more defined frequency flank in turn decreases the optimal offset and thus also allows for a smaller offset if this is required for the spectroscopic question at hand.

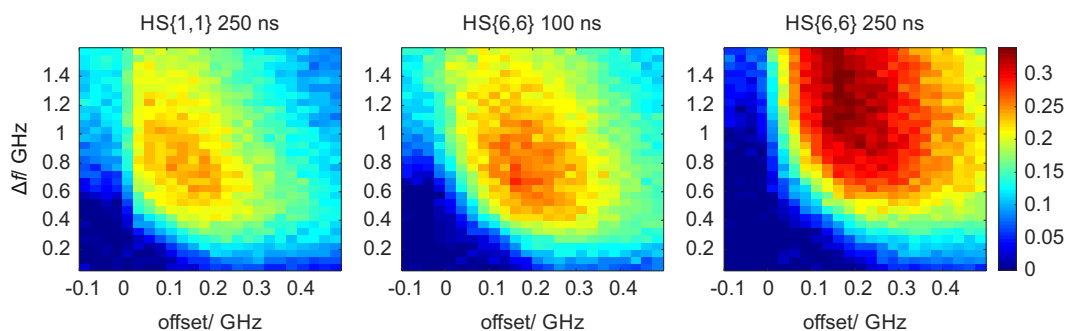


Figure 7.4. Two-point optimization for Q-band DEER experiments with pump pulses of different shape and length. Observer pulses were monochromatic (12 ns) and placed at the maximum of the spectrum. The difference between the signal intensity at t_0 and $t_0 + 1 \mu\text{s}$ is plotted, normalized to the maximal echo intensity at t_0 .

Further note that the experiments presented in Figure 7.4 were performed with the sweep rate of the pump pulses adapted to the $\nu_1(f)$ profile of the resonator. We compared these results to experiments without compensation and found the same trends (data not shown). Note however, that the higher uniformity of the compensated pulses should simplify interpretation of the DEER data, in particular if orientation selection must be considered.

In summary, we found that an individual optimization of the pump pulse parameters for a given combination of spectrometer, resonator and spin system is advantageous. HS6 pulses of length restricted by $t_p < \frac{T_{\text{dd}}}{4}$ appear generally to be a robust choice for a broad range of 'optimal' pulse bandwidth Δf . We expect these observations to hold true not only for DEER measurements between Cu(II) centres but between any two spin 1/2 systems with broad and potentially overlapping spectra.

The optimized pump pulses were applied in DEER measurements with monochromatic observer pulses, see Figure 7.5(a). The traces were compared to a DEER measurement with the shortest monochromatic pulse of 7 ns length available in the centre of the Q-band broadband resonator as pump pulse, which resulted in a modulation depth λ of 6%. The modulation depth λ was significantly increased to 17% for a HS1 pump pulse of length 250 ns. With a HS6 pulse

of the same length, 27% modulation depth were achieved. Reducing the length of a HS6 pump pulse to 100 ns still yielded $\lambda=20\%$.

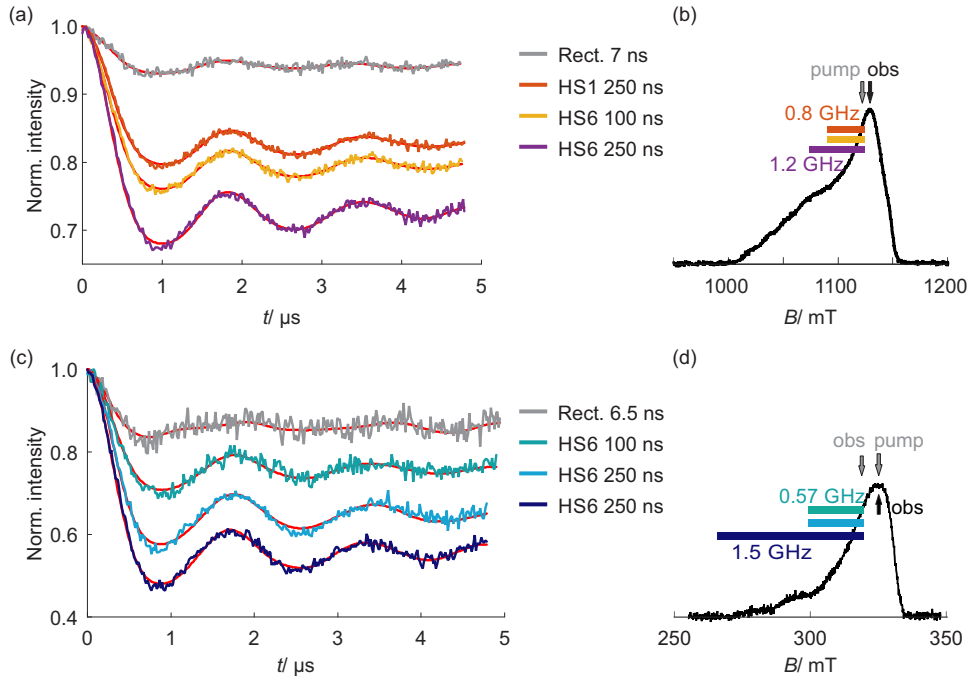


Figure 7.5. DEER with UWB pump pulses. The 12/12 ns observer pulses were monochromatic and placed as indicated. (a) Q-band DEER background-corrected form factors, (b) Q-band echo-detected field sweep with ranges covered by the pulses indicated, (c) X-band DEER background-corrected form factors, (d) X-band echo-detected field sweep with pulse ranges and positions indicated. (a, c) Form factor fits are overlaid in red.

These observations roughly correspond to the predictions made from the two-point optimizations, cf. Figure 7.4. As discussed there, a shorter pump pulse has to be used for shorter r_{\min} . These DEER traces therefore confirm that the maximal sensitivity gain by shaping the pump pulse will be lower if shorter distances r_{\min} are of interest.

The noise level $n_{1,M}$ and initial signal intensity $S(0)$ of the individual DEER traces appear to be rather similar between the traces with different pump pulses. Thus the sensitivity η for distance determination is strongly increased in the DEER traces with HS6 pump pulses in comparison to the monochromatic pump pulse. For details see Table D.2 in Appendix D.

In Figure 7.5(b), the pulse bandwidth Δf is cast on a field axis and overlaid on the echo-detected field sweep. From this direct comparison it is clear that many more spins are included into the experiment by the use of the HS compared to the monochromatic pump pulse. However, a significant fraction of the spins is not yet excited in the Q-band DEER traces. For the Cu-PyMTA ruler studied here, this manifests in residual orientation selection: the fit corresponding to a superposition of Pake patterns and the experimental traces deviate slightly for dipolar evolution times between 0.9 and 1.1 μs in Figure 7.5(a). Orientation selection is discussed in detail in Section 7.3.5. For now it suffices to note that not all spins take part in the Q-band experiments with shaped pump pulses. However, a much larger fraction of all spins is excited than in the case of a monochromatic pump pulse.

In X band, the spectrum of the Cu-PyMTA complex spans about 80 mT, which is less than half of the spectral width in Q band. Thus a significant fraction of the spectrum can be excited in X band already by the shortest available monochromatic pulse of 6.5 ns (~ 150 MHz) pumping

on B_{\max} . This in turn increases λ to 14%, shown as grey trace in Figure 7.5(c). However, the noise level $n_{1,M}$ in the time domain data is slightly higher in the X-band than the Q-band DEER traces as concentration sensitivity is higher. These two effects partly compensate each other with respect to the sensitivity η of DEER measurements, resulting in similar sensitivity for DEER with a monochromatic pump pulse in X band and in Q band, see Table D.2 in Appendix D.

X-band DEER measurements with shaped pump pulse were performed with the monochromatic observer pulses positioned at B_{\max} . A trace recorded with a HS6 pump pulse of 100 ns length and 0.57 GHz bandwidth Δf , is compared to a DEER trace with a pump pulse of the same Δf but a length of 250 ns in green and light blue in Figure 7.5(c). The modulation depth was drastically increased to 24% and 36% for the 100 ns and 250 ns-long HS6 pump pulse, respectively. From the overlay of the bandwidth Δf of the pulses and the echo-detected field sweep spectrum in Figure 7.5(d) it becomes clear that a much larger fraction of the spins take part in the experiment. However, the fit by a superposition of Pake patterns in Figure 7.5(c) still deviates from the experimental data for dipolar evolution times of 0.9 to 1.1 μs . This residual orientation selection can be reduced by increasing the bandwidth Δf of the pump pulse to 1.5 GHz, i.e. covering the entire low-field shoulder of the spectrum. The corresponding DEER trace is shown dark blue in Figure 7.5(c). The change in the shape of the DEER data – including an increase in modulation depth to 44% – proves that a different set of pumped spins participates in the experiment. Indeed, the shape of the form factor agrees much better with the fit by a superposition of Pake patterns. Note also that this modulation depth is similar to the one achieved for nitroxide pairs with monochromatic pulses.

Despite the increased noise level $n_{1,M}$ in X band compared to Q band, we found the sensitivity η of X-band DEER with shaped pump pulses to be similar to the one of Q-band DEER (see Table D.2 in Appendix D) due to the increased modulation depth λ .

To summarize, we found a strong increase in modulation depth and thus sensitivity by substituting the monochromatic pump pulse by a shaped one for DEER experiments both in X and Q band. With a 250 ns pump pulse, corresponding to $r_{\min} > 3.73$ nm, the increase in the fraction of the spectrum excited by the pump pulse resulted in even larger sensitivity gains. Due to the narrower spectrum in X band, it was possible to include nearly the whole spectrum in the experiment. The gain in coupled spin pairs cancelled the lower concentration sensitivity of X vs. Q band and lead to a similar sensitivity of X-band and Q-band DEER.

All pulses shaped

Shaped observer pulses were combined with a shaped pump pulse for DEER measurements. In order to assess the individual gain by sweeping the frequency of either the observer or the pump band, we investigated all possible combinations, i.e. monochromatic observer pulses with monochromatic pump pulse (M_oM_p), monochromatic observer pulses and shaped pump pulse (M_oS_p), shaped observer pulses and monochromatic pump pulse (S_oM_p) and shaped observer pulses with shaped pump pulse (S_oS_p). The traces are compared in Figure 7.6(a).

All shaped pulses had a width of $\Delta f = 0.9$ GHz and were placed on one side of the resonator each: the observer pulse frequency range began 50 MHz above and the pump pulse frequency range began 50 MHz below the centre of resonator f_0 at $B = B_{\max} - 104$ G, respectively. The regions of the spectrum covered by the individual pulses are cast on a field axis and overlaid over the echo-detected field sweep in Figure 7.6(b). They were kept constant between all traces, so

that for example the shaped pump pulse (S_p) had the same frequency range for the setup with monochromatic M_oS_p as for the shaped S_oS_p observer pulse. Note that this corresponds to a pulse setup with lower sensitivity for M_oM_p than setting the observer position onto the spectral maximum as was done for the measurements in Figure 7.5(a).

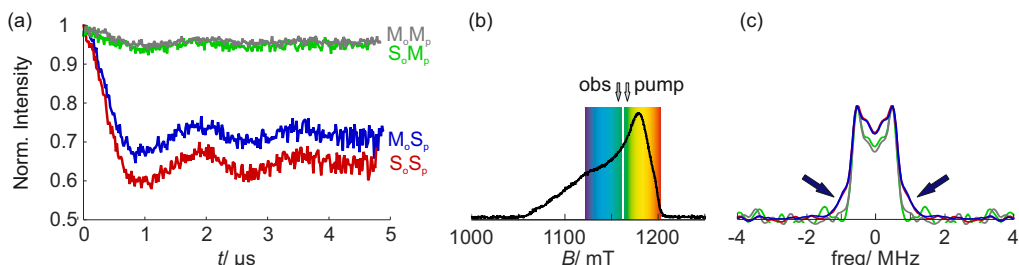


Figure 7.6. Q-band DEER with monochromatic (M) and shaped (S) observer (o) and pump pulses (p) at 20 K: M_oM_p (grey), S_oM_p (green), M_oS_p (blue), S_oS_p (red). (a) DEER background-corrected form factors, (b) echo-detected field sweep with pulse ranges indicated by coloured boxes, (c) dipolar spectra.

Analogously to the observations made above in Figure 7.5(a), the M_oS_p setup resulted in a large gain in modulation depth λ over the M_oM_p setup from 4% to 28%. In contrast, the S_oM_p setup did not result in a significant increase in λ (5%). Both these observations agree with considerations of orientation selection for geometrically correlated systems: The observer frequency selects the orientation(s) of the molecular system with respect to the external magnetic field B_0 . The pump pulse induces a contribution to the modulation only if the resonance frequency of the coupled spin for this orientation of the molecular axis system corresponds to the pump pulse frequency band. In other words, the pump frequency range determines λ within the observer-selected molecular frame. For the M_oS_p setup this corresponds to an increase in λ as the range in pump frequencies is broadened, which increases the probability that the resonance frequency of the geometrically restricted partner spin lies within the pump band. In contrast, a broadened observer frequency range selects more of the randomly oriented spins in the sample to participate in the experiment which in turn should increase sensitivity. However, a broader observer frequency range only increases the probability of the partner spin to resonate at the pump frequency, if the constrained geometry requires a specific frequency offset, which was not excited before with narrowband (monochromatic) observation. A broadened observer frequency range therefore often does not have a significant influence on λ , as we find it here when comparing the S_oM_p and M_oM_p setup.

A further increase in modulation depth λ to 35% was observed for the combination of shaped observer pulses with a shaped pump pulse (S_oS_p). We tentatively explain this increase in λ to orientation selection for this geometrically correlated Cu-PyMTA ruler system: the additional spins that are excited by the broadened observer frequency range in comparison to the monochromatic observer pulse select a set of molecular orientations that due to the geometrical constraint have a higher probability that their partner spin is resonant with the pump frequency band.

The dipolar spectra shown in Figure 7.6(c) provide no arguments in favour of or against this hypothesis. Dipolar spectra detected with the M_oS_p and S_oS_p setups are very similar, i.e. the set of detected orientations of the spin–spin vector with respect to the external magnetic field B_0 are similar. However, it would still be possible that the probability of the observed spin to be the partner spin of one of the pumped spin packets is increased by the S_oS_p setup, which would

then results in the higher λ . Furthermore, the dipolar spectra for the setups with shaped pump pulse closely resemble a superposition of Pake patterns. This suggests that a larger subspace of θ values is sampled by the shaped pulses applied here. In contrast, the M_oM_p and the S_oM_p dipolar spectra both do not resemble a superposition of Pake patterns. The subspace of sampled θ values is thus clearly not sufficient for detection of the complete Pake pattern. A comparison of the distance distributions computed with neglect of orientation selection is presented in Appendix D, Figure D.5.

Unexpectedly, with shaped observer pulses the observed noise level $n_{1,M}$ was slightly higher than for the otherwise equivalent setup with monochromatic observer pulses in Figure 7.6(a). This observation was made with monochromatic (M_p) as well as with shaped pump pulses (S_p). A yet larger increase in $n_{1,M}$ was observed in S_oS_p with respect to M_oS_p DEER measurements for a setup, in which the observer bandwidth was placed around B_{\max} with Δf_{obs} set to 0.5 GHz, as optimized for sensitivity in Section 7.3.2. Here, Δf_{pump} was 1.2 GHz, the data are shown in Figure D.11 in Appendix D. The highest noise levels were found for S_o compared to M_o DEER measurements with a similar setup as in Figure 7.6 but with the observer and pump band inverted, i.e. the observer band covering B_{\max} and the pump band the spectral region towards the low-field shoulder, see Figure D.12. All noise levels are provided in Table D.2. It thus appears as if the increase in noise level was more pronounced when the observer pulses were placed around the maximum of the Cu(II) spectrum compared to placing the observer pulses towards the low-field shoulder. As discussed above in Section 7.3.2, the increase in detectable coherence saturates for $\Delta f > 0.5$ GHz for shaped observer pulses are placed around B_{\max} and no pump pulse is applied. We currently do not understand why shaped observer pulses lead to increased noise levels in dipolar data despite the fact that more spins are observed in the experiment. A thorough understanding of this observation requires a dedicated study.

Note that in some cases we also observed higher noise levels $n_{1,M}$ in the DEER trace when the pump pulse was shaped instead of a monochromatic pulse, see Fig. 7.6(a). This increase in noise $n_{1,M}$ was observed in the form factor in time domain, however, in some cases it was masked in the noise evaluation $n_{1,FT}$ from dipolar spectra by the improved modulation depth (Table D.2, Appendix D). The increase in noise $n_{1,M}$ for shaped pump pulses was large in the measurements where the observer was far from the spectral maximum in Figure 7.6(a), however it was not significant when the observer pulse was positioned on the spectral maximum, see Fig. 7.5(a). We tentatively explain this increase in noise level $n_{1,M}$ by off-resonant Bloch-Siegert phase shifts ϕ_{BS} caused by the individual pumped spin packets on the observer spin packets. Due to the disparity in ϕ_{BS} for different offsets, destructive interference results in echo reduction. Such phase shifts have been observed before in Gd(III)-Gd(III) UWB DEER and were alleviated there by application of two pump pulses, one on either side of the observer frequency.¹¹⁵ This effect is expected to be amplified if the observer pulses are shaped: ϕ_{BS} now depends on the offset of each specific observer spin packet to its respective pumped spin packet and the Bloch-Siegert shift is accumulated over a longer pulse.

To conclude our findings for DEER experiments with shaped pulses, we found very large improvements in sensitivity when substituting the monochromatic pump pulse by a shaped one in DEER experiments with monochromatic observer pulses. This effect was especially strong in X band, where nearly the whole spectrum can be included in the experiment.

Combining shaped observer pulses with a shaped pump pulse did result in an increase in nominal modulation depth over the equivalent experiment with monochromatic observer pulses.

We attribute this otherwise unexpected finding to orientation selection effects. Shaped observer pulses lead to an increase in noise level that is contradicting the increase in peak intensity in the echo transients. Sweeping only the observer pulses did not increase the modulation depth significantly. This is in agreement with expectations as the modulation depth in DEER corresponds to the fraction of B spins that are pumped for the observer-selected molecular orientations. A broader observer band thus detects more molecular orientations (as A spins), but might not necessarily increase the probability that the coupled spin resonates within the pump band. Dipolar spectra closely resembling a superposition of Pake patterns were detected in the measurements using shaped pump pulses provided Δf_{pump} covered a significant part of the spectrum. This suggests that orientation selection was largely suppressed. In the following, we will explore the sensitivity of RIDME experiments with monochromatic as well as shaped observer pulses before we discuss orientation selection in DEER and RIDME in detail in Section 7.3.5.

7.3.4. RIDME experiments

Rectangular pulses

In contrast to the DEER experiment, where inversion of the B spins is achieved by applying a pump pulse at a second frequency band, in RIDME B spins are inverted by stochastic longitudinal relaxation events and thus a single frequency band is sufficient. This poses lower technical requirements to (i) the spectrometer and (ii) the resonator. Further, the observer frequency can be placed freely in the resonator, and in the EPR spectrum of the A spins, so that the position of highest sensitivity can be chosen. This implies that the performance of the RIDME technique is drastically improved in resonators with a higher quality factor Q , which induce a higher signal intensity at the same spin concentration (see Table D.1 and D.2 for a comparison of the loop-gap and TE₁₀₂ box resonator.)

The modulation depth is determined by the time allowed for longitudinal spin flips during the mixing block and builds up according to the probability P_{odd} of an odd number of spin flips during the mixing block:⁷⁴

$$P_{\text{odd}} = \frac{1}{2} \left[1 - \exp\left(-\frac{T_{\text{mix}}}{T_{1,B}}\right) \right]. \quad (7.7)$$

Note that this equation uses the assumption that longitudinal relaxation of paramagnetic centres in frozen glasses is mono-exponential as well as that it neglects correlated flip-flops of the A-B pairs. The latter effect can cause a reduction of the limiting value for the maximal achievable modulation depth.

As in the DEER experiment, an initial preparation period creates electron coherence, which is in RIDME subsequently stored in the direction of the external static magnetic field in form of a polarization grating. This results in a loss of half of the originally excited magnetization. After the mixing time, the magnetization is transferred back into the transverse plane, where it is eventually detected after refocusing by another π -pulse. By adjusting the length of the mixing interval T_{mix} several parameters can be tuned. A long mixing time leads to a higher probability of B-spin flips and thus efficient spin inversion, which in turn results in large modulation depths. However, also some A spins will lose their phase information by longitudinal spin flips and thus

the signal intensity is reduced. Further, a longer mixing block allows for more efficient spectral diffusion in that time and thus the background decay is accelerated.¹⁷⁹

These findings are presented for a set of mixing times in Figure 7.7(a, b). Figure 7.7(b, c) further shows that the shapes of the RIDME form factors in time domain as well as in frequency domain for different mixing times remain largely constant apart from some zero-frequency components which we attribute to imperfect background correction. The consistency in form factor shape for different mixing times supports the assumption, that no orientation selection due to different relaxation of the various spin packets is introduced to the Cu(II)-Cu(II) dipolar evolution data - at least for this very sample over the studied range.

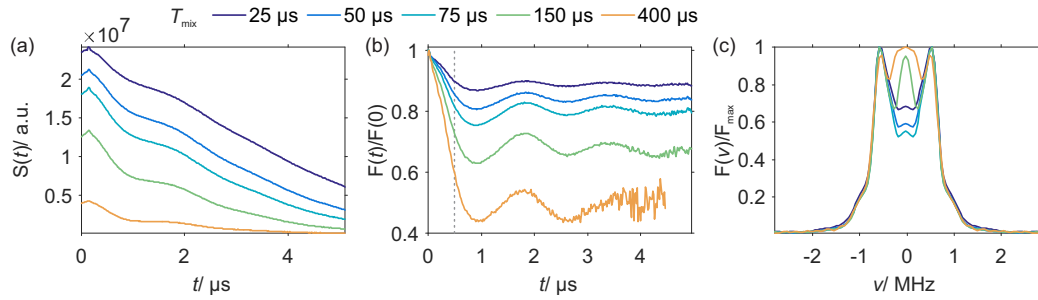


Figure 7.7. Dependence of RIDME traces on mixing time in Q band and at 20 K. (a) Primary data, (b) background-corrected form factors in time and (c) frequency domain. The different mixing times are colour coded. The grey dashed line in (b) corresponds to the second time point used in the two-point optimization in Figure 7.8.

A fast and simple experiment to probe the optimal length of the mixing block is depicted in Figure 7.8. It is based on a similar idea as the two-point optimization for the DEER pump pulse parameters shown in Figure 7.4. Two points of a RIDME trace are measured while the mixing time is varied: the zero time point, representing the maximum signal intensity $S(t=0)$ (Figure 7.8(a)) and a later time point before the minimum of the first oscillation, e.g. 500 ns after the zero time point $S(t)$ indicated by the grey, dashed line in Figure 7.7(b). The intensity difference between the two time points can serve as an estimate λ_{2P} of the modulation depth (Figure 7.8(b)) and, if well chosen, can reproduce the measured modulation depth for a full RIDME trace (see dark blue diamonds in Figure 7.8(b)). Note that the steep background decay can cause deviations between λ_{2P} and the true modulation depth. The product of signal intensity and modulation depth serves as estimate for the sensitivity $\eta_{2P} = S(0) \cdot \lambda_{2P}$ of the experiment.

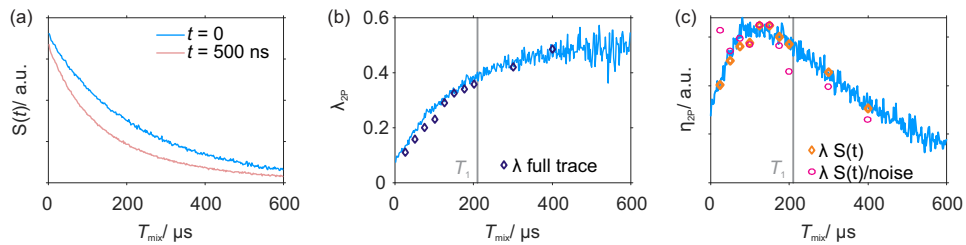


Figure 7.8. Two-point optimization curves for RIDME experiments. (a) Signal intensity for $t = 0$ (blue) and $t = 500$ ns (rose). (b) Estimate of modulation depth λ_{2P} based on difference of signal intensity at $t = 0$ and $t = 500$ ns (blue). Dark blue diamonds give the modulation depth λ extracted from full RIDME traces. (c) Sensitivity estimate η_{2P} from product of signal intensity at $t = 0$ and modulation depth estimate λ_{2P} (blue), the same product for full RIDME traces (orange diamonds) and a sensitivity estimate taking noise into account (purple). The grey vertical lines mark the longitudinal relaxation time T_1 extracted from fitting $c \cdot \exp(-t/T_1)^x$ to the inversion recovery experiment at the same measurement temperature and detection position.

Figure 7.8(c) shows that there is a range of mixing times with best sensitivity, resulting from the trade-off between best signal intensity and highest modulation depth. The trends resulting from this estimate are in qualitative agreement with sensitivity measures from full RIDME traces, that also take noise into account (purple circles, see Table D.1). Note that the two-point optimization underestimates noise contributions at the end of long time traces as noise is not equally distributed over the background-corrected RIDME form factor. Noise strongly increases towards the end of the dipolar evolution time due to the shape of the background function. Thus, it is recommended to use a value of T_{mix} towards the end of the region of best mixing times in the two-point optimization for short time traces and a value of T_{mix} towards the beginning of this range for long time traces. The latter one is also true for conditions with very strong background curvature, where the background might already be significantly decayed for short time traces, i.e. in protonated solvent.

For the Cu-PyMTA ruler presented here, highest sensitivity is achieved at a mixing time of approximately $T_{\text{mix}} \sim 3/4 \cdot T_1$ with a modulation depth of about 30%. A maximal modulation depth of almost 50% can be achieved at the cost of signal intensity and faster background decay for longer T_{mix} . Non-negligible contributions of A-spin flips induced by B-spin flips may cause some reduction in modulation depth. Note that echo-crossings around the zero-time¹¹⁴ may slightly overestimate the modulation depth presented here. A similar effect was observed in a study of copper-nitroxide rulers in our lab.¹⁹⁸

Depending on the interplay of background decay and trace length required to access the distance of interest, the maximal mixing time may be restricted. In addition to the DEER background decay from intermolecular interactions, contributions from spectral diffusion arise during the mixing block in the RIDME experiment. The longer the mixing block the more pronounced these effects become and the background decay is accelerated (see Chapter 5). A comparison of the background decay for the DEER and the RIDME experiment is shown in Appendix D, Figure D.3. The efficiency of the electron-nuclear spectral diffusion process depends on the surrounding nuclei and thus on the solvent, e.g. the effect will be more pronounced in proton-rich than in deuterated environments (see Chapter 5). Thus, the choice of the solvent is not only an important parameter in terms of transverse evolution time, but also for the curvature of the RIDME background decay. On the other hand, for short distances and consequently short time traces, loss in signal intensity and faster background decay are less significant so that longer mixing times may be used to increase the modulation depth.

To summarize, we observed an increase of the modulation depth accompanied by a decrease in signal intensity with increasing T_{mix} in RIDME measurements. A two-point optimization was found to provide a good basis to choose T_{mix} with respect to sensitivity. The choice of T_{mix} further depends on the distance of interest as the background decay is accelerated at longer mixing times. This effect is expected to be particularly strong in protonated environment.

RIDME with shaped pulses

We also explored the use of shaped pulses in RIDME measurements. Optimization of the shaped observer pulses for RIDME is simpler than in DEER for two reasons: (i) In contrast to DEER, only one frequency band is necessary for excitation in RIDME and thus the shaped observer pulses can be placed symmetrically in the centre of the resonator. (ii) The observer pulses could

be placed freely in the spectrum, as the excitation bandwidth for the B spins is not limited by excitation in the RIDME experiment.

We compared RIDME traces recorded with monochromatic pulses to RIDME traces acquired with HS6 pulses of bandwidth $\Delta f = 0.5$ GHz. This bandwidth was found to provide optimal sensitivity for two-pulse echoes of shaped pulses in Section 7.3.2. The shaped observer pulses were sweeping a frequency range which was placed symmetrically around the maximum of the Cu(II) spectrum. This choice was motivated by highest signal intensity as well as by the fact that most orientations of the spin-spin vector contribute in this region, which should reduce orientation selection.²⁴²

Despite the larger excitation band of the shaped pulses, we observed a reduction in SNR in the RIDME traces with shaped pulses compared to using monochromatic pulses (data not shown). In order to compare form factors with high SNR, in Figure 7.9 we show traces that were recorded with different numbers of scans. Two effects contribute to the better SNR with monochromatic pulses. First, RIDME measurements with monochromatic pulses were acquired in a resonator with larger sample size and higher Q -value. Second, the higher noise levels found in DEER measurements with the same shaped observer pulses are expected to reduce SNR of RIDME experiments with these pulses.

The shape of the RIDME form factors detected by pulses covering 0.5 GHz slightly changes compared to the form factors obtained with monochromatic pulses with pulse bandwidth $\Delta f \sim 40$ MHz. The dipolar spectra detected by RIDME recorded with shaped as well as with monochromatic pulses deviate from each other for higher dipolar frequencies, i.e. the contributions corresponding to $\theta = 0^\circ$. This indicates an influence of orientation selection, which will be discussed in Section 7.3.5. Both types of pulses were positioned symmetrically at and around the maximum of the Cu(II) spectrum, respectively. For now we note that the weighting of this frequency contribution is yet different for field-averaged RIDME data, but no additional frequencies occur. This finding corroborates the assumption that both perpendicular and parallel orientations of the spin-spin vector with respect to the external field contribute at this detection position.

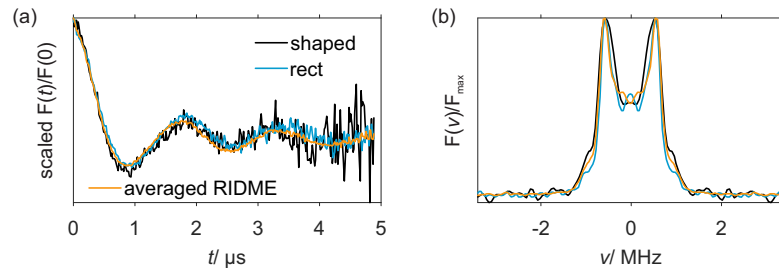


Figure 7.9. Comparison of Q-band RIDME data for shaped (black) and rectangular pulses (blue) at 20 K, $T_{\text{mix}} = 75 \mu\text{s}$. Data from field averaged RIDME measurements are overlaid in orange ($T_{\text{mix}} = 30 \mu\text{s}$). (a) Scaled form factors in time domain $F(t)$ and (b) dipolar spectrum $F(v)$.

The RIDME background decay does not significantly vary with the pulse bandwidth (see Appendix D, Figure D.3). This suggests that instantaneous diffusion due to the microwave pulses negligibly contributes to the RIDME background decay in deuterated frozen glassy matrices at the given spin concentration and that for these conditions the RIDME background shape is dominated by spectral diffusion during the mixing block.

To conclude, we found a similar reduction in SNR when using shaped compared to monochromatic observer pulses in the RIDME experiment and in the DEER experiment. The shape of the RIDME form factor and thus the dipolar spectrum were only slightly affected by the change from monochromatic to shaped observer pulses with larger bandwidth for detection at the maximum of the Cu(II) spectrum.

7.3.5. Orientation selection in DEER and RIDME

The spectral width of the Cu-PyMTA EPR spectrum in Q band does not allow for its full excitation even on a spectrometer with high-power microwave output and broadband pulse shaping capabilities. This leads to the afore-mentioned orientation selection effects.⁶⁸

In Section 7.3.4, it was shown that the RIDME form factors are largely constant over a wide range of mixing times from $T_1/10$ to $2T_1$. We thus assume that the probability of longitudinal relaxation is approximately equal across the full spectrum and orientation selection from the inverted spin can be neglected, even though longitudinal relaxation times do slightly vary across the spectrum (see Appendix D, Figure D.2). Therefore, in the case of the RIDME experiments only orientation selection from the observer spin contributes that restricts the dipolar angle θ if the system has a fixed geometry. The latter effect needs to be studied for a set of different detection positions across the Cu(II) spectrum.

In contrast, the detected subspace of θ is further limited in the DEER experiment by the restriction that the frequency of the coupled (pumped) spin for the observer-selected geometry has to be contained in the pump-pulse excitation band and in Figures 7.5 and 7.6, we observed changes in the dipolar spectra with the bandwidth Δf of the pump pulse in UWB DEER.

In the following we investigate how the restriction of the detected dipolar angles θ by an UWB pump pulse ($\Delta f_{\text{pump}} = 0.8$ GHz) in DEER compares to a B-spin flip by inversion in RIDME experiments for the stiff Cu-PyMTA ruler compound with correlated g -tensor orientations of the Cu(II) centres at several field positions. In both experiments, the observer pulses were monochromatic and the field position is indicated with respect to the observer frequency. For the DEER experiments, two data sets were acquired: one, in which the pump band was positioned below the observer frequency ($\nu_{\text{pump}} < \nu_{\text{obs}}$), and the other one with the opposite arrangement $\nu_{\text{obs}} < \nu_{\text{pump}}$. The sum of the two traces with same ν_{obs} were compared to the RIDME traces as well as the individual data sets. This is illustrated in Figure 7.11(a-d) for detection at the maximum of the Cu(II) spectrum. The full comparison of DEER and RIDME traces at all fields is shown in Figure D.7. The different detection positions and DEER setups are illustrated in Figure D.6. Note that for the comparison of different detection positions presented here, the g -value of the free electron g_e was used in data analysis.

Figure 7.10 shows the dipolar spectra for detection at (a) the maximum and (b, c) in the low- and high-field regions of the spectrum. For both techniques, the dominant dipolar frequency changes from 0.6 MHz for observation at fields $\leq B_{\text{max}}$ (Figure 7.10(a,b)) to 1.2 MHz at higher fields than B_{max} (Figure 7.10 (c)). The strongest differences between the summed DEER trace and RIDME are observed in regions in which mainly x/y -orientations of the g - and A -tensors contribute, e.g. at B_{max} and at higher fields as shown in Figure 7.10(a, c). For these field positions, the DEER traces are sensitive to the position of the pump pulse: either the perpendicular or the parallel contribution to the dipolar signal is enhanced as demonstrated for detection at B_{max}

in Figure 7.11(a-d). At lower fields, the dipolar spectra from RIDME and the different DEER setups largely agree.

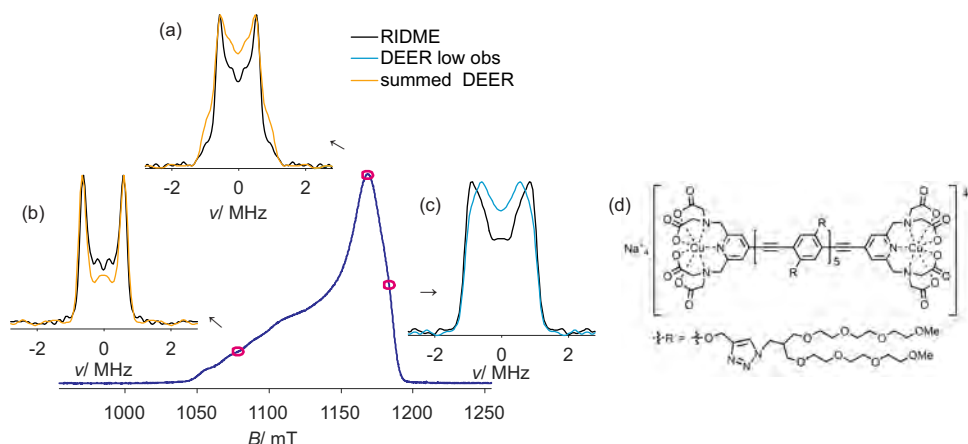


Figure 7.10. Comparison of Q-band DEER (coloured) and RIDME (black) normalized dipolar spectra at different field positions indicated on Cu-PyMTA spectrum (purple curve). (a) Detected at maximum field B_{\max} , (b) $B_{\max} - 90$ mT and (c) $B_{\max} + 15$ mT. (a, b) DEER traces obtained by summing over both setups (yellow) and (c) $\nu_{\text{obs}} < \nu_{\text{pump}}$ (low obs, blue). (d) Structure of the Cu-PyMTA ruler.

Averaging over a full set of RIDME as well as DEER data does result in the same distance information. The summed dipolar data are shown in Figure 7.11(e-h). This suggests that with the applied averaging scheme most of the dipolar frequencies are detected. However, fitting such data with DeerAnalysis which assumes a superposition of Pake patterns in frequency domain reveals slight deviations between the experimental data and the fit around $\theta = 0^\circ$ (arrows in Figure 7.11(g)) indicating residual orientation selection. We observed similar effects for bis-nitroxides in Q band, which will be discussed elsewhere.

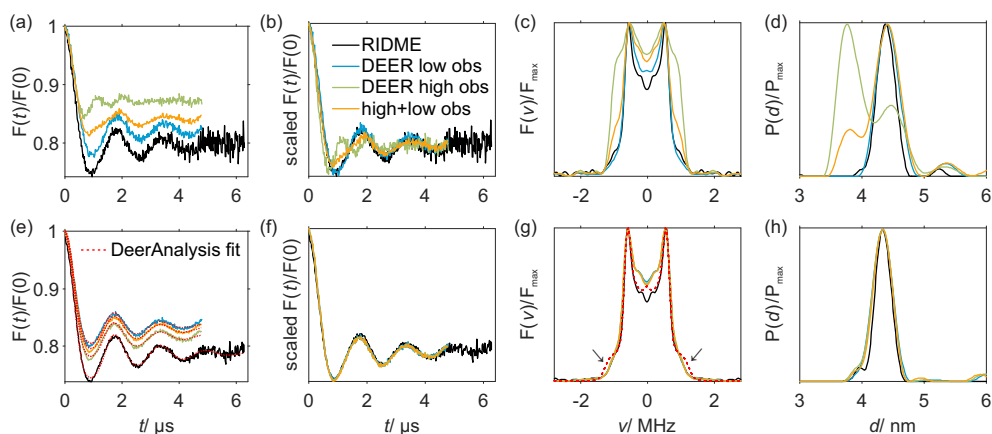


Figure 7.11. Comparison of Q-band RIDME (black) and DEER (coloured lines) recorded with different relative positions of the pump pulse with respect to the observer position. (a-d) Detected at maximum field B_{\max} and (e-f) field averaged. DEER setups were recorded with $\nu_{\text{obs}} < \nu_{\text{pump}}$ (low obs, blue) and $\nu_{\text{pump}} < \nu_{\text{obs}}$ (high obs, green). (a, e) Form factors in time domain and corresponding fits (red, dashed lines), (b, f) modulation-depth scaled form factors in time domain, (c, g) dipolar spectrum, (d, h) apparent distance distributions. The arrows in (g) indicate positions where deviations between the dipolar spectra and the fit are observed.

Furthermore, for the system studied here and detection at B_{\max} – where both parallel and perpendicular orientations contribute – the RIDME experiment as well as the DEER experiment with $\nu_{\text{obs}} < \nu_{\text{pump}}$ already closely resemble an average over the full Cu(II) spectrum and the

resulting changes in the apparent distance distributions are small, but noticeable, see Appendix D Figure D.5.

The g -tensor can be extracted from lineshape analysis as described in Appendix D. It allows us to calculate an effective g -value as an average over all orientations according to Equation (7.3) and averaging over the full angular space. For Cu-PyMTA, an effective g_{eff} -value of 2.131 is obtained. This already deviates significantly from the g -value of the free electron, which is typically assumed for distance analysis.

Figure 7.12 shows the influence of the g -value on the apparent distance distribution. Two different situations are compared: the use of the g -value of the free electron ($g_e = 2.0023$) as implemented in DeerAnalysis and the effective g_{eff} -value to compute the dipolar coupling constant w_{dd} (Equation (7.2)). The difference in g -values leads to a shift of $\sim 2 \text{ \AA}$ in the extracted Cu(II)–Cu(II) mean distance: from 4.3 to 4.5 nm.

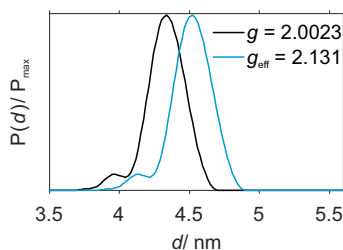


Figure 7.12. Influence of g -value on distance distribution for the field-averaged RIDME data in Q band, 20 K, $T_{\text{mix}} = 30 \mu\text{s}$.

The distance of $\sim 4.5 \text{ nm}$ is much closer to the distance of $\sim 4.7 \text{ nm}$ measured for the same molecular rulers with Gd(III)^{101;115;197} or Mn(II)⁹³ as metal centres. A small shift towards shorter distances is not astonishing in the case of Cu-PyMTA due to the smaller ionic radius of Cu(II),²⁶³ although this effect is expected to be smaller than 0.2 nm. Further, the Cu(II) ion is most probably more strongly coordinated by the three nitrogen atoms and thus is expected to sit closer to the pyridine ring. In addition, the shorter distance might also indicate a higher spin density at the coordinated nitrogen atoms for the Cu-PyMTA complex as compared to Gd-PyMTA and Mn-PyMTA. Nevertheless, the distance of 4.5 nm is much more likely to be correct than the one of 4.3 nm. We thus conclude that g -values should be adjusted in distance analysis routines of spin tags with significant deviation of g_{eff} from g_e .

Note that using the effective g -values as computed from Equation (7.3) and averaging over the full angular space is an approximation. In principle, the true g -value average also depends on the relative orientation of both spins and is given as $\langle g_A \cdot g_B \rangle$, while in our approach we assumed no correlation, i.e. $\langle g_A \cdot g_B \rangle = \langle g_A \rangle \cdot \langle g_B \rangle$, and ignored the angular dependencies of both g -values. The influence of the correlation and angular dependencies is expected to be much smaller than the shift between g_e and g_{eff} , but it might cause complications in quantitative analysis of orientation selection. Note further that the effective g -value is calculated in the spin Hamiltonian after the Bleaney transformation, which tilts the magnetic field experienced by the spin with respect to the direction of the static magnetic field. Thus, also the quantization axes of the \hat{S}_z operators in Equation (7.1) do no longer coincide with the direction of the static magnetic field. However, this is expected to cause only a weak perturbation in the case of about 10% g -anisotropy presented here. The problem can become relevant for spin systems with yet larger g -anisotropy.

Eventually, Figure 7.10 reveals that excitation of dominantly perpendicular orientations of the axial g -/ A -tensors favour a parallel orientation of the inter-spin vector with respect to the external magnetic field ($\theta = 0^\circ$). In contrast, excitation of the z -orientation of the Cu(II) spectrum correlates to the perpendicular orientation ($\theta = 90^\circ$). This indicates that the parallel orientations of the g -/ A -tensor are along the long axis of the molecular ruler and the perpendicular tensor orientations are along the short axis of the molecular ruler.

7.3.6. Advantages and disadvantages of DEER and RIDME

After individual optimization of the two pulse sequences in the previous sections, in the following we discuss their relative performance for different experimental conditions. This includes the microwave frequency band, the available pulse power and shape, the resonator bandwidth and B_1 as well as intrinsic sample properties such as the distance of interest or the spin centre environment, e.g. the degree of solvent protonation.

We found that similar sensitivity can be achieved by the two techniques if the experimental conditions are optimized for each method (see Table D.1 and D.2 in Appendix D). For UWB DEER, we found a large increase in modulation depth λ and thus sensitivity by the use of a shaped pump pulse. Due to the narrower spectrum, the gain was particularly large in X band where $\lambda = 44\%$ was feasible in the commercial MS3 resonator combined with a TWT with nominally 1 kW output power. The gain in sensitivity for UWB DEER depends on the shortest distance r_{\min} due to the limitation of the pump pulse length t_p by $t_p < \frac{T_{\text{dd}}}{4}$. In our case this translated to a λ of 24% compared to 36% for $r_{\min} > 2.75$ nm and 3.7 nm in Q band, respectively. On the other hand, in RIDME measurements a trade-off between modulation depth λ and signal intensity was observed with increased length of the mixing block T_{mix} . Furthermore, the choice of T_{mix} depends on the background decay. For the compound studied here a maximal λ of nearly 50% was observed, while the λ for best sensitivity was found in the order of 30%.

UWB DEER benefits from high resonator bandwidth and B_1 , while this is not beneficial for the RIDME technique. If only a resonator and low bandwidth is available, the gain in modulation depth in UWB DEER is smaller. Spectrometers with low microwave power (and thus low B_1) and high sensitivity-detection with small bandwidth, accompanied by a resonator with higher Q , yield favourable results for the RIDME experiment with monochromatic pulses. Note also the simplified setup in comparison to UWB DEER and that a single frequency source is sufficient.

However, the requirements of high power and high bandwidth are reintroduced for RIDME in combination with shaped observer pulses. Yet, shaped observer pulses in Q band did not introduce any additional dipolar frequencies for detection in the region of B_{max} . Instead, the SNR of DEER and RIDME traces with shaped observer pulses around B_{max} was decreased even though the peak echo intensity was found to be increased for broader observer pulse bandwidth Δf_{obs} . This matter appears to deserve a dedicated study. Thus, we currently conclude that frequency-swept observer pulses do not seem to be beneficial in terms of higher sensitivity. However, they appear more promising for experiments in which a good separation between different microwave frequency bands is necessary^{53;54;264} or in which the full spectrum can be excited. This enables correlation of EPR and dipolar spectra²⁵⁹ or simplifies orientation averaging.¹⁹⁸ Note that for the Cu-PyMTA ruler studied here, it is impossible to excite the full EPR spectrum with a single broadband pulse with the given EPR setup in Q band.

For the stiff Cu-PyMTA ruler studied here, the same dipolar spectrum was attained by field averaging of UWB DEER and RIDME traces. Detection at individual field positions revealed differences between DEER and RIDME for $B \geq B_{\max}$ as well as for different positioning of the pump band relative to the observer band in DEER. These observations are in line with partial excitation of orientations. Selective excitation by the pump band might be an advantage and a disadvantage of UWB DEER at the same time: while it maintains the possibility for orientation selection studies it needs to be taken into account for accurate distance determination in very rigid systems. In contrast to UWB DEER, orientation selection in RIDME was solely dominated by the observer pulses. Thus, RIDME data might be easier to interpret for systems with highly correlated geometry. Finally, the quality of RIDME data is expected to remain the same independent of the width of the B-spin spectrum and spectral separation, i.e. for systems with broader spectra or different spin labels with well-separated EPR spectra.^{180;181;198;244;265}

Electron Spin Echo Envelope Modulation (ESEEM) introduces hyperfine frequencies to the dipolar evolution data due to coupling of the electron spin to nearby nuclei that interfere with the distance analysis. These effects are less important at high frequencies (W band and above), since at those conditions the nuclear Zeeman interaction is typically much larger than the hyperfine coupling, which suppresses ESEEM contributions. Due to the nature of the pulse sequence, these effects are more pronounced in the RIDME experiment^{79;179;180} and might hinder application of the RIDME technique at low frequencies. For instance, deuterium ESEEM is often pronounced in X band and complete suppression of nuclear modulations in RIDME was found to be difficult (see Chapter 6). UWB DEER therefore appears advantageous over RIDME for measurements at lower frequencies, in particular in X band. In X band, the sensitivity of UWB DEER was even found to be similar to Q-band DEER on our home-built spectrometer. On the other hand, the RIDME technique may be beneficial at high frequencies where EPR spectra of some spin labels become very broad while broadband resonators and high microwave power outputs are currently less common and more difficult to construct.

Lastly, the steeper background decay in RIDME experiments may restrict the distance range and complicate data analysis, especially for long distances. This problem is notably enhanced in protonated solvents for which spectral diffusion is much more efficient (see Chapter 5). On the other hand, at both X- and Q-band frequencies, the quality of the UWB DEER data was increased with increasing r_{\min} due to the possibility to use a longer pump pulse. It follows that UWB DEER may be advantageous for the detection of long dipolar evolution times, i.e. long spin–spin distances, and RIDME for shorter spin–spin distances.

To summarize, the choice of technique depends on the following factors:

(i) The spectrometer: In X band, UWB DEER performed well whereas RIDME measurements would be more difficult due to nuclear modulation effects. Low amplifier power, i.e. low B_1 , would hinder application of UWB DEER. Broadband experiments may impose strict requirements on spectral purity of the excitation, for instance on sufficient suppression of the local oscillator frequency. The RIDME setup neither requires high spectrometer bandwidth nor a second frequency source.

(ii) The resonator: Resonators with higher Q and with low bandwidth Δf_{res} improve the sensitivity of RIDME experiments while the lower average B_1 limits the modulation depth in UWB DEER. The opposite is true for resonators that can be operated at low Q like the X-band MS3 resonator or Q-band loop-gap resonators.^{257;258;266}

(iii) The distance of interest: For long dipolar evolution times, the RIDME signal might be already significantly decayed due to background contributions. Thus, background correction of the RIDME data can strongly enhance the noise level towards the end of the time trace. At the same time, the sensitivity of UWB DEER is limited by the shortest distance r_{\min} which in turn limits the pump pulse length. The sensitivity in UWB DEER increases with increasing r_{\min} for the same length of DEER traces. Eventually, the longest distance of interest is limited by the detectable trace length, which depends on the phase memory time. In RIDME, the signal might be potentially decayed to zero due to the background decay already before the phase memory limit is reached.

(iv) The sample geometry: Albeit the same dipolar spectrum was obtained from field-averaged RIDME and UWB-DEER for the sample studied here, this might not be a general result. Orientation selection might be more difficult to average by UWB-DEER in some other samples, whereas it may also be less critical than observed here for Cu(II) labels attached to a protein by a flexible linker. In cases where information on the relative orientation is sought, RIDME can not deliver this information unless relaxation is strongly anisotropic.

(v) The solvent: A higher degree of deuteration generally prolongs the decay of observable coherence both in DEER and RIDME. In case of the RIDME technique, solvent deuteration also strongly reduces the contribution of electron-nuclear spectral diffusion to the RIDME background decay, i.e. the curvature of the background. However, depending on the microwave frequency and the strength of forbidden transitions, deuteration might introduce nuclear modulations which might be more difficult to average for RIDME, especially at X-band frequencies and below. For protonated environments, the DEER background decay is less curved and can therefore be fitted more reliably.

(vi) The combination of spin labels: Large spectral separation in systems with two different spin labels might hinder applicability of UWB DEER while performance of RIDME is expected to be unaffected.

7.4. Conclusions

We compared RIDME and DEER experiments for the measurement of dipolar couplings in a Cu-PyMTA ruler and investigated the use of shaped pulses in both pulse sequences. The two techniques require different optimization of instrumental parameters, as for example the resonator bandwidth. Furthermore, their relative performance varies with the spectrometer band and the sample requirements. We found both methods to provide high-quality data with good and similar sensitivity if the experimental setup was adjusted for the respective sequence. From our findings it becomes apparent that there is not one best method, but that the optimal choice depends on the system under investigation.

Application of a shaped pump pulse to substitute the monochromatic pump pulse of the DEER sequence led to large gains in modulation depth and correspondingly in sensitivity in X and Q band. At X-band frequencies and with a commercial MS3 resonator, it was possible to include nearly the whole spectrum in the experiment. These are very promising results, especially with respect to the ongoing development of Cu(II) spin labels, which are often anchored with little conformational flexibility. For such systems, distance determination with good sensitivity and without orientation selection presents a challenge, which X-band DEER with a shaped pump pulse might help to address in the future.

Orientation selection in RIDME was found to be independent of the mixing time. A trade-off between signal intensity and modulation depth was found depending on the measurement parameters. A simple two-point optimization experiment provides a good estimate for finding the mixing time which yields the highest sensitivity. The choice of mixing time is further influenced by the background decay.

Application of shaped observer pulses resulted in shorter echoes with higher peak intensity. However, evaluation of echo-integrated DEER and RIDME data revealed increased noise levels. The reason remains to be fully understood and calls for a dedicated study.

Orientation selection in DEER and RIDME was compared for Q-band traces with monochromatic observer pulses and a shaped pump pulse for DEER. In both cases, the dipolar spectrum changes with the observer position and for DEER it also changes with the position of the pump band relative to the observer band. Field-averaged data resulted in the same dipolar spectrum for RIDME and DEER measurements. The agreement between the dipolar spectra obtained by two methods that differ fundamentally in the selection of the pumped spins indicates that orientation selection is largely suppressed in the field-averaged data.

Based on our findings, the development of experiments using a relaxation block or shaped pulses is certainly promising large sensitivity gains for excitation of broad spectra – not only for high-spin centres^{63;64} – but also for spin 1/2 systems, such as Cu(II) studied here. Using spin 1/2 systems alleviates problems occurring in high-spin systems, as for example distortions of distance distributions by level mixing¹⁹⁷ or harmonic overtones of the dipolar frequency.^{73;115}

Broadband excitation of spins that are not directly observed in echoes from shaped pulses, e.g. the pumped spins in the DEER experiment, certainly proved beneficial. Sweeping also the observer pulses appears to yield lower sensitivity or even deteriorates sensitivity yet promises other improvements, e.g. for orientation averaging. For example, an experiment in which the whole X-band Cu(II) spectrum is observed by an experiment based on a single frequency band using shaped observer pulses could be imagined. Currently it appears that shaped observer pulses may be more promising for experiments designed for Fourier Transform Evaluation than for experiments based on evaluation by echo integration. In this regard, we hope to inspire dedicated studies of echo intensities and noise levels in traces from shaped observer pulses.

Computing Distance Distributions from Dipolar Evolution Data with Overtones: RIDME Spectroscopy with Gd(III)-Based Spin Labels

The previous chapter revealed large modulation depths and high sensitivity for RIDME measurements on low-spin molecular Cu(II) rulers. Even larger modulation depths were found for the same molecular ruler compounds with Gd(III) as paramagnetic metal centre due to its high-spin nature. However, extraction of distance distributions between high-spin paramagnetic centres from RIDME data is affected by the presence of multiples of the dipolar frequency. This chapter addresses if and how reliable such overtone frequencies can be removed in data analysis routines. To this end, a modified kernel function with overtone frequency contributions is introduced in Tikhonov regularization. The performance of this approach is analysed for a series of model compounds with the Gd-PyMTA complex serving as paramagnetic high-spin label. The calibration of the overtone coefficients for the RIDME kernel is described. The accuracy of distance distributions obtained with this approach is demonstrated and it is shown that for the studied series of Gd-rulers the RIDME technique provides more accurate distance distributions than Gd(III)-Gd(III) double electron-electron resonance (DEER). The established analysis routine of RIDME data including harmonic overtones is implemented in the MATLAB-based program OvertoneAnalysis, which is available as open-source software from the web page of ETH Zurich. This approach opens a perspective for the routine use of the RIDME technique with high-spin labels in structural biology and structural studies of other soft matter.

This chapter is reproduced from Ref.¹¹⁴ with permission from the PCCP Owner Societies and edited for consistency of notation: 'Katharina Keller, Valerie Mertens, Mian Qi, Anna I. Nalepa, Adelheid Godt, Anton Savitsky, Gunnar Jeschke and Maxim Yulikov: Computing distance distributions from dipolar evolution data with overtones: RIDME spectroscopy with Gd(III)-based spin labels, *Phys. Chem. Chem. Phys.*, 2017, 19, 17856-17876'.

The synthesis of the model compound was performed by M. Qi in the group of A. Godt. Most EPR measurements were performed by K. Keller with contributions from A. I. Nalepa, V. Mertens, A. Savitsky and M. Yulikov. The analysis of RIDME data and calibration of harmonic overtones was performed by V. Mertens and K. Keller. Data analysis routines were modified from DeerAnalysis by G. Jeschke and K. Keller.

8.1. Introduction

Combination of site-directed spin labelling (SDSL) with EPR-based distance determination is a powerful tool in molecular biology that allows access to site-to-site distances up to about 10 nm.^{16–18;20–22;41} The most widely used approach for distance distribution measurements utilizes nitroxide-based spin labels^{16–18;20;21;23} together with the DEER experiment.^{75;76;174} During the last decade, several other types of spin labels, such as lanthanide, manganese or copper chelates,^{20;26;237;238;267–269} as well as trityl radicals^{270–273} have attracted attention. This also lead to the reconsideration of a number of previously introduced, but so far much less exploited EPR techniques for distance determination, such as relaxation enhancement,²⁷⁴ DQC,^{175;176} ‘2+1’,²⁷⁵ SIFTER¹⁷⁷ or RIDME.^{66;67;179} In this report, we consider accurate determination of distance distributions from RIDME data obtained from spin-label pairs based on high-spin metal ions. We will explicitly consider Gd(III)-Gd(III) pairs with electron group spin $S=7/2$. However, our general approach and the qualitative findings should be transferable to other high-spin paramagnetic labels, such as Mn(II)^{93;178} or to pairs of paramagnetic labels with one low-spin species and one high-spin species, with the most important example being a pair of a nitroxide radical and a metal ion.^{180–182}

EPR-based distance measurements utilizing paramagnetic metal centres attract attention both from a practical and a methodological point of view. First, metal ions are naturally present at many active sites of bio-macromolecules. Second, spin labels based on metal ions can be chemically more stable than nitroxide labels in the reducing cell environment. Third, use of spectroscopically orthogonal spin labels allows for spectroscopic selection of individual distances in multi-spin systems,²⁷ i.e. selective measurement of individual distances in multiply spin-labelled biomolecules or biomolecular complexes.^{26;28} Moreover, application of transition metal complexes with rather broad EPR spectra as spin labels was one of the key motivations for development of ultra-wide band (UWB) EPR techniques.^{60–62;115;117} Here, we concentrate our efforts on nanometre range distance distribution determination between high-spin Kramers-type metal ions, with the most important examples being Gd(III) ($S=7/2$) and Mn(II) ($S=5/2$) centres. Gd(III) complexes were intensely studied as spin labels for high-field applications as well as for spectroscopic orthogonal detection schemes.^{26;28} Besides this, lanthanide(III) ions are good paramagnetic substitutes for diamagnetic ions in biomolecules, such as Gd(III) for Ca(II) as was demonstrated in the context of paramagnetic NMR spectroscopy.^{276;277} The Gd(III) ion has a half-filled f shell, which results in a very weak contribution of the orbital momentum to the total momentum of these centres. This leads to a weak zero-field splitting (ZFS) that is smaller than the electron Zeeman (EZ) interaction at X-band microwave frequencies (~ 9.5 GHz) and much smaller than the EZ interaction in Q band (≈ 34 GHz) and higher frequencies. Furthermore, longitudinal and transverse relaxation of metal ions with half-filled d or f shells is slow compared to other high-spin paramagnetic metal centres, so that Gd(III) centres in glassy frozen solutions can be used in nearly any pulse EPR technique at temperatures up to at least 30 K. Kramers-type metal centres have an odd number of unpaired electrons and thus a half-integer spin with a particularly narrow central $m_s = -1/2 \rightarrow m_s = 1/2$ transition, which is broadened by the ZFS interaction only to second order of a perturbation series. Very conveniently for high-field/high-frequency applications, this central transition narrows with increasing magnetic field.²⁸

The DEER technique,^{174;278} commonly applied to pairs of two nitroxide radicals, is applicable to Gd(III)-Gd(III) pairs as well. However, the bandwidth of the microwave pump pulse covers a

much smaller fraction of the Gd(III) spectrum than what can be covered for nitroxide radicals leading to a low modulation depth.²⁸ Furthermore, the distance distribution may be distorted since pseudo-secular terms of the dipole-dipole coupling mix spin states near level crossings in high-spin systems,⁴⁴ which poses limitations in the application of this technique. While the modulation depth can be increased by application of UWB pump pulses,^{60;61;115;117} such an approach requires high microwave power as well as a microwave resonator with a broad mode and thus a low quality factor, which decreases detection sensitivity. In the RIDME technique, the inversion pulse is replaced by spontaneous spin flips due to longitudinal relaxation, while the part of the magnetization, which is to be eventually detected, is stored along the magnetic field direction. Relaxation is not bandwidth limited, so that larger modulation depths can be achieved. Furthermore, the spin echo signal can be detected in the mode centre of the resonator whose quality factor is limited only by the required detection bandwidth and at the maximum of the Gd(III) spectrum, both without compromising on the modulation depth. The virtually unlimited bandwidth of spin inversion reduces the fraction of spin pairs in a state mixing regime and thus removes the distortions in the distance distribution that arise from such mixing.¹¹³ RIDME on Gd(III) ions thus has the potential to provide more accurate distance distributions than DEER at higher sensitivity.

However, this potential is currently not realized, since RIDME produces dipolar evolution data with strong contributions of dipolar frequency overtones, stronger than what is typically observed with broad-band inversion pulses in DEER experiments.⁷³ Such contributions are minor in DEER experiments with broadband inversion pulses when the observer is set to the maximum of the Gd(III) spectrum and the pump pulses in the wings at both sides where modulation depth can reach 17%.¹¹⁵ Further complications arise from an additional contribution to the background decay in RIDME compared to DEER, which may limit application to long distances. A detailed analysis of these background contributions is beyond the scope of this chapter and is described in Chapter 5. Here, we focus on data analysis procedures that improve accuracy of the distance distribution in the presence of overtone contributions. Previously, it has been shown that RIDME time traces for Gd(III)-Gd(III) pairs are well approximated by a linear combination of contributions at the fundamental dipolar frequency (f) along with the first ($2f$) and the second ($3f$) overtone frequencies. It has been proposed that the overtone contributions can be considered by adaptation of the kernel used in the Tikhonov regularization procedure that extracts the distance distribution from the time-domain data.⁷³ In this work we demonstrate that the use of such a modified, overtone-containing kernel indeed allows analysing RIDME data in a way that is very similar to the conventional processing of DEER data, and leads to accurate distance distributions for simulated data and to the anticipated distance distributions for model compounds. An analogous analysis of RIDME data for Mn(II)-PyMTA ruler compounds has been reported in Ref.⁹³ (Chapter 9.5). Note also the recent work on Mn(II)-DOTA.¹⁷⁸ We have also used this approach without verification for processing Gd(III)-Gd(III) RIDME data in a report demonstrating the suppression of ESEEM artefacts (Chapter 6).⁷⁹

Here, we study in detail for the Gd(III)-based spin label Gd(III)-PyMTA⁹⁴ in a glassy water/glycerol matrix how the overtone coefficients for the kernel function can be calibrated and how robust the procedure is with respect to changes in temperature and mixing time. Our aim is to provide a calibration procedure that can be applied to other ligands for Gd(III) and for other high-spin ion/ligand combinations in any matrix. We propose that, after such calibration of the kernel function, RIDME-based distance determination on high-spin ions with half-filled d or f

shells can provide more accurate distance distributions than the DEER experiment, in particular, in the lower range of distances accessible by pulsed dipolar spectroscopy techniques. Application of the RIDME technique to studies on structure and function of bio-macromolecules thus appears attractive. It may, however, require kernel calibration for each particular metal ion complex and, possibly, for each particular matrix. This work provides a data analysis software and describes an approach for the calibration of dipolar kernel coefficients that make it possible to address these questions in future studies.

8.2. Theoretical background

Dipolar interaction. Apart from spin-orbit contributions that are small for organic radicals and metal ions with half-filled d or f shells, the magnetic dipole-dipole interaction between an observer spin A and a spin B can be expressed in a form¹⁹

$$\begin{aligned}\hat{H}_{\text{dd}} &= \frac{\mu_0 g_e^2 \mu_B^2}{4\pi\hbar} \frac{(\hat{S}_A, \hat{S}_B) - 3(\hat{S}_A, \hat{n}_{AB})(\hat{S}_B, \hat{n}_{AB})}{r_{AB}^3} \\ &\approx 52.04 \text{ MHz} \frac{(\hat{S}_A, \hat{S}_B) - 3(\hat{S}_A, \vec{n}_{AB})(\hat{S}_B, \vec{n}_{AB})}{(r_{AB}/1 \text{ nm})^3}\end{aligned}\quad (8.1)$$

Here, $\vec{n} = \vec{r}_{AB}/r_{AB}$ is a unit length vector along the inter-spin direction, μ_0 is the magnetic permeability of vacuum, μ_B the Bohr magneton and g_e the g -value of the free electron. In the context of DEER experiments, the pump pulse inverts the B-spin transitions, whereas in the context of RIDME experiments, the B-spin state changes by relaxation. In both cases, this causes a change of the dipolar field at the A spin, which in turn leads to a shift of the resonance frequency of the A spin.

The dipolar term in the spin Hamiltonian is much weaker than the electron Zeeman and the ZFS terms. If all pairs of levels coupled by H_{dd} have an energy difference in the absence of this coupling that is much larger than the coupling, only the secular part of the dipolar interaction needs to be retained and the non-secular parts can be neglected. We briefly discuss a relevant exception below. Typical D parameters for the ZFS of various Gd(III) complexes are below 2 GHz and thus small compared to the electron Zeeman frequency in Q band (34 GHz) as well as at higher microwave frequencies. Thus, at these frequencies the eigenstates of a single Gd(III) centre are approximately equivalent to the eigenstates $|m_A\rangle$ and $|m_B\rangle$ of the operators, assuming the external magnetic field is directed along the z axis. Hence, the states of the coupled system are $|m_A, m_B\rangle$ states. For these conditions, the secular part of the dipolar interaction has the form

$$\hat{H}_{\text{dd,sec.}} = \omega_{\text{dd}} \hat{S}_{A,z} \hat{S}_{B,z} (1 - 3 \cos^2 \theta), \quad (8.2)$$

with $\omega_{\text{dd}} = \mu_0 g_e^2 \mu_B^2 / (4\pi\hbar r_{AB}^3)$ and θ being the angle between the inter-spin vector and the direction of the external magnetic field. At low detection frequencies (9 GHz and below) or for complexes with very strong ZFS, deviations from this description become apparent and the actual eigenstates of the spin Hamiltonian are admixtures of states with different spin projections. This leads to an appearance of additional contributions that have different angular dependencies.^{110;132}

Importantly, for all Gd(III) complexes studied to date, rather broad distributions of the ZFS parameters were observed. Thus, no correlation of the orientation of the ZFS tensor frame (and, accordingly, the local molecular frame of the Gd(III) complex) with the position in the Gd(III)

EPR spectrum could be observed. This property excludes so-called orientation selection effects⁶⁸ in Gd(III)-Gd(III) dipolar spectroscopy experiments. Note, however, that in case of distance determination between a Gd(III) centre and a paramagnetic centre with spectrally resolved molecular frame orientation selection effects may be relevant.²⁷⁹ Another important correction to Equation (8.2) is required close to energy level crossings of two interacting Gd(III) centres.⁴⁴ For some of these crossings, the zero-quantum term of the dipole-dipole coupling

$$\hat{H}_{\text{dd,pseud.-sec.}} = -\frac{\omega_{\text{dd}}}{4}(\hat{S}_{\text{A,+}}\hat{S}_{\text{B,-}} + \hat{S}_{\text{A,-}}\hat{S}_{\text{B,+}})(1 - 3\cos^2\theta), \quad (8.3)$$

becomes pseudo-secular and mixes the near-degenerate levels.⁴⁴ In particular, the zero-quantum operator has off-diagonal matrix elements that connect the $|m_{\text{A}}, m_{\text{B}}\rangle = |-1/2, +1/2\rangle$ and $|+1/2, -1/2\rangle$ levels, which for a half-integer spin with isotropic g value are split only by the second-order (or even higher order) ZFS contribution and by hyperfine couplings, which are small for Gd(III) complexes. Hence, for all orientations, where the second-order ZFS contribution is smaller than or comparable to \hat{H}_{dd} , these two levels are mixed. For all spin pairs, where one of these levels is involved in a pumped or observer transition, the observer frequency does not change by \hat{H}_{dd} , as it would be assumed in data analysis, when B spin inversion involves the $|m_{\text{B}}\rangle = |-1/2\rangle$ or $|m_{\text{B}}\rangle = |+1/2\rangle$ level. Rather, the frequency change depends on the magnitude of the second-order ZFS and thus on orientation, which leads to an apparent shift to longer distances and to an apparent broadening of the distance distribution. The effect is significant in DEER, where the frequency difference between A and B spin transitions is usually relatively small, so that only pairs with $|-3/2\rangle, |-1/2\rangle, |+1/2\rangle$, and $|+3/2\rangle$ states of the individual spins and orientations with moderate ZFS take part in the experiment.⁴⁴ Such mixing can be avoided by a large offset between observer and pump frequency, a strategy that does, however, require a specialized bimodal resonator.¹³⁰ Alternatively, long UWB pump pulses at larger offsets can be applied after storage of the A spin magnetization along the direction of the static magnetic field in the CIDME experiment.¹¹⁶

In Gd(III)-Gd(III) RIDME experiments, the highest spin echo intensity is obtained when the detection position (A spins) is set to the maximum of the Gd(III) EPR spectrum, which corresponds to the $|+1/2\rangle \leftrightarrow |-1/2\rangle$ transition. Since the bandwidth for the B spins is virtually infinite, most B spin inversion events involve levels other than $|\pm 1/2\rangle$ and orientations with such a ZFS value that the second-order ZFS contribution is sufficiently larger than the dipole-dipole interaction to prevent strong level mixing by the pseudo-secular contribution.¹¹³ Furthermore, in RIDME experiments the detection position within the Gd(III) spectrum can be freely chosen, and, for instance, selecting any transition that does not involve an $|m_{\text{A}}\rangle = |-1/2\rangle$ or $|+1/2\rangle$ level would remove distortions due to level crossings. Of course, such a detection position strongly reduces the intensity of the detected echo signal compared to detection on the central transition. However, level crossing effects should only be important at short spin-spin distances and their measurement requires a short length of the dipolar evolution time traces. For such short time traces the loss of spin echo signal due to transverse relaxation is usually not large. Therefore, the reduction of the RIDME signal intensity due to the shift in the detection position in the Gd(III) EPR spectrum might be tolerable.

Dipolar evolution for high-spin centres. A pulse EPR technique designed to detect the static dipole-dipole interaction provides a time trace as output, which, ideally speaking, contains

evolution solely due to the secular part of the dipole-dipole interaction in the form described by Equation (8.2). Under the common assumption that the distribution of the spin-spin vectors with respect to the external magnetic field is isotropic, the time-domain signal in DEER and most other pulsed dipolar spectroscopy experiments is given by the equation

$$F(t) = \int \int p(r) \cos(\omega(r, \theta) \cdot t) \sin(\theta) d\theta dr \quad (8.4)$$

The evolution frequency is determined according to Equation (8.2) as $\omega = \omega_{\text{dd}}(1 - 3 \cos^2 \theta)/2$. Note that the spin Hamiltonian in Equation (8.2) is written in the angular frequency units. The distance distribution $p(r)$ is varied by the data analysis routines to match the computed time evolution $F(t)$ to the experimental time trace. The function

$$K(r, t) = \int \cos(\omega(r, \theta) \cdot t) \sin(\theta) d\theta \quad (8.5)$$

is called kernel function, and its Fourier transform with respect to t for a fixed r is the so called Pake pattern.⁷⁵ The kernel function is the core of any distance distribution fitting procedure. For high-spin metal centres, both in DEER and in RIDME experiments overtone frequencies appear. These overtone frequency contributions are very weak in conventional Gd(III)-Gd(III) DEER, but are apparent in DEER experiments with broad band pump pulses, in particular, if a pump pulse with large adiabaticity is applied at the central transition.¹¹⁵ These overtones can be included in the kernel function, as earlier suggested,⁷³ in a rather straightforward way:

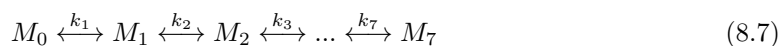
$$K_{\text{mod}}(r, t) = \int [P_1 \cos(\omega(r, \theta) \cdot t) + P_2 \cos(2\omega(r, \theta) \cdot t) + P_3 \cos(3\omega(r, \theta) \cdot t)] \sin(\theta) d\theta. \quad (8.6)$$

In Equation (8.6) we took into account that only double and triple dipolar frequencies were found to have measurable contributions to RIDME time evolution data and that higher overtone frequencies can thus be neglected.⁷³ Since only the ratios of the weighting coefficients P_1 , P_2 , and P_3 influence the shape of the dipolar evolution trace, it is convenient to normalize these coefficients by the condition $P_1 + P_2 + P_3 = 1$. With this normalization, the new kernel function has two free parameters, and thus requires calibration on a set of well-defined model compounds. Note that the Equations (8.4)-(8.6) do not rely on a particular relation between the strength of ZFS and electron Zeeman interaction. However, for non-Kramers ions (integer spin) with non-axial ZFS larger than the thermal energy, the dipole-dipole interaction will be quenched.²⁸⁰ In other regimes, Equation (8.3) cannot simply be applied to non-Kramers ions. Describing such cases would require appropriate change of the $\omega(r, \theta)$ dependencies.

Build-up of the dipolar modulation during the mixing block of the RIDME experiment. The pulse sequence of the RIDME experiment is shown in Figure 8.1(a). Instead of applying a pump pulse, as in the DEER experiment, inversion of the B spins is achieved by storing the magnetization of A spins along the direction of the external magnetic field for a mixing time period T_{mix} . During this time, B spins change their state $|m_B\rangle$ by relaxation with a certain probability, thus creating a change in the dipolar field at the A spin, and, accordingly, inducing the modulation of the detected echo signal. Of course, such spontaneous spin flips also happen during the signal evolution of the A spins in the transverse plane. However, these latter flips will

happen at random times and will thus contribute to the background decay, rather than to the RIDME form factor signal. During the mixing time the stored magnetization of A spins decays, which reduces the resulting echo intensity. It is natural to assume that the relaxation of the A spins is independent or only weakly dependent on the states of the spins in remote molecules. We can thus disregard such relaxation processes of A spins while describing the spin flip kinetics for the B spins. We shall see below that the detailed mechanism of relaxation of the B spins, coupled to A spins, needs to be considered to understand the relative intensities of the dipolar frequency overtones in RIDME data.

Consider a series of ensembles $\{E\}_k$ with $k = 0, 1, 2, \dots, 7$, such that the ensemble $\{E\}_k$ describes all spin pairs for which one spin is always of type A, i.e. it is excited by the microwave pulses and contributes to the detected spin echo signal, and the second spin is always of type B (non-resonant) and spontaneously undergoes a state change with $k = \Delta m_B$ during the mixing time due to one or several relaxation events. This ensemble of spin pairs will be responsible for the whole modulation of the RIDME echo signal with the dipolar frequency overtone $k\omega_{dd}$. The magnetization of the A spins, stored along the z direction, will have a contribution for which the state $|m_B\rangle$ of the B spin has not changed, which we call M_0 (ensemble $\{E\}_0$), as well as contributions for which the B spin has flipped by $\Delta m_B = 1$ (M_1), $\Delta m_B = 2$ (M_2) and so on (ensembles $\{E\}_1$, $\{E\}_2$, etc.). We now consider the time evolution during the mixing block (Figure 8.1(a)). The initial time point of this evolution ($t_e = 0$) is after the first $\pi/2$ pulse of the mixing block, and the last time point ($t_e = T_{\text{mix}}$) is just before the second $\pi/2$ pulse of the mixing block. At $t_e = 0$ all A spins belong to $\{E\}_0$ and thus $M(0) = M_0$, and no dipolar modulation of the RIDME echo would be observed if the second $\pi/2$ pulse would follow instantly after the first $\pi/2$ pulse. As the time t_e increases, other contributions to the magnetization $M(t_e)$ grow up on the expense of the decaying value of M_0 . One can write that $M(t_e) = M_0 + M_1 + M_2 + M_3 + \dots + M_7$. Experimentally, these contributions can be determined from the relative weight of the non-modulated echo signal (M_0) to the echo signal modulated with the fundamental dipolar frequency ω_{dd} (M_1), and its higher harmonics ($M_2 \dots M_7$). It has been demonstrated that at least contributions of the main dipolar frequency ω_{dd} and of the two lowest overtones ($2\omega_{dd}$ and $3\omega_{dd}$) can be experimentally determined with reasonable accuracy, but that higher overtones cannot be observed within experimental uncertainty.⁷³ By monitoring the build-up of the dipolar modulation we can thus make some important conclusions on the longitudinal relaxation processes of the Gd(III) centres. If we assume that at each relaxation event the spin projection of a B spin can only change by one, this would lead to a chain-like kinetic scheme:



In such a scheme each ‘higher order’ contribution to the A spin magnetization appears on expense of the previous or next order magnetization. Such time evolution schemes are well known, for instance in chemical kinetics or in chain reaction studies, and their mathematical properties are understood in detail. An important property of such kinetic schemes is that during the whole equilibration process the relative contributions of different orders M_i are continuously changing. For instance, at short mixing times one can approximately write

$$M_1(t_e) \approx M_0 k_1 t_e; \quad M_2(t_e) \approx M_0 k_1 k_2 \frac{t_e^2}{2}; \quad M_3(t_e) \approx M_0 k_1 k_2 k_3 \frac{t_e^3}{6} \text{ etc.} \quad (8.8)$$

These equations predict that at short mixing times the modulation of the main dipolar harmonic should grow first, whereas higher harmonics should appear only later with increasing mixing time. Such behaviour was not experimentally observed.⁷³ We can thus exclude this simplest chain-like kinetic scheme, at least for the type of Gd(III) complexes at hand. To date, we observed in RIDME experiments nearly constant relative fractions of different dipolar harmonics independent on the mixing time and only very weakly dependent on temperature. More detailed data, presented below in the Results section, are in line with our earlier observations. A kinetic scheme that could explain such behaviour requires direct processes with a change of m_B by at least two and three:



For the frequency ranges corresponding to contributions from higher-order dipolar harmonics M_4 to M_7 the frequency-domain experimental RIDME data show very low signal intensity (see, for instance, Figure 8.7). Thus, for data analysis the corresponding kinetic constants are set to zero for all events with $\Delta m_B > 3$. It was shown that such a kinetic scheme is, indeed, capable of explaining the nearly constant fractions of different dipolar harmonics in a rather broad range of mixing times.⁷³ We will come back to further details of the dipolar signal build-up after discussing the experimental data.

We should, however, make a remark on the physical origin of such higher-order relaxation events. To do so we need to consider the spin-orbit coupling term in the spin Hamiltonian. Orbach as well as Raman relaxation mechanisms²⁸¹ involve two phonons, i.e. spin-orbit coupling ‘acts twice’ in a single relaxation event. According to the general form of this interaction, terms up to S^2 are present in the spin-orbit coupling operator,⁴⁸ and, thus, acting twice during the relaxation process, these terms can induce spin flips up to four units of the spin projection operator in a single relaxation event.

Note also that we observe longitudinal relaxation for Gd(III) centres that is not mono-exponential, i.e. the relaxation rate is not the same for all paramagnetic centres. Furthermore, for a single Gd(III) centre the relaxation rate might be different for each individual transition. However, these effects would not change the qualitative picture presented here.

The last important point to be discussed is the effect of B spin flips on the longitudinal relaxation of A spins. Due to the presence of $S_A^\pm S_B^\mp$ terms in the dipole-dipole interaction, flip-flop type processes would accompany each flip of a B spin with a certain rate. In magnetic resonance such events are the origin of spin diffusion. In the RIDME experiment, such flip-flop processes would result in a higher loss of the echo intensity for the fraction of A spins for which multiple B spin flips have occurred. Depending on the strength of the dipole-dipole interaction with respect to the resonance frequency offset between A and B spin, in each spin pair the contribution of the spin flip-flops would vary. We shall see below that RIDME experiments on model compounds with short spin-spin distances (< 3 nm) suggest a significant impact of such flip-flops on the RIDME signal. Furthermore, it is likely that spin flip-flops explain the absence of higher-frequency overtones even in RIDME experiments with long mixing times. These processes might also play a role in preserving nearly constant overtone weight coefficients over a large range of experimental conditions in Gd(III)-Gd(III) RIDME measurements.

8.3. Experimental details

Materials and methods. To study the influence of the harmonic overtones on RIDME data, the Gd-rulers $\mathbf{1}_n$ and $\mathbf{2}_n$ with Gd(III)-PyMTA as the spin label, as shown in Figure 8.1(c), were used. Because of their geometry and the rather high stiffness of the spacer the Gd-Gd distances are well-defined. In this study Gd-Gd-distances from 2.1 to 6.0 nm were considered. The synthesis of the Gd-rulers is described elsewhere.^{94;101;131} For low temperature distance measurements the Gd-rulers were dissolved in a 1:1 mixture of D₂O:glycerol-d₈ (v:v) to obtain solutions with concentrations between 25 and 300 μ M. The solutions were filled into 0.6 mm inner diameter quartz sample tubes and subsequently shock-frozen by immersion into liquid nitrogen. EPR experiments were performed on a commercial Bruker Elexsys E680 X-/W-band spectrometer as well as on a modified Bruker Elexsys E680 W-Band spectrometer,¹⁹³⁻¹⁹⁵ both operating at roughly 94 GHz. A home-built ENDOR cavity with a microwave frequency bandwidth of 130 MHz was used with the latter spectrometer,¹⁹³ and a Bruker TE011 resonator with the former one. Q-band data were acquired at a Bruker Elexsys E580 Q-Band spectrometer equipped with a home-built cavity operating at about 34.5 GHz.⁹⁷ For Q-Band measurements and in cases where high-SNR measurements in W band revealed ESEEM oscillations, ESEEM averaging was performed according to Ref.⁷⁹. To study the temperature dependence of the RIDME signal the sample temperature was adjusted to 10, 20 or 30 K using a helium flow cryostat. The RIDME pulse sequence is shown in Figure 8.1(a) with $(\pi/2)$ -pulses being set to 12 ns and (π) -pulses to 24 ns if not stated differently. The interpulse delays were set to $d_1 = 400$ ns and $d_{12,\text{init}} = -120$ ns, while d_2 was adjusted to the required trace length from 2.5 to 9.4 μ s. The time increment t was chosen to obtain traces with approximately 300 data points. The mixing time is given by T_{mix} and was varied to study its influence on the signal evolution. In this study mixing times in the range of 4 to 200 μ s were probed. The longitudinal relaxation $1/e$ decay times ($T_1(1/e)$) at 10 K, 20 K and 30 K were determined at the maximum of the Gd(III) spectrum with the inversion recovery experiment. For field-dependent longitudinal relaxation data on Gd(III)-PyMTA see Ref.⁷³. T_{mix} of the RIDME experiments shown in the main part of the paper was varying around the value of $T_1(1/e)$, ranging from about $T_1(1/e)/3$ to about $2T_1(1/e)$. In Appendix E RIDME data for mixing times up to $6T_1(1/e)$ are shown. To remove echo crossing and phase offsets, an eight-step phase cycle as described by Milikisyants et al.⁶⁷ was applied. For $\pi/2$ and π pulses of equal length the MPFU unit and for $t(\pi) = 2t(\pi/2)$ the SPFU unit was used for phase cycling. Unless stated differently, RIDME traces were detected at the maximum of the Gd(III)-spectrum as denoted in Figure 8.1(b).

Analysis of RIDME time traces, calculation of distance distributions and generation of simulated data. The analysis of the RIDME signal was performed using the software package OvertoneAnalysis, which can be obtained free of charge from www.epr.ethz.ch/software. The software package is based on the well-known DeerAnalysis package⁷⁸ with a modified kernel function that consists of a linear combination of the primary dipolar frequency ω_{dd} (P_1) and the high frequency overtones $2\omega_{\text{dd}}$ (P_2) and $3\omega_{\text{dd}}$ (P_3). Data processing with OvertoneAnalysis follows in principal the known procedure for the extraction of distance distributions using the DeerAnalysis software package.⁷⁸ A detailed description can be found in Appendix E.

In contrast to DeerAnalysis, the form factor panel in OvertoneAnalysis provides the additional option to account for 2nd and 3rd harmonic overtone fractions P_2 and P_3 , respectively. The fraction of the fundamental frequency (P_1) is given by $P_1 = 1 - P_2 - P_3$. Yet higher harmonic

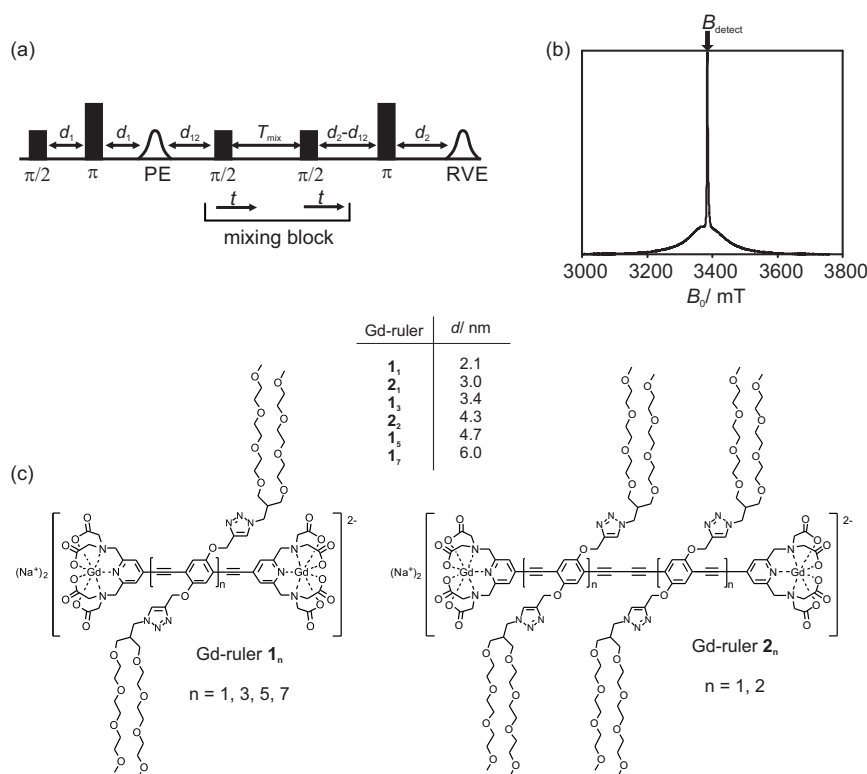


Figure 8.1. (a) RIDME pulse sequence, (b) W-band echo-detected EPR spectrum of the Gd-ruler **1₃** at 10 K. The arrow denotes the spectral position for RIDME experiment, if not stated otherwise. (c) Structural formulae and expected mean distances d of the Gd-rulers used in this study. These Gd-rulers consist of two Gd(III)-PyMTA moieties kept at a well-defined distance by spacers of high stiffness. The expected distances were calculated as described.⁴⁴

overtone were neglected, since their contributions to the RIDME signals appear to be very small and could not be observed in our experiments. Tikhonov regularization is then performed using the modified kernel function given in the Theory section (Equation (8.6)). A comparison of using an ‘overtone-free’ or an ‘overtone-containing’ kernel in Tikhonov regularization is shown in Figure E.4. The extraction of the distance information is then performed as described for DeerAnalysis. Note that harmonic overtones only occur for spin systems with $S > 1/2$ and thus the analysis presented here is only relevant for those cases. Simulated data were created using home-written Matlab scripts available, with slight modifications, from the DeerAnalysis software package. The scripts are added in the OvertoneAnalysis software package. As input, a Gaussian distance distribution with specified mean and width is entered. The form factor is then calculated from the distance distribution according to Ref.²⁶ using the modified kernel function given in Equation (8.6) and selected P_2 and P_3 ratio. In this work, a simulated RIDME signal of 3.4 nm mean distance and a Gaussian distribution with a full width at half maximum (FWHM) of 0.5 nm was used (Figures 8.2-8.5). In some cases, specified in the text, the width of the Gaussian distribution was varied. The dipolar modulation depth in the simulated data was 0.3 for a normalized form factor signal with starting amplitude of 1.0. The dipolar overtone coefficients $P_1 = 0.4$, $P_2 = 0.5$, and $P_3 = 0.1$ were used to simulate this data set. In some cases, specified in the text, an additional background function or white noise were added. Root mean square deviations (rmsd) are shown in the figures for the form factor fits in time and frequency domain, as well as, in some cases, for the comparison of distance distributions. While trends in

the rmsd are general and reflect the changes of overtone coefficients, the particular values are specific for the given examples and can at most be used as indicative values in other applications.

8.4. Results and discussion

Our analysis of the extraction of distance distributions from RIDME data is organized as follows. First, we show the determination of dipolar overtone coefficients for simulated data, and discuss the positions of artefact peaks as well as their appearance due to a mismatch of fitted and actual, simulated dipolar overtone coefficients. Second, we investigate the accuracy of computing form factor traces from simulated RIDME data with artificial noise and stretched exponential background decays. The stability of the distance analysis procedure is tested for these cases. Third, we perform a calibration of the dipolar overtone coefficients for the Gd-rulers $\mathbf{1}_n$ and $\mathbf{2}_n$ and discuss the uncertainties of this calibration. Fourth, we discuss the dependence of the determined coefficients on measurement temperature, mixing time, microwave frequency and detection position within the ED EPR spectrum of the Gd(III)-PyMTA moieties of the rulers. Fifth, we preliminarily analyse the distance dependence of the dipolar overtone coefficients. Note that at short distances (< 3 nm), where this dependence appears rather steep, a larger data set with smaller steps in the Gd(III)-Gd(III) distance is needed to make a detailed analysis. Thus, here we only make semi-quantitative conclusions. Finally, we compare distance distribution calculations based on Gd(III)-Gd(III) RIDME data and on conventional Gd(III)-Gd(III) DEER data measured in Q band with rectangular 12 ns pulses.

8.4.1. Analysis of simulated RIDME data

Optimization of the overtone coefficients. Let us, as a thought experiment, consider an ideal RIDME signal that conforms to the kernel given by Equation (8.6) for the simple case that P_2 and P_3 are constant within the distance distribution, and ask the question whether one can determine P_2 and P_3 coefficients by fitting this signal, provided the distance distribution is unknown. It turns out that this is not the case. Assume that the true distance distribution is $p_{\text{id}}(r)$ and the overtone coefficients are P_2 and P_3 . The same signal can be perfectly fitted with $P_2 = P_3 = 0$ and the apparent distance distribution $p_{\text{app}}(r) = (1 - P_2 - P_3) \cdot p_{\text{id}}(r) + P_2 \cdot p_{\text{id}}(2^{-1/3}r) + P_3 \cdot p_{\text{id}}(3^{-1/3}r)$. Infinitely many other sets (P_2, P_3) will also provide perfect fits with other linear combinations of the original distance distribution and its two contracted copies, with the only condition that the $p_{\text{app}}(r)$ must be non-negative at all distances.

In a more realistic description of RIDME data, one should assume some distribution of the overtone coefficients over the different Gd(III)-Gd(III) pairs in the sample. It can be still appropriate to fit such data using a simplified kernel function with one fixed set of dipolar frequency overtone coefficients. However, in an attempt to fit a RIDME trace measured on such a sample, one would have to approximate dipolar evolution data for each contributing distance by stretching one particular kernel function of a fixed shape. Should there be some deviations from this approximation, e.g. weakly distance dependent kernel coefficients, this might result in an increase of the root-mean square deviation (rmsd) between the fitted trace and the experimental data. In contrast to this, if we set all overtone coefficients to zero, and only keep the main dipolar frequency contribution in the kernel, there would be no restriction on the relative contributions from any two particular dipolar frequencies, and the best rmsd between the fitted

and experimental data would be achieved. This means that with the ‘overtone-containing’ kernel ($P_1, P_2, P_3 \neq 0$) one would never be able to fit a dipolar evolution trace better than with a ‘overtone-free’ kernel ($P_1 = 1, P_2 = P_3 = 0$). However, the opposite might happen for samples with a variation of the dipolar frequency overtone coefficients through the spin pairs.

It follows that the overtone coefficients can only be calibrated when the distance distribution is known or, at least, an accurate distance distribution can be distinguished from a distribution with overtone artefacts. The latter condition is fulfilled if the expected distribution is sufficiently narrow, so that the contracted copies contribute non-zero probability density only at distances where the true distribution is zero. In other words, the contracted copies must be resolved from the true distribution. This suggests the use of a series of model compounds with predictable Gd(III)-Gd(III) mean distance and quite narrow distance distribution.^{24;44;73;117} Thus, our approach was to adjust the RIDME kernel coefficients such that the calculated distance distributions have no or minimal possible artefact peaks at distances other than the expected Gd(III)-Gd(III) distances in the given model compounds. A small deviation between experimental and fitted form factors is used as a secondary criterion, as it excludes those solutions where the contracted copies would add unphysical negative probability density. The deviation between experimental and fitted form factor data is typically more pronounced for solutions that assume larger overtone coefficients P_2 or P_3 than the true ones. This is best visible in frequency domain.

First, we tested this approach on an artificially generated ‘high-spin RIDME form factor trace’ with $\langle r \rangle = 3.4$ nm, a Gaussian shape of distance distribution with $\sigma = 0.21$ nm (FWHM ≈ 0.5 nm) and the dipolar overtone coefficients $P_{1,\text{sim}} = 0.4$, $P_{2,\text{sim}} = 0.5$ and $P_{3,\text{sim}} = 0.1$. Figure 8.2 shows an example for fitting this simulated form factor trace with different combinations of overtone coefficients in the RIDME kernel function. As expected, the use of correct coefficients in the kernel function results in an accurate reproduction of the intrinsic distance distribution, while an ‘overtone-free’ kernel does show pronounced artefact peaks at distances corresponding to $2\omega_{\text{dd}}$ and $3\omega_{\text{dd}}$ (see orange line in Figure 8.2(g)). Thus it can be observed that in case of a mismatch between the kernel function coefficients and the intrinsic coefficients $P_{i,\text{sim}}$, artefact peaks appear at shorter or longer distances, and the relative intensities of these artefact peaks can serve as a measure of the mismatch of the dipolar overtone coefficients. Furthermore, in many cases, the position of these artefact peaks with respect to the correct mean distance $\langle r_{\text{sim}} \rangle$ can reveal the particular type of the mismatch.

Positions of artefact peaks in cases of mismatch of overtone coefficients. The analysis shows that if an overtone coefficient P_2 or P_3 assumed in the kernel function is smaller than the simulated value $P_{2,\text{sim}}$ or $P_{3,\text{sim}}$, (‘under-correction’), then artefact peaks appear at distances smaller than $\langle r_{\text{sim}} \rangle$, namely and for P_2 and P_3 , respectively, in agreement with the compensation by contracted copies of the true distance distribution discussed above. Nevertheless, especially in frequency domain data, a deviation in intensity between fit and simulated pattern can be observed in this ideal case of constant P_i throughout the whole distance distribution. The deviations are best seen at the positions $\omega = \pm 2\omega_{\text{dd}}$, where the edges of the Pake pattern of the main dipolar frequency and the ‘horns’ of the Pake pattern for the double frequency overtone are situated. These deviations are also seen in rmsd. In case of ‘over-correction’, when $P_2 > P_{2,\text{sim}}$ or $P_3 > P_{3,\text{sim}}$, the situation is more complicated. Proper compensation would be possible only by subtracting the contracted copies with appropriate weighting, which is prevented by the applied Tikhonov regularization algorithm that ensures $p(r) \geq 0$ at all r . One can see instead that in the

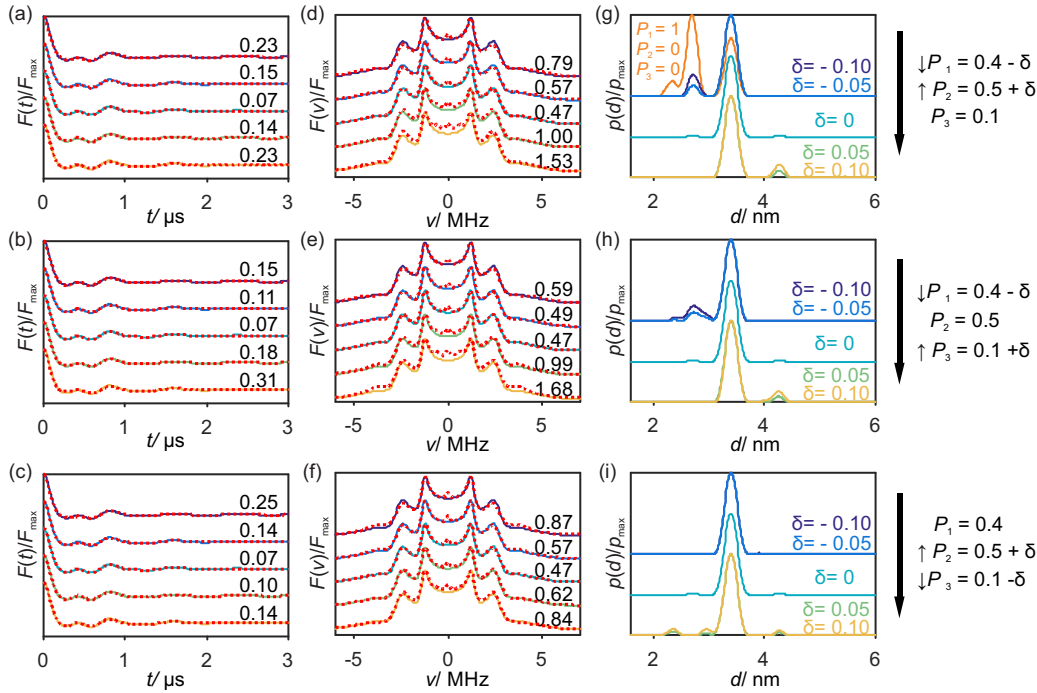


Figure 8.2. Influence of harmonic overtone coefficients P_i on data analysis for simulated RIDME data: 3.4 nm mean distance, Gaussian distribution with a FWHM of 0.5 nm. Analysis results for different coefficients are vertically shifted. The coefficients were set to $P_{1,\text{sim}} = 0.4$, $P_{2,\text{sim}} = 0.5$ and $P_{3,\text{sim}} = 0.1$. The rmsd values (multiplied by a factor of 100) between input trace and the different fits for each set of overtone coefficients are given next to the corresponding trace. (a, b, c) Background corrected form factors in time domain and corresponding fits (red dotted lines); (d, e, f) dipolar spectra and corresponding fits (red dotted lines); (g, h, i) distance distributions. (a, d, g) Variation of coefficients P_1 and P_2 , P_3 is kept constant. The orange line in (g) shows the distance distribution resulting from an overtone-free kernel ($P_1 = 1$, $P_2 = P_3 = 0$). (b, e, h) Variation of coefficients P_1 and P_3 , P_2 is kept constant. (c, f, i) Variation of coefficients P_2 and P_3 , P_1 is kept constant. δ gives the deviation from the simulated fraction of each frequency.

fitted RIDME data artefact peaks appear at distances longer than the real distance. Apparently, adding dipolar evolution time traces for such artefact distances can somewhat compensate the mismatch in the overtone coefficients for the real distance distribution. However, the quality of form factor fit is more reduced in the case of over-correction, as compared to the case of under-correction (see also rmsd values in Figure 8.2). This is best seen in the higher intensity of the P_2 horns in the dipolar spectra. Figure 8.2 shows that at a mismatch of any single coefficient P_2 or P_3 of 0.05 (accordingly, P_1 is also altered by 0.05 as $P_1 + P_2 + P_3 = 1$) the artefact peak intensity in the distance distribution is already about 10% of the actual main peak and thus visible with confidence in the analysis of RIDME data. In the case at hand, a signal to noise ratio (SNR) of 20 or more would be sufficient to discriminate such cases. Note that this SNR value is not universal, and might depend, e.g., on the width of the tested distance distribution. As a very rough estimate the SNR should be at least of the order of magnitude of $1/\delta$.

In contrast, if only the ratio $P_2 : P_3$ is varied, while keeping their sum, and, thus P_1 , constant, changes become less pronounced. Figure 8.3 shows the simultaneous mismatch of all three overtone coefficients. For a mismatch of P_2 and P_3 in the same direction (here both under-corrected, thus, P_1 over-corrected), the artefacts, originating for the mismatch of only P_2 or P_3 , add up. The simultaneous mismatch of both P_2 and P_3 coefficients in opposite directions (here over-correction for P_2 and under-correction for P_3) can partially compensate each other and the relative intensities of the artefact peaks are smaller. Such compensation may cause a

shift of the artefact peaks (see Figure 8.3(f)), thus making them less predictable. This can be qualitatively understood by looking at the frequency-domain representation of the RIDME form factor (Figure 8.2 and 8.3, middle panel). The Pake pattern corresponding to $3\omega_{\text{dd}}$ is the broadest and it forms a ‘background’ contribution under the double-frequency horns at $\pm 2\omega_{\text{dd}}$. Thus, if the double-frequency peaks get reduced in intensity, but simultaneously the triple-frequency contribution increases (or vice versa), the total amplitude at the double dipolar frequency in the RIDME pattern does not change very much (Figure 8.2 and 8.3 for simulated data and Figure 8.7 for real data). From this, we can conclude that the shape of the RIDME kernel function is most sensitive to the correct value of P_1 or equivalently, to the sum $P_2 + P_3$. Our data suggest that this dependence is easier to calibrate, while anti-correlated variations of P_2 and P_3 in a small range around the correct values (keeping P_1 constant) have only a minor impact on the shape of the RIDME form factor and distance distribution. Thus, it seems to be more difficult to calibrate the ratio of the overtone coefficients P_2/P_3 . Yet, thorough inspection of time- and frequency-domain data may allow identification of this ratio up to some reasonable accuracy as small changes in the rmsd can be observed (see Figure 8.2, 8.3 and 8.7). On the other hand, precise calibration of this ratio is less critical for obtaining accurate distance distributions in later application of the kernel to data from other samples.

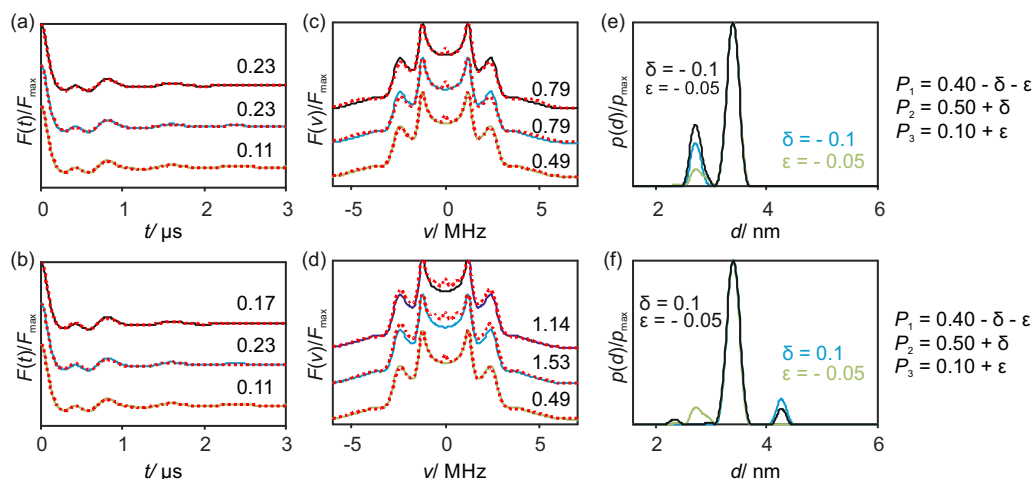


Figure 8.3. Influence of harmonic overtone coefficients P_i on data analysis. Analysis results for different coefficients are vertically shifted. Studied for simulated data: 3.4 nm mean distance, Gaussian distribution with FWHM of 0.5 nm. The coefficients were set to $P_{1,\text{sim}} = 0.40$, $P_{2,\text{sim}} = 0.50$ and $P_{3,\text{sim}} = 0.10$. The rmsd values (multiplied by a factor of 100) between input trace and the different fits for each set of overtone coefficients are given next to the corresponding trace. (a, b) Background corrected form factors in time domain and corresponding fits (red dotted lines), (c, d) dipolar spectra and corresponding fits (red dotted lines), (e, f) distance distributions. (a, c, e) Under-correction of both harmonic overtones P_2 and P_3 ; (b, d, f) Under-correction of P_2 but over-correction of P_3 .

Analysis of RIDME data in presence of an intermolecular background decay.

Next, we evaluated the stability of the distance determination procedure with modified kernel functions in the presence of noise and intermolecular contributions. A detailed study of RIDME background behaviour is beyond the scope of this chapter. At present, we make a phenomenological assumption that, like in the DEER case, the intramolecular and intermolecular contributions are factorizable, and that the background function in RIDME experiments can be modelled by a stretched exponential function: $B(t) = c \cdot \exp(-(\tau/\tau_0)^{d/3})$, with c being a vertical scaling factor, τ_0 being the $1/e$ decay time and $d/3$ being the stretching exponent. This assumed background

model works for all experimental data that we have obtained to date. A detailed description of the RIDME background is given in Chapter 5.

Whereas in DEER, D is the fractional dimension of a homogeneous distribution of spins in other molecules, this is no longer true for RIDME, where an additional contribution to the background decay arises. This contribution is related to the storage of observer spin magnetization during the mixing block in the form of a polarization grating, i.e., in an oscillatory polarization pattern as a function of resonance offset Ω . Periodicity of this grating depends on time d_{12} that has passed between the previous refocusing and the $\pi/2$ storage pulse, as the oscillation is of the form $\cos(d_{12}\Omega)$. During the mixing time T_{mix} , spectral diffusion erases part of the grating by destructive interference. Such erasure is the more efficient the finer the grating is, i.e., the larger the absolute value of d_{12} is. This spectral diffusion decay multiplies with the decay from intermolecular dipole-dipole interactions that is also observed in DEER, which is a disadvantage of the RIDME experiment. Thus, spectral diffusion decay becomes more pronounced at longer mixing times.

Despite the mentioned obstacles, background correction of RIDME data performs similar to the one of DEER data. If the longest intramolecular distances are much shorter than the typical intermolecular distances, then in frequency domain an over- or under-correction of the background function is visible as a sharp hole or peak at zero frequency (Figure 8.4(a)). In case of under-correction (meaning that the stretched exponential is more flat than the ground truth), the sharp peak at zero frequency is incorporated into the distance distribution by a series of weak artefact peaks at long distances. The artefact peak widths are determined by the used regularization parameter of the Tikhonov regularization procedure. In case of an over-correction of the background (meaning that the stretched exponential is steeper than the ground truth), the deep hole at zero frequency cannot be fitted by the kernel function and thus a deviation between the original time trace and the fit appears. Importantly, even in cases of moderately strong over- or under-correction of the intermolecular background, the main distance peak is not shifted and its width remains unaffected. An over-correction of the background slightly reduces the intensity of the peak at the primary dipolar frequency and induces weak artefacts at shorter distances, similar to an under-correction of the P_2 coefficient. Note that background artefact peaks can become significant at low modulation depth or for broad distance distributions. As has been discussed earlier for DEER,^{20;21} the length of the form factor trace determines up to what distances the shape, width, and mean value of the distance distribution can be trusted.

Generally, for all types of dipolar evolution data a reasonable separation of form factor and background contributions from each other can be obtained as long as the intramolecular distance distribution is narrow enough to produce oscillating dipolar evolution data, and the time trace is long enough to observe at least one full oscillation in the time-domain data. For one full oscillation, it is possible to determine the mean distance with less than about 5% error, while the width estimate is useless. If two full oscillations can be observed, the width estimate is reliable.^{20;21} A stretched exponential background function cannot incorporate oscillations and thus leaves such a form factor rather well determined. If the second maximum of the dipolar oscillation cannot be observed due to too broad distance distribution, longer time traces may help, since in such traces the form factor contribution has already decayed to zero for a large part of the time trace and this part can be analysed as a pure background decay function. In critical cases, when no oscillations can be observed in the form factor and the length of the time trace is rather limited, the DEER technique has an advantage in comparison to RIDME, since

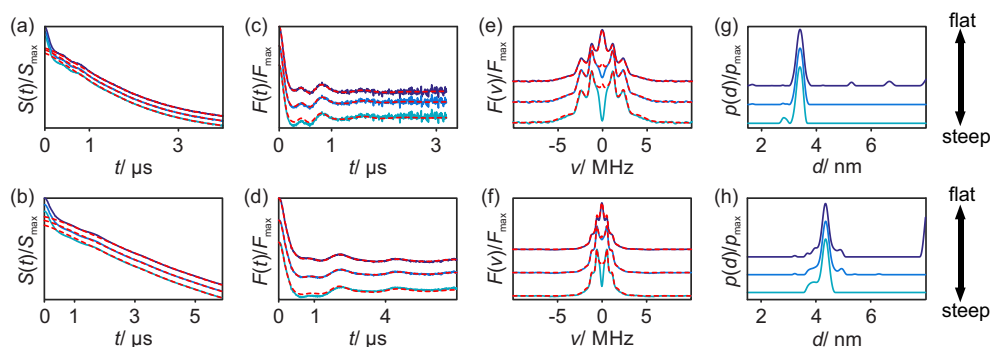


Figure 8.4. Influence of background correction on data analysis. Analysis results with different background decay are vertically shifted. (a, b) Normalized primary data and corresponding background fits (red dotted lines), (c, d) background corrected form factors in time domain and corresponding fits (red dotted lines), (e, f) dipolar spectra and corresponding fits (red dotted lines), (g, h) distance distributions. (a, c, e, g) Simulated data with 3.4 nm mean distance (0.5 nm FWHM), noise level of about 6% and coefficients $P_{1,\text{sim}} = 0.4$, $P_{2,\text{sim}} = 0.5$ and $P_{3,\text{sim}} = 0.1$; (b, d, f, h) Gd-ruler **22** ruler measured in W band and 10 K. The mixing time was set to 8 μs . The raw data were truncated as described in Appendix E. Coefficients used for analysis were set to $P_1 = 0.51$, $P_2 = 0.40$ and $P_3 = 0.09$ based on previous calibration.

the additional spectral diffusion decay makes the background functions in RIDME steeper and more curved than the ones in DEER. For such complicated cases, more practical experience is required to assess the robustness of background correction in RIDME experiments. In those cases where the trace is sufficiently long to see at least one full dipolar oscillation the background correction can be considered as reasonably reliable. The accuracy of the background correction further improves, if a larger number of full oscillations can be detected. Note that for the longest detected distance (compound **17**, Figure E.20) we actually detected two full oscillations with the primary dipolar frequency, and, accordingly, four oscillations of the double-frequency overtone. The extraction of overtone coefficients was only performed using such data.

Since the RIDME background is steeper than the background in the DEER experiment, and since the extraction of the form factor contribution is performed by division of the primary time trace by the background function to deconvolute broadening of the distance distribution, noise towards the end of the form factor is more enhanced in RIDME data than in DEER data. In cases of particularly weak SNR and for traces acquired with long mixing times, which induce a steep spectral-diffusion background decay, the noise enhancement at the end of the RIDME trace can even become very strong and a truncation of the trace might be required as illustrated in Figure E.2 in Appendix E. This is a general property of the RIDME technique common to $S = 1/2$ and $S > 1/2$ species and is unrelated to the distance analysis procedure discussed here.

Influence of noise on RIDME data analysis. To investigate the stability of the Tikhonov regularization-based data analysis using modified kernel functions with respect to noise in dipolar evolution data, such analysis was performed on a series of simulated RIDME time traces with stretched exponential background decay and different levels of artificially constructed white noise (Figure 8.5). One can observe that at all practically relevant noise levels the position of the peak in the distance distribution is quite stable, and its shape starts being distorted only at very high noise levels (at $\text{SNR} \approx 6$). In this respect the performance of the RIDME kernel is again very close to the one of the DEER kernel.¹⁶⁹

RIDME data analysis in case of broad distance distributions. If the distribution of intramolecular metal-metal distances is broad, positions of primary dipolar frequencies and

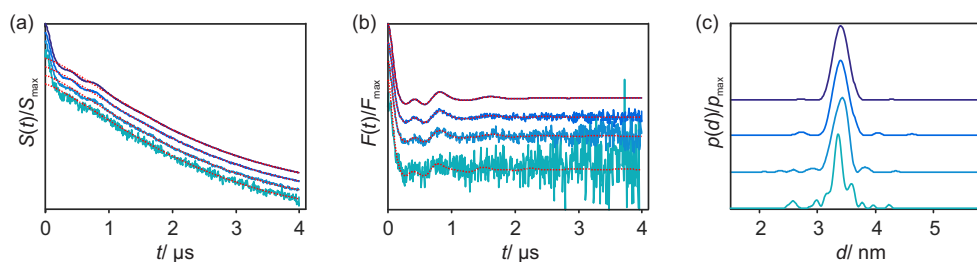


Figure 8.5. Influence of noise on data analysis for simulated data: 3.4 nm mean distance, Gaussian distribution with FWHM of 0.5 nm and added white noise. Traces with different noise level are vertically shifted. The coefficients were set to $P_{1,\text{sim}} = 0.4$, $P_{2,\text{sim}} = 0.5$ and $P_{3,\text{sim}} = 0.1$. Added white noise is increasing from top (dark blue) to bottom (light green). (a) Normalized primary data, (b) background corrected form factors and corresponding fits (red dotted lines), (c) distance distributions. Up to a noise level of about 1/6 with respect to the modulation depth the Tikhonov regularization approach performs well and a low level of artefacts is introduced through noise in primary data.

dipolar frequency overtones may overlap. Analysis of simulated data for such cases reveals that it is not possible to calibrate the dipolar frequency overtone coefficients based on the presence or absence of satellite distance peaks or the quality of the form factor and dipolar spectrum fits. If the metal-metal distance distribution is known accurately from an independent source (e.g. DEER data), then the calibration can still be performed, but to lower precision. This is demonstrated on simulated data in Figure 8.6. For under-correction of the P_2/P_3 coefficients the artefact peaks at shorter distances are not resolved, but the mean distance shifts to shorter distances and the distance distribution becomes asymmetric. Accordingly, the over-correction of the P_2/P_3 coefficients leads to a shift in the mean distance to longer distances and the distance distribution becomes asymmetric as well. If correct coefficients are set in the RIDME kernel function, the actual distance distribution is well reproduced. Some imperfections are noticed in comparison to the original distance distribution possibly due to the enforced constant smoothness of the distance distribution in the whole distance range in the Tikhonov regularization procedure. While the deviation between the form factor or dipolar spectrum fit (see rmsd values in Figure 8.6) barely changes for different sets of overtone coefficients, the deviation from the input distance distribution can be observed. Similar as in the case of narrow distance distributions, the correct ratio of P_1 to the sum of P_2 and P_3 already results in a better recovery of the anticipated distance distribution compared to a mismatch in the P_1 ratio. Looking at the form factor fits in Figure 8.6 it becomes apparent that the overtone coefficients cannot be obtained by minimizing the mean square deviation of the fit from the experimental data. One can thus state that, while the distance calculations should work fine both for narrow and broad distance distributions, the calibration of the RIDME kernel is more accurate on samples with narrow metal-metal distance distributions. The analysis for two distance distributions with intermediate width is shown in Figure E.7-E.9 in Appendix E along with the broad distribution presented here.

8.4.2. Analysis of experimental RIDME data for a series of Gd rulers.

Analysis of RIDME kernel coefficients. Figure 8.4(b-h) shows the background correction for the Gd-ruler **2**₂ with a Gd(III)-Gd(III) mean distance of 4.3 nm. An under- or over-correction of the background function can be clearly seen in the frequency-domain representation of the corresponding form factor trace as a peak or hole at zero frequency. Figure 8.7 illustrates the procedure of the dipolar frequency overtone coefficient calibration on this sample, indicating

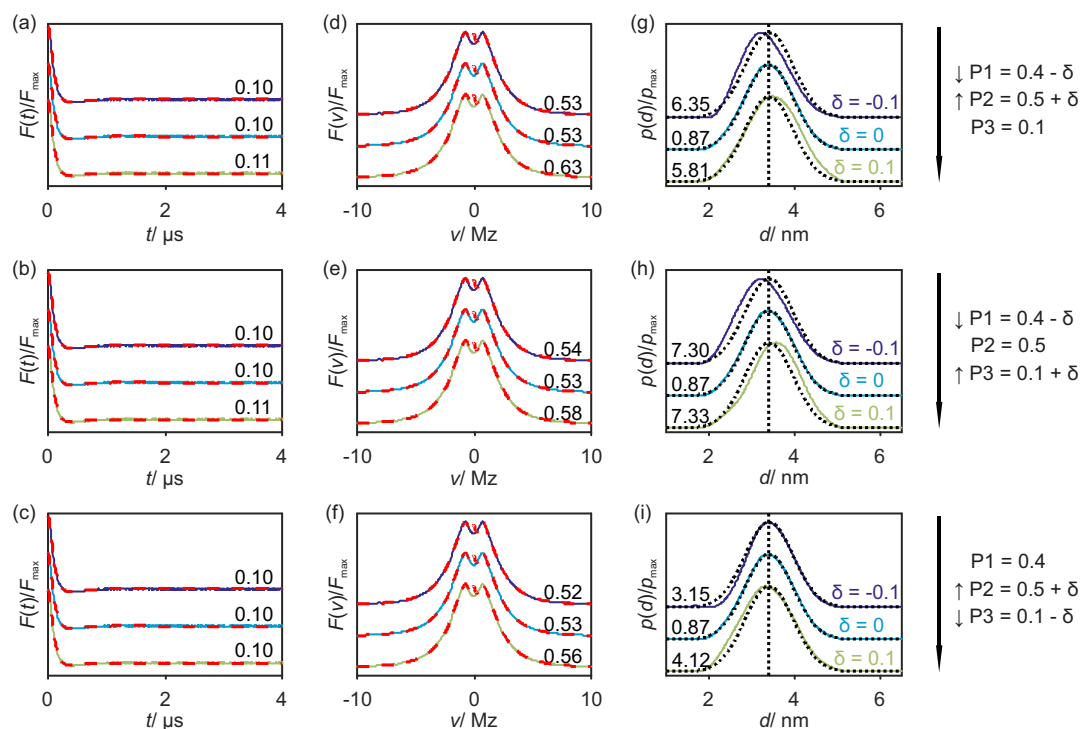


Figure 8.6. Influence of harmonic overtone coefficients P_i on data analysis for simulated data: 3.4 nm mean distance (indicated by dashed, black vertical lines in (g, h, i)), Gaussian distribution with FWHM of 1.3 nm plotted as dashed, black traces on top of the calculated distance distributions in g, h, i). rmsd values (multiplied by a factor of 100) between the data trace and the different fits or the computed and input distance distribution are displayed at the corresponding trace. (a, b, c) Background corrected form factors in time domain and corresponding fits (red dotted lines), (d, e, f) dipolar spectra and corresponding fits (red dotted lines), (g, h, i) distance distributions. The coefficients were set to $P_{1,\text{sim}} = 0.4$, $P_{2,\text{sim}} = 0.5$ and $P_{3,\text{sim}} = 0.1$. (a, d, g) Variation of coefficients P_1 and P_2 , P_3 is kept constant. (b, e, h) Variation of coefficients P_1 and P_3 , P_2 is kept constant. (c, f, i) Variation of coefficients P_2 and P_3 , P_1 is kept constant. The parameter δ gives the deviation from the simulated fraction of each frequency used during Tikhonov regularization.

that a rather clean distance distribution is obtained for the set of coefficients $P_1 = 0.51$; $P_2 = 0.40$; $P_3 = 0.09$. Note that in contrast to the simulated RIDME data we could not manage to remove all small artefact peaks from the distance distribution even by scanning through a wide range of dipolar frequency overtone coefficients. This indicates the presence of additional effects, missing in our approach. The good fits of the form factor and dipolar spectra make it unlikely that the presence of overtones of higher order than three is such a missing effect. Furthermore, orientation selection or level-mixing by the pseudo-secular part of the dipole-dipole interaction are unlikely to influence RIDME results.⁷³ In any case, one can appreciate a good reproduction of the expected narrow distance distribution and a low level of artefact peaks. Further information on the calibration of the RIDME kernel coefficients for this and other Gd-rulers can be found in Appendix E. An example of a L-curve for such a distance analysis is given in Figure E.3(d), showing the corner point for the regularization parameter $\alpha = 1$, which was then consequently used in the distance analysis of all model compounds. It is also worth mentioning that, whenever this was tested, the Tikhonov regularization procedure with RIDME kernel functions resulted in L-curves with well-defined corner points for all model compounds.

The influence of a variation of overtone coefficients using the validation tool in Overtone-Analysis is shown in Figure 8.8. The validation tool allows computing distance distribution

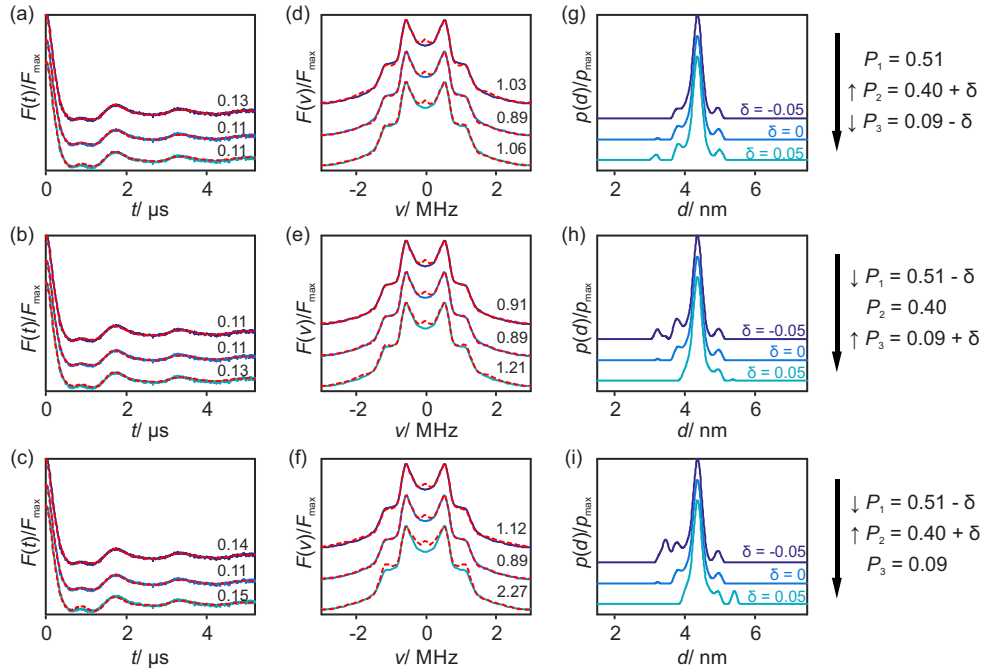


Figure 8.7. Influence of harmonic overtone coefficients P_i on data analysis for the Gd-ruler 2_2 measured in W band and at 10 K. Analysis results for different overtone coefficients are vertically shifted. The mixing time was set to $8 \mu\text{s}$. The raw data were truncated as described in Appendix E resulting into a modulation depth of 12%. rmsd values (multiplied by a factor of 100) between the data trace and the different fits are displayed at the corresponding trace. (a, b, c) background corrected form factors in time domain and corresponding fits (red dotted lines), (d, e, f) dipolar spectra and corresponding fits (red dotted lines), (g, h, i) distance distributions.

and form factor fits for a grid of overtone coefficients similar to the variation of the background starting position in DeerAnalysis. This provides an estimate for the uncertainty of the distance distribution if an estimate for the uncertainty of the overtone coefficients is given. The automatically displayed distance distribution after computation of all trials, the ‘Prune’ as well as the ‘!’ button of the validation tool should not be used in conjunction with overtone coefficient variation, as these features select parameter sets by rmsd of the form factor fit. This rmsd is not a suitable criterion for detecting good overtone coefficient sets as we discussed above. An example of validation is shown in Figure 8.8. Using the validation tool, it is seen that a small variation of 10% around the calibrated values $P_1 = 0.51$, $P_2 = 0.40$, $P_3 = 0.09$ (Figure 8.8(a)) does not induce significant changes to the distance distribution, but may help to identify the origin of artefact peaks and may reveal those artefact peaks, which are independent of the overtone coefficients. Importantly, even for a larger variation of the overtone coefficients the true distance peak is present for each individual fit, while artefact peaks at longer and shorter distances appear and disappear, depending on the particular combination of the three RIDME kernel coefficients (Figure 8.8(b, c)). However, if the deviation between the overtone coefficient used for analysis and the actual overtone coefficient is large, also real peaks can be suppressed or even artificial peaks can occur (Figure 8.8(d)). In other words, it appears from the case presented in Figure 8.8, where the actual RIDME kernel coefficients P_1 and P_2 are large, and P_3 is rather small, that any trial kernel, in which at least one of the large coefficients - P_1 or P_2 has a magnitude of at least 0.1, results in the true distance peak besides the artefact peaks.

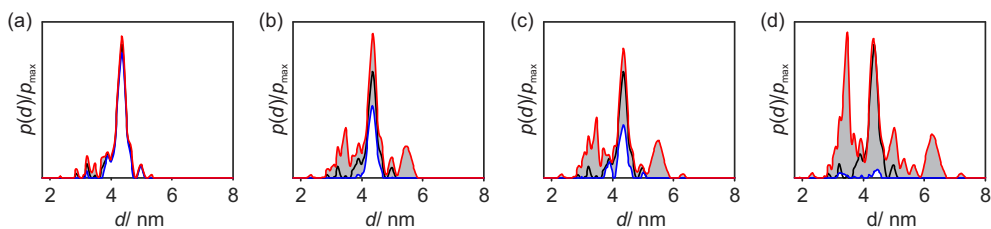


Figure 8.8. Performance of the validation tool for overtone coefficients P_2/P_3 for the Gd-ruler $\mathbf{2}_2$ measured in W Band and 10 K. The mixing time was set to $8 \mu\text{s}$. (a) Distance distributions for overtone coefficients varying 10% around the chosen set $P_1 = 0.51$, $P_2 = 0.40$, $P_3 = 0.09$ (black line). The red line gives the maximum envelope around all calculated distance distributions, while the blue line gives the minimum envelope; (b) distance distribution if P_2 is varied from 0 to 0.6, while P_3 is varied from 0 to 0.3. Colours as in (a), (c) distance distributions if P_2 is varied from 0 to 1, while P_3 is kept constant at 0. Colours as in (a); (d) distance distribution if P_3 is varied from 0 to 1, while P_2 is kept constant at 0. Colours as in (a).

Stability of kernel coefficients with temperature and mixing time. In this work a detailed study of the dependence of the RIDME form factor traces on the measurement temperature and mixing time has been performed for all Gd-rulers. Our principal findings are demonstrated in Figure 8.9 on the example of the Gd-ruler $\mathbf{1}_3$. Further data are presented in Appendix E. Again, the form factor fits are of such a good quality that the presence of overtones higher than $3\omega_{\text{ad}}$ at a significant level can be excluded. Notably, virtually no change in the shape of the RIDME form factor traces is recognized upon variation of the mixing time (Figure 8.9(c)) in these series of measurements. The dependence of temperature is shown in Figure 8.9(d). With increasing temperature, minor changes in the form factors were observed, but distance distributions remained stable up to differences in the shapes and positions of weak artefacts, but without increase of the artefact amplitudes. In accordance with this, the analysis of the entire series of RIDME traces with the same RIDME kernel coefficients $P_1 = 0.51$; $P_2 = 0.40$; $P_3 = 0.09$ resulted in a low level of artefacts in the distance distributions being similar at all temperatures and mixing times. Note that all these measurements were performed at the maximum intensity position of the Gd(III) EPR spectrum and, as we will discuss below, a change of the observer field does have an influence on the overtone coefficients. In all cases, an increasing mixing time as well as increasing temperature leads to a larger modulation depth and an accelerated background decay can be observed.

ESEEM and echo crossing artefacts in RIDME data. All five pulses in the RIDME experiment are applied at the same frequency, and the moving block of two $\pi/2$ pulses produces electron spin echo envelope modulations (ESEEM), which need to be taken into account at X-, Q- and in some cases even at W-band microwave frequencies.^{67;79;179;180} Another important drawback of the RIDME experiment is the generation of multiple electron spin echoes by the five microwave pulses. In particular, three strong echoes cross at the zero-time point of the RIDME trace, i.e. at the point when the first $\pi/2$ pulse of the mixing block overlaps with the primary Hahn echo generated by the first two pulses in the RIDME pulse sequence. The three echoes are the so called refocused virtual echo (RVE), which we use in this work for detection, the refocused stimulated echo (RSE), and the two-pulse Hahn echo (PE_2) resulting from the last $\pi/2$ pulse and the last π pulse in the RIDME sequence.⁶⁷ Especially for long mixing times, the two-pulse echo can be very strong compared to the RVE and clean detection of the RIDME signal, thus, relies on accurate phase cycling. In practice, we rarely managed to perform perfect phase cycling on our spectrometers. The imperfections typically resulted in a small 'bump' close to the zero time in the RIDME form factor trace. In our experimental data the exact position of

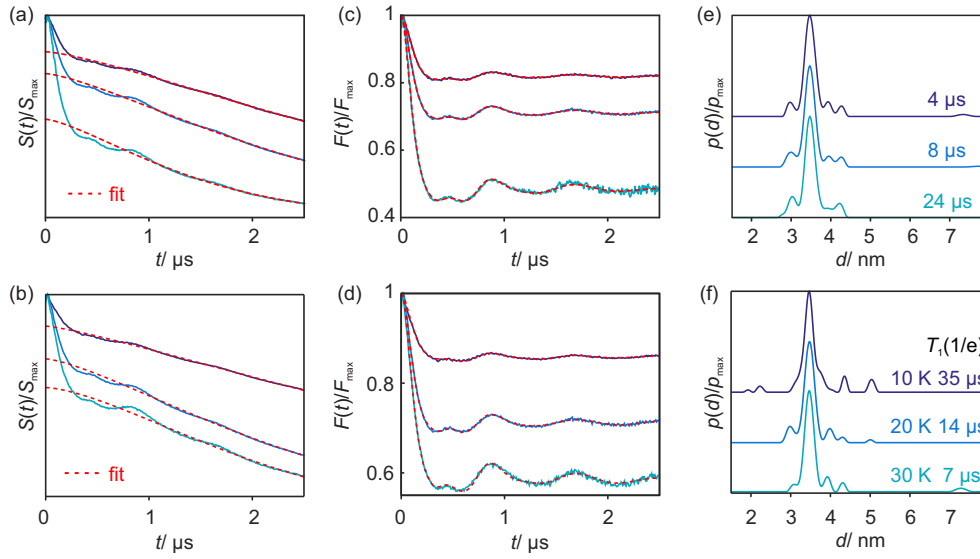


Figure 8.9. Influence of mixing time and temperature on harmonic overtone coefficients P_i for the Gd-ruler $\mathbf{1}_3$ in W band. The coefficients were set to $P_1 = 0.51$, $P_2 = 0.40$ and $P_3 = 0.09$. (a, b) Normalized primary data and corresponding background fits (red dotted lines), (c, d) background corrected form factors in time domain and corresponding fits (red dotted lines), (e, f) distance distributions. (a, c, e) Increasing mixing time from top to bottom measured at 20 K. T_{mix} is in the order of $T_1(1/e)$, ranging from about $T_1(1/e)/3$ to about $2T_1(1/e)$. (b, d, f) Increasing temperature from top to bottom using a mixing time of $8 \mu\text{s}$. The longitudinal relaxation time was estimated from the $1/e$ decay time and is given in the figure for each temperature.

this bump is shifted from zero by approximately the difference in the pulse lengths of the $\pi/2$ and π pulses (here 12 ns). Under the approximation that the entire lengths of the microwave pulses can be disregarded in the computation of the transverse time evolution of spin packets, the actual echo crossing point of the three mentioned echoes with respect to the zero time ($d_{12} = 0$) is at the time $d_{12}^* = \tau_p(\pi) - \tau_p(\pi/2)$, which is equal to the difference of the pulse lengths of the π pulse ($\tau_p(\pi)$) and the $\pi/2$ pulse ($\tau_p(\pi/2)$). This approximate rule is fulfilled up to a π pulse lengths of about 120 ns as demonstrated in Appendix E, Figure E.10. For measurements of long distances, this bump artefact is clearly visible at the beginning of the RIDME traces and can be filtered out, which reduces the apparent modulation depth as shown in Figure 8.10. The procedure is discussed in more detail in Appendix E. For short metal-metal distances, the period of dipolar oscillations becomes comparable to the width of the echo crossing artefact and accurate artefact removal becomes problematic. This might lead to a shift of the apparent zero time, calculated as the position of maximum intensity in the RIDME trace, and, accordingly, to a less accurate distance determination. This problem should be resolved on new generation EPR spectrometers using a single microwave pulse channel and an arbitrary waveform generator (AWG) to perform phase cycling.^{60–62} For long metal-metal distances, the choice of zero time does not have a significant influence on the overtone coefficients or on the distance distribution (compare Figure 8.10(c, d)). In the presented data series (Figure 8.14) the echo crossing artefact was filtered for the Gd-ruler $\mathbf{2}_2$ (10 K, $8 \mu\text{s}$ mixing time), $\mathbf{1}_5$ (10 K, $24 \mu\text{s}$ mixing time) and $\mathbf{1}_7$ (10 K, $16 \mu\text{s}$ mixing time). The impact of the filtering on the computed distance distribution is given in the Figure 8.10 (for the Gd-ruler $\mathbf{2}_2$) and for all other samples in Figure E.11. For the Gd-rulers $\mathbf{1}_1$, $\mathbf{1}_3$, and $\mathbf{2}_1$ and the mixture of Gd-rulers $\mathbf{1}_3$ and $\mathbf{1}_5$ no such filtering was performed.

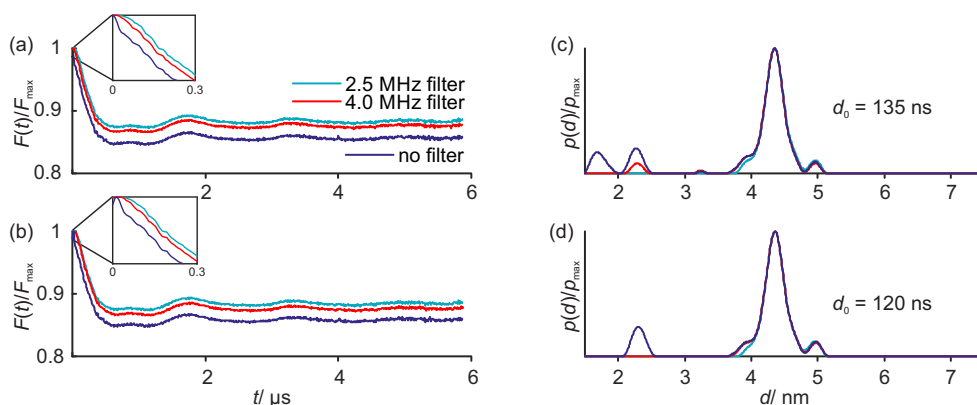


Figure 8.10. Influence of filtering the bump artefact in the beginning of RIDME traces and choice of zero time d_0 . Data for the Gd-ruler $\mathbf{2}_2$, measured at 10 K using a mixing time of $8 \mu\text{s}$. The overtone coefficients were set to $P_1 = 0.51$, $P_2 = 0.40$ and $P_3 = 0.09$. (a, b) Form factors of raw data (violet lines), data filtered for high-frequency components above noise level with 4 MHz (red lines) and 2.5 MHz (cyan lines). (a, c) $d_0 = 135 \text{ ns}$ and (b, d) $d_0 = 120 \text{ ns}$.

Comparison of the Q-band and W-band data. Figure 8.11 shows the very close similarity of RIDME time traces measured in Q and W band on the example of the Gd-ruler $\mathbf{1}_3$ (mean distance 3.4 nm). In this case, the Q-band RIDME measurement was performed with deuterium ESEEM averaging according to the previously published protocol.⁷⁹ This very close similarity of the two dipolar evolution traces is important, since it allows performing the RIDME kernel coefficients calibration at one microwave frequency and later use the calibration data at other frequencies. Of course, the applicability of this conclusion to microwave bands other than W and Q band is yet to be proven.

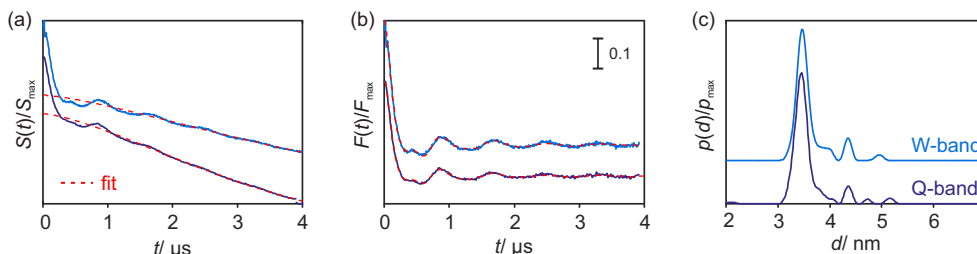


Figure 8.11. RIDME experiments for the Gd-ruler $\mathbf{1}_3$ at 20 K. Comparison of RIDME data acquired in W band (blue line) and Q band (purple line). The mixing time was set to $16 \mu\text{s}$. Overtone correction was performed with $P_1 = 0.51$, $P_2 = 0.40$ and $P_3 = 0.09$. (a) Normalized primary data and corresponding background fits (red dotted lines), (b) background corrected form factors in time domain and corresponding fits (red dotted lines). The time traces reveal different background decay behaviour, while the form factors remain fairly constant, (c) distance distributions.

RIDME kernel coefficients at short spin-spin distances. The only significant change of the optimal RIDME kernel coefficients was found for the Gd-ruler $\mathbf{1}_1$ with a Gd(III)-Gd(III) distance of 2.1 nm. The RIDME data for this Gd-ruler are shown in Figure 8.12. At a given measurement temperature and mixing time (10 K and $24 \mu\text{s}$) the dipolar modulation depth as well as the shape of the RIDME form factor signal depend on the detection position within the Gd(III) EPR spectrum. Furthermore, at the maximum of the Gd(III) spectrum the relative contributions of the double and triple dipolar frequency overtones to the RIDME signal are substantially weaker than for the Gd-rulers with larger Gd(III)-Gd(III) distances. Essentially, for

this sample the distance analysis of the RIDME trace detected at the spectral maximum can be performed with an overtone-free kernel ($P_2 = P_3 = 0$) with only a moderate level of artefacts (see Appendix E, Figure E.13). If the detection position is shifted away from the maximum of the EPR spectrum, the RIDME modulation depth increases and a clear contribution from the dipolar frequency overtones is recognized. Note also that for this Gd-ruler, for detection at the central transition, the RIDME modulation depth is smaller than for the other Gd-rulers at the same measurement conditions (compare Figures E.17-E.22).

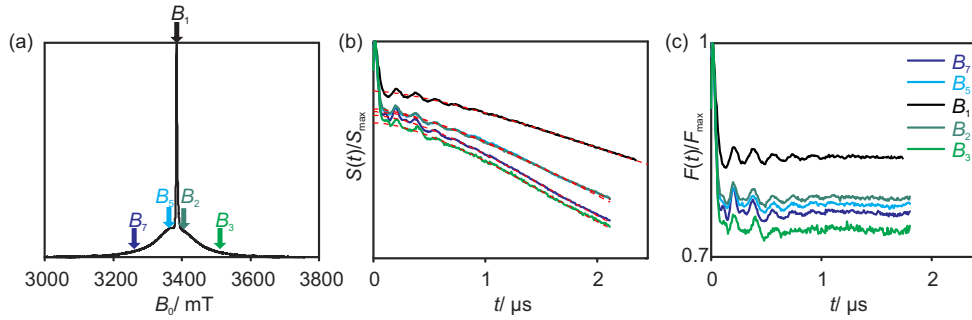


Figure 8.12. W-band RIDME experiments at different detection positions within the Gd(III) spectrum for the Gd-ruler 1_1 at 10 K. The mixing time was set to $24 \mu\text{s}$. (a) EDEPR spectra with the different detection positions denoted by arrows, (b) RIDME raw data obtained at different detection positions and corresponding background fits (red dotted lines), (c) Background corrected form factors.

As discussed in the Theoretical Background section, we propose that the magnetic dipole-dipole interaction between Gd(III) species is an important channel for the decay of non-equilibrium magnetization during the mixing block. This hypothesis allows to consistently interpret a number of experimental facts regarding the Gd(III)-Gd(III) RIDME measurements. If we ignore this decay channel, then, after numerous longitudinal flips of the B-spins in the A-B spin pairs, the distribution of the dipolar frequency overtones detected with the A spins should conform to a ‘steady state’. In such a case every possible initial and final spin state of the B-spin would be equally probable, and the relative weights of the dipolar frequencies, including the zero frequency, can be calculated to be $P(0) = 8/64$; $P(\omega_{\text{dd}}) = 14/64$; $P(2\omega_{\text{dd}}) = 12/64$; $P(3\omega_{\text{dd}}) = 10/64$; $P(4\omega_{\text{dd}}) = 8/64$; $P(5\omega_{\text{dd}}) = 6/64$; $6P(\omega_{\text{dd}}) = 4/64$; $P(7\omega_{\text{dd}}) = 2/64$ by counting state pairs with the required $|\Delta m_B|$. This restricts the total modulation depth for the first three non-zero frequencies (ω_{dd} , $2\omega_{\text{dd}}$ and $3\omega_{\text{dd}}$) to a value of $36/64$, which is exceeded in our experiments (see Appendix E Figures, E.17-E.22). Furthermore, this steady state assumption predicts a ratio of P_3/P_2 , which is higher than our experimental calibration results. It also predicts an ultimate weight of $20/64$ or 31% for yet higher dipolar frequency overtones ($4\omega_{\text{dd}}$ to $7\omega_{\text{dd}}$). However, in our RIDME experiments we do not register any detectable intensity in the frequency domain representation at these frequencies. These inconsistencies with the steady-state statistics can be qualitatively explained if we assume a certain probability for the signal of the observer A spin to decay upon every flip of the B spin together with low or zero transition probabilities for $|\Delta m_B| > 3$ in a single longitudinal flip. For a substantial probability of A spin memory decay in a single B spin flip, the relative contribution of the main dipolar frequency and lower overtones would be enhanced, while the contribution of the higher overtones would be suppressed. This would be also in line with the stronger suppression of the overtone frequencies at short Gd(III)-Gd(III) distances where the magnetic dipole-dipole interaction is stronger and, accordingly, all related

transition probabilities are higher. Likewise, the enhancement of the dipolar frequency overtones outside of the maximum of the Gd(III) EPR spectrum is in line with this hypothesis. The density of Gd(III) EPR transition frequencies at these field positions is lower than at the maximum of the Gd(III) EPR spectrum. Thus, at these field positions the probability would be lower to have an approximate match between the difference of the A spin and B spin transition frequencies and the dipole-dipole interaction. Therefore, the probability of B-spin induced relaxation of A spins is lower at these field positions, and this enhances the contributions of the overtone frequencies to the RIDME trace. Note that for longer Gd(III)-Gd(III) distances field dependence of the overtone coefficients is also observed. Here, the form factors for different detection positions reveal small differences and the modulation depth is slightly increased. Overtone correction with the same coefficients $P_1 = 0.51$, $P_2 = 0.40$ and $P_3 = 0.09$ results in the same main distance, but a shift of the artefact peaks to shorter distances is observed for detection positions away from the field maximum. This indicates an under-correction of the overtone coefficients and thus the increase of $P_2 + P_3$ compared to P_1 (see Figure 8.13 for the Gd-ruler $\mathbf{1}_3$ and Figure E.21(d, e) for results on the Gd-ruler $\mathbf{1}_5$). In agreement with our hypothesis, it is weaker than for the 2.1 nm distance. Note again that here orientation selection effects can be excluded, as for Gd(III) chelate complexes, and, in particular, for Gd(III)-PyMTA, the ZFS parameters are broadly distributed (for Gd(III)-PyMTA the ZFS parameter D has a Gaussian distribution centred approximately at $\langle D \rangle = 1060$ MHz with a width of about $\langle D \rangle/2$).¹³²

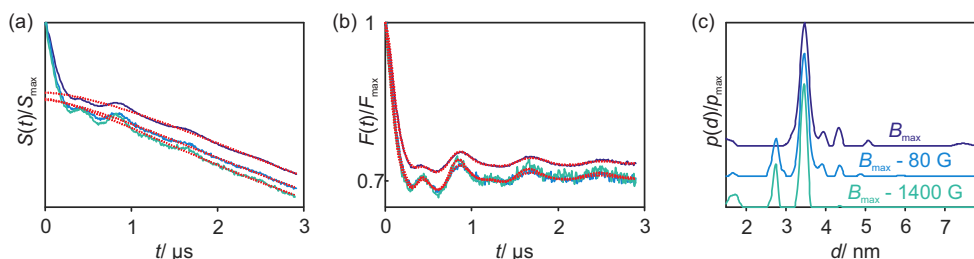


Figure 8.13. RIDME data of the Gd-ruler $\mathbf{1}_3$ in W band and at 10 K for different detection positions: Maximum of Gd(III) spectrum (purple line), 80 G down field from maximum (blue line), 1400 G down field from maximum (cyan line). The mixing time was set to 24 μs . (a) Normalized primary data and corresponding background fits (red dotted lines), (b) background corrected form factors in time domain and corresponding fits (red dotted lines), (c) distance distributions using $P_1 = 0.51$, $P_2 = 0.40$ and $P_3 = 0.09$.

The B-spin induced relaxation channel for non-equilibrium longitudinal magnetization of A spins might influence two further important features of RIDME data. First, as we systematically demonstrate in this work, and as it was noted already in our first report,⁷³ the RIDME kernel coefficients are nearly independent on the mixing time. To explain this property, we have earlier suggested a parallel kinetics model that assumes non-zero rates for B spin flips with a change $\Delta m_B = 2$ or 3 in a single event.⁷³ Possibly, inclusion of the B-spin driven relaxation into the kinetic model for the dipolar modulation build-up in the RIDME experiments would help to explain that the overtone coefficients remain constant over such a broad range of mixing times. Of course, this and the suppression of higher overtones of the dipolar frequency in such a modified kinetic scheme need to be tested by computations. We plan to study a series of model compounds with different Gd(III)-Gd(III) distances below 3 nm, in order to obtain sufficient experimental data for a calibration of the RIDME kernel coefficients at short spin-spin distances. We intend to perform kinetic modelling of the dipolar modulation build-up in RIDME experi-

ments and compare the results of these calculations with such an extended set of experimental data.

Numerical stability of regularization with the overtone kernel. Tikhonov regularization is used in the conversion of dipolar evolution data to distance distributions since the problem is ill-posed. Even in the absence of overtones, the kernel matrix has a large condition number, i.e., a large ratio of the largest to the smallest singular value. Since the overtones correspond to other rows of the kernel matrix, the condition number could potentially increase for a kernel containing overtone contributions. First we note that the kernel is not expected to become singular, i.e. to introduce strict linear dependence of kernel rows. A large increase in the condition number would, however, lead to larger optimal regularization parameters and thus to stronger artificial broadening of distance distributions. We tested for this effect by Monte Carlo variation of P_2 and P_3 and computation of the condition number of the overtone-containing kernels. The logarithm of the condition number was found to decrease by up to 2% and to increase by up to 10%. The largest condition numbers that we encountered are still in a regime where regularization remains stable.

Comparison of Gd(III)-Gd(III) RIDME and Gd(III)-Gd(III) DEER data. The RIDME-based distance distributions computed for a series of Gd-rulers with expected mean distances larger than 3 nm (up to 6 nm) are shown in Figure 8.14. Within this distance range we found that the use of one set of RIDME kernel coefficients $\{P_1 = 0.51; P_2 = 0.40; P_3 = 0.09\}$ always results in distance distributions with relatively weak artefact peaks for all temperatures and mixing times. For none of the rulers, significant contributions by overtones higher than $3\omega_{\text{dd}}$ are indicated in the form factor fits. Additionally, an experiment was performed on a 1:1 mixture of the Gd-rulers $\mathbf{1}_3$ and $\mathbf{1}_5$. It demonstrates the ability of the overtone data analysis procedure to treat bimodal distance distributions. Note that a thorough inspection of the deviations between fits and primary data, as well as the position of artefacts in the distance distribution on a larger set of data (see Appendix E, Figures E.17-E.20), indicates a slight trend towards lower P_1 values and thus a larger sum $P_2 + P_3$ for longer distances. This is in line with our above considerations on the dipolar frequency build-up kinetics.

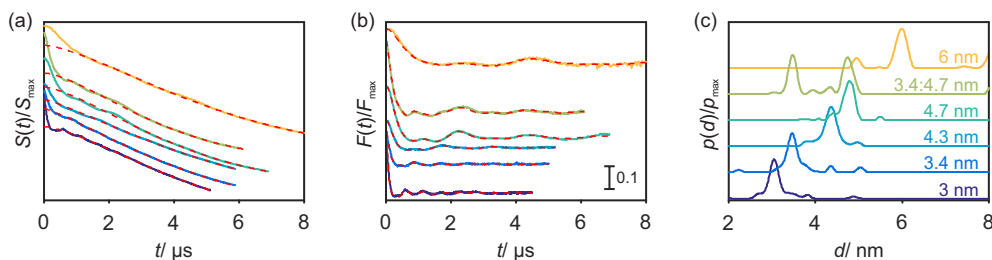


Figure 8.14. Analysis of W-band RIDME data at 10 K performed on various Gd-rules. From top to bottom: Gd-ruler $\mathbf{1}_7$ (6 nm) – 16 μs mixing time, truncated primary data; 1:1 mixture of Gd-rulers $\mathbf{1}_3$ and $\mathbf{1}_5$ (3.4 nm and 4.7 nm) – 24 μs mixing time, truncated primary data; Gd-ruler $\mathbf{1}_5$ (4.7 nm) – 24 μs mixing time, truncated primary data; Gd-ruler $\mathbf{2}_2$ (4.3 nm) – 8 μs mixing time, truncated primary data; Gd-ruler $\mathbf{1}_3$ (3.4 nm) – 8 μs mixing time and Gd-ruler $\mathbf{2}_1$ (3.0 nm) – 24 μs mixing time. (a) Normalized primary data and corresponding background fits (red dashed lines), (b) background corrected form factors in time domain and corresponding fits (red dashed lines), (c) distance distributions.

In Figure 8.15 we compare the results of RIDME-based distance determination with the ones from DEER data. To this end, we performed Q-band Gd(III)-Gd(III) DEER measurements on selected samples using the most conventional detection scheme with the pump pulse on the

maximum of the Gd(III) spectrum and the observer pulse in the wings. All pulse lengths were set to 12 ns and the offset between pump and detection frequency was 150 MHz. Note that, as compared to the previous report⁴⁴ on artificial broadening of DEER-based Gd(III)-Gd(III) distance distributions, we conducted our DEER measurements at lower microwave frequency at which the central peak in the Gd(III) EPR spectrum is broadened.^{26;28} Furthermore, we used shorter microwave pulses with broader excitation profiles, as compared to the cited work. Both modifications should have reduced the effect of level crossing artefacts on Gd(III)-Gd(III) distance determination. However, even in this case we observe notable broadening and stronger artefact peaks in Gd(III)-Gd(III) DEER measurements as compared to the corresponding RIDME data (Figure 8.15). In the studied distance range, the comparison of the shape of DEER- and RIDME-based distance distributions suggests better performance of the Gd(III)-Gd(III) RIDME technique for the Gd-rulers used in this study and therefore for the Gd-PyMTA as the spin label. However, the faster background decay in RIDME experiments reduces the maximum detectable time range, and thus for longer distances, the benefits of RIDME-based distance measurements diminish. It is obvious from Figure 8.15 that for detecting Gd(III)-Gd(III) distances longer than 6 nm one would need to reduce RIDME mixing time T_{mix} in order to obtain a less steep background decay. This would result in lower dipolar modulation depths of such RIDME traces. It is difficult to give an accurate estimate of the longest detectable distance in the Gd(III)-Gd(III) RIDME experiment, but we suspect the distance would be comparable to or shorter than the corresponding distance limit using the Gd(III)-Gd(III) DEER technique.

It is an important observation that RIDME-based Gd(III)-Gd(III) distance distributions are narrower than the ones obtained through Gd(III)-Gd(III) DEER experiments (see Figure 8.15) and are thus better in line with expectations based on the flexibility of the used spacers. This is rationalized by taking into account significant changes in the secular part of dipolar interaction for the cases of level crossing in the Gd(III)-Gd(III) two-spin system. In the conventional DEER setup these effects are strongly affecting the dipolar evolution signal, and strong artificial broadening of the distance distribution peaks is observed, especially for distances below 3.5 nm.⁴⁴ Already in our first report on Gd(III)-Gd(III) RIDME we approximated the Gd(III)-Gd(III) distance distribution by a Gaussian function with a width smaller than the width of the peak in the data obtained through DEER.⁷³ The same effect was later observed and discussed for Gd-DOTA as the spin label.¹¹³ As explained in the theoretical background section, the small frequency difference between the observer and pump excitation bands in DEER leads to a larger fraction of spin pairs with dipolar frequencies that are influenced by level mixing, whereas this fraction is small in the RIDME case, where the typical frequency differences are of the order of the ZFS parameter D . It might be speculated that some artefact peaks in the distance distributions computed here from RIDME data are still due to remaining level crossing distortions, and not due to the mismatch of the RIDME kernel coefficients. Such an explanation would be in line with the fact that some of the artefact peaks cannot be removed by further varying the overtone coefficients. This point might be better understood after molecular rulers with other types of Gd(III) chelate complexes, with significantly different strengths of ZFS, are studied.

8.5. Conclusions

We have demonstrated that the distance analysis based on overtone-adapted kernel functions in Tikhonov regularization is sufficiently accurate and robust to be broadly applied for the processing

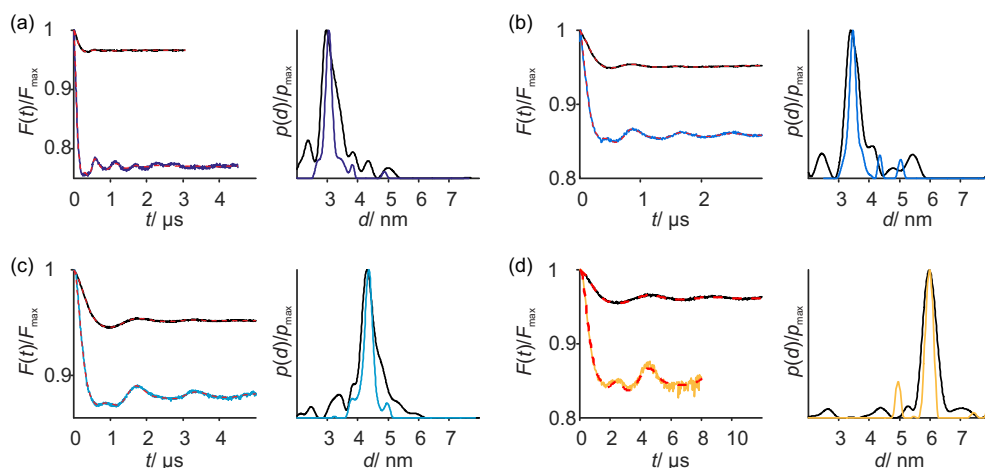


Figure 8.15. Comparison between conventional DEER (black lines) and RIDME (coloured lines, colour coding of Figure 8.14 maintained) measurements at 10 K. Simulated form factors are shown in red, dashed lines. RIDME distance distributions were calculated with $P_1 = 0.51$, $P_2 = 0.40$ and $P_3 = 0.09$. (a) Gd-ruler $\mathbf{2}_1$ (3.0 nm) – 24 μs mixing time, (b) Gd-ruler $\mathbf{1}_3$ (3.4 nm) – 8 μs mixing time, (c) Gd-ruler $\mathbf{2}_2$ (4.3 nm) – 8 μs mixing time and (d) Gd-ruler $\mathbf{1}_7$ (6.0 nm) – 16 μs mixing time, truncated primary data used.

of RIDME data on high-spin paramagnetic centres, given that the overtone coefficients can be calibrated, as it is done here on an example of Gd(III)-Gd(III) rulers. We propose to use the set of the dipolar frequency overtone coefficients $P_1 = 0.51$; $P_2 = 0.40$; $P_3 = 0.09$ with Gd(III)-PyMTA for distances above 3 nm. At distances shorter than 3 nm the RIDME kernel coefficients start to be strongly dependent on the spin-spin distance and an additional calibration is required to obtain accurate distance distributions in this range. Note that the general analysis presented here for Gd(III), which does not rely on any particular values of the RIDME kernel coefficients, should be valid for all types of high-spin paramagnetic centres with half-filled d or f shells and moderate zero-field splittings, such as, most notably, Mn(II) complexes.^{93;178} For high-spin centres with strong ZFS the basic scheme of constructing the RIDME kernel would stay unchanged, but the angular dependencies in the dipolar frequency patterns need to be reconsidered.

We showed in this work that the most reliable way of calibrating the RIDME kernel coefficients is to use model compounds with narrow spin-spin distance distributions and to find the coefficients by relying on the intensities of the artefact distance peaks and the quality of form factor fits in time- and frequency-domain. It is encouraging that in our Gd(III)-Gd(III) and Mn(II)-Mn(II) RIDME experiments⁹³ with Gd- and Mn-rulers, respectively, the RIDME kernel coefficients were found to be independent on mixing time, only weakly dependent on temperature and on the spin-spin distance within a metal-metal distance range of 3-6 nm. The use of RIDME spectroscopy for distance determination with other types of metal complexes, even if only the type of ligand is changed, may require a similar RIDME kernel calibration, which in turn requires corresponding model compounds with narrow distance distributions. While this is certainly a drawback of the technique, such calibration is straightforward if the required rulers can be prepared. The experiments in this work were performed on samples in frozen water/glycerol mixtures that are very similar to the buffer/glycerol mixtures typically used in the pulse EPR studies of soluble biomacromolecules. Although we do not expect changes in the overtone coefficients upon use of the Gd(III)-PyMTA attached to biomacromolecules, robustness of these coefficients in such scenarios needs to be tested prior to application.

Accurate distance analysis has been previously performed with Mn(II)-Mn(II) RIDME data obtained with Mn(II)-PyMTA as the spin label and using a similar set of overtone coefficients of $P_1 = 0.41$; $P_2 = 0.50$; $P_3 = 0.09$.⁹³ For Mn(II)-DOTA complexes, a similar set of coefficients $P_1 = 0.5$; $P_2 = 0.5$; $P_3 = 0.0$ or $P_1 = 0.425$; $P_2 = 0.425$; $P_3 = 0.15$ was found to work well depending on microwave frequency and mixing time.¹⁷⁸ The particular values for the dipolar frequency overtone coefficients determined in this work are expected to be applicable for RIDME experiments in Q and W band with the Gd(III)-PyMTA complex as the spin label. It is possible that the same coefficients are valid at other frequencies. However, this proposal needs to be confirmed experimentally.

Thus, we observed that RIDME data, measured in great detail for Gd(III)-PyMTA complexes, reveal encouraging persistence of kernel overtone coefficients with respect to the change of several key conditions. One can list a few considerations which bring hope that this might be a rather general property. First, Gd(III)-PyMTA and Mn(II)-PyMTA RIDME data can be analysed with similar sets of overtone coefficients. Second, both Gd(III) and Mn(II) chelate complexes are characterized by broad distributions of ZFS coefficients. This means that the obtained coefficients are not specific for a particular ZFS strength and symmetry, but can describe broad ensembles. Specifically for Gd(III), we can further note that the longitudinal relaxation, which is the origin of the dipolar modulation build-up in the RIDME experiment, is very similar for many different Gd(III) chelate complexes.¹⁰⁷ The mechanism of differential relaxation, which we proposed to explain the absence of the fourth and higher overtones in the Gd(III)-Gd(III) RIDME data, is also general and does not depend on any specific properties of Gd(III)-PyMTA. However, the distance range, where the overtone coefficients are distance dependent, might vary with the strength of ZFS.

The currently used procedure of distance distribution calculations only allows considering dipolar frequency overtone coefficients in the kernel functions that do not depend on distance. Once the distance dependencies of the overtone coefficients are determined, the incorporation of these data into the distance distribution calculation procedure would be rather straightforward, and would simply require a slight modification of kernel construction. Variation of the condition number of the kernel would need to be tested again. The mathematical procedure to determine distance distributions from overtone-containing dipolar evolution data is implemented in the MATLAB based program OvertoneAnalysis. The program is a modification of the well-known open-source DeerAnalysis software for the processing of DEER data.^{75;76;174} OvertoneAnalysis can be downloaded free of charge from the web page of the EPR group at ETH Zurich (<http://www.epr.ethz.ch/software.html>).

Note also that in dipolar spectroscopy measurements on high-spin paramagnetic centres using broad-band chirp pulses, dipolar frequency overtones can be excited with certain probability.¹¹⁵ Thus, the proposed distance analysis approach would be applicable to those data as well. However, it is not yet clear how the kernel coefficients would depend on the excitation bandwidth of the UWB pulses.

To summarize, the presented analysis of RIDME data acquired for high-spin paramagnetic centres is efficient and may bring RIDME spectroscopy with high-spin labels closer to becoming a routine distance determination technique in bio-EPR applications.

Towards high-spin RIDME in structural biology

The previous chapter introduced an accurate and robust analysis routine for the processing of high-spin RIDME data, given that the relative contributions of the different harmonic overtone frequencies are known. This chapter addresses important steps towards routine applications of high-spin RIDME in structural biology, such as the stability of the harmonic overtone contributions for Mn(II) or Gd(III) complexes as paramagnetic spin probes. To that end, calibration of the dipolar overtone coefficients for the RIDME kernel is performed for ruler compounds with Mn-PyMTA as paramagnetic spin tag. The stability of overtone coefficients is investigated for different molecular rulers with Mn(II) or Gd(III) and different chelator moieties, based on PyMTA, PymiMTA and DOTA. Such RIDME measurements confirmed a fairly high stability of dipolar frequency overtone coefficients for different mixing times and measurement temperatures, and for the metal-metal distances above ~ 3 nm. In the distance range of about 3 to 6 nm and probably also longer distances, the set of $P_1 = 0.5$, $P_2 = 0.4$, $P_3 = 0.1$ seems to be applicable in data analysis routines for Gd-PyMTA, Gd-PymiMTA and Gd-DOTA spin tags, detected at the central transitions. Some deviations are observed for short spin-spin distances and other detection positions in the EPR spectrum. For Mn-PyMTA, Mn-PymiMTA and Mn-DOTA, at least for distances $a \geq 3.4 \dots 3.7$ nm, the set $P_1 = 0.4$, $P_2 = 0.5$, $P_3 = 0.1$ appears to be suitable for detection on the 3rd line of the hyperfine sextet or at higher fields.

RIDME experiments performed on Gd-labelled recombinant proteins reproduce distance distributions obtained by earlier DEER measurements if harmonic overtone frequencies are included in data analysis. The measurements for three different protein mutants labelled with Gd-DOTA indicate fairly high stability of the dipolar evolution data obtained for different mixing times and measurement temperatures in spin-labelled proteins.

Signal enhancements up to 150% in Gd(III) and 25% in Mn(II) can be achieved using linear frequency-swept (chirp) pulses for pre-polarization of the central transition of these high-spin centres. The optimal RIDME measurement conditions (in terms of signal-to-noise ratio, detectable distance range and modulation depth) are found to be different for Mn(II) or Gd(III) metal ions and dependent on the distance of interest.

Most parts of this chapter are prepared for publication. Section 9.5 is reproduced as part of Ref.⁹³ with permission from the PCCP Owner Societies and edited for consistency: 'Katharina Keller, Michal Zalibera, Mian Qi, Vanessa Koch, Julia Wegner, Henrik Hintz, Adelheid Godt, Gunnar Jeschke, Anton Savitsky, Maxim Yulikov, EPR characterization of Mn (II) complexes for distance determination with pulsed dipolar spectroscopy, Phys. Chem. Chem. Phys., 218 (2016) 25120-25135'.

The synthesis of the molecular rulers was performed in the group of A. Godt (Bielefeld University) by M. Qi, Xuemei Yao, H. Hintz and M. Hülsman. C. Gmeiner prepared the protein mutants, performed MMM simulations and DEER measurements for the protein samples. Other data presented here were measured by K. Keller. References to relaxation measurements from Ref.⁹³ performed by M. Zalibera are indicated. F. Breitgoff and K. Keller implemented the AWG setup in W band with support from R. Tschaggelar. Data analysis was performed by K. Keller.

9.1. Introduction

Throughout this thesis, we have presented the power of EPR to access distance distributions on the nanometre scale.^{20–22;41} Cu(II),^{29–31} Mn(II)^{268;282} and Gd(III)^{24;28} centres have been studied as promising alternatives to the commonly utilized nitroxide-based spin labels in site-directed spin labelling approaches.^{16–18;23} Such metal centres also attract attention by their natural presence at many active sites of bio-macromolecules^{32–36;239;241;267;283} or their suitability for paramagnetic metal-ion substitution as presented in the preceding chapter for Mg(II) by Mn(II) or Gd(III) for Ca(II) as was demonstrated in the context of paramagnetic NMR spectroscopy.^{276;277} Even though, spin labelling and distance measurements using nitroxides are currently more reliable¹⁹² and well described,^{20;21} orthogonal spin labels have been proven valuable in spectroscopic selection schemes of individual distances in multi-spin systems.^{26–28} Pre-polarization schemes based on population transfer in high-spin centres have been shown to increase the sensitivity of pulsed EPR spectroscopy.^{117;284} Efficient population transfer became possible by the development of ultra-wide band pulses.^{60–62} Such pulses with much better defined excitation and inversion profiles also allowed the development of new and the reconsideration of former experimental schemes.^{116;261;264;285–287}

The RIDME experiment^{66;67} has been recognized as valuable alternative in measuring spin-spin distance on spin tags with broad EPR lines.^{73;93;113;178–184} It profits from a very simple setup and low technical requirements. Yet, its combination with frequency-swept pulses can increase the observer bandwidth¹⁹⁸ and the sensitivity in measurements of high-spin centres by pre-polarization schemes as demonstrated here. However, harmonic overtones present in high-spin RIDME data⁷³ complicate data analysis routines as described in Chapter 8. Therefore, reliable application in structure determination requires a priori knowledge of the harmonic overtone weighting coefficients and their stability upon changing some experimental conditions, such as sample concentration, measurement temperature, mixing time or other pulse delay settings.

This chapter describes the recent progress towards the use of RIDME spectroscopy on high-spin paramagnetic tags in routine applications, for example in structural biology. To this end, first some considerations important to the choice of experimental parameters are presented. Next, signal enhancement schemes based on frequency-modulated pulses are demonstrated for Gd(III) and Mn(II) complexes. Calibration of harmonic frequency overtones has been discussed for Gd(III) in Chapter 8, a calibration for Mn(II) complexes is presented in Section 9.5. These results have been reported in Ref.⁹³ This is followed by a discussion of the stability of the overtone coefficients in protonated and deuterated nuclear spin bath and variations in the ligand structure. Finally, the application of the RIDME technique to a recombinant protein is explored.

9.2. Experimental

Synthesis of molecular rulers. Figure 9.1 shows the structure of the studied molecular ruler compounds. The synthesis of the PyMTA-based ruler compounds 1_n can be found in Refs.^{94;101;131}. Synthesis of the DOTA and TAHA-based rulers will be described elsewhere.

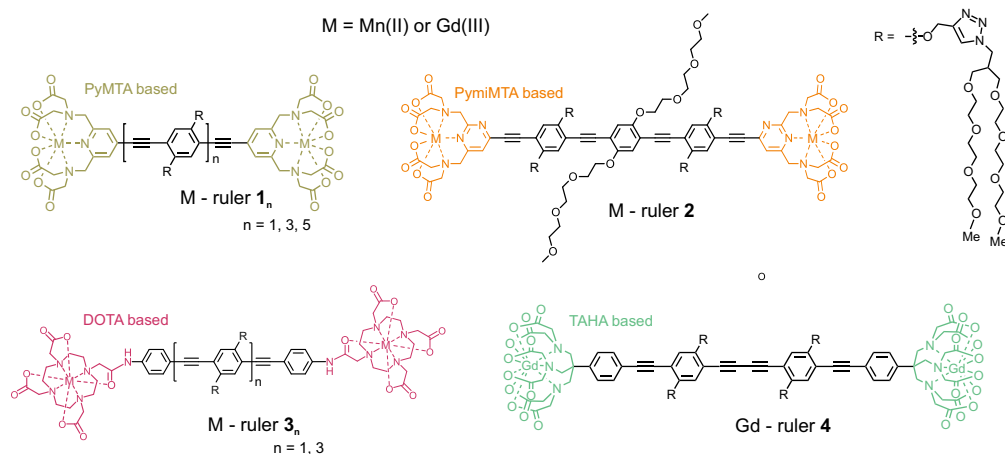


Figure 9.1. Molecular ruler compounds studied in this chapter. The different metal ligands are colour coded. Dashed lines mark possible coordination sites.

Expression of protein mutants. Cysteine residues were inserted following two consecutive site-directed mutageneses into a cysteine-free version of the RNA-binding domains (RBD), also known as RNA recognition motifs (RRM), RBD1, RBD2 and RBD34 of the polypyrimidine tract-binding protein (PTB). The mutation positions were close to or within the α -helical regions of each RBD. The respective site pairs (see Table F.1 in Appendix F) were selected to address distance ranges between 2 to 4 nm (RBD1; T71C/T109C), 2 to 3 nm (RBD2; S205C/S240C) and 3 to 5 nm (RBD34; Q388C/S475C), respectively. The mutageneses, protein expression and purification of the different constructs are described elsewhere.¹⁹² Distance distributions simulated with the rotamer library approach²⁸⁸ and the amino acid sequences of the cysteine-mutated RBDs are given in Appendix F.1.

Protein double mutants were spin labelled with 10-fold excess of Gd-maleimido-DOTA (abbreviated as Gd-DOTA) at ambient temperature. The overnight labelling reaction was performed in a labelling buffer containing 50 mM MOPS, 500 mM NaCl, 10% glycerol, pH: 6.5) under gentle shaking. Unreacted spin label was washed out using PD10 desalting columns (GE Healthcare) and eluted protein was concentrated and rebuffered into low-salt (LS) buffer (10 mM NaPO₄, 20 mM NaCl, pH: 6.5). Further, all samples were analysed for cysteine-mediated dimerization by SDS PAGE under non-reducing conditions.

Due to the broad EPR spectrum of Gd(III) in X band (9.6 GHz) and ambient temperature, quantitative determination of the labelling efficiencies similar to nitroxide radicals is hardly feasible. Therefore, all Gd-DOTA-labelled RBDs were analysed by electrospray ionization mass spectrometry (ESI-MS), according to previous studies.¹⁹² A mass shift corresponding to twice the spin-label mass and the change in the amino acid sequence indicated double Gd-labelled RBDs.

EPR sample preparation. Stock solutions of the molecular rulers were diluted to 100 μ M spacer concentration in a 1:1 (v:v) D₂O:glycerol-d₈. To study the influence of the nuclear spin bath,

Gd-ruler $\mathbf{1}_n$ ($n = 1, 3$) stock solutions were lyophilized and rediluted in a 1:1 (v:v) H_2O :glycerol mixture to 100 μM molecular ruler concentration.

RBD1 T71C/T109C was directly mixed with d_8 -glycerol in a 1:1 (v:v) ratio to a final concentration of about 27 μM . RBD2 S205C/S240C and RBD34 Q388C/S475C were rebuffed into D_2O (99%, Sigma Aldrich) and afterwards mixed with glycerol- d_8 to a final concentration of 25 μM and 19 μM , respectively.

Sample solutions were filled into 0.5 mm inner diameter quartz tubes for W-band measurements. 3 mm outer diameter quartz sample tubes were used in Q band measurements. Subsequently, samples were shock-frozen by immersion into liquid nitrogen.

EPR measurements. W-band EPR experiments were performed on a Bruker Elexsys E680 X-/W-band spectrometer and homebuilt W-band microwave bridge unit with a 2 Watt solid state amplifier. The samples were placed in a Bruker TE_{011} resonator. The spectrometer was extended with an AWG as described in Ref.⁶⁰ to enable the application of frequency-modulated pulses. Q-band data were acquired at two different high power (200 Watt) spectrometers: a commercial Bruker Elexsys E580 and a homebuilt spectrometer.⁹⁶ Both spectrometers were equipped with a home-built rectangular cavity operating at about 34.5 GHz.⁹⁷ A helium flow cryostat (ER 4118 CF, Oxford Instruments) was used to adjust and stabilize the measurement temperature at any chosen value between 10 K and 30 K.

EPR absorption spectra were measured with a $\pi/2 - \tau - \pi - \tau$ -echo sequence ($t_p(\pi/2) = 12$ ns and $t_p(\pi) = 24$ ns at the central transition). The interpulse delay τ was set to 400 ns. Hahn echo decay curves were measured using the same sequence and incrementing the interpulse delay τ (delay time increment depending on decay rate). Longitudinal relaxation traces were measured using the inversion recovery sequence $\pi - T - \pi/2 - \tau - \pi - \tau$ -echo as described in Chapter 2.5.4. A soft detection sequence ($t_p(\pi/2) = 54$ or 60 ns, $t_p(\pi) = 2t_p(\pi/2)$, $\tau = 400$ ns) was used in combination with hard inversion pulses ($t_{\text{inv}} = 8$ or 12 ns). The delay T was incremented starting from the initial delay of 600 ns or 1 μs . Relaxation data were acquired at different field positions as indicated in the text.

Distance measurements were performed using the refocused RIDME experiment⁶⁷ and the conventional 4-pulse DEER experiment¹⁷⁷ to record reference distance distributions. The pulse sequences are shown in Figure 9.2.

DEER measurements were performed with an offset of 150 MHz between pump and detection frequency. All pulses were set to 12 ns. The pump frequency was set to the centre position of the Gd(III) or a hyperfine line of the Mn(II) spectrum. An 8-step nuclear modulation averaging was performed by incrementing the first interpulse delay d_1 by 16 ns ($d_{1,0} = 400$ ns). The second delay time d_2 was set between 1.5 and 5.2 μs , according to the expected distances. In RIDME experiments, the detection position was set to the centre of the resonator. Nuclear modulation averaging was performed according to Ref.⁷⁹. The mixing time T_{mix} was varied to study its influence on the signal evolution in a range of 4 to 260 μs . $\pi/2$ - π -pulses were set to 12-24 ns. The interpulse delays were set to $d_1 = 400$ ns, while d_2 was adjusted to the required trace length from 1.8 to 10.2 μs . For both experiments, the initial time delay d_{12} was - 120 ns and the time step increment was 8, 12 or 16 ns, depending on the distance of interest.

For pre-polarized EDEPR and RIDME experiments, two consecutive linear chirps ($t_p = 2$ μs , 30 ns rise time) were applied prior to the first $\pi/2$ pulse of each sequence. The sweep ranges are indicated in Figure 9.2(d). The optimized pulse parameters are given in Table 9.1. The parameter

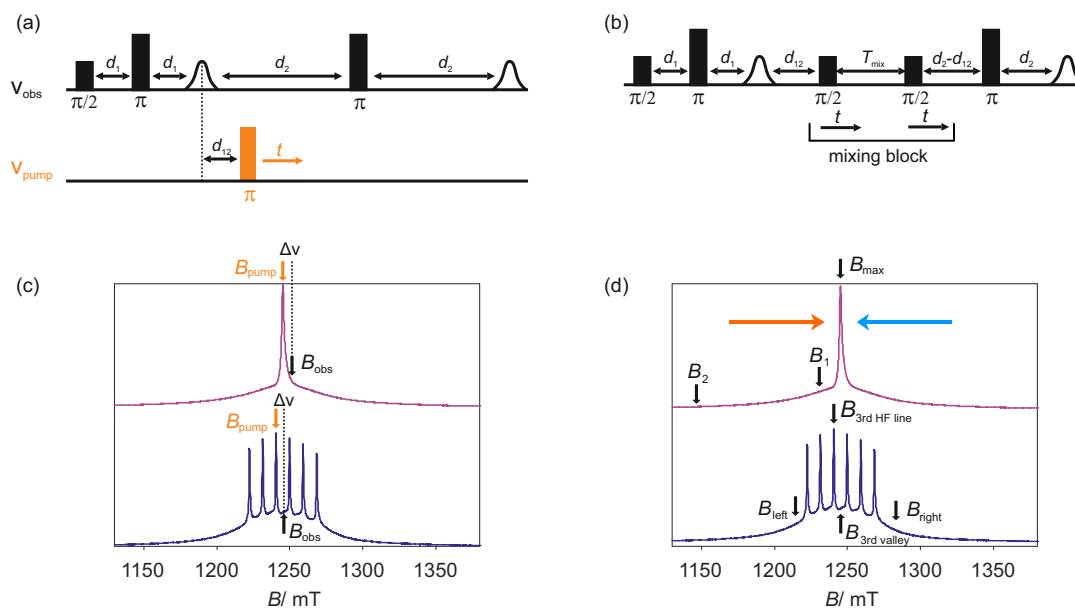


Figure 9.2. (a) DEER and (b) RIDME pulse sequences. (c, d) Q-band EDEPR absorption spectra at 10 K for M-DOTA M=Gd(III) (purple) and Mn(II) (violet). (c) DEER pump (orange) and detection positions (black), (d) different observer positions studied in the RIDME experiment and illustration of frequency-swept pulses used in the pre-polarization scheme: up-chirp (orange), down-chirp (blue).

optimization is shown in Section F.3 and was performed according to Ref.¹¹⁷. Heating effects and noise amplification are given in Appendix F, Figure F.4.

MW band	Molecular ruler	up-chirp/ GHz	down-chirp/ GHz
Q band	Mn-ruler 1 ₅	-1.69 to -0.79	2.74 to 1.56
Q band	Gd-ruler 1 ₃	-1.42 to -0.23	1.78 to 0.22
W band	Gd-ruler 1 ₃	-0.9 to -0.18	1.25 to 0.85

Table 9.1. Optimized pulse parameters used in pre-polarization schemes. The chirp frequencies are defined with respect to the observer frequency.

Data analysis. All recorded dipolar evolution traces were analysed using the software package OvertoneAnalysis.¹¹⁴ Primary data were background corrected using a stretched exponential function as described in Reference,¹¹⁴ prior to Tikhonov regularization. The program, which evolved from the well-known DeerAnalysis package,⁷⁸ allows to use modified kernel functions that consist of a linear combination of the primary dipolar frequency ω_{dd} (P_1) and the high frequency overtones $2\omega_{dd}$ (P_2) and $3\omega_{dd}$ (P_3). The overtone coefficients P_2 , P_3 ($P_1 = 1 - P_2 - P_3$) need to set by the user. For DEER measurement the coefficients P_2 and P_3 were set to zero ($P_1 = 1$). In RIDME experiments different sets of overtone coefficients are tested and are given next to the resulting distance distributions. The regularization parameter α was chosen following the L-curve criterion.

9.3. Choice of experimental parameters

In Chapter 3, we discussed the importance of relaxation times in pulsed dipolar spectroscopy and the influence of the ligand on the central metal ion therein. In complexes of Mn(II) and

Gd(III), the electron spin relaxation times were found to be longer in complexes with weaker ZFS. For negligible electron spin-spin interactions phase memory times for Gd(III) or Mn(II) chelates were similar, while longitudinal relaxation times were up to a factor of three larger in Mn(II)-complexes. For a given metal complex, e.g. used as spin tag or paramagnetic probe in molecular rulers, relaxation times are influenced by the spin concentration, solvent, microwave frequency, measurement temperature and detection position within the EPR spectrum.

A quantitative discussion of relaxation is beyond the scope of this study, but Figure 9.3 shows some qualitative trends at the example of the PyMTA-ruler. When optimizing signal-to-noise (SNR) or dipolar modulation depth versus sample temperature in RIDME distance measurements between two spins of similar relaxation properties, one has to keep in mind that longitudinal relaxation should be fast but not too similar to the transverse relaxation (see discussion in Chapter 3).

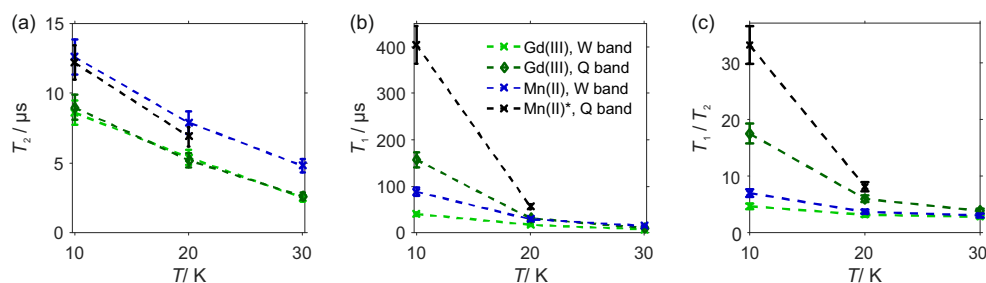


Figure 9.3. Relaxation properties of 100 μM PyMTA-based rulers with Mn(II) or Gd(III) as central ion. *100 μM Mn-PyMTA in Q band. (a) Phase memory times T_m , (b) longitudinal relaxation times T_1 , (c) quotient T_1/T_m .

For Mn- and Gd-PyMTA, phase memory times are found to decrease approximately linear with increasing measurement temperature in the range of 10 to 30 K. Note, the accelerated phase memory times due to increased electron spin-spin interactions in the molecular rulers (200 μM metal ion) as compared to the measurements presented in Chapter 3. The effect is stronger in Gd(III), because of its higher spectral density at the central transition. Within experimental uncertainty, no differences were observed between phase memory times in Q and W band. For these compounds distance measurements in the range of 10 to 30 K appear feasible, while longer time traces can be detected at lower temperature. Longitudinal relaxation times of both Gd(III) and Mn(II) show a steeper temperature dependence than transverse relaxation, and for both metal ions it is faster in W band than in Q band. Differences in longitudinal relaxation times between Mn(II) and Gd(III) at a given microwave frequency as well as corresponding relaxation time differences for a given metal ion at two different microwave bands become smaller at higher temperatures. Thus, by the choice of measurement temperature and microwave frequency the ratio of T_1/T_m can be adjusted. With respect to RIDME experiments between like spins, a ratio of $T_1/T_m \sim 5$ is considered to be close to optimal.⁹³ In the systems under investigation, such a ratio is typically encountered at higher measurement temperatures for Mn(II)- compared to Gd(III)-complexes. For instance, for the maleimide-DOTA spin tag (100 μM), a ratio of $T_1/T_m = 5$ was found at 14 K for Gd-maleimide-DOTA and at 27 K for Mn-maleimide-DOTA in W band.⁹³ For these particular complexes and spin concentration, the transverse relaxation times of the two metal ions were found to be nearly the same at this 'optimal' measurement temperature. The same observation holds for longitudinal relaxation. For PyMTA as ligand and 200 μM spin concentration, such a ratio was found in a similar range in W band (see Figure

9.3(c)). Changing from W to Q band, requires for the same T_1/T_m ratio a higher measurement temperature, which in turn reduces the phase memory time. Thus, longer distances will be potentially better accessible at higher microwave frequencies in RIDME experiments on like spins.

Phase memory times are also strongly affected by solvent deuteration, which thus can increase the range of accessible distances.^{50;289;290} Electron spin-spin contributions influence transverse relaxation rates at spin concentrations down to $\sim 25 \mu\text{M}$ for Gd(III) (see Chapter 5) and $\sim 100 \mu\text{M}$ for Mn(II),⁹³ respectively. Longitudinal relaxation appears to be less sensitive to spin concentration and deuteration in the investigated systems,^{93;107} (Chapter 5), so that the T_1/T_m ratio can be modulated. Both, spin concentration and degree of solvent deuteration also strongly affect the RIDME background as described in Chapter 5.

Lastly, it should be noted that Gd(III) ions show a strong dependence of the transverse relaxation rates on the type of EPR transition ($m_s \leftrightarrow m_s + 1$) due to transient ZFS fluctuations,⁴⁷ while longitudinal relaxation rates are approximately constant (see for instance Chapter 5). The transverse relaxation is slowest and the EPR intensity is largest at the central transition of Gd(III) ions. Therefore, whenever possible, for these metal ions detection on the central transition is preferred in terms of sensitivity. For Mn(II) complexes, similar effects seem to appear and some dependencies on the detection position are presented in the Appendix F, Figure F.2. However, such effects were not investigated in detail.

If now all parameters mentioned above are chosen according to the experimental problem at hand, the RIDME sequence itself still contains the mixing time as free parameter to influence the modulation depth and SNR. Simultaneous optimization of both modulation depth and echo SNR is not possible since they have opposite dependences on the RIDME mixing time. A simple experiment can be designed to find the best compromise in measurements of intermediate distances as illustrated in Figure 9.4 and described in detail in Chapter 7 for low-spin Cu(II) ions. However, in cases of long distances or protonated solvents, the background decay may limit the mixing time, while the SNR condition is weakened for measurements of short spin-spin distances. In cases of low labelling efficiency, where modulation depth is very low, it might be beneficial to sacrifice signal intensity for reaching a minimal modulation depth, necessary for the dipolar modulations to exceed the level of any electronics-related or experimental artefacts. Such an increase of the modulation depth, would then come at the cost of longer measurement times for the same SNR level. A low modulation depth is particularly disadvantageous in RIDME time traces, as compared e.g. to DEER, due to the echo crossing artefacts that can almost never be perfectly removed in measurements on like spins.

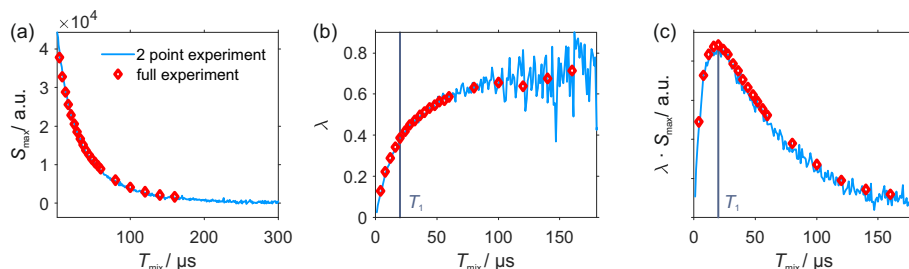


Figure 9.4. Two-point optimization scheme for RIDME experiments at the example of the Gd-ruler **1₃** in Q band at 20 K. (a) Maximal signal intensity S_{max} , (b) modulation depth λ , (c) sensitivity estimate as $\lambda \cdot S_{\text{max}}$. Light blue: two-point RIDME experiment; Red: full RIDME time trace. The characteristic T_1 time is indicated by the vertical line.

The initial refocused virtual echo signal intensity in the RIDME experiment (Figure 9.4(a)) decreases for increasing mixing time due to additional spectral diffusion contributions, while the modulation depth increases, potentially, up to the steady state value of $\lambda_{\text{steady state}} = 1 - 1/(2S + 1)$. This would correspond to a modulation depths of 0.88 for Gd(III) and 0.83 for Mn(II). In practice, the steady state value has not been reached, but larger modulation depths were observed in Gd(III) than in Mn(II) chelates as shown in Figure 9.5(a, c). Deviations from the steady-state value may be caused by correlated flip-flop processes in the A-B pairs or the presence of non-coupled, resonant spins.

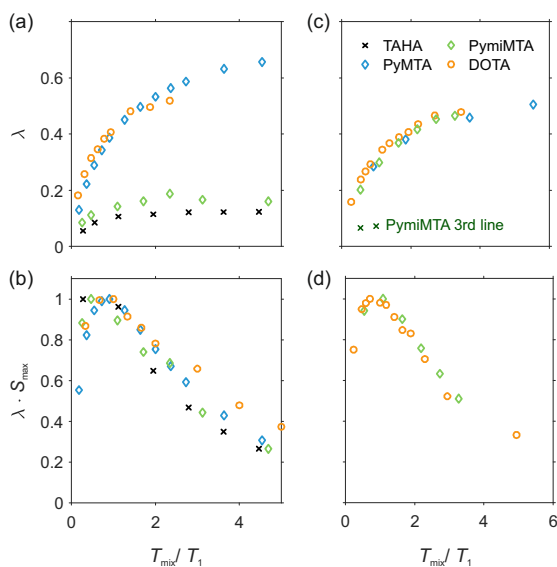


Figure 9.5. (a, c) Modulation depth λ and (b, d) estimated sensitivity $\lambda \cdot S_{\text{max}}$ for the studied molecular rulers. (a, b) Gd(III) and (c, d) Mn(II) as central metal ion.

The panels (b) and (d) in Figure 9.5 show estimated sensitivities by the product of initial signal intensity and modulation depth extracted from full RIDME traces for the studied set of molecular rulers. Best sensitivity was found to be in the order of $T_{\text{mix}} \sim T_1/2 - T_1$ for Gd(III) complexes and about $T_{\text{mix}} \sim 1/2 - 3/4 T_1$ for Mn(II) complexes. Additional two-point optimization curves are shown in Section F.8 in Appendix F.

Modulation depth is reduced by the presence of non-coupled, resonant spins as illustrated for a 1:1 (v:v) mixture of Gd-PyMTA and the corresponding molecular ruler compound in Figure 9.6. While this does not change the mixing time of optimal sensitivity, it might pose the requirement for a longer mixing time to regain the loss in the modulation depth.

The much lower modulation depth of the TAHA-based (only Gd(III)) and PymiMTA-based ruler compounds indicate incomplete loading in these complexes or the presence of unloaded metal ions. Indeed, the much larger modulation depth of the Mn-PymiMTA ruler, detected at the 3rd hyperfine valley compared to the of 3rd hyperfine lines, suggest the presence of free Mn(II) ions in form of the hexa-aqua complex. This complex encompasses narrow EPR lines, so that its relative contribution is reduced at the satellite transitions. This finding is supported by a strong contribution of a narrow hyperfine splitting pattern to the much broader absorption spectrum of the Mn-PymiMTA-based ruler (see Figure F.19(a)). In case of Gd(III)-complexes such a spectroscopic trick is not easily realized, because the spectrum of the aqua-ion has similar spectral width as known Gd(III)-labels (see Figure F.19(b)).

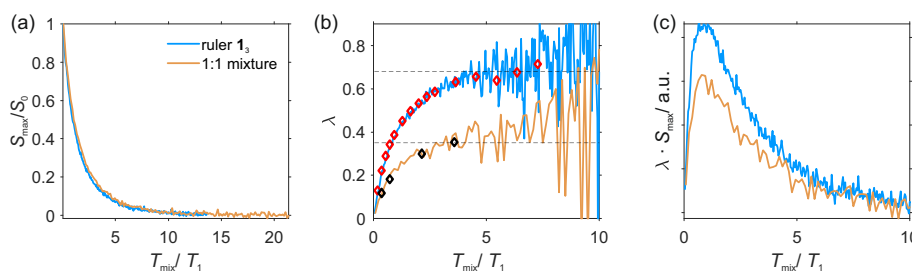


Figure 9.6. Reduction of modulation depth for partially labelled samples at the example of a 1:1 mixture of Gd-PyMTA and the Gd-ruler **13** in Q band at 20 K. (a) Maximal signal intensity S_{\max} normalized to first T_{mix} -value, (b) modulation depth λ , (c) sensitivity estimate as $\lambda \cdot S_{\max}$. Light blue/ orange data points: two-point RIDME experiment; Red/ black diamonds: full RIDME time trace.

9.4. Sensitivity enhancement by pre-polarization

Linear chirps have been shown to enhance the sensitivity of DEER distance measurements using Gd(III).¹¹⁷ Similarly, rapid magnetic field sweeps over a sub-spectrum of the EPR transitions concomitantly with low power microwave irradiation, have been used to increase the sensitivity of Mn(II) absorption spectra.²⁸⁴ Such experiments are based on successive exchange of populations between pairs of levels in a multi-level high-spin system. Such a series of ‘population inversions’ can be used to enhance the EPR signal intensity at the EPR transitions of interest by selectively moving highest and lowest populations to the two neighbouring energy levels as illustrated in Figure 9.7. This can be achieved by application of two frequency-swept pulses: One pulse drives magnetization from the low lying levels to central level sweeping from low to high frequency and consequently inverting the populations of the energy levels: $-7/2 \leftrightarrow -5/2 \leftrightarrow -3/2 \leftrightarrow -1/2$). The second pulse acts vice versa, inverting the $7/2 \leftrightarrow 5/2 \leftrightarrow 3/2 \leftrightarrow 1/2$ transitions by sweeping from high frequency to low frequency.

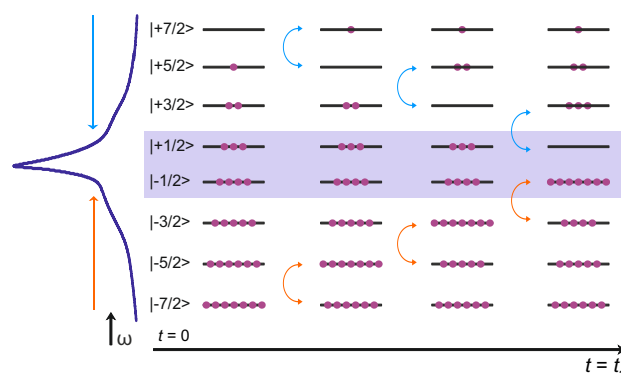


Figure 9.7. Schematic illustration of polarization enhancement by population transfer.

Resulting enhancement in EPR absorption spectra and RIDME time traces for Gd/ Mn-rulers are shown in Figure 9.8. Nicely, the enhancement factors observed in absorption spectra do translate into a sensitivity enhancement in the RIDME experiments.

The largest signal enhancement of 150% is achieved for Gd(III) in Q band. The larger signal enhancement in Q band than in W band can be explained, by the larger resonator bandwidth and higher microwave power available at this frequency. For Mn(II), only a moderate enhancement of about 25% is observed.

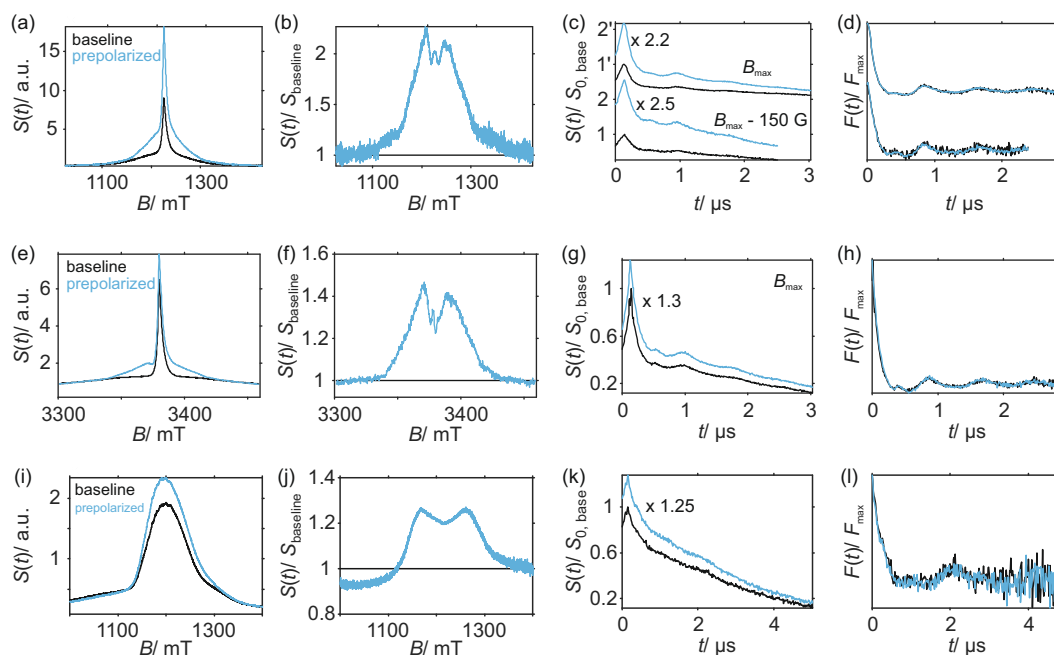


Figure 9.8. Pre-polarization in RIDME experiments at 20 K. (a-h) Gd-ruler $\mathbf{1}_3$ and (i-l) Mn-ruler $\mathbf{1}_5$. (a-d, i-l) Q band (resonator $Q \sim 100$) and (e-h) W band (resonator $Q \sim 1000$). (a, e, i) Conventional (black) and pre-polarized (blue) absorption spectra; (b, f, j) Pre-polarized absorption spectra normalized by conventional absorption spectra; (c, g, k) conventional (black) and pre-polarized (blue) RIDME raw data; (d, h, l) Normalized and background-corrected form factors.

Very conveniently only echoes generated with contributions from the initial $\pi/2 - \pi$ preparation period contribute to the signal enhancement, which is illustrated in Figure 9.9 for the two RIDME echoes (refocused virtual echo RVE and refocused stimulated echo RSE). The echo generated by the last two pulses (PE_2) in the RIDME sequence, which strongly contributes to the echo-crossing artefact at zero time, is not enhanced. Therefore, pre-polarization schemes may help to reduce the relative intensity of such parasite echoes and therefore also artefact peaks in RIDME experiments. E.g. a reduction of the two-pulse echo contribution might be particularly beneficial in partially labelled samples.

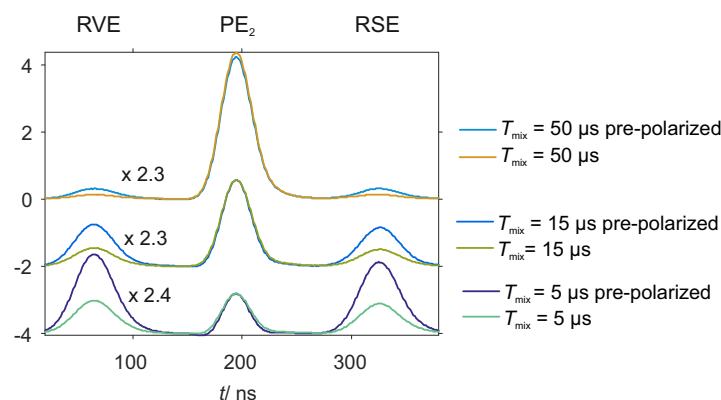


Figure 9.9. Enhancement of different echoes resulting from a pre-polarized RIDME sequence. RVE - refocused virtual echo, used for detection; RSE refocused stimulated echo and PE_2 - two-pulse echo generated from the last two pulses.

9.5. Calibration of overtone coefficients for Mn(II)

The computation of distance distribution for dipolar evolution data with harmonic overtones has been introduced in the previous chapter. This approach requires knowledge of the overtones coefficients. This section investigates their contribution to Mn-Mn based RIDME experiments at the example of the Mn-rulers $\mathbf{1}_n$. The result have been described in Ref.⁹³.

Figure 9.10 presents the dependence of the dipolar modulation in Mn-Mn RIDME time traces on mixing time and temperature for the Mn-ruler $\mathbf{1}_3$ with an expected Mn-Mn distance of about 3.4 nm. Further data on this compound as well as data of Mn-ruler $\mathbf{1}_5$ with an expected Mn-Mn distance of about 4.7 nm are presented in Appendix F (Figures F.6-F.8 and F.9-F.11, respectively).

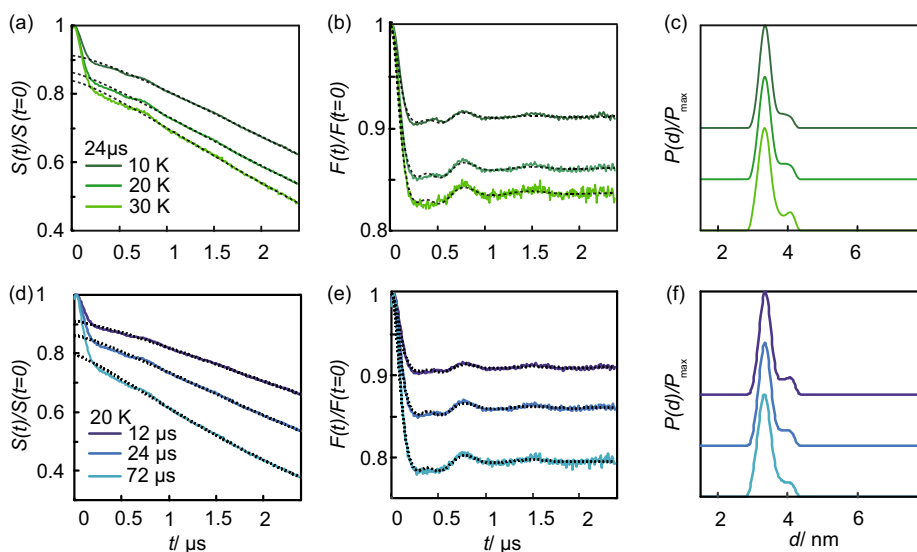


Figure 9.10. W-band RIDME data for the Mn-ruler $\mathbf{1}_3$ in 1:1 D_2O /glycerol- d_8 , with a mixing time of $24 \mu s$ and at different temperatures (a-c), and with different mixing times at 20 K (d-f). (a, b) Renormalized primary data with fitted background functions (dashed black lines), (c, d) normalized form factors with corresponding fits (black dashed lines) and (e, f) extracted distance distributions for the coefficients: $P_1 = 0.41$, $P_2 = 0.50$ and $P_3 = 0.09$.

By comparing the Mn-Mn RIDME form factors for different mixing times, one can conclude that the shape of dipolar evolution is nearly identical in all cases, a situation also found in the case of Gd-Gd RIDME (previous Chapter 9). This allows to compute distance distributions using a single set of overtone coefficients: $P_1 = 0.41$, $P_2 = 0.50$ and $P_3 = 0.09$. Still, with increasing temperature (Figure 9.10) and changing the detection position (Figure 9.11), one can recognize some minor differences between the different RIDME time traces in the region of the first minimum (300–600 ns in Figure 9.10, F.5), so that analysis with adjusted kernel coefficients is able to further reduce the artefact level (see Appendix F.4). Figures 9.10, 9.11 and F.6-F.11 show the relatively low level of artefacts in the distance distributions, resulting from analysis of the whole data set with constant dipolar overtone coefficients $P_1 - P_3$ ($P_1 = 0.41$, $P_2 = 0.50$ and $P_3 = 0.09$). Concurrent with the observations for Gd(III), longer mixing times induce larger dipolar modulation depths in Mn-Mn RIDME experiments, while in parallel the background decay is accelerated.

Figure 9.11 presents Mn-Mn RIDME traces detected at a few different positions in the absorption spectrum of Mn-ruler $\mathbf{1}_5$. A larger set of field positions is presented in Appendix

F, Figure F.12 for the Mn-ruler **1**₃. Interestingly, the dipolar modulation depth increases as one shifts the detection frequency away from the top of hyperfine components of the central $|+1/2\rangle \leftrightarrow |-1/2\rangle$ transition although longitudinal relaxation rates are approximately constant throughout the spectrum, so that strong contributions from the hexa-aqua complex are not expected. For Gd(III) it was found that at short interspin distances the dipolar evolution in Gd-Gd DEER experiments gets distorted, most probably due to multiple level crossings in the range of the central transition and level mixing by the pseudo-secular part of dipolar interaction.⁴⁴ In the case of Mn-Mn RIDME, effects of similar origin may lead to a partial decay of the resonant spins (A spins) upon every spin flip event of B spins in the A-B spin pairs. Such a decay mechanism should be pronounced for detection in the frequency range of the central transition. Indeed, detecting at the position B_3 , which is most remote from the six central hyperfine peaks, we obtained the largest RIDME modulation among the three tested positions $B_1 - B_3$ (Figure 9.11(c)). This type of problem would be reduced if measurements are performed at lower field/microwave frequency or using metal complexes with larger ZFS, since both these modifications lead to spectral broadening and thus spreading of the positions of different level crossing points,. Therefore also the fraction of paramagnetic centres for which level crossing plays a role at a particular detection position is reduced.

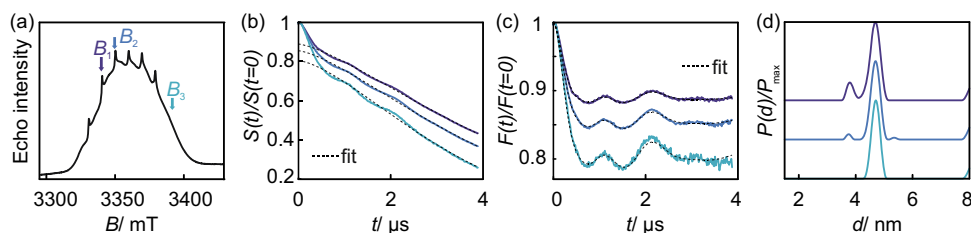


Figure 9.11. W-band data for the Mn-ruler **1**₅ in 1:1 D₂O/glycerol-D₈ acquired at different field positions and 10 K: (a) EDEPR spectrum with three detection field positions (B_1 , B_2 , B_3) marked by arrows; (b) renormalized primary RIDME traces with fitted background functions; (c) normalized RIDME form factors with Tikhonov regularization-based fits (for overtone coefficients: $P_1 = 0.41$, $P_2 = 0.50$ and $P_3 = 0.09$); (d) distance distributions, according to the fits presented in (c). In (b-d) top curve – position B_1 , middle curve – position B_2 , bottom curve – position B_3 ; in addition, time traces and distance distributions are coloured according to the colour code of the detection position marks in (a). Background fits in (b) and form factor fits in (c) are plotted as dashed black lines.

Further, there is a consistent trend of a short-distance shoulder in RIDME experiments detected at the low field side of the EPR spectrum as presented above and in Figure F.12 for the Mn-ruler **1**₃. This peak does not seem to be clearly related to contributions of overtone coefficients (see Figure F.13 in the Appendix F), but its origin remained unclear. The frequency distribution can also be clearly identified by a kink in the primary data around 400 ns for the Mn-ruler **1**₅ and 200 ns for the Mn-ruler **1**₃, respectively. In terms of distance measurement, it appears that this contribution can be circumvented by detection at the centre of the Mn(II) spectrum or at the high field side.

To summarise, the overtone coefficients in Mn-PyMTA rulers appear to be approximately stable with mixing time, measurement temperature and detection position within the EPR spectrum. Therefore, data analysis with a set of overtone coefficients $P_1 = 0.41$, $P_2 = 0.50$ and $P_3 = 0.09$ results into the anticipated distance distribution with a relatively low level of artefacts for the studied distances of 3.4 and 4.7 nm. Application of this set of overtones to Mn-rulers based on the DOTA-ligand is presented in the following section.

9.6. Stability of overtone coefficients

Before RIDME experiments can be routinely applied in biological systems, the stability of overtone coefficients in different environments needs to be tested. This section investigates if such stability is observed when changing the nuclear spin bath as well as the ligand field of the paramagnetic metal complexes.

9.6.1. Nuclear spin bath

In this subsection we address if changes occur in RIDME form factors when deuterons are exchanged by protons. The nuclear spin bath causes fluctuating hyperfine fields at the site of the electron spin that in turn lead to a loss of electron phase coherence. These fluctuations are much stronger in the case of protons than deuterons. Longitudinal relaxation at low temperature in frozen glassy solution is dominated by spin-lattice interactions due to two-phonon processes, which are expected to be independent of the hyperfine field observed at site of the electron spin. Therefore, longitudinal relaxation rates are roughly unaffected in protonated solvents, while much faster transverse relaxation rates are observed.¹⁰⁷ In addition, we saw in Chapter 5 that proton hyperfine fields contribute more efficiently to spectral diffusion processes and therefore cause fast RIDME background decays. Nevertheless, if the nature of longitudinal relaxation mechanisms does not change, we expect that the harmonic overtone coefficients build-up as described in Chapter 8.

Figure 9.12(a-d) shows the much faster background decay in RIDME measurement on the Gd-ruler **13** in protonated as compared to deuterated glasses and thus the maximal possible trace length is strongly reduced. The steep background decay, which is then dominated by nuclear spectral diffusion, makes the separation of inter- and intramolecular contributions much more difficult. The steepness of the background decay (see Figure 9.12(e-h)) is reduced for detection at the outer transitions of the Gd(III) spectrum. Similarly, transverse magnetization decays initially faster at the outer transitions, however, lasts longer than at the central line (see Figure F.18). It may thus be beneficial to detect RIDME traces in protonated solvents at the outer transitions.

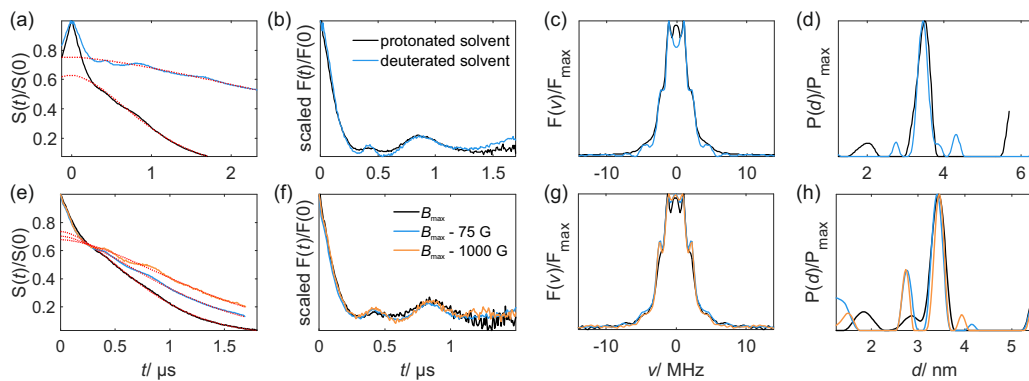


Figure 9.12. W-band RIDME measurements on the Gd-ruler **13**. (a-d) Comparison of RIDME measurements in protonated (black, $T_{\text{mix}} = 12 \mu\text{s}$) and deuterated (blue, $T_{\text{mix}} = 10 \mu\text{s}$) solvent, detected at maximum field B_{max} and 20 K. (e-h) For different field positions, $T = 10 \text{ K}$, $T_{\text{mix}} = 24 \mu\text{s}$. (a, e) Raw data and corresponding background fits (red dashed lines), (b, f) scaled form factors in time domain, (c, g) form factors in frequency domain, (d, h) resulting distance distributions with $P_2 = 0.40$, $P_3 = 0.09$.

Small deviations are observed in the form factor traces in protonated and deuterated glasses as well as for different mixing times and measurement temperatures (see Figure F.14, F.15).

Those deviations are most probably caused by inadequacies in background correction. Distance distributions in protonated glasses obtained by Tikhonov regularisation with the set of overtone coefficients calibrated in deuterated glasses ($P_1 = 0.5$, $P_2 = 0.41$ and $P_3 = 0.09$) agree well with the measurements in deuterated environment. As in the deuterated glass, an increase in overtone coefficients is observed for a shift of the detection position away from the central line (Figure 9.12(e-h)).

Similarly, the Gd-ruler **1**₁ shows significantly steeper background decay in protonated than deuterated glasses, while the form factor shape and distance distribution are relatively unaffected (Figure 9.13(a-d) and Figure F.16, F.17). As described in Chapter 8 almost overtone-free time traces are observed for detection at the central transition and the harmonic overtones are reintroduced accompanied by an increase in modulation depth at field positions moved away from the central transition as shown in Figure 9.13(e-h).

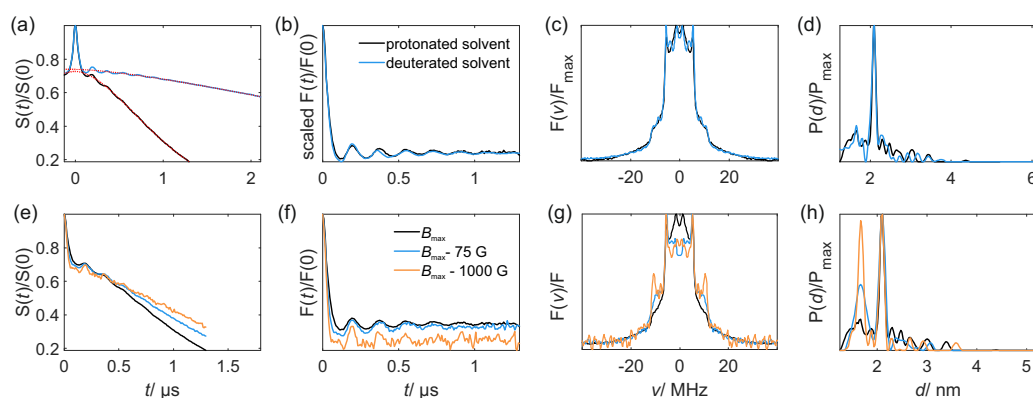


Figure 9.13. W-band RIDME measurements on the Gd-ruler **1**₁. (a-d) Comparison of RIDME measurements in protonated (black) and deuterated (light blue) solvent, detected at maximum field B_{\max} , $T_{\text{mix}} = 12 \mu\text{s}$ and 20 K. (e-h) For different field positions, $T = 10 \text{ K}$, $T_{\text{mix}} = 12 \mu\text{s}$. (a, e) Raw data and corresponding background fits (red dashed lines), (b, f) scaled form factors in time domain, (c, g) form factors in frequency domain, (d, h) resulting distance distributions with $P_2 = 0.40$, $P_3 = 0.09$.

Summarising, no substantial changes are observed with respect to harmonic overtone coefficients in protonated environments. Nevertheless, due to the very strong contributions of spectral diffusion the use of fully or partially deuterated solvents is recommended, e.g. by adding deuterated glycerol.

9.6.2. Ligand field

After studying the influence of solvent molecules on the harmonic overtones, this sub-section examines the influence of changes in the ligand structure. First, we investigate the influence of an additional nitrogen in the pyridine ring in PymiMTA as compared to PyMTA, before turning to a different ligand structure in DOTA- or TAHA-based ruler compounds.

PymiMTA-rulers

Figure 9.14 shows distance distribution obtained from measurements on the Gd- and Mn-ruler **1**₃ (ligand = PyMTA, blue lines) and ruler **2** (ligand = PymiMTA, black lines). For the rulers with Gd(III) as central ion (Figure 9.14(c, d)), both distributions are identical within the artefact level using the same overtone coefficients ($P_2 = 0.40$, $P_3 = 0.09$). However, for a similar mixing time, the dipolar modulation depth is strongly reduced in the PymiMTA-based ruler **2**, which indicates the presence of free metal ions or incomplete loading. In agreement with the smaller

ionic radius of Mn(II), the Mn-ruler distances (Figure 9.14(b)) are slightly shorter. The somewhat broader distance distributions in the Mn(II) pairs as compared to the Gd(III) case, might be caused by larger spin delocalization in the metal-ligand interactions for the $3d$ orbitals of Mn(II) as compared to the $4f$ orbitals of Gd(III). This effect appears to increase in the PymiMTA based compounds, which is in agreement with the modification of the ligand structure. As for Gd(III), in the Mn-PymiMTA based ruler **2** the overtone coefficients calibrated on the Mn-PyMTA rulers $\mathbf{1}_n$ ($P_2 = 0.5, P_3 = 0.1$) do result into the anticipated distance distributions and the modulation depth is reduced with respect to the Mn-PyMTA ruler.

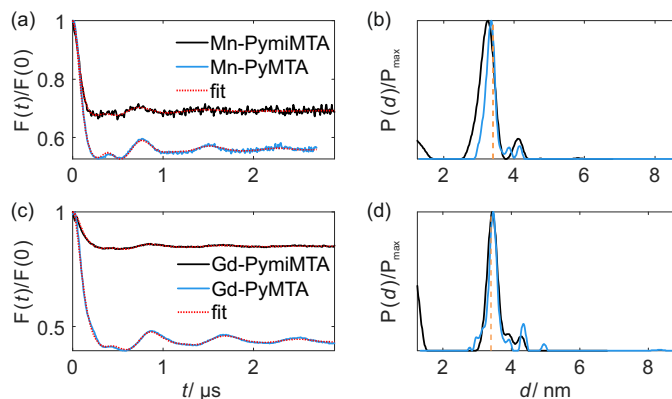


Figure 9.14. Comparison of W-band RIDME measurements on M-PyMTA $\mathbf{1}_3$ and M-PymiMTA-rulers **2** at 20 K. (a, b) $M = \text{Gd(III)}$, detected at maximum field, $T_{\text{mix}} = 22 \mu\text{s}$ for Gd-PymiMTA and $T_{\text{mix}} = 24 \mu\text{s}$ for Gd-PyMTA. (c, d) $M = \text{Mn(II)}$, detected at 3rd valley of hyperfine sextet, $T_{\text{mix}} = 30 \mu\text{s}$. (a, c) Form factors in time domain and corresponding fits (red dashed lines); (b, d) resulting distance distributions with (b) $P_2 = 0.40, P_3 = 0.09$ and (d) $P_2 = 0.5, P_3 = 0.1$.

Figure 9.15 shows the influence of measurement temperature and detection position for the Gd-ruler **2**. The variation of mixing time is shown in Appendix F, Figures F.20 and F.21. Similar to the PyMTA-based ruler compounds, described in detail in Chapter 8, the form factors are relatively stable with measurement temperature and mixing time, so that the same set of overtone coefficients can be used. Moving the detection position away from the central $m_S = |-1/2\rangle \leftrightarrow |1/2\rangle$ transition does increase contributions from higher harmonics as it was observed earlier for Gd-PyMTA based rulers.

Correspondingly, Figure 9.16 shows the influence of measurement temperature and detection position for the Mn-ruler **2**. The variation of mixing time is shown in Figure F.22. As presented in the previous section for the Mn-PyMTA based ruler compounds, changes in measurement temperature as well as mixing time do not significantly alter the form factor shape. Thus, analysis can be performed with the same set of overtone coefficients. In the case of PymiMTA, no strong deviations can be observed for different detection positions within the EDEPR spectrum, which may be related to the larger spectral width and thus stronger overlap of the central and satellite transitions. However strikingly, the modulation depth is strongly reduced for detection at the central transition. This indicates, in combination with rather narrow lines in the EDEPR spectrum of the PymiMTA-ruler compared to the PymiMTA-complex (Figure F.19), the presence of free Mn(II) ions in form of the hexa-aqua complex. Because of the small ZFS in the hexa-aqua complex, its relative contribution is largest at the hyperfine lines of the central transition and can be reduced by detection on the satellite transitions.

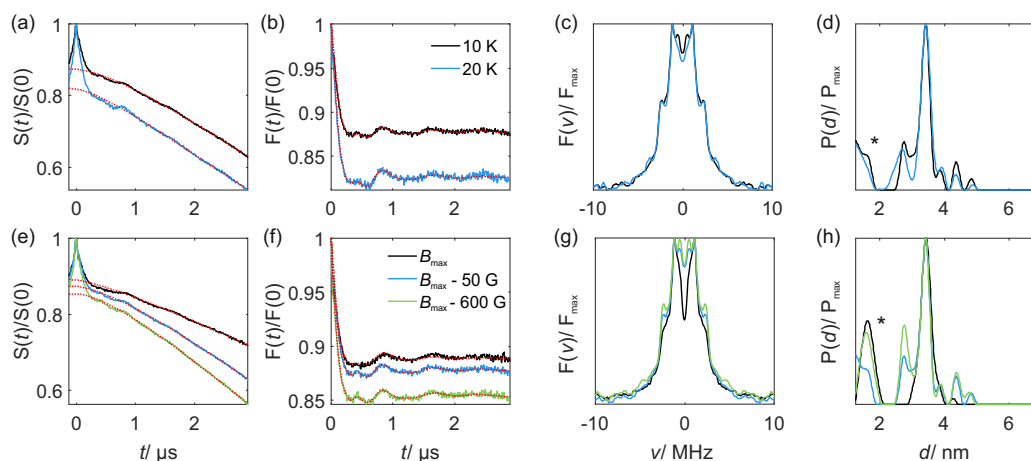


Figure 9.15. W-band RIDME measurements on the Gd-ruler **2**. (a-d) 10 K (black) and 20 K (light blue) detected at maximum field B_{\max} , $T_{\text{mix}} = 15 \mu\text{s}$. (e-h) Detected at different field positions, $T = 10 \text{ K}$, $T_{\text{mix}} = 15 \mu\text{s}$. (a, e) Raw data and corresponding background fits (red dashed lines), (b, f) form factors in time domain and corresponding fits (red dashed lines), (c, g) form factors in frequency domain, (d, h) resulting distance distributions with $P_2 = 0.40$, $P_3 = 0.09$. *contribution from echo-crossing artefact.

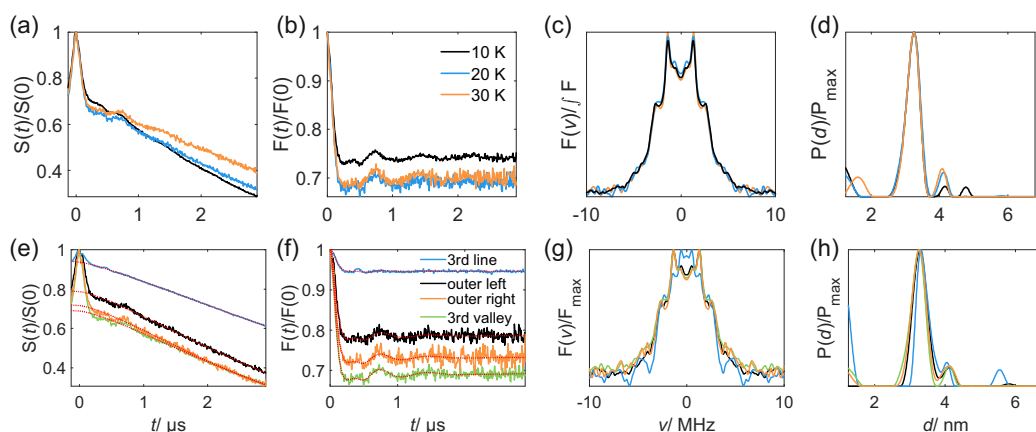


Figure 9.16. Influence of measurement temperature and detection position for W-band RIDME measurements on the Mn-ruler **2**. (a-d) Detected at 3rd valley, $T_{\text{mix}} \approx T_1$. (e-h) Detected at different field positions, $T = 20 \text{ K}$, $T_{\text{mix}} = 30 \mu\text{s}$. (a, e) Raw data and corresponding background fits (red dashed lines), (b, f) form factors in time domain and corresponding fits (red dashed lines), (c, g) form factors in frequency domain, (d, h) resulting distance distributions with $P_2 = 0.50$, $P_3 = 0.10$.

In summary, the minor change in the ligand structure introduced by the additional nitrogen in the pyridine ring does not induce a change in the overtone coefficients or spectroscopic behaviour of molecular rulers compounds beyond experimental uncertainties.

DOTA-based rulers

It is promising that small changes in the central metal ion environment do not cause changes in the overtone coefficients. Let us now turn to the DOTA ligand with smaller ZFS and longer longitudinal relaxation times. It is commercially available for Gd-based protein labelling with maleimido linker chemistry. Figure 9.17 shows a comparison of DEER and RIDME distance measurements for the Gd-ruler **3_n**, with $n = 1$ (a-d), $n = 3$ (e-h).

First, one immediately notices the faster background decay in RIDME-based measurements, as compared to DEER, but also a significant increase in modulation depth. The form factors in time- and frequency domain exhibit features of harmonic overtones, which result in at least

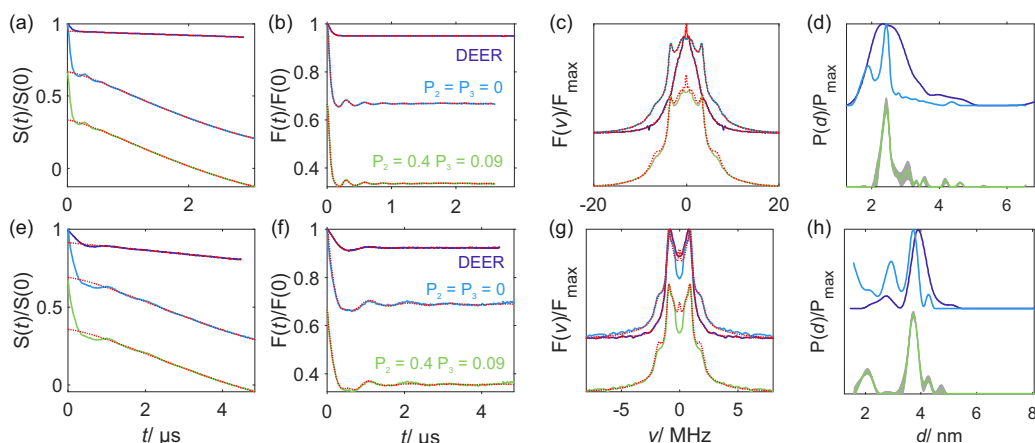


Figure 9.17. Distance measurements on the Gd-ruler $\mathbf{3}_n$. Purple: Q-band DEER at 10 K; Blue/ Green RIDME at 20 K, detected at maximum field. (a-d) Gd-ruler $\mathbf{3}_1$ in Q band, $T_{\text{mix}} = 50 \mu\text{s}$, (e-h) Gd-ruler $\mathbf{3}_3$ in W band, $T_{\text{mix}} = 30 \mu\text{s}$. (a, e) Raw data and corresponding background fits (red dashed lines), (b, f) form factors in time domain and corresponding fits (red dashed lines), (c, g) form factors in frequency domain and corresponding fits (red dashed lines), (d, h) resulting distance distributions with $P_2 = P_3 = 0$ (upper half, blue lines) and $P_2 = 0.40$, $P_3 = 0.09$ (lower half, green lines). The grey error bands marks a 20 % variation of overtone coefficients $P_2 = 0.40$, $P_3 = 0.09$.

bimodal distance distributions upon Tikhonov regularization with the standard DEER kernel. The contribution of harmonic overtones is larger in case of the longer ruler $\mathbf{3}_3$. For this compound, the DEER distance measurement resulted in a mean spin-spin distance of $d_{\text{mean}} \sim 3.7$ nm. For the corresponding RIDME data application of a modified kernel function with the same overtone coefficients as obtained for the PyMTA-based rulers ($P_2 = 0.4$, $P_3 = 0.09$, Figure 9.17(h), green trace) returned a single peak at the same mean distance as in DEER up to the artefact level. The width of the distance distribution computed from the RIDME data is narrower than in DEER, a finding that supports earlier results for PyMTA (see Figure 8.15 in Chapter 8). For spin-spin distance < 3 nm, level mixing⁴⁴ leads to broadening of the DEER distance distribution, which is observed for the short ruler compound $\mathbf{3}_1$ (Figure 9.17(d), green trace). Distance distributions extracted with the RIDME technique are narrower, which is in agreement with previous measurements on PyMTA-based rulers (Chapter 8) and results presented in literature for Gd-DOTA RIDME measurements.¹¹³ The contribution of harmonic overtones in the RIDME data was found to be reduced in the distance range below 3 nm.¹¹⁴ In the Gd-DOTA ruler $\mathbf{3}_1$ besides a mean peak at 2.4 nm a shorter distance peak corresponding to harmonic overtones can be recognized. Analysis of this data set, with the overtone coefficients obtained for PyMTA-based rulers does remove the short distance peak at 1.9 nm ($\hat{=} 2\omega_{\text{dd}}$), yet, induces peaks at longer distances that indicate overcorrection. Therefore, as described earlier for PyMTA, precise artefact correction will require a careful calibration of overtone coefficients for different distance ranges. Such an approach requires the synthesis of a set of molecular rulers with distances in the short distance ($d_{\text{mean}} < 2.4$ nm) and uncertainty range ($2.4 \text{ nm} < d_{\text{mean}} < 3.7$ nm), which are currently not at hand. Precise calibration is therefore omitted until such samples become available and in the subsequent analysis no overtone coefficients are used in the data analysis of the short compound $\mathbf{3}_1$. For the long compound $\mathbf{3}_3$, coefficients calibrated for the PyMTA-based rulers ($P_2 = 0.40$, $P_3 = 0.09$) are applied.

For the long Gd-DOTA based ruler compound $\mathbf{3}_3$ RIDME time traces and resulting distance distributions are relatively stable for changing mixing times and measurement temperature as

presented in Figure 9.18(a-d) and Figures F.27, F.25, F.26 in Appendix F. Like for the other PyMTA- and PymiMTA based rulers, changing the detection positions does lead to an increase in the overtone coefficients as presented in Figure 9.18(e-h).

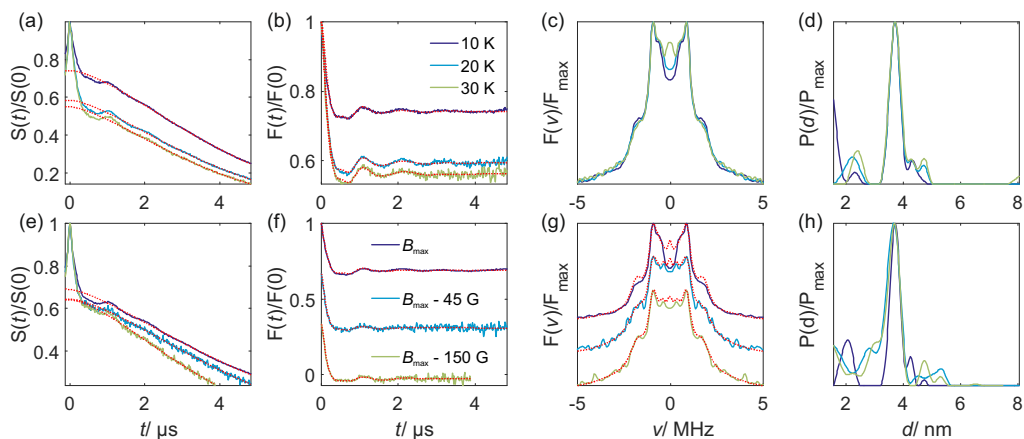


Figure 9.18. Influence of measurement temperature (a-d) and detection position (e-h) in W-band RIDME measurements on the Gd-ruler $\mathbf{3}_3$. (a-d) $T_{\text{mix}} = 30 \mu\text{s}$, detected at B_{max} ; (e-h) 20 K, $T_{\text{mix}} = 15 \mu\text{s}$. (a, e) Raw data and corresponding background fits (red dashed lines), (b, f) form factors in time domain and corresponding fits (red dashed lines), (c, g) form factors in frequency domain and corresponding fits (red dashed lines), (d, h) resulting distance distributions with $P_2 = 0.40$, $P_3 = 0.09$.

Some instabilities are observed in RIDME data at increasing mixing time as well as measurement time for the short DOTA-ruler $\mathbf{3}_1$. However, they might be related to an insufficient description of the background function as high-frequency contributions remain in the frequency-domain data (see Figures 9.19(a-d), F.23 and F.24). Clear deviations in the form factors are observed for detection of RIDME traces at the outer Gd(III) transitions as shown in Figure 9.19(e-h).

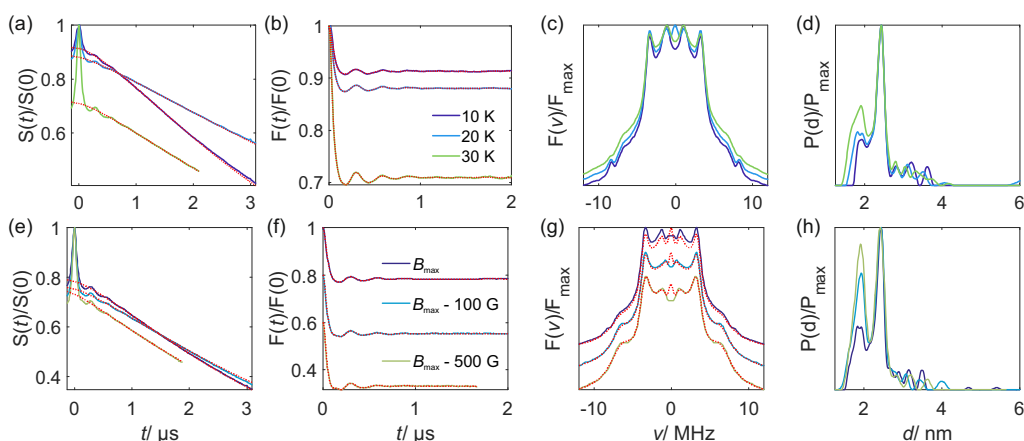


Figure 9.19. Influence of measurement temperature (a-d) and detection position (e-h) in Q-band RIDME measurements on the Gd-ruler $\mathbf{3}_1$. (a-d) detected at B_{max} , $T_{\text{mix}} = 40 \mu\text{s}$ at 10 K, $T_{\text{mix}} = 10 \mu\text{s}$ at 20/30 K; (e-h) 20 K, $T_{\text{mix}} = 24 \mu\text{s}$. (a, e) Raw data and corresponding background fits (red dashed lines), (b, f) form factors in time domain and corresponding fits (red dashed lines), (c, g) form factors in frequency domain and corresponding fits (red dashed lines), (d, h) resulting distance distributions with $P_2 = P_3 = 0$.

For the short compound $\mathbf{3}_1$, we also investigated differences between Q and W band as the contribution of the outer transitions to the central line should be higher in Q band due to a weaker electron Zeeman contribution. Consequently, contributions from higher harmonics should

be larger in Q band than in W band. Such a difference, albeit weak, is observed experimentally, however the uncertainty introduced by background correction for this compound is comparable to the form factor difference between Q- and W-band RIDME data.

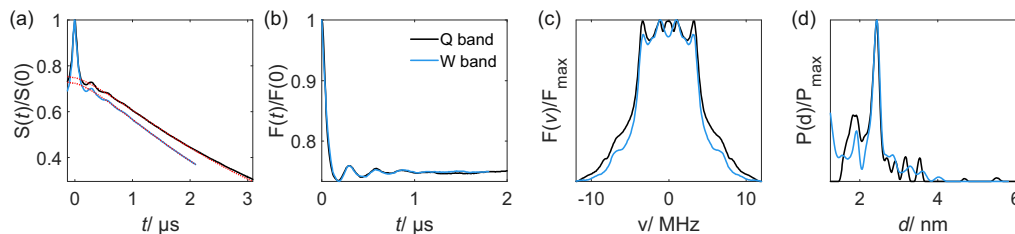


Figure 9.20. Influence of microwave band in RIDME measurements on the Gd-ruler $\mathbf{3}_1$ detected at maximum field. $T_{\text{mix}} = 30 \mu\text{s}$. (a) Raw data and corresponding background fits (red dashed lines), (b) form factors in time domain, (c) form factors in frequency domain, (d) resulting distance distributions with $P_2 = P_3 = 0$.

Let's now turn to the Mn-DOTA based ruler compounds. Figure 9.22 shows a comparison of both RIDME and DEER measurements as well as Gd(III) and Mn(II) as central ion. Distance distributions for the longer DOTA-rulers $\mathbf{3}_3$ are very similar between RIDME and DEER as well as Gd(III) and Mn(II). It can be noticed that the distance distribution of the Mn-ruler is broader and slightly shifted towards longer distances, which is counter-intuitive considering the smaller ionic radius of Mn(II). However, spin delocalization is larger in $3d$ than $4f$ orbitals, which might cause the larger width of the distance distribution. In addition, the DOTA-complex of the ruler compound offers up to eight ligand arms for coordination, but Mn(II) typically only coordinates six. Considering the structure of the DOTA-ruler (Figure 9.21), it is possible that the oxygen in the ruler backbone does not take part in coordination, which would allow for a higher freedom of rotation of the sp^3 carbon and a broader distribution of torsional angles N-C-C=O (purple bonds in Figure 9.21) between the ligand attachment site to the spacer unit.

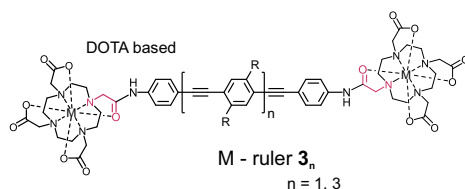


Figure 9.21. DOTA-based molecular ruler $\mathbf{3}_n$ ($n = 1, 3$). $M = \text{Mn(II)}$ or Gd(III)

On the other hand, for the short compound $\mathbf{3}_1$ and Mn(II) as central metal ion severe deviations, in the RIDME distribution width as well as mean position are observed. With the currently available experimental data, we can only speculate that the relatively large shift of about 3 \AA and much broader distributions are caused by the presence of several conformations. Potentially, also interference effects between ZFS, dipolar coupling and nuclear frequencies occur resulting into additional distance peaks. Such additional peaks can be identified in Figure 9.23 when the regularisation parameter in OvertoneAnalysis is reduced to match the main peak of the Gd-ruler $\mathbf{3}_1$ (overlaid in black). Analysis with such reduced regularisation parameter shows that the same peak (green band in Figure 9.23 is present in the Mn-ruler $\mathbf{3}_1$ for analysis with (orange curve) and without (blue curve) harmonic overtone coefficients. However, also peaks at short and longer distances occur in both cases. The short distance peaks can be mostly removed by analysis including harmonic overtones, while the peaks at longer distances ($\sim 2.7 \text{ nm}$) remains.

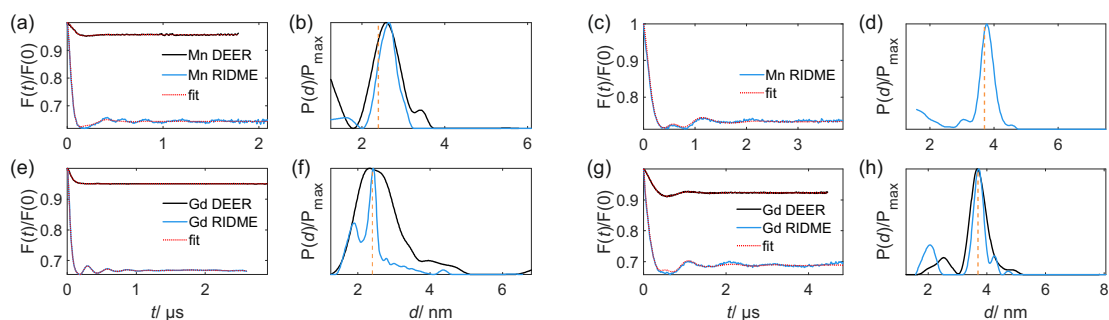


Figure 9.22. Distance measurements on M-DOTA-rulers $\mathbf{3}_n$. Black: Q-band DEER at 10 K; blue: W-band RIDME at 20 K. (a, b) Mn-ruler $\mathbf{3}_1$, $T_{\text{mix}} = 20 \mu\text{s}$, detected at 3rd hyperfine line; (c, d) Mn-ruler $\mathbf{3}_3$, $T_{\text{mix}} = 15 \mu\text{s}$, detected at 3rd hyperfine line; (e, f) Gd-ruler $\mathbf{3}_1$, $T_{\text{mix}} = 50 \mu\text{s}$, detected at maximum field; (g, h) Gd-ruler $\mathbf{3}_3$, $T_{\text{mix}} = 30 \mu\text{s}$, detected at maximum field. (a, c, e, g) Form factors in time domain and corresponding fits (red dashed lines), (b, d, f, h) resulting distance distributions. (b, d) $P_2 = 0.5$, $P_3 = 0.1$, (f) $P_2 = P_3 = 0$, (h) $P_2 = 0.40$, $P_3 = 0.09$.

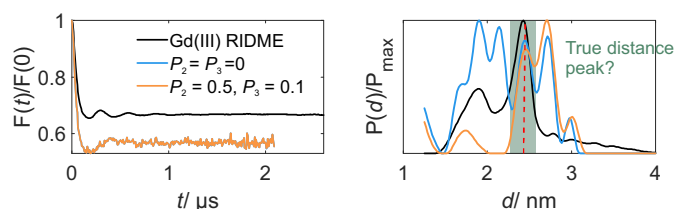


Figure 9.23. Distance contributions for the Mn-ruler $\mathbf{3}_1$ at 20 K, $T_{\text{mix}} = 70 \mu\text{s}$, detected on high-field shoulder of satellite transitions. Data analysis presented for $P_2 = P_3 = 0$ (blue), $P_2 = 0.5$, $P_3 = 0.1$ (orange) and reduced regularisation parameter compared to Figure 9.22. Corresponding Gd-ruler $\mathbf{3}_1$ at 20 K, $T_{\text{mix}} = 50 \mu\text{s}$, detected at maximum field is shown in black. The red dashed, line and grey band mark the expected peak.

Further, Figure 9.24 shows significant deviations in the RIDME data at different mixing times for the same compound (Mn-ruler $\mathbf{3}_1$). This behaviour remains when the measurement temperature or the detection position is modified (see Figure F.28). Potentially, these frequency variations are caused by higher harmonic overtones or by nuclear-electron spin type RIDME. They do not induce major changes in the resulting distance distributions with $P_2 = 0.5$, $P_3 = 0.1$, yet form factor fits can not reproduce the experimental features around 200 ns (see Figure F.28). To study these effects a better understanding of the molecular ruler geometry is needed.

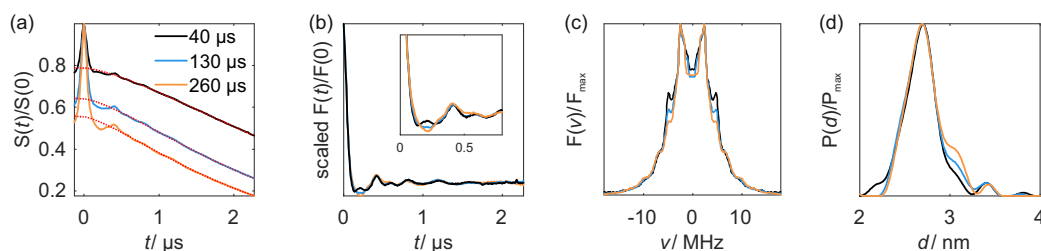


Figure 9.24. Influence of mixing time in W-band RIDME measurements on the Mn-ruler $\mathbf{3}_1$ at 10 K, detected at 3rd hyperfine line. (a) Raw data and corresponding background fits (red dashed lines), (b) form factors in time domain, (c) form factors in frequency domain, (d) resulting distance distributions with $P_2 = 0.5$, $P_3 = 0.1$. The inset in (b) shows a zoom of the presented form factors in the region from 0 to 800 ns.

In contrast, the longer Mn-DOTA-based ruler $\mathbf{3}_3$ is well-behaved and performs very similar to the Mn(II)-rulers based on PyMTA or PymiMTA and the data can be analyzed with the same set of overtone coefficients. Almost no changes can be observed by changing the mixing time or

measurement temperature, as shown in Figure 9.25 and Figures F.29 - F.31 in Appendix F. As for the Mn-PyMTA rulers, towards the low-field side of the EPR spectrum an additional shoulder can be observed. The distance distribution is most narrow when detected on the 3rd hyperfine line.

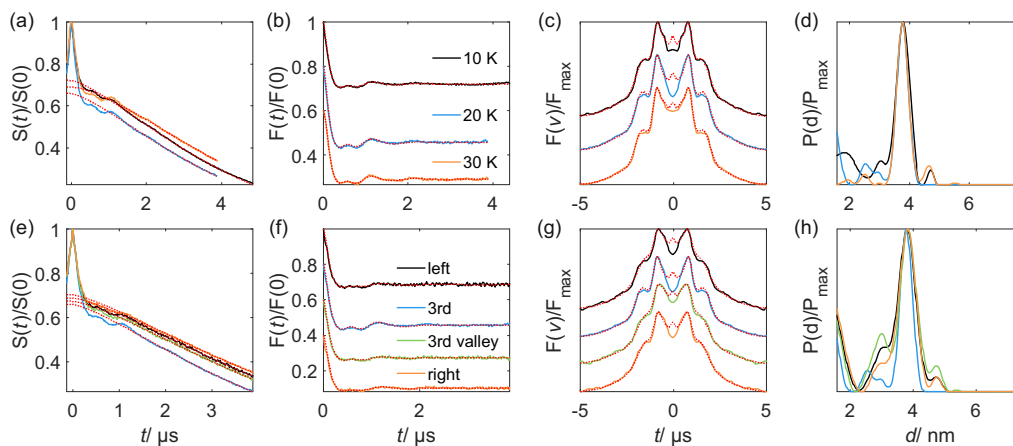


Figure 9.25. Influence of measurement temperature (a-d) and detection position (e-h) in W-band RIDME measurements on the Mn-ruler $\mathbf{3}_3$. (a-d) 3rd hyperfine line, $T_{\text{mix}} \sim T_1$; (e-h) 20 K, $T_{\text{mix}} = 34 \mu\text{s}$ at 3rd hyperfine line, else $T_{\text{mix}} = 20 \mu\text{s}$ (a, e) Raw data and corresponding background fits (red dashed lines), (b, f) form factors in time domain and corresponding fits (red dashed lines), (c, g) form factors in frequency domain and corresponding fits (red dashed lines), (d, h) resulting distance distributions with $P_2 = 0.5$ $P_3 = 0.1$.

In summary, DOTA-based rulers and Gd(III) as metal ion behave very similar to rulers with PyMTA or PymiMTA as ligands and the same set of overtone coefficients can be used in data analysis routines at least for distances above ~ 3 nm. For short distances a reduction of overtone coefficients is observed. In case of Mn(II), rulers of longer distance ($d \geq 3.4 \dots 3.7$ nm) seem to be well-behaved, however, severe deviations occur in the case of the short spin-spin distance ($d \sim 2.5$ nm). It is currently unclear if this is related to the geometry of the ruler itself or to a spectroscopic effect.

TAHA-ruler

To conclude the study of the influence of ligand field a Gd-TAHA based ruler $\mathbf{4}$ was investigated. The ZFS of Gd-TAHA ($\langle D \rangle_{\text{TAHA}} = 1361 \pm 69$) is about 10% larger than in Gd-PyMTA ($\langle D \rangle_{\text{PyMTA}} = 1213 \pm 60$) and in both cases broadly distributed ($\sigma_D \simeq \langle D \rangle / 3$).⁹⁵ DEER and RIDME experiments on this compound exhibit a very low modulation depth, which indicates incomplete loading or the presence of unbound Gd(III). From the sample preparation 80% of the molecular rulers are expected to contain two Gd(III) ions. Assuming a modulation depth of about ~ 0.7 for fully loaded ruler compounds based on measurement of Gd-ruler $\mathbf{1}_3$ (see Figure 9.4) a modulation depth on the order of 0.56 would be expected. In RIDME experiments, however, a maximal modulation of 0.13 was observed at 10 K in Q band, which is more than a factor of 4 smaller than the expectation. This indicates that loading of Gd(III) ions into the TAHA ligands is hindered and some unbound Gd(III) remains in solution.

Unfortunately, the obtained distance distributions exhibit a high level of artefacts and are rather broad, which makes precise determination of overtone coefficients difficult. The data suggest that the overtones extracted for PyMTA-based molecular rulers are too small. More symmetric distance distributions are obtained using somewhat higher harmonic overtones of

$P_2 = 0.45$ and $P_3 = 0.12$ (see Figure 9.26 and Supporting Information Figure F.33). The harmonic overtones appear to be stable with mixing time as presented in Figure F.32). Currently available measurements at field positions shifted away from the central line suffer from low signal-to-noise ratio and strong contribution of echo-crossing artefacts. For such traces no significant difference between different detection positions can be observed (see Figure F.32).

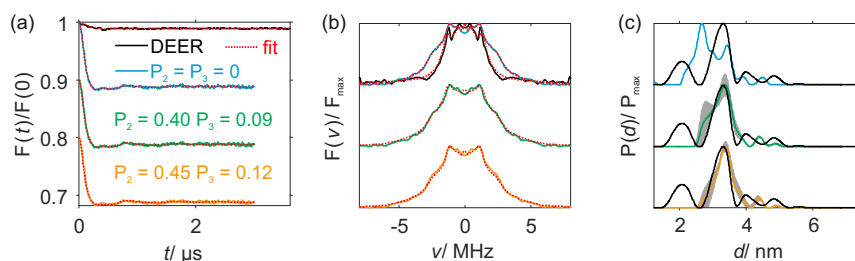


Figure 9.26. Comparison of Q-band DEER and W-band RIDME data for the Gd-ruler **4** at 10 K. $T_{\text{mix}} = 84 \mu\text{s}$. (a) Form factors in time domain and corresponding fits (red dashed lines), (b) form factors in frequency domain and corresponding fits (red dashed lines), (c) resulting distance distributions: top (blue lines) with $P_2 = P_3 = 0$; middle (green lines) $P_2 = 0.4$ $P_3 = 0.09$; bottom (orange lines) $P_2 = 0.45$ $P_3 = 0.12$. The grey error bands show a 20% variation of the overtone coefficients around the chosen values.

Interestingly, overtone coefficients found to generate symmetric distance distribution in the case of the Gd-TAHA ruler **4** ($P_2 = 0.45$ and $P_3 = 0.12$), reduce artefact contributions in cases where the coefficients calibrated for the central transition of the PyMTA-based ruler **1₃** ($P_2 = 0.4$ and $P_3 = 0.09$) were found to be somewhat underestimated (see Chapter 8), as shown in Figure F.35 for detection at the satellite transitions of the Gd-ruler **1₃** and larger spin-spin distances in the Gd-ruler **1₇**.

Due to the larger ZFS of Gd-TAHA complexes, distortions induced by level mixing for high-spin pairs with insufficient difference in the resonance offset between the different transitions should be smaller or potentially suppressed and such coefficients may represent time traces that do not contain or contain only small contributions from such effects, as they are present in the case of PyMTA, PymiMTA as well as DOTA ligand. From a methodological point of view, it would therefore be interesting to study molecular rulers with large, broadly distributed ZFS and well defined distance distributions to allow for careful calibration of such overtone coefficients if such model compounds can be synthesized with good loading efficiency. In such a study, careful calibrations of overtone coefficients for RIDME experiments on rulers with weaker ZFS, e.g. Gd-PyMTA, at larger spin-spin distance and detection at satellite transitions for smaller spin-spin distance could be added, so that potentially one set of overtone coefficients can be found for RIDME traces with no or only minor contributions from level mixing effects.

To summarize, the overtone coefficients calibrated for each central ion appear to be relatively stable with measurement temperature and mixing time. Moving the detection position to the satellite transitions introduces some changes, which might be reduced for spin probes with large ZFS complexes and long spin-spin distances. The precise determination of overtone coefficients at shifted detected position and different spin-spin distance should be studied once further model compounds are available.

However, it is promising that some uncertainty in the overtone coefficients does not lead to a breakdown of the proposed analysis approach. For narrow distance distributions, a 20% variation of overtone coefficients shifts artefact peaks from left to right with respect to the mean distance and they can thus be identified by following the peaks in a validation procedure as shown for

simulated data in Figure 9.27(e, f). For broad distributions (Figure 9.27(g, h)) the resulting shapes become mainly more asymmetric with only a small shift of the detected mean distance. However for such data, uncertainties in background removal may be equally large. Note that in Chapter 8 it was observed that a simultaneous mismatch of P_2 and P_3 in opposite direction can partially compensate each other and thus that the shape of the RIDME kernel function is most sensitive to the correct ratio of $P_1:P_2 + P_3$.

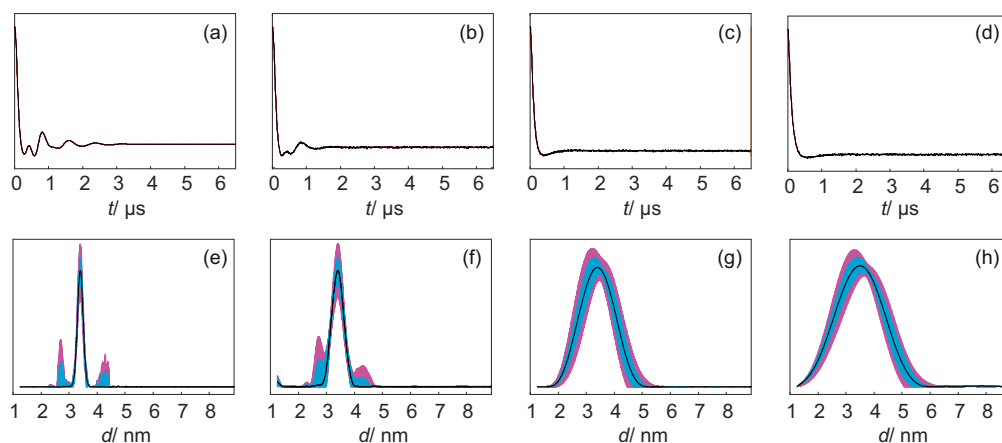


Figure 9.27. Influence of overtone deviations for simulated Gaussian distance distributions with $d_{\text{mean}} = 3.4$ nm and harmonic overtone contributions $P_2 = 0.5$, $P_3 = 0.1$. (a-d) Simulated form factors and (e-h) distance distributions. Blue bands mark deviations of overtone coefficients up to 10% and purple bands deviations up to 20%.

9.7. RIDME on proteins

Based on the promising results obtained with respect to overtone stability in molecular Gd-rulers, we now turn to RIDME measurements in spin-labelled protein mutants using commercially available Gd-maleimide-DOTA spin tags. Figure 9.28 shows a set of RIDME measurements for three different cysteine-mutants of a cysteine-free version of the polypyrimidine-tract binding (PTB) protein. As observed in the model compounds, the RIDME time traces contain harmonic overtone contributions, which seem to be stable with mixing time and measurement temperature (see also Figures F.37 - F.39). The modulation depths can be increased relative to DEER measurements depending on the mixing time. Distance distributions resulting from Tikhonov regularization with modified kernel functions and coefficients calibrated on Gd-PyMTA based molecular rulers ($P_2 = 0.4$, $P_3 = 0.09$) are similar to the ones obtained by earlier DEER measurements.¹⁹² Distance distributions from analysis with an overtone-free ($P_2 = P_3 = 0$) kernel, as well as a variation of overtone coefficients are shown in Appendix F.7, Figure F.36.

In case of the RNA-binding domains (RBD) RBD1 and RBD2, also known as RNA recognition motifs (RRMs), variations of the overtone coefficients by 20%, indicated by grey bands, do not decrease the asymmetry or width of the distance distributions. For RBD1 the resulting distance distribution is narrower than in the case of DEER and it is shifted towards shorter distance, which is in better agreement with simulated distance distributions using the Multiscale Modeling of Macromolecules (MMM) software²⁹¹ based on existing RBD structures.¹⁹² This might indicate level-mixing distortions⁴⁴ in the DEER data. However, the RIDME distance distributions for RBD2 with a slightly shorter mean distance are almost perfectly identical to the DEER distance

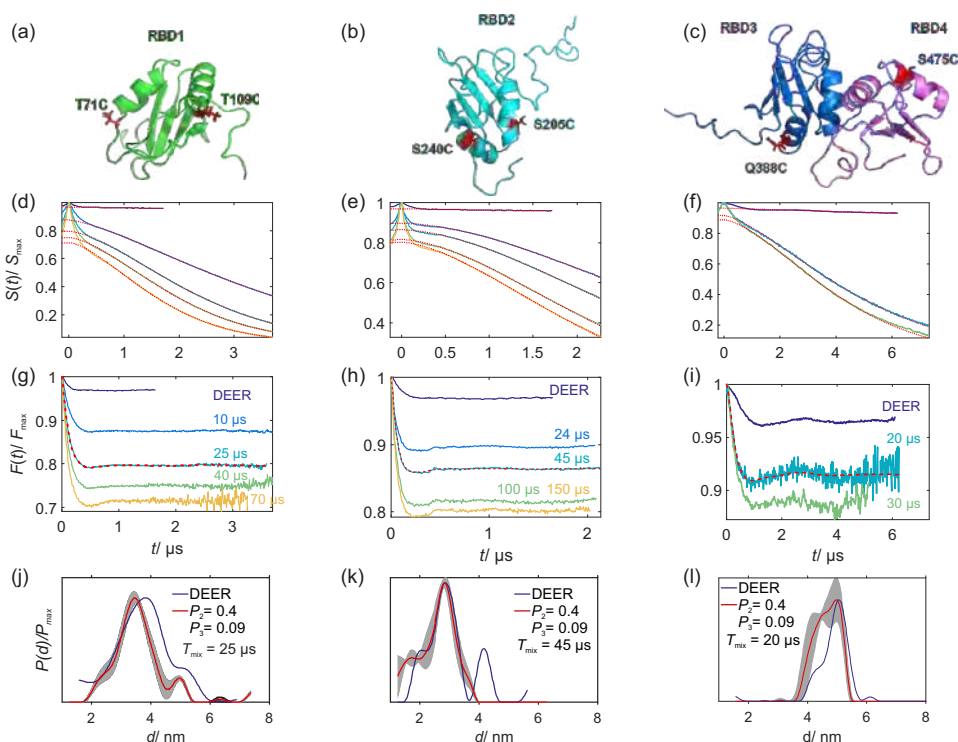


Figure 9.28. RIDME and DEER¹⁹² experiments on different protein double mutants (a-c). (d-f) RIDME raw data and corresponding background fits (red dashed lines); (g-i) background-corrected form factors, red dashed line: form factor fits corresponding to distance distributions in (j-l); (j-l) distance distributions, the grey bands mark a 20 % uncertainty in overtone coefficients. (a, d, g, j) T71C/ T109C in RBD1; (b, e, h, k) S240C/ S205C in RBD2; (c, f, i, l) Q388C/ S475C in RBD34.

distribution, apart from a missing long-distance peak centred at 4.2 nm, which is probably an artefact contribution. Hence, the difference between RIDME and DEER results for RBD1 is more likely related to uncertainty of background correction. As observed for molecular ruler compounds, a shift of the detection position increases the modulation depth as well as the contribution of harmonic overtones, the latter effect is however largely smeared out by the broad distance distribution (see Appendix F Figure F.38). Lastly, in RBD34, the RIDME distance distribution has a larger relative fraction of short distances as compared to the DEER measurement. This contribution can be reduced (see Appendix F Figure F.36), but never perfectly removed by higher harmonic overtones at the cost of introducing additional long distance peaks that are caused by overtone correction. This is in agreement with the imperfect correction of overtone coefficients observed for longer spin-spin distances in the Gd-PyMTA ruler **17**. Structure calculation predicts a mean distance of 4.5 nm, which would be in better agreement with the RIDME measurement. However, rotamer library predictions for this label may not be sufficiently accurate to draw a firm conclusion. The need of relatively long time traces in this distance range requires the use of relatively short mixing times. Thus, the modulation depth gain is no longer so striking as compared to DEER. Yet, the RIDME modulation depth in these experiments still exceeded the one in DEER by at least a factor of two. Further, difficulties in separation of inter- and intramolecular contributions start to occur, because at the required trace length, the background can not be well fitted by a single stretched exponential. This was observed earlier on a protein single mutant described in Chapter 5. Therefore, the measurement of long distances likely remains more reliable with the DEER technique. Results of further variation of experimental parameters

as measurement temperature or detection positions are shown in Appendix F.7, but no significant changes were observed.

In brief, the apparent consistency of the overtone coefficients for Gd-labelled protein mutants and model ruler compounds is promising and is a good step towards the application of the RIDME technique in structural biology, in particular for determining short spin-spin distances. However, the complicated background decay may remain the major obstacle towards routine applications for broad or long distance distributions, even if stable overtone coefficients can be confirmed.

9.8. Conclusions

Being a single-frequency technique, RIDME poses low technical requirements on spectrometer hardware. It provides the option to rather freely choose the detection position within the EPR spectrum and to work with resonators of narrower bandwidth, which allows choosing the highest EPR signal intensity position and the most sensitive detection in resonators with moderate quality factors. The RIDME technique provides high modulation depth for Mn(II) and Gd(III) chelate complexes that are promising as alternatives to the more commonly used nitroxide-based spin labels. Sensitivity enhancement in RIDME can be achieved by population transfer for both these metals using linear chirp pulses. For the systems investigated in this chapter Gd-complexes appeared to be more reliable in terms of overtone coefficient stability, and might therefore be preferable as spin tags. However, Mn(II) is a good substitute for Mg(II) in paramagnetic metal-ion substitutions approaches as demonstrated in the next chapter.

RIDME performed on biological systems showed promising results towards an application in structural biology. It confirms larger modulation depths and in some cases narrower distance distributions than the DEER experiment if harmonic overtones are considered in data analysis routines. A drawback is the steep background decay due to spectral diffusion processes, which limits the detectable trace length or at least the modulation depth on account of shorter mixing times T_{mix} . The effect is particularly strong in protonated environments, where it proved beneficial to move the detection position to satellite transitions. Therefore, whenever possible, solvent deuteration should be performed for RIDME-based distance measurements. Another problem that can occur for deuterated solvents and long time traces is the shape of the RIDME background itself that is no longer fit by a single stretched exponential as discussed in Chapter 5. The problem can be circumvented by cutting the time trace, as for instance in the RIDME measurements in RBD34, however, it strongly limits the detectable trace length and thus the distance range. For well-resolved dipolar frequency oscillations, it may be possible to fit more complicated background shapes, e.g. a polynomial or a double stretched-exponential, but such an approach will introduce major uncertainties or even fail when applied to samples with broad intramolecular distance distributions. The strong dependence of the RIDME background on the electron spin environment also makes the detection of a reference background for the corresponding single mutants more difficult. For that reason the benefits of the RIDME compared to the DEER technique diminish at longer spin-spin distances ($\simeq 5\text{-}6$ nm), unless reliable background models can be found in certain experimental conditions. On the other hand, the strong dependence of the RIDME background on the coupling to protons may provide another source of information, e.g. for the study of local or mid-range surrounding of spin labels in mono-radicals.

The contribution of overtone coefficients appears to be relatively stable for Gd(III) as metal ion in protonated and deuterated glasses. For complexes with relatively small ZFS

($\langle D \rangle_{\text{Gd-DOTA}} = 714 \pm 43$ MHz, $\langle D \rangle_{\text{Gd-PyMTA}} = 1213 \pm 60$ MHz) and detection at the central transition, the set of overtone coefficients $P_2 = 0.40$, $P_3 = 0.09$ (no large deviations were observed for $P_3 = 0.1$) appears to be suitable for distance analysis in the range of $\simeq 3$ to 6 nm in molecular rulers as well as proteins. For longer spin-spin distances, this set of coefficients may slightly under-correct the harmonic overtone contributions. In all cases, a variation of the overtone coefficients in the order of 20% should be included in the data analysis to test if a lower level of artefacts emerge from a different set of overtone coefficients. Prior to data analysis including harmonic overtones, the maximal detectable distances should always be estimated by $P_2 = P_3 = 0$. If longer distance peaks appear upon inclusion of harmonic overtones, this strongly points to an over-correction. Such an approach will also help to identify distance peaks stemming from higher frequency overtones, which should be reduced or ideally disappear without creating new peaks at longer distances upon inclusion of harmonic overtones - in reality some artefact contributions have been observed to remain.

For Gd-DOTA and Gd-PyMTA by moving the detection position away from the central transition or at any detection position for the Gd-TAHA complex with larger ZFS ($\langle D \rangle_{\text{Gd-TAHA}} = 1361 \pm 69$ MHz, spin-spin distance of 3.4 nm) an increase in overtone coefficients is observed. The change with detection position is particularly pronounced at short spin-spin distances (< 3 nm), e.g. approximately overtone-free time traces are observed at the central transition of the Gd-PyMTA ruler **1**₁ with a spin-spin distance of 2.1 nm. The larger overtone-coefficients in such cases may represent dipolar evolution traces with negligible or no contributions of level mixing effects. The precise determination of overtone coefficients for such data still needs to be investigated for several spin-spin distances at different detected positions, considering small ZFS (e.g. Gd-PyMTA and Gd-DOTA) and ideally also large ZFS complexes. Synthesis of such model compounds is in progress. Potentially, detection on the outermost Gd(III) transitions may help to circumvent the need for precise calibration of overtone coefficients for a range of short spin-spin distances, which might also vary with the strength of ZFS for different Gd(III) complexes.

It is promising that some uncertainty in the overtone coefficients does not lead to a breakdown of the proposed analysis approach. For narrow distance distributions small artefact peaks may be introduced beyond the level of typical noise artefacts, while for broad distributions the resulting shapes would be overly asymmetric assuming that the deviations do not exceed approximately 20%. In the end, assuming that the primary dipolar frequency is always present up to at least 30% and no other harmonic overtone frequency is strongly dominating, the RIDME technique may be at least used to estimate the upper distance limit using $P_2 = P_3 = 0$.

In most cases of Mn-Mn RIDME measurements, form factors were found to be relatively stable for different mixing times and measurement temperatures. The overtone coefficients $P_2 = 0.5$ and $P_3 = 0.09/0.1$ were used in data analysis routines of all compounds. This is in agreement with overtone coefficients proposed in literature for a different type of Mn-DOTA ruler: $P_1 = 0.5$; $P_2 = 0.5$; $P_3 = 0.0$ or $P_1 = 0.425$; $P_2 = 0.425$; $P_3 = 0.15$ were found to work well depending on microwave frequency and mixing time.¹⁷⁸ In some cases, dipolar evolution traces detected at the low field side of the spectrum contained additional short-distance shoulders or peaks that did not clearly relate to harmonic overtone contributions. For the Mn-ruler **3**₁ (ligand = DOTA) based on the DOTA complex (spin-spin distance ~ 2.5 nm), deviations were observed, which may however be related to ambiguous ligation.

The values for the dipolar frequency overtone coefficients presented here are expected to be applicable for Q- and W-band RIDME measurements. It is possible that the same coefficients are valid at other frequencies, but this should be established experimentally.

On a final note, it is important to keep in mind that RIDME measurements, in particular at low mw frequencies, are sensitive to ESEEM modulations that can contribute additional distance peaks as described in Chapter 6.

EPR Spectroscopy of Mn²⁺-Substituted ATP-Fuelled Protein Engines

This last chapter, demonstrates the applicability of EPR techniques to ATP-fuelled motor proteins by paramagnetic metal ion substitution. Paramagnetic metal ions deliver structural information both in EPR and solid-state NMR experiments, offering a profitable synergetic approach to study bio-macromolecules. The chapter investigates the spectral consequences of Mg²⁺/ Mn²⁺ substitution and the resulting information contents for two different ATP:Mg²⁺-fuelled protein engines, a DnaB helicase from *Helicobacter pylori* active in the bacterial replisome, and the ABC transporter BmrA, a bacterial efflux pump. It is shown that EPR can report on metal binding and can provide information on the geometry of the metal centres in the proteins. This work was published as part of Ref.²²³, where in addition paramagnetic relaxation enhancements identified in the NMR spectra could be used to localize residues at the binding site. Protein engines are ubiquitous and the methods described herein should be applicable in a broad context.

This chapter was published as part of Ref.²²³ and Ref.¹: 'Thomas Wiegand, Denis Lacabanne, Katharina Keller, Riccardo Cadalbert, Lauriane Lecoq, Maxim Yulikov, Laurent Terradot, Gunnar Jeschke, Beat H. Meier and Anja Böckmann: Solid-state NMR and EPR Spectroscopy of Mn²⁺-Substituted ATP Fueled Protein Engines, *Angew. Chem. Int. Ed.* 2017, 56, 3369–3373' and 'Katharina Keller, Thomas Wiegand, Riccardo Cadalbert, Beat H. Meier, Anja Böckmann, Gunnar Jeschke, and Maxim Yulikov: High-spin Metal Centres in Dipolar EPR Spectroscopy, *CHIMIA* 2018, 72, 216–220'. Both publications are combined and edited for consistent presentation.

R. Cadalbert prepared the *HpDnaB* samples and D. Lacabanne the BmrA samples. The EPR measurements presented here were performed by K. Keller. T. Wiegand and D. Lacabanne performed the NMR measurements (data not shown). L. Terradot developed the homology model.

10.1. Introduction

Nucleotide binding domains (NBDs) are part of multipurpose engines which convert the chemical energy released on nucleoside triphosphate hydrolysis into mechanical movement or switching. They are found in a set of proteins for which conformational change and molecular motion is needed for function,^{292;293} with adenosine triphosphate (ATP) being a common fuel for these engines. We herein inquire what information on ATP binding to NBDs can be obtained from EPR spectroscopy when Mg²⁺ as a cofactor of ATP hydrolysis is replaced by Mn²⁺. For this investigation, we focus on a helicase (*HpDnaB*)²⁹⁴ and an ABC transporter (BmrA)²⁹⁵ as two proteins whose functions rely on NBDs,²⁹⁶ but with nucleotide-binding dissociation constants

(K_d) differing by roughly two orders of magnitude.^{297–299} In Ref.²²³ we combined this work with complementary information from paramagnetic solid-state NMR,^{300–303} for which we only report the key findings here.

For ATP hydrolysis, which provides the energy source for the engine, the NBDs require a divalent metal ion, typically Mg^{2+} , as cofactor. Both proteins show multiple ATP binding sites: 6 (12) for *HpDnaB*, and two for *BmrA*. Each domain contains conserved structured motifs, such as Walker A and Walker B motifs,³⁰⁴ the latter containing an aspartate that coordinates Mg^{2+} . While in the helicase the NBDs maintain contact throughout the functional cycle, they are spatially separated in the ABC transporter *BmrA* in the open conformation and assemble to bind and hydrolyse ATP:Mg^{2+} . To mimic nucleotide-bound states, poorly hydrolysable analogues can be used, such as adenylyl imidodiphosphate (AMP-PNP), which binds with high affinity to *HpDnaB*.^{294;305} The dissociation constants of *BmrA*-nucleotide complexes in the absence of substrate²⁹⁹ are larger than the ones of *DnaB*^{297;298} and large amounts of AMP-PNP/metal would be needed for the preparation of samples showing high occupancy of the binding sites, thus we used $\text{ATP:Mg}^{2+}:\text{VO}_4^{3-}$ instead. After ATP hydrolysis in the presence of vanadate, the NBDs are expected to remain blocked in an $\text{ADP:Mg}^{2+}:\text{VO}_4^{3-}$ bound state, with the VO_4^{3-} ion mimicking the γ -phosphate of ATP.³⁰⁶

The characterization of the interaction between ATP and the NBDs is essential for understanding the functioning of such ATP-fuelled proteins. By substituting the diamagnetic Mg^{2+} by paramagnetic Mn^{2+} , the binding sites become EPR observable^{221;307} and a distance-dependent paramagnetic relaxation enhancement (PRE) is induced for the NMR resonances.^{222;308–311} This provides contrast between the binding site and the part of the system remote from it. Owing to the similar coordination behaviour, charge, and ionic radius of Mg^{2+} and Mn^{2+} ions, most often the function is retained.^{223;312}

We added Mn^{2+} and ATP analogues to the two proteins to demonstrate the effects of nucleotide: Mn^{2+} binding on NMR (data not shown) and EPR spectra. This approach allows the occupation of nucleotide binding sites to be determined, to probe the geometry of the multimeric assemblies, as well as to identify the residues in the neighbourhood of Mn^{2+} . In this chapter, we describe first how metal binding can be followed by changes in the EPR lineshape and electronic relaxation measurements. Second, we discuss Mn^{2+} - Mn^{2+} distance measurements on such samples. Details on sample preparation and EPR experiments can be found in the Appendix G.1.

10.2. Monitoring metal binding

EPR spectroscopy allows to monitor the binding of Mn^{2+} to the NBD. Figure 10.1(a) shows the room-temperature X-band CW spectra of the *HpDnaB*:AMP-PNP: Mn^{2+} complex in solution, as well as of AMP-PNP: Mn^{2+} and MnCl_2 solutions as reference. The spectrum of the MnCl_2 solution consists of a resolved sextet for the $| -1/2, m_I \rangle \leftrightarrow | 1/2, m_I \rangle$ transitions arising from the electron-⁵⁵Mn hyperfine splitting, as expected for the fast tumbling high-spin Mn^{2+} hexaaquo complex ($S = 5/2$ and $I = 5/2$). Coordination of Mn^{2+} to AMP-PNP induces a pronounced change in the lineshape that is related to a longer rotational correlation time of the larger complex with lower symmetry inducing an anisotropic broadening of the six hyperfine lines. The change in zero-field splitting (ZFS) leads to additional spectral features. Addition of *HpDnaB* (1:12 Mn^{2+} :*HpDnaB* monomer ratio) causes a further change of the spectrum by even stronger prolongation of the rotational correlation time as well as by changes in the ZFS due to a different

ligand field. The change in ZFS is also observed in the echo-detected EPR spectra of glassy frozen solutions (Figure 10.1(b)) as the width of the outer envelope of the Mn^{2+} spectra scales with the strength of the ZFS. The observed spectrum indicates quantitative formation of the nucleotide metal complex for the case of a 1:12 Mn^{2+} :*HpDnaB* monomer ratio. The complex with 1:1 Mn^{2+} :*HpDnaB* monomer shows CW spectra (Figure G.1(a)) with additional contributions from NBD-unbound Mn^{2+} :AMP-PNP, which is further quantified below by relaxation measurements.

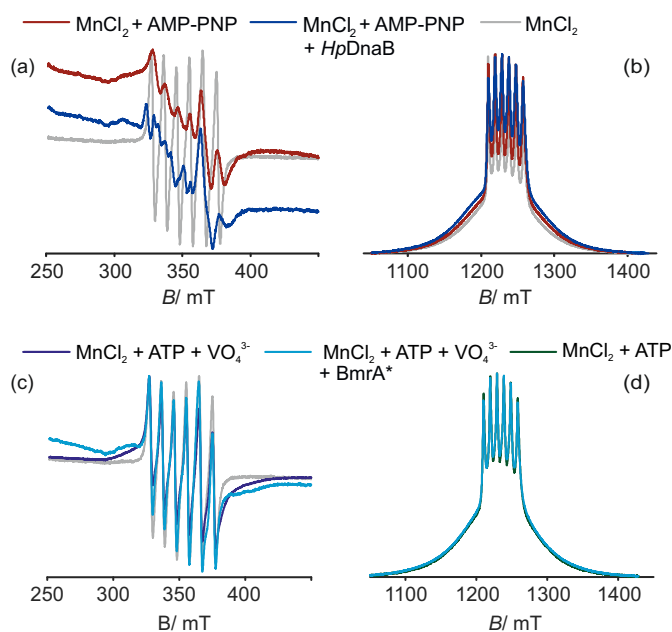


Figure 10.1. (a, c) Room-temperature X-band CW and (b, d) Q-band echo-detected (ED) EPR spectra at (b) 20 K and (d) 10 K. (a, b) AMP-PNP: Mn^{2+} (red) and *HpDnaB*:AMP-PNP: Mn^{2+} solution (dark blue, *HpDnaB*: Mn 12:1 in (a) and 1:1 in (b)). (c, d) ADP: Mn^{2+} : VO_4^{3+} (purple) and *BmrA*:ADP: Mn : VO_4^{3+} * (light blue). *Note deviations in sample preparations for pulsed and CW EPR experiments as detailed in Appendix G.1. Mn^{2+} reference solution in grey.

To study the effects of Mn^{2+} for a protein which shows lower nucleotide binding constants, we investigated the ABC transporter *BmrA*, for which a larger excess of Mn^{2+} compared to a *BmrA* monomer is used to obtain quantitative binding (300-fold excess to protein monomer compared to 5-fold in *HpDnaB*). The CW EPR lineshape of the ADP: Mn^{2+} : VO_4^{3+} complex (Figure 10.1(c)) varies from the AMP-PNP: Mn^{2+} complex, indicating a different coordination geometry of the Mn^{2+} ion. Upon addition of *BmrA* protein (300 fold excess and consequent washing after incubation as detailed in Appendix G.1) a broader feature in the spectrum can be observed, which suggests that a fraction of Mn^{2+} ions is bound. Samples for pulsed EPR measurements were prepared without the washing step to ensure occupation of the binding site. The EDEPR spectra detected at 10 K reveal only minor changes between the ATP: MnCl_2 reference solution and the protein sample, indicating that a large fraction of Mn^{2+} remained unbound.

Protein binding can be further quantified by relaxation measurements. The presence of several paramagnetic metal centres in close vicinity of each other in the *DnaB* multimer, and the use of a protonated protein and deuterated buffer lead to a strong difference in the transverse relaxation behaviour for the Mn^{2+} centres bound to NBDs as compared to Mn^{2+} coordinated to AMP-PNP in deuterated solution (Figure 10.2(a)). The main contribution to this difference is spin diffusion of protons that are more abundant near the protein metal binding sites. This

spin diffusion causes a stronger stochastic fluctuation of the local hyperfine field at the electron spin for bound Mn^{2+} ions compared to free ones. Assuming that not all Mn^{2+} ions are bound to the protein, the electron spin echo decay would be a superposition of the contribution from protein-bound Mn^{2+} as well as solvent-exposed Mn^{2+} . Indeed, the transverse relaxation curve shows a fast initial decay, dominated by the bound species, and a slower decaying tail stemming from the unbound species. Using the Mn^{2+} :AMP-PNP echo decay as a reference for the slowly relaxing species, we can remove the contribution of the solvent-exposed Mn^{2+} by dividing the two time traces under the assumption that the relaxation pathway for the protein-bound species is independent of all other channels, and that the total relaxation rate is a sum of the rates of all relaxation pathways, i.e. relaxation processes are uncorrelated.^{104;223;313} The division trace (Figure 10.2(b)) reveals the fast component of the protein-bound relaxation pathway added to an approximately constant contribution resulting for the unbound relaxation pathway. That the contribution from unbound species is not constant might be related to additional intermolecular interactions as well as to correlation between relaxation processes. The crossing point rather accurately marks the relative fraction of bound to unbound species, which is in the presented case about 3 to 2. This leads to a K_d value in the order of 10^{-5} M^{223} that is in agreement with published values for similar proteins.^{297;298}

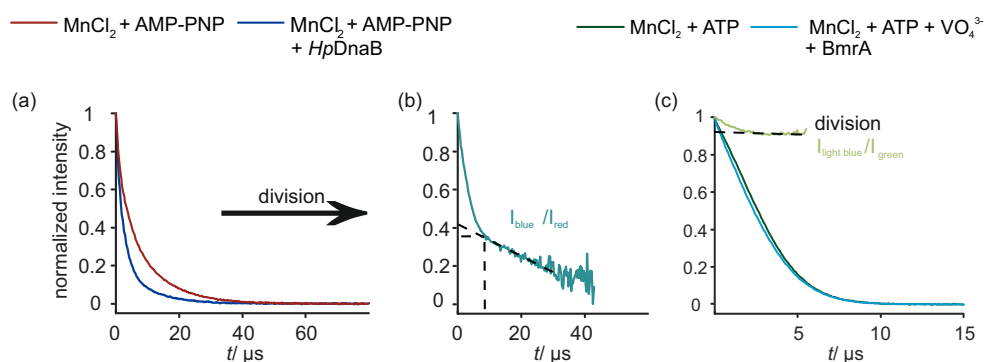


Figure 10.2. Hahn-echo decay traces in Q band. (a) AMP-PNP: Mn^{2+} (red) and *HpDnaB*:AMP-PNP: Mn^{2+} (dark blue, *HpDnaB*: Mn 1:1) at 20 K. (b) Division of the normalized decaying functions of *HpDnaB*:AMP-PNP: Mn^{2+} (dark blue) by AMP-PNP: Mn^{2+} (red) from (a). (c) *BmrA*:ADP: Mn : VO_4^{3-} (light blue), ATP: MnCl_2 reference solution (green) and division (light green).

For *BmrA*, a detailed analysis is hampered by the unknown Mn^{2+} excess resulting from sedimentation and buffer replacement (see Appendix G.1). Nevertheless, relaxation measurements can indicate that about 8% of Mn^{2+} ions in the sample are bound to the *BmrA* protein (Figure 10.2(c)).

10.3. Information on geometric assemblies

Spin-spin distance distributions can be obtained, for example from DEER or RIDME measurements as described in Chapter 2.5.5 and demonstrated for Cu^{2+} , Mn^{2+} and Gd^{3+} compounds in the preceding chapters. In this section we demonstrate the application of UWB-DEER to the two ATP: Mg^{2+} -fuelled protein engines, in which Mg^{2+} is substituted by Mn^{2+} . RIDME is applied to the *HpDnaB* protein complex.

For the *HpDnaB* protein complex, even for deuterated *DnaB* samples used to measure dipole-dipole interactions, the relaxation of Mn^{2+} ions bound to NBDs is faster than in the free

state (Figure G.2(a)). For the case of incomplete binding, this leads to a very small modulation depth in the DEER experiment. The modulation depth is further reduced due to the broad EPR spectra of Mn^{2+} ions (Figure 10.1(b)). Therefore the distribution of the Mn^{2+} - Mn^{2+} distances was determined by double electron electron resonance (DEER) with broadband chirp pump pulses (see Appendix G.1) to obtain a measurable dipolar modulation depth in spite of the large width of the Mn^{2+} EPR spectrum.^{115;174;268;314} To reduce contributions from the unbound Mn^{2+} , distance distributions were detected in the second valley of the hyperfine sextet.

Figure 10.3(b) shows the DEER form factor trace obtained as a sum of two measurements on the *HpDnaB*:AMP-PNP: Mn^{2+} sample (see Appendix G.3 and Figure G.3 for a detailed description), and Figure 10.3(c) shows the resulting distance distribution obtained by Tikhonov regularization analysis.⁷⁸ Distances of 3 nm and, with lower significance, of 5 - 6 nm are found, showing that the (double-)hexameric assembly in *HpDnaB* (see inset Figure 10.3(b)) is conserved, with slight deviations from the homology model based on the *AaDnaB*:ADP: Mg^{2+} complex³¹⁵ being expected. Peaks in the range between 3.4 and 4 nm are less significant and may be related to flexibility or to unspecifically bound Mn^{2+} . At least a full dipolar oscillation needs to be detected to extract the corresponding distances (see colour coding in Figure 10.3(c, g, i)). Thus, distances larger than 7 nm are not accessible from the data presented.²²³ Owing to the low inversion efficiency of even the ultra-wideband pump pulses, multispin contributions in the multimeric assembly^{316;317} are not expected in our case.

Even with the use of wideband pump pulses only a low inversion efficiency of about 1.5% could be achieved (see Figure 10.3(b)). Therefore, we investigated if the use of the RIDME sequence can improve the inversion efficiency. RIDME data were acquired in W band (94 GHz) due to the stronger appearance of electron spin echo envelope modulations in the RIDME experiment in Q band (34 GHz).^{79;180;318} The resulting time trace is shown in Figure 10.3(d). After background correction, the depth of dipolar modulation amounts to about 6% for a mixing time of $\sim 0.8T_1$ considering that the first sharp initial decay is attributed to an artefact peak (Figure 10.3(e)). Larger modulation depth might be possible with longer mixing times. The time trace is about four times shorter than the UWB-DEER time traces, since longer RIDME traces exhibited strong artefact peaks. For shorter time traces the modulation depth is expected to increase also for DEER measurements (see Figure G.2(b)), however, an increase by a factor of 4 or more is unlikely. Processing of the data with the standard data analysis routine leads to the observation of two distinct peaks around 2.4 and 3 nm in Figure 10.3(f), black curve. This corresponds exactly to a primary dipolar frequency ω_{dd} of a 3 nm distance as well as its first harmonic overtone $2\omega_{\text{dd}}$, that is typically observed in high-spin RIDME experiments. If the modified kernel function as described in the proceeding Chapters 8, 9 with coefficients $P_2 = 0.5$, $P_3 = 0.1$ - as calibrated for Mn^{2+} ruler compounds in Section 9 - is used for data processing, a relatively clean distance distribution (Figure 10.3(f), cyan curve) is obtained in agreement with the DEER data presented above. Yet, for the currently available trace length, we cannot detect distances longer than 4 nm. It is promising that the RIDME overtone coefficients are similar for *DnaB* and for earlier published Mn^{2+} - Mn^{2+} model compounds^{93;178} and the RIDME traces presented in the previous Chapter 9. However, more examples are required to ascertain that the calibrated overtone coefficients are generally applicable. Furthermore, it is necessary to reduce artefacts in RIDME - one strategy may be to use pre-polarized sequences and thus selectively increase the signal intensity for the detected refocused virtual echo compared to the Hahn-echo of the last two pulses (see Figure 9.9 in Chapter 9.4). Such a setup was not implemented in W band at the time of these measurements.

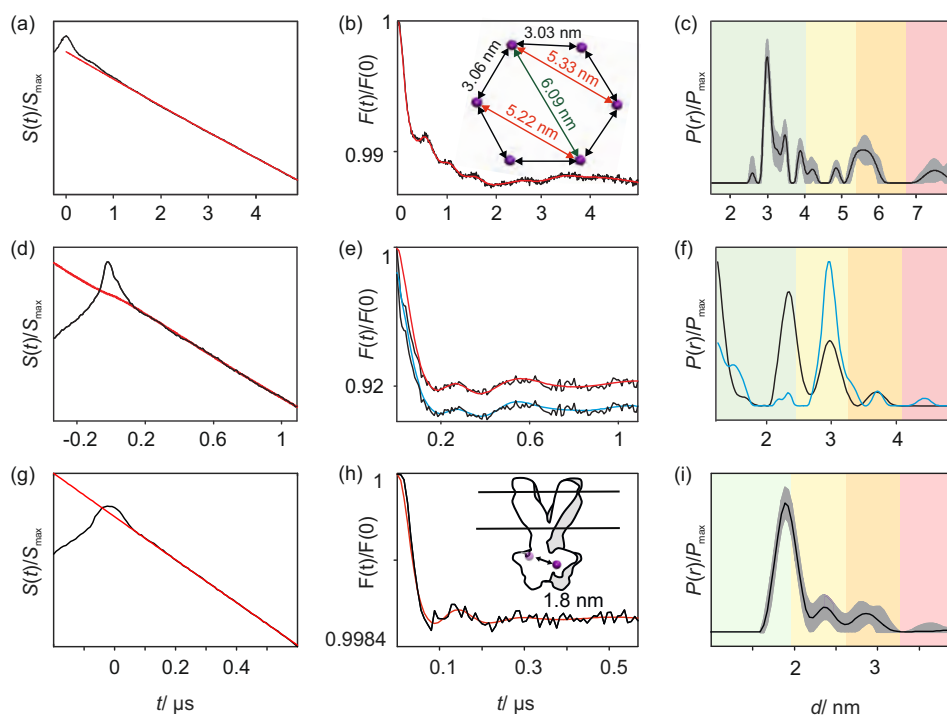


Figure 10.3. Data obtained from (a-c, g-i) DEER, (d-f) RIDME measurements on (a-f) a *HpDnaB*:AMP-PNP: Mn^{2+} system and (g-i) a *BmrA*:ADP:Mn: VO_4^{3-} system. (a, d, g) Primary data and background fit (red line), (b, e, h) background-corrected form factors (black lines) and corresponding fit (coloured lines), (c, f, i) resulting distance distributions. The colour-coding indicates reliability ranges resulting from the limited length of the dipolar evolution trace. Pale green: Shape of distance distribution is reliable. Pale yellow: Mean distance and width are reliable. Pale orange: Mean distance is reliable. Pale red: Long-range distance contributions may be detectable, but cannot be quantified. (b) The inset shows the model obtained by homology for DnaB. (e) Red: fit using an overtone-free kernel, blue: fit using overtone-containing kernel with $P_2 = 0.5$ and $P_3 = 0.1$. (f) Black: using the overtone-free kernel, blue: using an overtone-containing kernel with $P_2 = 0.5$ and $P_3 = 0.1$. (h) The inset shows the model obtained by homology for BmrA. (c, i) The shaded areas give an error estimate of the distance distribution from a validation procedure.

Mn^{2+} - Mn^{2+} distance distributions in *BmrA*:ADP: Mn^{2+} : VO_4^{3-} could be determined by DEER experiments in combination with broadband inversion pulses. Yet, the modulation depths was very low caused by the larger amount of free Mn^{2+} (see Figures 10.3(g-i) and for details Appendix G.3). The resulting distance distribution has a maximum at about 1.9 nm, which is in agreement with the Mn^{2+} - Mn^{2+} distances in the homology model of *BmrA*:ADP: Mn^{2+} : VO_4^{3-} representing the closed form (1.8 nm) of the protein assembly. RIDME experiments were omitted for this sample due to its susceptibility to echo-crossing artefacts, in particular in the presence of unbound Mn^{2+} , giving rise to artefact peaks in exactly the same distance region.

Complementary, the measurement of paramagnetic relaxation enhancements (PREs) in solid-state NMR spectra allows identifying residues close to the binding site unambiguously as described in detail in Ref. ²²³. The radius of view is about 15 Å. This is in contrast to chemical shift perturbations that cannot distinguish direct and allosteric effects. For *BmrA*, additional unspecific binding to solvent-exposed side-chains was observed due to the higher Mn^{2+} concentrations. They act, however, in a smaller radius of a few Å and do not hinder the characterization of the binding site. The combination of both techniques shows the high benefit of combining different techniques to obtain deeper insights in the systems under investigation. ²²³

10.4. Conclusions

In summary, we have demonstrated on two examples that NBD engines in proteins can be investigated by the exchange of diamagnetic Mg^{2+} with paramagnetic Mn^{2+} . No tagging is necessary, and there is no distribution of metal positions, unlike with flexible tags. Pulsed EPR methods, in particular ultrawideband DEER, allow for the evaluation of distances between paramagnetic centers in the multimers. First results obtained from the RIDME techniques are promising with contributions from harmonic overtones as observed previously in molecular ruler systems. The measurement of PREs in solid-state NMR spectra localizes residues close to the binding site. The radius of view is on the order of 15 Å for residue identification and on the order of 20 - 65 Å for assembly geometry. The spectroscopic approaches described herein should be generally applicable to the study of the many proteins with ATP-fuelled engines, and a combination of EPR and NMR approaches allows deeper insights in the mechanisms powering these machines, and also in the remote conformational changes driven by the engines. Such integrative approaches, that may include other complementary methods, are thus valuable in structural biology.

Conclusions & Outlook

A combination of site-directed spin labelling with EPR-based distance measurements has become a powerful tool in structural biology and site-to-site distances up to 16 nm have been accessed.²¹⁶ Currently, the most common approach employs nitroxide spin labels,^{16;17;20} while over the last years also other types of spin labels, such as metal ions,^{20;26;237;238;267;268} as well as trityl radicals^{270–273} have been examined with greater attention.

This thesis contributes to that development by investigating the suitability of a large set of paramagnetic metal chelates for pulsed dipolar spectroscopy (PDS) experiments. The selection of a particular complex for PDS was found to depend on several factors and should be considered individually for each particular type of PDS experiment. For example, spin 1/2 systems alleviate some problems occurring in high-spin systems as distortions of distance distributions by level mixing⁴⁴ or harmonic overtones,⁷³ yet, high-spin centres exhibit higher sensitivity at high fields. What is the 'best' spin tag also depends on the spin-spin distances or on geometric considerations.

Zero-field splitting (ZFS) parameters are known to influence several spectroscopic effects, such as distortions of the Gd(III)-Gd(III) distance distributions by level mixing⁴⁴ or echo reduction.^{104;110} An understanding of these effects requires determination of the ZFS parameters of the Gd(III) complex(es) in use. The current state of quantum chemistry calculations does not allow for the prediction of the ZFS parameters of Gd(III) complexes with a sufficient precision¹³³ and determination of these parameters through fitting of the EPR spectra is currently the most accurate way of obtaining such values. In this thesis the model proposed by Raitsimring *et al.*,¹³⁴ with the addition of an allowance for asymmetry of the bimodal D distribution, appeared to provide the most adequate description of ZFS distributions for Gd(III) complexes in frozen glassy solutions. These data allowed for development of a superposition model to predict ZFS parameters, which may be useful in predicting the strength of ZFS for Gd(III) complexes, e.g. based on optimized geometry calculations, and, thus, may help to design tailored Gd(III) complexes prior to any synthesis efforts. All fitting routines and simulated libraries were made available at www.epr.ethz.ch/software.

However, the large width of the EPR spectra of metal centres calls for the development of broadband methods. The RIDME technique with virtual infinite bandwidth for spin inversion meets exactly this requirement, while posing low technical requirements on the spectrometer hardware. As a single-frequency technique it also allows choosing the detection position freely within the EPR spectrum and the most sensitive detection position within the resonators.

Consequently, the RIDME technique was found to provide high modulation depth and good sensitivity for Cu(II), Mn(II) and Gd(III) chelate complexes. The experiment appeared to be characterized by a trade-off between signal intensity and modulation depth depending on the length

of the mixing block that also influences the background decay. A simple two-point optimization experiment was proposed as a good estimate to assess the mixing time of highest sensitivity. Further, sensitivity enhancement was demonstrated in RIDME experiments on high-spin metal centres based on polarization transfer from satellite transitions to the central transition using broadband linear frequency-swept pulses. Orientation selection was confirmed to be reduced in RIDME compared to DEER experiments on molecular Cu(II) rulers - the remaining contribution being related to the excited tensor orientations from the observer pulses. The following difficulties that hinder routine use of this technique in structural biology and beyond were addressed:

(i) The RIDME background: analytical equations for the RIDME background describe the key trends observed in experimental RIDME traces and allow for understanding the most important practical aspects of intermolecular RIDME background measurements. However, the steepness of the background decay due to spectral diffusion processes remains a drawback of the technique and limits the detectable trace length. The strong dependence of the RIDME background on the electron spin environment also makes the detection of a reference background as means for background correction more difficult. For that reasons the benefits of the RIDME compared to the DEER technique diminish at longer spin-spin distances ($\sim 5\text{-}6$ nm), unless reliable background models can be found in certain experimental conditions. On the other hand, the observed proton-driven electron spectral diffusion appears to be very interesting for elucidation of some steps in polarization transfer from electron spins to the nuclear spin bath, which would be valuable information for low-temperature DNP techniques. Further, proton-driven spectral diffusion processes might be utilized to construct a new RIDME-based approach for singly labelled proteins in the studies of local or mid-range surrounding of spin labels.

(ii) ESEEM modulations: an averaging procedure was developed for RIDME-based distance measurements with improved signal-to-noise ratio as compared to previously suggested ESEEM removal schemes.^{67;179;180} However, due to the incomplete nuclear modulation averaging, suppression of ESEEM frequencies is not sufficient for large ESEEM modulation depths, i.e. ^2D ESEEM in X band. In such cases, combination with long transverse evolution intervals¹⁹⁸ may be shown in the future to further reduce ESEEM peaks, however, again at the cost of signal intensity.

(iii) The occurrence of multiples of the dipolar frequency in the dipolar signal of high-spin systems can be included in the data analysis routine by overtone-adapted kernel functions in Tikhonov regularization. The corresponding program *OvertoneAnalysis* can be obtained from www.epr.ethz.ch/software. The approach was found to be sufficiently accurate and robust to be broadly applied for processing of high-spin RIDME data, in cases where the overtone coefficients are constant or exhibit a known dependence, e.g. on distance. Encouraging, for either high-spin metal centre studied here, Mn(II) or Gd(III), the harmonic overtone coefficients were found to be relatively stable for spin-spin distances > 3 nm, pulse sequence parameters, measurement temperature and spin environment. Some deviations were observed for short spin-spin distances and for shifting the detection position away from the maximum in the spectrum of Gd(III) or towards the low-field part of the Mn(II) spectrum. These deviations shall be investigated in more detail in follow-up studies. Some uncertainty in the overtone coefficients did not lead to a breakdown of the proposed analysis approach, which is promising for routine applications. Particularly, deviations not exceeding 20%, were found to somewhat overestimate the artefact level for narrow distance distributions, while for broad distributions the resulting shapes were overly asymmetric. Lastly, assuming that the primary dipolar frequency is always present and no overtone frequency is dominating at least an upper distance limit can be estimated.

Nicely, Mn(II)-Mn(II) as well as Gd(III)-Gd(III) RIDME measurements performed on biological systems provided larger modulation depths and in some cases narrower distance distributions than the DEER experiment if harmonic overtones - calibrated on molecular rulers - are considered in data analysis routines. In these studies paramagnetic metal-ion substitution of Mg(II) by Mn(II) was found to provide valuable means to follow metal binding in nucleotide binding domains of ATP-fuelled proteins as well as for assessing geometric assemblies through measurement of spin-spin distances.

Importantly, a comparison of RIDME and broadband-DEER experiments for molecular Cu(II) rulers revealed that there is not one best method, but that the optimal choice is dependent on the system under investigation and especially on the available spectrometer hardware. In this respect, RIDME appears to be beneficial for situations with limited power over a broad range and notably can also be applied on spectrometers with a single-frequency source.

Based on the findings within this thesis and results presented in literature, the design of future experiments using a relaxation block, possibly combined with frequency-swept excitation pulses, is promising large sensitivity gains for excitation of broad EPR spectra. In particular frequency-swept broadband observer pulses open the door for improved orientation averaging and for new experimental schemes correlating different frequencies.^{259;261;264;286;287}

'Poets say science takes away from the beauty of the stars - mere globs of gas atoms. I too can see the stars on a desert night, and feel them. But do I see less or more?'

Richard P. Feynman

In 'Astronomy', The Feynman Lectures on Physics (1961), 1, 3-6.

Bibliography

- [1] K. Keller, T. , R. Cadalbert, B. H. Meier, A. Böckmann, G. Jeschke, M. Yulikov, High-spin Metal Centres in Dipolar EPR Spectroscopy, *CHIMIA* 72 (2018) 216–220.
- [2] A. Bruckner, In Situ Electron Paramagnetic Resonance: A Unique Tool for Analyzing Structure-Reactivity Relationships in Heterogeneous Catalysis, *Chem. Soc. Rev.* 39 (2010) 4673–4684.
- [3] S. Van Doorslaer, D. M. Murphy, EPR Spectroscopy in Catalysis, in: M. Drescher, G. Jeschke (Eds.), *EPR Spectroscopy: Applications in Chemistry and Biology*, Springer Berlin Heidelberg, Berlin, Heidelberg, 2012, pp. 1–39.
- [4] E. Carter, D. M. Murphy, The Role of Low Valent Transition Metal Complexes in Homogeneous Catalysis: An EPR Investigation, *Topics in Catalysis* 58 (2015) 759–768.
- [5] D. M. Martino, H. van Willigen, M. T. Spitler, FT-EPR Study of Photoinduced Electron Transfer at the Surface of TiO Nanoparticles, *J. Phys. Chem. B* 101 (1997) 8914–8919.
- [6] Z. E. X. Dance, Q. Mi, D. W. McCamant, M. J. Ahrens, M. A. Ratner, M. R. Wasielewski, Time-Resolved EPR Studies of Photogenerated Radical Ion Pairs Separated by p-Phenylene Oligomers and of Triplet States Resulting from Charge Recombination, *J. Phys. Chem. B* 110 (2006) 25163–25173.
- [7] R. Davydov, B. M. Hoffman, Active Intermediates in Heme Monooxygenase Reactions as Revealed by Cryoreduction/Annealing, EPR/ENDOR Studies, *Arch. Biochem. Biophys.* 507 (2011) 36–43.
- [8] W. Lubitz, E. Reijerse, M. van Gastel, [NiFe] and [FeFe] Hydrogenases Studied by Advanced Magnetic Resonance Techniques, *Chem. Rev.* 107 (2007) 4331–4365.
- [9] R. Britt, K. A. Campbell, J. M. Peloquin, M. Gilchrist, C. P. Aznar, M. M. Dicus, J. Robblee, J. Messinger, Recent pulsed EPR studies of the Photosystem II oxygen-evolving complex: Implications as to water oxidation mechanisms, *Biochimica et Biophysica Acta (BBA) - Bioenergetics* 1655 (2004) 158–171.
- [10] S. Van Doorslaer, E. Vinck, The Strength of EPR and ENDOR Techniques in Revealing Structure-Function Relationships in Metalloproteins, *Phys. Chem. Chem. Phys.* 9 (2007) 4620–4638.
- [11] R. Cammack, Electron Paramagnetic Resonance Spectroscopy of Metalloproteins, in: C. Jones, B. Mulloy, A. H. Thomas (Eds.), *Spectroscopic Methods and Analyses: NMR,*

- Mass Spectrometry, and Metalloprotein Techniques, Humana Press, Totowa, NJ, 1993, pp. 327–344.
- [12] G. D. Watkins, EPR of defects in semiconductors: Past, present, future, *Phys. Solid State* 41 (1999) 746–750.
- [13] G. Jeschke, Determination of the Nanostructure of Polymer Materials by Electron Paramagnetic Resonance Spectroscopy, *Macromol. Rapid Commun.* 23 (2002) 227–246.
- [14] V. I. Krinichnyi, 2mm waveband saturation transfer electron paramagnetic resonance of conducting polymers, *J. Chem. Phys.* 129 (2008) 134510.
- [15] D. Hinderberger, EPR spectroscopy in polymer science., *Top. Curr. Chem.* 321 (2012) 67–89.
- [16] J. P. Klare, H.-J. Steinhoff, Spin labeling EPR, *Photosynthesis Research* 102 (2009) 377–390.
- [17] E. Bordignon, Site-directed spin labeling of membrane proteins., *Top. Curr. Chem.* 321 (2012) 121–157.
- [18] W. L. Hubbell, C. J. Lopez, C. Altenbach, Z. Yang, Technological advances in site-directed spin labeling of proteins., *Curr. Opin. Struct. Biol.* 23 (2013) 725–733.
- [19] A. Schweiger, G. Jeschke, Principles of pulse electron paramagnetic resonance, Oxford University Press, 2001.
- [20] G. Jeschke, DEER distance measurements on proteins., *Annu. Rev. Phys. Chem.* 63 (2012) 419–446.
- [21] G. Jeschke, Y. Polyhach, Distance measurements on spin-labelled biomacromolecules by pulsed electron paramagnetic resonance, *Phys. Chem. Chem. Phys.* 9 (2007) 1895–1910.
- [22] O. Schiemann, T. F. Prisner, Long-range distance determinations in biomacromolecules by EPR spectroscopy, *Quart. Rev. Biophys.* 40 (2007) 1–53.
- [23] G. E. Fanucci, D. S. Cafiso, Recent advances and applications of site-directed spin labeling., *Curr. Opin. Struct. Biol.* 16 (2006) 644–653.
- [24] M. Qi, A. Groß, G. Jeschke, A. Godt, M. Drescher, Gd(III)-PyMTA Label Is Suitable for In-Cell EPR, *J. Am. Chem. Soc.* 136 (2014) 15366–15378.
- [25] A. Martorana, G. Bellapadrona, A. Feintuch, E. Di Gregorio, S. Aime, D. Goldfarb, Probing Protein Conformation in Cells by EPR Distance Measurements using Gd³⁺ Spin Labeling, *J. Am. Chem. Soc.* 136 (2014) 13458–13465.
- [26] M. Yulikov, Chapter 1 Spectroscopically orthogonal spin labels and distance measurements in biomolecules, *Electron Paramag. Reson.* 24 (2015) 1–31.
- [27] E. Narr, A. Godt, G. Jeschke, Selective Measurements of a Nitroxide–Nitroxide Separation of 5 nm and a Nitroxide–Copper Separation of 2.5 nm in a Terpyridine-Based Copper(II) Complex by Pulse EPR Spectroscopy, *Angew. Chem. Int. Ed.* 41 (2002) 3907–3910.

- [28] D. Goldfarb, Gd^{3+} Spin Labeling for Distance Measurements by Pulse EPR Spectroscopy., *Phys. Chem. Chem. Phys.* 16 (2014) 9685–9699.
- [29] A. Lewin, J. P. Hill, R. Boetzel, T. Georgiou, R. James, C. Kleanthous, G. R. Moore, Site-specific labeling of proteins with cyclen-bound transition metal ions, *Inorganica Chimica Acta* 331 (2002) 123–130.
- [30] T. F. Cunningham, M. D. Shannon, M. R. Putterman, R. J. Arachchige, I. Sengupta, M. Gao, C. P. Jaroniec, S. Saxena, Cysteine-Specific Cu^{2+} Chelating Tags Used as Paramagnetic Probes in Double Electron Electron Resonance, *J. Phys. Chem. B* 119 (2015) 2839–2843.
- [31] Z. Yang, M. Ji, T. F. Cunningham, S. Saxena, Chapter Seventeen - Cu^{2+} as an ESR Probe of Protein Structure and Function, in: P. Z. Qin, K. Warncke (Eds.), *Methods in Enzymology*, volume 563, Academic Press, 2015, pp. 459–481.
- [32] R. Meng, J. Becker, F.-T. Lin, S. Saxena, S. G. Weber, Binding of Copper(II) to Thyrotropin-Releasing Hormone (TRH) and Its Analogs, *Inorganica Chimica Acta* 358 (2005) 2933–2942.
- [33] S. Jun, J. S. Becker, M. Yonkunas, R. Coalson, S. Saxena, Unfolding of Alanine-Based Peptides Using Electron Spin Resonance Distance Measurements, *Biochemistry* 45 (2006) 11666–11673.
- [34] C. W. M. Kay, H. El Mkami, R. Cammack, R. W. Evans, Pulsed ELDOR Determination of the Intramolecular Distance between the Metal Binding Sites in Dicumpric Human Serum Transferrin and Lactoferrin, *J. Am. Chem. Soc.* 129 (2007) 4868–4869.
- [35] B.-k. Shin, S. Saxena, Direct Evidence That All Three Histidine Residues Coordinate to Cu(II) in Amyloid-*b*1-16, *Biochemistry* 47 (2008) 9117–9123.
- [36] K. J. Waldron, J. C. Rutherford, D. Ford, N. J. Robinson, Metalloproteins and Metal Sensing, *Nature* 460 (2009) 823.
- [37] Z. Yang, M. R. Kurpiewski, M. Ji, J. E. Townsend, P. Mehta, L. Jen-Jacobson, S. Saxena, ESR spectroscopy identifies inhibitory Cu^{2+} sites in a DNA-modifying enzyme to reveal determinants of catalytic specificity, *PNAS* 109 (2012) E993–E1000.
- [38] A. Abragam, B. Bleaney, *Electron Paramagnetic Resonance of Transition Metal Ions*, Clarendon, Oxford, 1970.
- [39] L. J. Berliner, S. S. Eaton, G. R. Eaton, *Distance measurements in biological systems by EPR*, volume 19, Springer Science & Business Media, 2006.
- [40] G. Gabrielse, D. Hanneke, T. Kinoshita, M. Nio, B. Odom, New Determination of the Fine Structure Constant from the Electron g Value and QED, *Phys. Rev. Lett.* 97 (2006) 030802.
- [41] I. Krstic, B. Endeward, D. Margraf, A. Marko, T. F. Prisner, Structure and Dynamics of Nucleic Acids, *Top. Curr. Chem.* 321 (2012) 159–198.
- [42] H. A. Kramers, *Proc. Amsterdam Acad.* 33 (1930) 959.
- [43] G. Jeschke, *PC IV: Magnetic Resonance, Chapters 10-14: Electron Paramagnetic Resonance Spectroscopy*, ETH Zürich, Laboratorium für Physikalische Chemie, 2010.

- [44] A. Dalaloyan, M. Qi, S. Ruthstein, S. Vega, A. Godt, A. Feintuch, D. Goldfarb, Gd(III)-Gd(III) EPR distance measurements - the range of accessible distances and the impact of zero field splitting, *Phys. Chem. Chem. Phys.* 17 (2015) 18464–18476.
- [45] O. Sørensen, G. Eich, M. Levitt, G. Bodenhausen, R. Ernst, Product operator formalism for the description of NMR pulse experiments, *Progr. Nucl. Magn. Reson. Spec.* 16 (1984) 163–192.
- [46] C. Slichter, *Principles Of Magnetic Resonance.*, Springer-Verlag Berlin Heidelberg New York, 3rd edition, 1978.
- [47] A. Raitsimring, A. Dalaloyan, A. Collauto, A. Feintuch, T. Meade, D. Goldfarb, Zero field splitting fluctuations induced phase relaxation of Gd^{3+} in frozen solutions at cryogenic temperatures., *J. Magn. Reson.* 248 (2014) 71–80.
- [48] L. D. Landau, E. M. Lifshitz, *Course of Theoretical Physics Vol 3 Quantum Mechanics*, Pergamon Press, 1958.
- [49] L. J. Berliner, S. S. Eaton, G. R. Eaton, *Time Domain Electron Spin Resonance.*, edited by Larry Kevan, Robert N. Schwartz, New York, Wiley, 1979.
- [50] H. El Mkami, D. G. Norman, Chapter Five - EPR Distance Measurements in Deuterated Proteins, in: P. Z. Qin, K. Warncke (Eds.), *Methods in Enzymology*, volume 564, Academic Press, 2015, pp. 125–152.
- [51] J. R. Harbridge, S. S. Eaton, G. R. Eaton, "comparison of electron spin relaxation times measured by carr–purcell–meiboom–gill and two-pulse spin-echo sequences", *J. Magn. Reson.* 164 (2003) 44 – 53.
- [52] P. P. Borbat, E. R. Georgieva, J. H. Freed, Improved Sensitivity for Long-Distance Measurements in Biomolecules: Five-Pulse Double Electron–Electron Resonance, *J. Phys. Chem. Lett.* 4 (2013) 170–175.
- [53] P. E. Spindler, I. Waclawska, B. Endeward, J. Plackmeyer, C. Ziegler, T. F. Prisner, Carr–Purcell Pulsed Electron Double Resonance with Shaped Inversion Pulses, *J. Phys. Chem. Lett.* 6 (2015) 4331–4335.
- [54] F. D. Breitgoff, J. Soetbeer, A. Doll, G. Jeschke, Y. O. Polyhach, Artefact suppression in 5-pulse double electron electron resonance for distance distribution measurements, *Phys. Chem. Chem. Phys.* 19 (2017) 15766–15779.
- [55] J. Soetbeer, M. Hülsmann, A. Godt, Y. Polyhach, G. Jeschke, Dynamical decoupling of nitroxides in o-terphenyl: A study of temperature, deuteration and concentration effects, *Phys. Chem. Chem. Phys.* 20 (2018) 1615–1628.
- [56] R. K. Wangsness, F. Bloch, The dynamical theory of nuclear induction, *Phys. Rev.* 89 (1953) 728.
- [57] A. G. Redfield, On the theory of relaxation processes, *IBM J. Res. Dev.* 1 (1957) 19–31.
- [58] E. Zavoisky, *Journal of Physics-USSR* 8 (1944) 377–380.

- [59] S. Stoll, A. Schweiger, EasySpin, a comprehensive software package for spectral simulation and analysis in EPR., *J. Magn. Reson.* 178 (2006) 42–55.
- [60] A. Doll, S. Pribitzer, R. Tschaggelar, G. Jeschke, Adiabatic and fast passage ultra-wideband inversion in pulsed EPR, *J. Magn. Reson.* 230 (2013) 27–39.
- [61] P. E. Spindler, S. J. Glaser, T. E. Skinner, T. F. Prisner, Broadband inversion PELDOR spectroscopy with partially adiabatic shaped pulses., *Angew. Chem. Int. Ed.* 52 (2013) 3425–3429.
- [62] A. Doll, G. Jeschke, Fourier-transform electron spin resonance with bandwidth-compensated chirp pulses, *J. Magn. Reson.* 246 (2014) 18–26.
- [63] A. Doll, G. Jeschke, Wideband frequency-swept excitation in pulsed EPR spectroscopy, *J. Magn. Reson.* 280 (2017) 46–62.
- [64] P. E. Spindler, P. Schöps, A. M. Bowen, B. Endeward, T. F. Prisner, Shaped pulses in EPR, *Emagres* (2017) 1477–1492.
- [65] P. E. Spindler, P. Schöps, W. Kallies, S. J. Glaser, T. F. Prisner, Perspectives of shaped pulses for EPR spectroscopy, *J. Magn. Reson.* 280 (2017) 30–45.
- [66] L. Kulik, S. Dzuba, I. Grigoryev, Y. Tsvetkov, Electron dipole–dipole interaction in ESEEM of nitroxide biradicals, *Chem. Phys. Lett.* 343 (2001) 315–324.
- [67] S. Milikisyants, F. Scarpelli, M. G. Finiguerra, M. Ubbink, M. Huber, A pulsed EPR method to determine distances between paramagnetic centers with strong spectral anisotropy and radicals: The dead-time free RIDME sequence, *J. Magn. Reson.* 201 (2009) 48–56.
- [68] R. G. Larsen, D. J. Singel, Double electron–electron resonance spin–echo modulation: Spectroscopic measurement of electron spin pair separations in orientationally disordered solids, *J. Chem. Phys.* 98 (1993) 5134–5146.
- [69] A. G. Maryasov, Y. D. Tsvetkov, J. Raap, Weakly coupled radical pairs in solids: ELDOR in ESE structure studies, *Appl. Magn. Reson.* 14 (1998) 101–113.
- [70] A. Bencini, D. Gatteschi, *EPR of Exchange Coupled Systems*, Springer Verlag: Berlin, 1990.
- [71] S. S. Eaton, K. M. More, B. M. Sawant, G. R. Eaton, Use of the esr half-field transition to determine the interspin distance and the orientation of the interspin vector in systems with two unpaired electrons, *J. Am. Chem. Soc.* 105 (1983) 6560–6567.
- [72] S. A. Dzuba, P. Gast, A. J. Hoff, ESEEM study of spin-spin interactions in spin-polarised P^+QA^- pairs in the photosynthetic purple bacterium *Rhodobacter sphaeroides* R26, *Chem. Phys. Lett.* 236 (1995) 595 – 602.
- [73] S. Razzaghi, M. Qi, A. I. Nalepa, A. Godt, G. Jeschke, A. Savitsky, M. Yulikov, RIDME Spectroscopy with Gd(III) Centers., *J. Phys. Chem. Lett.* 5 (2014) 3970–3975.

- [74] A. Savitsky, A. A. Dubinskii, M. Flores, W. Lubitz, K. Mobius, Orientation-resolving pulsed electron dipolar high-field EPR spectroscopy on disordered solids: I. Structure of spin-correlated radical pairs in bacterial photosynthetic reaction centers., *J. Phys. Chem. B* 111 (2007) 6245–6262.
- [75] G. Jeschke, A. Koch, U. Jonas, A. Godt, Direct Conversion of EPR Dipolar Time Evolution Data to Distance Distributions., *J. Magn. Reson.* 155 (2002) 72–82.
- [76] G. Jeschke, G. Panek, A. Godt, A. Bender, H. Paulsen, Data analysis procedures for pulse ELDOR measurements of broad distance distributions, *Appl. Magn. Reson.* 26 (2004) 223–244.
- [77] Y.-W. Chiang, P. P. Borbat, J. H. Freed, The determination of pair distance distributions by pulsed ESR using Tikhonov regularization, *J. Magn. Reson.* 172 (2005) 279–295.
- [78] G. Jeschke, V. Chechik, P. Ionita, A. Godt, H. Zimmermann, J. Banham, C. R. Timmel, D. Hilger, H. Jung, DeerAnalysis2006—a comprehensive software package for analyzing pulsed ELDOR data, *Appl. Magn. Reson.* 30 (2006) 473–498, <http://www.epr.ethz.ch/software.html>.
- [79] K. Keller, A. Doll, M. Qi, A. Godt, G. Jeschke, M. Yulikov, Averaging of nuclear modulation artefacts in RIDME experiments, *J. Magn. Reson.* 272 (2016) 108–113.
- [80] J. R. Pilbrow, *Transition Ion Electron Paramagnetic Resonance*, Clarendon Press, Oxford, 1990.
- [81] P. Caravan, J. J. Ellison, T. J. McMurry, R. B. Lauffer, Gadolinium(III) Chelates as MRI Contrast Agents: Structure, Dynamics, and Applications, *Chem. Rev.* 99 (1999) 2293–2352.
- [82] I. Kaminker, H. Yagi, T. Huber, A. Feintuch, G. Otting, D. Goldfarb, Spectroscopic selection of distance measurements in a protein dimer with mixed nitroxide and Gd^{3+} spin labels, *Phys. Chem. Chem. Phys.* 14 (2012) 4355–4358.
- [83] P. Lueders, G. Jeschke, M. Yulikov, Double Electron-Electron Resonance Measured Between Gd^{3+} Ions and Nitroxide Radicals, *J. Phys. Chem. Lett.* 2 (2011) 604–609.
- [84] M. Symons, J. Baker, Epr and endor in the lanthanides, in: *Electron Spin Resonance*, 1993, pp. 131–177.
- [85] S. K. Misra, Spin hamiltonians and site symmetries for transition ions, *Multifrequency Electron Paramagnetic Resonance: Theory and Applications* (2011) 327–384.
- [86] J. Huheey, E. Keiter, R. Keiter, *Anorganische Chemie*, Gruyter, Walter de Berlin New York, 3. Auflage, 2003.
- [87] D. R. Lide, *CRC handbook of chemistry and physics: a ready-reference book of chemical and physical data*, volume 85 edition, CRC press, 2004.
- [88] D. G. Karraker, Coordination of trivalent lanthanide ions, *J. Chem. Educ.* 47 (1970) 424.
- [89] V. Chaurin, E. C. Constable, C. E. Housecroft, What is the coordination number of copper(II) in metallocsupramolecular chemistry?, *New J. Chem.* 30 (2006) 1740–1744.

- [90] L. Garbuio, B. Lewandowski, P. Wilhelm, L. Ziegler, M. Yulikov, H. Wennemers, G. Jeschke, Shape Persistence of Polyproline II Helical Oligoproline., *Chemistry* 21 (2015) 10747–10753.
- [91] H. El Mkami, R. Ward, A. Bowman, T. Owen-Hughes, D. G. Norman, The spatial effect of protein deuteration on nitroxide spin-label relaxation: Implications for EPR distance measurement, *J. Magn. Reson.* 248 (2014) 36–41.
- [92] H. Y. Carr, E. M. Purcell, Effects of Diffusion on Free Precession in Nuclear Magnetic Resonance Experiments, *Phys. Rev.* 94 (1954) 630–638.
- [93] K. Keller, M. Zalibera, M. Qi, V. Koch, J. Wegner, H. Hintz, A. Godt, G. Jeschke, A. Savitsky, M. Yulikov, EPR characterization of Mn(II) complexes for distance determination with pulsed dipolar spectroscopy, *Phys. Chem. Chem. Phys.* 18 (2016) 25120–25135.
- [94] M. Qi, M. Hülsmann, A. Godt, Synthesis and Hydrolysis of 4-Chloro-PyMTA and 4-Iodo-PyMTA Esters and Their Oxidative Degradation with Cu(I/II) and Oxygen, *Synthesis* 48 (2016) 3773–3784.
- [95] J. A. Clayton, K. Keller, M. Qi, J. Wegner, V. Koch, H. Hintz, A. Godt, S. Han, G. Jeschke, M. S. Sherwin, M. Yulikov, Quantitative analysis of zero-field splitting parameter distributions in Gd(III) complexes, *Phys. Chem. Chem. Phys.* 20 (2018) 10470–10492.
- [96] I. Gromov, J. Shane, J. Forrer, R. Rakhmatoullin, Y. Rozentzwaig, A. Schweiger, A Q-Band Pulse EPR/ENDOR Spectrometer and the Implementation of Advanced One- and Two-Dimensional Pulse EPR Methodology, *J. Magn. Reson.* 149 (2001) 196–203.
- [97] R. Tschaggelar, B. Kasumaj, M. G. Santangelo, J. Forrer, P. Leger, H. Dube, F. Diederich, J. Harmer, R. Schuhmann, I. García-Rubio, G. Jeschke, Cryogenic 35 GHz pulse ENDOR probehead accommodating large sample sizes: Performance and applications, *J. Magn. Reson.* 200 (2009) 81–87.
- [98] Y. Polyhach, E. Bordignon, R. Tschaggelar, S. Gandra, A. Godt, G. Jeschke, High sensitivity and versatility of the DEER experiment on nitroxide radical pairs at Q-band frequencies, *Phys. Chem. Chem. Phys.* 14 (2012) 10762–10773.
- [99] J. E. Lovett, A. M. Bowen, C. R. Timmel, M. W. Jones, J. R. Dilworth, D. Caprotti, S. G. Bell, L. L. Wong, J. Harmer, Structural information from orientationally selective DEER spectroscopy, *Phys. Chem. Chem. Phys.* 11 (2009) 6840–6848.
- [100] S. Feng, L. Ma, G. Feng, Y. Jiao, M. Zhu, Dinuclear copper (ii) complexes hold by crab-shaped pincer ligands: Syntheses, structures, luminescent and magnetic properties, *Journal of Molecular Structure* 1059 (2014) 27–32.
- [101] M. Qi, M. Hülsmann, A. Godt, Spacers for Geometrically Well-Defined Water-Soluble Molecular Rulers and Their Application, *J. Org. Chem.* 81 (2016) 2549–2571.
- [102] A. Kulikov, G. Likhtenstein, The use of spin relaxation phenomena in the investigation of the structure of model and biological systems by the method of spin labels, *Adv. Mol. Relax. Interact.* 10 (1977) 47 – 79.

- [103] H. Jäger, A. Koch, V. Maus, H. Spiess, G. Jeschke, Relaxation-based distance measurements between a nitroxide and a lanthanide spin label, *J. Magn. Reson.* 194 (2008) 254 – 263.
- [104] P. Lueders, S. Razzaghi, H. Jäger, R. Tschaggelar, M. A. Hemminga, M. Yulikov, G. Jeschke, Distance determination from dysprosium induced relaxation enhancement: A case study on membrane-inserted WALP23 polypeptides, *Mol. Phys.* 111 (2013) 2824–2833.
- [105] W. Low, Hyperfine structure and nuclear moments of gadolinium from paramagnetic resonance spectrum, *Phys. Rev.* 103 (1956) 1309–1309.
- [106] S. Un, L. C. Tabares, N. Cortez, B. Y. Hiraoka, F. Yamakura, Manganese(II) Zero-Field Interaction in Cambialistic and Manganese Superoxide Dismutases and Its Relationship to the Structure of the Metal Binding Site, *J. Am. Chem. Soc.* 126 (2004) 2720–2726.
- [107] L. Garbuio, K. Zimmermann, D. Haussinger, M. Yulikov, Gd(III) complexes for electron-electron dipolar spectroscopy: Effects of deuteration, pH and zero field splitting., *J. Magn. Reson.* 259 (2015) 163–173.
- [108] F. Bloch, A. Siegert, Magnetic resonance for nonrotating fields, *Phys. Rev.* 57 (1940) 522.
- [109] M. K. Bowman, A. G. Maryasov, Dynamic phase shifts in nanoscale distance measurements by double electron electron resonance (DEER), *J. Magn. Reson.* 185 (2007) 270–282.
- [110] M. Yulikov, P. Lueders, M. F. Warsi, V. Chechik, G. Jeschke, Distance measurements in Au nanoparticles functionalized with nitroxide radicals and Gd³⁺-DTPA chelate complexes., *Phys. Chem. Chem. Phys.* 14 (2012) 10732–10746.
- [111] P. Lueders, H. Jäger, M. A. Hemminga, G. Jeschke, M. Yulikov, Distance measurements on orthogonally spin-labeled membrane spanning WALP23 polypeptides, *J. Phys. Chem. B* 117 (2013) 2061–2068.
- [112] H. Y. Vincent Ching, P. Demay-Drouhard, H. C. Bertrand, C. Policar, L. C. Tabares, S. Un, Nanometric Distance Measurements between Mn(II)DOTA Centers., *Phys. Chem. Chem. Phys.* 17 (2015) 23368–23377.
- [113] A. Collauto, V. Frydman, M. D. Lee, E. H. Abdelkader, A. Feintuch, J. D. Swarbrick, B. Graham, G. Otting, D. Goldfarb, RIDME distance measurements using Gd(III) tags with a narrow central transition, *Phys. Chem. Chem. Phys.* (2016).
- [114] K. Keller, V. Mertens, M. Qi, A. Nalepa, A. Godt, A. Savitsky, G. Jeschke, M. Yulikov, Computing Distance Distributions from Dipolar Evolution Data with Overtones: RIDME Spectroscopy with Gd(III)-Based Spin Labels, *Phys. Chem. Chem. Phys.* (2017).
- [115] A. Doll, M. Qi, N. Wili, S. Pribitzer, A. Godt, G. Jeschke, Gd(III)-Gd(III) Distance Measurements with Chirp Pump Pulses., *J. Magn. Reson.* 259 (2015) 153–162.
- [116] A. Doll, M. Qi, A. Godt, G. Jeschke, CIDME: Short distances measured with long chirp pulses, *J. Magn. Reson.* 273 (2016) 73–82.
- [117] A. Doll, M. Qi, S. Pribitzer, N. Wili, M. Yulikov, A. Godt, G. Jeschke, Sensitivity enhancement by population transfer in Gd(III) spin labels., *Phys. Chem. Chem. Phys.* 17 (2015) 7334–7344.

- [118] R. Viguier, G. Serratrice, A. Dupraz, C. Dupuy, New Polypodal Polycarboxylic Ligands - Complexation of Rare-Earth Ions in Aqueous Solution, *Eur. J. Inorg. Chem.* 2001 (2001) 1789–1795.
- [119] E. M. Chellquist, R. Searle, An LC method for measuring complex formation equilibria by competitive chelation, *J. Pharm. Biomed. Anal.* 11 (1993) 985–992.
- [120] A. Collauto, A. Feintuch, M. Qi, A. Godt, T. Meade, D. Goldfarb, Gd(III) complexes as paramagnetic tags: Evaluation of the spin delocalization over the nuclei of the ligand., *J. Magn. Reson.* 263 (2016) 156–163.
- [121] B. M. Sawant, A. L. W. Shroyer, G. A. Eaton, S. S. Eaton, Metal-nitroxyl interactions. 24. Electron spin delocalization in vanadyl and copper(II) bis (. beta.-diketonates), *Inorg. Chem.* 21 (1982) 1093–1101.
- [122] A. Feintuch, G. Otting, D. Goldfarb, Gd³⁺ Spin Labeling for Measuring Distances in Biomacromolecules: Why and How?, in: *Methods in Enzymology*, volume 563, 2015, pp. 415–457.
- [123] E. H. Abdelkader, X. Yao, A. Feintuch, L. A. Adams, L. Aurelio, B. Graham, D. Goldfarb, G. Otting, Pulse EPR-enabled interpretation of scarce pseudocontact shifts induced by lanthanide binding tags, *J. Biomol. NMR* 64 (2016) 39–51.
- [124] E. A. Sutura, D. Häussinger, K. Zimmermann, L. Garbuio, M. Yulikov, G. Jeschke, I. Kuprov, Model-free extraction of spin label position distributions from pseudocontact shift data, *Chem. Sci.* 8 (2017) 2751–2757.
- [125] J.-C. G. Bünzli, Lanthanide Luminescence for Biomedical Analyses and Imaging, *Chem. Rev.* 110 (2010) 2729–2755.
- [126] E. Debroye, T. N. Parac-Vogt, Towards polymetallic lanthanide complexes as dual contrast agents for magnetic resonance and optical imaging, *Chem. Soc. Rev.* 43 (2014) 8178–8192.
- [127] J. G. Reifernberger, P. Ge, P. R. Selvin, Progress in Lanthanides as Luminescent Probes, in: C. D. Geddes, J. R. Lakowicz (Eds.), *Reviews in Fluorescence*, Springer US, 2005, pp. 399–431.
- [128] S. Cotton, *Lanthanide and actinide chemistry*, John Wiley & Sons, 2013.
- [129] D. J. Newman, W. Urban, Interpretation of S-state ion E.P.R. spectra, *Advances in Physics* 24 (1975) 793–844.
- [130] M. Ramirez Cohen, V. Frydman, P. Milko, M. A. Iron, E. H. Abdelkader, M. D. Lee, J. D. Swarbrick, A. Raitsimring, G. Otting, B. Graham, A. Feintuch, D. Goldfarb, Overcoming artificial broadening in Gd³⁺–Gd³⁺ distance distributions arising from dipolar pseudo-secular terms in DEER experiments, *Phys. Chem. Chem. Phys.* 18 (2016) 12847–12859.
- [131] J. A. Clayton, M. Qi, A. Godt, D. Goldfarb, S. Han, M. S. Sherwin, Gd³⁺–Gd³⁺ distances exceeding 3 nm determined by very high frequency continuous wave electron paramagnetic resonance, *Phys. Chem. Chem. Phys.* 19 (2017) 5127–5136.

- [132] A. M. Raitsimring, C. Gunanathan, A. Potapov, I. Efremenko, J. M. L. Martin, D. Milstein, D. Goldfarb, Gd^{3+} complexes as potential spin labels for high field pulsed EPR distance measurements., *J. Am. Chem. Soc.* 129 (2007) 14138–14139.
- [133] A. Lasoroski, R. Vuilleumier, R. Pollet, Vibrational dynamics of zero-field-splitting hamiltonian in gadolinium-based MRI contrast agents from ab initio molecular dynamics., *J. Chem. Phys.* 141 (2014) 014201.
- [134] A. M. Raitsimring, A. V. Astashkin, O. G. Poluektov, P. Caravan, High-Field Pulsed EPR and ENDOR of Gd^{3+} Complexes in Glassy Solutions, *Appl. Magn. Reson.* 28 (2005) 281–295.
- [135] M. Benmelouka, J. Van Tol, A. Borel, M. Port, L. Helm, L. C. Brunel, A. E. Merbach, A High-Frequency EPR Study of Frozen Solutions of Gd(III) Complexes: Straightforward Determination of the Zero-Field Splitting Parameters and Simulation of the NMRD Profiles, *J. Am. Chem. Soc.* 128 (2006) 7807–7816.
- [136] H. A. Buckmaster, Y. H. Shing, A survey of the EPR spectra of Gd^{3+} in single crystals, *Physica Status Solidi (a)* 12 (1972) 325–361.
- [137] A. M. Raitsimring, A. V. Astashkin, P. Caravan, High-Frequency EPR and ENDOR Characterization of MRI Contrast Agents, *Biological Magnetic Resonance* 28 (2009) 581–621.
- [138] W. Blumberg, The EPR of high spin Fe^{3+} in rhombic fields, *Magnetic resonance in biological systems* (A. Ehrenberg, B.G. Malmström, T. Vännngård, eds), Pergamon, Oxford (1967) 119–133.
- [139] M. Azarkh, E. J. Groenen, Simulation of multi-frequency EPR spectra for a distribution of the zero-field splitting, *J. Magn. Reson.* 255 (2015) 106–113.
- [140] W. R. Hagen, Wide zero field interaction distributions in the high-spin EPR of metalloproteins, *Molecular Physics* 105 (2007) 2031–2039.
- [141] J. T. Weisser, M. J. Nilges, M. J. Sever, J. J. Wilker, Epr investigation and spectral simulations of iron-catecholate complexes and iron-peptide Models of marine adhesive cross-links, *Inorg. Chem.* 45 (2006) 7736–7747.
- [142] A. P. Golombek, M. P. Hendrich, Quantitative analysis of dinuclear manganese(II) EPR spectra, *J. Magn. Reson.* 165 (2003) 33–48.
- [143] G. Scholz, R. Stösser, M. Krossner, J. Klein, Modelling of multifrequency ESR spectra of Fe^{3+} ions in crystalline and amorphous materials: A Simplified approach to determine statistical distributions of spin-spin coupling parameters, *Appl. Magn. Reson.* 21 (2001) 105–123.
- [144] E M Yahiaoui and R Berger and Y Servant and J Kliava and L Cugunov and A Mednis, Electron paramagnetic resonance of Fe^{3+} ions in borate glass: computer simulations, *J. Phys. Condens. Matter* 6 (1994) 9415.

- [145] A. Yang, B. Gaffney, Determination of relative spin concentration in some high-spin ferric proteins using E/D-distribution in electron paramagnetic resonance simulations, *Biophys. J.* 51 (1987) 55–67.
- [146] M. Benmelouka, J. Van Tol, A. Borel, S. Nellutla, M. Port, L. Helm, L.-C. Brunel, A. E. Merbach, Multiple Frequency and Variable Temperature EPR study of Gd(III) polyaminocarboxylates: Analysis and comparison of the magnetically dilute powder and the frozen solution spectra, *Helvetica Chimica Acta* 92 (2009) 2173–2185.
- [147] S. Takahashi, L.-C. Brunel, D. T. Edwards, J. Van Tol, G. Ramian, S. Han, M. S. Sherwin, Pulsed electron paramagnetic resonance spectroscopy powered by a free-electron laser, *Nature* 489 (2012) 409–413.
- [148] D. T. Edwards, Z. Ma, T. J. Meade, D. Goldfarb, S. Han, M. S. Sherwin, Extending the distance range accessed with continuous wave EPR with Gd^{3+} spin probes at high magnetic fields, *Phys. Chem. Chem. Phys.* 15 (2013) 11313–11326.
- [149] M. Weger, Passage Effects in Paramagnetic Resonance Experiments, *Bell System Technical Journal* 39 (1960) 1013–1112.
- [150] A. Portis, Rapid passage effects in electron spin resonance, *Phys. Rev.* 100 (1955) 1219–1221.
- [151] W. Low, Paramagnetic Resonance Spectrum of Manganese in Cubic MgO and GaF, *Phys. Rev.* 105 (1957) 793–800.
- [152] V. I. Krinichnyi, Investigation of biological systems by high resolution 2-mm wave band ESR, *J. Biochem. Biophys. Methods* 23 (1991) 1–30.
- [153] A. V. Astashkin, A. M. Raitisimring, Electron spin echo envelope modulation theory for high electron spin systems in weak crystal field, *J. Chem. Phys.* 117 (2002) 6121–6132.
- [154] C. Gateau, M. Mazzanti, J. Pécaut, F. A. Dunand, L. Helm, Solid-state and solution properties of the lanthanide complexes of a new nonadentate tripodal ligand derived from 1,4,7-triazacyclo- nonane, *Dalton Trans.* (2003) 2428–2433.
- [155] S. Aime, P. Anelli, M. Botta, F. Fedeli, M. Grandi, P. Paoli, F. Uggeri, Gd(III) Complexes of DOTA-like Ligand Derivatives, *Inorg. Chem* 31 (1992) 2422–2428.
- [156] C. Gunanathan, Y. Diskin-Posner, D. Milstein, Lanthanide-organic framework of a rigid bis-gd complex: Composed by carbonate ions spacers, *Cryst. Growth Des.* 10 (2010) 4235–4239.
- [157] M. Le Fur, M. Beyler, N. Lepareur, O. Fougère, C. Platas-Iglesias, O. Rousseaux, R. L. Tripier, Pyclen Tri-n-butylphosphonate ester as potential chelator for targeted radiotherapy: from Yttrium(III) complexation to ^{90}Y radiolabeling, *Inorg. Chem.* 55 (2016) 8003–8012.
- [158] Chang, C. Allen and Francesconi, Lynn C. and Malley, Mary F. and Kumar, Krishan and Gougoutas, Jack Z. and Tweedle, Michael F. and Lee, Daniel W. and Wilson, Lon J., Synthesis, characterization, and crystal structures of $M(DO3A)$ ($M = \text{iron, gadolinium}$) and $Na[M(DOTA)]$ ($M = \text{Fe, yttrium, Gd}$), *Inorg. Chem.* 32 (1993) 3501–3508.

- [159] F. Benetollo, G. Bombieri, L. Calabi, S. Aime, M. Botta, Structural Variations Across the Lanthanide Series of Macrocyclic DOTA Complexes: Insights into the Design of Contrast Agents for Magnetic Resonance Imaging, *Inorg. Chem.* 19 (2003) 1319.
- [160] G. Bombieri, N. Marchini, S. Ciattini, A. Mortillaro, S. Aime, The crystallized solvent could influence the lanthanide water bonding?, *Inorganica Chimica Acta* 359 (2006) 3405–3411.
- [161] L. K. Templeton, D. H. Templeton, A. Zalkin, H. W. Ruben, Anomalous scattering by praseodymium, samarium and gadolinium and structures of their ethylenediaminetetraacetate (edta) salts, *Acta Crystallographica Section B Structural Crystallography and Crystal Chemistry* 38 (1982) 2155–2159.
- [162] A. Bianchi, L. Calabi, C. Giorgi, P. Losi, P. Mariani, P. Paoli, P. Rossi, B. Valtancoli, M. Virtuani, Thermodynamic and structural properties of Gd^{3+} complexes with functionalized macrocyclic ligands based upon 1,4,7,10- tetraazacyclododecane, *J. Chem. Soc. Dalton Trans* (2000) 697–705.
- [163] L. S. Natrajan, N. M. Khoabane, B. L. Dadds, C. A. Muryn, R. G. Pritchard, S. L. Heath, A. M. Kenwright, I. Kuprov, S. Faulkner, Probing the structure, conformation, and stereochemical exchange in a family of lanthanide complexes derived from tetrapyrridyl-appended cyclen, *Inorg. Chem.* 49 (2010) 7700–7709.
- [164] M. S. Konings, W. C. Dow, D. B. Love, K. N. Raymond, S. C. Quay, S. M. Rocklage, Gadolinium complexation by a new DTPA-amide ligand. Amide oxygen coordination, *Inorg. Chem.* 29 (1990) 1488–1491.
- [165] S. W. A. Bligh, N. Choi, E. G. Evagorou, M. Mcpartlin, W. J. Cummins, J. D. Kelly, Synthesis and crystal structure of a gadolinium(III) complex of a tetraimine schiff-base macrocycle: A potential contrast agent for magnetic resonance imaging, *Polyhedron* 11 (1992) 2571–2573.
- [166] Hervé Daubric and Janis Kliava and Philippe Guionneau and Daniel Chasseau and Jean-François Létard and Olivier Kahn, Spin transition in $[Fe(PM-BiA)_2(NCS)_2]$ studied by the electron paramagnetic resonance of the Mn^{2+} ion, *J. Phys. Condens. Matter* 12 (2000) 5481.
- [167] L. C. Tabares, N. Cortez, I. Agalidis, S. Un, Temperature-Dependent Coordination in *E. coli* Manganese Superoxide Dismutase, *J. Am. Chem. Soc.* 127 (2005) 6039–6047.
- [168] T. Gupta, G. Rajaraman, Modelling spin Hamiltonian parameters of molecular nanomagnets, *Chem. Commun. Chem. Commun* 8972 (2016) 8972–9008.
- [169] G. Jeschke, Interpretation of Dipolar EPR Data in Terms of Protein Structure, *Struct. Bond.* 152 (2014) 83–120.
- [170] R. Igarashi, T. Sakai, H. Hara, T. Tenno, T. Tanaka, H. Tochio, M. Shirakawa, Distance Determination in Proteins inside *Xenopus laevis* Oocytes by Double Electron-Electron Resonance Experiments, *J. Am. Chem. Soc.* 132 (2010) 8228–8229.

- [171] I. Krstić, R. Hänsel, O. Romainczyk, J. W. Engels, V. Dötsch, T. F. Prisner, Long-Range Distance Measurements on Nucleic Acids in Cells by Pulsed EPR Spectroscopy, *Angew. Chem. Int. Ed.* 123 (2011) 5176–5180.
- [172] Z. Yang, Y. Liu, P. Borbat, J. L. Zweier, J. H. Freed, W. L. Hubbell, Pulsed ESR Dipolar Spectroscopy for Distance Measurements in Immobilized Spin Labeled Proteins in Liquid Solution, *J. Am. Chem. Soc.* 134 (2012) 9950–9952.
- [173] G. Y. Shevelev, O. A. Krumkacheva, A. A. Lomzov, A. A. Kuzhelev, O. Y. Rogozhnikova, D. V. Trukhin, T. I. Troitskaya, V. M. Tormyshev, M. V. Fedin, D. V. Pyshnyi, E. G. Bagryanskaya, Physiological-Temperature Distance Measurement in Nucleic Acid using Triarylmethyl-Based Spin Labels and Pulsed Dipolar EPR Spectroscopy, *J. Am. Chem. Soc.* 136 (2014) 9874–9877.
- [174] M. Pannier, S. Veit, A. Godt, G. Jeschke, H. Spiess, Dead-Time Free Measurement of Dipole–Dipole Interactions between Electron Spins, *J. Magn. Reson.* 142 (2000) 331–340.
- [175] S. Saxena, J. H. Freed, Double quantum two-dimensional Fourier transform electron spin resonance: Distance measurements, *Chem. Phys. Lett.* 251 (1996) 102–110.
- [176] P. P. Borbat, J. H. Freed, Multiple-quantum ESR and distance measurements, *Chem. Phys. Lett.* 313 (1999) 145–154.
- [177] G. Jeschke, M. Pannier, A. Godt, H. Spiess, Dipolar spectroscopy and spin alignment in electron paramagnetic resonance, *Chem. Phys. Lett.* 331 (2000) 243–252.
- [178] D. Akhmetzyanov, H. Y. V. Ching, V. Denysenkov, P. Demay-Drouhard, H. C. Bertrand, L. C. Tabares, C. Policar, T. F. Prisner, S. Un, RIDME spectroscopy on high-spin Mn^{2+} centers, *Phys. Chem. Chem. Phys.* 18 (2016) 30857–30866.
- [179] A. V. Astashkin, Chapter Ten - Mapping the Structure of Metalloproteins with RIDME, in: Peter Z. Qin and Kurt Warncke (Ed.), *Meth. Enzymol.*, volume Volume 563, Academic Press, 2015, pp. 251–284.
- [180] D. Abdullin, F. Duthie, A. Meyer, E. S. Muller, G. Hagelueken, O. Schiemann, Comparison of PELDOR and RIDME for Distance Measurements between Nitroxides and Low-Spin Fe(III) Ions., *J. Phys. Chem. B* 119 (2015) 13534–13542.
- [181] A. Meyer, D. Abdullin, G. Schnakenburg, O. Schiemann, Single and double nitroxide labeled bis(terpyridine)-copper(II): Influence of orientation selectivity and multispin effects on PELDOR and RIDME, *Phys. Chem. Chem. Phys.* 18 (2016) 9262–9271.
- [182] A. Meyer, O. Schiemann, PELDOR and RIDME Measurements on a High-Spin Manganese(II) Bisnitroxide Model Complex, *J. Phys. Chem. A* 120 (2016) 3463–3472.
- [183] A. Giannoulis, M. Oranges, B. E. Bode, Monitoring Complex Formation by Relaxation-Induced Pulse Electron Paramagnetic Resonance Distance Measurements, *ChemPhysChem* 18 (2017) 2318–2321.
- [184] A. Giannoulis, C. L. Motion, M. Oranges, M. Bühl, G. M. Smith, B. E. Bode, Orientation selection in high-field RIDME and PELDOR experiments involving low-spin Co(II) ions, *Phys. Chem. Chem. Phys.* 20 (2018) 2151–2154.

- [185] A. D. Milov, A. G. Maryasov, Y. D. Tsvetkov, "pulsed electron double resonance (peldor) and its applications in free-radicals research", *Appl. Magn. Reson.* 15 (1998) 107–143.
- [186] A. M. Portis, Spectral diffusion in magnetic resonance, *Phys. Rev.* 104 (1956) 584–588.
- [187] J. R. Klauder, P. W. Anderson, Spectral diffusion decay in spin resonance experiments, *Phys. Rev.* 125 (1962) 912.
- [188] W. B. Mims, Phase Memory in Electron Spin Echoes, Lattice Relaxation Effects in CaWO_4 : Er, Ce, Mn, *Phys. Rev.* 168 (1968) 370–389.
- [189] P. Hu, S. R. Hartmann, Theory of spectral diffusion decay using an uncorrelated-sudden-jump model, *Phys. Rev. B* 9 (1974) 1–13.
- [190] K. M. Salikhov, S. A. Dzuba, A. M. Raitsimring, The theory of electron spin-echo signal decay resulting from dipole-dipole interactions between paramagnetic centers in solids, *J. Magn. Reson.* 42 (1981) 255–276.
- [191] C. Gmeiner, D. Klose, E. Mileo, V. Belle, S. R. A. Marque, G. Dorn, F. H. T. Allain, B. Guigliarelli, G. Jeschke, M. Yulikov, Orthogonal Tyrosine and Cysteine Site-Directed Spin Labeling for Dipolar Pulse EPR Spectroscopy on Proteins, *J. Phys. Chem. Lett.* 8 (2017) 4852–4857.
- [192] C. Gmeiner, G. Dorn, F. H. T. Allain, G. Jeschke, M. Yulikov, Spin labelling for integrative structure modelling: A case study of the polypyrimidine-tract binding protein 1 domains in complexes with short RNAs, *Phys. Chem. Chem. Phys.* 19 (2017) 28360–28380.
- [193] A. Nalepa, K. Mobius, W. Lubitz, A. Savitsky, High-field ELDOR-detected NMR study of a nitroxide radical in disordered solids: Towards characterization of heterogeneity of microenvironments in spin-labeled systems., *J. Magn. Reson.* 242 (2014) 203–213.
- [194] N. Cox, W. Lubitz, A. Savitsky, W-band ELDOR-detected NMR (EDNMR) spectroscopy as a versatile technique for the characterisation of transition metal–ligand interactions, *Mol. Phys.* 111 (2013) 2788–2808.
- [195] L. Rapatskiy, N. Cox, A. Savitsky, W. M. Ames, J. Sander, M. M. Nowaczyk, M. Rogner, A. Boussac, F. Neese, J. Messinger, W. Lubitz, Detection of the water-binding sites of the oxygen-evolving complex of Photosystem II using W-band ^{17}O electron-electron double resonance-detected NMR spectroscopy., *J. Am. Chem. Soc.* 134 (2012) 16619–16634.
- [196] J. L. Baber, J. M. Louis, G. M. Clore, Dependence of Distance Distributions Derived from Double Electron–Electron Resonance Pulsed EPR Spectroscopy on Pulse-Sequence Time, *Angew. Chem. Int. Edit.* 54 (2015) 5336–5339.
- [197] A. Dalaloyan, M. Qi, S. Ruthstein, S. Vega, A. Godt, A. Feintuch, D. Goldfarb, EPR distance measurements – the range of accessible distances and the impact of zero field splitting, *Phys. Chem. Chem. Phys.* 17 (2015) 18464–18476.
- [198] I. Ritsch, H. Hintz, G. Jeschke, A. Godt, M. Yulikov, Improving the accuracy of Cu(II)-nitroxide RIDME in the presence of orientation correlation in water-soluble Cu(II)-nitroxide rulers, *Phys. Chem. Chem. Phys.* 21 (2019) 9810–9830.

- [199] W. Kaim, B. Schwederski, A. Klein, *Bioinorganic Chemistry—Inorganic Elements in the Chemistry of Life: An Introduction and Guide*, John Wiley & Sons, 2013.
- [200] T. R. Hvidsten, A. Læg Reid, A. Kryshatfovych, G. Andersson, K. Fidelis, J. Komorowski, A comprehensive analysis of the structure-function relationship in proteins based on local structure similarity, *PloS one* 4 (2009) e6266.
- [201] C. R. Timmel, J. R. Harmer, *Structural Information from Spin-Labels and Intrinsic Paramagnetic Centres in the Biosciences*, volume 152, Springer, 2014.
- [202] P. Borbat, A. Costa-Filho, K. Earle, J. Moscicki, J. Freed, Electron spin resonance in studies of membranes and proteins, *Science* 291 (2001) 266–269.
- [203] M. Smyth, J. Martin, *X-Ray Crystallography*, *Molecular Pathology* 53 (2000) 8.
- [204] A. Lapinaite, B. Simon, L. Skjaerven, M. Rakwalska-Bange, F. Gabel, T. Carlomagno, The structure of the box c/d enzyme reveals regulation of rna methylation, *Nature* 502 (2013) 519.
- [205] H. J. de Groot, Solid-state NMR spectroscopy applied to membrane proteins, *Curr Opin Struct Biol* 10 (2000) 593–600.
- [206] B. C. Bohrer, S. I. Merenbloom, S. L. Koeniger, A. E. Hilderbrand, D. E. Clemmer, Biomolecule analysis by ion mobility spectrometry, *Annu. Rev. Anal. Chem.* 1 (2008) 293–327.
- [207] F. Lanucara, S. W. Holman, C. J. Gray, C. E. Eyers, The power of ion mobility-mass spectrometry for structural characterization and the study of conformational dynamics, *Nature chemistry* 6 (2014) 281.
- [208] L. Sleno, D. A. Volmer, Ion activation methods for tandem mass spectrometry, *J. Mass Spectrom.* 39 (2004) 1091–1112.
- [209] D. Suckau, Y. Shi, S. C. Beu, M. W. Senko, J. P. Quinn, F. Wampler, F. W. McLafferty, Coexisting stable conformations of gaseous protein ions., *PNAS* 90 (1993) 790–793.
- [210] E. Boeri Erba, C. Petosa, The emerging role of native mass spectrometry in characterizing the structure and dynamics of macromolecular complexes, *Protein Science* 24 (2015) 1176–1192.
- [211] E. Haas, The study of protein folding and dynamics by determination of intramolecular distance distributions and their fluctuations using ensemble and single-molecule fret measurements, *ChemPhysChem* 6 (2005) 858–870.
- [212] B. Schuler, W. A. Eaton, Protein folding studied by single-molecule FRET, *Curr Opin Struct Biol* 18 (2008) 16–26.
- [213] J. Lepault, F. Booy, J. Dubochet, Electron microscopy of frozen biological suspensions, *J. Microsc.* 129 (1983) 89–102.
- [214] R. Fernandez-Leiro, S. H. Scheres, Unravelling biological macromolecules with cryo-electron microscopy, *Nature* 537 (2016) 339.

- [215] T. Prisner, M. Rohrer, F. MacMillan, Pulsed EPR Spectroscopy: Biological Applications, *Annu. Rev. Phys. Chem.* 52 (2001) 279–313.
- [216] T. Schmidt, M. A. Wälti, J. L. Baber, E. J. Hustedt, G. M. Clore, Long Distance Measurements up to 160 Å in the GroEL Tetradecamer Using Q-Band DEER EPR Spectroscopy, *Angew. Chem. Int. Edit.* 55 (2016) 15905–15909.
- [217] G. Jeschke, The contribution of modern EPR to structural biology, *Emerging Top. Life Sci.* 2 (2018) 9–18.
- [218] R. Sundaramoorthy, A. L. Hughes, V. Singh, N. Wiechens, D. P. Ryan, H. El-Mkami, M. Petoukhov, D. I. Svergun, B. Treutlein, S. Quack, et al., Structural reorganization of the chromatin remodeling enzyme Chd1 upon engagement with nucleosomes, *Elife* 6 (2017) e22510.
- [219] O. Duss, E. Michel, M. Yulikov, M. Schubert, G. Jeschke, F. H.-T. Allain, Structural Basis of the Non-Coding RNA RsmZ Acting as a Protein Sponge, *Nature* 509 (2014) 588–592.
- [220] L. C. Dickinson, M. Symons, Electron spin resonance of haemoglobin and myoglobin, *Chem. Soc. Rev.* 12 (1983) 387–414.
- [221] M. Bennati, M. Hertel, J. Fritscher, T. Prisner, N. Weiden, R. Hofweber, M. Spoerner, G. Horn, H.-R. Kalbitzer, High-Frequency 94 GHz ENDOR Characterization of the Metal Binding Site in Wild-Type Ras-GDP and Its Oncogenic Mutant G12V in Frozen Solution, *Biochemistry* 45 (2006) 42–50.
- [222] G. Otting, Protein NMR using paramagnetic ions, *Annual review of biophysics* 39 (2010) 387–405.
- [223] T. Wiegand, D. Lacabanne, K. Keller, R. Cadalbert, L. Lecoq, M. Yulikov, L. Terradot, G. Jeschke, B. H. Meier, A. Böckmann, Solid-state NMR and EPR Spectroscopy of Mn²⁺-Substituted ATP-Fueled Protein Engines, *Angew. Chem. Int. Ed.* 56 (2017) 3369–3373.
- [224] T. F. Cunningham, M. D. Shannon, M. R. Putterman, R. J. Arachchige, I. Sengupta, M. Gao, C. P. Jaroniec, S. Saxena, Cysteine-Specific Cu²⁺ Chelating Tags Used as Paramagnetic Probes in Double Electron Electron Resonance, *J. Phys. Chem. B* 119 (2015) 2839–2843.
- [225] T. F. Cunningham, M. R. Putterman, A. Desai, W. S. Horne, S. Saxena, The Double-Histidine Cu²⁺-Binding Motif: A Highly Rigid, Site-Specific Spin Probe for Electron Spin Resonance Distance Measurements, *Angew. Chem. Int. Ed.* 54 (2015) 6330–6334.
- [226] S. Ghosh, M. J. Lawless, G. S. Rule, S. Saxena, The Cu²⁺-Nitrilotriacetic Acid Complex Improves Loading of α -Helical Double Histidine Site for Precise Distance Measurements by Pulsed ESR, *J. Magn. Reson.* 286 (2018) 163–171.
- [227] M. J. Lawless, S. Ghosh, T. F. Cunningham, A. Shimshi, S. Saxena, On the use of the Cu²⁺-iminodiacetic acid complex for double histidine based distance measurements by pulsed ESR, *Phys. Chem. Chem. Phys.* 19 (2017) 20959–20967.

- [228] G. E. Merz, P. P. Borbat, A. R. Muok, M. Srivastava, D. N. Bunck, J. H. Freed, B. R. Crane, Site-Specific Incorporation of a Cu²⁺ Spin Label into Proteins for Measuring Distances by Pulsed Dipolar Electron Spin Resonance Spectroscopy, *J. Phys. Chem. B* 122 (2018) 9443–9451.
- [229] R. Hänsel, L. M. Luh, I. Corbeski, L. Trantirek, V. Doetsch, In-cell NMR and EPR spectroscopy of biomacromolecules, *Angew. Chem. Int. Edit.* 53 (2014) 10300–10314.
- [230] G. Jeschke, Distance measurements in the nanometer range by pulse EPR, *ChemPhysChem* 3 (2002) 927–932.
- [231] G. Jeschke, Dipolar Spectroscopy–Double-Resonance Methods, *eMagRes* (2007) 1459–1476.
- [232] J. S. Becker, S. Saxena, Double Quantum Coherence Electron Spin Resonance on Coupled Cu(II)–Cu(II) Electron Spins, *Chem. Phys. Lett.* 414 (2005) 248–252.
- [233] S. Ruthstein, M. Ji, P. Mehta, L. Jen-Jacobson, S. Saxena, Sensitive Cu²⁺–Cu²⁺ Distance Measurements in a Protein–DNA Complex by Double-Quantum Coherence ESR, *J. Phys. Chem. B* 117 (2013) 6227–6230.
- [234] A. Milov, A. Ponomarev, Y. Tsvetkov, Electron-electron double resonance in electron spin echo: Model biradical systems and the sensitized photolysis of decalin, *Chem. Phys. Lett.* 110 (1984) 67–72.
- [235] D. M. Engelhard, A. Meyer, A. Berndhäuser, O. Schiemann, G. H. Clever, Di-Copper (II) DNA G-Quadruplexes as EPR Distance Rulers, *ChemComm* (2018).
- [236] E. Narr, A. Godt, G. Jeschke, Selective Measurements of a Nitroxide–Nitroxide Separation of 5 nm and a Nitroxide–Copper Separation of 2.5 nm in a Terpyridine-Based Copper(II) Complex by Pulse EPR Spectroscopy, *Angew. Chem. Int. Edit.* 41 (2002) 3907–3910.
- [237] Z. Yang, J. Becker, S. Saxena, On Cu(II)–Cu(II) distance measurements using pulsed electron electron double resonance., *J. Magn. Reson.* 188 (2007) 337–343.
- [238] B. E. Bode, J. Plackmeyer, T. F. Prisner, O. Schiemann, PELDOR measurements on a nitroxide-labeled Cu(II) porphyrin: Orientation selection, spin-density distribution, and conformational flexibility., *J. Phys. Chem. A* 112 (2008) 5064–5073.
- [239] I. M. C. van Amsterdam, M. Ubbink, G. W. Canters, M. Huber, Measurement of a Cu–Cu Distance of 26 Å by a Pulsed EPR Method, *Angew. Chem. Int. Edit.* 42 (2003) 62–64.
- [240] Z. Yang, M. Ji, S. Saxena, Practical Aspects of Copper Ion-Based Double Electron Electron Resonance Distance Measurements, *Appl. Magn. Reson.* 39 (2010) 487–500.
- [241] Z. Yang, D. Kise, S. Saxena, An Approach towards the Measurement of Nanometer Range Distances Based on Cu²⁺ Ions and ESR, *J. Phys. Chem. B* 114 (2010) 6165–6174.
- [242] A. M. Bowen, C. E. Tait, C. R. Timmel, J. R. Harmer, Orientation-Selective DEER Using Rigid Spin Labels, Cofactors, Metals, and Clusters, Springer Berlin Heidelberg, Berlin, Heidelberg, pp. 283–327.

- [243] D. Abdullin, N. Florin, G. Hagelueken, O. Schiemann, Epr-based approach for the localization of paramagnetic metal ions in biomolecules, *Angew. Chem. Int. Edit.* 127 (2015) 1847–1851.
- [244] A. Giannoulis, C. L. Motion, M. Oranges, M. Bühl, G. M. Smith, B. E. Bode, Orientation selection in high-field RIDME and PELDOR experiments involving low-spin Co(II) ions, *Phys. Chem. Chem. Phys.* 20 (2018) 2151–2154.
- [245] P. E. Spindler, Y. Zhang, B. Endeward, N. Gershernzon, T. E. Skinner, S. J. Glaser, T. F. Prisner, Shaped optimal control pulses for increased excitation bandwidth in EPR, *J. Magn. Reson.* 218 (2012) 49–58.
- [246] I. Kaminker, R. Barnes, S. Han, Arbitrary waveform modulated pulse EPR at 200 GHz, *J. Magn. Reson.* 279 (2017) 81–90.
- [247] A. Band, M. P. Donohue, B. Epel, S. Madhu, V. A. Szalai, Integration of a versatile bridge concept in a 34 GHz pulsed/CW EPR spectrometer, *J. Magn. Reson.* 288 (2018) 28–36.
- [248] T. Kaufmann, T. J. Keller, J. M. Franck, R. P. Barnes, S. J. Glaser, J. M. Martinis, S. Han, DAC-board based X-band EPR spectrometer with arbitrary waveform control, *J. Magn. Reson.* 235 (2013) 95–108.
- [249] P. Neugebauer, D. Bloos, R. Marx, P. Lutz, M. Kern, D. Aguilà, J. Vaverka, O. Laguta, C. Dietrich, R. Clérac, et al., Ultra-broadband EPR spectroscopy in field and frequency domains, *Phys. Chem. Chem. Phys.* 20 (2018) 15528–15534.
- [250] M. Teucher, E. Bordignon, Improved signal fidelity in 4-pulse DEER with Gaussian pulses, *J. Magn. Reson.* 296 (2018) 103–111.
- [251] G. Jeschke, S. Pribitzer, A. Doll, Coherence Transfer by Passage Pulses in Electron Paramagnetic Resonance Spectroscopy, *J. Phys. Chem. B* (2015) 150513145858008.
- [252] M. Silver, R. Joseph, C.-N. Chen, V. Sank, D. Hoult, Selective population inversion in NMR, *Nature* 310 (1984) 681.
- [253] A. Tannus, M. Garwood, et al., Improved performance of frequency-swept pulses using offset-independent adiabaticity, *Journal of Magnetic Resonance-Series A* 120 (1996) 133–137.
- [254] T. Bahrenberg, Y. Rosenski, R. Carmieli, K. Zibzener, M. Qi, V. Frydman, A. Godt, D. Goldfarb, A. Feintuch, Improved sensitivity for W-band Gd (III)-Gd (III) and nitroxide-nitroxide DEER measurements with shaped pulses, *J. Magn. Reson.* 283 (2017) 1–13.
- [255] J. S. Hyde, J. W. Sidabras, R. R. Mett, Uniform Field Resonators for EPR Spectroscopy: A Review, *Cell Biochemistry and Biophysics* (2018) 1–12.
- [256] J. W. Sidabras, T. Sarna, R. R. Mett, J. S. Hyde, Uniform field loop-gap resonator and rectangular TEU02 for aqueous sample EPR at 94 GHz, *J. Magn. Reson.* 282 (2017) 129–135.
- [257] R. Tschaggelar, F. D. Breitgoff, O. Oberhänsli, M. Qi, A. Godt, G. Jeschke, High-Bandwidth Q-Band EPR Resonators, *Appl. Magn. Reson.* 48 (2017) 1273–1300.

- [258] V. Denysenkov, P. van Os, T. F. Prisner, Q-Band Loop-Gap Resonator for EPR Applications with Broadband-Shaped Pulses, *Appl. Magn. Reson.* 48 (2017) 1263–1272.
- [259] A. Doll, G. Jeschke, EPR-correlated dipolar spectroscopy by Q-band chirp SIFTER, *Phys. Chem. Chem. Phys.* 18 (2016) 23111–23120.
- [260] S. Pribitzer, T. F. Segawa, A. Doll, G. Jeschke, Transverse interference peaks in chirp FT-EPR correlated three-pulse ESEEM spectra, *J. Magn. Reson.* 272 (2016) 37–45.
- [261] P. Schöps, P. E. Spindler, A. Marko, T. F. Prisner, Broadband spin echoes and broadband SIFTER in EPR, *J. Magn. Reson.* 250 (2015) 55–62.
- [262] A. Tannús, M. Garwood, Adiabatic pulses, *NMR in Biomedicine: An International Journal Devoted to the Development and Application of Magnetic Resonance In Vivo* 10 (1997) 423–434.
- [263] R. D. Shannon, Revised effective ionic radii and systematic studies of interatomic distances in halides and chalcogenides, *Acta Cryst. A* 32 (1976) 751–767.
- [264] S. Pribitzer, M. Sajid, M. Hülsmann, A. Godt, G. Jeschke, Pulsed triple electron resonance (TRIER) for dipolar correlation spectroscopy, *J. Magn. Reson.* 282 (2017) 119–128.
- [265] M.-E. Boulon, A. Fernandez, E. M. Pineda, N. F. Chilton, G. Timco, A. J. Fielding, R. E. Winpenney, Measuring Spin-Spin Interactions between Heterospins in a Hybrid [2] Rotaxane, *Angew. Chem. Int. Edit.* 129 (2017) 3934–3937.
- [266] R. Mett, J. Sidabras, J. Hyde, Uniform radio frequency fields in loop-gap resonators for EPR spectroscopy, *Appl. Magn. Reson.* 31 (2007) 573.
- [267] M. Ji, S. Ruthstein, S. Saxena, Paramagnetic metal ions in pulsed ESR distance distribution measurements., *Acc. Chem. Res.* 47 (2014) 688–695.
- [268] H. V. Ching, P. Demay-Drouhard, H. C. Bertrand, C. Policar, L. C. Tabares, S. Un, Nanometric distance measurements between Mn(II) DOTA centers, *Phys. Chem. Chem. Phys.* 17 (2015) 23368–23377.
- [269] D. Akhmetzyanov, J. Plackmeyer, B. Endeward, V. Denysenkov, T. F. Prisner, Pulsed Electron-Electron Double Resonance Spectroscopy between a High-Spin Mn^{2+} Ion and a Nitroxide Spin Label., *Phys. Chem. Chem. Phys.* 17 (2015) 6760–6766.
- [270] G. Y. Shevelev, O. A. Krumkacheva, A. A. Lomzov, A. A. Kuzhelev, O. Y. Rogozhnikova, D. V. Trukhin, T. I. Troitskaya, V. M. Tormyshev, M. V. Fedin, D. V. Pyshnyi, E. G. Bagryanskaya, Physiological-temperature distance measurement in nucleic acid using triarylmethyl-based spin labels and pulsed dipolar EPR spectroscopy., *J Am Chem Soc* 136 (2014) 9874–9877.
- [271] G. Y. Shevelev, O. A. Krumkacheva, A. A. Lomzov, A. A. Kuzhelev, D. V. Trukhin, O. Y. Rogozhnikova, V. M. Tormyshev, D. V. Pyshnyi, M. V. Fedin, E. G. Bagryanskaya, Triaryl-methyl Labels: Toward Improving the Accuracy of EPR Nanoscale Distance Measurements in DNAs., *J. Phys. Chem. B* 119 (2015) 13641–13648.

- [272] G. W. Reginsson, N. C. Kunjir, S. T. Sigurdsson, O. Schiemann, Trityl radicals: Spin labels for nanometer-distance measurements., *Chemistry* 18 (2012) 13580–13584.
- [273] Z. Yang, Y. Liu, P. Borbat, J. L. Zweier, J. H. Freed, W. L. Hubbell, Pulsed ESR Dipolar Spectroscopy for Distance Measurements in Immobilized Spin Labeled Proteins in Liquid Solution, *J. Am. Chem. Soc.* 134 (2012) 9950–9952.
- [274] T. R. Krugh, Spin-label-induced nuclear magnetic resonance relaxation studies of enzymes, *Spin labeling: Theory and applications* 1 (1976) 339–372.
- [275] V. V. Kurshev, A. M. Raitsimring, Y. D. Tsvetkov, Selection of dipolar interaction by the “2+ 1” pulse train ese, *J. Magn. Reson.* (1969) 81 (1989) 441–454.
- [276] M. Allegrozzi, I. Bertini, M. B. L. Janik, Y.-M. Lee, G. Liu, C. Luchinat, Lanthanide-Induced Pseudocontact Shifts for Solution Structure Refinements of Macromolecules in Shells up to 40 Å from the Metal Ion, *J. Am. Chem. Soc.* 122 (2000) 4154–4161.
- [277] C. F. G. C. Geraldes, C. Luchinat, Lanthanides as Shift and Relaxation Agents in Elucidating the Structure of Proteins and Nucleic Acids, *Met Ions Biol Syst* 40 (2003) 513–588.
- [278] A. D. Milov, S. KM, S. MD, Application of ELDOR in electron-spin echo for investigation of paramagnetic center space distribution in solids., *Fiz. Tverd. Tela* (1981) 957–982.
- [279] I. Kaminker, I. Tkach, N. Manukovsky, T. Huber, H. Yagi, G. Otting, M. Bennati, D. Goldfarb, W-Band Orientation Selective DEER Measurements on a Gd³⁺/Nitroxide Mixed-Labeled Protein Dimer with a Dual Mode Cavity., *J. Magn. Reson.* 227 (2013) 66–71.
- [280] A. G. Maryasov, M. K. Bowman, Y. D. Tsvetkov, Dipole-Dipole Interactions of High-Spin Paramagnetic Centers in Disordered Systems, *Appl. Magn. Reson.* 30 (2006) 683.
- [281] R. Orbach, *Proc. Phys. Soc.(London)* 77 (1961) 821.
- [282] Y. Yang, Y.-J. Gong, A. Litvinov, H.-K. Liu, F. Yang, X.-C. Su, D. Goldfarb, Generic tags for Mn(II) and Gd(III) spin labels for distance measurements in proteins, *Phys.Chem. Chem. Phys.* 19 (2017) 26944–26956.
- [283] Z. Yang, G. Jiménez-Osés, C. J. López, M. D. Bridges, K. N. Houk, W. L. Hubbell, Long-Range Distance Measurements in Proteins at Physiological Temperatures Using Saturation Recovery EPR Spectroscopy, *J. Am. Chem. Soc.* 136 (2014) 15356–15365.
- [284] I. Kaminker, A. Potapov, A. Feintuch, S. Vega, D. Goldfarb, Population transfer for signal enhancement in pulsed EPR experiments on half integer high spin systems, *Phys. Chem. Chem. Phys.* 11 (2009) 6799–6806.
- [285] S. Pribitzer, L. F. Ibanez, C. Gmeiner, I. Ritsch, D. Klose, M. Sajid, M. Hülsmann, A. Godt, G. Jeschke, Two-Dimensional Distance Correlation Maps from Pulsed Triple Electron Resonance (TRIER) on Proteins with Three Paramagnetic Centers, *Appl. Magn. Reson.* 49 (2018) 1253–1279.
- [286] N. Wili, G. Jeschke, Chirp echo Fourier transform EPR-detected NMR, *J. Magn. Reson.* 289 (2018) 26–34.

- [287] T. F. Segawa, A. Doll, S. Pribitzer, G. Jeschke, Copper ESEEM and HYSCORE through ultra-wideband chirp EPR spectroscopy, *J. Chem. Phys.* 143 (2015) 044201.
- [288] Y. Polyhach, E. Bordignon, G. Jeschke, Rotamer libraries of spin labelled cysteines for protein studies, *Phys. Chem. Chem. Phys.* 13 (2011) 2356–2366.
- [289] G. Jeschke, A. Bender, H. Paulsen, H. Zimmermann, A. Godt, Sensitivity enhancement in pulse EPR distance measurements, *J. Magn. Reson.* 169 (2004) 1 – 12.
- [290] R. Ward, A. Bowman, E. Sozudogru, H. El-Mkami, T. Owen-Hughes, D. G. Norman, EPR distance measurements in deuterated proteins, *J. Magn. Reson.* 207 (2010) 164 – 167.
- [291] G. Jeschke, MMM: A toolbox for integrative structure modeling, *Protein Science* 27 (2018) 76–85.
- [292] P. I. Hanson, S. W. Whiteheart, AAA⁺ proteins: have engine, will work, *Nat Rev Mol Cell Biol.* 6 (2005) 519.
- [293] D. C. Rees, E. Johnson, O. Lewinson, ABC transporters: the power to change, *Nat Rev Mol Cell Biol.* 10 (2009) 218.
- [294] A. Bazin, M. V. Cherrier, I. Gutsche, J. Timmins, L. Terradot, Structure and primase-mediated activation of a bacterial dodecameric replicative helicase, *Nucleic Acids Res.* 43 (2015) 8564–8576.
- [295] E. Steinfelds, C. Orelle, J.-R. Fantino, O. Dalmas, J.-L. Rigaud, F. Denizot, A. Di Pietro, J.-M. Jault, Characterization of YvcC (BmrA), a multidrug ABC transporter constitutively expressed in *Bacillus subtilis*, *Biochemistry* 43 (2004) 7491–7502.
- [296] C. Geourjon, C. Orelle, E. Steinfelds, C. Blanchet, G. Deléage, A. Di Pietro, J.-M. Jault, A common mechanism for ATP hydrolysis in ABC transporter and helicase superfamilies, *Trends Biochem Sci* 26 (2001) 539–544.
- [297] W. Bujalowski, M. M. Klonowska, Negative cooperativity in the binding of nucleotides to *Escherichia coli* replicative helicase DnaB protein. Interactions with fluorescent nucleotide analogs, *Biochemistry* 32 (1993) 5888–5900.
- [298] M. J. Jezewska, U.-S. Kim, W. Bujalowski, Interactions of *Escherichia coli* primary replicative helicase DnaB protein with nucleotide cofactors., *Biophys. J.* 71 (1996) 2075.
- [299] A. Siarheyeva, R. Liu, F. J. Sharom, Characterization of an asymmetric occluded state of P-glycoprotein with two bound nucleotides: implications for catalysis, *J. Biol. Chem.* (2010) jbc–M109.
- [300] C. P. Jaroniec, Structural studies of proteins by paramagnetic solid-state NMR spectroscopy, *J. Magn. Reson.* 253 (2015) 50–59.
- [301] I. Bertini, L. Emsley, M. Lelli, C. Luchinat, J. Mao, G. Pintacuda, Ultrafast MAS solid-state NMR permits extensive ¹³C and ¹H detection in paramagnetic metalloproteins, *J. Am. Chem. Soc.* 132 (2010) 5558–5559.

- [302] G. Pintacuda, N. Giraud, R. Pierattelli, A. Böckmann, I. Bertini, L. Emsley, Solid-State NMR Spectroscopy of a Paramagnetic Protein: Assignment and Study of Human Dimeric Oxidized Cu^{II}-Zn^{II} Superoxide Dismutase (SOD), *Angew. Chem. Int. Edit.* 46 (2007) 1079–1082.
- [303] S. J. Ullrich, S. Hölper, C. Glaubitz, Paramagnetic doping of a 7TM membrane protein in lipid bilayers by Gd³⁺-complexes for solid-state NMR spectroscopy, *J. Biomol. NMR* 58 (2014) 27–35.
- [304] J. E. Walker, M. Saraste, M. J. Runswick, N. J. Gay, Distantly related sequences in the alpha-and beta-subunits of ATP synthase, myosin, kinases and other ATP-requiring enzymes and a common nucleotide binding fold., *EMBO J.* 1 (1982) 945–951.
- [305] T. Wiegand, R. Cadalbert, C. Gardiennet, J. Timmins, L. Terradot, A. Böckmann, B. H. Meier, Monitoring ssDNA Binding to the DnaB Helicase from *Helicobacter pylori* by Solid-State NMR Spectroscopy, *Angew. Chem. Int. Ed.* 55 (2016) 14164–14168.
- [306] C. Orelle, F. Gubellini, A. Durand, S. Marco, D. Lévy, P. Gros, A. Di Pietro, J.-M. Jault, Conformational change induced by ATP binding in the multidrug ATP-binding cassette transporter BmrA, *Biochemistry* 47 (2008) 2404–2412.
- [307] H. Witt, A. Wittershagen, E. Bill, B. Kolbesen, B. Ludwig, Asp-193 and Glu-218 of subunit II are involved in the Mn²⁺-binding of *Paracoccus denitrificans* cytochrome c oxidase, *FEBS letters* 409 (1997) 128–130.
- [308] E. Bonneau, P. Legault, NMR localization of divalent cations at the active site of the *Neurospora VS* ribozyme provides insights into RNA–metal-ion interactions, *Biochemistry* 53 (2014) 579–590.
- [309] I. Bertini, C. Luchinat, G. Parigi, R. Pierattelli, NMR spectroscopy of paramagnetic metalloproteins, *ChemBioChem* 6 (2005) 1536–1549.
- [310] H. Kaur, A. Lakatos, R. Spadaccini, R. Vogel, C. Hoffmann, J. Becker-Baldus, O. Ouari, P. Tordo, H. Mchaourab, C. Glaubitz, The ABC exporter MsbA probed by solid state NMR—challenges and opportunities, *Biol. Chem.* 396 (2015) 1135–1149.
- [311] H. Tamaki, A. Egawa, K. Kido, T. Kameda, M. Kamiya, T. Kikukawa, T. Aizawa, T. Fujiwara, M. Demura, Structure determination of uniformly ¹³C, ¹⁵N labeled protein using qualitative distance restraints from MAS solid-state ¹³C-NMR observed paramagnetic relaxation enhancement, *J. Biomol. NMR* 64 (2016) 87–101.
- [312] G. Mukhopadhyay, N. R. Choudhury, P. Mehra, R. K. Soni, S. K. Dhar, Functional characterization of *Helicobacter pylori* DnaB helicase, *Nucleic Acids Res* 31 (2003) 6828–6840.
- [313] S. Razzaghi, E. K. Brooks, E. Bordignon, W. L. Hubbell, M. Yulikov, G. Jeschke, EPR Relaxation-Enhancement-Based Distance Measurements on Orthogonally Spin-Labeled T4-Lysozyme, *ChemBioChem* 14 (2013) 1883–1890.
- [314] D. Banerjee, H. Yagi, T. Huber, G. Otting, D. Goldfarb, Nanometer-Range Distance Measurement in a Protein Using Mn²⁺ Tags, *J. Phys. Chem. Lett.* 3 (2012) 157–160.

- [315] M. S. Strycharska, E. Arias-Palomo, A. Y. Lyubimov, J. P. Erzberger, V. L. O'Shea, C. J. Bustamante, J. M. Berger, Nucleotide and Partner-Protein Control of Bacterial Replicative Helicase Structure and Function, *Mol Cell* 52 (2013) 844–854.
- [316] C. Pliotas, R. Ward, E. Branigan, A. Rasmussen, G. Hagelueken, H. Huang, S. S. Black, I. R. Booth, O. Schiemann, J. H. Naismith, Conformational state of the MscS mechanosensitive channel in solution revealed by pulsed electron–electron double resonance (PELDOR) spectroscopy, *PNAS* 109 (2012) E2675–82.
- [317] S. Valera, K. Ackermann, C. Pliotas, H. Huang, J. H. Naismith, B. E. Bode, Accurate extraction of nanometer distances in multimers by pulse EPR, *Chem. Eur. J.* 22 (2016) 4700–4703.
- [318] A. V. Astashkin, B. O. Elmore, W. Fan, J. G. Guillemette, C. Feng, Pulsed EPR determination of the distance between heme iron and FMN centers in a human inducible nitric oxide synthase., *J. Am. Chem. Soc.* 132 (2010) 12059–12067.
- [319] J. R. Taylor, *An Introduction to Error Analysis: the study of uncertainties in physical measurements*, University Science Books, 1997.
- [320] A. Volkov, C. Dockter, T. Bund, H. Paulsen, G. Jeschke, Pulsed EPR determination of water accessibility to spin-labeled amino acid residues in LHCIIB, *c* 96 (2009) 1124–1141.
- [321] F. C. Oberstrass, S. D. Auweter, M. Erat, Y. Hargous, A. Henning, P. Wenter, L. Reymond, B. Amir-Ahmady, S. Pitsch, D. L. Black, et al., Structure of PTB bound to RNA: specific binding and implications for splicing regulation, *Science* 309 (2005) 2054–2057.
- [322] P. J. Simpson, T. P. Monie, A. Szendrői, N. Davydova, J. K. Tyzack, M. R. Conte, C. M. Read, P. D. Cary, D. I. Svergun, P. V. Konarev, et al., Structure and RNA interactions of the N-terminal RRM domains of PTB, *Structure* 12 (2004) 1631–1643.
- [323] F. Vitali, A. Henning, F. C. Oberstrass, Y. Hargous, S. D. Auweter, M. Erat, F. H.-T. Allain, Structure of the two most C-terminal RNA recognition motifs of PTB using segmental isotope labeling, *EMBO J.* 25 (2006) 150–162.
- [324] A. Joshi, M. B. Coelho, O. Kotik-Kogan, P. J. Simpson, S. J. Matthews, C. W. Smith, S. Curry, Crystallographic analysis of polypyrimidine tract-binding protein-Raver1 interactions involved in regulation of alternative splicing, *Structure* 19 (2011) 1816–1825.
- [325] H. Yaginuma, S. Kawai, K. V. Tabata, K. Tomiyama, A. Kakizuka, T. Komatsuzaki, H. Noji, H. Imamura, Diversity in ATP concentrations in a single bacterial cell population revealed by quantitative single-cell imaging, *Scientific reports* 4 (2014) 6522.
- [326] B. D. Bennett, E. H. Kimball, M. Gao, R. Osterhout, S. J. Van Dien, J. D. Rabinowitz, Absolute metabolite concentrations and implied enzyme active site occupancy in *Escherichia coli*, *Nature chemical biology* 5 (2009) 593.
- [327] G. Hagelueken, W. J. Ingledew, H. Huang, B. Petrovic-Stojanovska, C. Whitfield, H. Elmkami, O. Schiemann, J. H. Naismith, PELDOR Spectroscopy Distance Fingerprinting of the Octameric Outer-Membrane Protein Wza from *Escherichia coli*., *Angew. Chem. Int. Edit.* 48 (2009) 2904–2906.

- [328] B. E. Bode, D. Margraf, J. Plackmeyer, G. Dürner, T. F. Prisner, O. Schiemann, Counting the monomers in nanometer-sized oligomers by pulsed electron-electron double resonance, *J. Am. Chem. Soc.* 129 (2007) 6736–6745.

A

Supplementary Information to Chapter 4

A.1. Characterization of ZFS tensor eigenvalue distributions by anisotropy and axiality

In a spin operator expansion up to second order, the ZFS leads to a coupling **SDS** of the spin vector operator **S** with itself that is described by a traceless second-rank tensor **D**, which depends on the spin density distribution. In this work, we are not interested in the eigenframe of **D**, but only in its eigenvalues D_1 , D_2 , and D_3 . Without loss of generality we assume $D_1 > D_2 > D_3$.

If the eigenvalues D_i ($i = 1 \dots 3$) are all similar between two configurations, the two parameters by which we characterize the traceless ZFS tensor should also be similar. This is not the case for the parameters D and E using the usual convention. As an example, consider the two sets $(D_{1,a}, D_{2,a}, D_{3,a}) = (800, -4, -796)$ MHz and $(D_{1,b}, D_{2,b}, D_{3,b}) = (796, 4, -800)$ MHz. The first set is characterized by $D_a = 1200$ MHz and $E_a = 396$ MHz, while the second set is characterized by $D_a = -1200$ MHz and $E_a = -396$ MHz. A very small change in the spin density distribution can cause a sign change of the parameters D and E . For the set $(D_{1,c}, D_{2,c}, D_{3,c}) = (800, 0, -800)$ MHz, two different assignments of D_y and D_z to D_1 and D_3 are possible, which lead to different signs for D and E . The two parameters are often discussed as characterizing the magnitude (D) and deviation from axial symmetry (E) of the ZFS. However, in the case of broad distributions with significant probability density near $E/D = 1/3$, mean values of D and E are ill-defined due to the unphysical discontinuity of the sign.

This problem can be solved without giving up the convention of assigning D_x , D_y , and D_z and computing the parameters D and E by defining two additional parameters that are well-behaved when comparing broad distributions. These parameters $\Delta = |D_z|$ and $\xi = 2(D_y + D_z)/\Delta$ characterize the anisotropy and the proximity to a tensor with axial symmetry, respectively. The sign of the axiality ξ is the sign of the principal value of **D** with the largest magnitude. We have $-1 \leq \xi \leq 1$ with $\xi = -1$ and $+1$ corresponding to the cases with axial symmetry and $\xi = 0$ corresponding to $E/D = 1/3$. For $\xi = 0$, assignment of the principal values is not strictly defined by the established convention and we follow common usage by assigning $D_z = \Delta$, $D_y = -\Delta$, $D_x = 0$. For $\xi \neq 0$, we find

$$D_x = -\xi \frac{\Delta}{2}, \quad (\text{A.1})$$

$$D_y = [\xi - 2 \text{sign}(\xi)] \frac{\Delta}{2}, \quad (\text{A.2})$$

$$D_z = \text{sign}(\xi) \Delta, \quad (\text{A.3})$$

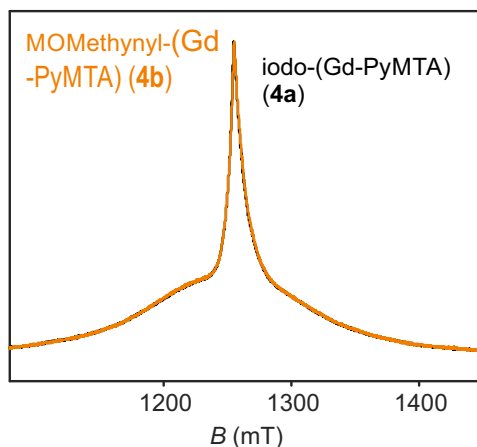


Figure A.1. Q-band (34 GHz) EDEPR spectra of iodo-(Gd-PyMTA) (**4a**) (black curve) and MOMethynyl-(Gd-PyMTA) (**4b**) (orange curve) at 10 K.

$$D = \frac{3}{2} \text{sign}(\xi) \Delta, \quad (\text{A.4})$$

and

$$E = [\text{sign}(\xi) - \xi] \frac{\Delta}{2}. \quad (\text{A.5})$$

Equations (A.1 - A.5) are applicable at $\xi = 0$ if the sign function is substituted by unity.

For Models 1, 2, and 3, as well as for small perturbations of a given ligand geometry in the superposition Model B, anisotropy Δ exhibits a monomodal distribution. The distribution of axially ξ extends from -1 to 1 in all four models. The sign of the mean value $\bar{\xi}$ is directly related to the asymmetry of the low-temperature G-band spectrum and the standard deviation σ_{ξ} to broadening of the shoulders of the spectrum.

A.2. Q-band EDEPR spectra of R-(Gd-PyMTA) (**4ab**)

In the course of this project due to changes in availability, we performed EPR measurements on Gd-PyMTA complexes with two different substituents. Figure A.1 shows the Q-band EDEPR spectra of both R-(Gd-PyMTA) (**4ab**) complexes. It is observed that the spectra overlay almost perfectly. Thus, for this study, it was assumed the ZFS distribution parameters are not strongly influenced by the substituent of R-(Gd-PyMTA).

A.3. Further details of the numerical simulations

A.3.1. Orientation averaging

Orientation averaging was performed in 3 degree increments and a 10-fold interpolation of the orientation grid (Opt.nKnots = [31 10] in EasySpin), although reducing the orientation resolution to 10 degree increments did not have a large influence on the spectra given a sufficient number of points in the D and E distributions (Figures A.2(a) and A.3(a)). Computation time is reduced by reducing the resolution of the orientation averaging.

A.3.2. Range and number of magnetic field points

The number of field points was set to 8000 to reach sufficient convergence (Figures A.2(b) and A.3(b)). This is especially important to avoid deviations for EPR spectra simulated at 240 GHz. The magnetic field range for simulation was chosen to well cover the experimental one, as the EasySpin function *pepper* forces the computed spectra to zero at its boundaries (Figures A.2(c) and A.3(c)). The range of the magnetic field and the number of points sampled within this range were found to not largely influence the computation time for the values tested.

A.3.3. Regular grid vs. Monte Carlo sampling of the ZFS parameter distributions

Two different approaches to the sampling of the $P(D)$ and $P(E)$ (or $P(E/D)$) distributions were investigated. First, the distributions were sampled using a regular grid of linearly spaced points. This approach allows for uniform sampling of all relevant D and E values, however a significant fraction of the total computational cost is spent on computing spectra with D and E parameters far away from the maxima of the probability distributions. Additionally, when sampling in the vicinity of $D = 0$, a sharp peak will be generated in the simulated EPR spectra corresponding to the smallest sampled value of D . In particular, if the point $D = 0$ is present in the sampling set, this produces an artefact peak with the intrinsic line width at the Gd(III) g -value position (Figure A.4). Such a sharp peak is not expected, nor is it observed in the experimental data, since for nearly symmetric cases ($D \approx 0$, $E \approx 0$) the width of the central transition of Gd(III) will be dominated by inhomogeneous broadening mechanisms. In particular, higher-order ZFS terms are expected to play a significant role for the small fraction of cases where $D \approx 0$ and $E \approx 0$, and any small g anisotropy or unresolved hyperfine couplings also contribute to the width of the central transition.

As an alternative to the regular grid sampling, we inspected a Monte Carlo approach in which a large set of randomly distributed (D, E) pairs is first generated, and then the overall EPR spectrum is computed as a linear combination of the EPR spectra for all of the (D, E) pairs. For the $P(D)$ distribution, which is Gaussian in all three models, the required stream of pseudo-random numbers can be generated by the MATLAB function *randn()*. The polynomial distribution for $P(E/D)$ in Models 2/3 was generated by numeric calculation of the corresponding $E/D = A$ values from the uniformly distributed cumulative probability $X = P(E/D \leq A)$. Using this method ensures that the number of points sampled in a particular range of D and E parameters corresponds to the relative weight of this range in the overall EPR spectrum, resulting in minimal computational cost.

Both sampling methods require careful calibration of the convergence criteria. Monte Carlo sampling requires calibration of the convergence of simulated EPR spectrum with respect to the number N of random steps, and the regular grid sampling requires calibration of the step size of the grid. The minimum requirement for convergence is dependent of the strength of the ZFS. Given known convergence criteria for a particular set of ZFS parameter values, the convergence criteria for any arbitrary ZFS can be reasonably extrapolated since the number of sampling points required scales nearly linearly with the strength of the ZFS (assuming the weak ZFS/strong field case). In this work, random Monte Carlo sampling was used with $N = 40000$ random points to ensure sufficient convergence for any ZFS within the range of values typically found for Gd(III) complexes (Figures A.2(d) and A.3(d)).

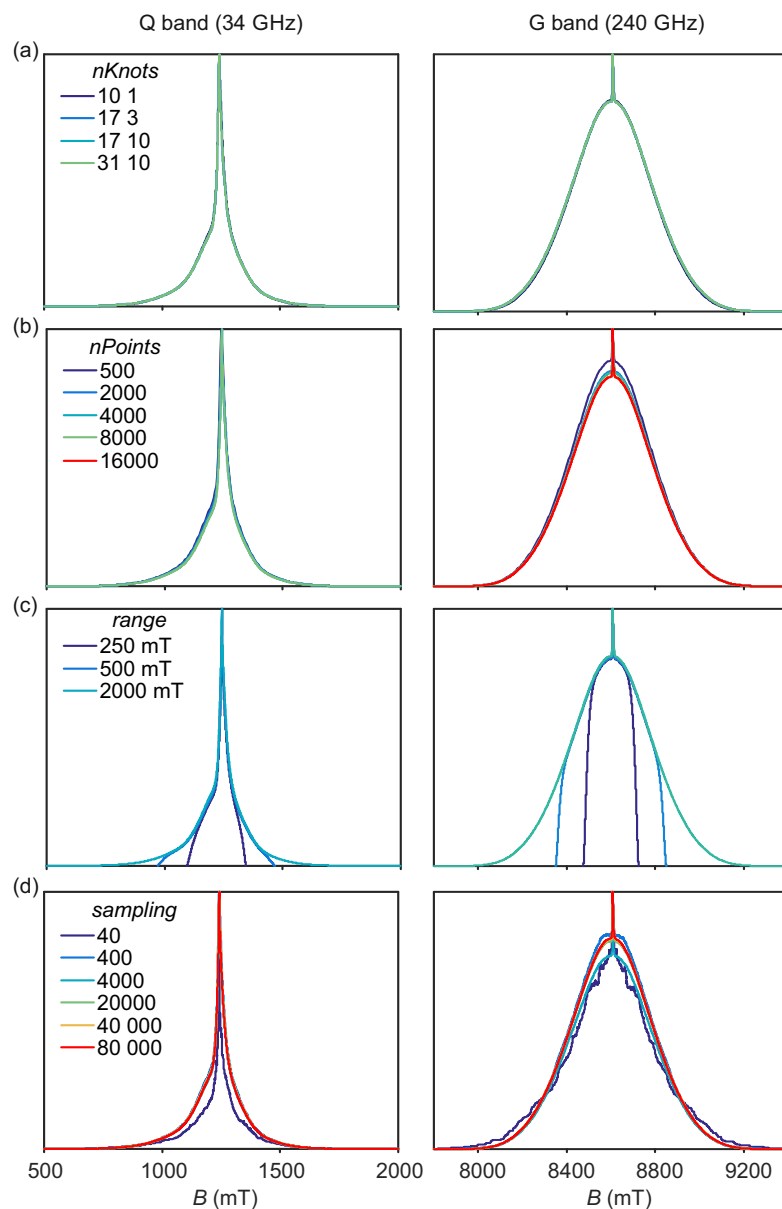


Figure A.2. Influence of simulation options on the convergence of simulated EPR spectra in Q band (left) and G band (right) using Model 2, $D = 1820$ MHz and $\sigma_D = 520$ MHz. a) orientation resolution (nKnots), b) number of field points ($nPoints$), c) field range ($Range$), d) number of random points in $P(D)$ distribution sampled by Monte Carlo integration. No additional line broadening is included.

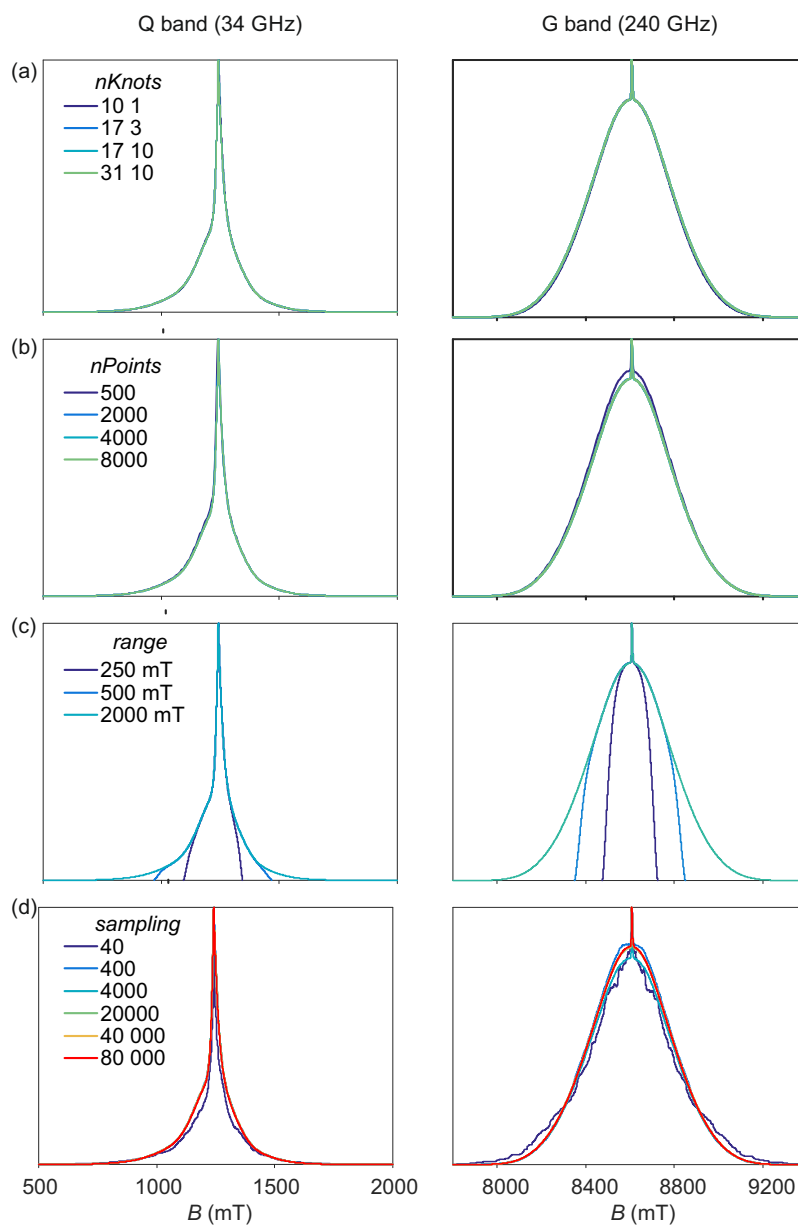


Figure A.3. Influence of simulation options on the convergence of simulated EPR spectra in Q band (left) and G band (right) using Model 2, $D = 1820$ MHz and $\sigma_D = 520$ MHz. a) orientation resolution ($nKnots$), b) number of field points ($nPoints$), c) field range ($Range$), d) number of random points in $P(D)$ distribution sampled by Monte Carlo integration. An additional convolutional line broadening term was included in these simulations ($lwpp = [1 \ 0.1]$). It was found that including a convolutional line broadening term resulted into faster convergence of the simulated spectra for given simulation options.

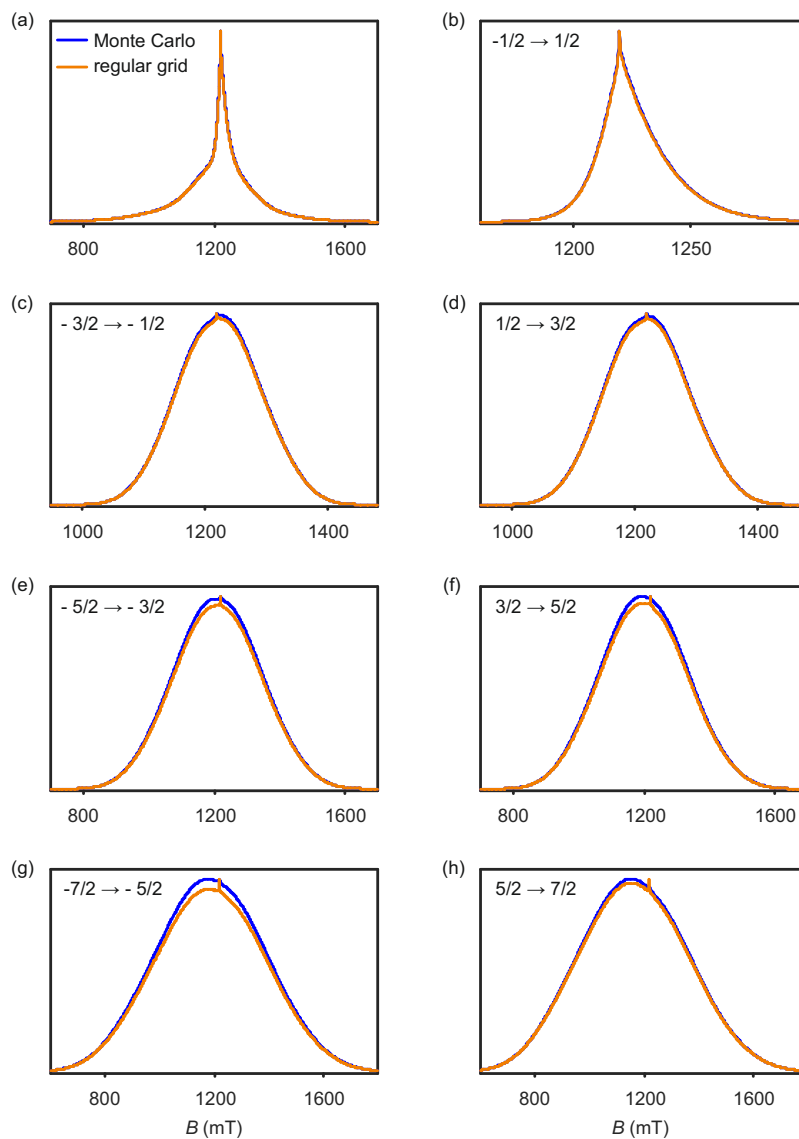


Figure A.4. Comparison of Q-band EPR spectra simulated using Monte-Carlo (blue) or regular grid sampling (orange). The regular grid was set to include the point $D = 0$, resulting in an artefact peak at the Gd(III) g -value position. Simulations were performed using Model 2 with $D = 1820$ MHz and $\sigma_D = 520$ MHz. (a) final simulated spectra after summing of all transitions, (b) $| -1/2 \rangle \rightarrow | 1/2 \rangle$ transition, (c) $| -3/2 \rangle \rightarrow | -1/2 \rangle$ transition, (d) $| 1/2 \rangle \rightarrow | 3/2 \rangle$ transition, (e) $| -5/2 \rangle \rightarrow | -3/2 \rangle$ transition, (f) $| 3/2 \rangle \rightarrow | 5/2 \rangle$ transition, (g) $| -7/2 \rangle \rightarrow | -5/2 \rangle$ transition, (h) $| 5/2 \rangle \rightarrow | 7/2 \rangle$ transition.

Figure A.4 illustrates the similarity of the calculated Gd(III) EPR spectra computed with a regular grid of (D, E) values compared to the use of a random ensemble of (D, E) values and Monte Carlo integration. The only difference between the resulting calculated spectra can be found at the peak of the simulated EPR spectrum. This deviation is smeared out if an intrinsic linewidth is included in the calculations.

A.3.4. Line broadening

The effect of an isotropic convolutional line broadening parameter ($Sys.lwpp = [\text{Gaussian Lorentzian}]$ in EasySpin) on the simulated spectra is shown in Figures A.5 and A.6. The broadening parameter primarily influences the sharp feature at the central peak of the EPR spectrum, leaving the shape of the outer envelope largely unaffected. Increasing the amount of Gaussian and/or Lorentzian broadening results in broadening of the central peak of the EPR spectrum. Thus, the relative intensity of the central peak with respect to the outer envelope of the EPR spectrum is influenced by broadening of the central peak and scaling of the simulated spectra to the maximum of the experimental spectra can result in an overestimation of the ZFS if unresolved broadening are neglected (Figure A.5(a) and Figure A.24(a-c)). Scaling only to the broad outer envelope of the EPR spectrum, as it was done in this work, circumvents this problem.

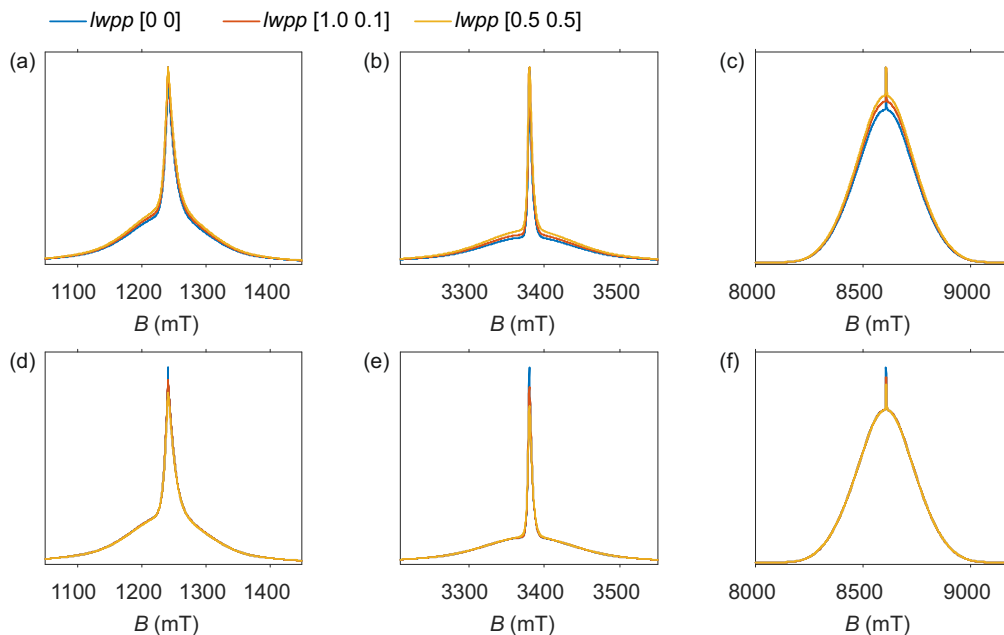


Figure A.5. Influence of the addition of an isotropic line broadening parameter ($Sys.lwpp = [\text{Gaussian Lorentzian}]$ in EasySpin) on the line shape of simulated EPR spectra in Q band (34 GHz) (a, d), W band (94 GHz) (b, e), and G band (240 GHz) (c, f). Spectra were simulated using Model 2, $D = 1350$ MHz and $\sigma_D = D/3.5$ for line broadenings of $lwpp = [0\ 0]$, $lwpp = [1.0\ 0.1]$, and $lwpp = [0.5\ 0.5]$. Peak-to-peak line broadenings ($lwpp$) are given in units of mT. (a - c) Simulated spectra scaled to maximum intensity and (d - f) simulated spectra scaled to the outer envelope.

The effect of an additional line broadening parameter is also demonstrated for the W-band (94 GHz) spectra of Gd-NO₃Pic (Figure A.6(a)) and Gd-PyDTTA (Figure A.6(b)). Adding a line broadening to the simulation helps improve the match between the experimental and simulated Gd(III) EPR spectra. However, the line broadening term is a phenomenological parameter and its interpretation is not straightforward.

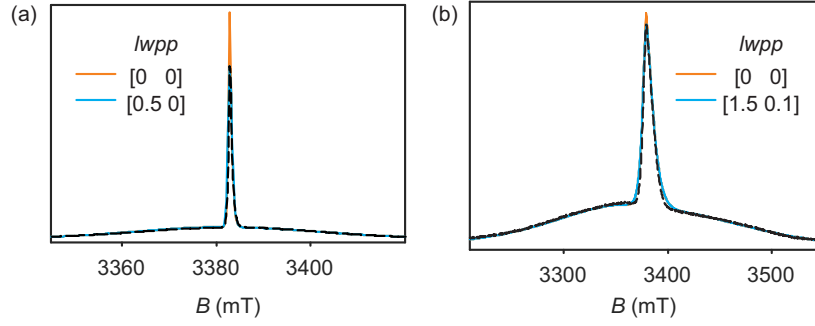


Figure A.6. Influence of isotropic line broadening ($Sys.lwpp = [Gaussian Lorentzian]$ in EasySpin) on the line shape of simulated EPR spectra (Model 3, ZFS parameters from table A.8) for the complexes (a) Gd-NO₃Pic ($D = 470$ MHz, $\sigma_D = 134$ MHz) and (b) Gd-PyDTTA ($D = 1860$ MHz, $\sigma_D = 465$ MHz) at W band (94 GHz). Peak-to-peak line broadening is given in units of mT. Simulated spectra are scaled to the outer envelope of the experimental data (black dashed lines).

A.3.5. Flip angle correction for Q-/W-band simulations

For the Q-/W-band spectra, which were obtained experimentally from EDEPR measurements, a flip angle correction was included in the simulation. Each allowed transition was computed separately, and then the final simulated spectra were obtained by summing the contributions of the individual transitions according to their effective flip angles (Table A.1). The relative contribution of each transition P_m to the normalized echo intensity upon a $\pi/2 - \tau - \pi - \tau$ pulse sequence is given by

$$\begin{aligned}
 P_m &= \sin(\alpha\pi/2) \cos(\alpha\pi), \\
 \alpha &= \langle m_S | \hat{S}^+ | m_S + 1 \rangle / \langle -1/2 | \hat{S}^+ | +1/2 \rangle \\
 &= \frac{\sqrt{S(S+1) - m_S(m_S+1)}}{\sqrt{S(S+1) + 1/4}} = \sqrt{\frac{63 - 4 \cdot m_S(m_S+1)}{64}},
 \end{aligned} \tag{A.6}$$

which results in the normalized transition probabilities given in Table A.1. Figure A.7 illustrates the change in line shape from an equally weighted sum to a sum according to these transition probabilities.

Transition(s)	P_m
$ -7/2 \rangle \leftrightarrow -5/2 \rangle, +5/2 \rangle \leftrightarrow +7/2 \rangle$	0.419
$ -5/2 \rangle \leftrightarrow -3/2 \rangle, +3/2 \rangle \leftrightarrow +5/2 \rangle$	0.893
$ -3/2 \rangle \leftrightarrow -1/2 \rangle, +1/2 \rangle \leftrightarrow +3/2 \rangle$	0.994
$ -1/2 \rangle \leftrightarrow +1/2 \rangle$	1

Table A.1. Flip angle correction applied to each allowed transition, given by the relative contribution of each transition P_m to the normalized echo intensity for a $\pi/2 - \tau - \pi - \tau$ pulse sequence.

Note that the weight coefficients listed in the Table A.1 are only valid with good precision when the electron spin echo is tuned at the maximum of the Gd(III) EPR spectrum. If the spin echo is instead set up at the high-field or low-field side of the spectrum, the power of the microwave pulses will be optimized for the $| -7/2 \rangle \leftrightarrow | -5/2 \rangle$ and $| +5/2 \rangle \leftrightarrow | +7/2 \rangle$ transitions, resulting in over-flipping of the other Gd(III) transitions.

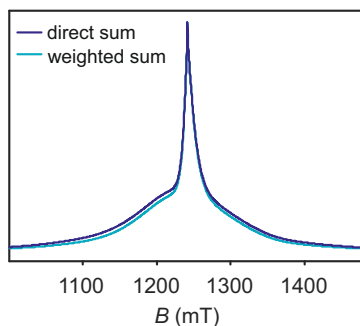


Figure A.7. Comparison between an equally weighted sum of transitions (called direct sum, violet) and a transition-specific weighted sum (called weighted sum, cyan) of the allowed Gd(III) transitions according to Table A.1. The simulation is shown for Q band (34 GHz) using Model 2 with the parameters $D = 1350$ MHz, $\sigma_D = 386$ MHz and no additional line broadening.

A.4. Parameters used for simulations with Model 1

For simulations with Model 1, $N = 40000$ random steps were used for Monte Carlo sampling of the $P(D)$ and $P(E)$ distributions. The field range was set to well cover the experimental spectra (the same as the *Exp.Range* values in Table A.2). Additionally an isotropic line broadening term $lwpp$ was added. Other simulation parameters were set as described in section A.3.5 and in the main text. The simulation frequency and temperature for each Gd(III) complex were set to the values given in Table A.5.

A.5. Simulation parameters used for generation of rmsd error maps for Models 2 and 3

For Models 2 and 3, a large library of simulated EPR spectra were generated for use in computing the rmsd error maps. This library contains a set of simulations for each measurement frequency and temperature employed in this work (i.e. Q band and 10 K, W band and 10 K, G band and 5 K, Table A.2), and maps out a region of the parameter space of (D, σ_D) parameter values. The range of D and σ_D parameter values was chosen to include the ZFS parameter values for each of the Gd(III) complexes studied here, as estimated by visual inspection. These considerations resulted in the library of simulations sampling a grid spanning $D = 300 - 1950$ MHz and $\sigma_D = 50 - 600$ MHz in steps of 50 MHz. The contributions to the simulated lineshape from the positive and negative modes of the bimodal $P(D)$ distribution were saved separately, allowing for the same library of simulations to be used for both Models 2 and 3.

mwFreq (GHz)	Range (mT)	Temperature (K)
34.50	[219 2219]	10
94.25	[2380 4380]	10
240	[7608 9608]	5

Table A.2. Experimental parameters used as EasySpin inputs to generate a large library of simulated spectra for the determination of ZFS parameter value with Models 2 and 3.

These simulations employed Monte-Carlo sampling of the $P(D)$ and $P(E/D)$ distributions, with the number of random steps set to $N = 20000$. The magnetic field range for each measurement frequency was chosen to well cover the experimental spectrum for all Gd(III) complexes studied

here (Table A.2). The number of magnetic field points sampled was set to $Exp.nPoints = 8000$, and the orientational averaging was set to $Opt.nKnots = [31\ 10]$. No additional line broadening was included.

A.6. Procedure for determining best-fit ZFS parameter values and associated error bars from rmsd error maps (Models 2 and 3)

For Models 2 and 3, the best-fit ZFS parameter values were determined from the rmsd error maps computed using the library of simulations for each measurement frequency. The library of simulations used maps out a region of (D, σ_D) parameter space in increments of 50 MHz. The asterisk on these contour plots indicates the (D, σ_D) parameter values which give the minimum rmsd value on the 50 MHz grid. As a conservative estimate of the error on these parameter values, we take as an acceptable fit those values which are bounded by a contour of twice this minimum rmsd value, indicated by the first contour line in figures throughout this manuscript. Further, the 50 MHz grid of ZFS parameters available in the library of simulated EPR spectra is a somewhat coarse sampling of these parameter values, particularly for complexes with small ZFS. In order to interpolate the ZFS parameter values on this grid, we make the assumption that the contour bounding the region of twice the minimum rmsd value should be smooth given arbitrarily fine sampling of the (D, σ_D) parameter space. Therefore, we estimate this first contour by fitting an ellipse, as shown for Gd-NO₃Pic (**1**) in Figure A.8. The best-fit values of D and σ_D were taken to be given by the centre of an ellipse fit to this first contour line.

Uncertainties on the determined best-fit D and σ_D parameter values at each frequency were taken as the lengths of the semi-minor and semi-major axes of the fitted ellipses. These best-fit D and σ_D parameter values and their associated uncertainties for each measurement frequency are given in Tables A.3 and A.4 for Models 2 and 3, respectively.

Gd(III) Complex	Experiment	D (MHz)	σ_D (MHz)
Gd-NO ₃ Pic (1)	G band	443 ± 48	140 ± 108
	W band	499 ± 26	160 ± 78
	Q band	539 ± 37	200 ± 87
Gd-DOTA (2)	G band	642 ± 124	238 ± 331
Gd-maleimide-DOTA (3)	W band	813 ± 158	400 ± 375
Gd-maleimide-DOTA (3)	Q band	594 ± 155	594 ± 338
iodo-(Gd-PyMTA) (4a)	G band	1146 ± 286	327 ± 115
MOMethynyl-(Gd-PyMTA) (4b)	W band	1273 ± 156	529 ± 171
MOMethynyl-(Gd-PyMTA) (4b)	Q band	1301 ± 194	582 ± 491
Gd-TAHA (5)	G band	1262 ± 111	366 ± 249
	W band	1397 ± 120	568 ± 373
	Q band	1400 ± 200	350 ± 350
iodo-(Gd-PCTA-[12]) (6)	G band	1750 ± 411	450 ± 500
	W band	1900 ± 326	400 ± 500
	Q band	1850 ± 300	350 ± 500
Gd-PyDTTA (7)	G band	1750 ± 378	450 ± 500
	W band	1900 ± 383	350 ± 500
	Q band	1800 ± 226	300 ± 500

Table A.3. Best-fit D and σ_D parameter values for each measurement frequency, as determined by the above described ellipse fitting procedure using simulations with Model 2 and the region about the central peak excluded from the analysis.

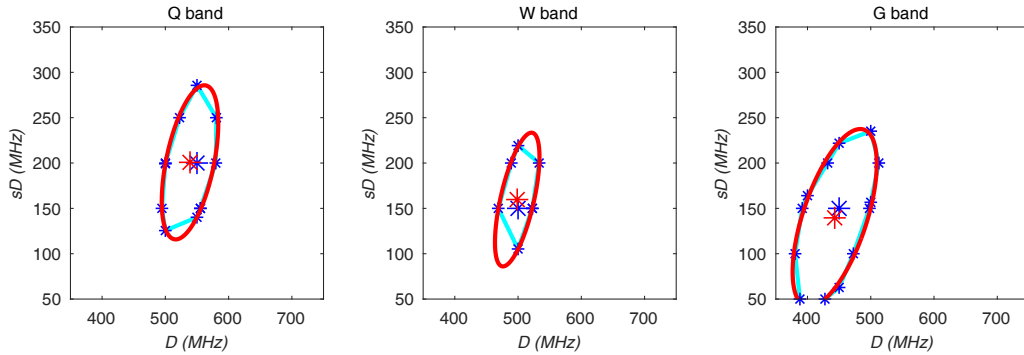


Figure A.8. Contour plots of constant rmsd for Gd-NO₃Pic (1) using Model 2 with the region about the central transition excluded for calculation of rmsd errors. The blue asterisk indicates the position of minimum rmsd on the 50 MHz grid of tested (D, σ_D) parameter values and the first contour line bounding the region of (D, σ_D) parameter space where the minimum rmsd doubles is plotted in cyan (other contour lines have been omitted for clarity). This first contour was fit by an ellipse (in red), whose centre is denoted by a red asterisk.

Gd(III) Complex	Experiment	D (MHz)	σ_D (MHz)
Gd-NO ₃ Pic (1)	G band	447 ± 27	143 ± 42
	W band	503 ± 48	166 ± 136
	Q band	541 ± 37	203 ± 92
Gd-DOTA (2)	G band	630 ± 58	224 ± 132
Gd-maleimide-DOTA (3)	W band	817 ± 69	436 ± 162
Gd-maleimide-DOTA (3)	Q band	852 ± 185	617 ± 401
iodo-(Gd-PyMTA) (4a)	G band	1155 ± 86	346 ± 206
MOMethynyl-(Gd-PyMTA) (4b)	W band	1254 ± 98	468 ± 228
MOMethynyl-(Gd-PyMTA) (4b)	Q band	1301 ± 155	526 ± 373
Gd-TAHA (5)	G band	1290 ± 108	350 ± 251
	W band	1395 ± 98	553 ± 283
	Q band	1480 ± 214	621 ± 572
iodo-(Gd-PCTA-[12]) (6)	G band	1750 ± 266	450 ± 600
	W band	1900 ± 201	500 ± 500
	Q band	1850 ± 192	350 ± 350
Gd-PyDTTA (7)	G band	1750 ± 175	450 ± 450
	W band	1900 ± 182	400 ± 500
	Q band	1850 ± 192	350 ± 350

Table A.4. Best-fit D and σ_D parameter values for each measurement frequency, as determined by the above described ellipse fitting procedure using simulations with Model 3 and the region about the central peak excluded from the analysis.

In order to determine the cumulative best-fit ZFS parameter values and associated errors quoted in the main text, the results from the three data-sets (in Q band, W band, and G band) were combined by taking a weighted average³¹⁹

$$x_{wav} = \frac{\sum w_i x_i}{\sum w_i} \quad (\text{A.7})$$

where the w_i are the weights of each measurement, given by the reciprocal square of the corresponding uncertainty $w_i = 1/\sigma_i^2$ for each measurement. The uncertainty in the weighted average was calculated by propagating the errors, giving

$$\sigma_{wav} = \frac{1}{\sqrt{\sum w_i}}. \quad (\text{A.8})$$

A.7. Parameters used for final simulations with best fit ZFS parameter values

After determination of the 'best fit' ZFS parameter values for each of the Gd(III) complexes using Models 1, 2, and 3, a set of simulations was run using these ZFS parameter values and the exact experimental parameter values (given in Table A.5). $N = 40000$ random steps were used for Monte Carlo sampling of the $P(D)$ and $P(E/D)$ distributions. The magnetic field range for each measurement frequency was chosen to well cover the experimental spectrum for all Gd(III) complexes studied here (Table A.2). The number of magnetic field points sampled was set to $Exp.nPoints = 8000$, and the orientational averaging was set to $Opt.nKnots = [31\ 10]$. Unless otherwise noted in the text, no additional line broadening was included in the simulations.

Gd(III) Complex	mwFreq (GHz)	Temperature (K)
Gd-NO ₃ Pic (1)	240	4.92
	94.31686	10
	34.370	10
Gd-DOTA (2) Gd-maleimide-DOTA (3) Gd-maleimide-DOTA (3)	240	5.17
	94.24218	10
	34.794	10
iodo-(Gd-PyMTA) (4a) MOMethynyl-(Gd-PyMTA) (4b) MOMethynyl-(Gd-PyMTA) (4b)	240	4.82
	94.21278	10
	34.452	10
Gd-TAHA (5)	240	4.94
	94.2422	10
	34.612	10
iodo-(Gd-PCTA-[12]) (6)	240	4.97
	94.24496	10
	34.370	10
Gd-PyDTTA (7)	240	5.17
	94.2117	10
	34.371	10

Table A.5. Measured microwave frequency and sample temperature for each EPR spectrum used in this work.

A.8. Model 1 - additional results

For analysis with Model 1, EPR spectra recorded at the three measurement frequencies were fit by visual inspection. For selected 'best' fit data the reordered ZFS distributions were computed, as discussed in Section 4.2.1. Selected ZFS parameters (before reordering of the indices) are presented in Table 4.2 of the main text, with the corresponding simulated spectra presented in Figure A.9. Table A.6 gives the selected D and σ_D parameter values for Model 1, before and after reordering of the indices according to Equations (4.3) and (4.4).

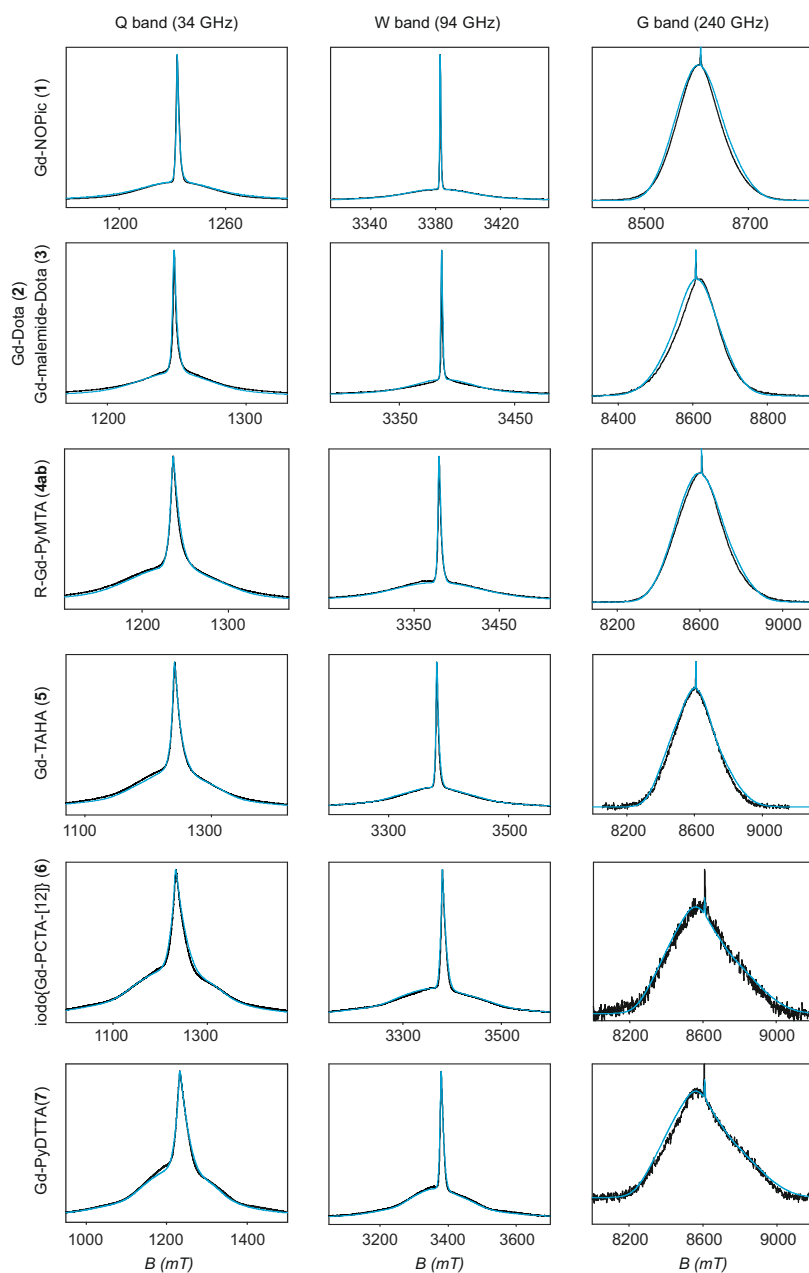


Figure A.9. Simulations using Model 1 and selected ZFS parameter values (light blue lines) compared to experimental spectra (black lines) for all measured frequency bands and Gd(III) complexes.

Gd(III) Complex	D_{init}	D_{pos}	D_{neg}	$\sigma_{D,\text{init}}$	$\sigma_{D,\text{pos}}$	$\sigma_{D,\text{neg}}$	$\frac{P(+D)}{P(-D)}$
Gd-NO ₃ Pic (1)	420	472	- 418	140	124	111	1.4
Gd-DOTA (2)/ Gd-maleimide-DOTA (3)	-600	515	- 675	240	160	204	0.6
R-(Gd-PyMTA) (4ab)	1070	1200	- 1065	357	316	288	1.4
Gd-TAHA (5)	1250	1400	- 1117	417	311	272	1.4
iodo-(Gd-PCTA-[12]) (6)	1780	1850	- 1370	508	440	318	3.3
Gd-PyDTTA (7)	1800	1845	- 1275	514	439	271	3.3

Table A.6. Change in $\langle D \rangle$ and σ_D upon reordering the ZFS parameters in Model 1 according to Equations (4.3) and (4.4). Units are given in MHz.

A.9. Model 2 - additional results with central peak excluded from analysis

Figure A.10 shows rmsd error maps for the ZFS parameters D and σ_D computed using Model 2, with the region about the central transition excluded from the analysis. In Figures A.11 and A.12 are presented the best-fit spectra for Model 2 using the best-fit ZFS parameters D and σ_D determined with the region about the central peak excluded from analysis (Table 4.2).

For the Q- and W-band spectra, Model 2 gives very reasonable fits of the experimental data, despite the fixed equal ratio between the positive and negative components of the $P(D)$ distribution. In particular, the position and width of the central peak is well reproduced by the simulations in Q and W band even though the region of this peak was excluded from the fit. However, the spectra measured at 240 GHz show strong deviations between the experimental data and their respective fits with Model 2. The strongest mismatches are observed with Gd-DOTA (**2**)/Gd-maleimide-DOTA (**3**), iodo-(Gd-PCTA-[12]) (**6**), and Gd-PyDTTA (**7**) (Figure A.22). The cases of the Q-band spectra of Gd-NO₃Pic (**1**) and Gd-maleimide-DOTA (**3**) appear to be outliers, possibly because a too broad region about the central peak was excluded from the fit. Most likely, by conservatively cutting only the region of the steeply rising peak so that the shoulders of the central transition remain in the fit range, the fit could be better stabilized.

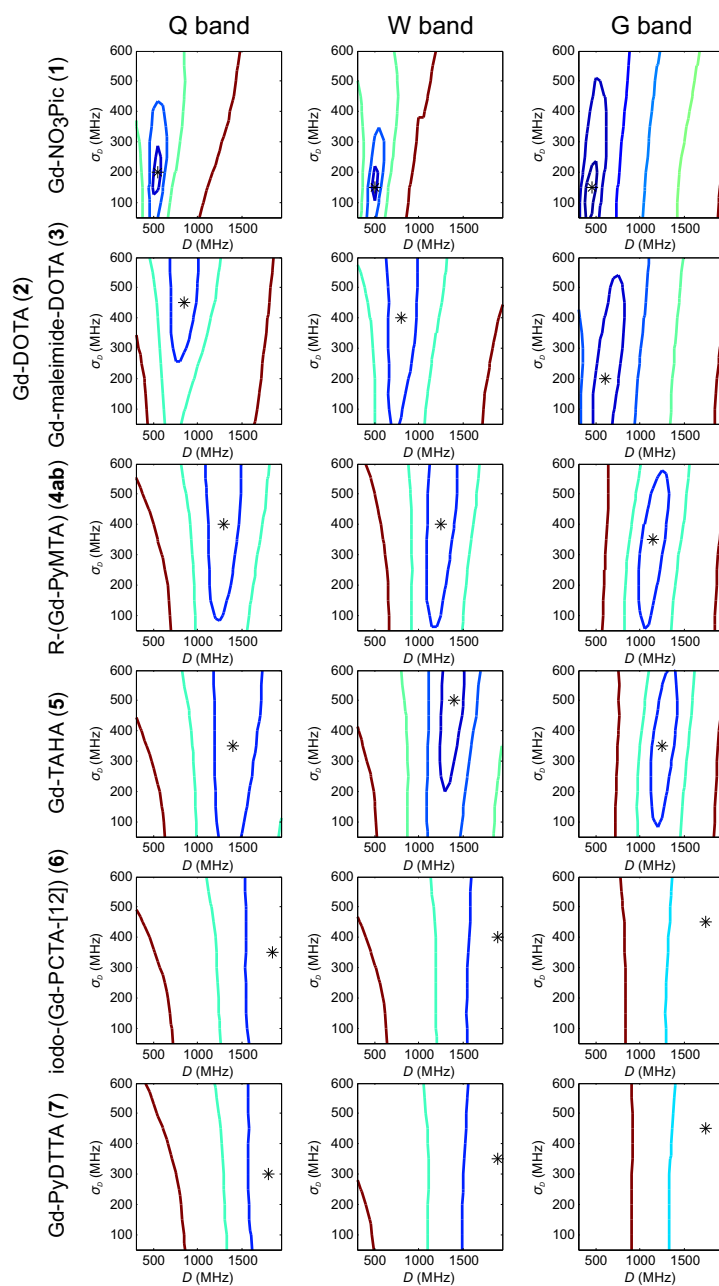


Figure A.10. Contours of constant rmsd as a function of D and σ_D parameter values using Model 2 with the region about the central peak excluded from the calculation of rmsd errors. Simulated spectra were normalized to the experimental data using only the outer shoulders of the spectra. The asterisk denotes the position of minimum rmsd on the 50 MHz grid of (D, σ_D) parameter values.

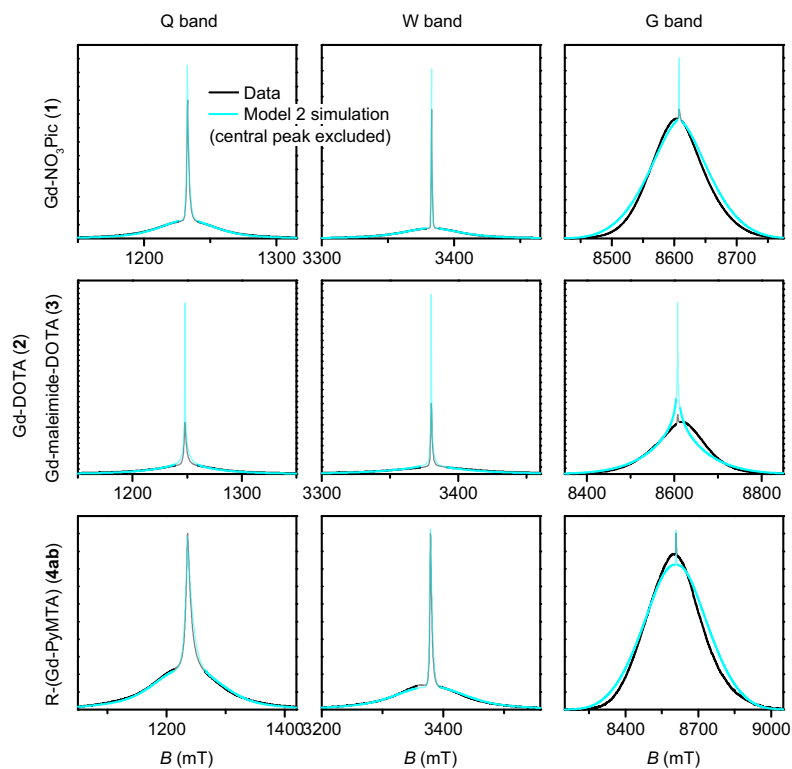


Figure A.11. EPR spectra simulated using Model 2 with the best-fit ZFS parameters determined with the region about the central peak (faded regions) excluded from the analysis (Table 4.2).

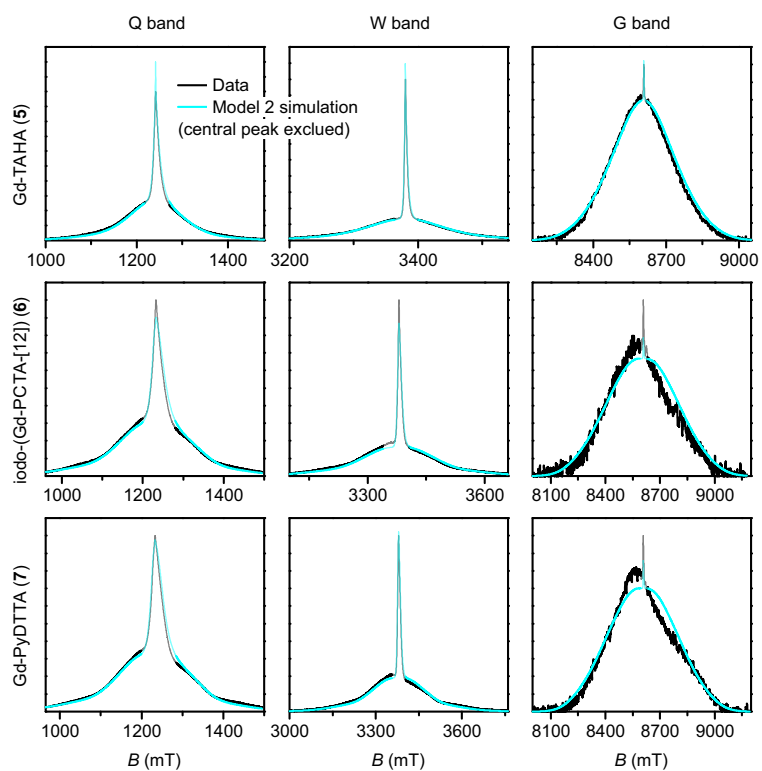


Figure A.12. EPR spectra simulated using Model 2 with the best-fit ZFS parameters determined with the region about the central peak (faded regions) excluded from the analysis (Table 4.2).

A.10. Model 3 - rmsd error maps with central peak excluded from analysis

In Figure A.13 are presented the rmsd error maps for the ZFS parameters D , σ_D , and $P(+D)/P(-D)$ computed using Model 3, with the region about the central transition excluded from the analysis. Spectra simulated using the best-fit ZFS parameters determined from these rmsd error maps are given in the main text.

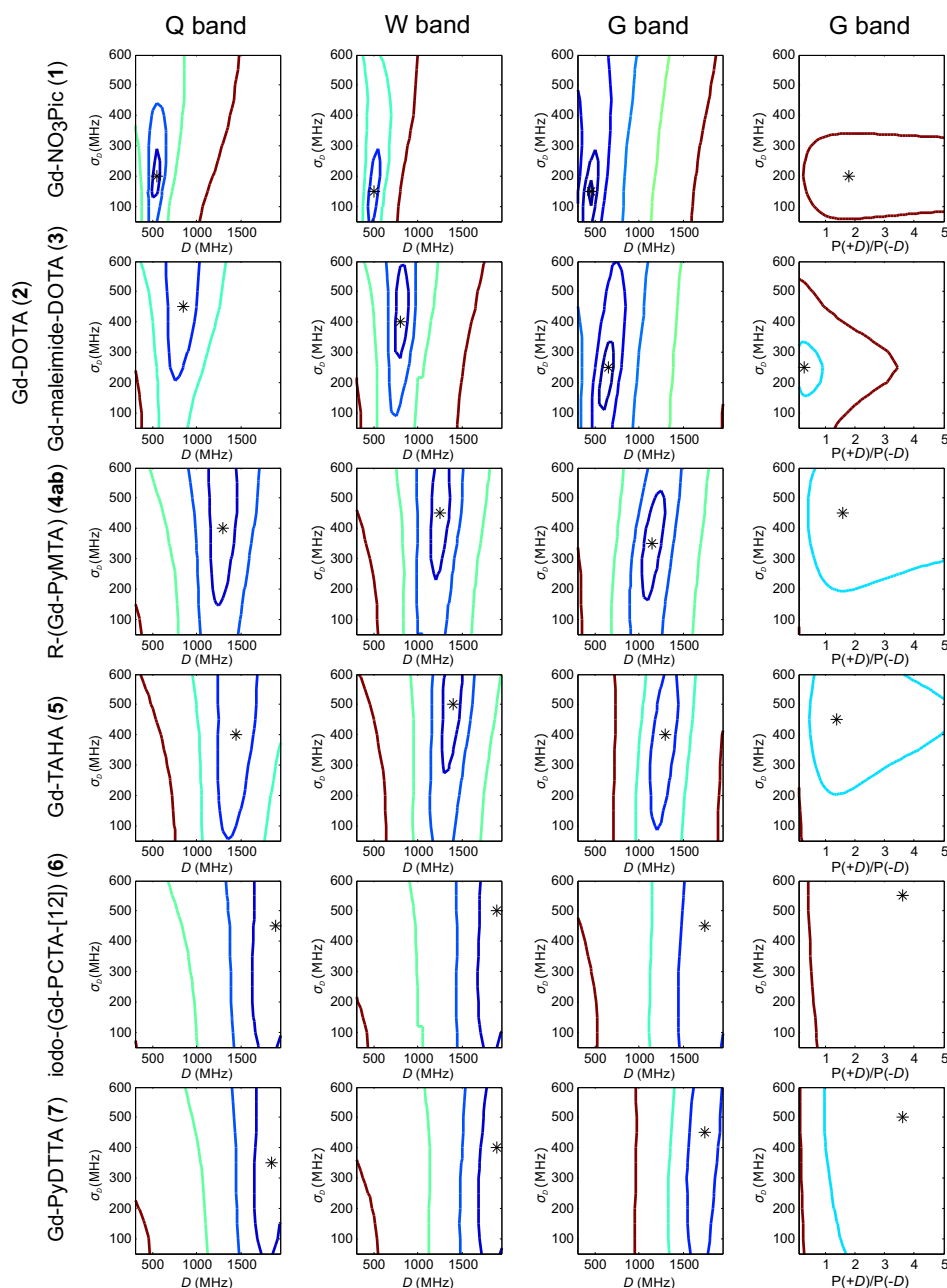


Figure A.13. Contours of constant rmsd as a function of D and σ_D parameter values, and as a function of σ_D and $P(+D)/P(-D)$ parameter values, using Model 3 with the region about the central peak excluded from the calculation of rmsd errors. Simulated spectra were normalized to the experimental data using only the outer shoulders of the EPR spectra. The asterisk denotes the position of minimum rmsd.

A.11. Model 3 - $P(+D)/P(-D)$ parameter error estimation

The criterion of an acceptable fit as being those values which are within the region bounded by a contour of twice the minimum rmsd overestimates the error on the asymmetry parameter $P(+D)/P(-D)$ in Model 3. The most obvious effect of this parameter on the simulated spectra is to set the relative position of the broad component of the EPR spectrum with respect to the sharp central peak corresponding to the $| - 1/2 \rangle \rightarrow | 1/2 \rangle$ transition, particularly in the high-field data. The width of this central peak is so narrow compared to the broad component of the 240 GHz EPR spectrum that it has a relatively small impact on the overall rmsd of the fit, though there is enough of an effect on the rmsd to assign a position of minimum rmsd in a contour plot of $P(+D)/P(-D)$ and σ_D , as was done to determine the other parameter values for Models 2 and 3. For consistency, the $P(+D)/P(-D)$ and σ_D rmsd error maps were used to determine the best-fit value for $P(+D)/P(-D)$.

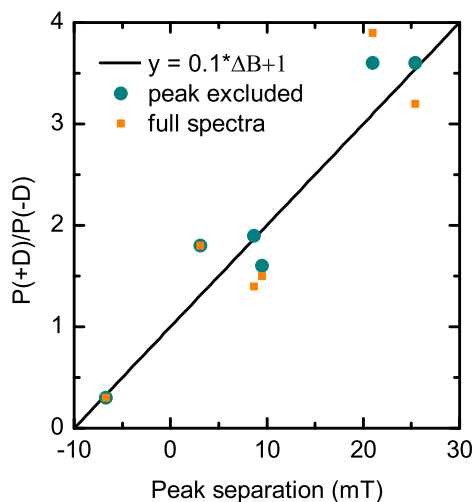


Figure A.14. Plot of determined $P(+D)/P(-D)$ parameter values vs the separation in field of the $| - 1/2 \rangle \rightarrow | 1/2 \rangle$ transition and the peak of the broad component of the 240 GHz EPR spectra, for analysis in which the central transition was excluded from the calculation of the rmsd error maps and analysis using the full 240 GHz EPR spectra.

In order to estimate a better-constrained value for the error on the $P(+D)/P(-D)$ parameter value, we looked at a plot of the separation of the position of the $| - 1/2 \rangle \rightarrow | 1/2 \rangle$ transition and the peak of the broad component of the 240 GHz EPR spectra with the value determined for $P(+D)/P(-D)$ via rmsd error maps. This is shown in Figure A.14, for analysis conducted with and without the region about the central transition included in the calculation of rmsd error maps. The plot of the determined $P(+D)/P(-D)$ parameter value vs the peak separation for the various Gd(III) complexes falls on a line. The average deviation in the determined $P(+D)/P(-D)$ values from this line is 0.24 for the analysis excluding the central transition and 0.43 for analysis using the full 240 GHz EPR spectra.

A.12. Models 2 and 3 - fit results using the full EPR spectra

In the main body of the paper, results presented for Models 2 and 3 were calculated with the region about the central transition excluded from the analysis (Figures A.15/ A.18) and the corresponding lineshape fits (Figures A.16,A.17/A.19,A.20) . Here, we present the rmsd contour plots computed using the full EPR spectra, including the central peak, and the corresponding calculated best-fit ZFS parameters (Table A.7).

Figure A.21 shows an example of the effect of scaling the best-fit simulated spectra only to the outer shoulders of the experimental EPR spectra vs scaling to the full EPR spectra with the central peak included.

Model	Complex	D (MHz)	σ_D (MHz)	$\frac{\sigma_D}{D}$	$\frac{P(+D)}{P(-D)}$
2	Gd-NO3Pic	494 ± 36	126 ± 89	0.26	—
	Gd-DOTA/ Gd-maleimide-DOTA	700 ± 71	218 ± 213	0.31	—
	R-(Gd-PyMTA)	1214 ± 71	331 ± 194	0.27	—
	Gd-TAHA	1307 ± 59	359 ± 159	0.28	—
	iodo-(Gd-PCTA-[12])	1821 ± 210	526 ± 305	0.29	—
	Gd-PyDTTA	1829 ± 198	467 ± 346	0.26	—
	3	Gd-NO3Pic	473 ± 30	130 ± 71	0.28
Gd-DOTA/ Gd-maleimide-DOTA		660 ± 50	210 ± 125	0.32	0.3
R-(Gd-PyMTA)		1203 ± 60	339 ± 160	0.28	1.5
Gd-TAHA		1307 ± 54	365 ± 144	0.28	1.4
iodo-(Gd-PCTA-[12])		1812 ± 160	520 ± 230	0.29	3.2
Gd-PyDTTA		1814 ± 138	459 ± 258	0.25	3.9

Table A.7. Extracted D and σ_D values using Model 2 and the full EPR spectra for analysis, and extracted D , σ_D , and $P(+D)/P(-D)$ values using Model 3 and the full EPR spectra for analysis.

A.13. Models 2 and 3 - minimum rmsd errors of the D and σ_D parameter contour plots

In Figure A.22 are plotted the minimum rmsd values in the contour plots for Models 2 and 3 (denoted by an asterisk in the contour plots). The rmsd errors for the 240 GHz spectra are about an order of magnitude larger than for the Q-/W-band spectra. For the Q-/W-band spectra, the minimum rmsd error does not change significantly whether Model 2 or Model 3 is used, but for the 240 GHz spectra the addition of the asymmetry parameter $P(+D)/P(-D)$ significantly reduces the minimum rmsd. The asymmetry parameter has the largest effect on the minimum rmsd value at 240 GHz for Gd-DOTA (**2**), iodo-(Gd-PCTA-[12]) (**6**), and Gd-PyDTTA (**7**). In general, the minimum rmsd error is smaller if the region about the sharp central peak is excluded, particularly for the Q-/W-band spectra where the $| -1/2 \rangle \rightarrow | 1/2 \rangle$ transition makes up a significant portion of the EPR spectra and is particularly sensitive to any additional broadening terms (e.g., higher-order ZFS or hyperfine interactions), which may be present but are not accounted for in the simulations with Models 2 and 3.

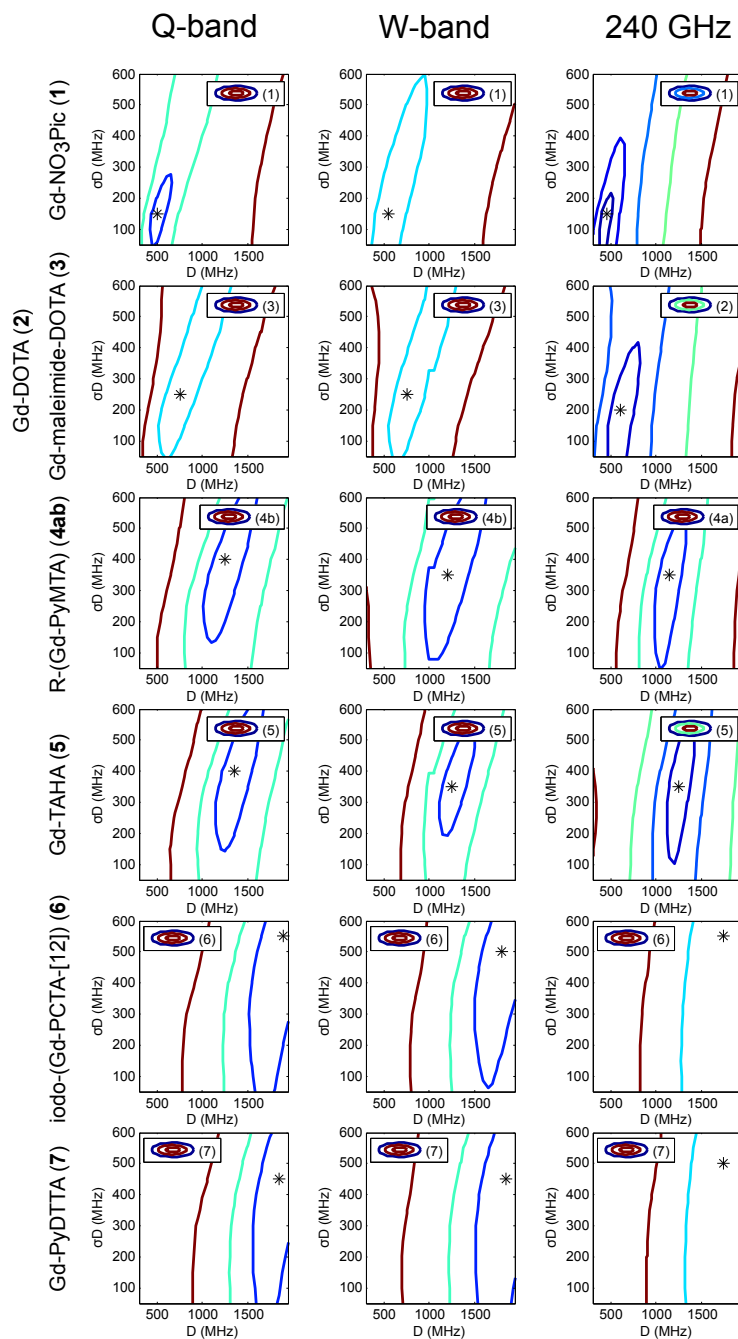


Figure A.15. Contours of constant rmsd as a function of D and σ_D parameter values using Model 2 with the full EPR spectra used for calculation of the rmsd errors. Simulated spectra were normalized to the experimental data using the full spectrum, including the region of the central peak. The asterisk denotes the position of minimum rmsd.

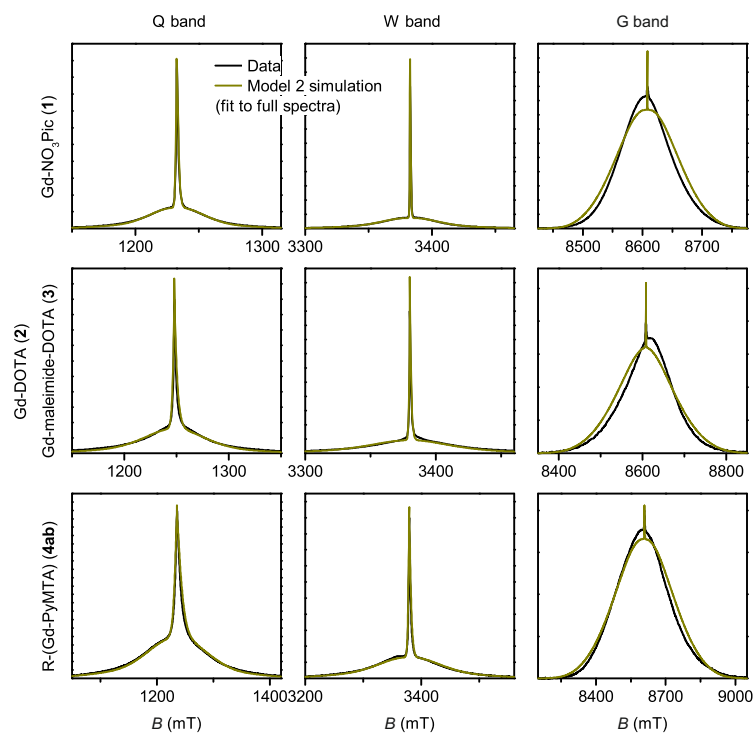


Figure A.16. Measured EPR spectra at Q-/W-band and 240 GHz for the Gd(III) complexes Gd-NO₃Pic (**1**), Gd-DOTA (**2**) (240 GHz spectra)/Gd-maleimide-DOTA (**3**) (Q-/W-band spectra), and iodo-(Gd-PyMTA) (**4a**) (240 GHz spectra)/MOMethynyl-(Gd-PyMTA) (**4b**) (Q-/W-band spectra). Overlaid are simulations with Model 2 using the best-fit ZFS parameters determined using the full EPR spectra in the calculation of rmsd error maps, presented in Table A.7.

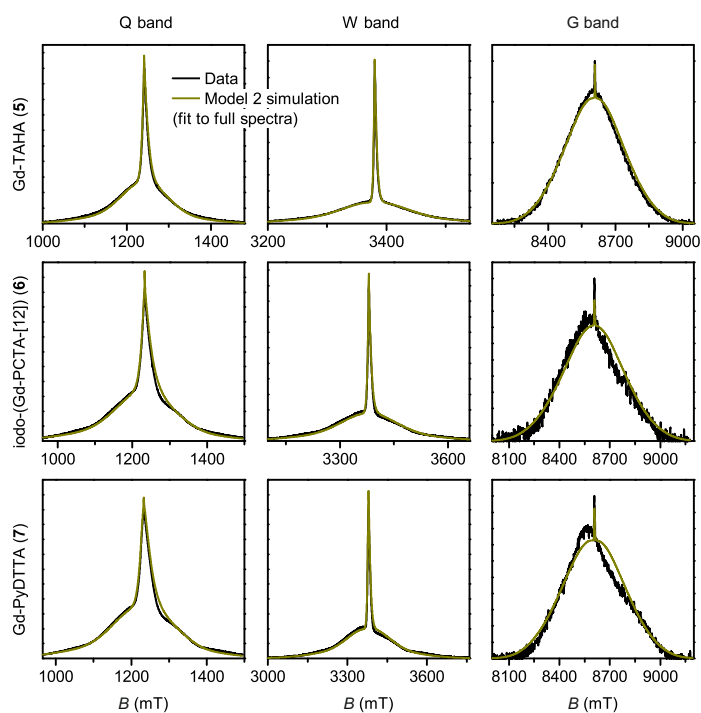


Figure A.17. Measured EPR spectra at Q-/W-band and 240 GHz for the Gd(III) complexes Gd-TAHA (**5**), iodo-(Gd-PCTA-[12]) (**6**), and Gd-PyDTTA (**7**). Overlaid are simulations with Model 2 using the best-fit ZFS parameters determined using the full EPR spectra in the calculation of rmsd error maps, presented in Table A.7.

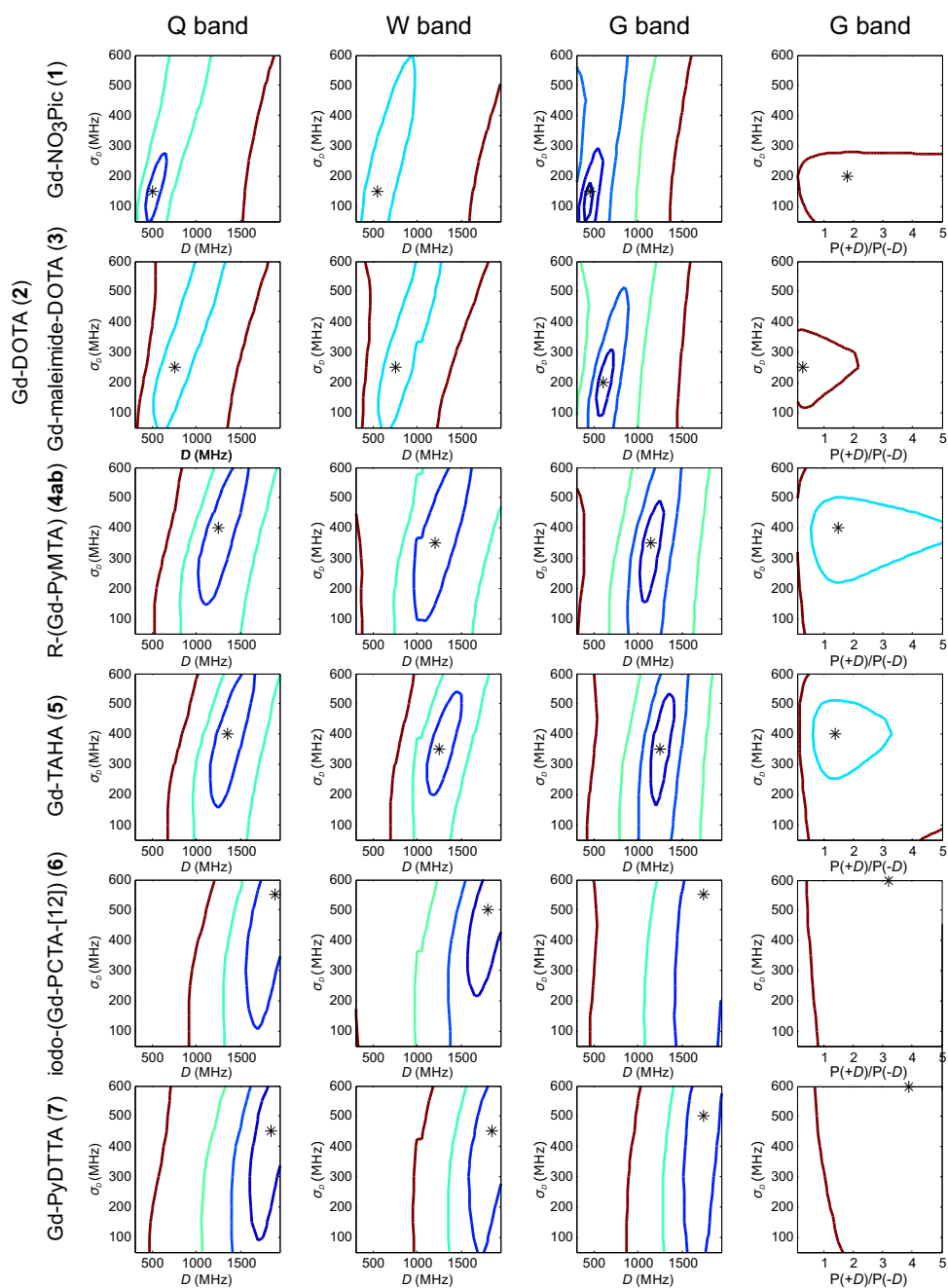


Figure A.18. Contours of constant rmsd as a function of D and σ_D parameter values, and $P(+D)/P(-D)$ and σ_D parameter values, using Model 3 with the full EPR spectra used for calculation of the rmsd errors. Simulated spectra were normalized to the experimental data using the full spectrum, including the region of the central peak. The asterisk denotes the position of minimum rmsd.

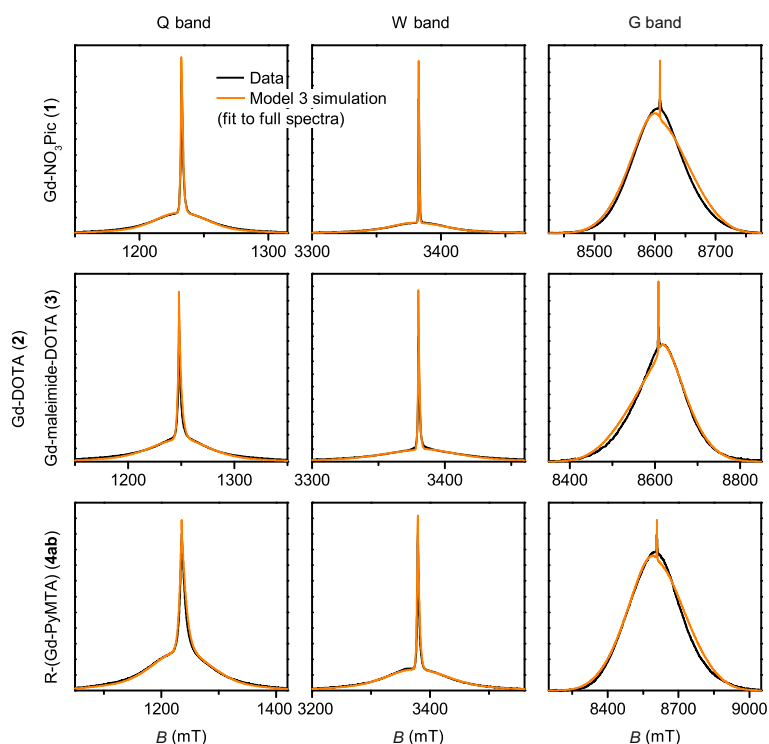


Figure A.19. Measured EPR spectra at Q-/W-band and 240 GHz for the Gd(III) complexes Gd-NO₃Pic (1), Gd-DOTA (2) (240 GHz spectra)/Gd-maleimide-DOTA (3) (Q-/W-band spectra), and iodo-(Gd-PyMTA) (4a) (240 GHz spectra)/MOMethynyl-(Gd-PyMTA) (4b) (Q-/W-band spectra). Overlaid are simulations with Model 3 using the best-fit ZFS parameters determined using the full EPR spectra in the calculation of rmsd error maps, presented in Table A.7.

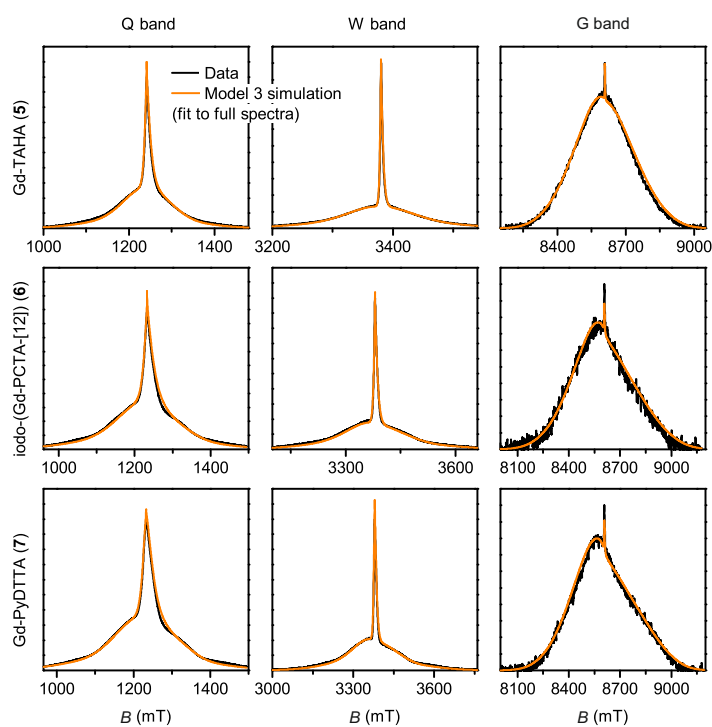


Figure A.20. Measured EPR spectra at Q-/W-band and 240 GHz for the Gd(III) complexes Gd-TAHA (5), iodo-(Gd-PCTA-[12]) (6), and Gd-PyDTTA (7). Overlaid are simulations with Model 3 using the best-fit ZFS parameters determined using the full EPR spectra in the calculation of rmsd error maps, presented in Table A.7.

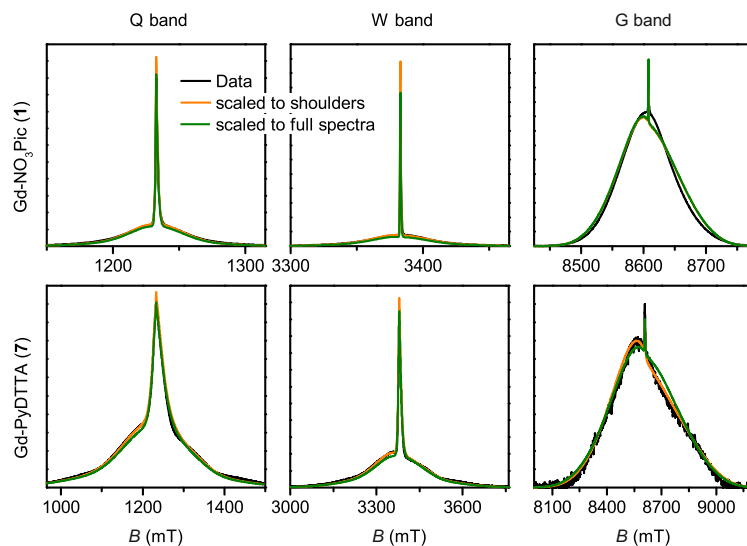


Figure A.21. Effect of scaling best-fit simulated spectra to only the shoulders of the EPR spectra compared to scaling to the full EPR spectra, including the region of the central transition. Simulations were computed using the best-fit parameters for Model 3 using the full EPR spectra, with ZFS parameter values listed in Table A.7. Shown are examples for the complexes Gd-NO₃Pic (**1**) and Gd-PyDTTA (**7**).

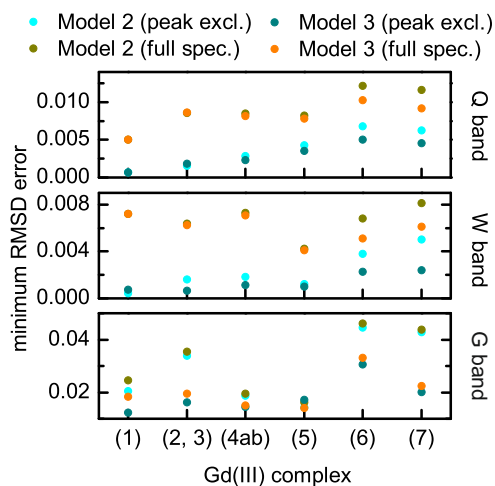


Figure A.22. Minimum rmsd errors from the D and σ_D parameter contour plots for Models 2 and 3, with and without the region about the central peak excluded in the calculation of rmsd errors. Structural formulae and naming for the Gd(III) complexes **1** - **7** are given in Figure 4.2.

A.14. Influence of D and σ_D on the EPR line shape and Model 3 fits obtained by visual inspection

There are several approaches to obtain a match between simulated and experimental EPR data. Given the rather large error bars for the D and σ_D values, it is difficult to argue why the rigorous analysis described in the main text for determining ZFS distribution parameters has to be performed in every case, and it is tempting to simplify the protocol for fitting of ZFS distribution parameters.

One can, for example, conduct a fit based solely on a search for minimum rmsd between the simulated and experimental spectra. However, this limits the result to a single set of parameter values which give the minimum rmsd. This is also difficult to conduct in practice, given the long computation times required to generate artefact-free simulations with sufficient convergence using the protocols described in this manuscript. Alternatively, one can scan the parameter space of the ZFS parameters manually and qualitatively compare simulated and experimental data for a range of parameters by visual inspection. In this way, one gains intuition on the influence of the different fit parameters on the shape of the Gd(III) EPR spectrum. In the case of Model 3, the fit parameters are D , σ_D and the asymmetry $P(+D)/P(-D)$. Some trends with these parameters are shown in Figure A.24. This visual inspection represents a sparse sampling of the parameter space, which was described by the rmsd contour plots in the main body of this manuscript. If performed carelessly, such visual fits can be strongly influenced by the operator and one has to keep in mind that rather large variations of D and σ_D values lead to relatively small changes in rmsd. For instance, one can choose ZFS parameter values which qualitatively reproduce certain weak yet clearly visible features of the Gd(III) EPR spectra as fitting criteria, e.g. the curvature patterns of the outer-envelope shoulders of the spectrum. However, such criteria are more related to physical intuition of the particular person performing this fit, rather than to the formal requirement of rmsd minimization. Nevertheless, such visual inspection gives useful insight compared to a fit solely determined by one minimum rmsd value.

In the course of this work, the EPR data were first investigated by visual inspection using the three tested models, both to ensure convergence of the computational approach and to narrow down the parameter space. To extract the final reported values, the more objective best-fit determination method of creating rmsd error maps was employed for Models 2 and 3.

Selected results of the visual inspection for Model 3 are shown in Figure A.23, with the corresponding ZFS parameter values given in Table A.8. Note that the fits by visual inspection include an additional line broadening term, which was not included in the fitting via rmsd error maps described in the main text. Other adjustable parameter in the simulations were set as described in A.7. In the majority of cases (see Table 4.2), the values of D and σ_D determined by visual inspection lie within the accuracy ranges determined by the rmsd contour plots. For Gd-DOTA (**2**)/Gd-maleimide-DOTA (**3**), the estimated ranges for the D value differ for the case when the central peak is included and excluded. The mean D value for each of these two calculations does not fit into the estimated error band of the other one. However, both error bands do overlap to a certain extent. The manually estimated D values for Gd-DOTA (**2**)/Gd-maleimide-DOTA (**3**) for Model 3, lie within the error band of the rmsd analysis for the whole field range, but are out of the error band for the rmsd analysis excluding the central peak. If a fit-by-eye approach is to be used, we recommend reporting a range of variations about the selected values, rather than a single 'best-fit' set of D and σ_D values.

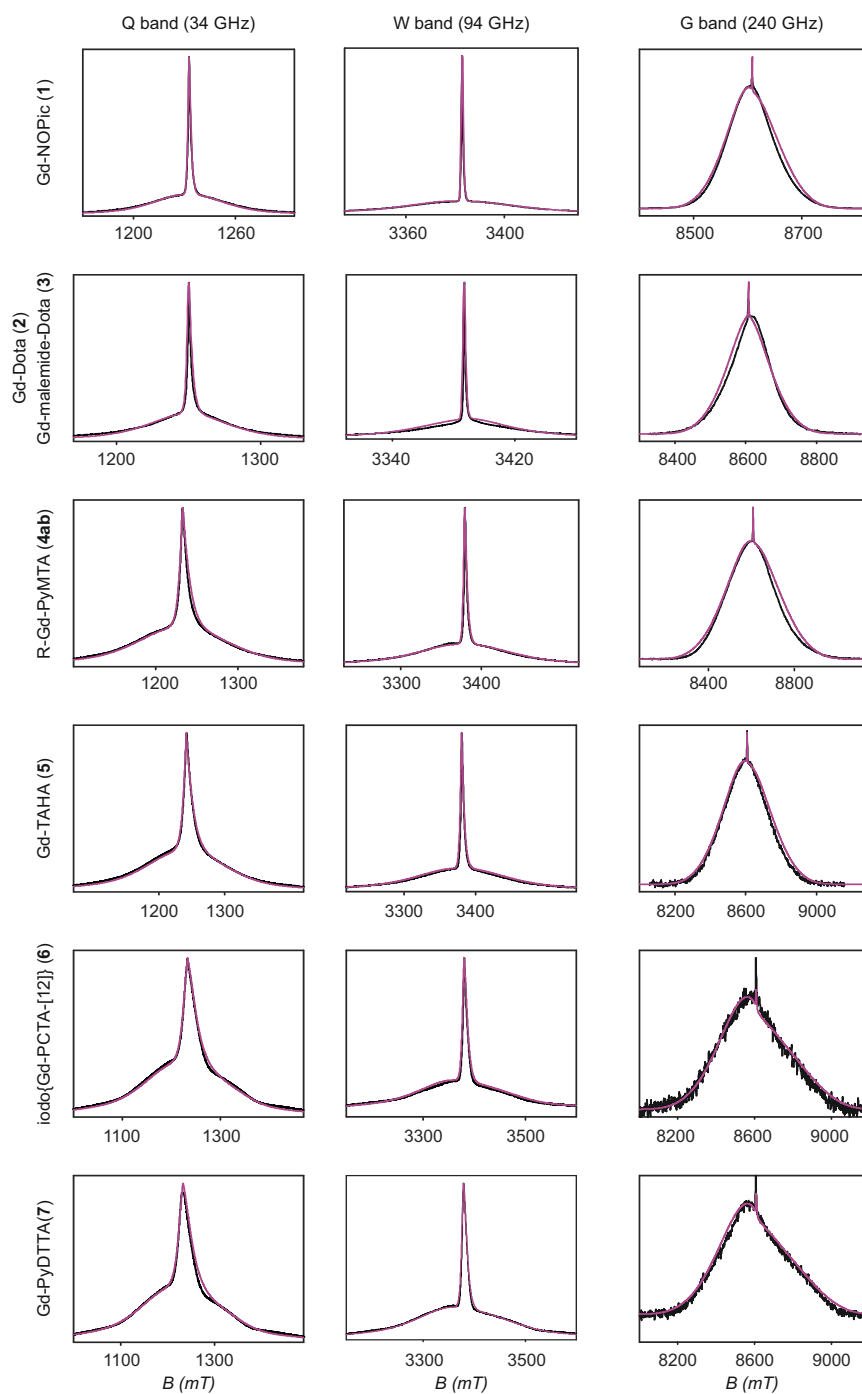


Figure A.23. Model 3 visual fits (purple lines) compared to experimental spectra (black lines).

Figure A.24 illustrates how the ZFS parameters D , σ_D and $P(+D)/P(-D)$ alter the simulated EPR line shape. Increasing the magnitude of the mean D value leads to an increasing contribution of the envelope of the outer transitions compared to the central transition. Additionally, the width of the envelope increases with increasing D , while the shape of the curvature remains the same (Figure A.24(a-c)). The curvature of the EPR lineshape is influenced primarily by the width σ_D of the distribution (Figure A.24(d-f)). If σ_D is reduced, the EPR lineshape becomes more curved (Figure A.24(d-f), blue lines) and the flanks of the envelope are steeper compared to simulations

Complex	D (MHz)	σ_D (MHz)	$\frac{\sigma_D}{D}$	$\frac{P(+D)}{P(-D)}$	$lwpp$ (MHz)
Gd-NO ₃ Pic	470	134	0.29	1.5	[0.5 0]
Gd-DOTA/ Gd-maleimide-DOTA	650	216	0.33	0.4	[1.25 0]
R-(Gd-PyMTA)	1230	351	0.29	1.2	[0.8 0]
Gd-TAHA	1350	386	0.29	1.2	[0.6 0]
iodo-(Gd-PCTA-[12])	1820	455	0.25	4	[0.8 0.1]
Gd-PyDTTA	1860	465	0.25	4	[1.5 0.1]

Table A.8. ZFS parameters extracted by visual fitting with Model 3. $lwpp$ is a convolutional peak-to-peak line broadening term, where the first entry in brackets is the Gaussian component of the broadening, and the second entry is the Lorentzian component.

with larger σ_D . Further, the ratio of central-to-outer transitions is larger for larger σ_D . Figure A.24(g-i) shows that the asymmetry $P(+D)/P(-D)$ of the bimodal Gaussian distribution of D primarily influences the G-band lineshapes. However, slight changes can also be observed in the Q- and W-band lineshapes. The maximum intensity of the broad envelope is shifted to the left of the central peak for $P(+D)/P(-D) > 1$, corresponding to an overall positive value of D . For $P(+D)/P(-D) \gg 1$, the flank on the left side of the central peak becomes more curved, while the flank on the right side falls off more steeply. If instead $P(+D)/P(-D) < 1$, the reverse is observed, wherein the maximum intensity of the broad envelope is shifted to the right of the sharp central peak corresponding to an overall negative value of D . To visualize the impact of only $P(+D)$ as well as $P(-D)$, its line shape is displayed Figure A.24(j-l) in yellow and blue, respectively.

Note that the impact of the ZFS parameter values on the EPR spectra is different for the central and for the outer transitions of Gd(III). For the outer transitions, the width of the spectrum scales linearly with respect to the value of D , so long as the high-field approximation holds. For the central peak, the ZFS terms broaden the $|-1/2\rangle \rightarrow |1/2\rangle$ sub-spectrum only to second order in perturbation theory, so that the width of the $|-1/2\rangle \rightarrow |1/2\rangle$ sub-spectrum scales quadratically with the value of D . Fitting a model for the ZFS parameter distribution to the full EPR spectra is expected to stabilize the fit and enhance the confidence in the determined ZFS parameter distributions. However, due to this difference in scaling for different regions of the EPR spectrum, the interpretation of the rmsd error becomes complicated if the full spectrum is used for fitting. In particular, if there are additional broadenings (higher-order ZFS parameters, hyperfine interactions, etc.) present in the region of the central transition which are not included in the model, the ZFS parameters D and E will be overestimated by the fit.

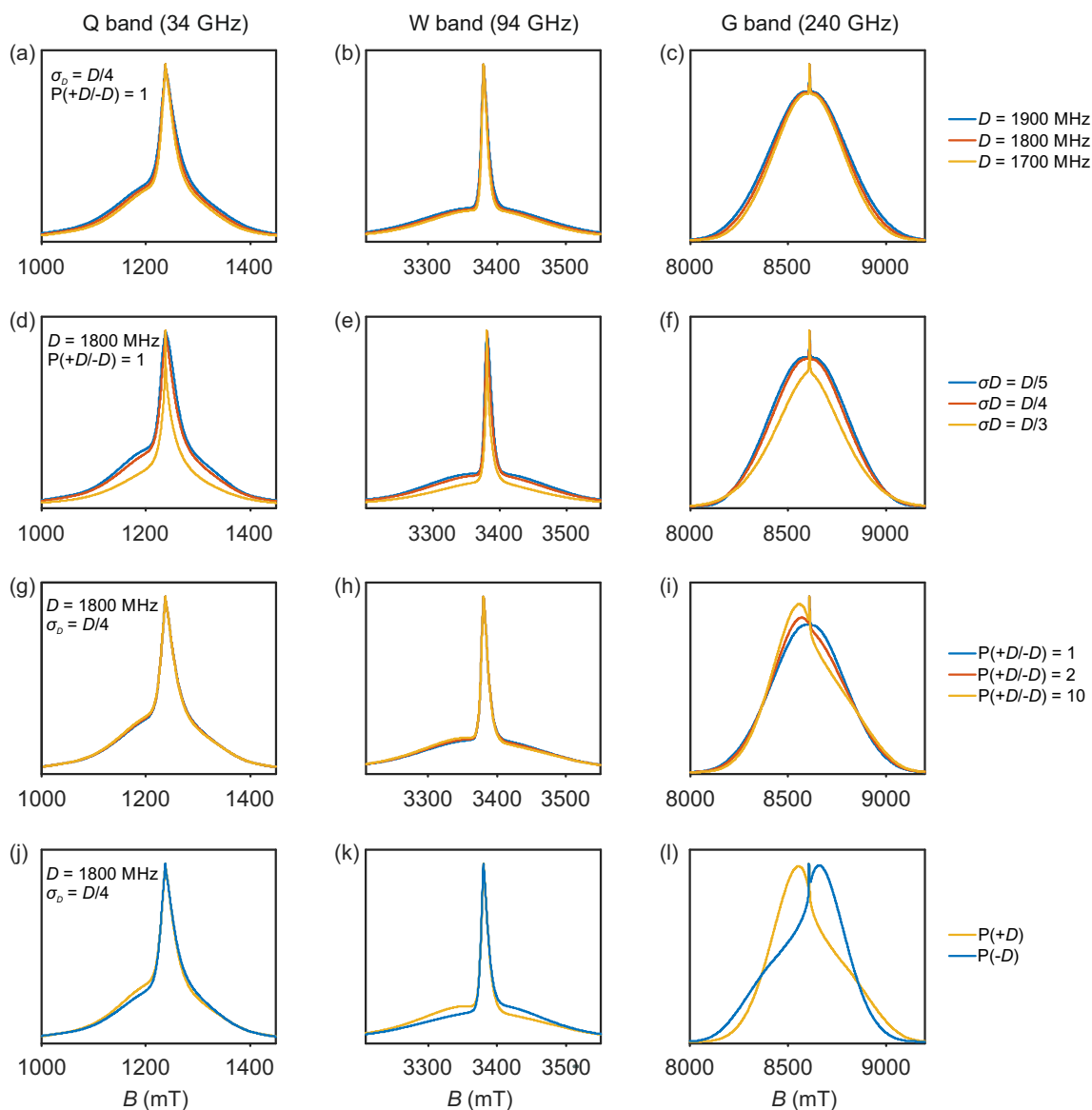


Figure A.24. Influence of parameters D , σ_D , and $P(+D)/P(-D)$ on the simulated EPR line shape for Models 2/3. (a)-(c) Variation of D , (d)-(f) variation of σ_D , (g)-(i) variation of $P(+D)/P(-D)$, (j-l) lineshape of $P(+D)$ as well as $P(-D)$. (a), (d), (g), (j) Q-band. (b), (e), (h), (k) W-band. (c), (f), (i), (l) G-band. For comparison, all spectra are scaled to 1 at maximum intensity.

A.15. Comparison of $P(D)$ and $P(D/E)$ distributions for Models 1 and 3

Figure A.25 shows the $P(D)$ and $P(E/D)$ distributions for Models 1 and 3 using the best-fit ZFS parameter values determined for each model. For Model 1, the $P(D)$ and $P(E)$ distributions were rearranged according to the conventional definitions Equation (4.2) to produce the $P(D)$ and $P(E/D)$ distributions shown in Figure A.25. The ZFS parameter values for Model 3 were taken directly and are given in Table 4.2. For Model 1 the initial values of D and σ_D as well as the value obtained after reordering are found in Table A.6.

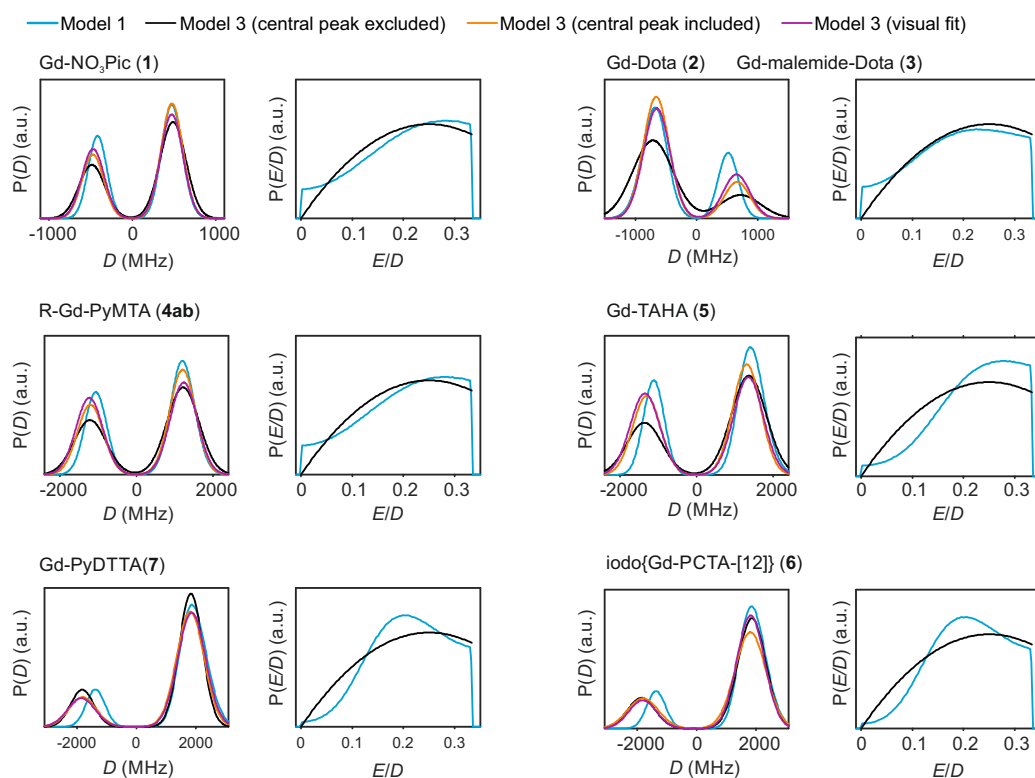


Figure A.25. Comparison of $P(D)$ and $P(E/D)$ distributions for Model 1 (light blue lines), Model 3 excluding the central peak of the spectrum (black lines), Model 3 including the central peak of the spectrum (orange lines) and Model 3 obtained by visual inspection (purple lines) for the different Gd(III) complexes. Spectra are normalized so that the area under the curves integrates to 1. Note that the $P(E/D)$ curves for the three flavours of Model 3 superimpose exactly.

A.16. Calculated absolute ZFS magnitude and ZFS axially for Model 1 and 3

Gd(III) complex	$\overline{ D }_1$	$\overline{ D }_3$	$(\sigma_{ D })_1$	$(\sigma_{ D })_3$	$\overline{\xi}_1$	$\overline{\xi}_3$	$ \overline{\xi} _1$
Gd-NO ₃ Pic (1)	452	485	122	155	0.103	0.114	0.398
Gd-DOTA (2)/ Gd-maleimide-DOTA (3)	635	717	208	320	0.181	-0.209	0.425
R-(Gd-PyMTA) (4ab)	1152	1214	312	417	0.102	0.092	0.398
Gd-TAHA (5)	1321	1362	355	457	0.088	0.124	0.337
iodo-(Gd-PCTA-[12]) (6)	1811	1861	469	467	0.279	0.226	0.373
Gd-PyDTTA (7)	1831	1830	467	390	0.280	0.226	0.374

Table A.9. Mean absolute ZFS magnitude $\overline{|D|} = 3\overline{\Delta}/2$, standard deviation $\sigma_{|D|}$ of the absolute ZFS magnitude, mean ZFS axially $\overline{\xi}$, and mean absolute ZFS axially $|\overline{\xi}|$ for fits to experimental data by Models 1 and 3. The mean absolute ZFS axially for Model 3 is fixed by Equation (4.8) at $|\overline{\xi}| = 0.4$.

B

Supplementary Information to Chapter 5

B.1. Synthesis of Cu-PyMTA

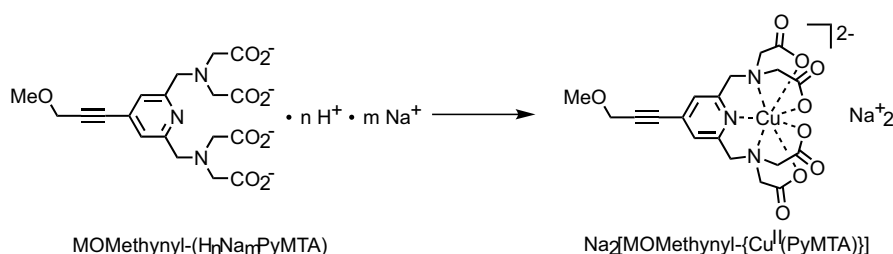


Figure B.1. Synthesis route of Cu-PyMTA.

$\text{Na}_2[\text{MOMethynyl-(Cu}^{\text{II}}\text{(PyMTA))}]$. MOMethynyl-($\text{H}_n\text{Na}_m\text{PyMTA}$)⁹³ (2.652 mg, contains 5.45 μmol of the structural motif $[(4\text{-MOMethynyl-H}_4\text{PyMTA}) - 4 \text{H}^+]^{4-}$ as determined by quantitative ^1H NMR spectroscopy)⁹⁴ was dissolved in D_2O (500 μL). A solution of CuCl_2 in D_2O (0.05 M, 103.6 μL , 5.18 μmol), which had a very pale blue colour, was added whereupon the colour of the solution changed to blue. A solution of NaOD in D_2O (0.10 M, 150 μL , 15 μmol) was added to rise the pH of the solution to pH 8.2. The solution was diluted with D_2O (336.8 μL) to obtain a 5 mM solution of $\text{Na}_2[\text{MOMethynyl-(Cu}^{\text{II}}\text{(PyMTA))}]$ in D_2O containing NaCl . Mass-spectroscopy (ESI) shows the corresponding peaks: $m/z = 247.8$ $[\text{M} - 2\text{Na}]^{2-}$, 217.3 $[(4\text{-MOMethynyl-H}_4\text{PyMTA}) - 2\text{H}]^{2-}$.

B.2. Examples of the fitting procedure

RIDME traces were fitted by a stretched exponential function (SE model) of the form $c \cdot \exp(-(kt)^{d/3})$, a sum of two stretched exponential functions (SSE model) of the form $c_a \cdot \exp(-(k_a t)^{d_a/3}) + c_b \cdot \exp(-(k_b t)^{d_b/3})$ or a product of two stretched exponential functions (PSE model) of the form $c \cdot \exp(-(k_a t)^{d_a/3}) \cdot \exp(-(k_b t)^{d_b/3})$ using a nonlinear least-square fitting criterion without prior normalization. The zero time point of the data traces was set to the expected zero time of 120 ns based on the sequence settings used in the RIDME experiment. The start point of the fitting routine was either set to the zero time point or shifted forward, thus cutting out the echo crossing artefact at zero time (see for example Figure B.2). This allowed for estimating an additional error, introduced by the mentioned artefact as well as the variation of the stretched exponential parameters due to cut of an initial part of the trace. Each such time trace was fitted by applying 20 different, random starting parameter sets, and the best set of k

and d parameters out of these 20 runs was selected. The 95% confidence of this fit (MATLAB function 'nlparci') was used to estimate the error. The best d and k set of parameters was then computed as the average over the results for different starting positions. The resulting error was taken as the largest error between the single-start-time error estimate, and the width of the distribution of the best-fit values over the range of starting positions. If a later starting point resulted in a significantly poorer fit, it was not taken into account for calculating the average value of d as well as k . Similarly, if there was a clear mismatch of the initial region for the fit starting at the zero time point due to a strong echo crossing artefact, those data points were excluded. Figure B.2 and B.3 show two typical examples of such a fitting routine.

If the data trace was not decayed to at least the $1/e$ value, errors were approximately estimated by manually varying d and adjusting k according to $\{(k \cdot t_{\max})^{(d/d_{\text{var}})}/t_{\max}\}$, to match the best fit curve at the last time point. This was done because the largest error in fitting such short traces appears due to the correlated change of d and k , which is not caught by the 'nlparci' function. This approach must still have somewhat underestimated the errors for d and k , but it resulted in larger error bars than the gradient-based calculation for short RIDME background decay traces. We assume that these estimates are comparable to the actual error bars in RIDME background fits. The ultimately accurate error estimation would include the analysis of the local Hessian matrices, which would be computationally too expensive for such large sets of data. This is also the reason why such a procedure is not offered in the MATLAB package.

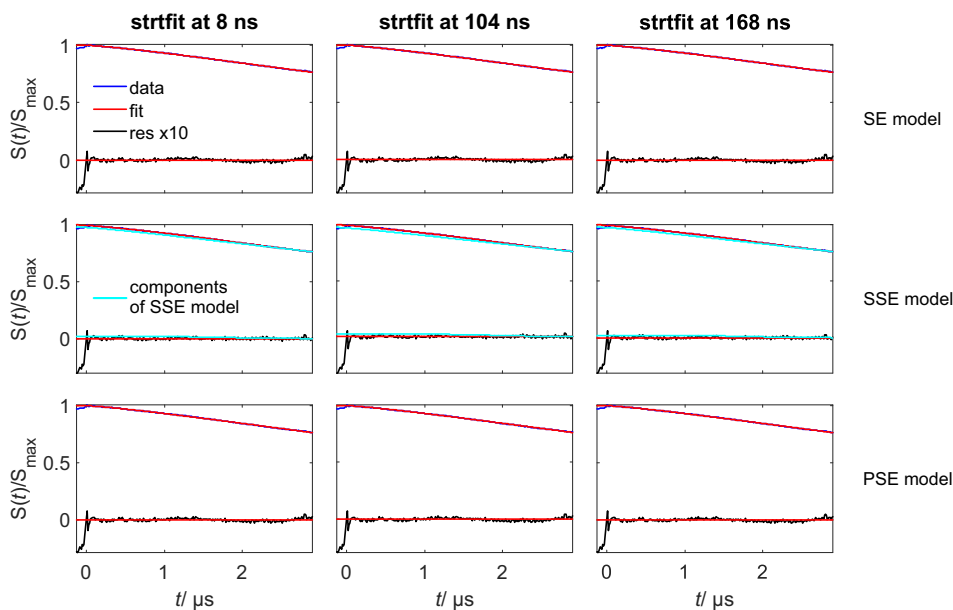


Figure B.2. RIDME background fits for 100 μM Gd-PyMTA in a deuterated matrix at 10 K in W band. $T_{\text{mix}} = 41 \mu\text{s}$, $d_1 = 0.4 \mu\text{s}$, $d_2 = 3.2 \mu\text{s}$. Top: Fit by SE model; Middle: Fit by SSE model; Bottom: Fit by PSE model. From left to right: increasing time of the fitting starting point after zero time. Note measurement are scaled to maximum intensity excluding the zero-time artefact.

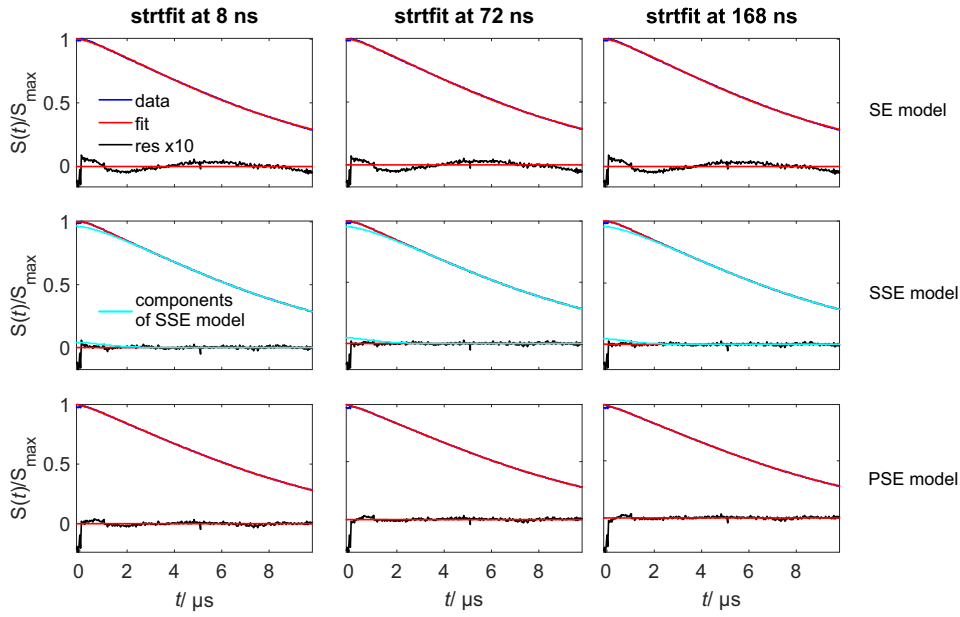


Figure B.3. RIDME background fits for $100 \mu\text{M}$ Gd-PyMTA in a deuterated matrix at 10 K in W band. $T_{\text{mix}} = 97 \mu\text{s}$, $d_1 = 10 \mu\text{s}$, $d_2 = 10.2 \mu\text{s}$. Top: Fit by SE model; Middle: Fit by SSE model; Bottom: Fit by PSE model. From left to right: increasing time of the fitting starting point after zero-time.

B.3. Influence of the detection position in RIDME background decays

Moving the detection position away from the centre of the Gd(III) spectrum induces a faster background decay in RIDME measurements of $100 \mu\text{M}$ Gd-PyMTA in a deuterated matrix.

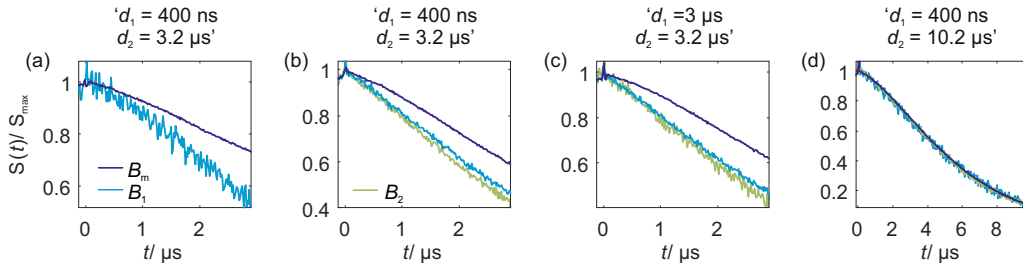


Figure B.4. Comparison of RIDME background decay of $100 \mu\text{M}$ Gd-PyMTA in a deuterated matrix in W band at various detection positions. $T_{\text{mix}} = 65 \mu\text{s} \approx T_1$; B_m corresponds to detection at maximum of Gd(III) spectrum (purple lines), $B_1 = B_m - 150 \text{ G}$ (blue lines), $B_2 = B_m - 750 \text{ G}$ (green lines), (a) 30 K. (b-d) 10 K. Note that signals are scaled to maximum intensity excluding the zero-time artefact.

It is accompanied by an increase of the characteristic decay rate k and a decrease in the background dimensionality d , thus leading to more mono-exponential functions. The effects diminish at longer dipolar evolution delays $d_2 > T_{\text{m,outer}}$, with $T_{\text{m,outer}}$ being the transverse relaxation time of the outer Gd(III) transitions.

B.4. Additional Figures to Section 5.4.3

Figure B.6 and B.7 show decay rates k with enlarged axis scales as addition to the Figures 5.7 and 5.8, respectively.

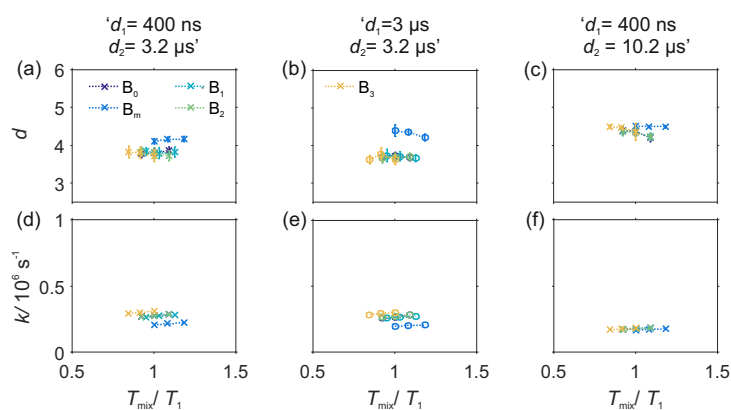


Figure B.5. Comparison of the stretching exponent d (a-c) and decay rate k (d-f) versus the relative mixing time T_{mix}/T_1 at given pulse sequence settings (left to right) for different detection fields in W band at 10 K for 100 μM Gd-PyMTA in deuterated matrix. (a, d) $d_1 = 0.4 \mu\text{s}$, $d_2 = 3.2 \mu\text{s}$; (b, e) $d_1 = 3 \mu\text{s}$, $d_2 = 3.2 \mu\text{s}$; (c, f) $d_1 = 0.4 \mu\text{s}$, $d_2 = 10.2 \mu\text{s}$. B_m corresponds to detection at maximum of Gd(III) spectrum (blue lines), $B_0 = B_m + 150 \text{ G}$ (purple lines), $B_1 = B_m - 75 \text{ G}$ (cyan lines), $B_2 = B_m - 150 \text{ G}$ (green lines), $B_3 = B_m - 750 \text{ G}$ (yellow lines).

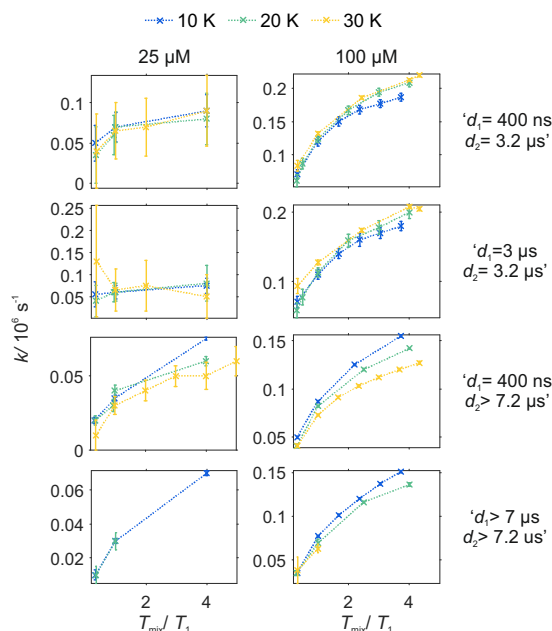


Figure B.6. Comparison of decay rate constant k versus the relative mixing time T_{mix}/T_1 obtained from the analysis of experimental W-band RIDME decays in deuterated solvent matrix at given pulse sequence settings (top to bottom) and spin concentration (left to right). The measurement temperature is colour encoded: blue 10 K, green 20 K, yellow 30 K.

B.5. Background decay in Cu-/Mn-PyMTA complexes

For Cu-PyMTA and Mn-PyMTA similar observations as for Gd-PyMTA were made. The best fits with a single stretched exponential function resulted in stretching exponent values d between 3 and 6. As in case of Gd-PyMTA, the d value was decreasing for longer d_2 values. There is also a slight trend for decreasing d with increasing T_{mix}/T_1 .

The decay rate k is increasing with T_{mix}/T_1 . As described in Chapter 5 for Gd-PyMTA, k is reduced when the temperature, the delay d_2 , and/or the delay d_1 are increased.

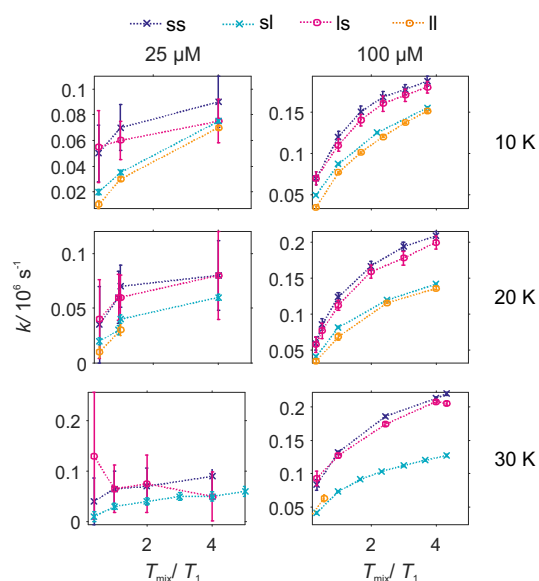


Figure B.7. Comparison of decay rate constant k versus the relative mixing time T_{mix}/T_1 obtained from the analysis of experimental W-band RIDME decays in deuterated solvent matrix at given measurement temperature (top to bottom) and spin concentration (left to right). The pulse sequence settings are colour encoded: purple line (ss): $d_1 = 0.4 \mu\text{s}$, $d_2 = 3.2 \mu\text{s}$; dark blue line (ls): $d_1 = 3 \mu\text{s}$, $d_2 = 3.2 \mu\text{s}$; light blue line (sl): $d_1 = 0.4 \mu\text{s}$, $d_2 = 10.2 \mu\text{s}$ and green line (ll): $d_1 = 10 \mu\text{s}$, $d_2 = 10.2 \mu\text{s}$. At 30 K, the long d_2 values was only set to $7.2 \mu\text{s}$ and correspondingly d_1 to $7 \mu\text{s}$. At 20 K the green line (lm) corresponds to $d_1 = 7 \mu\text{s}$, $d_2 = 7.2 \mu\text{s}$ and the yellow line (sm) to $d_1 = 0.4 \mu\text{s}$, $d_2 = 7.2 \mu\text{s}$. Cross marks correspond to a short interpulse delay d_1 of 400 ns; circles to a long d_1 on the order of d_2 .

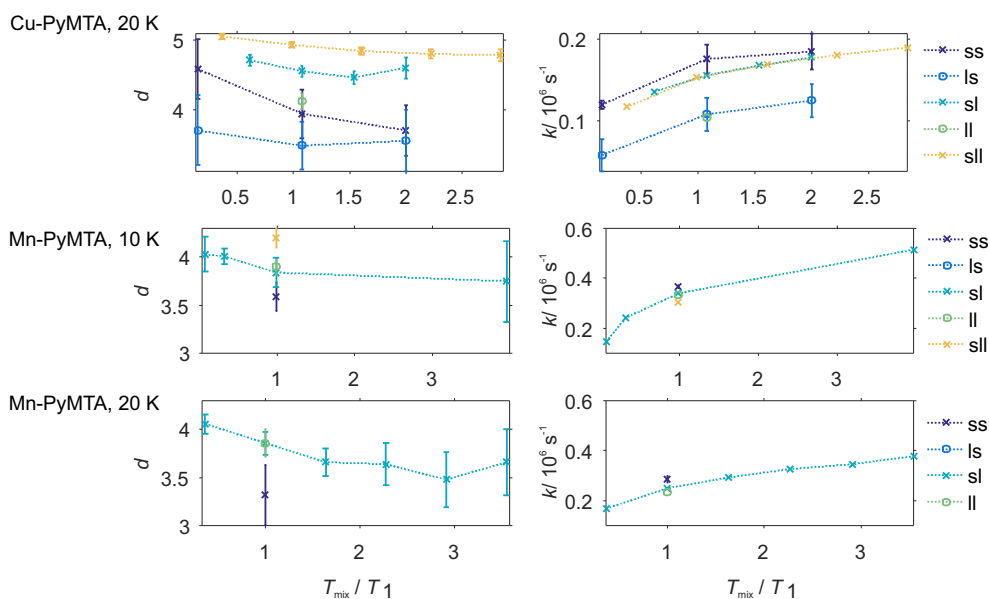


Figure B.8. Comparison of stretched exponential parameters d (left) and k (right) for Cu- and Mn-PyMTA each of $100 \mu\text{M}$ spin concentration in deuterated matrix and Q band. The sequence parameters were set as follows:

For Cu-PyMTA: short short (ss): $d_1 = 0.4 \mu\text{s}$, $d_2 = 2 \mu\text{s}$, long short (ls): $d_1 = 2 \mu\text{s}$, $d_2 = 2 \mu\text{s}$, short long (sl): $d_1 = 0.4 \mu\text{s}$, $d_2 = 5 \mu\text{s}$, long long (ll): $d_1 = 5 \mu\text{s}$, $d_2 = 5 \mu\text{s}$, short longer (sll) $d_1 = 0.4 \mu\text{s}$, $d_2 = 7 \mu\text{s}$;
 For Mn-PyMTA: short short (ss): $d_1 = 0.4 \mu\text{s}$, $d_2 = 2.2 \mu\text{s}$, short long (sl): $d_1 = 0.4 \mu\text{s}$, $d_2 = 4.2 \mu\text{s}$, long long (ll): $d_1 = 4 \mu\text{s}$, $d_2 = 4.2 \mu\text{s}$, short longer (sll) $d_1 = 0.4 \mu\text{s}$, $d_2 = 8.2 \mu\text{s}$.

B.6. Background decay in spin-labelled protein mutant RRM34 Q388C

The differences in the background fitting parameters for deuterated and protonated buffer solutions are shown in Figure B.9 and B.10. An increasing proton content leads to an increase in the decay rate k . Further, the decay rate k behaves as observed for the model compounds, with k increasing with increasing mixing time. However, the increase of k is slow and almost linear in the studied mixing time range due to the dominance of the approximately temperature-independent nuclear spin diffusion processes in the studied range. The similarity of the k parameters at different measurement temperatures further supports the assumption of temperature independence of nuclear spin diffusion processes in the studied range.

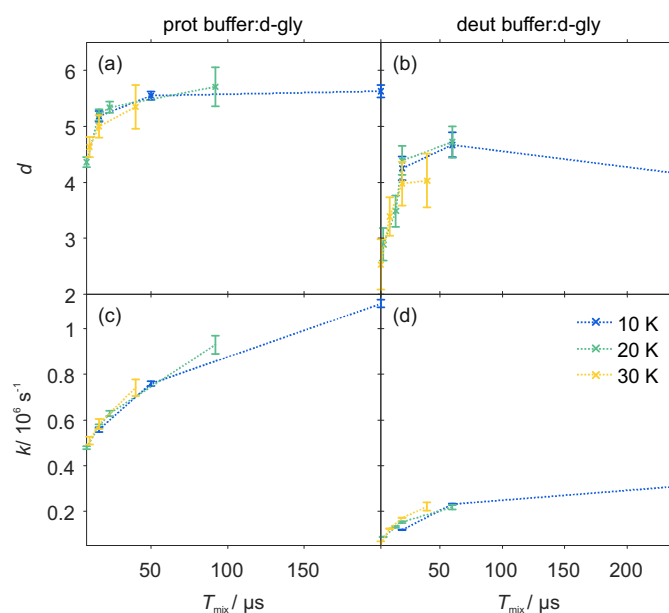


Figure B.9. Comparison of stretched exponential parameters d and k for RRM34 Q388C Gd-DOTA in W band. (a, c) In H_2O buffer:glycerol-d8 with $d_1 = 0.4 \mu\text{s}$, $d_2 = 4.2 \mu\text{s}$, $T_{1,e} = 50 \mu\text{s}$. (b, d) In D_2O buffer:glycerol-d8 with $d_1 = 0.4 \mu\text{s}$, $d_2 = 10.2 \mu\text{s}$. (a, b) Stretched exponent d and (c, d) decay rate k .

The dimensionality d exhibits a more Gaussian-like decay shape for proton-dominated environments. As for the decay rate k , the d parameters are very similar at different measurement temperatures. The dimensionality d is increasing with increasing d_1 as observed in the metal-PyMTA samples. Contrary to the metal-PyMTA complexes, for the RRM34 sample the stretching exponent d is reduced for longer dipolar evolution times d_2 (see Figure B.10(b)). However, it is important to note that traces of long d_2 were in most cases cut to allow for a sufficiently good fit using a single stretched exponential function. Overall fits by a sum of two stretched exponential functions were more suitable in the description of samples in deuterated buffer and long d_2 as shown in Figure 5.10.

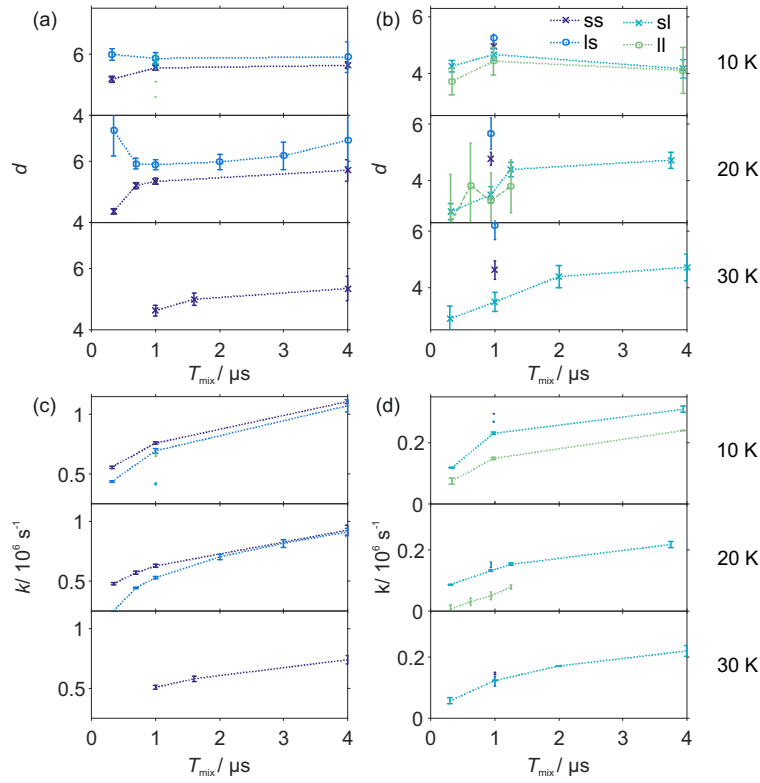


Figure B.10. Comparison of stretched exponential parameters d and k for RRM34 Q388C Gd-DOTA in W band. (a, c) In H_2O buffer:glycerol-d8, $T_{1(1/e)} = 50 \mu\text{s}$. (b, d) In D_2O buffer:glycerol-d8, $T_{1(1/e)} = 60 \mu\text{s}$. (a, b) Stretched exponent d and (c, d) decay rate k . The sequence parameters were set as follows: short short (ss): $d_1 = 0.4 \mu\text{s}$, $d_2 = 4.2 \mu\text{s}$, long short (ls): $d_1 = 4 \mu\text{s}$, $d_2 = 4.2 \mu\text{s}$, short long (sl): $d_1 = 0.4 \mu\text{s}$, $d_2 = 5.2$ (protonated case) or $10.2 \mu\text{s}$ (deuterated case), long long (ll): $d_1 = 10 \mu\text{s}$, $d_2 = 10.2 \mu\text{s}$. Note that the mixing time is normalized by the electronic relaxation times of Gd(III). The near absence of the changes in d and very weak changes in k for the changes in mixing time on the order of electronic T_1 confirm that the nuclear-driven mechanisms play the major role in these RIDME background shapes.

B.7. Relation of relaxation times to trace settings

The pulse sequence settings used in the systematic study on Gd-PyMTA at different spin concentration and measurement temperature are given in Table B.1.

	short short (ss)	short long (sl)	long short (ls)	long long (ll)
$d_1/\mu\text{s}$	0.4	0.4	3	10
$d_2/\mu\text{s}$	3.2	10.2	3.2	10.2
d_1/d_2	8	25.5	1.07	1.02
$(d_1 + d_2)/\mu\text{s}$	3.6	10.6	6.2	20.2
$(d_2 - d_1)/\mu\text{s}$	2.8	9.8	0.2	0.2

Table B.1. Pulse sequence combinations for the systematic study on Gd-PyMTA.

The fitted relaxation times using a SE model, the ratio T_m/T_1 and their relation to the dipolar evolution times d_2 are given in Table B.2.

Conc	T/ K	$T_m/ \mu s$	$T_1/ \mu s$	T_1/T_m	$d_{2,short}/T_1$	$d_{2,long}/T_1$
25 μM	10	23.3 ± 0.3	47.5 ± 1.3	2.04	0.07	0.22
	20	11.7 ± 0.1	17.4 ± 0.6	1.48	0.18	0.59
	30	6.2 ± 0.1	8.1 ± 0.3	1.30	0.40	1.26
100 μM	10	22.2 ± 0.2	41.3 ± 0.9	1.86	0.08	0.25
	20	11.7 ± 0.1	15.9 ± 0.3	1.36	0.20	0.64
	30	7.2 ± 0.1	8.7 ± 0.2	1.21	0.37	1.17
500 μM	10	11.2 ± 0.3	45.1 ± 1.8	4.03	0.07	0.23
	20	5.9 ± 0.1	15.3 ± 0.5	2.59	0.21	0.67
	30	4.7 ± 0.1	6.6 ± 0.3	1.40	0.48	1.55

Table B.2. W-band relaxation times T_m and T_1 in μs from 10 to 30 K for Gd-PyMTA at different concentrations (25, 100, 500 μM) in deuterated matrix. $d_{2,short} = 3.2 \mu s$; $d_{2,long} = 10.2 \mu s$.

Supplementary Information to Chapter 6

C.1. Averaging of the mixing block T_{mix}

At short mixing times, a reduction of the ESEEM oscillation amplitude can be achieved by varying the mixing time and averaging as the signal intensity varies with T_{mix} (Figure C.1(a, b)). Nevertheless, it can not be fully reduced and it can be shown that the reduction is larger using a certain value of T_{mix} (Figure C.1(b), light green trace). The effect of the mixing block length on the ESEEM oscillations vanishes at longer mixing times T_{mix} and averaging over T_{mix} does not result in a reduction of the ESEEM oscillations (Figure C.1(c, d)).

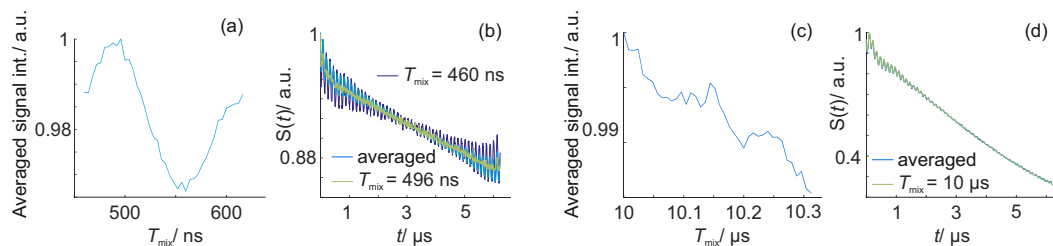


Figure C.1. Q-band RIDME data for the Gd-ruler (3.4 nm) acquired at 10 K. (a) Mean intensity of the primary RIDME traces as a function of $T_{\text{mix}} \sim 500$ ns. (b) Comparison of unprocessed primary data for $T_{\text{mix}} = 460$ ns, $T_{\text{mix}} = 496$ ns to a summation of all traces obtained in (a). (c) Mean intensity of the primary RIDME traces as a function of $T_{\text{mix}} \sim 10$ μs . (d) Comparison of unprocessed primary data for $T_{\text{mix}} = 10$ μs to a summation of all traces obtained in (c).

Although ESEEM oscillations can be reduced without averaging by working at short mixing times such a protocol is not recommended. Due to an incomplete decay of coherence, originating from the first two pulses, additional artefacts appear in the RIDME data for the accuracies of phase cycling that can usually be achieved. Furthermore, modulation depths become very low and thus sensitivity is drastically reduced.

C.2. Analytical calculations for a $S = 1/2$ and $I = 1/2$ spin system

To analyse the origin of ESEEM modulations in the RIDME experiment in more detail we present a closed expression for the five-pulse RIDME echo intensity in the case of an interacting spin $S = 1/2$ centre with one nuclear spin $I = 1/2$ obtained from product operator formalism⁴⁵ for electron-nuclear spin systems. Computations were performed with the SpinOp package in Mathematica [S. Beontges, personal communication]. Using the same notation as in Ref.¹⁹ the Hamiltonian in its eigenbasis is given by

$$\mathcal{H}_0 = \Omega_S S_z + \frac{\omega_+}{2} I_z + \omega_- S_z I_z. \quad (\text{C.1})$$

$\Omega_S = \omega_S - \omega_{mw}$ is the resonance offset and the combination frequencies $\omega_{+/-}$ are the sum or differences of the signed nuclear frequencies ω_{12} ($\alpha\alpha \rightarrow \alpha\beta$) and ω_{34} ($\beta\alpha \rightarrow \beta\beta$). The density operator at the time of the RIDME echo can be calculated using product operator formalism and the following scheme

$$\begin{aligned} \sigma_{eq} &\xrightarrow{\pi/2S_x} \xrightarrow{A} \xrightarrow{\mathcal{H}_0 d_1} \xrightarrow{-A} \xrightarrow{\pi S_x} \xrightarrow{A} \xrightarrow{\mathcal{H}_0 d_1} \xrightarrow{\mathcal{H}_0 d_{12}} \xrightarrow{-A} \xrightarrow{\pi/2S_x} \xrightarrow{A} \\ \mathcal{H}_0 T_{mix} &\xrightarrow{-A} \xrightarrow{\pi/2S_x} \xrightarrow{A} \xrightarrow{\mathcal{H}_0(d_2-d_{12})} \xrightarrow{-A} \xrightarrow{\pi S_x} \xrightarrow{A} \xrightarrow{\mathcal{H}_0 d_2} \xrightarrow{-A} \xrightarrow{\sigma_{echo}} \end{aligned} \quad (\text{C.2})$$

where free evolution is described in the eigenbasis, while ideal non-selective pulses are more easily calculated in the Cartesian product basis. Hereby we use that the transformation from the Cartesian product basis to the eigenbasis is effected by the unitary transformation $U_1 = \exp(-iA)$ and $A = \xi I_y + 2\eta S_z I_y$. The angles ξ and η are given by the secular A and pseudo-secular B hyperfine couplings, by $\xi = (\eta_\alpha + \eta_\beta)/2$ and $\eta = (\eta_\alpha - \eta_\beta)/2$ with $\eta_\alpha = \arctan(\frac{-B}{A+2\omega_I})$, $\eta_\beta = \arctan(\frac{-B}{A-2\omega_I})$. For detection, the density operator has to be transformed back into the Cartesian product basis. The amplitude of the transverse magnetization along the x - and y -axes is then proportional to the coefficients of the operators S_x and S_y in the product operator expansion of the echo. This simplified approach does not account for all possible high-spin effects, but provides correct dependencies on the different interpulse delays, which is essential for the following analysis.

In the case where the mixing block falls on top of the primary echo ($d_{12} = 0$), the analytical expression simplifies to the product of the modulation formula of the two-pulse ESEEM experiment before and after the mixing block and all other contributions refocus. Using the same notation as in Ref.¹⁹ one obtains for the modulation formula

$$\begin{aligned} V_{\text{RIDME}} &= V_{2p}(d_1) \cdot V_{2p}(d_2) = \\ &= \left(1 - \frac{1}{2}k + \frac{1}{2}k[\cos(\omega_\alpha d_1) + \cos(\omega_\beta d_1)] - \frac{1}{4}k[\cos(\omega_- d_1) + \cos(\omega_+ d_1)] \right) \\ &\cdot \left(1 - \frac{1}{2}k + \frac{1}{2}k[\cos(\omega_\alpha d_2) + \cos(\omega_\beta d_2)] - \frac{1}{4}k[\cos(\omega_- d_2) + \cos(\omega_+ d_2)] \right), \end{aligned} \quad (\text{C.3})$$

with the nuclear frequencies $\omega_\alpha = |\omega_{12}|$, $\omega_\beta = |\omega_{34}|$ and the combination frequencies ω_\pm as described above. k is the modulation depth parameter which can be expressed as

$$k = \left(\frac{B\omega_I}{\omega_\alpha \omega_\beta} \right)^2. \quad (\text{C.4})$$

Integrating Equation (C.3) over one period of the nuclear frequencies gives a constant contribution to the total echo intensity and subsequently the contribution of nuclear frequencies to the RIDME echo can be averaged out over one period of the corresponding nuclear frequency. In general the nuclear frequencies may not be commensurate. However, the major contribution to nuclear modulation in RIDME usually comes from matrix nuclei with $\omega_\alpha \sim \omega_\beta \sim \omega_I$, $\omega_+ \sim 2\omega_I$, $\omega_- \sim 0$, where ω_I is the nuclear Zeeman frequency. Averaging over a time $2\pi/\omega_I$ will then fully suppress the modulation.

If $d_{12} \neq 0$ the calculations become more difficult and are described in several steps in the following. The signal of the modulation formula at the time of the primary echo is given similar to the two pulse ESEEM formula¹⁹ by

$$\begin{aligned} V(t = 2d_1) &= -A_{2d_1} S_y = \\ &= - \left(1 - \frac{1}{2}k + \frac{1}{2}k[\cos(\omega_\alpha d_1) + \cos(\omega_\beta d_1)] - \frac{1}{4}k[\cos(\omega_- d_1) + \cos(\omega_+ d_1)] \right) S_y. \end{aligned} \quad (\text{C.5})$$

For the sake of simplicity, the following calculations are continued with S_y only. The pre-factor $-A_{2d_1}$ is dropped and needs to be multiplied to the final signal evolution.

The evolution is continued for the time interval d_{12} , the second $\pi/2$ pulse and the mixing time T_{mix} . During the mixing time, it is assumed that electron coherences defocus completely, but nuclear coherences are maintained. Thus all terms proportional to S_x or S_y are dropped at this point. In the eigenframe of the spin Hamiltonian we obtain for the nuclear coherences at the time $t_3 = 2d_1 + d_{12} + T_{\text{mix}}$

$$\begin{aligned} V(t_3) &= \frac{1}{2} \sin(2\eta) \sin(d_{12}\Omega_S) \left(I_y \left\{ S_z \left[\cos\left(\frac{d_{12}\omega_-}{2} + T_{\text{mix}}\omega_\alpha\right) \right. \right. \right. \\ &\quad \left. \left. - \cos\left(\frac{d_{12}\omega_+}{2} + T_{\text{mix}}\omega_\alpha\right) + \cos\left(T_{\text{mix}}\omega_\beta - \frac{d_{12}\omega_-}{2}\right) - \cos\left(\frac{d_{12}\omega_+}{2} + T_{\text{mix}}\omega_\beta\right) \right] \right. \\ &\quad \left. - \sin\left(\frac{T_{\text{mix}}\omega_+}{2}\right) \sin\left(\frac{1}{2}\omega_-(d_{12} + T_{\text{mix}})\right) + \sin\left(\frac{T_{\text{mix}}\omega_-}{2}\right) \sin\left(\frac{1}{2}\omega_+(d_{12} + T_{\text{mix}})\right) \right\} \\ + I_x \left\{ S_z \left[-\sin\left(\frac{d_{12}\omega_-}{2} + T_{\text{mix}}\omega_\alpha\right) + \sin\left(\frac{d_{12}\omega_+}{2} + T_{\text{mix}}\omega_\alpha\right) - \sin\left(T_{\text{mix}}\omega_\beta - \frac{d_{12}\omega_-}{2}\right) \right. \right. \\ &\quad \left. \left. + \sin\left(\frac{d_{12}\omega_+}{2} + T_{\text{mix}}\omega_\beta\right) \right] + \sin\left(\frac{T_{\text{mix}}\omega_-}{2}\right) \cos\left(\frac{1}{2}\omega_+(d_{12} + T_{\text{mix}})\right) \right. \\ &\quad \left. \left. - \cos\left(\frac{T_{\text{mix}}\omega_+}{2}\right) \sin\left(\frac{1}{2}\omega_-(d_{12} + T_{\text{mix}})\right) \right\} \right) \end{aligned} \quad (\text{C.6})$$

For the polarization terms we obtain:

$$\begin{aligned} V(t_3) &= \cos(d_{12}\Omega_S) S_z \left(\cos\left(\frac{d_{12}\omega_-}{2}\right) \cos(\eta)^2 + \cos\left(\frac{d_{12}\omega_+}{2}\right) \sin(\eta)^2 \right) \\ &\quad - \sin(d_{12}\Omega_S) I_z \left(2 \cos(\eta)^2 \sin\left(\frac{d_{12}\omega_-}{2}\right) S_z + \sin(\eta)^2 \sin\left(\frac{d_{12}\omega_+}{2}\right) \right). \end{aligned} \quad (\text{C.7})$$

From this point onwards, calculations were separated for terms proportional to S_z , $I_z + S_z I_z$, $I_y + S_z I_y$ and $I_x + S_z I_x$ and detection events evaluated separately. Detection from the evolution of the S_z terms from Equation (C.7) in y -direction results in a form

$$\begin{aligned} V_y(S_z) &= \frac{1}{16} \cos(d_{12}\Omega_S)^2 \left\{ 8 - 6k + 4 \cos(d_{12}\omega_-) + 4 \cos(d_{12}\omega_+) + k \left[2 \cos(d_2\omega_\alpha) \right. \right. \\ &\quad \left. \left. + 2 \cos(d_2\omega_\beta) - \cos(d_2\omega_-) - \cos(d_2\omega_+) + 2 \cos(d_{12}\omega_\alpha) + 2 \cos(d_{12}\omega_\beta) - 3 \cos(d_{12}\omega_-) \right. \right. \\ &\quad \left. \left. - 3 \cos(d_{12}\omega_+) + \cos(d_{12}\omega_\beta + d_2\omega_\alpha) + \cos(d_{12}\omega_\alpha + d_2\omega_\beta) + \cos(d_2\omega_\alpha - d_{12}\omega_\beta) \right. \right. \\ &\quad \left. \left. + \cos(d_{12}\omega_\alpha - d_2\omega_\beta) + \cos(d_2\omega_\alpha - d_{12}\omega_-) - \cos(d_{12}\omega_\alpha - d_2\omega_-) + \cos(d_2\omega_\alpha - d_{12}\omega_+) \right. \right. \\ &\quad \left. \left. - \cos(d_{12}\omega_\alpha - d_2\omega_+) + 2 \cos(\omega_\alpha(d_{12} - d_2)) + \cos(d_{12}\omega_- + d_2\omega_\beta) - \cos(d_{12}\omega_\beta + d_2\omega_-) \right. \right. \\ &\quad \left. \left. + \cos(d_2\omega_\beta - d_{12}\omega_+) - \cos(d_{12}\omega_\beta - d_2\omega_+) + 2 \cos(\omega_\beta(d_{12} - d_2)) - \cos(\omega_-(d_{12} - d_2)) \right. \right. \\ &\quad \left. \left. - \cos(\omega_+(d_{12} - d_2)) \right] + \cos(2\eta) \left[4 \left(\cos(d_{12}\omega_-) - \cos(d_{12}\omega_+) \right) + k \left(\cos(d_2\omega_\alpha - d_{12}\omega_\beta) \right. \right. \right. \\ &\quad \left. \left. - \cos(d_{12}\omega_\beta + d_2\omega_\alpha) - \cos(d_{12}\omega_\alpha + d_2\omega_\beta) + \cos(d_{12}\omega_\alpha - d_2\omega_\beta) + \cos(d_2\omega_\alpha - d_{12}\omega_-) \right. \right. \\ &\quad \left. \left. + \cos(d_{12}\omega_\alpha - d_2\omega_-) - \cos(d_2\omega_\alpha - d_{12}\omega_+) - \cos(d_{12}\omega_\alpha - d_2\omega_+) + \cos(d_{12}\omega_- + d_2\omega_\beta) \right. \right. \\ &\quad \left. \left. + \cos(d_{12}\omega_\beta + d_2\omega_-) - \cos(d_2\omega_\beta - d_{12}\omega_+) - \cos(d_{12}\omega_\beta - d_2\omega_+) - \cos(\omega_-(d_{12} - d_2)) \right. \right. \\ &\quad \left. \left. + \cos(\omega_+(d_{12} - d_2)) - \cos(d_{12}\omega_-) + \cos(d_{12}\omega_+) - \cos(d_2\omega_-) + \cos(d_2\omega_+) \right] \right\}. \end{aligned} \quad (\text{C.8})$$

Assuming excitation of an inhomogeneously broadened symmetric line at its centre, the term $\cos(d_{12}\Omega_S)^2$ averages to $1/2$. It is thus seen that the generated signal in y -direction oscillates with the nuclear frequencies, as well as their sum and difference and depends on the evolution times d_2 , d_{12} as well as sum and difference thereof.

In x -direction one obtains

$$\begin{aligned}
V_x(S_z) = & -\frac{1}{32} \sin(2d_{12}\Omega_S) \left\{ 8 - 6k + 4 \cos(d_{12}\omega_+) + 4 \cos(d_{12}\omega_-) + k \left[2 \cos(d_2\omega_\alpha) \right. \right. \\
& + 2 \cos(d_2\omega_\beta) - \cos(d_2\omega_+) - \cos(d_2\omega_-) + 2 \cos(d_{12}\omega_\alpha) + 2 \cos(d_{12}\omega_\beta) - 3 \cos(d_{12}\omega_+) \\
& \quad - 3 \cos(d_{12}\omega_-) + \cos(d_2\omega_\beta - d_{12}\omega_+) - \cos(d_{12}\omega_\beta - d_2\omega_+) + \cos(d_{12}\omega_- + d_2\omega_\beta) \\
& \quad - \cos(d_{12}\omega_\beta + d_2\omega_-) + \cos(d_2\omega_\alpha - d_{12}\omega_\beta) + \cos(d_{12}\omega_\alpha - d_2\omega_\beta) - \cos(\omega_-(d_{12} - d_2)) \\
& + \cos(d_{12}\omega_\beta + d_2\omega_\alpha) + \cos(d_{12}\omega_\alpha + d_2\omega_\beta) - \cos(d_{12}\omega_\alpha - d_2\omega_-) + \cos(d_2\omega_\alpha - d_{12}\omega_+) \\
& \quad - \cos(d_{12}\omega_\alpha - d_2\omega_+) + 2 \cos(\omega_\alpha(d_{12} - d_2)) + 2 \cos(\omega_\beta(d_{12} - d_2)) - \cos(\omega_+(d_{12} - d_2)) \\
& \left. + \cos(d_2\omega_\alpha - d_{12}\omega_-) \right] + \cos(2\eta) \left[4 \left(\cos(d_{12}\omega_-) - \cos(d_{12}\omega_+) \right) + k \left(-\cos(d_{12}\omega_\beta + d_2\omega_\alpha) \right. \right. \\
& \quad - \cos(d_{12}\omega_\alpha + d_2\omega_\beta) + \cos(d_{12}\omega_\alpha - d_2\omega_-) + \cos(d_2\omega_\alpha - d_{12}\omega_\beta) + \cos(d_{12}\omega_\alpha - d_2\omega_\beta) \\
& \quad - \cos(d_2\omega_\alpha - d_{12}\omega_+) - \cos(d_{12}\omega_\alpha - d_2\omega_+) + \cos(d_{12}\omega_- + d_2\omega_\beta) + \cos(d_{12}\omega_\beta + d_2\omega_-) \\
& \quad - \cos(d_2\omega_\beta - d_{12}\omega_+) - \cos(d_{12}\omega_\beta - d_2\omega_+) - \cos(\omega_-(d_{12} - d_2)) + \cos(\omega_+(d_{12} - d_2)) \\
& \quad \left. \left. + \cos(d_{12}\omega_+) + \cos(d_2\omega_+) - \cos(d_{12}\omega_-) - \cos(d_2\omega_-) \right) \right] \left. \right\}. \tag{C.9}
\end{aligned}$$

In this case, for excitation of an inhomogeneously broadened symmetric line at its centre, the signal vanishes, as $\sin(2d_{12}\Omega_S)$ is an odd function with respect to Ω_S .

Evolution of the nuclear polarization combined with the electron-nuclear two-spin order results into the following equations in y - and x -direction

$$\begin{aligned}
V_y(I_z, S_z I_z) = & \frac{1}{16} \sin(d_{12}\Omega_S)^2 \left\{ 8 - 6k - 4 \cos(d_{12}\omega_-) - 4 \cos(d_{12}\omega_+) + k \left[2 \cos(d_2\omega_\alpha) \right. \right. \\
& + 2 \cos(d_2\omega_\beta) - \cos(d_2\omega_-) - \cos(d_2\omega_+) + 3 \cos(d_{12}\omega_-) + 3 \cos(d_{12}\omega_+) + \cos(\omega_-(d_{12} - d_2)) \\
& \quad \left. + \cos(\omega_+(d_{12} - d_2)) - 2 \cos(d_{12}\omega_\beta) \cos(\omega_\alpha(d_{12} - d_2)) - 2 \cos(d_{12}\omega_\alpha) \cos(\omega_\beta(d_{12} - d_2)) \right] \\
& + \cos(2\eta) \left[4 \cos(d_{12}\omega_+) - 4 \cos(d_{12}\omega_-) - k \left(\cos(d_{12}\omega_-) - \cos(d_2\omega_\alpha - d_{12}\omega_+) \right. \right. \\
& \quad + \cos(\omega_-(d_{12} - d_2)) \cos(d_2\omega_\alpha - d_{12}\omega_-) + \cos(d_{12}\omega_- + d_2\omega_\beta) - \cos(d_2\omega_\beta - d_{12}\omega_+) \\
& \quad \left. \left. + \cos(\omega_+(d_{12} - d_2)) + \cos(d_{12}\omega_+) + \cos(d_2\omega_-) - \cos(d_2\omega_+) \right) \right] \left. \right\}, \tag{C.10}
\end{aligned}$$

and

$$\begin{aligned}
V_x(I_z, S_z I_z) = & \frac{1}{32} \sin(2d_{12}\Omega_S) \left\{ 8 - 6k + 2k \cos(d_2\omega_\alpha) + 2k \cos(d_2\omega_\beta) \right. \\
& - 4 \cos(d_{12}\omega_+) - k \left[\cos(d_2\omega_\alpha - d_{12}\omega_-) + \cos(d_2\omega_\alpha - d_{12}\omega_+) \right. \\
& + \cos(d_{12}\omega_- + d_2\omega_\beta) + \cos(d_2\omega_\beta - d_{12}\omega_+) - \cos(\omega_+(d_{12} - d_2)) \\
& \left. \left. - 3 \cos(d_{12}\omega_+) + \cos(d_2\omega_-) + \cos(d_2\omega_+) \right] + 8 \sin^2(\eta) \cos^4(\eta) \cos(\omega_-(d_{12} - d_2)) \right. \\
& - 8 \cos^6(\eta) \cos(d_{12}\omega_-) - \cos(2\eta) \left[k \left(\cos(d_2\omega_\alpha - d_{12}\omega_-) - \cos(d_2\omega_\alpha - d_{12}\omega_+) \right) \right. \\
& + \cos(d_{12}\omega_- + d_2\omega_\beta) - \cos(d_2\omega_\beta - d_{12}\omega_+) + \cos(\omega_+(d_{12} - d_2)) + \cos(d_{12}\omega_+) \\
& \left. \left. + \cos(d_2\omega_-) - \cos(d_2\omega_+) \right) - 4 \cos(d_{12}\omega_+) \right] \left. \right\}, \tag{C.11}
\end{aligned}$$

respectively. As in the previous case the signal in x -direction vanishes, while it oscillates with the nuclear frequencies as well as their sum and difference frequencies and the timings d_2 , d_{12} as well as corresponding combinations in y -direction.

Evolution of nuclear coherence gives for terms proportional to I_y

$$\begin{aligned}
V_y(I_y, S_z I_y) = & \frac{1}{8} k \sin(d_{12}\Omega_S)^2 \left\{ \cos\left(\frac{d_{12}\omega_-}{2} + d_4\omega_\alpha\right) - \cos\left(\frac{d_{12}\omega_+}{2} + d_4\omega_\alpha\right) \right. \\
& + \cos\left(d_4\omega_\beta - \frac{d_{12}\omega_-}{2}\right) - \cos\left(\frac{d_{12}\omega_+}{2} + d_4\omega_\beta\right) \left. \right\} \left\{ \cos^2(\eta) \left[-\cos\left(d_2\omega_\alpha - \frac{d_{12}\omega_+}{2}\right) \right. \right. \\
& - \cos\left(d_2\omega_\beta - \frac{d_{12}\omega_+}{2}\right) + \cos\left(\frac{1}{2}\omega_+(d_{12} - 2d_2)\right) + \cos\left(\frac{d_{12}\omega_-}{2}\right) \left. \right] \\
& + \sin^2(\eta) \left[\cos\left(d_2\omega_\alpha - \frac{d_{12}\omega_-}{2}\right) + \cos\left(\frac{d_{12}\omega_-}{2} + d_2\omega_\beta\right) \right. \\
& \left. \left. - \cos\left(\frac{1}{2}\omega_-(d_{12} - 2d_2)\right) - \cos\left(\frac{d_{12}\omega_+}{2}\right) \right] \right\}, \tag{C.12}
\end{aligned}$$

and

$$\begin{aligned}
V_x(I_y, S_z I_y) = & \frac{1}{16} k \sin(2d_{12}\Omega_S) \left\{ \cos\left(\frac{d_{12}\omega_-}{2} + d_4\omega_\alpha\right) - \cos\left(\frac{d_{12}\omega_+}{2} + d_4\omega_\alpha\right) \right. \\
& + \cos\left(d_4\omega_\beta - \frac{d_{12}\omega_-}{2}\right) - \cos\left(\frac{d_{12}\omega_+}{2} + d_4\omega_\beta\right) \left. \right\} \left\{ \cos^2(\eta) \left[-\cos\left(d_2\omega_\alpha - \frac{d_{12}\omega_+}{2}\right) \right. \right. \\
& - \cos\left(d_2\omega_\beta - \frac{d_{12}\omega_+}{2}\right) + \cos\left(\frac{1}{2}\omega_+(d_{12} - 2d_2)\right) + \cos\left(\frac{d_{12}\omega_-}{2}\right) \left. \right] \\
& + \sin^2(\eta) \left[\cos\left(d_2\omega_\alpha - \frac{d_{12}\omega_-}{2}\right) + \cos\left(\frac{d_{12}\omega_-}{2} + d_2\omega_\beta\right) \right. \\
& \left. \left. - \cos\left(\frac{1}{2}\omega_-(d_{12} - 2d_2)\right) - \cos\left(\frac{d_{12}\omega_+}{2}\right) \right] \right\}, \tag{C.13}
\end{aligned}$$

as well as for terms proportional to I_x at the end of the mixing block

$$\begin{aligned}
V_y(I_x, S_z I_x) &= \frac{1}{32} \sin^2(d_{12}\Omega_S) \left(-8 \sin(d_{12}\omega_-) \sin(d_2\omega_-) \sin^2(\xi) \cos^6(\eta) \right) \quad (\text{C.14}) \\
&+ 32 \sin^2\left(\frac{d_{12}\omega_-}{2}\right) \sin^2\left(\frac{d_2\omega_-}{2}\right) \sin^4(\xi) \cos^4(\eta) + 8 \sin(d_{12}\omega_-) \sin(d_2\omega_-) \sin^4(\xi) \cos^4(\eta) \\
&\quad + 32 \cos^2\left(\frac{d_2\omega_-}{2}\right) \cos(2\eta) \sin^2\left(\frac{d_{12}\omega_-}{2}\right) \sin^2(\xi) \cos^4(\eta) \\
&\quad + 32 \cos^2(\xi) \sin^2\left(\frac{d_{12}\omega_-}{2}\right) \sin^2\left(\frac{d_2\omega_-}{2}\right) \sin^2(\xi) \cos^4(\eta) \\
&\quad + 64 \cos\left(\frac{d_2\omega_-}{2}\right) \cos\left(\frac{d_2\omega_+}{2}\right) \sin^2\left(\frac{d_{12}\omega_-}{2}\right) \sin^2(\eta) \sin^2(\xi) \cos^4(\eta) \\
&\quad - 32 \cos\left(\frac{d_2\omega_+}{2}\right) \sin(d_{12}\omega_-) \sin\left(\frac{d_2\omega_-}{2}\right) \sin^2(\eta) \sin^2(\xi) \cos^4(\eta) \\
&+ 16 \cos\left(\frac{d_{12}\omega_-}{2}\right) \cos\left(\frac{1}{2}(d_{12} + d_4)\omega_+\right) \sin\left(\frac{d_4\omega_-}{2}\right) \sin(d_2\omega_-) \sin^2(\eta) \sin^2(\xi) \cos^4(\eta) \\
&\quad + 8 \sin(d_{12}\omega_-) \sin(d_2\omega_-) \sin^2(\eta) \sin^2(\xi) \cos^4(\eta) \\
&- 16 \cos\left(\frac{d_{12}\omega_-}{2}\right) \cos\left(\frac{d_4\omega_+}{2}\right) \sin(d_2\omega_-) \sin\left(\frac{1}{2}(d_{12} + d_4)\omega_-\right) \sin^2(\eta) \sin^2(\xi) \cos^4(\eta) \\
&\quad + 32 \cos(\xi) \sin\left(\frac{d_{12}\omega_-}{2}\right) \sin\left(\frac{d_{12}\omega_+}{2}\right) \sin^2\left(\frac{d_2\omega_+}{2}\right) \sin(\eta) \sin^3(\xi) \cos^3(\eta) \\
&\quad + 16 \cos\left(\frac{d_{12}\omega_+}{2}\right) \cos(\xi) \sin\left(\frac{d_{12}\omega_-}{2}\right) \sin(d_2\omega_+) \sin(\eta) \sin^3(\xi) \cos^3(\eta) \\
&\quad + 32 \cos^3(\xi) \sin\left(\frac{d_{12}\omega_-}{2}\right) \sin\left(\frac{d_{12}\omega_+}{2}\right) \sin^2\left(\frac{d_2\omega_+}{2}\right) \sin(\eta) \sin(\xi) \cos^3(\eta) \\
&\quad + 16 \cos\left(\frac{d_{12}\omega_+}{2}\right) \cos^3(\xi) \sin\left(\frac{d_{12}\omega_-}{2}\right) \sin(d_2\omega_+) \sin(\eta) \sin(\xi) \cos^3(\eta) \\
&\quad - 32 \cos^2\left(\frac{d_2\omega_+}{2}\right) \cos^2(\xi) \sin^2\left(\frac{d_{12}\omega_+}{2}\right) \sin^4(\eta) \cos^2(\eta) \\
&\quad + 64 \cos\left(\frac{d_2\omega_-}{2}\right) \cos\left(\frac{d_2\omega_+}{2}\right) \cos^2(\xi) \sin^2\left(\frac{d_{12}\omega_+}{2}\right) \sin^4(\eta) \cos^2(\eta) \\
&\quad - 32 \cos\left(\frac{d_2\omega_-}{2}\right) \cos^2(\xi) \sin(d_{12}\omega_+) \sin\left(\frac{d_2\omega_+}{2}\right) \sin^4(\eta) \cos^2(\eta) \\
&\quad + 8 \cos^2(\xi) \sin(d_{12}\omega_+) \sin(d_2\omega_+) \sin^4(\eta) \cos^2(\eta) \\
&- 64 \cos\left(\frac{d_2\omega_-}{2}\right) \cos\left(\frac{d_2\omega_+}{2}\right) \cos\left(\frac{1}{2}(d_{12} + d_4)\omega_+\right) \sin\left(\frac{d_{12}\omega_-}{2}\right) \sin\left(\frac{d_4\omega_-}{2}\right) \sin^4(\eta) \sin^2(\xi) \cos^2(\eta) \\
&+ 64 \cos\left(\frac{d_{12}\omega_-}{2}\right) \cos\left(\frac{d_2\omega_+}{2}\right) \cos\left(\frac{1}{2}(d_{12} + d_4)\omega_+\right) \sin\left(\frac{d_2\omega_-}{2}\right) \sin\left(\frac{d_4\omega_-}{2}\right) \sin^4(\eta) \sin^2(\xi) \cos^2(\eta) \\
&\quad - 16 \cos\left(\frac{d_{12}\omega_-}{2}\right) \cos\left(\frac{1}{2}(d_{12} + d_4)\omega_+\right) \sin(d_2\omega_-) \sin\left(\frac{d_4\omega_-}{2}\right) \sin^4(\eta) \sin^2(\xi) \cos^2(\eta) \\
&+ 64 \cos\left(\frac{d_2\omega_-}{2}\right) \cos\left(\frac{d_2\omega_+}{2}\right) \cos\left(\frac{d_4\omega_+}{2}\right) \sin\left(\frac{d_{12}\omega_-}{2}\right) \sin\left(\frac{1}{2}(d_{12} + d_4)\omega_-\right) \sin^4(\eta) \sin^2(\xi) \cos^2(\eta) \\
&- 64 \cos\left(\frac{d_{12}\omega_-}{2}\right) \cos\left(\frac{d_2\omega_+}{2}\right) \cos\left(\frac{d_4\omega_+}{2}\right) \sin\left(\frac{d_2\omega_-}{2}\right) \sin\left(\frac{1}{2}(d_{12} + d_4)\omega_-\right) \sin^4(\eta) \sin^2(\xi) \cos^2(\eta) \\
&\quad + 16 \cos\left(\frac{d_{12}\omega_-}{2}\right) \cos\left(\frac{d_4\omega_+}{2}\right) \sin(d_2\omega_-) \sin\left(\frac{1}{2}(d_{12} + d_4)\omega_-\right) \sin^4(\eta) \sin^2(\xi) \cos^2(\eta) \\
&- 32 \cos\left(\frac{1}{2}(d_{12} + d_4)\omega_+\right) \cos(\xi) \sin\left(\frac{d_4\omega_-}{2}\right) \sin\left(\frac{d_{12}\omega_+}{2}\right) \sin^2\left(\frac{d_2\omega_+}{2}\right) \sin^3(\eta) \sin^3(\xi) \cos(\eta) \\
&\quad + 32 \cos(\xi) \sin\left(\frac{d_{12}\omega_-}{2}\right) \sin^2\left(\frac{d_2\omega_-}{2}\right) \sin\left(\frac{d_{12}\omega_+}{2}\right) \sin^3(\eta) \sin^3(\xi) \cos(\eta) \\
&\quad + 16 \cos\left(\frac{d_{12}\omega_-}{2}\right) \cos(\xi) \sin\left(\frac{d_{12}\omega_+}{2}\right) \sin(d_2\omega_-) \sin^3(\eta) \sin^3(\xi) \cos(\eta) \\
&+ 32 \cos\left(\frac{d_4\omega_+}{2}\right) \cos(\xi) \sin\left(\frac{d_{12}\omega_+}{2}\right) \sin^2\left(\frac{d_2\omega_+}{2}\right) \sin\left(\frac{1}{2}(d_{12} + d_4)\omega_-\right) \sin^3(\eta) \sin^3(\xi) \cos(\eta)
\end{aligned}$$

$$\begin{aligned}
& -16 \cos\left(\frac{d_{12}\omega_+}{2}\right) \cos\left(\frac{1}{2}(d_{12} + d_4)\omega_+\right) \cos(\xi) \sin\left(\frac{d_4\omega_-}{2}\right) \sin(d_2\omega_+) \sin^3(\eta) \sin^3(\xi) \cos(\eta) \\
& +16 \cos\left(\frac{d_{12}\omega_+}{2}\right) \cos\left(\frac{d_4\omega_+}{2}\right) \cos(\xi) \sin\left(\frac{1}{2}(d_{12} + d_4)\omega_-\right) \sin(d_2\omega_+) \sin^3(\eta) \sin^3(\xi) \cos(\eta) \\
& -32 \cos\left(\frac{1}{2}(d_{12} + d_4)\omega_+\right) \cos^3(\xi) \sin\left(\frac{d_4\omega_-}{2}\right) \sin\left(\frac{d_{12}\omega_+}{2}\right) \sin^2\left(\frac{d_2\omega_+}{2}\right) \sin^3(\eta) \sin(\xi) \cos(\eta) \\
& \quad +32 \cos^3(\xi) \sin\left(\frac{d_{12}\omega_-}{2}\right) \sin^2\left(\frac{d_2\omega_-}{2}\right) \sin\left(\frac{d_{12}\omega_+}{2}\right) \sin^3(\eta) \sin(\xi) \cos(\eta) \\
& \quad +16 \cos\left(\frac{d_{12}\omega_-}{2}\right) \cos^3(\xi) \sin\left(\frac{d_{12}\omega_+}{2}\right) \sin(d_2\omega_-) \sin^3(\eta) \sin(\xi) \cos(\eta) \\
& +32 \cos\left(\frac{d_4\omega_+}{2}\right) \cos^3(\xi) \sin\left(\frac{d_{12}\omega_+}{2}\right) \sin^2\left(\frac{d_2\omega_+}{2}\right) \sin\left(\frac{1}{2}(d_{12} + d_4)\omega_-\right) \sin^3(\eta) \sin(\xi) \cos(\eta) \\
& -16 \cos\left(\frac{d_{12}\omega_+}{2}\right) \cos\left(\frac{1}{2}(d_{12} + d_4)\omega_+\right) \cos^3(\xi) \sin\left(\frac{d_4\omega_-}{2}\right) \sin(d_2\omega_+) \sin^3(\eta) \sin(\xi) \cos(\eta) \\
& +16 \cos\left(\frac{d_{12}\omega_+}{2}\right) \cos\left(\frac{d_4\omega_+}{2}\right) \cos^3(\xi) \sin\left(\frac{1}{2}(d_{12} + d_4)\omega_-\right) \sin(d_2\omega_+) \sin^3(\eta) \sin(\xi) \cos(\eta) \\
& +32 \cos^2\left(\frac{d_2\omega_+}{2}\right) \cos^2(\xi) \sin^2\left(\frac{d_{12}\omega_+}{2}\right) \sin^6(\eta) - 8 \cos^2(\xi) \sin(d_{12}\omega_+) \sin(d_2\omega_+) \sin^6(\eta) \\
& +32 \cos^4(\xi) \sin^2\left(\frac{d_{12}\omega_+}{2}\right) \sin^2\left(\frac{d_2\omega_+}{2}\right) \sin^4(\eta) + 8 \cos^4(\xi) \sin(d_{12}\omega_+) \sin(d_2\omega_+) \sin^4(\eta) \\
& -8k \cos\left(\frac{1}{2}(d_{12} + d_4)\omega_+\right) \sin\left(\frac{d_{12}\omega_-}{2}\right) \sin^2\left(\frac{d_2\omega_-}{2}\right) \sin\left(\frac{d_4\omega_-}{2}\right) \sin^4(\xi) \\
& -4k \cos\left(\frac{d_{12}\omega_-}{2}\right) \cos\left(\frac{1}{2}(d_{12} + d_4)\omega_+\right) \sin(d_2\omega_-) \sin\left(\frac{d_4\omega_-}{2}\right) \sin^4(\xi) \\
& +8k \cos\left(\frac{d_4\omega_+}{2}\right) \sin\left(\frac{d_{12}\omega_-}{2}\right) \sin^2\left(\frac{d_2\omega_-}{2}\right) \sin\left(\frac{1}{2}(d_{12} + d_4)\omega_-\right) \sin^4(\xi) \\
& +4k \cos\left(\frac{d_{12}\omega_-}{2}\right) \cos\left(\frac{d_4\omega_+}{2}\right) \sin(d_2\omega_-) \sin\left(\frac{1}{2}(d_{12} + d_4)\omega_-\right) \sin^4(\xi) \\
& -8k \cos\left(\frac{1}{2}(d_{12} + d_4)\omega_+\right) \cos^2(\xi) \sin\left(\frac{d_{12}\omega_-}{2}\right) \sin^2\left(\frac{d_2\omega_-}{2}\right) \sin\left(\frac{d_4\omega_-}{2}\right) \sin^2(\xi) \\
& -8k \cos^2\left(\frac{d_2\omega_-}{2}\right) \cos\left(\frac{1}{2}(d_{12} + d_4)\omega_+\right) \cos(2\eta) \sin\left(\frac{d_{12}\omega_-}{2}\right) \sin\left(\frac{d_4\omega_-}{2}\right) \sin^2(\xi) \\
& +8k \cos\left(\frac{d_4\omega_+}{2}\right) \cos^2(\xi) \sin\left(\frac{d_{12}\omega_-}{2}\right) \sin^2\left(\frac{d_2\omega_-}{2}\right) \sin\left(\frac{1}{2}(d_{12} + d_4)\omega_-\right) \sin^2(\xi) \\
& +8k \cos^2\left(\frac{d_2\omega_-}{2}\right) \cos\left(\frac{d_4\omega_+}{2}\right) \cos(2\eta) \sin\left(\frac{d_{12}\omega_-}{2}\right) \sin\left(\frac{1}{2}(d_{12} + d_4)\omega_-\right) \sin^2(\xi) \\
& \quad + \left(4 \sin\left(\frac{d_2\omega_+}{2}\right) \left(\sin\left(\frac{d_2\omega_+}{2}\right) + \sin\left(d_{12}\omega_+ - \frac{d_2\omega_+}{2}\right)\right) \sin^4(\eta) \right. \\
& \quad \quad \left. + \sin(d_2\omega_-) \left(2 \sin(d_{12}\omega_-) \cos^4(\eta)\right) \right. \\
& \quad \quad \left. + k \cos\left(\frac{d_{12}\omega_-}{2}\right) \left(\cos\left(\frac{d_4\omega_+}{2}\right) \sin\left(\frac{1}{2}(d_{12} + d_4)\omega_-\right) \right. \right. \\
& \quad \quad \left. \left. - \cos\left(\frac{1}{2}(d_{12} + d_4)\omega_+\right) \sin\left(\frac{d_4\omega_-}{2}\right)\right)\right) \sin^2(2\xi) \\
& +8k \cos\left(\frac{d_4\omega_-}{2}\right) \cos\left(\frac{1}{2}(d_{12} - d_2)\omega_+\right) \cos^2(\xi) \sin\left(\frac{d_2\omega_+}{2}\right) \sin\left(\frac{1}{2}(d_{12} + d_4)\omega_+\right) \\
& +8k \cos\left(\frac{d_2\omega_-}{2}\right) \cos\left(\frac{d_4\omega_-}{2}\right) \cos^2(\xi) \sin\left(\frac{1}{2}(d_{12} - d_2)\omega_+\right) \sin\left(\frac{1}{2}(d_{12} + d_4)\omega_+\right) \\
& +16k \cos\left(\frac{d_4\omega_-}{2}\right) \cos(2\eta) \cos^2(\xi) \sin\left(\frac{d_2\omega_\alpha}{2}\right) \sin\left(\frac{d_2\omega_\beta}{2}\right) \sin\left(\frac{1}{2}(d_{12} - d_2)\omega_+\right) \sin\left(\frac{1}{2}(d_{12} + d_4)\omega_+\right) \\
& \quad + \left(8 \cos(\eta) \left(\cos\left(\frac{d_{12}\omega_-}{2}\right) \sin\left(\frac{d_{12}\omega_+}{2}\right) \sin(d_2\omega_-) \right. \right. \\
& \quad \left. \left. + \cos\left(\frac{d_{12}\omega_+}{2}\right) \left(\cos\left(\frac{1}{2}(d_{12} + d_4)\omega_+\right) \sin\left(\frac{d_4\omega_-}{2}\right) \right. \right. \right. \\
& \quad \left. \left. \left. - \cos\left(\frac{d_4\omega_+}{2}\right) \sin\left(\frac{1}{2}(d_{12} + d_4)\omega_-\right)\right) \sin(d_2\omega_+) \right) \sin^5(\eta) \right)
\end{aligned}$$

$$\begin{aligned}
& -8 \left(\cos\left(\frac{d_{12}\omega_+}{2}\right) \cos^3(\eta) \left(\sin\left(\frac{d_{12}\omega_-}{2}\right) + \cos\left(\frac{1}{2}(d_{12} + d_4)\omega_+\right) \sin\left(\frac{d_4\omega_-}{2}\right) \right) \sin(d_2\omega_+) \right. \\
& \quad - \left(\cos^2\left(\frac{d_2\omega_-}{2}\right) (\cos(\eta) + \cos(3\eta)) \sin\left(\frac{d_{12}\omega_-}{2}\right) \right. \\
& \quad \left. \left. - \cos\left(\frac{d_{12}\omega_-}{2}\right) \cos^3(\eta) \sin(d_2\omega_-) \right) \sin\left(\frac{d_{12}\omega_+}{2}\right) \right) \sin^3(\eta) \\
& + 8 \cos^3(\eta) \left(\cos\left(\frac{d_{12}\omega_+}{2}\right) \sin\left(\frac{d_{12}\omega_-}{2}\right) \left(\sin(d_2\omega_+) - 4 \cos\left(\frac{d_2\omega_-}{2}\right) \sin\left(\frac{d_2\omega_+}{2}\right) \right) \cos^2(\eta) \right. \\
& \quad + 2 \cos\left(\frac{d_4\omega_-}{2}\right) \left(\cos\left(\frac{1}{2}(d_{12} - d_2)\omega_-\right) \sin\left(\frac{d_2\omega_-}{2}\right) \right. \\
& \quad \left. \left. + \cos\left(\frac{d_2\omega_-}{2}\right) \cos(2\eta) \sin\left(\frac{1}{2}(d_{12} - d_2)\omega_-\right) \sin\left(\frac{1}{2}(d_{12} + d_4)\omega_+\right) \right) \right) \sin(\eta) \\
& + 8 \cos^2\left(\frac{d_2\omega_+}{2}\right) \sin\left(\frac{d_{12}\omega_+}{2}\right) \left((\cos(\eta) + \cos(3\eta)) \left(\cos\left(\frac{1}{2}(d_{12} + d_4)\omega_+\right) \sin\left(\frac{d_4\omega_-}{2}\right) \right. \right. \\
& \quad \left. \left. - \cos\left(\frac{d_4\omega_+}{2}\right) \sin\left(\frac{1}{2}(d_{12} + d_4)\omega_-\right) \right) \sin^2(\eta) - 2 \cos^3(\eta) \cos(2\eta) \sin\left(\frac{d_{12}\omega_-}{2}\right) \right) \sin(\eta) \\
& \quad + \cos\left(\frac{d_{12}\omega_+}{2}\right) \cos\left(\frac{d_4\omega_+}{2}\right) \sin\left(\frac{1}{2}(d_{12} + d_4)\omega_-\right) \sin(d_2\omega_+) \sin^3(2\eta) \\
& \quad + 4k \cos\left(\frac{d_2\omega_-}{2}\right) \left(\cos\left(\frac{d_4\omega_+}{2}\right) \sin\left(\frac{1}{2}(d_{12} + d_4)\omega_-\right) \right. \\
& \quad \left. \left. - \cos\left(\frac{1}{2}(d_{12} + d_4)\omega_+\right) \sin\left(\frac{d_4\omega_-}{2}\right) \right) \sin\left(\frac{1}{2}(d_{12} - d_2)\omega_+\right) \sin(2\eta) \right. \\
& + 2 \cos\left(\frac{d_2\omega_+}{2}\right) \left(16 \cos\left(\frac{d_4\omega_-}{2}\right) \cos^3(\eta) \sin\left(\frac{1}{2}(d_{12} - d_2)\omega_-\right) \sin\left(\frac{1}{2}(d_{12} + d_4)\omega_+\right) \sin^3(\eta) \right. \\
& \quad + \sin\left(\frac{d_{12}\omega_+}{2}\right) \left(\cos\left(\frac{d_2\omega_-}{2}\right) \sin\left(\frac{d_{12}\omega_-}{2}\right) (5 \sin(2\eta) + \sin(6\eta)) \right. \\
& \quad \left. \left. - 16 \cos\left(\frac{d_{12}\omega_-}{2}\right) \cos(\eta) \sin\left(\frac{d_2\omega_-}{2}\right) \sin^5(\eta) \right) \right) \sin(2\xi) \\
& + 2 \cos\left(\frac{1}{2}(d_{12} + d_4)\omega_-\right) \sin\left(\frac{d_4\omega_+}{2}\right) \left(-32 \cos\left(\frac{d_2\omega_-}{2}\right) \cos^2(\xi) \sin\left(\frac{1}{2}(d_{12} - d_2)\omega_+\right) \sin^2(\eta) \cos^4(\eta) \right. \\
& \quad - 16 \cos(\xi) \sin\left(\frac{d_{12}\omega_-}{2}\right) \sin^2\left(\frac{d_2\omega_-}{2}\right) \sin(\eta) \sin^3(\xi) \cos^3(\eta) \\
& \quad - 16 \cos\left(\frac{1}{2}(d_{12} - d_2)\omega_-\right) \cos^3(\xi) \sin\left(\frac{d_2\omega_-}{2}\right) \sin(\eta) \sin(\xi) \cos^3(\eta) \\
& \quad + 8 \cos\left(\frac{d_{12}\omega_-}{2}\right) \cos(2\eta) \cos(\xi) \sin(d_2\omega_-) \sin(\eta) \sin(\xi) \cos^3(\eta) \\
& \quad - 8 \cos^2\left(\frac{d_2\omega_-}{2}\right) \cos(2\eta) \sin\left(\frac{d_{12}\omega_-}{2}\right) \sin(\eta) \sin(2\xi) \cos^3(\eta) \\
& \quad \left. \left. - 2 \cos\left(\frac{d_{12}\omega_-}{2}\right) \sin(d_2\omega_-) \sin(\eta) \sin(2\xi) \cos^3(\eta) \right) \right. \\
& + \cos\left(\frac{d_{12}\omega_-}{2}\right) \sin(d_2\omega_-) \sin(\eta) \sin(4\xi) \cos^3(\eta) - 2k \cos\left(\frac{d_{12}\omega_+}{2}\right) \cos^2(\xi) \sin(d_2\omega_+) \sin^2(\xi) \\
& \quad - k \sin\left(\frac{d_{12}\omega_+}{2}\right) \sin^2\left(\frac{d_2\omega_+}{2}\right) \sin^2(2\xi) - 4k \cos\left(\frac{1}{2}(d_{12} - d_2)\omega_+\right) \cos^4(\xi) \sin\left(\frac{d_2\omega_+}{2}\right) \\
& \quad + 4 \cos\left(\frac{d_2\omega_+}{2}\right) \left(k \cos(2\eta) \cos^2(\xi) \sin\left(\frac{1}{2}(d_{12} - d_2)\omega_+\right) \right. \\
& \quad \left. \left. - 4 \cos^3(\eta) \sin\left(\frac{1}{2}(d_{12} - d_2)\omega_-\right) \sin^3(\eta) \sin(2\xi) \right) \right),
\end{aligned}$$

and

$$\begin{aligned}
V_x(I_x, S_z I_x) &= \frac{1}{32} \cos(d_{12}\Omega_S) \sin(d_{12}\Omega_S) \left(-8 \sin(d_{12}\omega_-) \sin(d_2\omega_-) \sin^2(\xi) \cos^6(\eta) \right. \\
& \quad \left. - 64 \cos\left(\frac{d_2\omega_-}{2}\right) \cos\left(\frac{d_{12}\omega_+}{2}\right) \cos(\xi) \sin\left(\frac{d_{12}\omega_-}{2}\right) \sin\left(\frac{d_2\omega_+}{2}\right) \sin(\eta) \sin(\xi) \cos^5(\eta) \right)
\end{aligned} \tag{C.15}$$

$$\begin{aligned}
& +32 \sin^2\left(\frac{d_{12}\omega_-}{2}\right) \sin^2\left(\frac{d_2\omega_-}{2}\right) \sin^4(\xi) \cos^4(\eta) + 8 \sin(d_{12}\omega_-) \sin(d_2\omega_-) \sin^4(\xi) \cos^4(\eta) \\
& +32 \sin^2(\xi) \cos^4(\eta) \left(\cos^2\left(\frac{d_2\omega_-}{2}\right) \cos(2\eta) \sin^2\left(\frac{d_{12}\omega_-}{2}\right) + \cos^2(\xi) \sin^2\left(\frac{d_{12}\omega_-}{2}\right) \sin^2\left(\frac{d_2\omega_-}{2}\right) \right) \\
& \quad +64 \cos\left(\frac{d_2\omega_-}{2}\right) \cos\left(\frac{d_2\omega_+}{2}\right) \sin^2\left(\frac{d_{12}\omega_-}{2}\right) \sin^2(\eta) \sin^2(\xi) \cos^4(\eta) \\
& \quad -32 \cos\left(\frac{d_2\omega_+}{2}\right) \sin(d_{12}\omega_-) \sin\left(\frac{d_2\omega_-}{2}\right) \sin^2(\eta) \sin^2(\xi) \cos^4(\eta) \\
& +16 \cos\left(\frac{d_{12}\omega_-}{2}\right) \cos\left(\frac{1}{2}(d_{12} + d_4)\omega_+\right) \sin\left(\frac{d_4\omega_-}{2}\right) \sin(d_2\omega_-) \sin^2(\eta) \sin^2(\xi) \cos^4(\eta) \\
& \quad +8 \sin(d_{12}\omega_-) \sin(d_2\omega_-) \sin^2(\eta) \sin^2(\xi) \cos^4(\eta) \\
& -16 \cos\left(\frac{d_{12}\omega_-}{2}\right) \cos\left(\frac{d_4\omega_+}{2}\right) \sin(d_2\omega_-) \sin\left(\frac{1}{2}(d_{12} + d_4)\omega_-\right) \sin^2(\eta) \sin^2(\xi) \cos^4(\eta) \\
& \quad +32 \cos(\xi) \sin\left(\frac{d_{12}\omega_-}{2}\right) \sin\left(\frac{d_{12}\omega_+}{2}\right) \sin^2\left(\frac{d_2\omega_+}{2}\right) \sin(\eta) \sin^3(\xi) \cos^3(\eta) \\
& \quad +16 \cos\left(\frac{d_{12}\omega_+}{2}\right) \cos(\xi) \sin\left(\frac{d_{12}\omega_-}{2}\right) \sin(d_2\omega_+) \sin(\eta) \sin^3(\xi) \cos^3(\eta) \\
& +32 \cos^3(\xi) \sin\left(\frac{d_{12}\omega_-}{2}\right) \sin\left(\frac{d_{12}\omega_+}{2}\right) \sin^2\left(\frac{d_2\omega_+}{2}\right) \sin(\eta) \sin(\xi) \cos^3(\eta) \\
& \quad +16 \cos\left(\frac{d_{12}\omega_+}{2}\right) \cos^3(\xi) \sin\left(\frac{d_{12}\omega_-}{2}\right) \sin(d_2\omega_+) \sin(\eta) \sin(\xi) \cos^3(\eta) \\
& \quad -32 \cos^2\left(\frac{d_2\omega_+}{2}\right) \sin^2\left(\frac{d_{12}\omega_+}{2}\right) \cos^2(\xi) \sin^4(\eta) \cos^2(\eta) \\
& \quad -64 \cos\left(\frac{d_2\omega_-}{2}\right) \cos\left(\frac{d_2\omega_+}{2}\right) \sin^2\left(\frac{d_{12}\omega_+}{2}\right) \cos^2(\xi) \sin^4(\eta) \cos^2(\eta) \\
& \quad -32 \cos\left(\frac{d_2\omega_-}{2}\right) \cos^2(\xi) \sin(d_{12}\omega_+) \sin\left(\frac{d_2\omega_+}{2}\right) \sin^4(\eta) \cos^2(\eta) \\
& \quad +8 \cos^2(\xi) \sin(d_{12}\omega_+) \sin(d_2\omega_+) \sin^4(\eta) \cos^2(\eta) \\
& -64 \cos\left(\frac{d_2\omega_-}{2}\right) \cos\left(\frac{d_2\omega_+}{2}\right) \cos\left(\frac{1}{2}(d_{12} + d_4)\omega_+\right) \sin\left(\frac{d_{12}\omega_-}{2}\right) \sin\left(\frac{d_4\omega_-}{2}\right) \sin^4(\eta) \sin^2(\xi) \cos^2(\eta) \\
& +64 \cos\left(\frac{d_{12}\omega_-}{2}\right) \cos\left(\frac{d_2\omega_+}{2}\right) \cos\left(\frac{1}{2}(d_{12} + d_4)\omega_+\right) \sin\left(\frac{d_2\omega_-}{2}\right) \sin\left(\frac{d_4\omega_-}{2}\right) \sin^4(\eta) \sin^2(\xi) \cos^2(\eta) \\
& -64 \cos\left(\frac{d_2\omega_-}{2}\right) \cos\left(\frac{d_2\omega_+}{2}\right) \cos\left(\frac{1}{2}(d_{12} + d_4)\omega_+\right) \sin\left(\frac{d_{12}\omega_-}{2}\right) \sin\left(\frac{d_4\omega_-}{2}\right) \sin^4(\eta) \sin^2(\xi) \cos^2(\eta) \\
& +64 \cos\left(\frac{d_{12}\omega_-}{2}\right) \cos\left(\frac{d_2\omega_+}{2}\right) \cos\left(\frac{1}{2}(d_{12} + d_4)\omega_+\right) \sin\left(\frac{d_2\omega_-}{2}\right) \sin\left(\frac{d_4\omega_-}{2}\right) \sin^4(\eta) \sin^2(\xi) \cos^2(\eta) \\
& \quad -16 \cos\left(\frac{d_{12}\omega_-}{2}\right) \cos\left(\frac{1}{2}(d_{12} + d_4)\omega_+\right) \sin(d_2\omega_-) \sin\left(\frac{d_4\omega_-}{2}\right) \sin^4(\eta) \sin^2(\xi) \cos^2(\eta) \\
& +64 \cos\left(\frac{d_2\omega_-}{2}\right) \cos\left(\frac{d_2\omega_+}{2}\right) \cos\left(\frac{d_4\omega_+}{2}\right) \sin\left(\frac{d_{12}\omega_-}{2}\right) \sin\left(\frac{1}{2}(d_{12} + d_4)\omega_-\right) \sin^4(\eta) \sin^2(\xi) \cos^2(\eta)
\end{aligned}$$

$$\begin{aligned}
& -64 \cos\left(\frac{d_{12}\omega_-}{2}\right) \cos\left(\frac{d_2\omega_+}{2}\right) \cos\left(\frac{d_4\omega_+}{2}\right) \sin\left(\frac{d_2\omega_-}{2}\right) \sin\left(\frac{1}{2}(d_{12} + d_4)\omega_-\right) \sin^4(\eta) \sin^2(\xi) \cos^2(\eta) \\
& \quad + 16 \cos\left(\frac{d_{12}\omega_-}{2}\right) \cos\left(\frac{d_4\omega_+}{2}\right) \sin(d_2\omega_-) \sin\left(\frac{1}{2}(d_{12} + d_4)\omega_-\right) \sin^4(\eta) \sin^2(\xi) \cos^2(\eta) \\
& \quad - 2 \cos\left(\frac{1}{2}(d_{12} + d_4)\omega_-\right) \sin\left(\frac{d_4\omega_+}{2}\right) \sin(\eta) \left(4 \sin\left(\frac{d_{12}\omega_+}{2}\right) \sin^2\left(\frac{d_2\omega_+}{2}\right) \sin(\eta) \sin^2(2\xi)\right. \\
& + 2 \cos(\eta) \sin(2\xi) \left(4 \cos(2\eta) \sin\left(\frac{d_{12}\omega_-}{2}\right) \cos^2\left(\frac{d_2\omega_-}{2}\right) + 8 \cos\left(\frac{d_2\omega_+}{2}\right) \sin\left(\frac{1}{2}(d_{12} - d_2)\omega_-\right) \sin^2(\eta)\right. \\
& \quad \left. + \cos\left(\frac{d_{12}\omega_-}{2}\right) \sin(d_2\omega_-)\right) + 8 \cos(\xi) \left(2 \cos(\eta) \sin\left(\frac{d_{12}\omega_-}{2}\right) \sin^2\left(\frac{d_2\omega_-}{2}\right) \sin^3(\xi)\right) \\
& + \cos\left(\frac{d_{12}\omega_+}{2}\right) \cos(\xi) \sin(d_2\omega_+) \sin(\eta) \sin^2(\xi) + \cos(\eta) \left(2 \cos\left(\frac{1}{2}(d_{12} - d_2)\omega_-\right) \cos^2(\xi) \sin\left(\frac{d_2\omega_-}{2}\right)\right. \\
& \quad \left. - \cos\left(\frac{d_{12}\omega_-}{2}\right) \cos(2\eta) \sin(d_2\omega_-)\right) \sin(\xi) + \cos(\xi) \left(2 \cos\left(\frac{1}{2}(d_{12} - d_2)\omega_+\right) \sin\left(\frac{d_2\omega_+}{2}\right) \cos^2(\xi)\right. \\
& \quad \left. + \left(4 \cos\left(\frac{d_2\omega_-}{2}\right) \cos^2(\eta) - 2 \cos\left(\frac{d_2\omega_+}{2}\right) \cos(2\eta)\right) \sin\left(\frac{1}{2}(d_{12} - d_2)\omega_+\right)\right) \sin(\eta) \\
& \quad - \cos\left(\frac{d_{12}\omega_-}{2}\right) \cos(\eta) \sin(d_2\omega_-) \sin(4\xi) \cos^2(\eta) \\
& - 32 \cos\left(\frac{1}{2}(d_{12} + d_4)\omega_+\right) \cos(\xi) \sin\left(\frac{d_4\omega_-}{2}\right) \sin\left(\frac{d_{12}\omega_+}{2}\right) \sin^2\left(\frac{d_2\omega_+}{2}\right) \sin^3(\eta) \sin^3(\xi) \cos(\eta) \\
& \quad + 32 \cos(\xi) \sin\left(\frac{d_{12}\omega_-}{2}\right) \sin^2\left(\frac{d_2\omega_-}{2}\right) \sin\left(\frac{d_{12}\omega_+}{2}\right) \sin^3(\eta) \sin^3(\xi) \cos(\eta) \\
& \quad + 16 \cos\left(\frac{d_{12}\omega_-}{2}\right) \cos(\xi) \sin\left(\frac{d_{12}\omega_+}{2}\right) \sin(d_2\omega_-) \sin^3(\eta) \sin^3(\xi) \cos(\eta) \\
& + 32 \cos\left(\frac{d_4\omega_+}{2}\right) \cos(\xi) \sin\left(\frac{d_{12}\omega_+}{2}\right) \sin^2\left(\frac{d_2\omega_+}{2}\right) \sin\left(\frac{1}{2}(d_{12} + d_4)\omega_-\right) \sin^3(\eta) \sin^3(\xi) \cos(\eta) \\
& \quad - 16 \cos\left(\frac{d_{12}\omega_+}{2}\right) \cos\left(\frac{1}{2}(d_{12} + d_4)\omega_+\right) \cos(\xi) \sin\left(\frac{d_4\omega_-}{2}\right) \sin(d_2\omega_+) \sin^3(\eta) \sin^3(\xi) \cos(\eta) \\
& \quad + 16 \cos\left(\frac{d_{12}\omega_+}{2}\right) \cos\left(\frac{d_4\omega_+}{2}\right) \cos(\xi) \sin\left(\frac{1}{2}(d_{12} + d_4)\omega_-\right) \sin(d_2\omega_+) \sin^3(\eta) \sin^3(\xi) \cos(\eta) \\
& - 32 \cos\left(\frac{1}{2}(d_{12} + d_4)\omega_+\right) \cos^3(\xi) \sin\left(\frac{d_4\omega_-}{2}\right) \sin\left(\frac{d_{12}\omega_+}{2}\right) \sin^2\left(\frac{d_2\omega_+}{2}\right) \sin^3(\eta) \sin(\xi) \cos(\eta) \\
& \quad + 32 \cos^3(\xi) \sin\left(\frac{d_{12}\omega_-}{2}\right) \sin^2\left(\frac{d_2\omega_-}{2}\right) \sin\left(\frac{d_{12}\omega_+}{2}\right) \sin^3(\eta) \sin(\xi) \cos(\eta) \\
& \quad + 16 \cos\left(\frac{d_{12}\omega_-}{2}\right) \cos^3(\xi) \sin\left(\frac{d_{12}\omega_+}{2}\right) \sin(d_2\omega_-) \sin^3(\eta) \sin(\xi) \cos(\eta) \\
& + 32 \cos\left(\frac{d_4\omega_+}{2}\right) \cos^3(\xi) \sin\left(\frac{d_{12}\omega_+}{2}\right) \sin^2\left(\frac{d_2\omega_+}{2}\right) \sin\left(\frac{1}{2}(d_{12} + d_4)\omega_-\right) \sin^3(\eta) \sin(\xi) \cos(\eta) \\
& \quad - 16 \cos\left(\frac{d_{12}\omega_+}{2}\right) \cos\left(\frac{1}{2}(d_{12} + d_4)\omega_+\right) \cos^3(\xi) \sin\left(\frac{d_4\omega_-}{2}\right) \sin(d_2\omega_+) \sin^3(\eta) \sin(\xi) \cos(\eta) \\
& \quad + 16 \cos\left(\frac{d_{12}\omega_+}{2}\right) \cos\left(\frac{d_4\omega_+}{2}\right) \cos^3(\xi) \sin\left(\frac{1}{2}(d_{12} + d_4)\omega_-\right) \sin(d_2\omega_+) \sin^3(\eta) \sin(\xi) \cos(\eta) \\
& + 32 \cos^2\left(\frac{d_2\omega_+}{2}\right) \cos^2(\xi) \sin^2\left(\frac{d_{12}\omega_+}{2}\right) \sin^6(\eta) - 8 \cos^2(\xi) \sin(d_{12}\omega_+) \sin(d_2\omega_+) \sin^6(\eta) \\
& \quad + 32 \cos^4(\xi) \sin^2\left(\frac{d_{12}\omega_+}{2}\right) \sin^2\left(\frac{d_2\omega_+}{2}\right) \sin^4(\eta) + 8 \cos^4(\xi) \sin(d_{12}\omega_+) \sin(d_2\omega_+) \sin^4(\eta) \\
& \quad - 8k \cos\left(\frac{1}{2}(d_{12} + d_4)\omega_+\right) \sin\left(\frac{d_{12}\omega_-}{2}\right) \sin^2\left(\frac{d_2\omega_-}{2}\right) \sin\left(\frac{d_4\omega_-}{2}\right) \sin^4(\xi)
\end{aligned}$$

$$\begin{aligned}
& -4k \cos\left(\frac{d_{12}\omega_-}{2}\right) \cos\left(\frac{1}{2}(d_{12} + d_4)\omega_+\right) \sin(d_2\omega_-) \sin\left(\frac{d_4\omega_-}{2}\right) \sin^4(\xi) \\
& + 8k \cos\left(\frac{d_4\omega_+}{2}\right) \sin\left(\frac{d_{12}\omega_-}{2}\right) \sin^2\left(\frac{d_2\omega_-}{2}\right) \sin\left(\frac{1}{2}(d_{12} + d_4)\omega_-\right) \sin^4(\xi) \\
& + 4k \cos\left(\frac{d_{12}\omega_-}{2}\right) \cos\left(\frac{d_4\omega_+}{2}\right) \sin(d_2\omega_-) \sin\left(\frac{1}{2}(d_{12} + d_4)\omega_-\right) \sin^4(\xi) \\
& - 8k \cos\left(\frac{1}{2}(d_{12} + d_4)\omega_+\right) \cos^2(\xi) \sin\left(\frac{d_{12}\omega_-}{2}\right) \sin^2\left(\frac{d_2\omega_-}{2}\right) \sin\left(\frac{d_4\omega_-}{2}\right) \sin^2(\xi) \\
& - 8k \cos^2\left(\frac{d_2\omega_-}{2}\right) \cos\left(\frac{1}{2}(d_{12} + d_4)\omega_+\right) \cos(2\eta) \sin\left(\frac{d_{12}\omega_-}{2}\right) \sin\left(\frac{d_4\omega_-}{2}\right) \sin^2(\xi) \\
& + 8k \cos\left(\frac{d_4\omega_+}{2}\right) \cos^2(\xi) \sin\left(\frac{d_{12}\omega_-}{2}\right) \sin^2\left(\frac{d_2\omega_-}{2}\right) \sin\left(\frac{1}{2}(d_{12} + d_4)\omega_-\right) \sin^2(\xi) \\
& + 8k \cos^2\left(\frac{d_2\omega_-}{2}\right) \cos\left(\frac{d_4\omega_+}{2}\right) \cos(2\eta) \sin\left(\frac{d_{12}\omega_-}{2}\right) \sin\left(\frac{1}{2}(d_{12} + d_4)\omega_-\right) \sin^2(\xi) \\
& + \left(4 \sin\left(\frac{d_2\omega_+}{2}\right) \left(\sin\left(\frac{d_2\omega_+}{2}\right) + \sin\left(d_{12}\omega_+ - \frac{d_2\omega_+}{2}\right)\right) \sin^4(\eta) \right. \\
& + \sin(d_2\omega_-) \left(2 \sin(d_{12}\omega_-) \cos^4(\eta) + k \cos\left(\frac{d_{12}\omega_-}{2}\right) \left(\cos\left(\frac{d_4\omega_+}{2}\right) \sin\left(\frac{1}{2}(d_{12} + d_4)\omega_-\right) \right. \right. \\
& \left. \left. - \cos\left(\frac{1}{2}(d_{12} + d_4)\omega_+\right) \sin\left(\frac{d_4\omega_-}{2}\right)\right)\right) \sin^2(2\xi) + \left(-16 \cos(\eta) \cos(2\eta) \sin\left(\frac{d_{12}\omega_+}{2}\right) \sin(\eta) \right. \\
& \left. \left(\sin\left(\frac{d_{12}\omega_-}{2}\right) \cos^2(\eta) + \left(\cos\left(\frac{d_4\omega_+}{2}\right) \sin\left(\frac{1}{2}(d_{12} + d_4)\omega_-\right) \right. \right. \right. \\
& \left. \left. - \cos\left(\frac{1}{2}(d_{12} + d_4)\omega_+\right) \sin\left(\frac{d_4\omega_-}{2}\right)\right) \sin^2(\eta) \right) \cos^2\left(\frac{d_2\omega_+}{2}\right) \\
& + 4 \sin\left(\frac{d_{12}\omega_+}{2}\right) \left((4 - 2k) \cos\left(\frac{d_2\omega_-}{2}\right) \sin\left(\frac{d_{12}\omega_-}{2}\right) \sin(2\eta) \right. \\
& \left. - 8 \cos\left(\frac{d_{12}\omega_-}{2}\right) \cos(\eta) \sin\left(\frac{d_2\omega_-}{2}\right) \sin^5(\eta) \right) \cos\left(\frac{d_2\omega_+}{2}\right) \\
& + 4 \cos\left(\frac{d_2\omega_-}{2}\right) \left(2(\cos(\eta) + \cos(3\eta)) \sin\left(\frac{d_{12}\omega_+}{2}\right) \sin\left(\frac{1}{2}(d_{12} - d_2)\omega_-\right) \sin^3(\eta) \right. \\
& \left. + k \left(\cos\left(\frac{d_4\omega_+}{2}\right) \sin\left(\frac{1}{2}(d_{12} + d_4)\omega_-\right) - \cos\left(\frac{1}{2}(d_{12} + d_4)\omega_+\right) \right. \right. \\
& \left. \left. \sin\left(\frac{d_4\omega_-}{2}\right) \right) \sin\left(\frac{1}{2}(d_{12} - d_2)\omega_+\right) \sin(2\eta) + \cos\left(\frac{d_{12}\omega_+}{2}\right) \sin(d_2\omega_+) \left(8 \sin\left(\frac{d_{12}\omega_-}{2}\right) \right. \right. \\
& \left. \left. \sin(\eta) \cos^5(\eta) - 8 \left(\sin\left(\frac{d_{12}\omega_-}{2}\right) + \cos\left(\frac{1}{2}(d_{12} + d_4)\omega_+\right) \sin\left(\frac{d_4\omega_-}{2}\right)\right) \sin^3(\eta) \cos^3(\eta) \right. \right. \\
& \left. \left. + 8 \left(\cos\left(\frac{1}{2}(d_{12} + d_4)\omega_+\right) \sin\left(\frac{d_4\omega_-}{2}\right) - \cos\left(\frac{d_4\omega_+}{2}\right) \sin\left(\frac{1}{2}(d_{12} + d_4)\omega_-\right)\right) \sin^5(\eta) \cos(\eta) \right. \right. \\
& \left. \left. + \cos\left(\frac{d_4\omega_+}{2}\right) \sin\left(\frac{1}{2}(d_{12} + d_4)\omega_-\right) \sin^3(2\eta)\right) \sin(2\xi) + 8 \cos\left(\frac{d_4\omega_-}{2}\right) \sin\left(\frac{1}{2}(d_{12} + d_4)\omega_+\right) \right. \\
& \left. \left(2 \sin\left(\frac{1}{2}(d_{12} - d_2)\omega_-\right) \sin(\eta) \left(2 \cos\left(\frac{d_2\omega_+}{2}\right) \sin^2(\eta) + \cos\left(\frac{d_2\omega_-}{2}\right) \cos(2\eta)\right) \sin(2\xi) \cos^3(\eta) \right. \right. \\
& \left. \left. + \cos(\xi) \left(4 \cos\left(\frac{1}{2}(d_{12} - d_2)\omega_-\right) \sin\left(\frac{d_2\omega_-}{2}\right) \sin(\eta) \sin(\xi) \cos^3(\eta) \right. \right. \right. \\
& \left. \left. + k \cos\left(\frac{1}{2}(d_{12} - d_2)\omega_+\right) \cos(\xi) \sin\left(\frac{d_2\omega_+}{2}\right) \right. \right. \\
& \left. \left. + \cos(\xi) \sin\left(\frac{1}{2}(d_{12} - d_2)\omega_+\right) \left(8 \cos\left(\frac{d_2\omega_-}{2}\right) \cos^4(\eta) \sin^2(\eta) - k \cos\left(\frac{d_2\omega_+}{2}\right) \cos(2\eta)\right)\right)\right).
\end{aligned}$$

While evolution following from nuclear coherence proportional to I_y leads to rather a compact expression, the terms proportional to I_x result into a rather lengthy expression. Still, similar to the previous equations there is no detectable magnetization in x -direction. The signals in y -direction oscillate again with the nuclear frequencies, their sum and their difference for the time intervals d_2 , d_{12} and their combination. Furthermore, some terms depending on the mixing time T_{mix} remain. However, this effect is much weaker and for long enough mixing times the nuclear coher-

ences propagated here will decay. This is also seen experimentally as described above (Figure C.1).

As aforementioned, the major contribution to nuclear modulation in RIDME usually comes from matrix nuclei with $\omega_\alpha \sim \omega_\beta \sim \omega_I$, $\omega_+ \sim 2\omega_I$, $\omega_- \sim 0$. Integration over a time $2\pi/\omega_I$ will then fully suppress the corresponding modulation terms. Such an integration of all the detectable terms at the time point of the RIDME echo (refocused virtual echo) over both d_1 and d_2 for one period of nuclear modulation gives the reduced modulation formula:

$$\begin{aligned}
 V_{\text{RE}} = -\langle S_y \rangle = & \frac{1}{32}(2-k) \left\{ 8 - 6k + k \left(\cos(d_{12}\omega_\alpha) + \cos(d_{12}\omega_\beta) \right) \right. \\
 & + \left[\cos^2(\eta) \cos\left(\frac{d_{12}\omega_-}{2}\right) - \sin^2(\eta) \cos\left(\frac{d_{12}\omega_+}{2}\right) \right] \cdot \left[\cos\left(\frac{d_{12}\omega_-}{2} + T_{\text{mix}}\omega_\alpha\right) \right. \\
 & \left. \left. - \cos\left(\frac{d_{12}\omega_+}{2} + T_{\text{mix}}\omega_\alpha\right) + \cos\left(T_{\text{mix}}\omega_\beta - \frac{d_{12}\omega_-}{2}\right) - \cos\left(\frac{d_{12}\omega_+}{2} + T_{\text{mix}}\omega_\beta\right) \right] \right\}. \quad (\text{C.16})
 \end{aligned}$$

Hereby, we assume excitation of an inhomogeneously broad line, so that the terms $\cos(\tau\Omega_S)^2$ and $\sin(\tau\Omega_S)^2$ approximate 1/2. If we further assume that all coherences evolving during T_{mix} are decayed we obtain for the RIDME echo (refocused virtual echo)

$$V_{\text{RE}} = \frac{1}{32}(2-k)(8 - 6k + k[\cos(d_{12}\omega_\alpha) + \cos(d_{12}\omega_\beta)]). \quad (\text{C.17})$$

C.3. Experimental settings

The synthesis of Gd-PyMTA as well as the Gd-PyMTA ruler (3.4 nm) has been described in Qi, et al.^{94;101} and for Mn-DOTA, Mn-PyMTA and the Mn-PyMTA ruler (4.7 nm) in Keller et al.⁹³. The compounds were dissolved in a 1:1 D₂O:glycerol-d₈ (v:v) solution at concentrations 100 μM for the Gd-PyMTA mono-complex and for the Gd-PyMTA ruler in X band as well as 300 μM for the Gd-PyMTA ruler in Q band. Mn(II) containing samples were diluted to 100 μM . The solutions were filled into 3 mm (Q band), 4 mm (Gd-PyMTA ruler, X band) and 5 mm (Gd-PyMTA mono-complex, X band) outer diameter quartz sample tubes and subsequently shock-frozen by immersion into liquid nitrogen. Q-band EPR experiments were performed on a Bruker Elexsys E580 Q-band spectrometer equipped with a home-built cavity operating at about 34.5 GHz.⁹⁷ X-band data were recorded on a Bruker 380 spectrometer updated to an Elexsys system with a 5 mm dielectric resonator (Bruker). The temperature was adjusted to 20 K using a helium flow cryostat.

RIDME traces were acquired at the central $| -1/2 \rangle \leftrightarrow | 1/2 \rangle$ transition of the Gd-spectrum as shown in Figure 6.1 (Chapter 6). Figure 6.1(b) (Chapter 6) displays the RIDME pulse sequence. $\pi/2$ -pulses were set to 12 ns and π -pulses to 24 ns duration. If not stated otherwise, initial interpulse delays were set to $d_1 = 400$ ns and $d_{12} = -120$ ns, while d_2 was adjusted for each sample. d_{12} was incremented in steps of 8 ns. For simultaneous d_1 and d_2 averaging, we incremented both delay times at each step with identical increment $\Delta d_1 = \Delta d_2$. For averaging over only d_1 or d_2 , the corresponding delay time was incremented, and the other one was kept constant. The resulting traces were summed over a half or over a full period of the deuterium ESEEM oscillation. If not stated otherwise, the mixing time T_{mix} was set to 16 μs for the Gd-PyMTA ruler and 24 μs for the Gd-PyMTA mono-complex. An eight-step phase cycle was applied.⁶⁷ The

analysis of the RIDME traces was performed using the OvertoneAnalysis software¹¹⁴ with the dipolar overtone coefficients $P_2 = 0.40$, $P_3 = 0.09$ for the Gd-PyMTA ruler and $P_2 = P_3 = 0$ for the Mn-PyMTA ruler.

Three-pulse ESEEM data were detected as described in Section 2.5.3 using a $\pi/2 - \tau - \pi/2 - T - \pi/2 - \tau - \text{echo}$ sequence with a 4-step phase-cycle and different τ -values. The $\pi/2$ pulses had a length of 12 ns. The interpulse delay T had a starting value of 172 ns and was incremented in steps of 8 ns. For Mn-PyMTA τ was incremented starting from 104 ns in 5 steps of 20 ns and for Mn-DOTA τ was incremented starting from 104 ns in 10 steps of 12 ns to avoid blind spots. The three-pulse ESEEM experiments were performed at the maximum of the Mn(II) spectrum (3rd hyperfine line for Mn-DOTA and 4th hyperfine line for Mn-PyMTA). The traces for the different τ values were averaged and subsequently analysed with a home-written MATLAB program.³²⁰ The background decay was subtracted by division of a higher-order polynomial fit as given in the caption of Figure C.2 to the primary data. The spectrum was obtained after apodization with a Hamming window, zero filling, and finally computing the magnitude spectrum after Fourier transform.

C.4. Three-pulse ESEEM measurements for Mn-PyMTA and Mn-DOTA

Figure C.2 shows the three-pulse ESEEM data for the Mn-PyMTA as well as the Mn-DOTA mono-complex. Besides, the deuterium peak at ~ 7.8 MHz, several other low frequencies can be identified. In particular, the frequency at ~ 2.5 MHz observed in the RIDME background measurements is also present in the three-pulse ESEEM data.

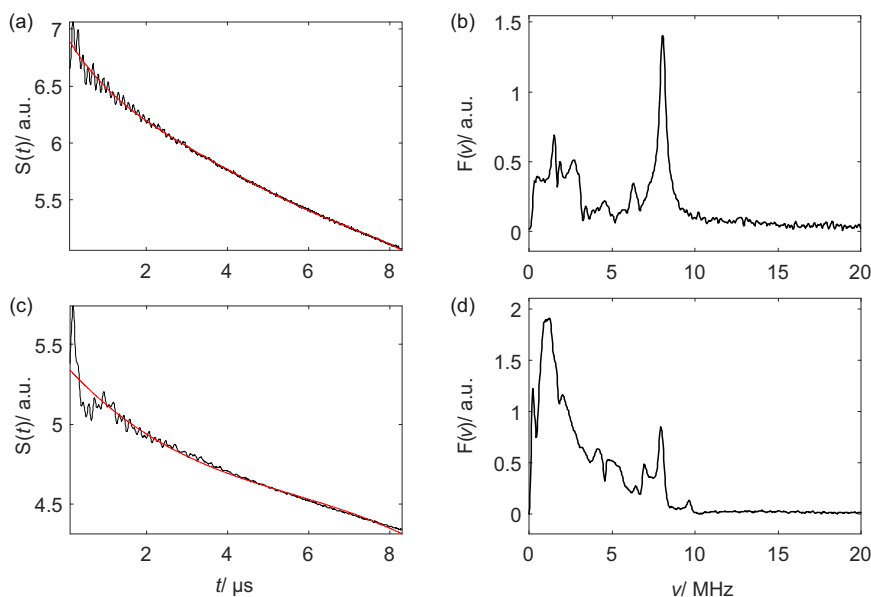


Figure C.2. Q-band three-pulse ESEEM experiments at 20 K. (a, b) Mn-PyMTA detected at the 4th hyperfine line, (c, d) Mn-DOTA detected at the 3rd hyperfine line. (a, c) Raw data (black) and corresponding background fit (red). Background function were fitted with (a) 5th and (c) 3rd order polynomial background correction. (b, d) Fourier transform.

C.5. Interference of nuclear and dipolar frequencies

Figure C.3 shows the interference of dipole-dipole coupling and ^2D nuclear frequency at two different mixing times for the Gd-PyMTA ruler in X band. For a short mixing time ($T_{\text{mix}} = 2 \mu\text{s}$) the dipolar modulation depth is weak and thus the resulting trace is dominated by the nuclear frequency with period of ~ 440 ns. For a longer mixing time ($T_{\text{mix}} = 36 \mu\text{s}$) the contribution of dipolar modulation depth is enhanced. Because the zero-time of the RIDME experiment was set to 100 ns, which corresponds to a minimum of the nuclear frequency, destructive interference is observed for both modulations.

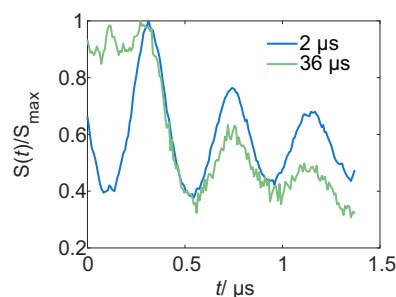


Figure C.3. X-band RIDME data for Gd-PyMTA ruler at 20 K. $T_{\text{mix}} = 2 \mu\text{s}$ (blue) and $36 \mu\text{s}$ (green).

C.6. Extraction of harmonic overtones in the presence of ESEEM contributions

Figure C.4 shows the analysis of a simulated time trace that contain contributions from ESEEM (2.3 MHz) as well as a 3.4 nm Gaussian distance distribution and its first ($2\omega_{\text{dd}}$, ~ 2.7 nm) and second ($3\omega_{\text{dd}}$, ~ 2.35 nm) harmonic overtone. It is observed that if $P_2 = P_3 = 0$ the actual distance peak is observed besides a broad, strong peak at about the ^2D ESEEM/ 1st harmonic overtone and a small side peak corresponding to the 2nd harmonic overtone. If the coefficients are matched, the peak intensity of the actual mean distance increases, but is also shifted away from the 3.4 nm mean value as part of the ^2D ESEEM is ‘corrected’ with the higher overtones. The ^2D ESEEM peak can be fully suppressed by an overcorrection of the harmonic overtones. However, this leads to a strong shift in the actual mean distance as the ESEEM peaks occur at slightly larger distance than the 1st harmonic of the dipolar frequency. The situation becomes yet more complicated if not only ESEEM from deuterons in X band ($\sim 2.3\text{MHz}$), but also other ESEEM frequencies are present (see Figure C.5). Peaks are shifted and full suppression cannot be obtained.

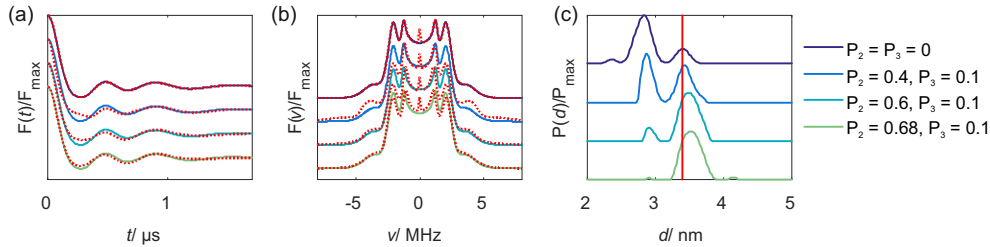


Figure C.4. Simulated data for 0.5 contribution of Gaussian distance distribution with mean distance of 3.4 nm including harmonic overtones with the fractions $P_2 = 0.4$, $P_3 = 0.1$ (representing the dipole-dipole coupling) and 0.5 contribution of Gaussian distance distribution with mean distance of 2.8 nm (representing an ESEEM contribution). Analysis of time and frequency domain data for different sets of harmonic overtones as colour coded. (a) Form factor in time domain and (b) in frequency domain. Red, dashed lines show corresponding fits. (c) Resulting distance distribution. The red vertical line marks 3.4 nm.

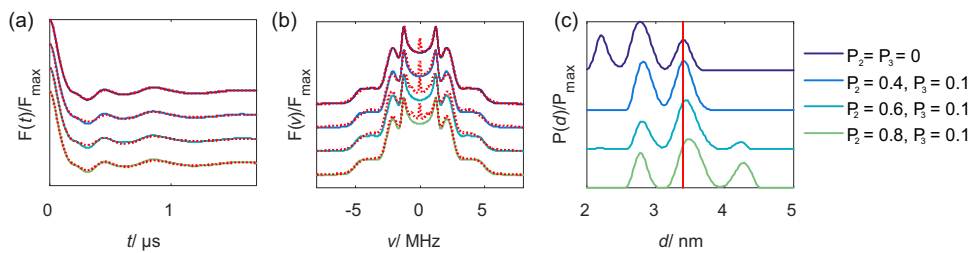


Figure C.5. Simulated data for 0.5 contribution of Gaussian distance distribution with mean distance of 3.4 nm including harmonic overtones with the fractions $P_2 = 0.4$, $P_3 = 0.1$ (representing the dipole-dipole coupling) and 0.3 contribution of Gaussian distance distribution with mean distance of 2.8 nm (2.3 MHz) as well as 2.2 nm (4.6 MHz) (representing ESEEM contributions). Analysis of time and frequency domain data for different sets of harmonic overtones as colour coded. (a) Form factor in time domain and (b) in frequency domain. Red, dashed lines show corresponding fits. (c) Resulting distance distribution. The red vertical line marks 3.4 nm.

D

Supplementary Information to Chapter 7

D.1. Lineshape analysis of Cu-PyMTA

Figure D.1 shows the X-band CW spectra of the Cu-PyMTA mono-complex and the Cu-PyMTA ruler at 140 K. As both spectra overlay, no significant change is expected in the spin density distribution upon ruler assembly and the validity of the point-dipole approximation is assumed for distance analysis. A fit of the EPR lineshape by using the software package *EasySpin* allows for extracting the spin Hamiltonian parameters. For Cu-PyMTA using axial g - and A -tensors caused deviations between lineshape fit and experimental data around 320 mT, which could only be reduced by assuming rhombic g - and A -tensors.

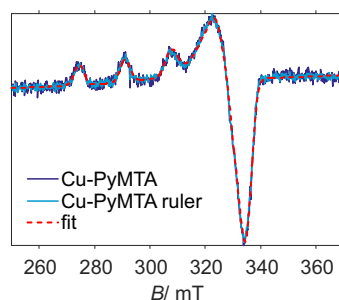


Figure D.1. Low temperature (140 K) X-band CW spectra of the Cu-PyMTA mono-complex (purple) and the [Cu-PyMTA]-[Cu-PyMTA] ruler (blue line). The corresponding lineshape fit is shown in red.

Note that the x/y region is not resolved in the broad EPR spectra and it is therefore challenging to determine such values unambiguously. The relatively large A_y was tested for significance by keeping it fixed at different values (30, 50, 60, 65, 70, 80, 90 MHz) and varying all other parameters as well as varying all fit parameters. The fit quality started to increase from 65 MHz onwards and decreased from 90 MHz onwards. The resulting fit parameters for A_y fixed between 65 and 90 MHz and varying all other parameters were used to extract the mean and standard deviation as uncertainty for the lineshape parameters of Cu-PyMTA: $g_x = 2.048 \pm 0.001$, $g_y = 2.078 \pm 0.001$, $g_z = 2.253 \pm 0.001$ with strains $g_x\text{strain} = 0.025 \pm 0.001$, $g_y\text{strain} = 0.038 \pm 0.001$, $g_z\text{strain} = 0.035 \pm 0$ and $A_x = 24 \pm 6$ MHz, $A_y = 76 \pm 10$ MHz, $A_z = 510 \pm 5$ MHz with strains $A_x\text{strain} = 4 \pm 4$ MHz, $A_y\text{strain} = 9 \pm 4$ MHz, $A_z\text{strain} = 25 \pm 1$ MHz. The necessity of introducing strains for g and A indicates that a distribution of slightly different conformations exist in the frozen glassy solutions.

D.2. Longitudinal relaxation across the Cu-PyMTA ruler spectrum

Figure D.2 presents the differences in longitudinal relaxation across the Cu(II) spectrum. Even though it varies somewhat across the spectrum, the form factor shape remained rather stable for mixing times in the range of $T_1/10$ to $2T_1$.

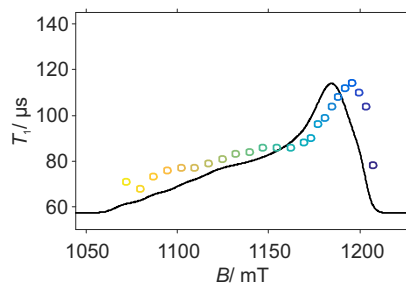


Figure D.2. Q-band longitudinal relaxation times in dependence of the detection positions at 20 K and in Q band. The relaxation times are extracted as fit parameter from stretched exponential fits of the form $c \cdot \exp(-(t/T_1)^x)$

D.3. Influence of pulse parameters on RIDME data

Figure D.3(c) shows the accelerated background decay in RIDME compared to DEER experiments. However, the RIDME background is unaffected by changes in the observer pulse settings (Figure D.3(a, b)), while slight differences in the modulation depth can be noticed.

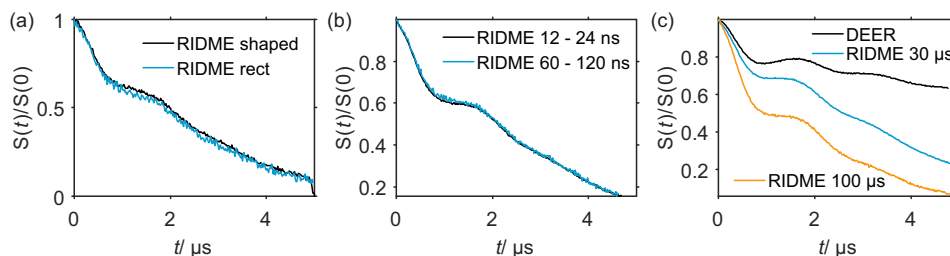


Figure D.3. Comparison of the background decay in Q band at 20 K with observer pulses centered around B_{\max} . (a) RIDME with shaped (black) and monochromatic rectangular (blue) observer pulses, $T_{\text{mix}} = 75 \mu\text{s}$. (b) RIDME with $\pi/2 - \pi = 12 - 24 \text{ ns}$ (black) and $\pi/2 - \pi = 60 - 120 \text{ ns}$ (blue) rectangular observer pulses, $T_{\text{mix}} = 50 \mu\text{s}$. (c) DEER (black) and RIDME with $T_{\text{mix}} = 30 \mu\text{s}$ (blue) $T_{\text{mix}} = 100 \mu\text{s}$ (orange). The DEER trace corresponds to a sum of low-obs and high-obs setup as in Figure 7.11(a-d).

For monochromatic pulses of different length, shown in Figure D.4, no significant changes are observed in the RIDME form factor shapes and consequently in the resulting distance distribution at a given detection position. Note that for this comparison in all cases the g -value of the free electron g_e was used in the data analysis.

D.4. Additional analysis with respect to orientation selection

Figure D.5(a-c) shows the comparison of the resulting, apparent distance distributions corresponding to the different DEER setups shown in Figure 7.6. Figure D.5(d-f) shows the difference between field averaging and detection at the maximum of the Cu(II) spectrum for DEER and RIDME. It can be observed that the relative strength of the dipolar frequencies slightly varies.

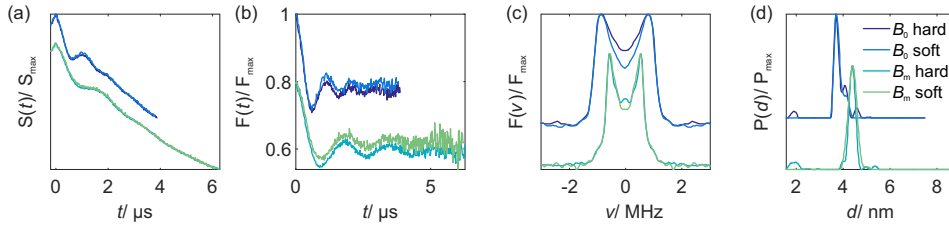


Figure D.4. Comparison of the performance of hard (12-24 ns) and soft detection pulses (60-120 ns) in the RIDME experiment at 20 K, Q band, $T_{\text{mix}} = 50 \mu\text{s}$. (a) Background decay, (b) time-domain and (c) frequency-domain form factors, (d) distance distributions.

The effect is stronger for DEER data, where orientation selection is influenced by two frequency bands. This induces a slight shift of mean distances in the apparent distributions for the different setups. Note that for this comparison in all cases the g -value g_e of the free electron was used.

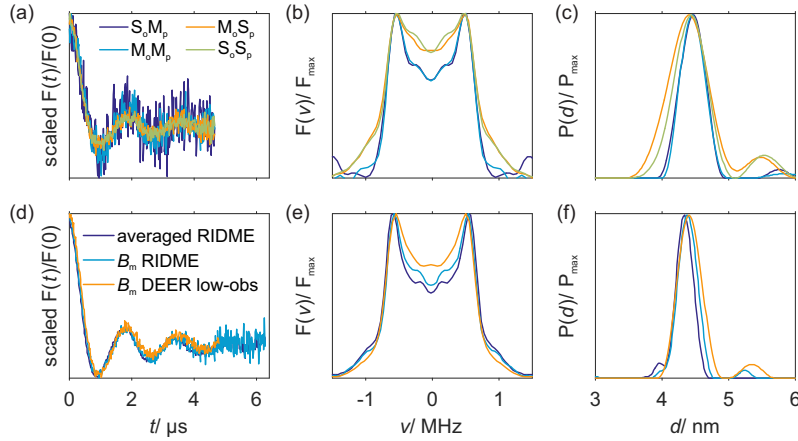


Figure D.5. (a-c) Comparison of the different DEER setups shown in Figure 7.6 with respect to the effect of the differences in the dipolar spectra on the extracted distance distribution. (d-f) Comparison of field-averaged RIDME data (black) and RIDME (blue) and DEER (green) data detected at maximum field B_m in Q band at 20 K, $T_{\text{mix}} = 30 \mu\text{s}$. In the DEER data the pump pulse was placed at the low-field side of the observer pulses. (a, d) Scaled form factors in time domain, (b, e) in frequency domain, (c, f) distance distribution.

Figure D.6 illustrates the detection positions of the DEER and RIDME measurements presented in Figure 7.11 (Chapter 7) and in Figure D.7. The field positions were equally spaced by 15 mT: $B_0 = B_{\max} + 15$ mT, $B_1 = B_{\max} - 15$ mT, $B_2 = B_{\max} - 2 \cdot 15$ mT, ... $B_7 = B_{\max} - 7 \cdot 15$ mT. For DEER two different setups were used: (i) *HighObs*: the pump pulse was set to lower frequency, i.e. higher on a field axis, than the observer frequency ($\nu_{\text{obs}} > \nu_{\text{pump}}$); (ii) *LowObs*: the relative position of the pump band was at higher frequency, i.e. lower on a field axis, than the observer ($\nu_{\text{obs}} < \nu_{\text{pump}}$).

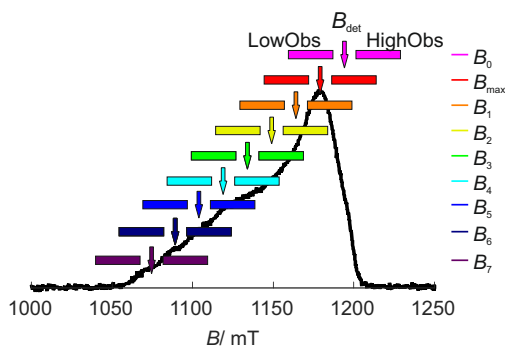


Figure D.6. Detection positions for field-stepped Q-band DEER and RIDME measurements. The arrows indicate the field B_{det} at which the observer frequency ν_{obs} was positioned. The pump bands are indicated as boxes, labelled *HighObs* for the setup with $\nu_{\text{obs}} > \nu_{\text{pump}}$ and *LowObs* for the setup with $\nu_{\text{obs}} < \nu_{\text{pump}}$.

Figure D.7 displays the comparison of RIDME and DEER data with differently positioned pump pulses for a large set of detection positions. Some deviations can be observed for detection above and just below the maximum. In the parallel region of the Cu(II) spectrum no significant changes can be observed. Note that for this comparison of different detection positions in all cases the g -value of the free electron g_e was used in Tikhonov regularization.

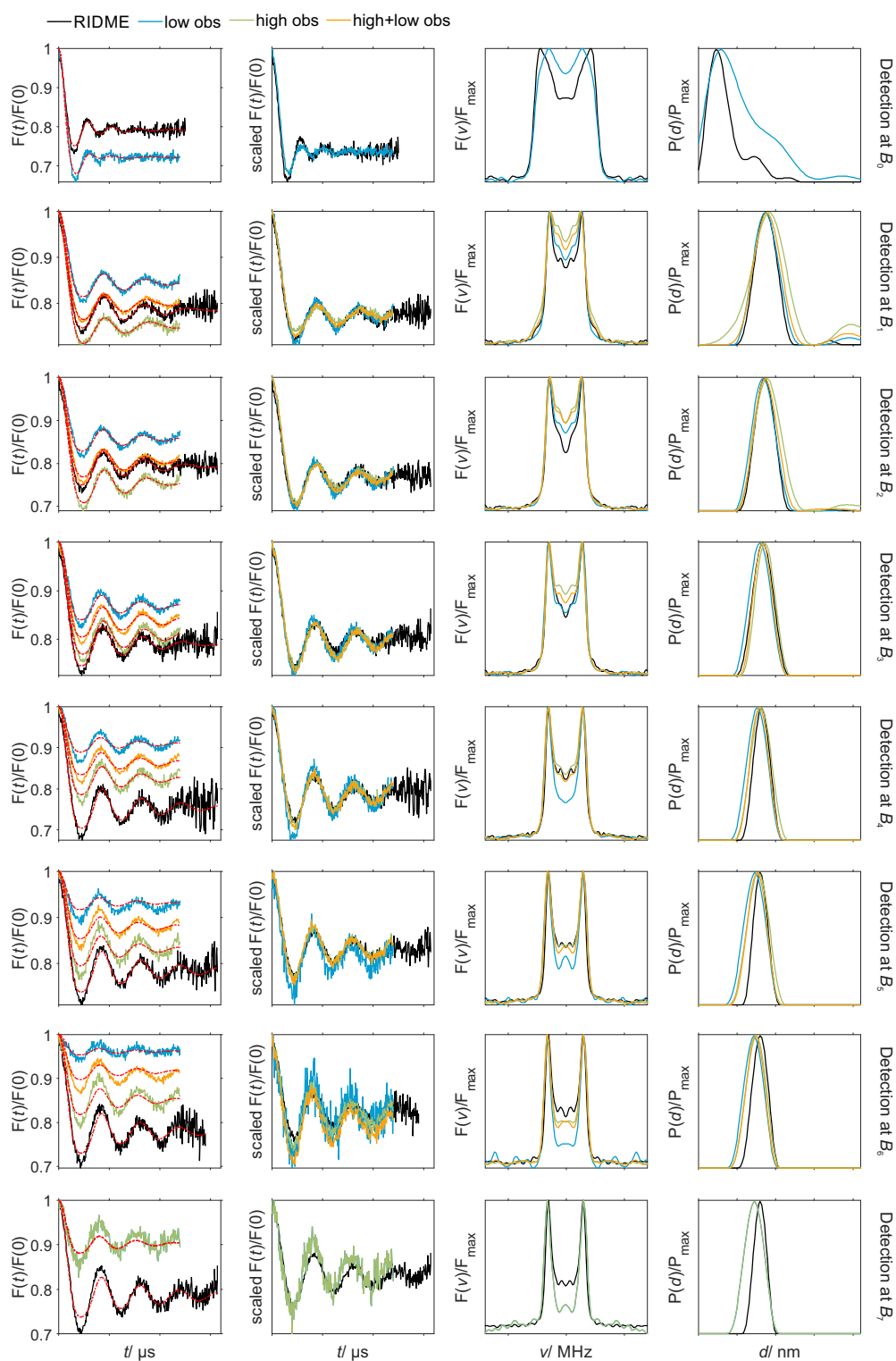


Figure D.7. Set of DEER (coloured) and RIDME (black) data at eight different field positions. B_0 indicates $B_{\max} + 15$ mT, while B_1 to B_7 correspond to $B_{\max} - n \cdot 15$ mT with $n = 1$ to 7 . From left to right: Form factor $F(t)$ with DeerAnalysis fit (red dashed lines), scaled form factor, dipolar spectrum $F(\nu)$, resulting distance distribution $P(d)$. For data acquired at B_{\max} see Figure 7.11(a-d) in Chapter 7.

D.5. Sensitivity in RIDME and DEER experiments

Table D.1 and D.2 give sensitivity estimates for the modified Bruker Elexys E580 spectrometer and the homebuilt AWG spectrometer, respectively. Note that deviations in modulation depth for RIDME measurements at the same mixing time, but in different sessions may be caused by somewhat different longitudinal relaxation, potentially caused by variations in glass quality, as well as contribution from echo-crossing artefacts¹¹⁴ at the beginning of the RIDME trace.

Setup	λ (%)	$\eta/10^3$	$n_{l,FT}/10^{-6}$	$n_{l,M}/10^{-4}$
RIDME T_{mix} 25 μs loop-gap	10	8	130	16
RIDME T_{mix} 50 μs loop-gap	16	11	94	17
RIDME T_{mix} 75 μs loop-gap	21	12	86	25
RIDME T_{mix} 150 μs loop-gap	32	8	115	44
DEER M_0S_p HS6 100 ns loop-gap	11	24	42	5
DEER M_0S_p HS6 250 ns loop-gap	12	20	51	5
Data in Figure 7.7				
RIDME T_{mix} 25 μs TE ₁₀₂ box	11	22	46	6
RIDME T_{mix} 50 μs TE ₁₀₂ box	16	20	54	9
RIDME T_{mix} 75 μs TE ₁₀₂ box	20	24	49	10
RIDME T_{mix} 100 μs TE ₁₀₂ box	24	25	51	10
RIDME T_{mix} 150 μs TE ₁₀₂ box	33	23	44	16
RIDME T_{mix} 300 μs TE ₁₀₂ box	46	14	73	41
RIDME T_{mix} 400 μs TE ₁₀₂ box	49	9	112	61
DEER M_0S_p HS6 100 ns TE ₁₀₂ box	3	9	1	2
DEER M_0S_p HS6 250 ns TE ₁₀₂ box	3	13	1	2

Table D.1. Sensitivity estimate for DEER and RIDME traces, performed at the commercial Q band spectrometer. Resonators: loop-gap resonator for UWB DEER measurements, loop-gap resonator or TE₁₀₂ box resonator for RIDME measurements. RIDME data for 3 mm resonator are shown in Chapter 7. Other data are not shown. Modulation depth λ , noise $n_{l,FT}$ as standard deviation of the dipolar spectra in the outer halves and sensitivity estimate $\eta = 1/n_{l,FT}$. The noise level $n_{l,M}$ is the standard deviation of the dipolar time domain trace and its moving average of 15 data points.

Setup	λ (%)	$\eta/10^2$	$n_{l,FT}/10^{-4}$	$n_{l,M}/10^{-4}$
Data in Figure 7.5(a)				
DEER M_oM_p 7 ns	6	10	10	44
DEER M_oS_p HS1 250 ns 800 MHz	17	41	2	35
DEER M_oS_p HS6 100 ns 800 MHz	20	55	2	44
DEER M_oS_p HS6 250 ns 1200 MHz	27	74	1	37
Data in Figure 7.5(c)				
DEER M_oM_p 6.5 ns X band	14	7	14	177
DEER M_oS_p 100 ns X band	24	21	5	132
DEER M_oS_p 250 ns X band	36	43	2	60
DEER M_oS_p 1.5 GHz X band	44	54	2	77
Data in Figure 7.6(a)				
DEER M_oM_p HS6 900 MHz	4	4	25	53
DEER S_oM_p HS6 900 MHz	5	3	35	73
DEER M_oS_p HS6 900 MHz	28	20	5	115
DEER S_oS_p HS6 900 MHz	35	24	4	129
Data in Figure D.11 (M_oS_p as in Figure 7.5(a))				
DEER S_oS_p HS6 250 ns 1.2 GHz	28	32	3	87
Data in Figure D.12				
DEER M_oM_p HS6 900 MHz	4	8	13	32
DEER S_oM_p HS6 900 MHz	5	2	65	219
DEER M_oS_p HS6 900 MHz	22	38	3	56
DEER S_oS_p HS6 900 MHz	29	10	10	293
RIDME T_{mix} 10 μ s loop-gap	9	10	10	80
RIDME T_{mix} 25 μ s loop-gap	12	11	9	114
RIDME T_{mix} 50 μ s loop-gap	18	13	8	171
RIDME T_{mix} 75 μ s loop-gap	22	10	10	239
RIDME T_{mix} 150 μ s loop-gap	39	12	8	298
RIDME T_{mix} 10 μ s TE ₁₀₂ box	9	21	5	42
RIDME T_{mix} 25 μ s TE ₁₀₂ box	13	23	4	69
RIDME T_{mix} 50 μ s TE ₁₀₂ box	19	24	4	94
RIDME T_{mix} 75 μ s TE ₁₀₂ box	25	30	3	104
RIDME T_{mix} 100 μ s TE ₁₀₂ box	28	26	4	140
RIDME T_{mix} 150 μ s TE ₁₀₂ box	35	22	5	198
RIDME T_{mix} 300 μ s TE ₁₀₂ box	47	11	9	435

Table D.2. Sensitivity estimate for all DEER and RIDME traces recorded on the home-built AWG spectrometer. Resonators: loop-gap resonator for UWB DEER measurements, loop-gap resonator or TE₁₀₂ box resonator for RIDME measurements. Q band unless otherwise specified. Data shown in Figures as indicated. Other data are not shown. Modulation depth λ , noise $n_{l,FT}$ as standard deviation of the dipolar spectra in the outer halves and sensitivity estimate $\eta = 1/n_{l,FT}$. The noise level $n_{l,M}$ is the standard deviation of the dipolar time domain trace and its moving average of 15 data points, provided as reference for the discussion to Figure 7.5.

D.6. Echoes from shaped pulses for the Cu-PyMTA mono-complex

Figure D.8 shows echo transients recorded for two-pulse echoes with chirp pulses of different bandwidth Δf for the Cu-PyMTA mono-complex. Similar to the results for the Cu-PyMTA ruler shown in Figure 7.3 in Chapter 7, inversion is largely uniform over the required bandwidth, yet does not reach more than about 70%. In this system, the dipolar coupling that is present in the Cu-PyMTA ruler is absent. The dipolar coupling thus does not appear to be the reason for the limited inversion efficiency.

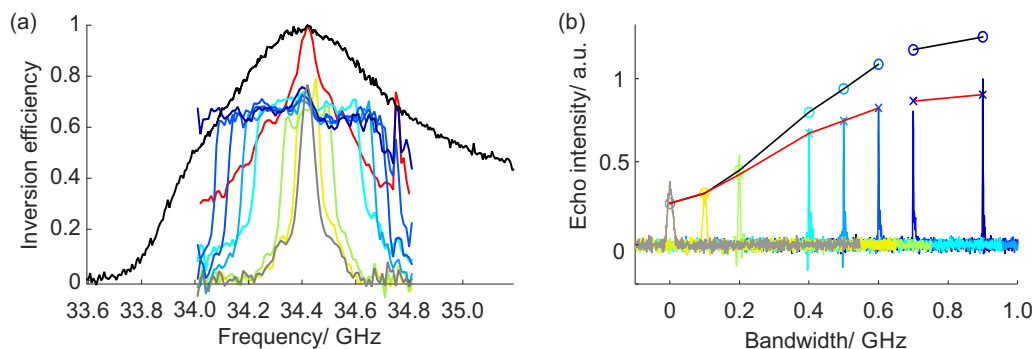


Figure D.8. Measurements with shaped pulses on the Cu-PyMTA mono-complex in Q band. (a) Inversion efficiencies $E(f)$ (coloured lines) overlaid on the echo-detected field sweep spectrum $I(f)$ (black) and the resonator profile $\nu_1(f)$ (red). (b) Echo transients for two-pulse chirp echoes centred around 0 and shifted according to the pulse bandwidth Δf . Predicted echo intensities $\int E(f) \cdot I(f) df$ (circles) and $\int E(f) \cdot I(f) \cdot \nu_1(f) df$ (shown as x). The predicted echo intensities were scaled so that the predicted echo intensity for a two-pulse echo of a 100 MHz chirp agrees with the experimentally observed echo intensity.

D.7. Pulse optimization for echoes from shaped pulses of different shapes

Two-pulse echoes from HS1, HS6, HS10 and chirp pulses were recorded on the Cu-PyMTA ruler while varying the pulse bandwidth Δf and pulse amplitude (Figure D.9) or the pulse length t_p and the pulse amplitude (Figure D.10). The maximal echo integral evaluated over 3 ns (six data points) was rather similar for all studied pulse shapes, i.e. all plots have the same range of the z-axis, except for HS1 pulses with pulse lengths 100/50 ns.

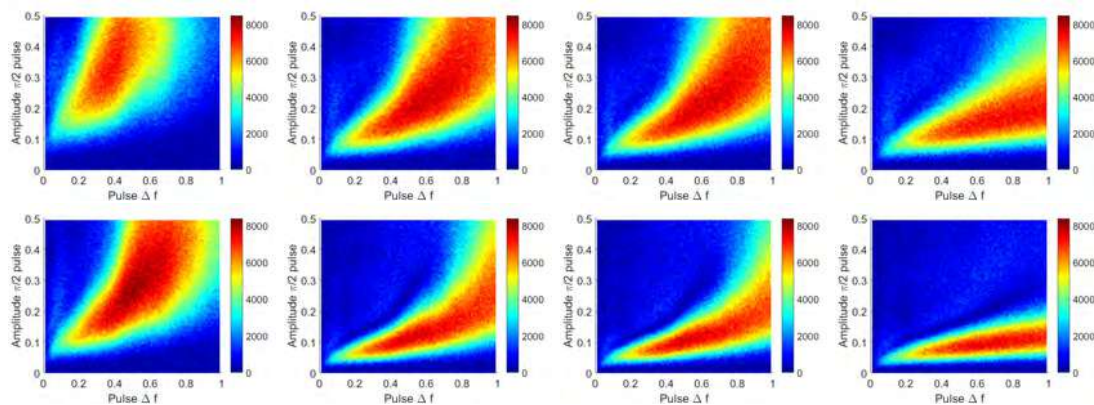


Figure D.9. Two-pulse echo optimization for different pulse shapes in Q band for the Cu-PyMTA ruler: Variation of pulse bandwidth Δf and microwave field amplitude. From left to right: HS1, HS6, HS10 and chirp. Pulse lengths were 100/50 ns (top) and 250/125 ns (bottom).

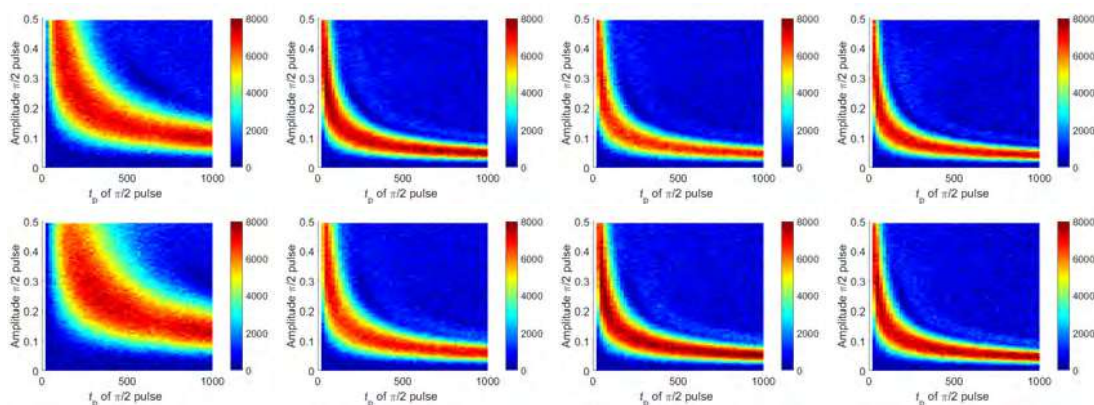


Figure D.10. Two-pulse echo optimization for different pulse shapes in Q band for the Cu-PyMTA ruler: Variation of pulse length and pulse amplitude for shaped pulses with $\Delta f = 0.5$ GHz. From left to right: HS1, HS6, HS10 and chirp. Shaped pulses were compensated for resonator ν_1 profile and amplitude non-linearity (top) or uncompensated (bottom). Pulse length ratios were 2:1 and the amplitude ratio was 1:2.

D.8. DEER experiments with the observer pulses positioned at the maximum of the Cu(II) spectrum

Figure D.11 and Figure D.12 show DEER experiments where the observer pulses cover the maximum of the Cu(II) spectrum. In both cases the noise level is higher in the traces recorded with shaped observer pulses compared to the same traces recorded with monochromatic observer pulses. In Figure D.12 modulation depths were 22 and 29% when the shaped 0.9 GHz pump pulse covered the region towards the low-field shoulder for the M_oS_p and the S_oS_p setup, respectively, see Figure D.12 and Table D.2. The modulation depths were thus slightly lower than for the setup in which the pump pulse was placed around B_{\max} , where 28 and 35% were observed with the M_oS_p and the S_oS_p setups, respectively. This is expected because less spins contribute in the low-field region of the spectrum.

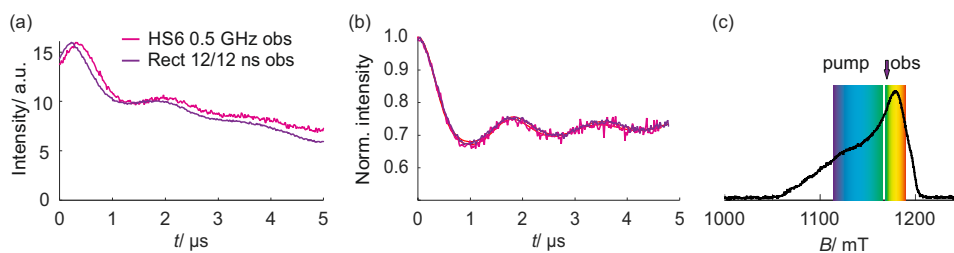


Figure D.11. Q-band DEER data for experiments with a HS6 pump pulse of 250 ns length and 1.2 GHz bandwidth Δf and monochromatic observer pulses (purple) or HS6 observer pulses with a bandwidth of 0.5 GHz at 20 K. (a) Raw DEER data, (b) form factors, (c) echo-detected field sweep with positioning of excitation bands indicated as coloured areas.

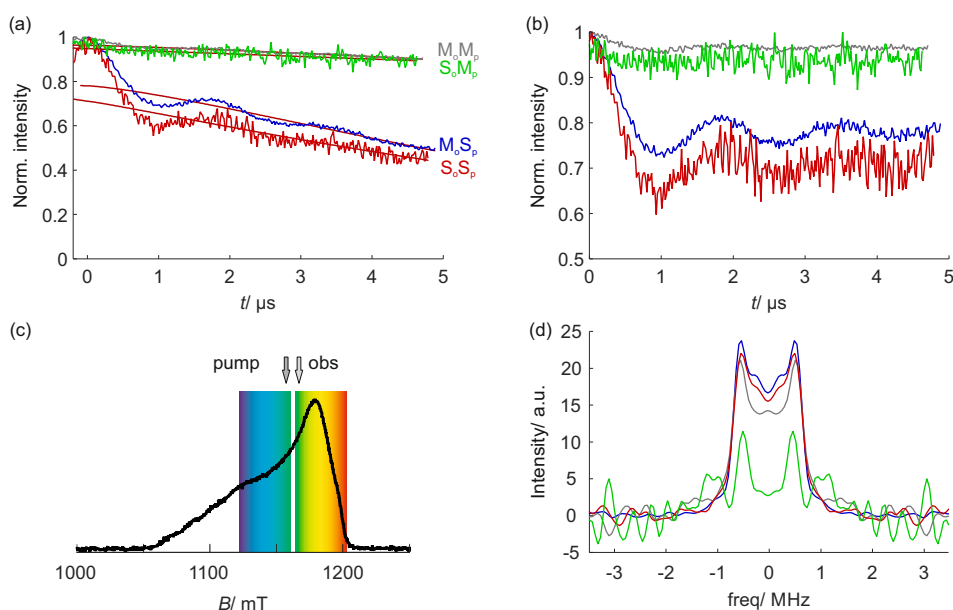


Figure D.12. Q-band DEER data at 20 K similar to Figure 7.6 but with the observer and pump pulses position inverted. Comparison of Monochromatic (M) and Shaped (S) observer (o) and pump pulses (p): M_oM_p (grey), S_oM_p (green), M_oS_p (blue), S_oS_p (red). (a) Primary DEER data, (b) form factors, (c) echo-detected field sweep with pulse ranges indicated, (d) dipolar spectra.

D.8.1. Primary DEER data for experiments with shaped pump pulse

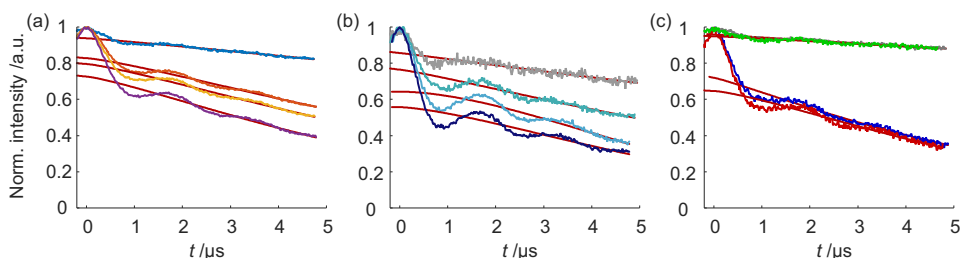


Figure D.13. Primary DEER data for the experiments (a, b) in Figure 7.5 and (c) in Figure 7.6 of Chapter 7. The colour code is the same as in Chapter 7. Background fits are overlaid in dark red.

D.8.2. Pulse setups for DEER experiments

X-band DEER measurements were performed with 12 ns monochromatic observer pulses set 0.04 GHz below the resonator center f_0 and shaped HS pump pulses of order 1 or 6 with a truncation parameter β of 10.4. The pump pulse bandwidth Δf was either 0.57 GHz or 1.5 GHz, the offset to the observer pulses 0.15 GHz. The observer pulses were placed on the maximum of the field-swept spectrum. In the M_oM_p setup, the observer pulses had a length of 8 ns and were offset by 0.2 GHz from the 6.5 ns monochromatic pump pulse. In this case, B_{\max} was set to the pump frequency.

Pulse setups for the Q-band DEER measurements in Figure 7.5(c) were as follows: ν_{obs} was 100 MHz below the resonator center f_0 . The monochromatic observer pulses were all 12 ns long. Shaped pump pulses were offset by 100 MHz. Δf was 0.8 GHz and 1.2 GHz for a HS6 pulse of length 100 ns and 250 ns, respectively. The HS1 pulse of length 100 ns had a bandwidth of 0.8

GHz. The observer pulse was exchanged for a HS6 pulse of 150 ns length and 0.5 GHz Δf for the S_oS_p setup in Figure D.11.

For the DEER measurements in Figure 7.6, the pulses were set up so that shaped observer pulses covered the frequency range 50-950 MHz above f_0 . Monochromatic observer pulses of length 12 ns were set 100 MHz above f_0 . The shaped pump pulse covered the frequency range 50-950 MHz below f_0 . The monochromatic pump pulse of 12 ns length was positioned 100 MHz below f_0 . The setup was inverted for the measurements in Figure D.12.

All parameters are provided in Table D.3.

Fig.	Setup	observer			pump			
		band /GHz	t_p	Shape	band /GHz	t_p	Shape	f /GHz for B_{\max}
7.5(c)	M_oM_p	$f_0 + 0.1$	7 ns	–	$f_0 - 0.1$	7 ns	–	$f_0 - 0.1$
	M_oSp	$f_0 - 0.1$	12 ns	–	$[f_0, f_0 + 0.8]$	250 ns	HS1	$f_0 - 0.1$
	M_oSp	$f_0 - 0.1$	12 ns	–	$[f_0, f_0 + 0.8]$	100 ns	HS6	$f_0 - 0.1$
	M_oSp	$f_0 - 0.1$	12 ns	–	$[f_0, f_0 + 1.2]$	250 ns	HS6	$f_0 - 0.1$
D.11	S_oSp	$[f_0 - 0.5, f_0]$	250/125 ns	HS6	$[f_0, f_0 + 1.2]$	250 ns	HS6	$f_0 - 0.25$
	M_oM_p	$f_0 + 0.1$	12 ns	–	$f_0 - 0.1$	12 ns	–	$f_0 - 0.3$
7.6	S_oM_p	$[f_0 + 0.05, f_0 + 0.95]$	250/250/125 ns	HS{1,10}	$f_0 - 0.1$	12 ns	–	$f_0 - 0.3$
	M_oM_p	$f_0 + 0.1$	12 ns	–	$[f_0 - 0.05, f_0 - 0.95]$	250 ns	HS{1,10}	$f_0 - 0.3$
	M_oSp	$[f_0 + 0.05, f_0 + 0.95]$	250/250/125 ns	HS{1,10}	$[f_0 - 0.05, f_0 - 0.95]$	250 ns	HS{1,10}	$f_0 - 0.3$
	S_oSp	$[f_0 + 0.05, f_0 + 0.95]$	250/250/125 ns	HS{1,10}	$[f_0 - 0.05, f_0 - 0.95]$	250 ns	HS{1,10}	$f_0 - 0.3$
D.12	M_oM_p	$f_0 - 0.1$	12 ns	–	$f_0 + 0.1$	12 ns	–	$f_0 - 0.3$
	S_oM_p	$[f_0 - 0.05, f_0 - 0.95]$	250/250/125 ns	HS{1,10}	$f_0 + 0.1$	12 ns	–	$f_0 - 0.3$
	M_oM_p	$f_0 - 0.1$	12 ns	–	$[f_0 + 0.05, f_0 + 0.95]$	250 ns	HS{1,10}	$f_0 - 0.3$
	M_oSp	$f_0 - 0.1$	12 ns	–	$[f_0 + 0.05, f_0 + 0.95]$	250 ns	HS{1,10}	$f_0 - 0.3$
7.10, D.7	S_oSp	$[f_0 - 0.05, f_0 - 0.95]$	250/250/125 ns	HS{1,10}	$[f_0 + 0.05, f_0 + 0.95]$	250 ns	HS{1,10}	$f_0 - 0.3$
	M_oSp	$f_0 - 0.26$	12 ns	–	$f_0 - 0.06, f_0 + 0.74$	100 ns	HS6	varied
7.5(a)	M_oM_p	$f_0 + 0.14$	8 ns	–	$f_0 - 0.06$	6.5 ns	–	$f_0 - 0.06$
	M_oSp	$f_0 - 0.04$	12 ns	–	$[f_0 + 0.11, f_0 + 0.68]$	100 ns	HS6	$f_0 - 0.04$
	M_oSp	$f_0 - 0.04$	12 ns	–	$[f_0 + 0.11, f_0 + 0.68]$	250 ns	HS6	$f_0 - 0.04$
	M_oSp	$f_0 - 0.04$	12 ns	–	$[f_0 + 0.11, f_0 + 1.61]$	250 ns	HS6	$f_0 - 0.04$

Table D.3. Pulse parameters for Q-band DEER measurements. M indicates a monochromatic pulse, S indicates a pulse which is amplitude- and frequency-modulated. All frequencies are indicated with respect to the center of the resonator mode f_0 . For monochromatic pulses, ν_{obs} is provided, for frequency-swept pulses the pulse edges in square brackets. HS6 pulses had a truncation parameter β of 10.4, HS{1,10} had $\beta = 8$.

Supplementary Information to Chapter 8

E.1. OvertoneAnalysis

The software package OvertoneAnalysis is based on the open-source DeerAnalysis package.⁷⁸ It is executed via MATLAB. The package differs from DeerAnalysis by using an extended kernel function in the Tikhonov regularization procedure to account for frequency overtones according to

$$K_{\text{mod}}(r, t) = \int [P_1 \cos(\omega(r, \theta) \cdot t) + P_2 \cos(2\omega(r, \theta) \cdot t) + P_3 \cos(3\omega(r, \theta) \cdot t)] \sin(\theta) d\theta. \quad (\text{E.1})$$

The fractions of the first (P_2) and second harmonic (P_3) overtone can be adjusted in the graphical user interface of OvertoneAnalysis (see Figure E.1), while the fraction of the fundamental frequency (P_1) is given by the requirement that the total sum of all three coefficients is one ($P_1 = 1 - P_2 - P_3$). Yet higher harmonic overtones are neglected since their contributions to the RIDME signals was unmeasurable small in the experimental data acquired to date. Tikhonov regularization is then performed using the modified kernel function with the given fractions P_i . The extraction of the obtained distance information can be performed in analogy to the procedure described for the DeerAnalysis software package.

In analogy to DeerAnalysis, the software package provides tools required for pre-processing of RIDME raw data as well as for the subsequent computation of the underlying distance distributions. After loading the experimental data in the designated **Data sets** panel, the primary RIDME data are displayed in the Original data section of the graphical interface of OvertoneAnalysis (see Figure E.1, top left corner). Pre-processing of the time traces should be performed by adjusting zero time and the phase of the signal. However, the background decay and thus its correction differ between DEER and RIDME. For RIDME data it is important to fit the correct background dimensionality of the homogeneous distribution, as it is dependent on the experimental conditions. In most of the cases at hand, due to the observable oscillations in the form factor traces, the background correction by stretched exponential model functions can be considered to be accurate. It was found that the optimum range for the background fit is located towards the end of the signal, where the contribution of dipolar oscillations has already almost decayed. The part of the signal which is utilized for fitting the background function is specified by the **Backgr.** edit field, which determines the starting point, and the **Cutoff** edit field, which marks the end of the considered part of the signal and thus the end of the range used for background fitting. The chosen interval is visualized by a blue and an orange line within the

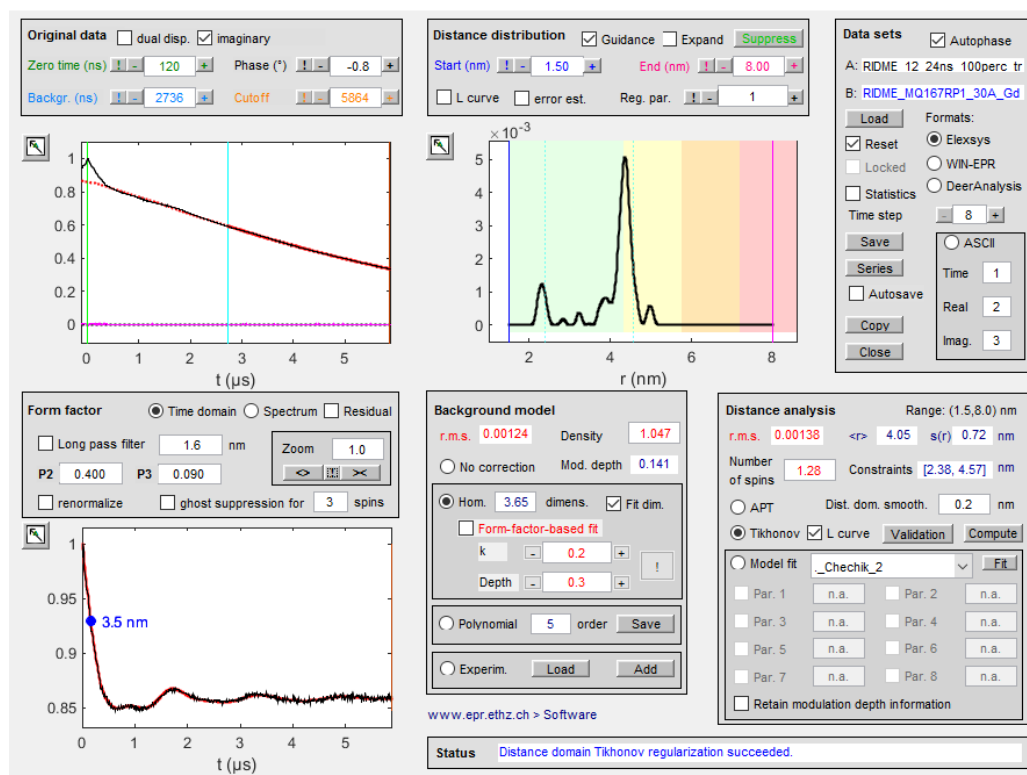


Figure E.1. Graphical interface of OvertoneAnalysis.

graphic (see Figure E.1, top left corner). In general, it is desirable to consider as much of the measured signal as possible. However, due to the fact that the RIDME background decay can be quite steep and that background correction involves division of the initial time trace by the background function, it is possible that the form factor (bottom left corner) is noisy towards the end of the trace (see Figure E.2). In such cases, or when artefacts at the end of the time domain data are present, cut-off at earlier times is required. Cutting off a significant amount of data will suppress noise, but background correction may become more difficult and will cause the suppression of long distances. In the studied data set, the range for background fitting, which was found automatically by pressing the two relevant ‘!’ buttons resulted in a reasonable background model. Nevertheless, it was verified for every investigated data set that the form factor in time and frequency domain exhibited the expected shape after removing the background contribution. For the form factor in time domain, this means a decay to a constant value and thus a flat line towards the end of the RIDME trace if the oscillations are completely decayed.

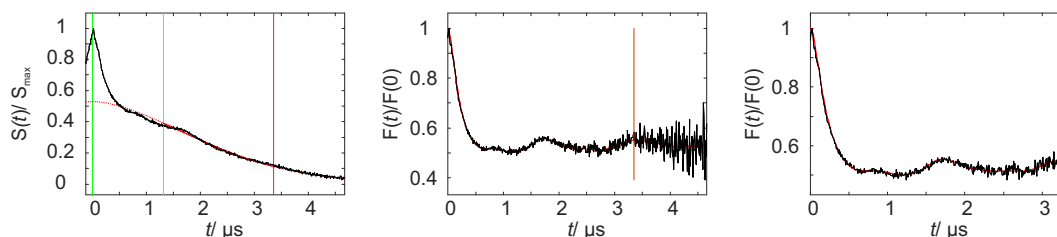


Figure E.2. Noise truncation by trace cut-off for the Gd-ruler **2**₂. Measured at 20 K using a mixing time of 24 μs.

Tikhonov regularization can then be executed using the modified kernel functions as well as different regularization parameters α . From the resulting L curve (Distance distribution panel), α_{opt} is determined (see DeerAnalysis manual, Figure E.3) and the corresponding distance distribution is displayed. As for DEER experiments, the reliability of distance distributions depends strongly on the maximum dipolar evolution time. Thus, the colour coding for reliability ranges in the Distance distribution panel are analogous to DeerAnalysis. Pale green: Shape of distance distribution is reliable. Pale yellow: Mean distance and width are reliable. Pale orange: Mean distance is reliable. Pale red: Long-range distance contributions may be detectable, but cannot be quantified. A scheme of the different steps within the analysis program is given in Figure E.3. For more details on the analysis program refer to the DeerAnalysis manual.

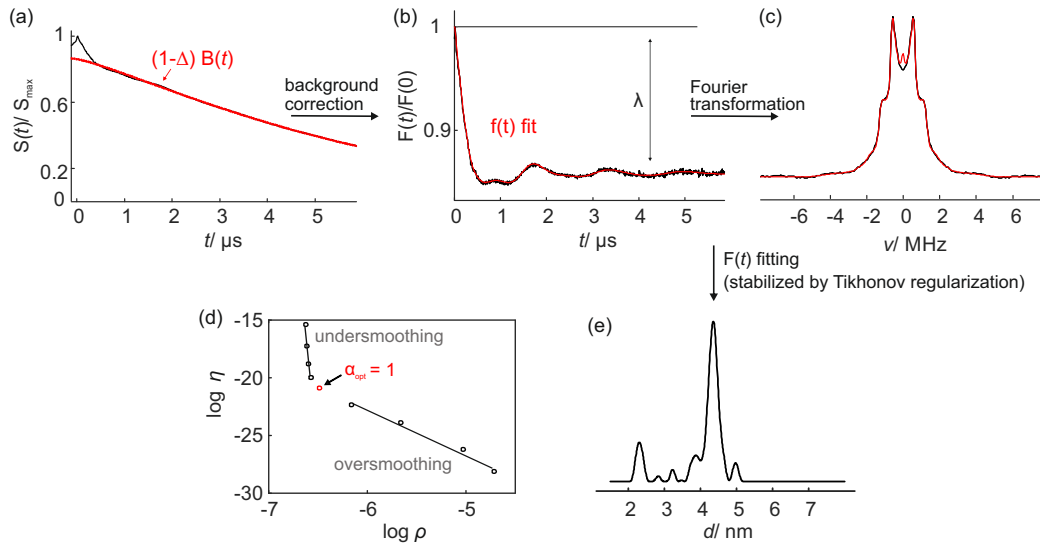


Figure E.3. Schematic representation for the extraction of distance distributions from RIDME raw data presented for the Gd-ruler $\mathbf{2}_2$ (10 K, 8 μs). (a) Normalized and phase-corrected primary RIDME data (black line) with background fit (red line); (b) RIDME form factor in time domain obtained after background correction and subsequent re-normalization (black line) and its fit (red line); (c) RIDME form factor in frequency domain (black line) and its fit (red line); (d) L-curve resulting from Tikhonov regularization using the extended kernel function and different regularization parameters; (e) resulting distance distribution $p(r)$ obtained by Tikhonov regularization with the extended kernel function (*artefact resulting from echo crossing).

Note that in the newest version of the DeerAnalysis software the fast Tikhonov regularization routines from Prof. P.C. Hansen (DTU) are used, which do not include the non-negativity constraint. The final calculation of the distance distribution with the selected regularization parameter is then done by considering the non-negativity condition. The published version of the OvertoneAnalysis software, being a 'daughter' of DeerAnalysis, is also based on this fast version of the Tikhonov regularization. However, the data analysis presented in this paper was still performed using the previous, slower version of the Tikhonov regularization procedure, including the non-negativity constraint at every step. Furthermore, both approaches use different definitions of the regularization parameter. For simulated data using a Gaussian distribution with FWHM of 0.5 nm and 3.4 nm mean distance, the value of 1, used in this work, corresponds to a value of 100 in the published version of OvertoneAnalysis. The old version of the software is available from the authors upon request.

A comparison of data analysis using an 'overtone-free' or an 'overtone-containing' kernel is shown in Figure E.4(a) for simulated data (3.4 nm mean distance, Gaussian distribution with

a FWHM of 0.5 nm, $\{P_{1,\text{sim}} = 0.4, P_{2,\text{sim}} = 0.5 \text{ and } P_{3,\text{sim}} = 0.1\}$) and in Figure E.4(b) for an experimental dataset (Gd-ruler **2**₂).

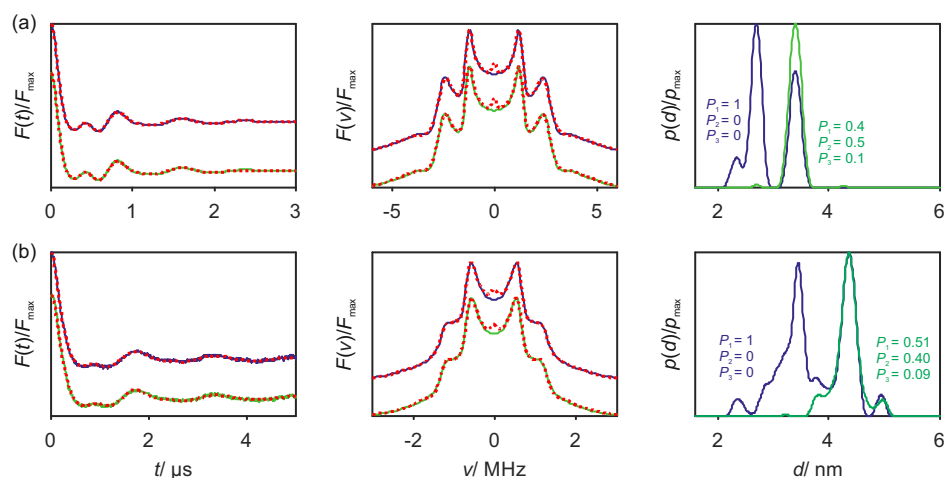


Figure E.4. Comparison of data analysis using an 'overtone-free' (purple line) and an 'overtone-containing' kernel (green line). (a) Simulated data of a Gaussian distribution with 3.4 nm mean distance, FWHM of 0.5 nm, modulation depth of 30% and coefficients $\{P_{1,\text{sim}} = 0.4, P_{2,\text{sim}} = 0.5 \text{ and } P_{3,\text{sim}} = 0.1\}$. The coefficients were set to the simulated values $\{P_1 = 0.4; P_2 = 0.5; P_3 = 0.1\}$ in the 'overtone-containing' kernel. (b) Gd-ruler **2**₂ measured at W-Band, 10 K and 8 μs mixing time. The raw data were truncated as described below resulting into a modulation depth of 12%. The coefficients were set to $\{P_1 = 0.51; P_2 = 0.40; P_3 = 0.09\}$ in the 'overtone-containing' kernel. From left to right: form factors and corresponding fits (red dashed lines), dipolar spectra and corresponding fits (red dashed lines), computed distance distribution and simulated distance distribution (black dashed lines).

E.2. Experimental set-up and measurement conditions

The RIDME pulse sequence creates a multitude of echoes. Thus, precise phase cycling is required to remove echo crossings and it is important to carefully adjust the phase settings prior to performing the RIDME experiment. Importantly, the amplification of the signal has to be adjusted at zero time of the dipolar evolution ($d_{12} = 0$) when the stimulated echo and the primary echo from the last two pulses fall on top of the refocused virtual echo, which is used for detection (see Figure E.5(b)). This situation corresponds to the largest total echo amplitude encountered during the whole experiment. The strong appearance of the stimulated echo as well as the primary echo from the last two pulses in the sequence can also be used to find the detected RIDME echo during set up: at $d_{12} = d_{12,\text{init}} = -120$ ns three echoes (Figure E.5(a)) can be observed, while at $d_{12} = 0$ the stimulated and primary echo will fall on top of the RIDME echo as shown in Figure E.5(b).

The strongest artefacts that can be observed during measurements are caused by the three echoes shown above. Note that further artefacts were sometimes observed at $t = 2d_1$ and at $t = d_2 - d_1$, which may distort the primary data and thus the distance distributions. The artefact level is dependent on the mixing time T_{mix} . For short mixing times $T_{\text{mix}} < T_m$ a higher artefact level was observed, resulting from an incomplete decay of the components of the transverse magnetization during the mixing block. Contrary, a very long mixing block increases the relative contribution of the primary echo (PE₂) from the last $\pi/2$ and π pulse, thus increasing the spike-like artefact around zero time. On another note, temperature (changes in relaxation properties) and mixing time influence modulation depth (m.d.) as well as background decay.

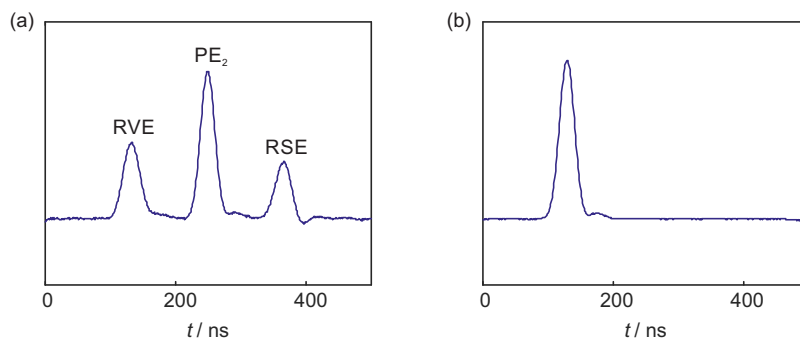


Figure E.5. Echoes resulting from the RIDME pulse sequence at the detection position. The refocused virtual echo (RVE, used for detection) occurs at $t_{\text{RVE}} = 2d_1 + 2d_2 + d_4$, while the stimulated echo (RSE) occurs at $t_{\text{RSE}} = t_{\text{RVE}} - 2d_{12}$ and the primary echo from the last two pulses (PE_2) at $t_{\text{PE}_2} = t_{\text{RVE}} - d_{12}$. Thus, the PE_2 and RSE change their position during the experiment, and cause echo crossings. Two different situations are displayed for (a) $d_{12} = -120$ ns and (b) $d_{12} = 0$.

For higher temperatures and longer mixing times the background decay is steeper, thus limiting the maximum detectable distance and reducing SNR. On the other hand, the m.d. is increased at those conditions. The maximum m.d. in the high-temperature limit is expected to achieve $\lambda = 1 - 1/(2S + 1)$ giving a value of 0.875 for Gd(III) in comparison for 0.5 for spin $S = 1/2$ systems.⁷³ Figure E.6 shows some of the properties related to temperature and mixing time for the Gd(III) ruler **1**₃.

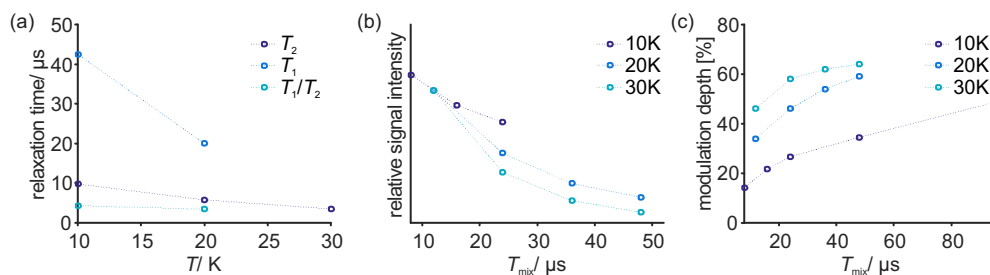


Figure E.6. Dependence of (a) relaxation times, (b) relative signal intensity (scaled to the signal intensity corresponding to 12 μs mixing time) and (c) modulation depth on mixing time and temperature for the Gd-ruler **1**₃.

E.3. Extraction of overtone coefficients for broad distance distributions

Figure E.7-E.9 show the decrease of overtone specific features upon broadening of the distance distribution. Thus, the higher-frequency overtones can no longer be identified in time- and frequency-domain data. Besides, the distance distribution does not exhibit artefacts peaks, but starts to become asymmetric. The mean distance is shifted for broad distributions if the overtone coefficients are mismatched. In such cases, either an a priori knowledge of the overtone coefficients is needed, or, for calibration, a control measurement using the DEER technique should be available. The latter strategy may run into problems for short distances, due to the distortion of distance distributions in the DEER experiments with high-spin centres. In that case, a CIDME¹¹⁶ control measurement may be preferable.

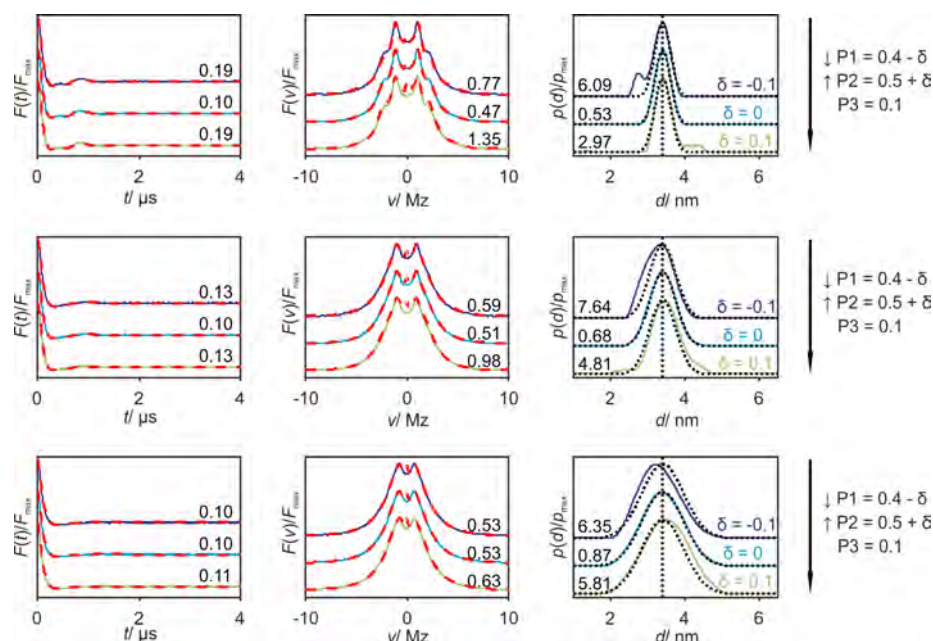


Figure E.7. Influence of the distance distribution width on dipolar evolution data with harmonic overtones studied on simulated data: Gaussian distribution with increasing width from top to bottom, 3.4 nm mean distance (indicated by black dashed vertical lines), added white noise, 30% modulation depth. The coefficients were set to $P_{1,\text{sim}} = 0.4$, $P_{2,\text{sim}} = 0.5$ and $P_{3,\text{sim}} = 0.1$. Variation of coefficients P_1 and P_2 , P_3 is kept constant. δ gives the deviation of P_i from the simulated fraction $P_{i,\text{sim}}$. RMSD values (multiplied by a factor of 100) between the data trace and the different fits or the computed and the simulated distance distribution are displayed at the corresponding trace. From left to right: form factors and corresponding fits (red dashed lines), dipolar spectra and corresponding fits (red dashed lines), computed distance distribution and simulated distance distribution (black dashed lines).

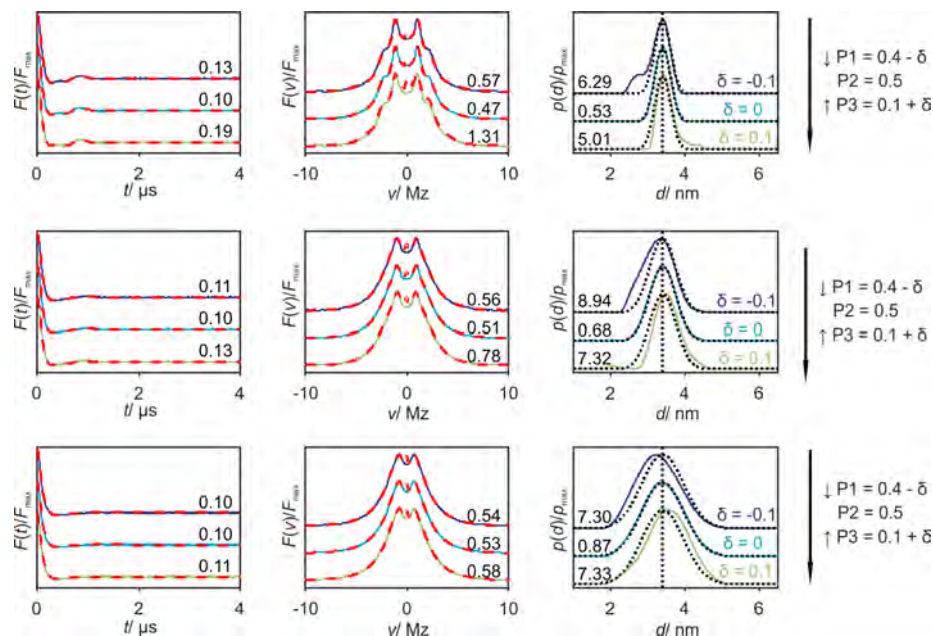


Figure E.8. Influence of the distance distribution width on dipolar evolution data with harmonic overtones studied on simulated data: Gaussian distribution with increasing width from top to bottom, 3.4 nm mean distance (indicated by black dashed vertical lines), added white noise, 30% modulation depth. The coefficients were set to $P_{1,\text{sim}} = 0.4$, $P_{2,\text{sim}} = 0.5$ and $P_{3,\text{sim}} = 0.1$. Variation of coefficients P_1 and P_3 , P_2 is kept constant. δ gives the deviation of P_i from the simulated fraction $P_{i,\text{sim}}$. RMSD values (multiplied by a factor of 100) between the data trace and the different fits or the computed and the simulated distance distribution are displayed at the corresponding trace. From left to right: form factors and corresponding fits (red dashed lines), dipolar spectra and corresponding fits (red dashed lines), computed distance distribution and simulated distance distribution (black dashed lines).

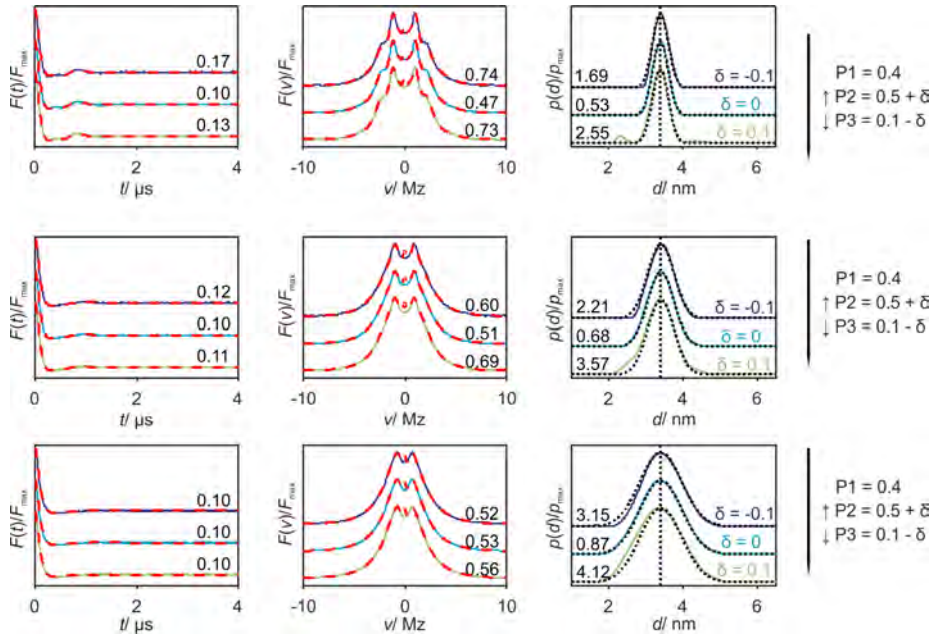


Figure E.9. Influence of the distance distribution width on dipolar evolution data with harmonic overtones studied on simulated data: Gaussian distribution with increasing width from top to bottom, 3.4 nm mean distance (indicated by black dashed vertical lines) added white noise, 30% modulation depth. The coefficients were set to $P_{1,\text{sim}} = 0.4$, $P_{2,\text{sim}} = 0.5$ and $P_{3,\text{sim}} = 0.1$. Variation of coefficients P_2 and P_3 , P_1 is kept constant. δ gives the deviation of P_i from the simulated fraction $P_{i,\text{sim}}$. RMSD values (multiplied by a factor of 100) between the data trace and the different fits or the computed and the simulated distance distribution are displayed at the corresponding trace. From left to right: form factors and corresponding fits (red dashed lines), dipolar spectra and corresponding fits (red dashed lines), computed distance distribution and simulated distance distribution (black dashed lines).

E.4. Filtering the artefact due to echo-crossing for long distances

Figure E.10 shows the dependence of the maximum signal intensity of the time trace on the pulse length. As described in the main text, the maximum is expected to be at the time where the three echoes cross ($d_{12} = 0$). However, experimentally we observe a shift of the apparent zero time from the expected value (d_0) by about the difference between the length of the π and the $\pi/2$ pulse. As the echoes cross at $d_0 + \tau_p(\pi) - \tau_p(\pi/2)$, the shift in zero time can be avoided by making pulses all of the same length.

The filtering approach is based on the fact that short-distance artefacts in the distance distribution correspond to high-frequency components in the time domain signal. In principle, such high-frequency components can be removed from the time trace by applying a digital low-pass filter, which in turn suppresses the short-distance artefacts. However, since this procedure also removes high-frequency noise, the original and the filtered data differ more than only by the unwanted, artefact-inducing frequency components, which is often not desired. This problem can be circumvented by subtracting the filtered data from the original primary data and only removing those components of the residual from the original signal that exceed the noise level. Doing so, the resulting time-domain signal differs from the original signal only by the absence of the unwanted high-frequency components. Such signals are referred to as truncated signals in this work. The described filtering procedure was performed for selected data sets of Gd-rulers **1₃**, **1₅**, **1₇**, and **2₂**. The resulting primary data and the change in distance distribution are shown in Figure E.11. To discuss the effect of truncation we will look at the example shown in Figures E.12.

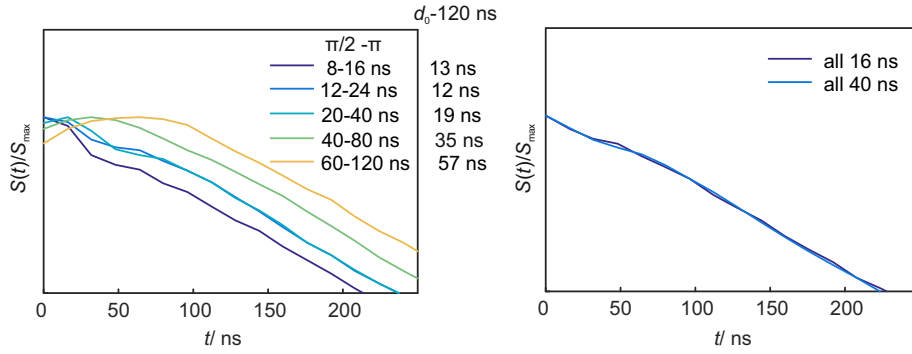


Figure E.10. Influence of the pulse length on the position of the maximum of RIDME signal measured for the Gd-ruler 15 at 20 K and 20 μ s mixing time. Left: $\pi/2 - \pi$ pulses with $t(\pi) = 2 * t(\pi/2)$. Right: $\pi/2 - \pi$ pulses of equal length. If phase cycling is incomplete, the echo crossing introduces an artefact in the RIDME primary data. The artefact in the primary data in turn causes a short-distance artefact in the distance distribution, which is not related to overtone coefficients. If this bump-like artefact can be clearly identified (e.g. for long distances, where the true dipolar oscillation is much slower) it can be filtered out from the primary data (see Figure E.11 for the samples studied here). It is seen that truncation of the bump artefact reduces m.d., but does not change the shape of the overall form factor and artefacts peaks < 3 nm can be filtered out. Furthermore, it is observed that the choice of zero time does not change the distance distribution significantly. However, it might become important if small changes need to be detected.

It is based on a Butterworth digital low pass filter and utilizes the MATLAB function `butter`. Its magnitude and phase response function is plotted in Figure E.12(a) and can be modified by the cut-off frequency and filter order. The resulting filtered data y_{filt} (red line) are shown in Figure E.12(b) on top of the RIDME raw data y (blue line). From filtered and raw primary data, truncated data y_{trunc} (green line) (Figure E.12(c)) are created as described above and are plotted on top of the RIDME raw data (blue line, Figure E.12c). The main deviation between the two time traces is observed in the region around the maxima. When adjusting the zero time, as demanded by theory, to 120 ns, this region coincides with the time origin of the primary signal. The high-frequency components, which are assumed to cause the observed short distance artefacts in the distance distribution (at $r < 3$ nm), therefore only contribute to the signal at initial times and manifest in terms of a bump-like artefact. This artefact in turn explains the observed non-coincidence of origin and maximum of the original primary signal as well as the observed sensitivity of the short distance artefacts in the distance distribution towards shifts in the zero-time (Figures E.11 and E.13-E.15). It is assumed that such distortion of the time trace at initial times is caused by echo crossings and may thus be attributed to incomplete phase-cycling.

E.5. Extraction of distance distributions for short distances (Gd-ruler 1₁)

Figure E.13 shows the extraction of the distance distribution for the Gd-ruler 1₁. If detection is performed at the maximum of the Gd(III) spectrum (Figure E.13, top row), Tikhonov regularization with coefficients $P_2 = P_3 = 0$ (cyan and violet line) results in the lowest level of artefacts. Nevertheless, the uncertainty in zero time (theoretical value of 120 ns versus maximal signal intensity) does change the level of artefacts and thus the overtone coefficients dramatically. With increasing field offset, dipolar frequencies of the harmonic overtones become more pronounced. This leads to a change in artefact level for the same overtone coefficients at different detection positions. Choosing the zero time at the maximum signal intensity of the primary traces yields, for the largest field offset, good agreement with the same set of coefficients as extracted for the other distances (bottom row, lower lines, yellow line). Setting the zero time to 120 ns indicates

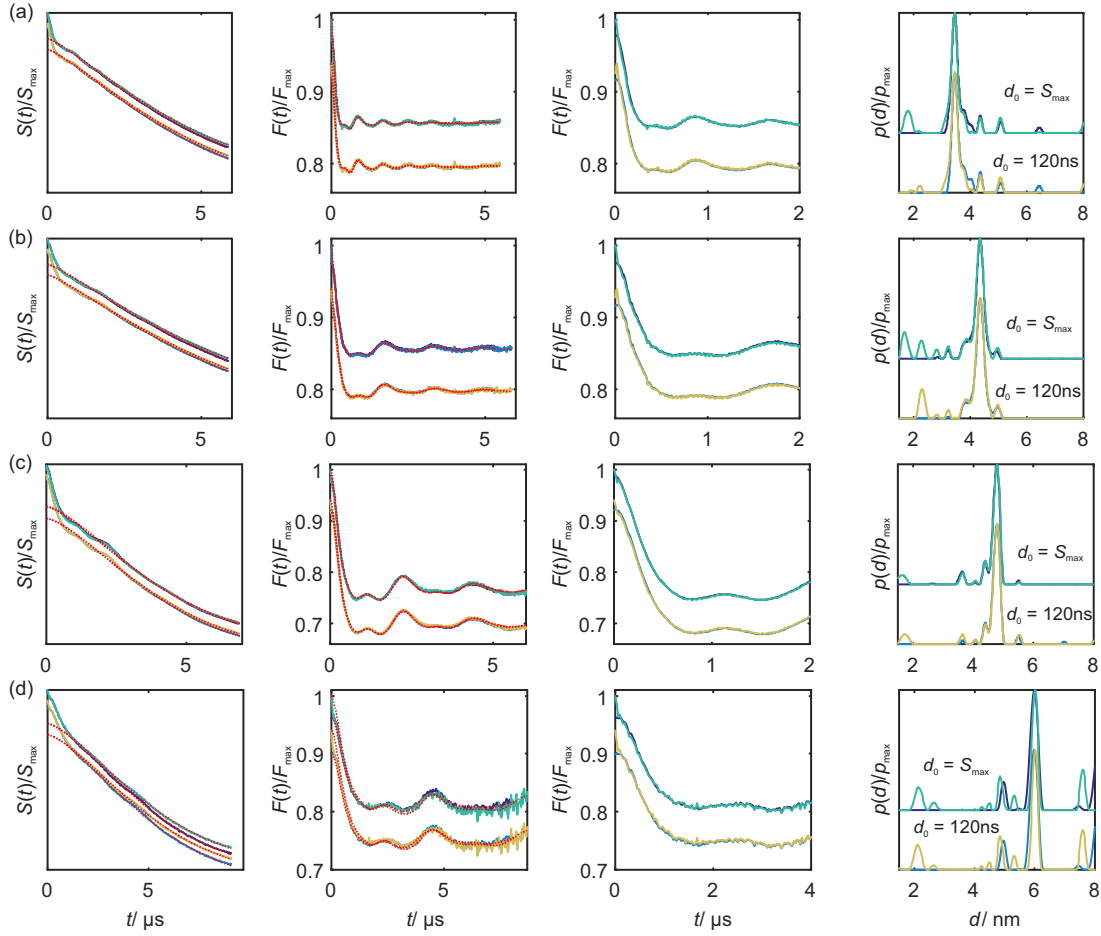


Figure E.11. Examples for filtering the bump-like artefact at zero time and influence of the choice of zero time on the distance distribution. (a) Gd-ruler 1₃ (10 K, 8 μ s), (b) Gd-ruler 2₂ (10 K, 8 μ s), (c) Gd-ruler 1₅ (10 K, 24 μ s) and (d) Gd-ruler 1₇ (10 K, 16 μ s). For each sub-figure: for the two upper lines zero time set to apparent maximum, RIDME raw data coloured in violet and truncated data in turquoise and for the two lower lines zero time set to 120 ns, RIDME raw data coloured in light blue and truncated data in yellow. Truncated data are y -shifted by the artefact amplitude.

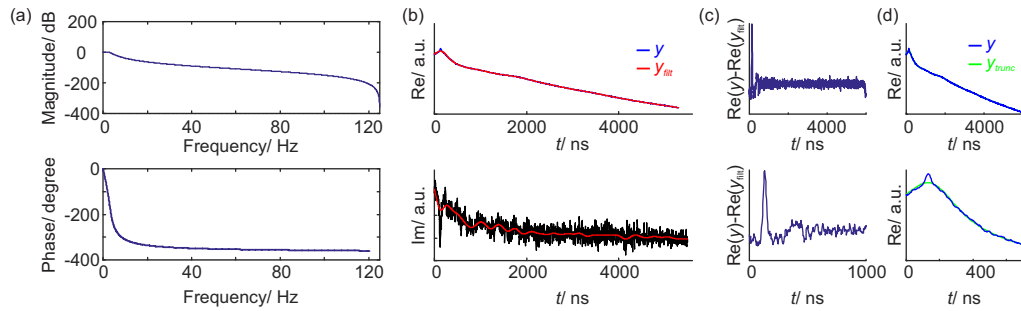


Figure E.12. Example of filtering RIDME raw data for the Gd-ruler 2₂ at 10 K and 8 μ s mixing time. (a) Magnitude (top) and phase (bottom) respond function of the filter, (b) real (top) and imaginary (bottom) RIDME raw data y (blue line) and data resulting from filtering y_{filt} (red line), (c) left residual between RIDME raw and (d) filtered data and right truncated RIDME data y_{trunc} (green line) overlaid with the detected RIDME raw data (real part). (c, d) The top line shows the complete trace, while the lower row shows an enlargement of the region around maximal signal intensity.

best agreement for a smaller contribution of P_2 and P_3 (bottom row, upper lines, blue line). This dependence of overtone coefficients on zero time is observed through all detection positions.

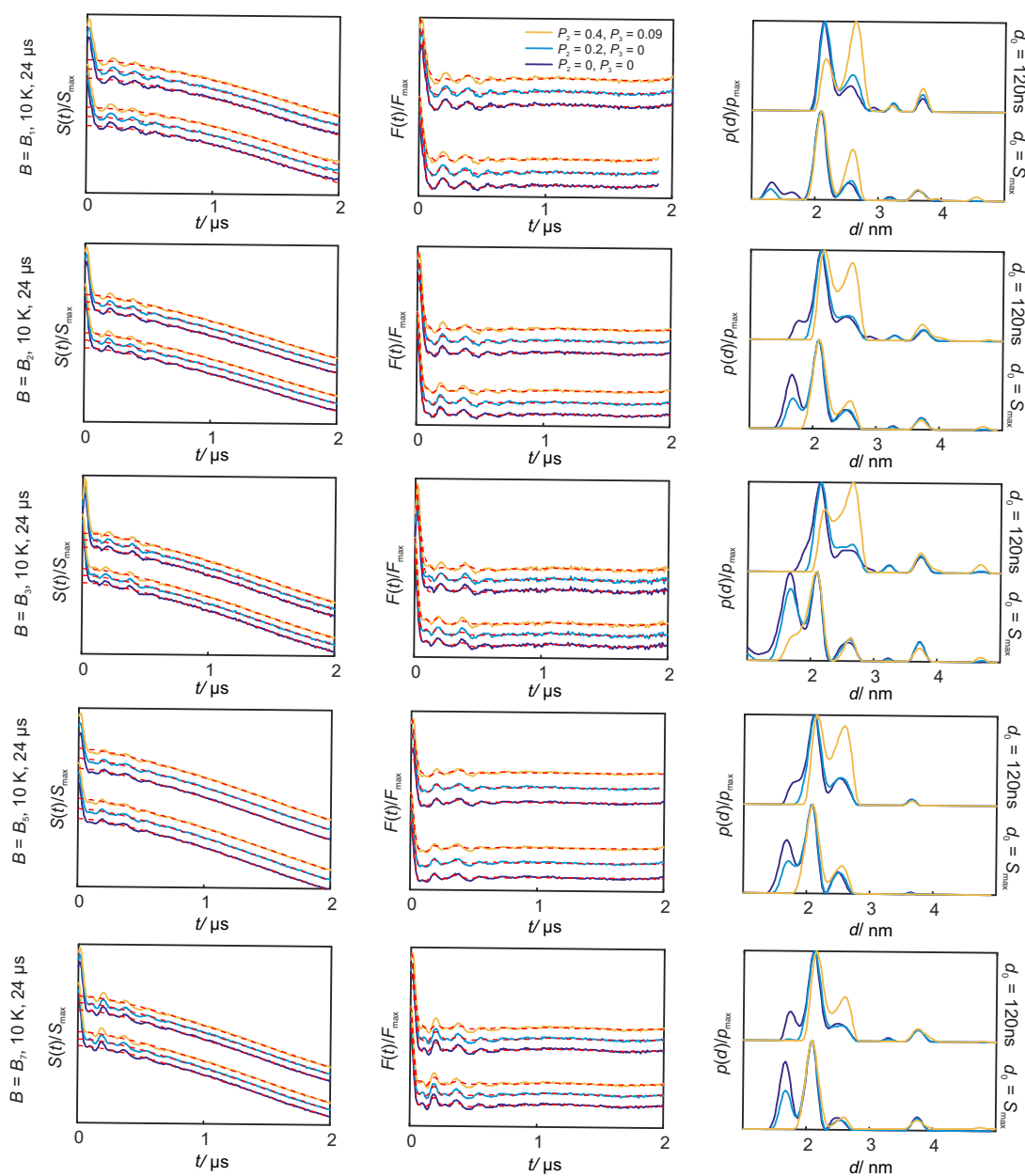


Figure E.13. Extraction of overtone coefficients for the Gd-ruler 1_1 . RIDME data were acquired at different field positions of the Gd(III) spectrum (see Figure 8.12 of the main text) at 10 K and a mixing time of $24 \mu\text{s}$. From left to right: Primary RIDME fit data (solid line) and corresponding background fit (red dashes line), background corrected form factor (solid line) and its fit (red dashed line), resulting distance distribution. The colour coding of the solid lines corresponds to a set of overtone coefficients and is retained throughout the whole figure. For each sub-figure: zero time set to 120 ns for the upper lines and zero time set to apparent maximum for the lower lines.

To avoid the uncertainty in zero time, measurements were performed with $\pi/2$ and π pulses of equal length at three different detection positions (B_1 , B_2 , B_3 , see Figure 8.12). The results are displayed in Figure E.14. Comparing the artefact level in the distance distribution it can be noted that the analysis with the zero time chosen at the maximum of the RIDME signal for 16-32 ns pulses and all 16 ns pulses yields very similar distance distributions. The small remaining differences may result from the different excitation bandwidth of the A spins. This effect is further studied in Figure E.15. However, remaining uncertainties from imperfect phase cycling cannot be

excluded. Based on these results we suggest to set the zero time close to the maximum signal intensity prior to Tikhonov regularization. For longer distances this uncertainty does not change the overtone coefficients or extraction of distances (see Figure E.11), for short distances ($d < 3$ nm) this should be carefully investigated.

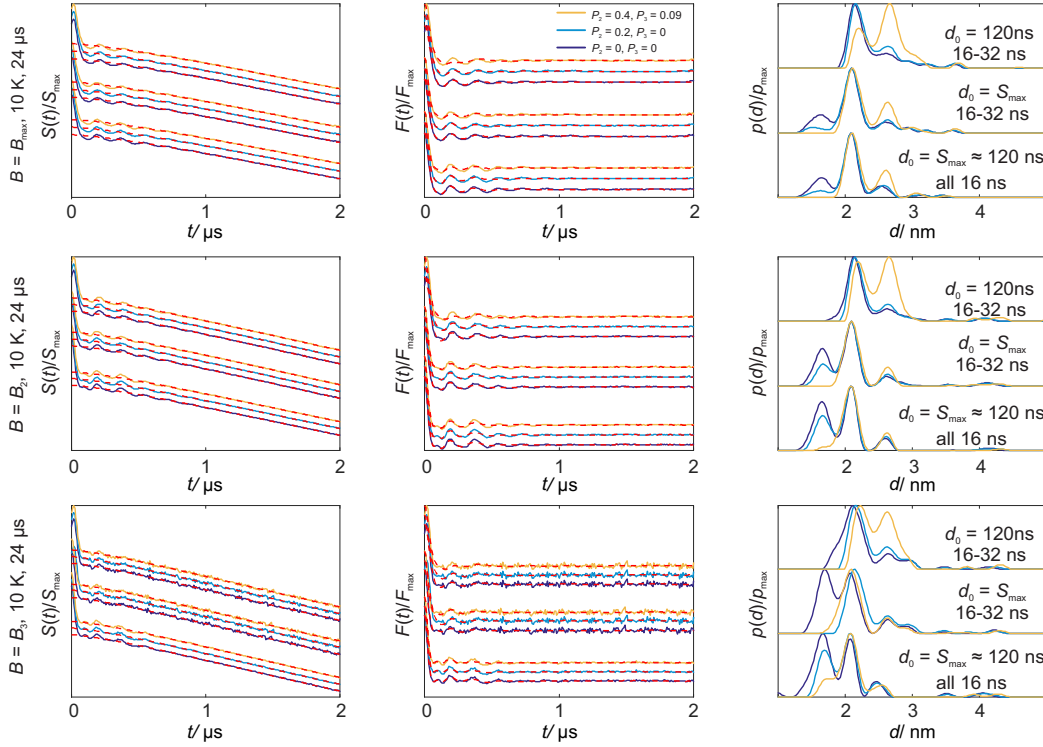


Figure E.14. Extraction of overtone coefficients for the Gd-ruler $\mathbf{1}_1$ using different pulse settings. RIDME data were acquired at different field positions of the Gd(III) spectrum (see Figure 8.12 of the main text) at 10 K and a mixing time of 24 μ s. From left to right: Primary RIDME data (solid line) and corresponding background fit (red dashed line), background corrected form factor (solid line) and its fit (red dashed line), resulting distance distribution. The colour coding of the solid lines corresponds to a set of overtone coefficients and is retained throughout the whole figure. The pulse length, for ($\pi/2$) and (π) pulses, is given in the figure next to the corresponding distance distributions.

Figure E.15 shows the effect of the observer pulse (A spin) bandwidth at two different detection positions for the Gd-ruler $\mathbf{1}_1$. Long, selective pulses only burn a narrow hole in the Gd(III) spectrum and thus only excite a small fraction of spins within a narrow frequency range. In these cases, higher harmonics are even more suppressed and the shape of the primary data gets distorted. For the very soft 80 ns pulses, the corresponding excitation bandwidth of 12 MHz, is already smaller than the width of the Pake pattern of the primary dipolar harmonic at the given average distance of 2.1 nm. Higher dipolar overtones are then strongly suppressed, and due to the incomplete Pake pattern excitation, artefacts at longer distances appear in the distance distribution for the case $P_2 = P_3 = 0$. Small changes in the shape of distance distribution, computed with the 'standard' set of dipolar overtone coefficients $\{P_1 = 0.51, P_2 = 0.40, P_3 = 0.09\}$, are already observed for short pulses (16 or 32 ns), which also lead to small deviations of the 'ideal' overtone coefficients. However, these effects are minor and differences of the coefficients are expected to be small, but may explain the remaining difference between $\pi/2$, π pulses of equal length with respect to π pulses being twice as long as $\pi/2$ pulses.

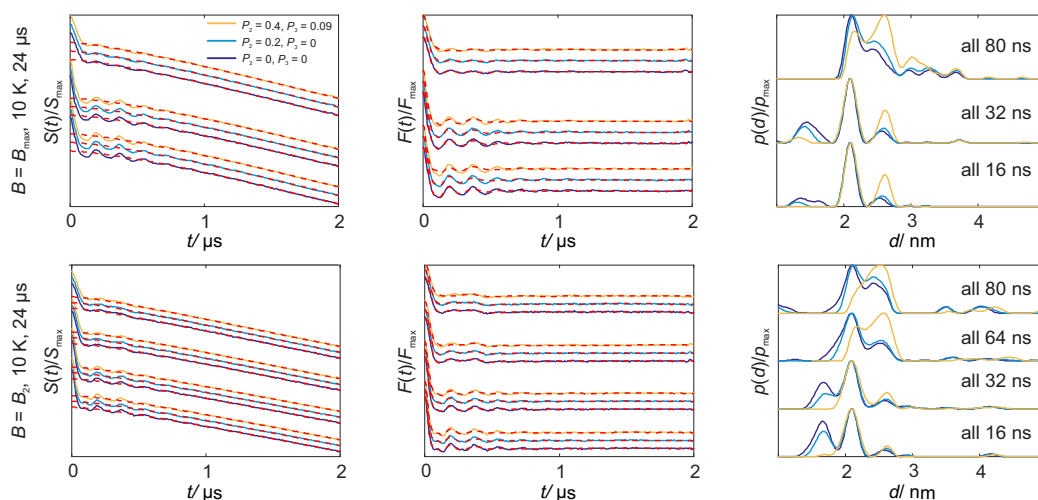


Figure E.15. Extraction of overtone coefficients for the Gd-ruler 1_1 using $(\pi/2)$ - (π) pulses of the same length, with varying bandwidth. RIDME data were acquired at different field positions of the Gd(III) spectrum (see Figure 8.12 of the main text) at 10 K and a mixing time of $24 \mu\text{s}$. From left to right: Primary RIDME data (solid line) and corresponding background fit (red dashes line), background corrected form factor (solid line) and its fit (red dashed line), resulting distance distribution. The colour coding of the solid lines corresponds to a set of overtone coefficients and is retained throughout the figure. The pulse length, identical for $(\pi/2)$ and (π) pulses, is given in the figure next to the corresponding distance distributions.

E.6. Calibration of overtone coefficients for a series of Gd-rulers

Table E.1 summarizes the data sets on which the calibration was performed. For calibration a wider range of overtone coefficients was scanned for a measurement of the Gd-ruler 1_3 . From that initial scanning procedure, a smaller set of coefficients $\{\{P_2 = 0.46, 0.40, 0.35\} \otimes \{P_3 = 0.05, 0.09\}\}$ was selected and applied to all data sets of Table E.1. Note that in some cases other variations were tested as well, but did not result in further improvement of distance distribution as well as form factor fit in time and frequency domain at the same time. It is important to keep in mind that a good fit does not necessarily imply a clean distance distribution (Figure E.16(a)). Likewise, a poor fit does not necessarily imply a wrong distance distribution (Figure E.16(b)). Thus, the major criteria for calibration was to find the best compromise between form factor/dipolar spectrum fit and clean anticipated distance distribution.

Over all data sets it was found that the set $\{P_1 = 0.51, P_2 = 0.40, P_3 = 0.09\}$ gives the best compromise between anticipated distance distribution and form factor/dipolar spectrum fit. As can be seen from Figures E.17-E.20, some slight variation of the optimal coefficients is observed with changing spin-spin distance (see figure captions for values). For short spin-spin distances the chosen combination rather over-corrects the harmonic contribution (artefact peaks on right side of mean distance), while for long distance the chosen combination rather under-corrects (artefact peaks on left side of mean distance). Nevertheless, for all measurements, the anticipated distance distribution and reasonable form factor/dipolar spectrum fits are obtained with the chosen coefficients (see Figures E.17-E.20 for the artefact levels). The remaining artefact level is smaller than typical distortions in distance distributions for biological samples that stem from noise or from small amounts of unfolded or aggregated material. Further, these coefficients were applied to all other measurements (Figures E.21-E.22 and Table E.2), giving relatively clean distance distributions and form factor/dipolar spectrum fits. For some cases the detected RIDME time trace is rather short compared to the distance of interest. This induces an uncertainty in

the background correction and might be the reason for an overall higher artefact level in the resulting distance distribution. On top, due to incomplete phase cycling, many measurements exhibit the bump-like artefact at about zero time inducing distance peaks < 3 nm. Such artefacts do not change with the choice of overtone coefficients. Still, as described in the main text, other effects might be responsible for the remaining artefacts. A validation tool incorporated into OvertoneAnalysis can help to distinguish overtone-specific artefacts from other artefacts (see Figure 8.8 of Chapter 8). In any case, validation is required if smaller side peaks are to be interpreted. Moreover, the whole data set (Figures E.18-E.22) suggests that RIDME form factors are stable with mixing time and approximately stable with temperature. With respect to these properties only small variations in the order of 0.05 for the 'best coefficients' are observed and we think it is reasonable to use one common set of coefficients for analysis. Moving the detection position away from the field maximum (Figure E.21(d, e) and Figure 8.13) does have a larger, systematic influence towards an under-correction of overtone coefficients (artefact peaks on left side of mean distance). The suggested under-correction is further supported by the deviation of experimental and fitted form factor.

Figure	Gd-ruler	$d_{\text{expected}}/ \text{nm}$	Temp/ K	Mixing time/ μs
Figure E.17	2 ₁	3	10 20	24, 48, 72 24
Figure E.18	1 ₃	3.4	10 20 30	4, 8, 16, 24, 48 4, 8, 16, 24 4, 8, 16
Figure E.19	2 ₂	4.3	10 20 30	4, 8, 16, 24, 48 4, 8, 16, 24 4, 8, 16
Figure E.20	1 ₇	6.0	10, 25 μM 20, 25 μM	16, 24 24

Table E.1. Summary of measurements for which the overtone variation was performed and corresponding Figure number.

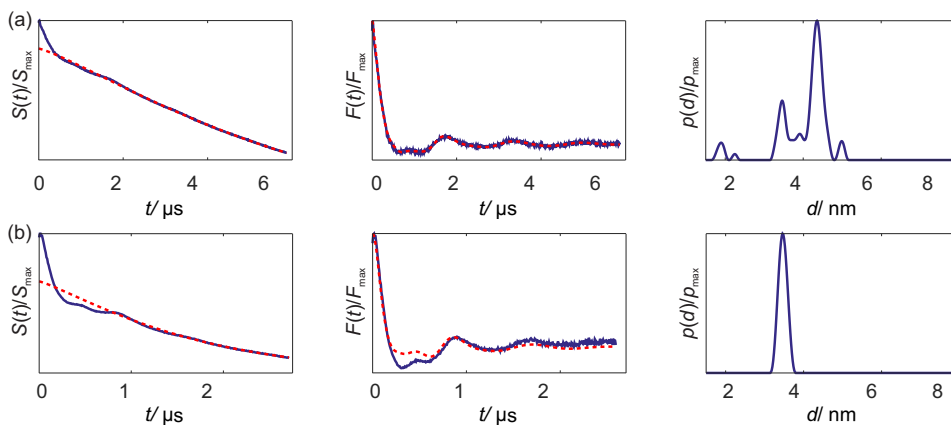


Figure E.16. Pitfalls during regularization procedure with harmonic overtones. (a) Good fit does not necessarily imply clean distance distribution. Gd-ruler **2**₂, W band, 10 K 16 μs , $\{P_1 = 0.6, P_2 = 0.2, P_3 = 0.3\}$; (b) Poor fit does not necessarily imply wrong distance distribution. Gd-ruler **1**₃, W band, 20 K 16 μs , $\{P_1 = 0.4, P_2 = 0.4, P_3 = 0.2\}$.

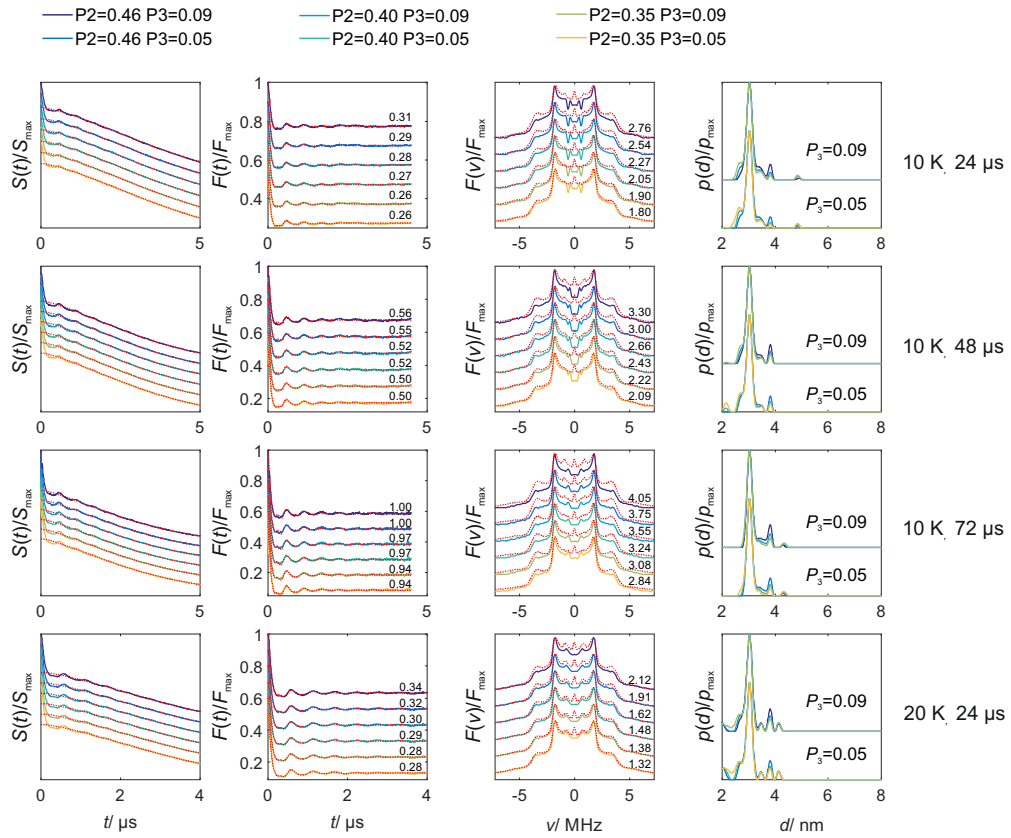
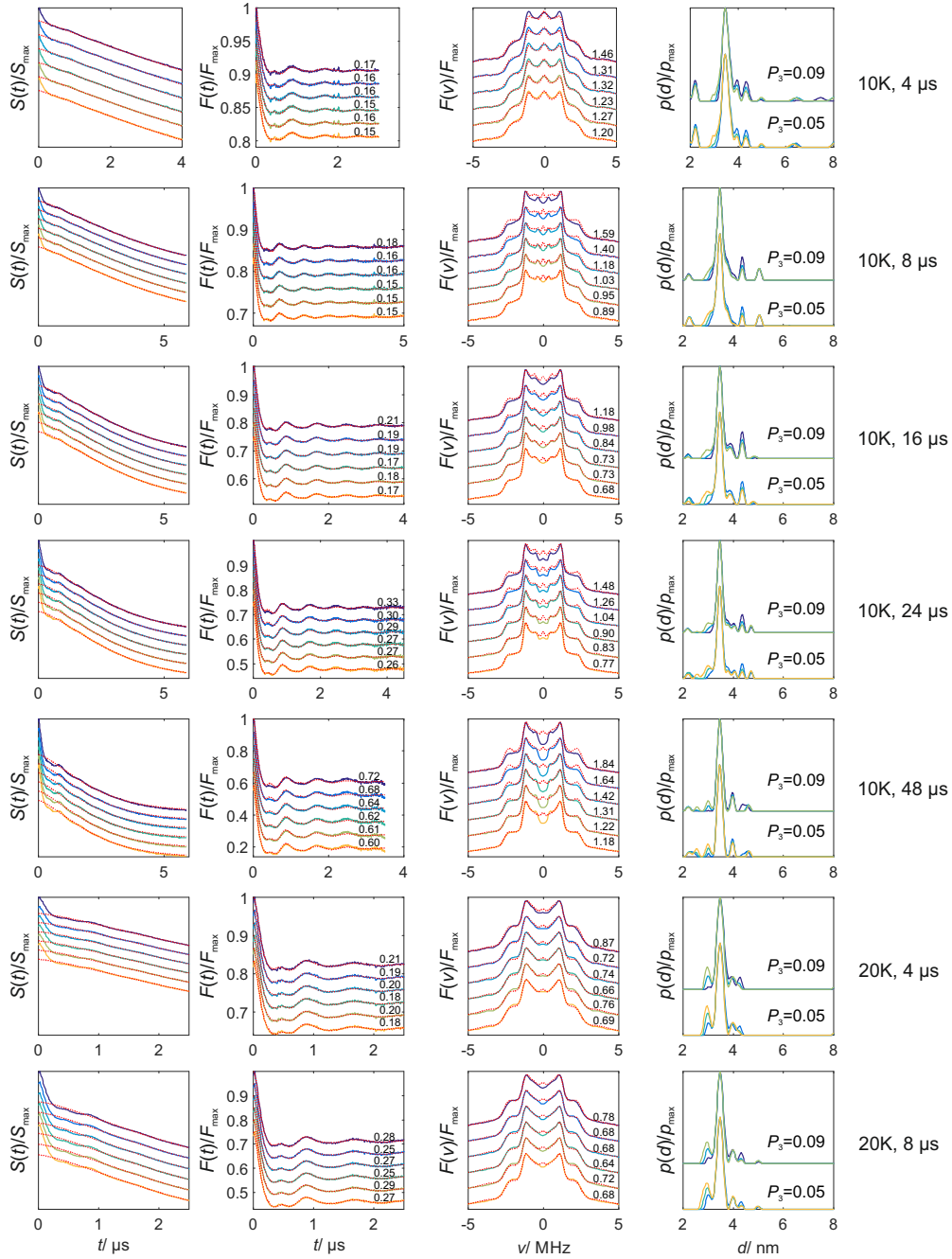


Figure E.17. Calibration for Gd-ruler **21** in W band. Rows: Variation of overtone coefficients for a given measurement (temperature and mixing time). From left to right: Primary data, form factor in time domain, form factor in frequency domain and distance distribution. Upper lines in distance distribution $P_3 = 0.09$. Lower lines in distance distribution $P_3 = 0.05$. Top to bottom: increasing mixing time and temperature – exact numbers are given next to each row. RMSD values (multiplied by a factor of 100) between the data trace and the different fits are given next to the corresponding trace. It can be observed that artefact peaks shift from left to right or increase in intensity on the right side with respect to the mean distance for assuming an increasing fraction of higher harmonics. On average the best compromise between distance distribution and form factor fit is obtained for $\{P_1 = 0.56, P_2 = 0.35, P_3 = 0.09\}$ or $\{P_1 = 0.55, P_2 = 0.40, P_3 = 0.05\}$, which indicates the uncertainty of the coefficients. Nevertheless, distance analysis using $\{P_1 = 0.51, P_2 = 0.40, P_3 = 0.09\}$ gives reasonable results in all cases.

Figure	Gd-ruler	d_{exp}/nm	Temp/ K	Mixing time/ μs
Figure E.21	1₅	4.7	10	8, 12, 16, 24, 56, 120, 200
			10	Field depend 24: max, -80 G, -1500 G
			20	8, 16, 24, 32, 40, 48, 56
			20	Field depend 24: max, -80 G, -1500 G
			30	4, 24
Figure E.22	mixture of 1₃ and 1₅	3.4:4.7	10	12, 24, 38
			20	12, 24
			30	12

Table E.2. Summary of measurements for which the set of overtone coefficients $\{P_1 = 0.51, P_2 = 0.40, P_3 = 0.09\}$ was applied.



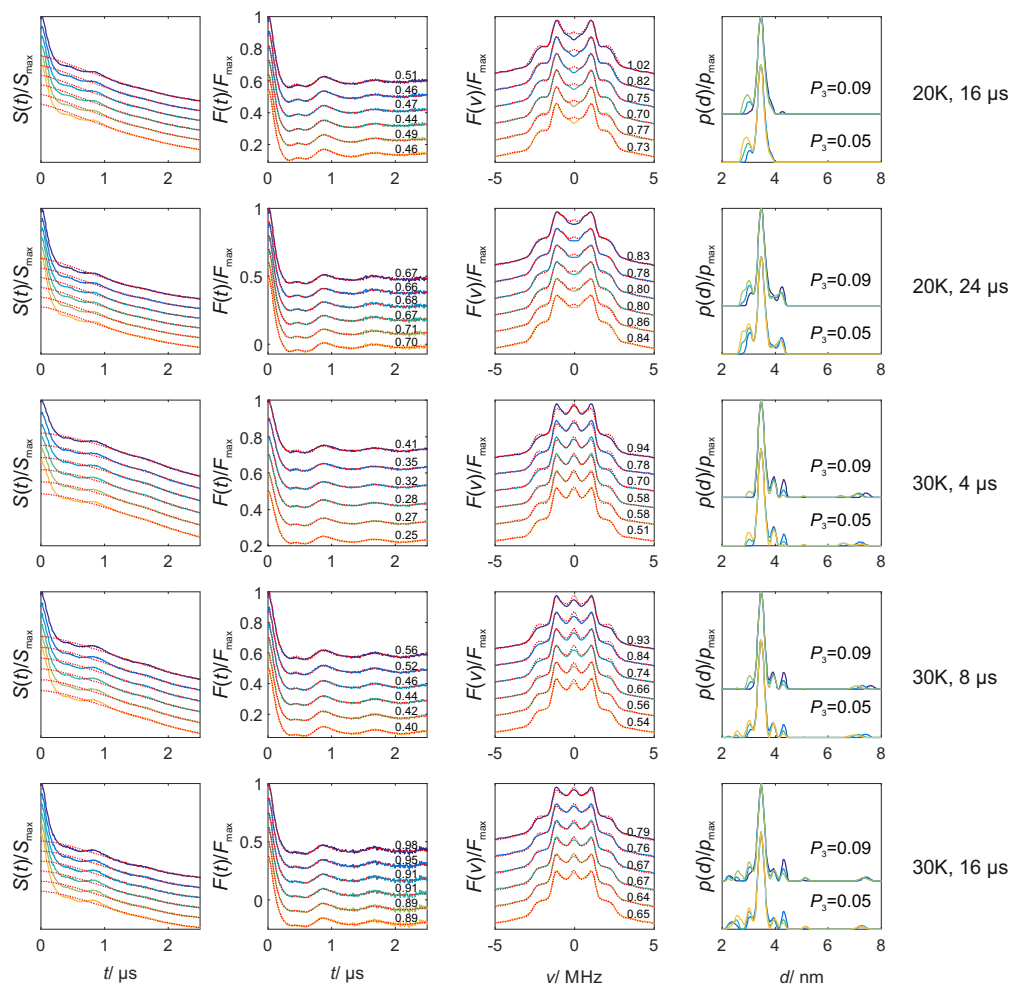
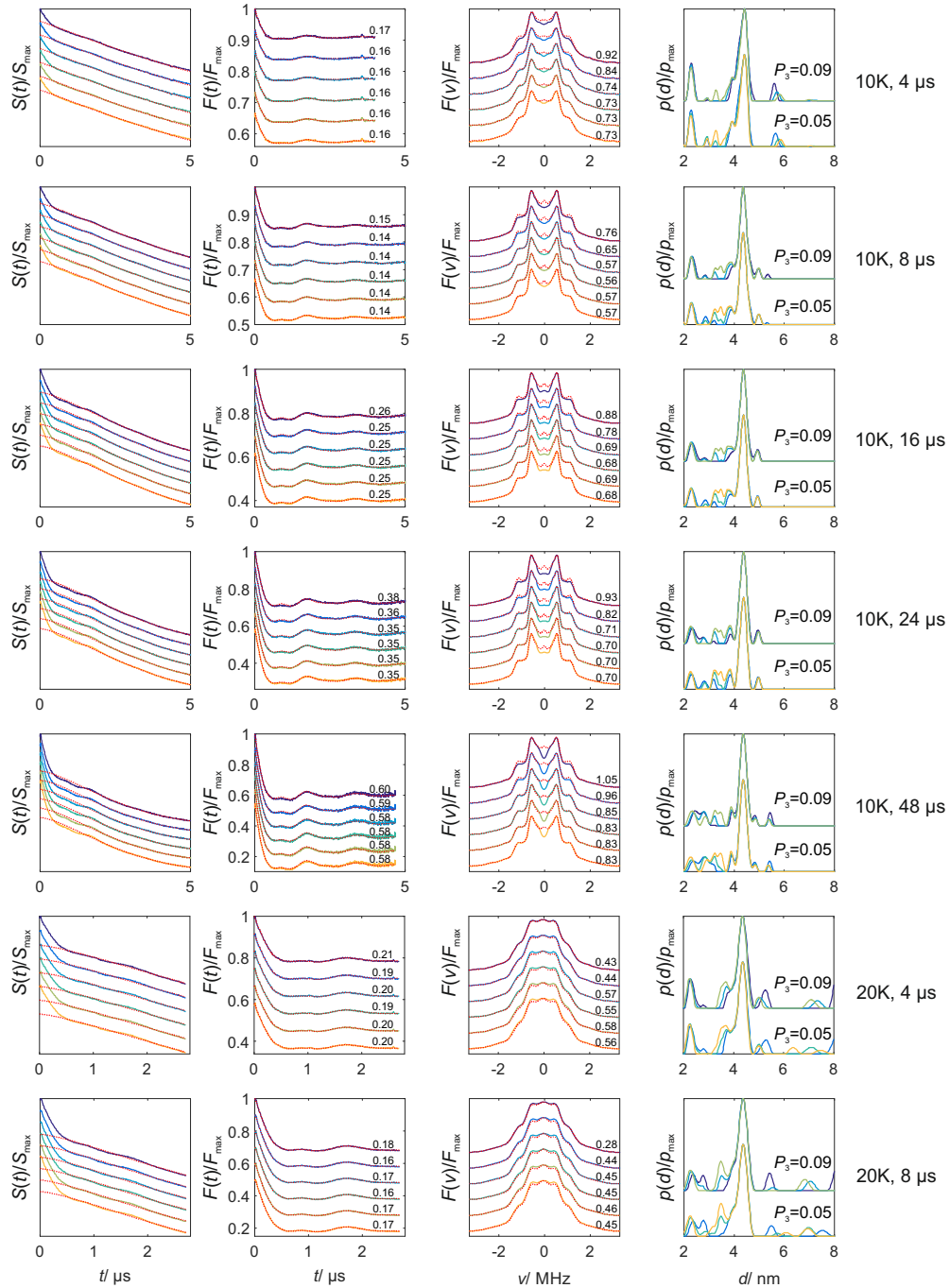


Figure E.18. Calibration for Gd-ruler 1_3 in W band. Rows: Variation of overtone coefficients for a given measurement. Colour coding is maintained from Figure E.17. From left to right: Primary data, form factor in time domain, form factor in frequency domain and distance distribution. Upper lines in distance distribution $P_3 = 0.09$. Lower lines in distance distribution $P_3 = 0.05$. Top to bottom: increasing mixing time and temperature – exact numbers are given next to each row. RMSD values (multiplied by a factor of 100) between the data trace and the different fits are given next to the corresponding trace. It is observed that artefact peaks do shift from left to right with respect to the mean distance as an increasing fraction of higher harmonics. On average the best compromise between distance distribution and form factor fit is obtained for $\{P_1 = 0.51, P_2 = 0.40, P_3 = 0.09\}$ or $\{P_1 = 0.55, P_2 = 0.40, P_3 = 0.05\}$. The spikes observed in the two upper rows at 2 or 4 μs are most likely artefacts remaining from crossing echoes due to the incomplete decay of the transverse magnetization during the mixing block as the mixing time (4 or 8 μs) is relatively short compared to the phase memory time ($\approx 10 \mu\text{s}$).



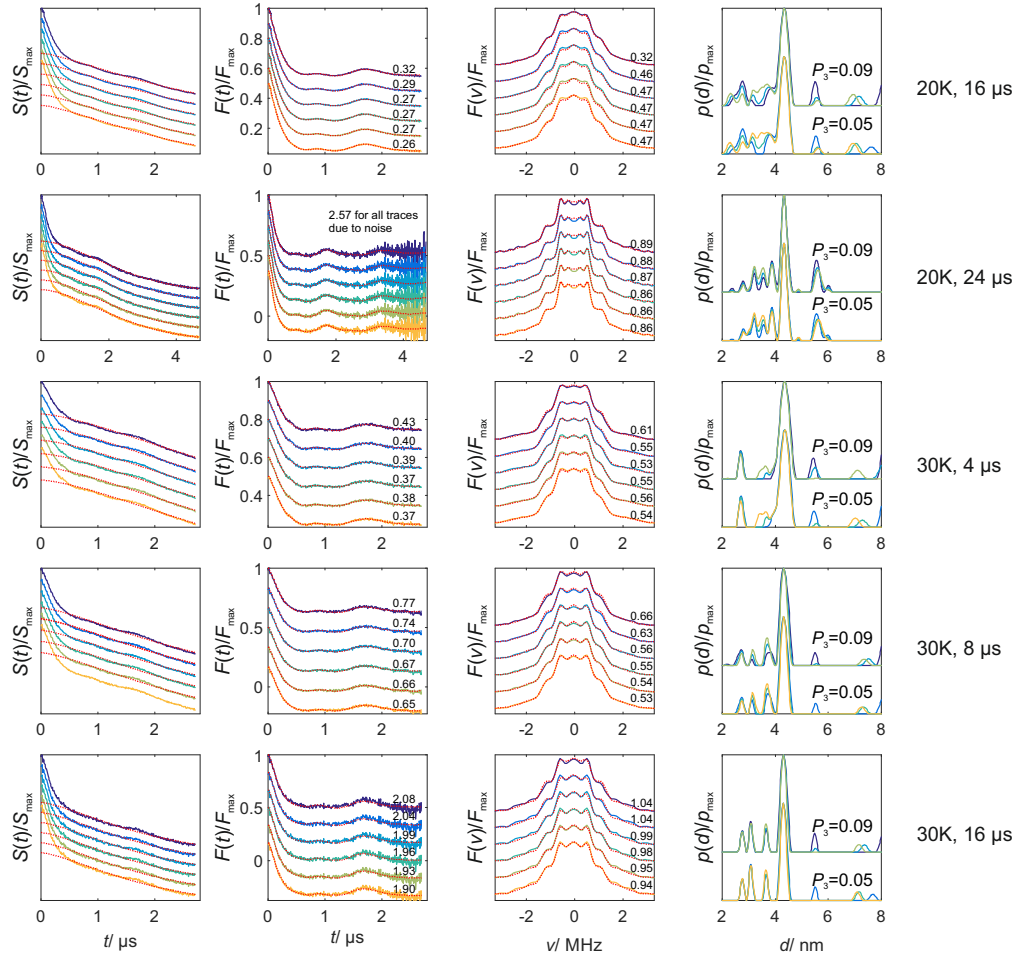


Figure E.19. Calibration for Gd-ruler 2_2 in W band. Rows: Variation of overtone coefficients for a given measurement. Colour coding is maintained from Figure E.17. From left to right: Primary data, form factor in time domain, form factor in frequency domain and distance distribution. Upper lines in distance distribution $P_3 = 0.09$. Lower lines in distance distribution $P_3 = 0.05$. Top to bottom: increasing mixing time and temperature – exact numbers are given next to each row. RMSD values (multiplied by a factor of 100) between the data trace and the different fits are given next to the corresponding trace. On average, it can be observed that artefact peaks do shift from left to right with respect to the mean distance for assuming an increasing fraction of higher harmonics. The best compromise between distance distribution and form factor fit is obtained for $\{P_1 = 0.51, P_2 = 0.40, P_3 = 0.09\}$.

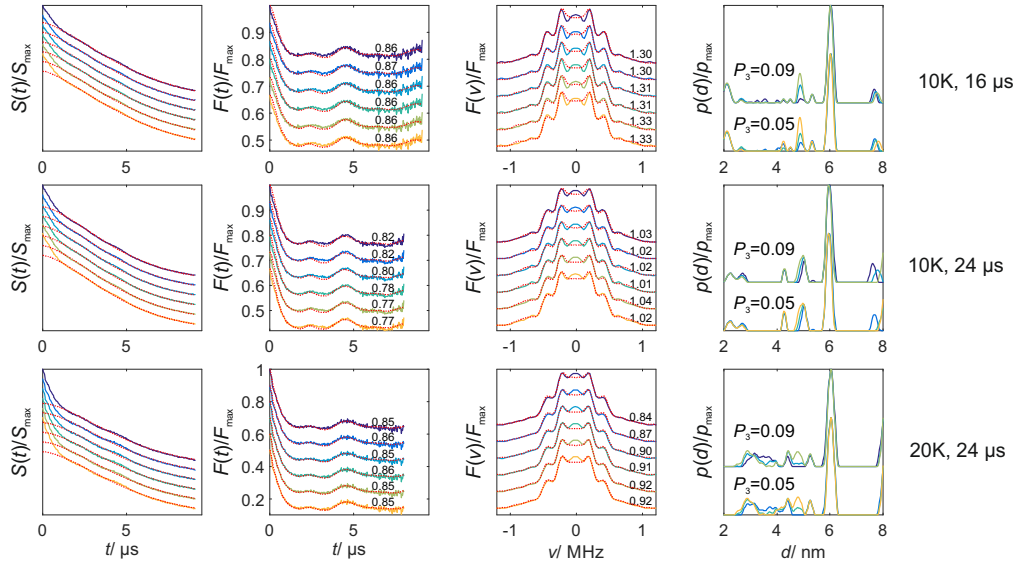


Figure E.20. Calibration for Gd-ruler 1_7 in W band. Rows: Variation of overtone coefficients for a given measurement. Colour coding is maintained from Figure E.17. From left to right: Primary data, form factor in time domain, form factor in frequency domain and distance distribution. Upper lines in distance distribution $P_3 = 0.09$. Lower lines in distance distribution $P_3 = 0.05$. Top to bottom: increasing mixing time and temperature – exact numbers are given next to each row. RMSD values (multiplied by a factor of 100) between the data trace and the different fits are given next to the corresponding trace. In the cases presented here, it can be observed that artefact peaks do not shift from left to right with respect to the mean distance, but only decrease in intensity for assuming an increasing fraction of higher harmonics. The best compromise between distance distribution and form factor fit is obtained for $\{P_1 = 0.45, P_2 = 0.46, P_3 = 0.09\}$ or $\{P_1 = 0.49, P_2 = 0.46, P_3 = 0.05\}$. Nevertheless, distance analysis using $\{P_1 = 0.51, P_2 = 0.40, P_3 = 0.09\}$ gives reasonable results in all cases.

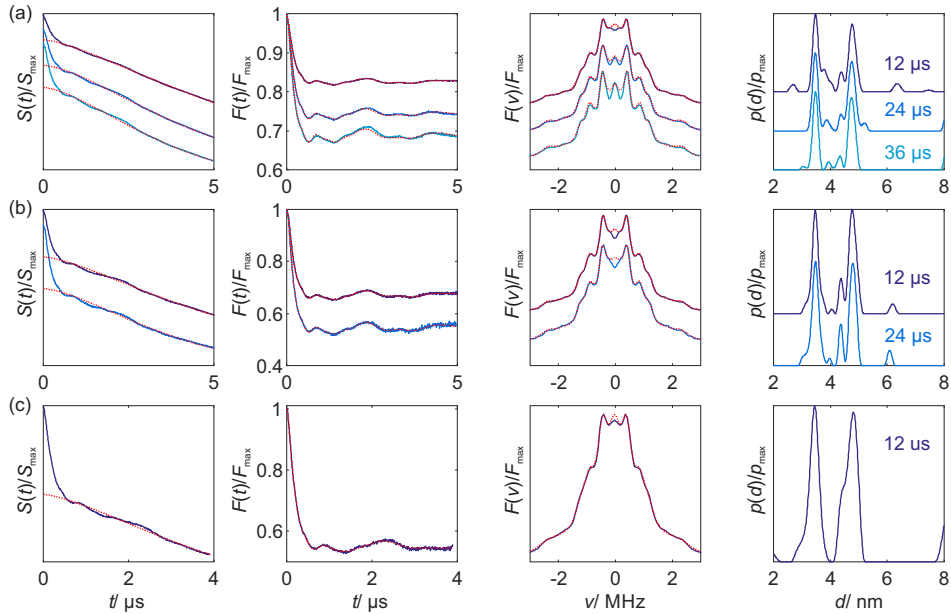


Figure E.21. Data for Gd-ruler 1_5 in W band. Raw data was truncated for the bump artefact at zero time. From left to right: Primary data, form factor in time domain, form factor in frequency domain and distance distributions using coefficients $\{P_1 = 0.51, P_2 = 0.40, P_3 = 0.09\}$. Form factors and distance distributions remain rather stable for different temperatures and mixing times. (a) 10 K, (b) 20 K, (c) 30 K, (d) field dependence at 10 K (24 μ s mixing time) and (e) field dependence at 20 K (24 μ s mixing time).

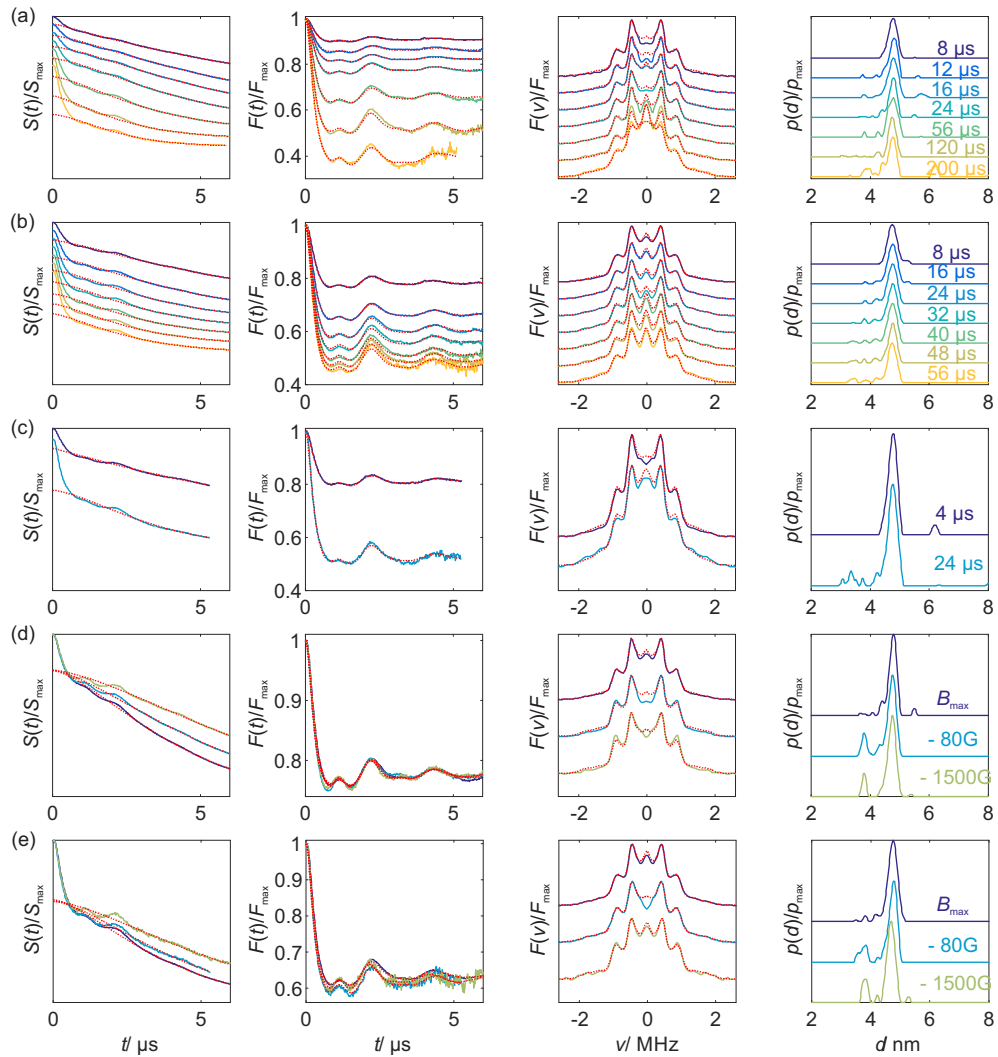


Figure E.22. Data for the mixture of Gd-rulers₁₃ and ₁₅ in W band. From left to right: Primary data, form factor in time domain, form factor in frequency domain and distance distribution using the set of coefficients $\{P_1 = 0.51, P_2 = 0.40, P_3 = 0.09\}$. Form factors and distance distribution remain rather stable for different temperatures and mixing times. (a) 10 K, (b) 20 K and (c) 30 K.

Supplementary Information to Chapter 9

F.1. Simulated distance distributions and protein sequence

The respective residues were selected for in *silico spin* labelling using the 3D-NMR structures of RBD1, RBD2 and RBD34 (pdb 2AD9, 2ADB, 2ADC).³²¹ Simulations of the distance distributions between the selected site pairs were done with the software Multiscale Modeling of Macromolecules (MMM).²⁹¹

Structure	pdb code	$\langle r \rangle$ / nm	r_{\max} / nm	$\sigma(r)$ / nm
RBD1	2AD9	3.13	3.25	0.41
T71C/T109C	1SJQ	2.70	2.90	0.52
	2N3O	3.31	3.35	0.47
RBD2	2ADB	2.22	2.40	0.42
S205C/S240C	1SJR	2.24	2.65	0.41
	3ZZY	2.17	2.40	0.41
RBD34	2ADC	4.51	4.60	0.40
Q388C/S475C	2EVZ	4.54	4.60	0.36

Table F.1. Analysed simulated distance distributions of all existing RBD structures of PTBP1. Mean distances $\langle r \rangle$, peak maxima (r_{\max}) and standard deviations $\sigma(r)$ were determined for the respective labelling sites using the spin label Gd-DOTA.

In total, three solution-NMR structures exist for RBD1 (pdb 2AD9, 1SJQ, 2N3O).^{321;322} In case of RBD2, two solution-NMR structures (pdb 2ADB, 1SJR) and one X-ray diffraction (XRD) structure (pdb 3ZZY) were determined and for RBD34 two solution-NMR structures (pdb 2ADC, 2EVZ).^{321;323;324} A comparison of the different structures of the single RBDs, determined by XRD and/or solution NMR, showed that the Gd-DOTA-simulated distance distributions for each RBD do not differ significantly as described recently (see Table F.1).¹⁹² The described similarities of all the simulated distance distributions for all existing RBD structures indicate that the presence of the short 5'-CUCUCU-3' RNA parts, which are included in the NMR structure determination of RBD1 (pdb 2AD9), RBD2 (2ADB) and RBD34 (2ADC), have no impact on the simulated spin clouds and therefore on the spin-to-spin distance distributions, which are shown in Figure F.1. Further, the respective sites where chosen to be close or within the α -helices oriented towards the opposite site of the RNA molecules.

Protein sequences in form of the one-letter amino-acid code of the studied protein mutants are given below. Mutations are marked in green.

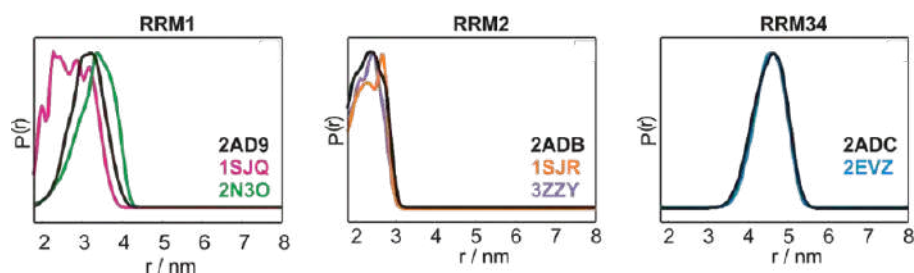


Figure F.1. Simulated distance distributions of all existing RBD structures of PTBP1.

RBD1(49-146):

GNDSKKFKGDSRSAGVPSRVIIHRLKLPIDV**T(71)**EGEVISLGLPFGKVTNLLML
 KGKNQAFIEMNTEEAAN**T(109)**MVNYTTSVTPVLRGQPIYIQFSNHKELKTD
 SSPNQARAQAALQAVNSVQSGNL

RBD2 (172-298):

AGQSPVLRRIIVENLFYPVTLVDLHQIFS**S(205)**KFGTVLKIITFTKNNQFQALLQY
 ADPVSAQHAKLS**(240)**LDGQNIYNASSTLRIDFSKLTSLNVKYNNDKSRDYTRP
 DLPSGDSQPSLDQTMAAAFGLSVPNVH GALAPLAIPSA

RBD34 (324-531):

GSHMGRIAIPGLAGAGNSVLLVSNLNERVTPQSLFILFGVYGDVQRVKILFNK
 KENALVQMADGNQA**Q(388)**LAMSHLNGHKLHGKPIRITLSKHQNVQLPREGQ
 EDQGLTKDYGNSPLHRFKKPGSKNFQNFPPSATLHLSNIPPSVSEEDLKVLF
S(475)SNGGVVKGFKFFQKDRKMALIQMGSVEEAVQALIDLHNHDLGENHHL
 RVSFSKSTI

F.2. Relaxation measurements for Mn-based rulers

Figure F.2 shows relaxation times measured for the Mn-ruler **3**₁ (ligand = DOTA) in W band. For both T_1 and T_m some transition dependence is observed. For the Mn-PyMTA-based rulers only one set of longitudinal relaxation data is available with respect to field dependencies. It does not exhibit a significant field dependence with respect to T_1 (Figure F.2(c)).

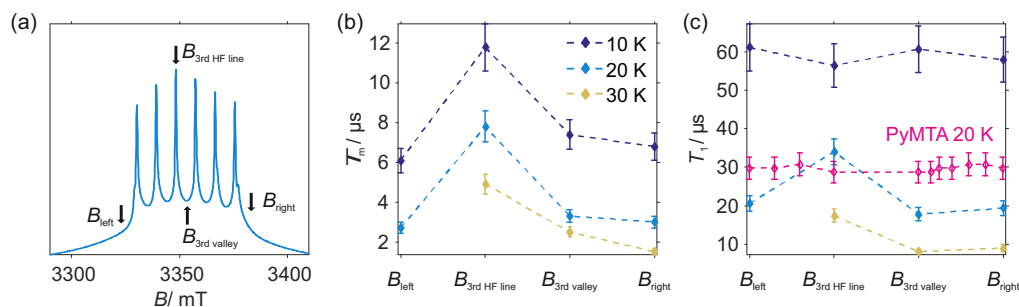


Figure F.2. Transition dependent relaxation in Mn-ruler **3**₃ (ligand=DOTA) in W band. (a) EDEPR at 30 K and marked detection positions, (b) phase memory times T_m given as 1/e time at 10 - 30 K, (c) longitudinal relaxation times T_1 given as 1/e time at 10 - 30 K. Pink lines give field-dependent longitudinal relaxation for the Mn-ruler **1**₅ (ligand = PyMTA) at 20 K and W band.

F.3. Optimization of pre-polarization pulses

Frequency-swept pulses were optimized using the following scheme:¹¹⁷ first the pulse offset was determined by variation of the offset of linear up and down chirps with a bandwidth of 750 MHz ($t_p = 1 \mu\text{s}$, 30 ns rise time), while detecting a standing Hahn echo (Figure F.3(a, c, e)). The linear chirp at the offset position with highest signal intensity was then chosen as optimal. Second, the bandwidth of the linear chirps was varied by modifying the starting frequency of the linear chirp (Figure F.3(b, d, f)).

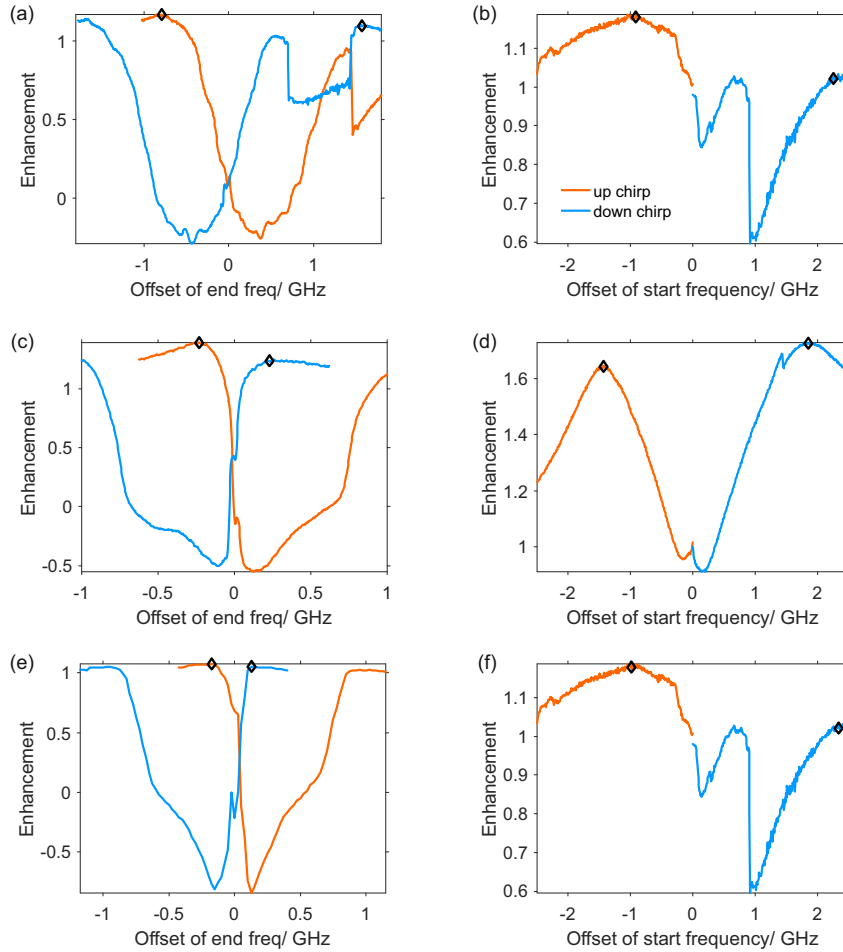


Figure F.3. Two-step optimization of pre-polarization pulses. (a-b) Mn-ruler **1**₅ at 20 K, Q band; (c, d) Gd-ruler **1**₃ at 20 K, Q band; (e, f) Gd-ruler **1**₃ at 20 K, W band. (a, c, e) Determination of final and (b, d, f) of initial frequency of linear chirp pulses. Orange: up-chirp (low to high frequency), blue: down-chirp (high to low frequency). The selected positions are marked by black diamonds.

Figure F.4 shows standing echo traces with and without pre-polarization pulses. Such traces are valuable to estimate a sample heating transient as well as noise amplification. No significant noise amplification can be observed in Q band. Some noise amplification is present in W band, which reduced the sensitivity compared to the signal enhancement. No significant heating transient can be observed in W band (2 W microwave power) or for the Mn(II) sample. Some heating transient are observed for the Gd-ruler **1**₃ in Q band (200 W microwave power). However, they are almost decayed by the zero time of the RIDME experiment and such transient

were not found to influence the form factor shape. Heating transients can be reduced by a larger number of shots per point or pre-heating as detailed in Ref.¹¹⁷.

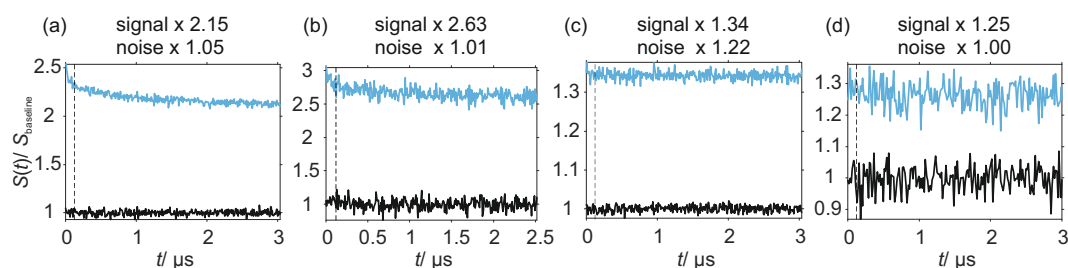


Figure F.4. Standing echo with (blue) and without (black) pre-polarization pulse at 20 K. The dashed vertical line marks the zero time of the RIDME experiment. (a) Gd-ruler $\mathbf{1}_3$ in Q band, detected at B_{\max} , $T_{\text{mix}} = 50 \mu\text{s}$; (b) Gd-ruler $\mathbf{1}_3$ in Q band, detected at $B_{\max} -150 \text{ G}$, $T_{\text{mix}} = 15 \mu\text{s}$; (c) Gd-ruler $\mathbf{1}_3$ in W band, detected at B_{\max} , $T_{\text{mix}} = 45 \mu\text{s}$; (d) Mn-ruler $\mathbf{1}_5$ in Q band, detected at maximum enhancement position, $T_{\text{mix}} = 20 \mu\text{s}$.

F.4. Calibration of overtone coefficients for Mn(II)

For better comparison of the form factors obtained for different mixing times and temperatures Figure F.5 shows a modulation depth scaled representation. Careful investigation shows that the form factors are indeed almost identical at various mixing times, though with changing temperature small deviations can be observed. This suggests the use of different overtone coefficients for analysis. Nevertheless, deviations between the 'optimal' coefficient are within 5% and an overall analysis using the same set of coefficients still leads to the anticipated mean distance with relatively low level of artefacts. This best set of coefficients $P_1 = 0.41$, $P_2 = 0.50$ and $P_3 = 0.09$ indicates nearly the same contribution of the main dipolar frequency and its first overtone (double frequency) to the dipolar evolution data. The contribution of the triple frequency is relatively small ($P_3 = 0.09$) but cannot be neglected.

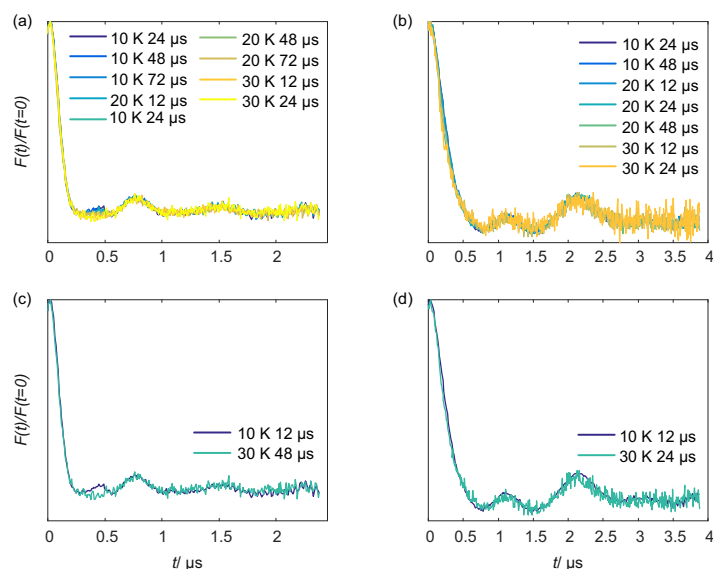


Figure F.5. Modulation-depth scaled RIDME form factors acquired in W band (94 GHz) for the Mn-rulers $\mathbf{1}_3$ and $\mathbf{1}_5$ in frozen solution of 1:1 D_2O /glycerol- D_8 at different temperatures. (a, b) Complete data set for the Mn-rulers $\mathbf{1}_3$ and $\mathbf{1}_5$, respectively. (c, d) Time traces with largest deviation for Mn-rulers $\mathbf{1}_3$ and $\mathbf{1}_5$. The strongest differences are observed between different temperatures.

The influence of the harmonic overtone coefficients is shown in Figure F.6 – Figure F.11. In most cases the cleanest distance distribution does not correspond to the best fit of time- and frequency-domain data. For the Mn-ruler $\mathbf{1}_3$ it is seen that with growing higher harmonics the form factor fit quality improves at the cost of intensification of the artefact at approximately 4 nm. E.g. at 10 K time- and frequency-domain data are best fitted with $P_2 = 0.50$ and $P_3 = 0.07$ or 0.09 , while the lowest artefact level is obtained for $P_2 = 0.46$ and $P_3 = 0.06$. Yet, higher coefficients do not improve the fitting, but clearly enlarge the artefact. Furthermore, precise determination of P_1 , P_2 , P_3 values is hampered by minor deviations in fit quality upon modification of the coefficients. For the 4.7 nm model compound the picture appears to be reversed. Cleaner distance distributions are obtained for coefficients that overfit the P_2 contribution in frequency domain. The coefficients for best fitted form factors intensify the artefact around 4 nm.

It is important to note that the artefact appearance is sensitive to background correction and a very 'clean' distance distribution can also be obtained with a clearly incorrect background fit as shown in Figure E.16 in the previous chapter. Besides the background correction, artefacts are also caused by noise or sample imperfections and thus cannot be suppressed by overtone correction. Nevertheless, these additional imperfections might be difficult to identify when they appear at the same distances as the overtone artefacts. In the following set of fitted RIDME data one can see that for the Mn-ruler $\mathbf{1}_3$ there seems to be a small trend towards lower overtone coefficients with increasing temperature.

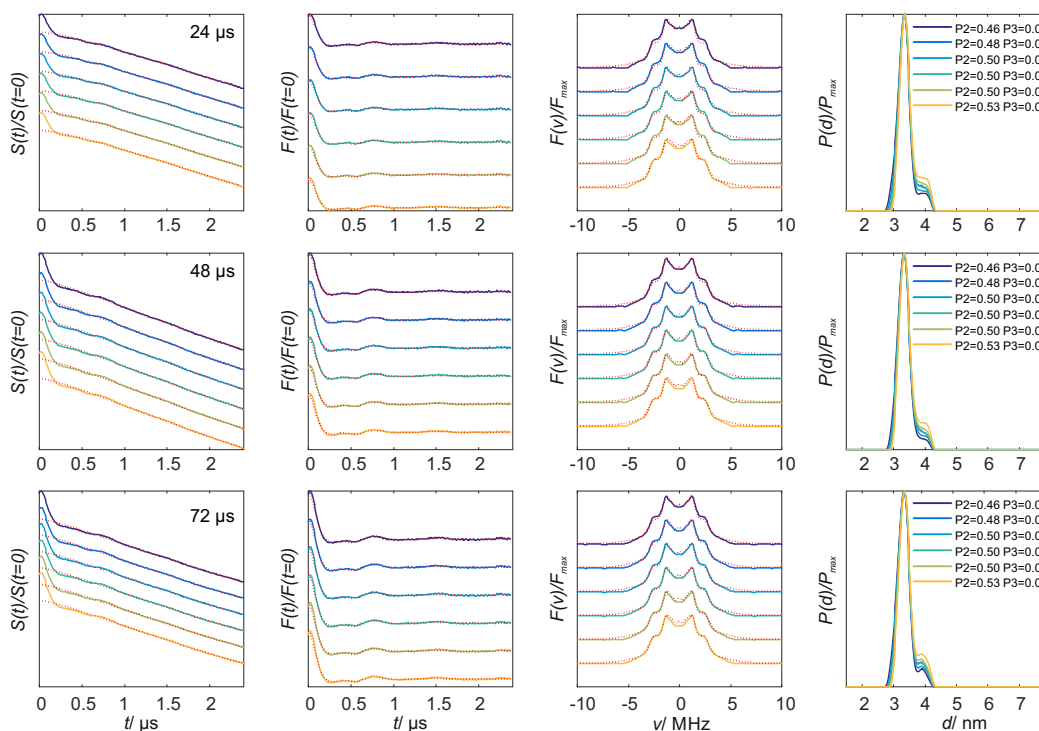


Figure F.6. Variation of overtone coefficients for the Mn-ruler $\mathbf{1}_3$ with increasing mixing times from top to bottom acquired in W band (94 GHz) in frozen solution of 1:1 D_2O /glycerol- D_8 at 10 K. Left to right: Primary data together with background fits, background corrected form factors and their corresponding form factor fit resulting from Tikhonov regularization, corresponding frequency domain spectra and extracted distance distributions. It is seen that the cleanest distance distribution ($P_2 = 0.46$ $P_3 = 0.06$) does not correspond to the best fit. With increasing higher harmonics, the fit quality improves however the artefact at approximately 4 nm is increases as well. Time and frequency domain are best fitted with $P_2 = 0.50$ and $P_3 = 0.07$ or 0.09 . Yet higher coefficients do not improve the fitting, but clearly increase the artefact level.

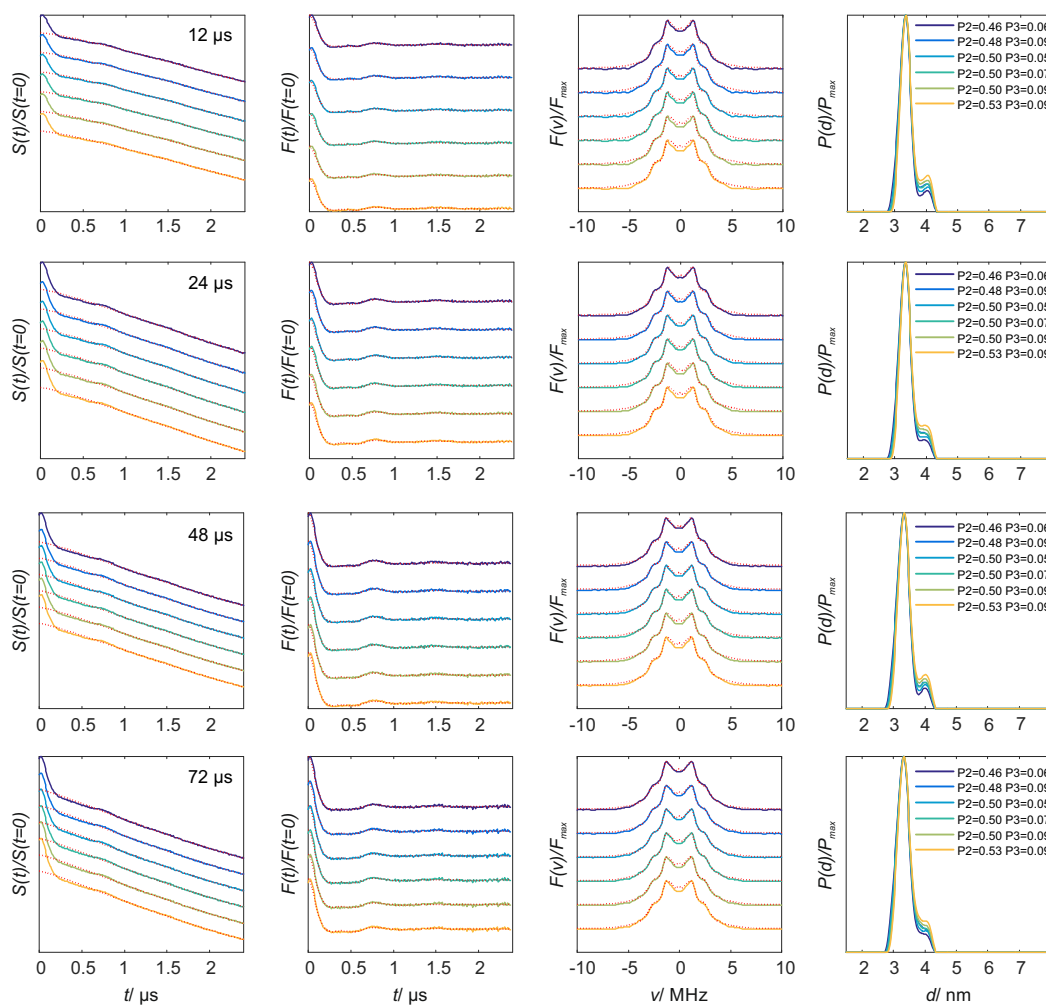


Figure F.7. Variation of overtone coefficients for the Mn-ruler 1_3 with increasing mixing times (from top to bottom) acquired in W band (94 GHz) in frozen solution of 1:1 D_2O /glycerol- D_8 at 20 K. Left to right: Primary data together with background fits, background corrected form factors and their corresponding form factor fit resulting from Tikhonov regularization, corresponding frequency domain spectra and extracted form distance distributions. It is seen that the cleanest distance distribution ($P_2 = 0.46$ $P_3 = 0.06$) does not correspond to the best fit. With increasing higher harmonics, the fit quality improves however the artefact at approx. 4 nm is increased as well. Time and frequency domain are best fitted with $P_2 = 0.50$ and $P_3 = 0.07$ or 0.05. Yet higher coefficients do not improve the fitting, but clearly increase the artefact level.

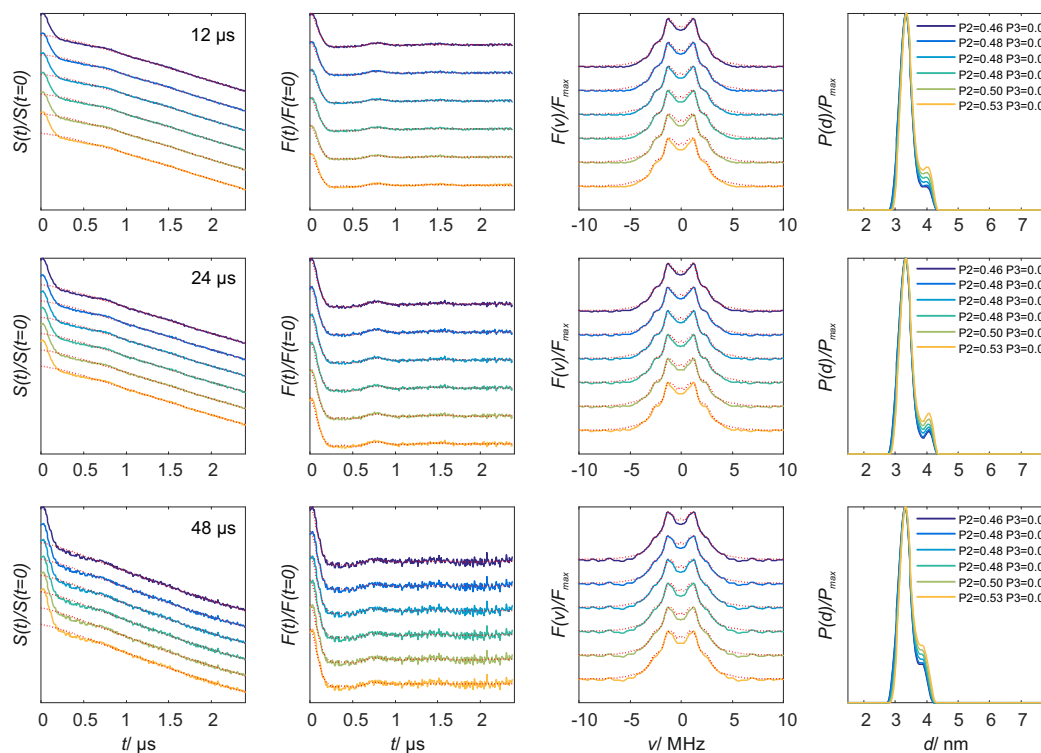


Figure F.8. Variation of overtone coefficients for the Mn-ruler 1_3 with increasing mixing times (from top to bottom) acquired in W band (94 GHz) in frozen solution of 1:1 D_2O /glycerol- D_8 at 30 K. Left to right: Primary data together with background fits, background corrected form factors and their corresponding form factor fit resulting from Tikhonov regularization, corresponding frequency domain spectra and extracted distance distributions. It is seen that the cleanest distance distribution ($P_2 = 0.46$ $P_3 = 0.06$) does not correspond to the best fit. Time and frequency domain are best fitted with $P_2 = 0.48$ and $P_3 = 0.07$ or 0.05 . Yet higher coefficients do not improve the fitting, but clearly increase the artefact level.

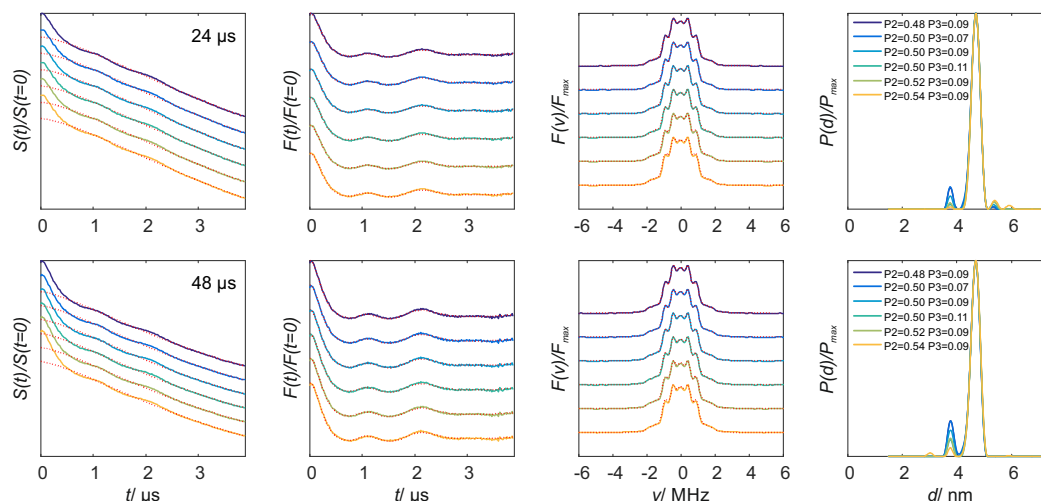


Figure F.9. Variation of overtone coefficients for the Mn-ruler 1_5 with increasing mixing times (from top to bottom) acquired in W band (94 GHz) in frozen solution of 1:1 D_2O /glycerol- D_8 at 10 K. Left to right: Primary data together with background fits, background corrected form factors and their corresponding form factor fit resulting from Tikhonov regularization, corresponding frequency domain spectra and extracted distance distributions. It is seen that the cleanest distance distribution ($P_2 = 0.52$ $P_3 = 0.09$) does not correspond to the best fit ($P_2 = 0.50$ $P_3 = 0.09$).

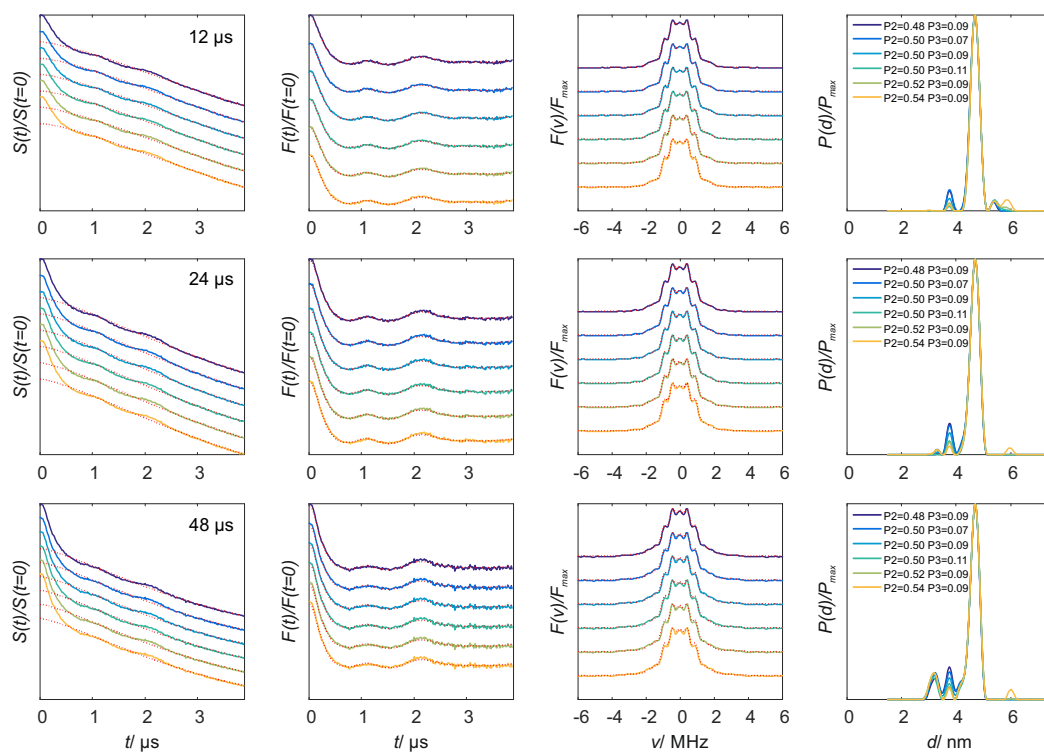


Figure F.10. Variation of overtone coefficients for the Mn-ruler 1_5 with increasing mixing times (from top to bottom) acquired in W band (94 GHz) in frozen solution of 1:1 D_2O /glycerol- D_8 at 20 K. Left to right: Primary data together with background fits, background corrected form factors and their corresponding form factor fit resulting from Tikhonov regularization, corresponding frequency domain spectra and extracted distance distributions. It is seen that the cleanest distance distribution ($P_2 = 0.52$ $P_3 = 0.09$) does not correspond to the best fit ($P_2 = 0.50$ $P_3 = 0.07$ or even $P_2 = 0.48$ $P_3 = 0.09$).

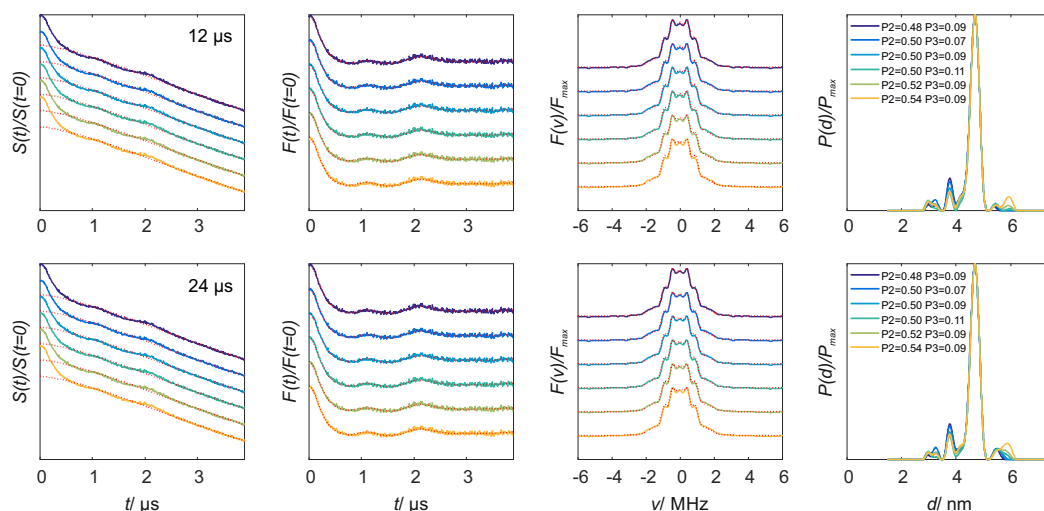


Figure F.11. Variation of overtone coefficients for the Mn-ruler 1_5 with increasing mixing times (from top to bottom) acquired in W band (94 GHz) in frozen solution of 1:1 D_2O /glycerol- D_8 at 20 K. Left to right: Primary data together with background fits, background corrected form factors and their corresponding form factor fit resulting from Tikhonov regularization, corresponding frequency domain spectra and extracted distance distributions. It is seen that the cleanest distance distribution ($P_2 = 0.52$ $P_3 = 0.09$) does not correspond to the best fit ($P_2 = 0.50$ $P_3 = 0.07$ or even $P_2 = 0.48$ $P_3 = 0.09$).

F.4.1. Field dependence in Mn-PyMTA based RIDME measurements

Figure F.12 shows a large set of RIDME measurements for the Mn-ruler $\mathbf{1}_3$ detected at different field positions. As described in Chapter 9, the modulation depth is higher and relatively constant for detection positions away from the central transition. For detection at different hyperfine lines of the central transition, modulation depth deviations up to 0.1 are observed. Distance distribution obtained from detection at the low-field side of the Mn(II) ED EPR spectra, enclose an additional shorter distance contribution.

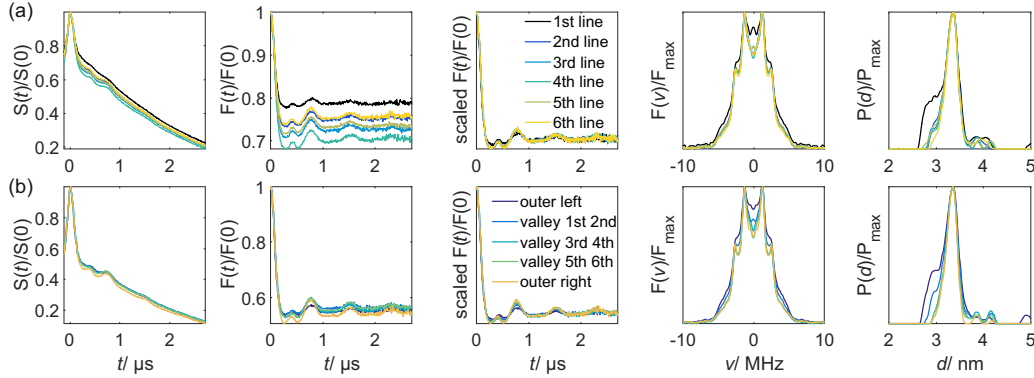


Figure F.12. W-band RIDME measurements for the Mn-ruler $\mathbf{1}_3$ (ligand = PyMTA) at 20 K. Detected (a) at the six hyperfine lines and (b) outside of the hyperfine lines as indicated in the legend. From left to right: Raw data, form factors in time domain, scaled form factors in time-domain, form factors in frequency domain; resulting distance distributions with $P_2 = 0.5$, $P_3 = 0.09$.

Figure F.13 shows additional analysis of overtone frequencies in measurements at the low-field side of the Mn(II) EDEPR absorption spectra (presented for detection on 1st hyperfine line). The vertical lines indicate the positions of distance peaks corresponding to overtone frequencies. For both compounds, a distance peak at frequencies faster than the third harmonic can be observed. Half of this faster frequency matches the additional short distance shoulder of distance distributions. Therefore the amplitude of the short distance shoulder/peak increases upon inclusion of harmonic overtones and this peak is not suppressed. Thus, it does not seem to be related to a harmonic overtone contribution.

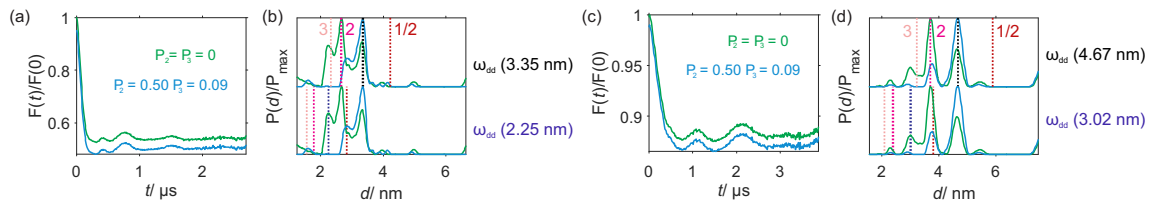


Figure F.13. Influence of harmonic overtones on distance distributions for the Mn-ruler $\mathbf{1}_n$ detected on the 1st hyperfine line. (a, b) $n = 3$ and (c, d) $n = 5$. (a, c) form factor in time domain; (b, d) resulting distance distributions with $P_2 = P_3 = 0$ (green trace) or $P_2 = 0.50$, $P_3 = 0.09$ (blue trace). The vertical coloured lines indicate distances from different frequency contributions: Black (top in subpanel) dipolar frequency corresponding to the expected distance, violet (bottom in subpanel) frequency corresponding to the short distance shoulder at 2.25 nm (ruler $\mathbf{1}_3$) and at 3.02 nm (ruler $\mathbf{1}_5$). The red lines mark half, the purple line double and the rose lines triple of the dipolar frequency.

F.5. RIDME in protonated solvent

Figure F.14 and F.15 show the dependence of RIDME traces on mixing time and detection position in Q and W band, respectively, for the Gd-ruler $\mathbf{1}_3$ (ligand = PyMTA) in 1:1 H₂O:glycerol. Note, the deviations in the frequency-domain data in Figure F.14(a, b) around ± 10 MHz are probably caused by echo-crossing artefact contributions around zero time of the experiment.

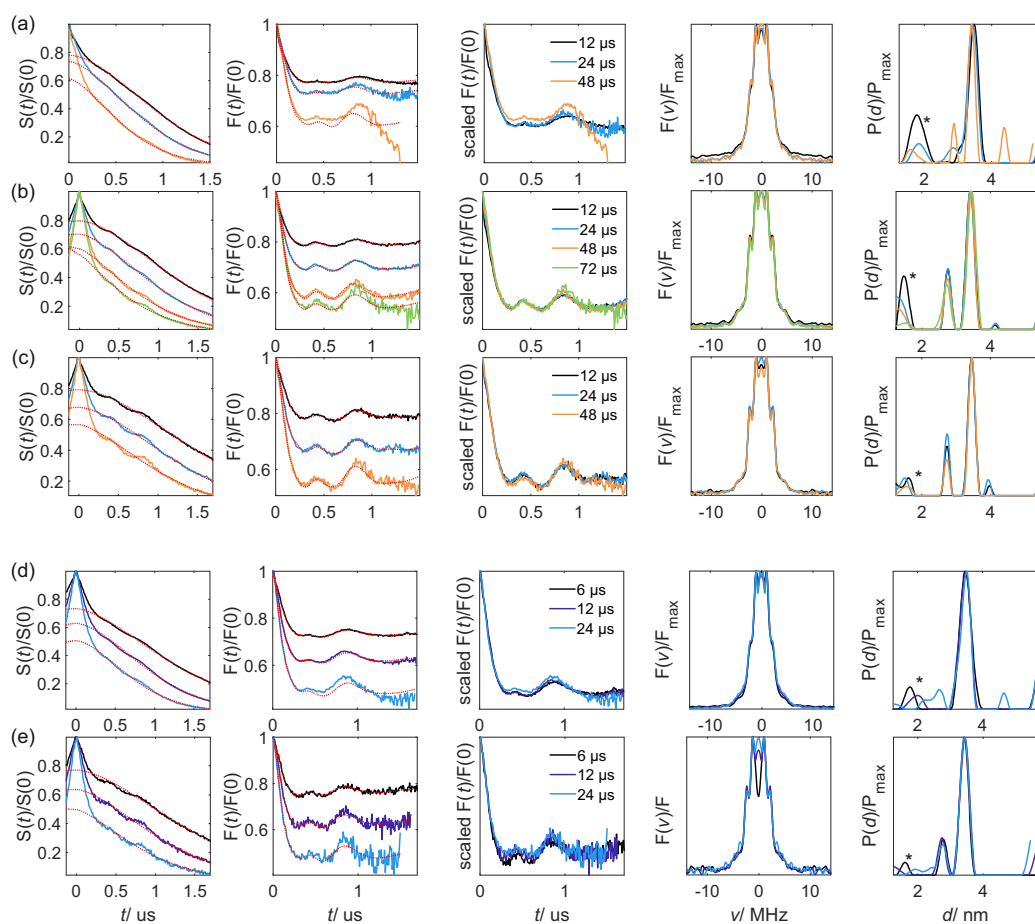


Figure F.14. W-band RIDME measurements on the Gd-ruler $\mathbf{1}_3$ (ligand = PyMTA) in 1:1 H₂O:glycerol. (a-c) 10 K, (d, e) 20 K. Detected (a, d) at maximum field B_{\max} and different mixing times (colour coded), (b, e) at $B_{\max} - 75$ G, (c) at $B_{\max} - 1000$ G. From left to right: Raw data and corresponding background fit (red dashed line), form factors in time domain and corresponding fits (red dashed lines), scaled form factors in time domain, form factors in frequency domain; resulting distance distributions with $P_2 = 0.4$, $P_3 = 0.09$. *echo-crossing artefact.

Background correction can be problematic in these samples, which leads to a high artefact level in distance distributions, as for example observed in RIDME traces detected at the central transition in Q band and at 10 K (Figure F.15(a)). In these samples for mixing times $\geq 50 \mu\text{s}$, the background decay becomes so steep that it becomes very difficult to separate the initial decay of the dipolar coupling from the background function. Further, the trace needs to be cut significantly with the result that one full oscillation of the primary dipolar frequency is just reached and the time trace is dominated by the second harmonic overtone frequency, which is believed to cause the over-representation of the resulting distance peak in the distance distributions. Therefore one has to be very careful calibrating overtone coefficients on samples with steep background decay and the mixing time should be reduced to be able to detect (at least) one and a half periods of the primary frequency of the dipolar oscillations even if it is already attenuated. Keep in mind that over- or under-correction of the background function was found to influence the overtone coefficients (Chapter 8, Figure 8.4).

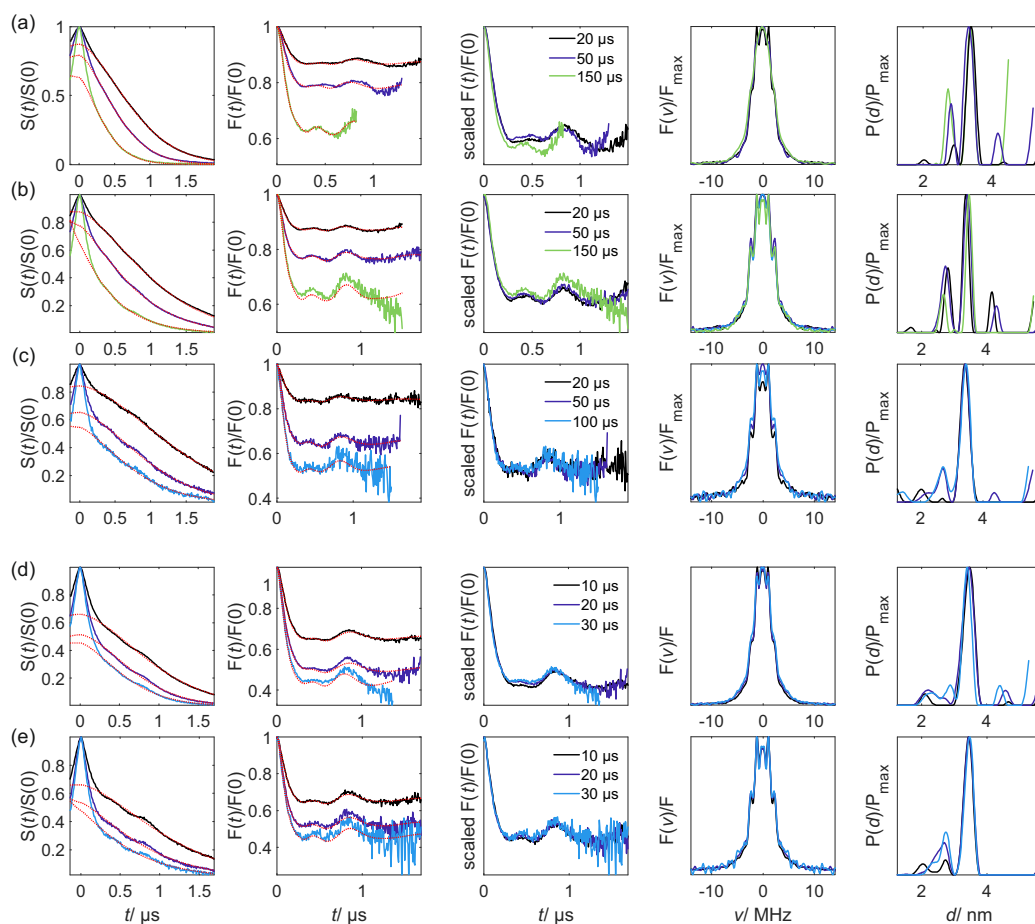


Figure F.15. Q-band RIDME measurements on the Gd-ruler $\mathbf{1}_3$ (ligand = PyMTA) in 1:1 H_2O :glycerol. (a-c) 10 K, (d, e) 20 K. Detected (a, d) at maximum field B_{max} and different mixing times (colour coded), (b, e) at $B_{\text{max}} - 150 \text{ G}$, (c) at $B_{\text{max}} - 1500 \text{ G}$. From left to right: Raw data and corresponding background fits (red dashed lines), form factors in time domain and corresponding fits (red dashed lines), scaled form factor in time-domain, form factors in frequency domain; resulting distance distributions with $P_2 = 0.4$, $P_3 = 0.09$.

Figure F.16 and F.17 show the same data for the Gd-ruler $\mathbf{1}_1$ in 1:1 H₂O:glycerol. Deviations between different mixing times seem to be caused by the performed background correction. Detection on satellite transitions increases the contribution of harmonic overtones for both rulers. This effect is much more pronounced in the short ruler compound ($\mathbf{1}_1$), for which detection at the central transitions yields almost overtone-free traces.

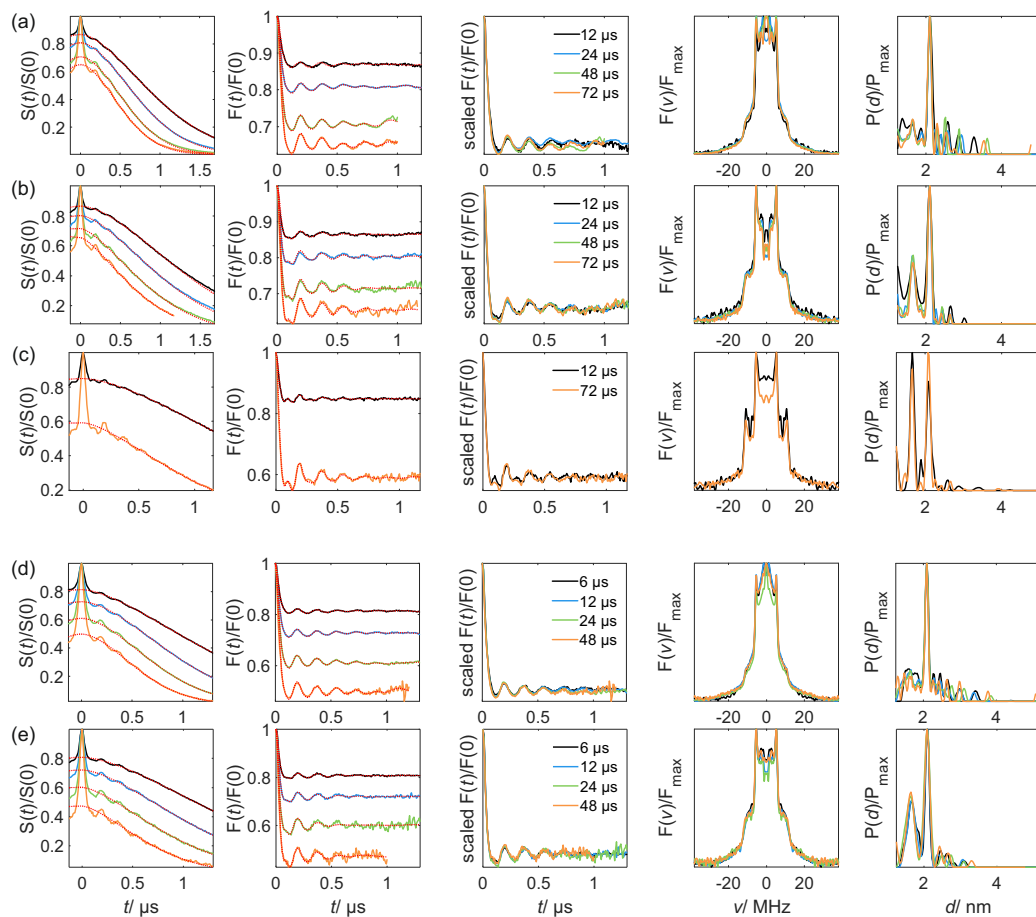


Figure F.16. W-band RIDME measurements on the Gd-ruler $\mathbf{1}_1$ (ligand = PyMTA) in 1:1 H₂O:glycerol. (a-c) 10 K, (d-f) 20 K. Detected (a, d) at maximum field B_{\max} and different mixing times (colour coded), (b, e) at $B_{\max} - 75$ G, (c, f) at $B_{\max} - 1000$ G. From left to right: Raw data and corresponding background fits (red dashed lines), form factor in time domain and corresponding fits (red dashed lines), scaled form factor in time-domain, form factors in frequency domain; resulting distance distributions with $P_2 = P_3 = 0$.

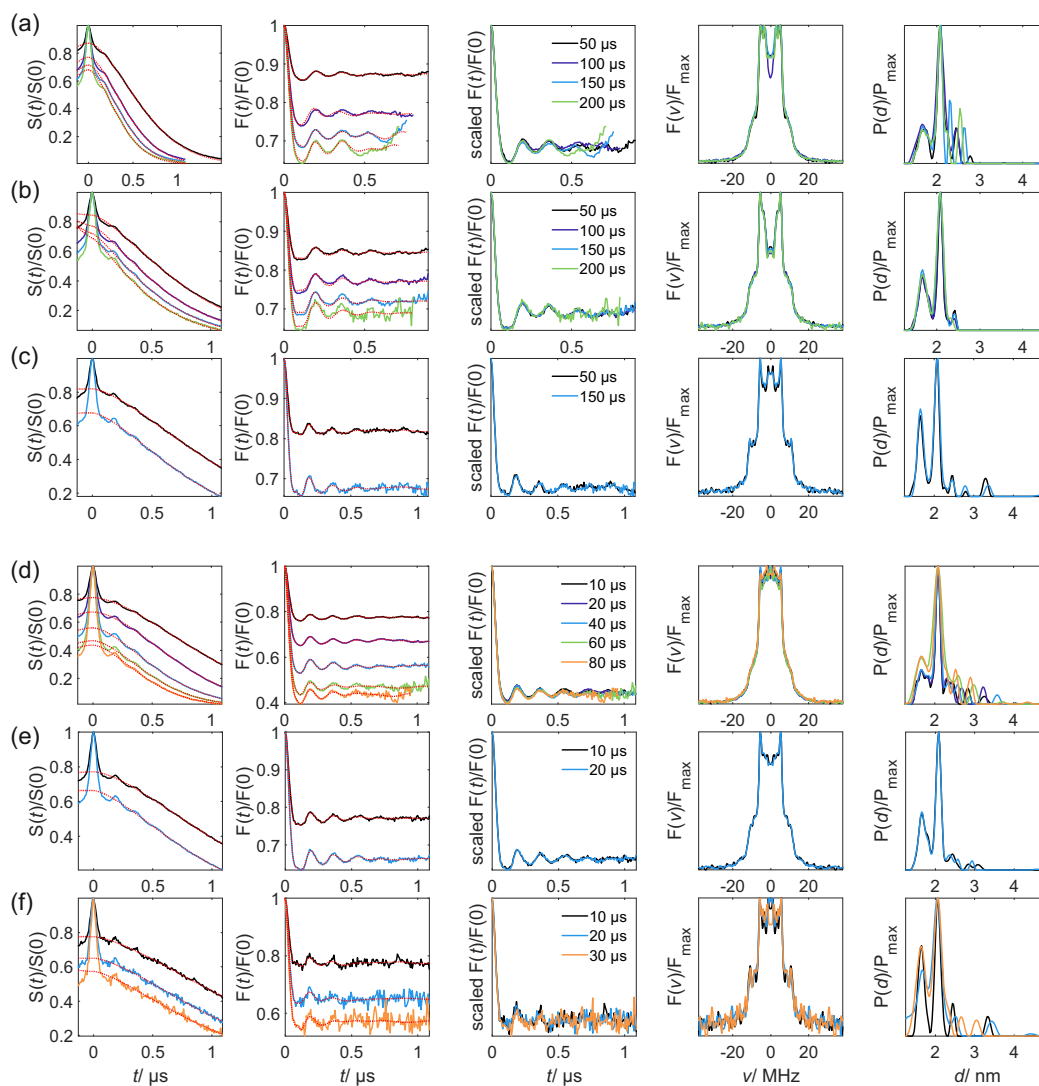


Figure F.17. Q-band RIDME measurements on the Gd-ruler $\mathbf{1}_1$ (ligand = PyMTA) in 1:1 H_2O :glycerol. (a-c) 10 K, (d-f) 20 K. Detected (a, d) at maximum field B_{max} and different mixing times (colour coded), (b, e) at $B_{\text{max}} - 150$ G, (c, f) at $B_{\text{max}} - 1500$ G. From left to right: Raw data and corresponding background fits (red dashed lines), form factors in time domain and corresponding fits (red dashed lines), scaled form factor in time-domain, form factors in frequency domain; resulting distance distributions with $P_2 = P_3 = 0$.

Figure F.18 shows Hahn-echo decays and inversion recovery data for the Gd-ruler $\mathbf{1}_3$ in 1:1 H₂O:glycerol in W band. Longitudinal relaxation is only slightly dependent on the detection position and similar in deuterated and protonated glasses (F.18(b)). On the other hand, phase memory times are strongly increased (F.18(a)). In protonated solvent at 10 K, the shape of the Hahn-echo decay is strongly transition dependent and spin-echo intensities becomes similar at different Gd(III) transition for times where the echo is decayed to approximately 10% of its initial value (black dashed lines). This effect is smaller at 20 K.

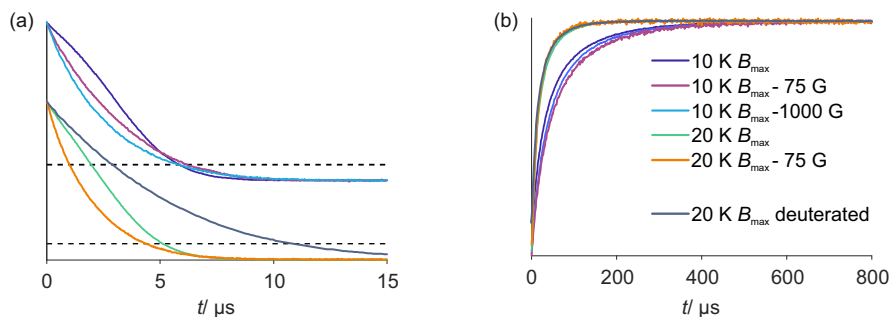


Figure F.18. W-band relaxation data for the Gd-ruler $\mathbf{1}_3$ in 1:1 H₂O:glycerol. (a) Hahn-echo decay. The black dashed lines mark the decay of the echo intensity to 10% of its initial value. (b) Inversion recovery. Measurement temperature and detection positions are colour coded. Measurements in 1:1 D₂O:glycerol-d₈ at 20 K are shown in dark grey.

F.6. Influence of ligand field

F.6.1. PymiMTA-based rulers

Figure F.19 shows EPR absorption spectra detected at 10 K. Based on Q-band absorption spectra, the spectral width of the Mn-ruler $\mathbf{2}$ should be larger than of the Mn-ruler $\mathbf{1}_3$ (Chapter 3). The sharp hyperfine sextet in addition to the broad envelop (Figure F.19(a)) is therefore assigned to free Mn(II) ions forming an hexa-aqua complex of small ZFS. Free Gd(III) ions have a spectral width rather similar to the PyMTA or PymiMTA complex (Figure F.19(b)).

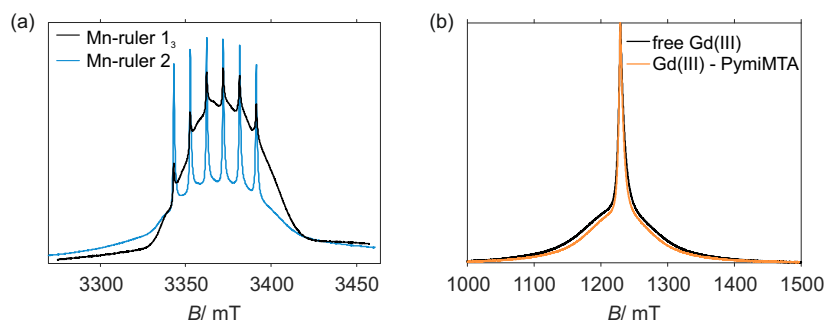


Figure F.19. W-band absorption spectra at 10 K. (a) Mn-ruler $\mathbf{1}_3$ (black, ligand = PyMTA) and Mn-ruler $\mathbf{2}$ (blue, ligand = PymiMTA). (b) Free Gd(III) (black) as well as the Gd-PymiMTA complex (orange).

Figures F.20 and F.21 show the influence of detection position and mixing time on the RIDME measurements for the Gd-ruler $\mathbf{2}$. No major deviations can be observed for primary data or extracted distance distributions at different mixing time and measurement temperature detected at the same transitions. Moving detection from the central to the satellite transitions does increase the contribution of harmonic overtones and a short distance peak appears. Note

that small variations are observed for the different form factors in frequency domain around ± 10 MHz, which most likely result from echo-crossing contributions around zero time.

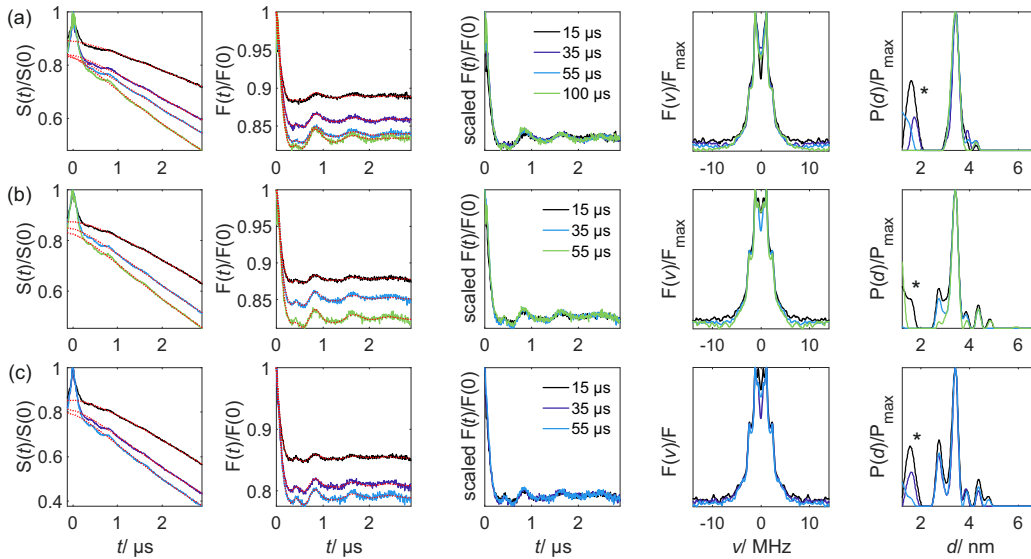


Figure F.20. W-band RIDME measurements on the Gd-ruler **2** (ligand = PymiMTA) at 10 K ($T_1 \simeq 32 \mu\text{s}$). Detected (a) at maximum field B_{max} and different mixing times (colour coded), (b) at $B_{\text{max}} - 50$ G, (c) at $B_{\text{max}} - 600$ G. From left to right: Raw data and corresponding background fits (red dashed lines), form factors in time domain and corresponding fits (red dashed lines), scaled form factor in time-domain, form factors in frequency domain; resulting distance distributions with $P_2 = 0.4$, $P_3 = 0.09$.

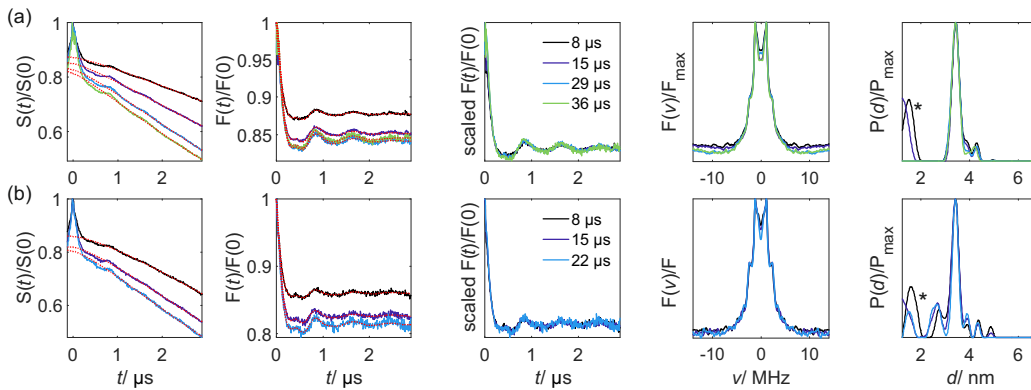


Figure F.21. W-band RIDME measurements on the Gd-ruler **2** (ligand = PymiMTA) at 20 K ($T_1 \simeq 22 \mu\text{s}$). (a) Detected at maximum field B_{max} and different mixing times (colour coded), (b) at $B_{\text{max}} - 50$ G. From left to right: Raw data and corresponding background fits (red dashed lines), form factors in time domain and corresponding fits (red dashed lines), scaled form factor in time-domain, form factors in frequency domain; resulting distance distributions with $P_2 = 0.4$, $P_3 = 0.09$.

Figure F.22 shows the corresponding data for the Mn-ruler **2**. Apart from a significantly reduced modulation depth for detection at the 3rd hyperfine line and a related higher level of echo-crossing artefacts in the time-domain data, no major deviations can be observed between different data sets.

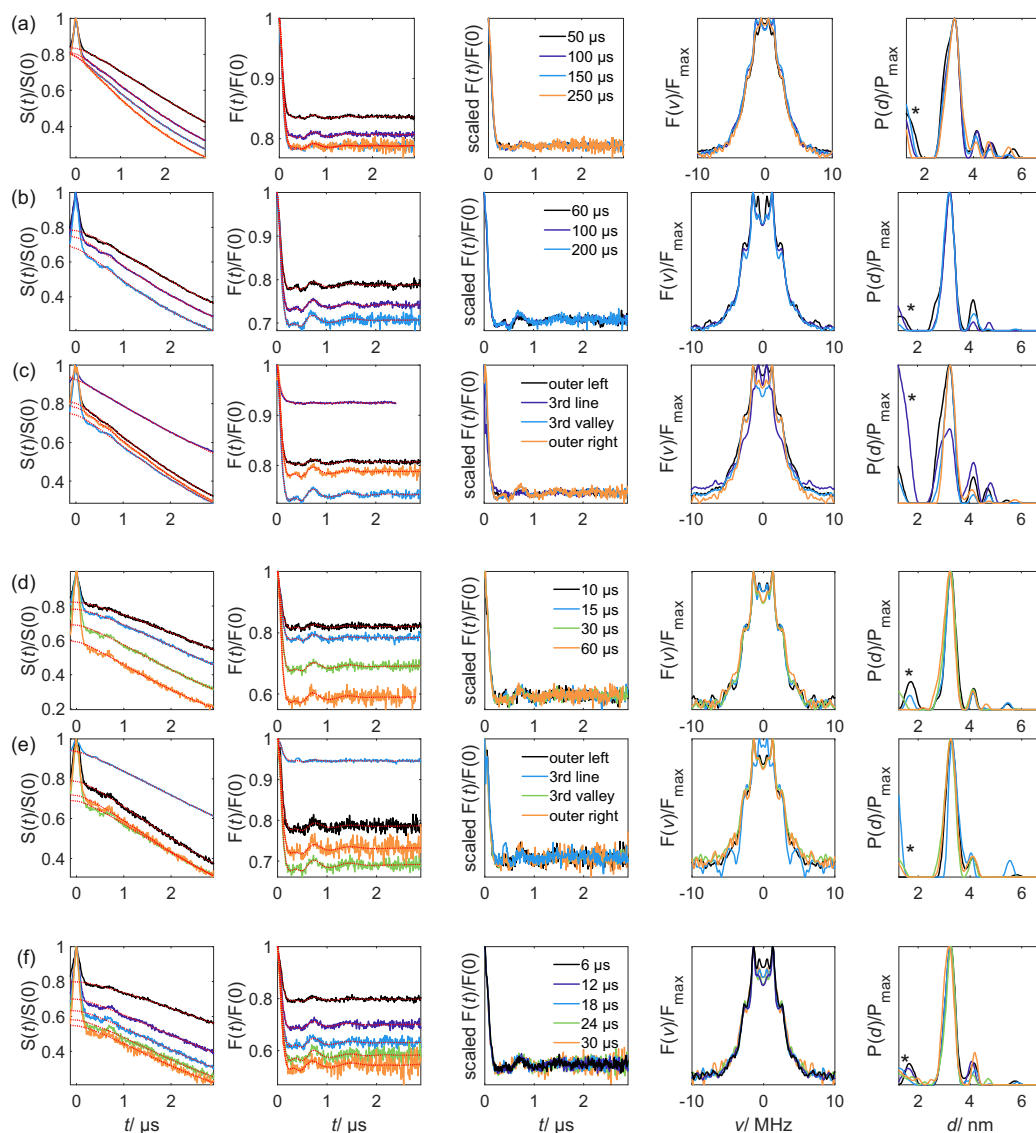


Figure F.22. Influence of detection position and mixing times in W-band RIDME measurements on the Mn-ruler **2** (ligand = PymiMTA). (a) 10 K, detected at low field side outside of hyperfine sextet (outer left); (b) 10 K, detected at 3rd valley in hyperfine sextet (3rd valley); (c) 10 K, $T_{\text{mix}} = T_1 \approx 100 \mu\text{s}$; (d) 20 K, detected at 3rd valley; (e) 20 K, $T_{\text{mix}} = T_1 \approx 30 \mu\text{s}$; (f) 30 K, detected at 3rd valley. From left to right: Raw data and corresponding background fits (red dashed lines), form factors in time domain and corresponding fits (red dashed lines), scaled form factors in time-domain, form factors in frequency domain; resulting distance distributions with $P_2 = 0.5$, $P_3 = 0.1$.

F.6.2. DOTA based rulers

Gd-DOTA based rulers

Figures F.23 and F.24 show the influence of detection position and mixing time for the Gd-ruler $\mathbf{3}_1$. Figures F.25, F.26 and F.27 show the same data for the Gd-ruler $\mathbf{3}_3$. No major deviations can be observed for primary data or extracted distance distributions at different mixing times and measurement temperatures detected at the same transition (F.23). For the shorter ruler $\mathbf{3}_1$ in Q band (F.24), the fractions of harmonic overtone seem to be slightly increasing from 10 to 30 K and with increasing mixing time, in particular at 30 K. Further, for the short ruler and especially for detection at the central transition, background correction appears to be difficult and it is not possible to remove zero-frequency contributions in the dipolar spectra. Moving from the central to the satellite transitions does increase the contribution of harmonic overtones significantly and a short distance peak appears.

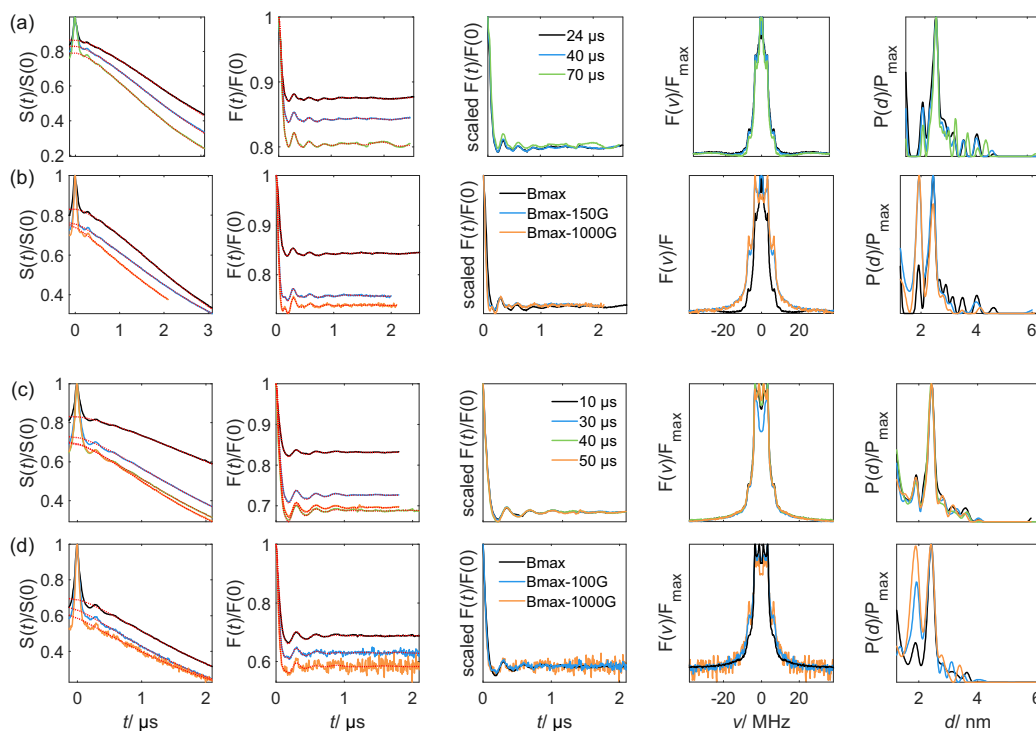


Figure F.23. Influence of mixing time (a, c) and detection position (b, d) in W-band RIDME measurements on the Gd-ruler $\mathbf{3}_1$. (a) 10 K, maximum field B_{\max} , (b) 10 K, $T_{\text{mix}} = 40 \mu\text{s}$, (c) 20 K, maximum field B_{\max} , (d) 20 K, $T_{\text{mix}} = 40 \mu\text{s}$. From left to right: Raw data and corresponding background fits (red dashed lines), form factors in time domain and corresponding fits (red dashed lines), scaled form factor in time-domain, form factors in frequency domain; resulting distance distributions with $P_2 = P_3 = 0$.

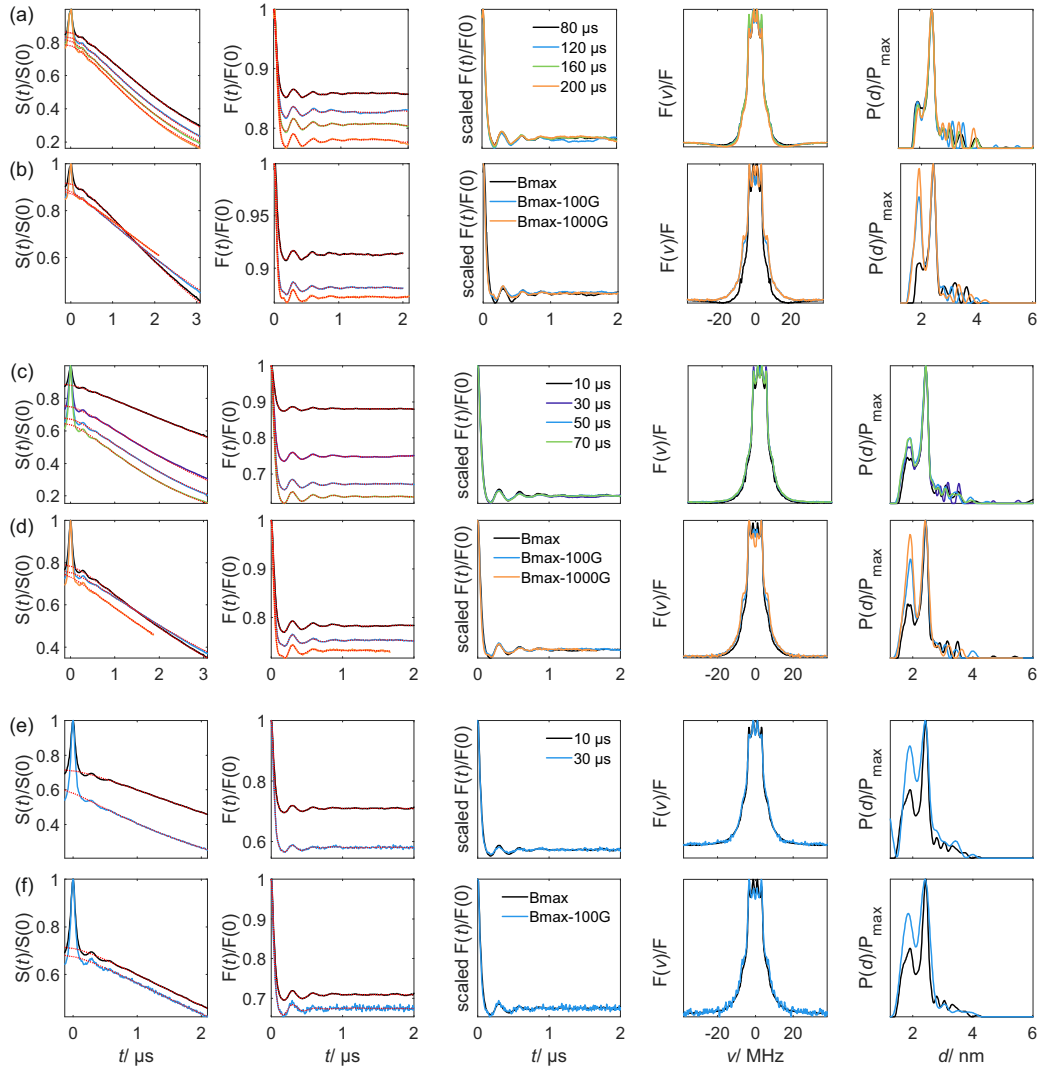


Figure F.24. Influence of mixing time (a, c, e) and detection position (b, d, f) in Q-band RIDME measurements on the Gd-ruler $\mathbf{3}_1$. (a) 10 K, detected at maximum field B_{\max} , (b) 10 K, $T_{\text{mix}} = 40 \mu\text{s}$, (c) 20 K, detected at maximum field B_{\max} , (d) 20 K, $T_{\text{mix}} = 24 \mu\text{s}$, (e) 30 K, detected at maximum field B_{\max} , (f) 30 K, $T_{\text{mix}} = 10 \mu\text{s}$. From left to right: Raw data and corresponding background fits (red dashed lines), form factors in time domain and corresponding fits (red dashed lines), scaled form factor in time-domain, form factors in frequency domain; resulting distance distributions with $P_2 = P_3 = 0$.

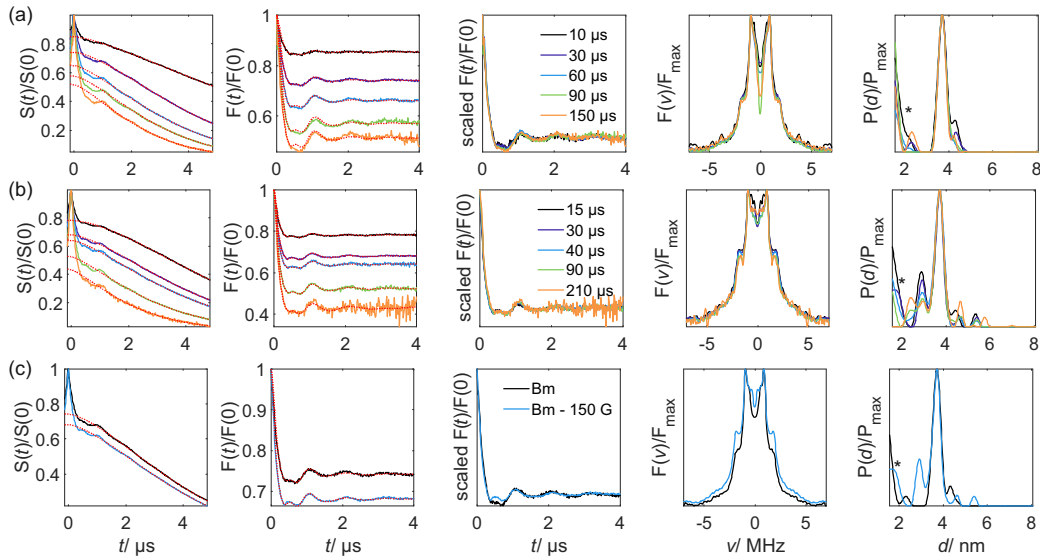


Figure F.25. Influence of mixing time and detection positions for W-band RIDME measurements on the Gd-ruler $\mathbf{3}_3$ at 10 K ($T_1 \simeq 35 \mu\text{s}$). (a) Detected at maximum field B_{max} and different mixing times (colour coded), (b) at $B_{\text{max}} - 150 \text{ G}$ and different mixing times (colour coded), (c) direct comparison of detection position for $T_{\text{mix}} = 30 \mu\text{s}$. From left to right: Raw data and corresponding background fits (red dashed lines), form factors in time domain and corresponding fits (red dashed lines), scaled form factor in time-domain, form factors in frequency domain; resulting distance distributions with $P_2 = 0.4, P_3 = 0.09$. *echo-crossing artefact.

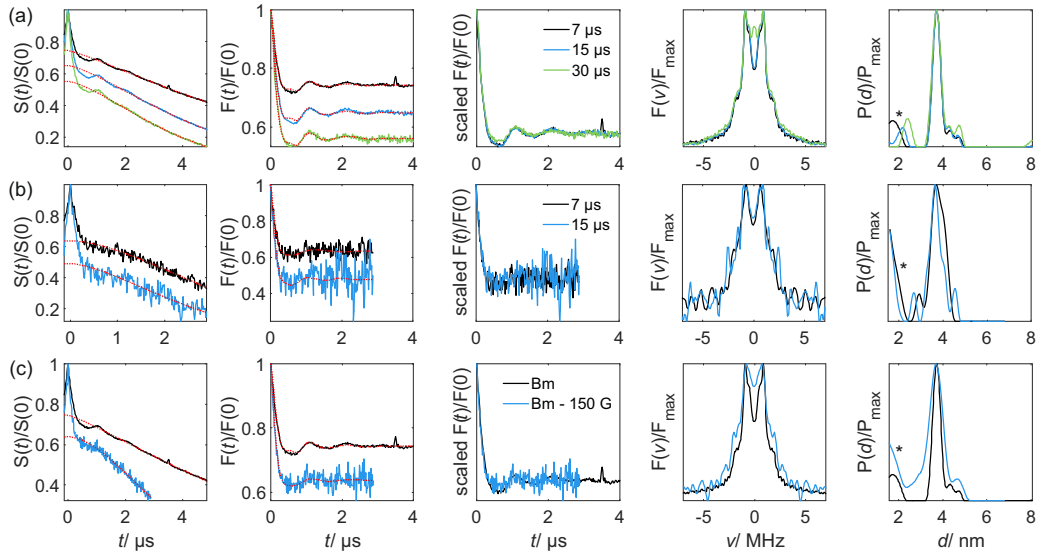


Figure F.26. Influence of mixing time and detection positions for W-band RIDME measurements on the Gd-ruler $\mathbf{3}_3$ at 30 K ($T_1 \simeq 7 \mu\text{s}$). (a) Detected at maximum field B_{max} and different mixing times (colour coded), (b) at $B_{\text{max}} - 150 \text{ G}$ and different mixing times (colour coded), (c) direct comparison of detection position for $T_{\text{mix}} = 7 \mu\text{s}$. From left to right: Raw data and corresponding background fits (red dashed lines), form factors in time domain and corresponding fits (red dashed lines), scaled form factor in time-domain, form factors in frequency domain; resulting distance distributions with $P_2 = 0.4, P_3 = 0.09$. *echo-crossing artefact.

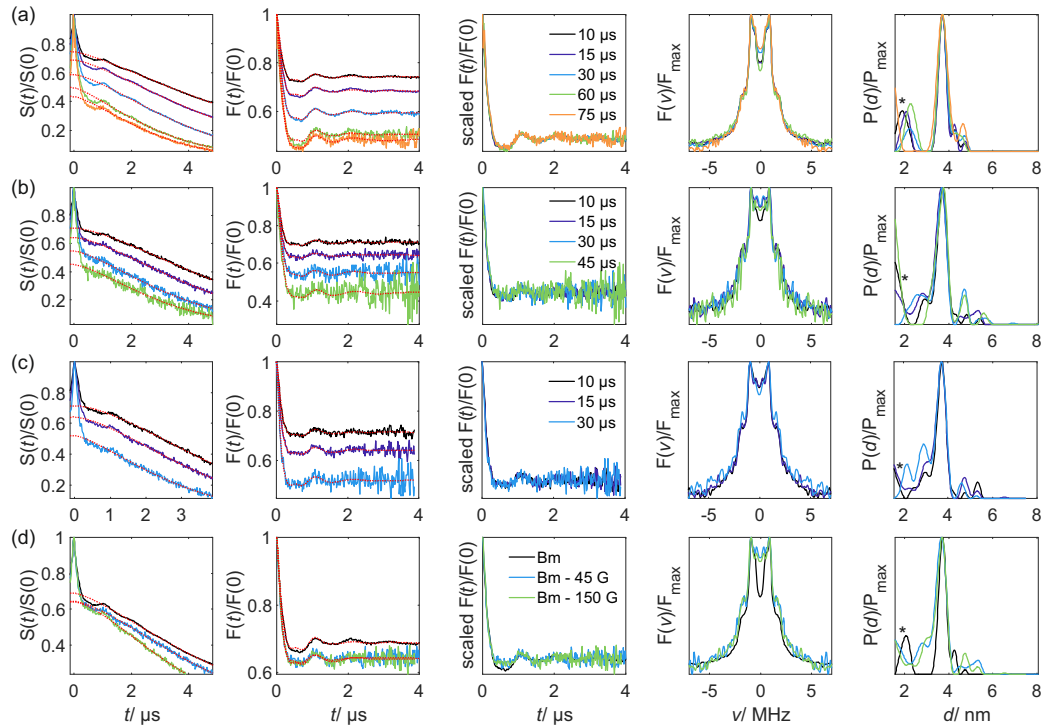


Figure F.27. Influence of mixing time and detection positions for W-band RIDME measurements on the Gd-ruler $\mathbf{3}_3$ at 20 K ($T_1 \simeq 15 \mu\text{s}$). (a) Detected at maximum field B_{max} and different mixing times (colour coded), (b) at $B_{\text{max}} - 45 \text{ G}$ and different mixing times (colour coded), (c) at $B_{\text{max}} - 150 \text{ G}$ and different mixing times (colour coded), (d) direct comparison of detection position for $T_{\text{mix}} = 15 \mu\text{s}$. From left to right: Raw data and corresponding background fits (red dashed lines), form factors in time domain and corresponding fits (red dashed lines), scaled form factor in time-domain, form factors in frequency domain; resulting distance distributions with $P_2 = 0.4$, $P_3 = 0.09$. *echo-crossing artefact.

Mn-DOTA based rulers

Figures F.28, F.30 and F.31 show the influence of detection position and mixing time for the Mn-ruler $\mathbf{3}_1$. Drastic changes are observed for different mixing times around 200 ns at all measurement temperatures and detection positions.

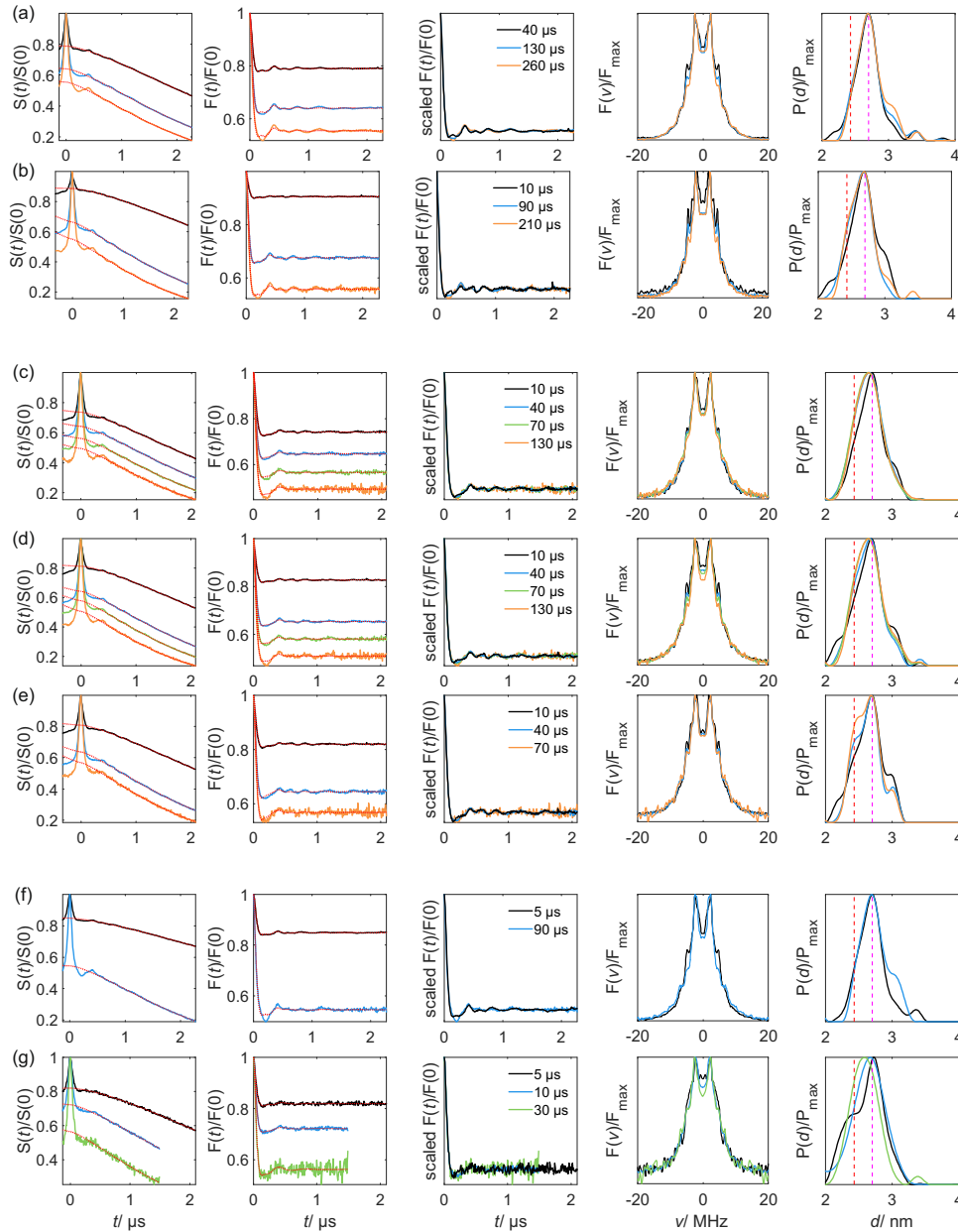


Figure F.28. W-band RIDME measurements on the Mn-ruler $\mathbf{3}_1$. (a-b) 10 K, (c-e) 20 K, (f-g) 30 K. (a, c, f) Detected at third hyperfine line; (d) in 3rd valley of hyperfine sextet; (b, e, g) high field of hyperfine sextet. From left to right: Raw data and corresponding background fits (red dashed lines), form factors in time domain and corresponding fits (red dashed lines), scaled form factor in time-domain, form factors in frequency domain; resulting distance distributions with $P_2 = 0.5$, $P_3 = 0.1$. Vertical lines indicate distance at 2.4 (red) and 2.7 (purple) nm.

Figures F.29, F.30 and F.31 show the influence of detection position and mixing time for the Mn-ruler **3**₃. No major deviations can be observed for primary data or extracted distance distributions at different mixing times and measurement temperatures detected at the same transition. Some smaller changes are observed for different detection positions.

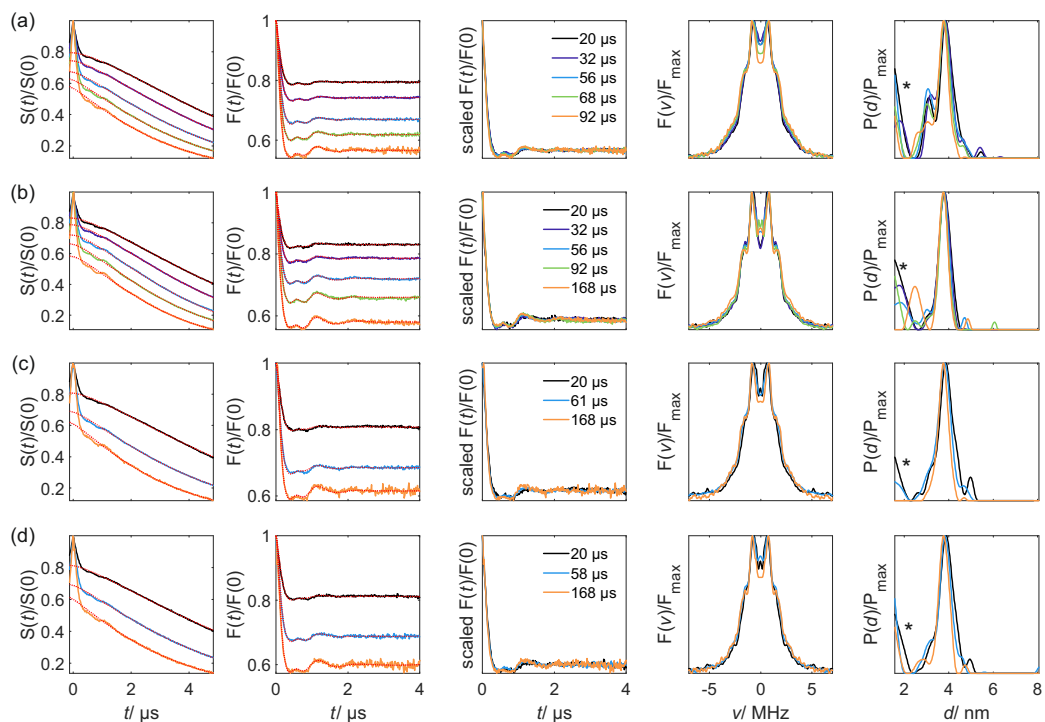


Figure F.29. W-band RIDME measurements on the Mn-ruler **3**₃ at 10 K ($T_1 \sim 60\mu\text{s}$). Detected at (a) low field of hyperfine sextet, (b) 3rd line of hyperfine sextet, (c) 3rd valley of hyperfine sextet, (d) high field of hyperfine sextet. From left to right: Raw data and corresponding background fits (red dashed lines), form factors in time domain and corresponding fits (red dashed lines), scaled form factor in time-domain, form factors in frequency domain; resulting distance distributions with $P_2 = 0.5, P_3 = 0.1$. *echo-crossing artefacts.

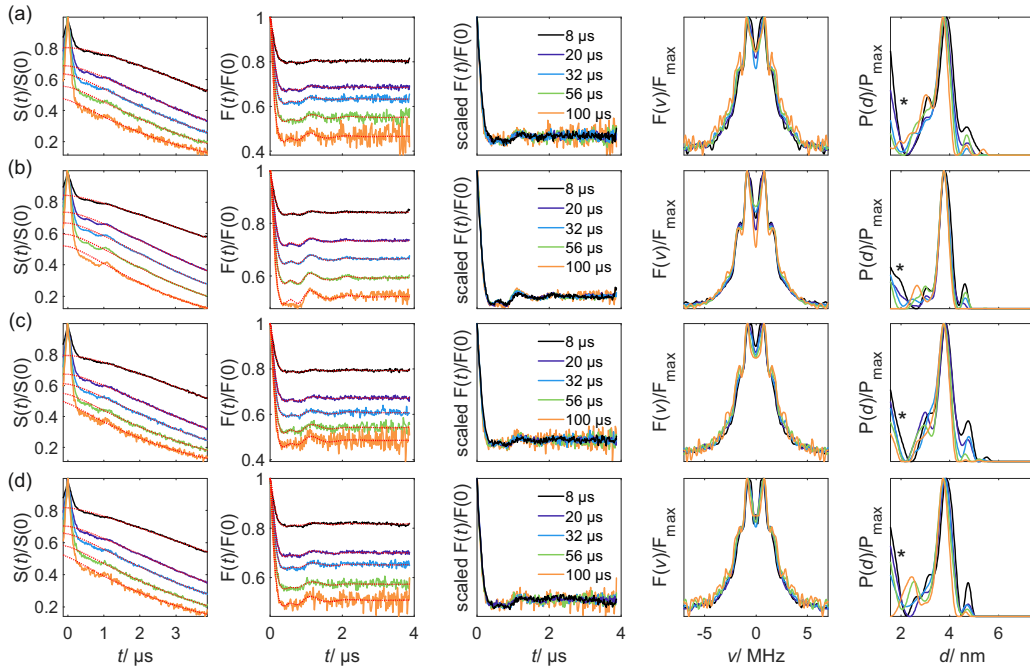


Figure F.30. W-band RIDME measurements on the Mn-ruler $\mathbf{3}_3$ at 20 K ($T_1 \sim 20/34 \mu\text{s}$). Detected at (a) low field of hyperfine sextet, (b) 3rd line of hyperfine sextet, (c) 3rd valley of hyperfine sextet, (d) high field of hyperfine sextet. From left to right: Raw data and corresponding background fits (red dashed lines), form factors in time domain and corresponding fits (red dashed lines), scaled form factor in time-domain, form factors in frequency domain; resulting distance distributions with $P_2 = 0.5, P_3 = 0.1$. *echo-crossing artefacts.

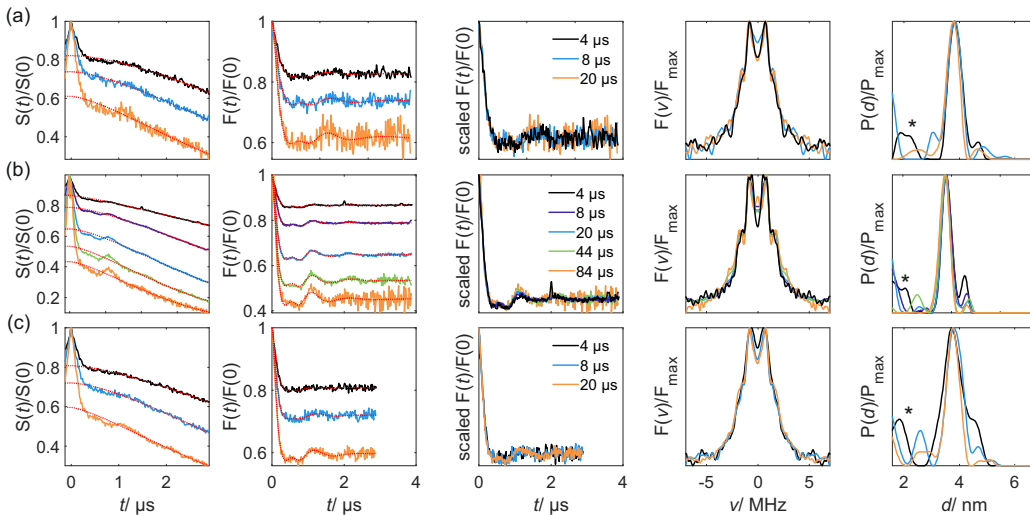


Figure F.31. W-band RIDME measurements on the Mn-ruler $\mathbf{3}_3$ at 30 K ($T_1 \sim 8/17 \mu\text{s}$). Detected at (a) low field of hyperfine sextet, (b) 3rd line of hyperfine sextet, (c) 3rd valley of hyperfine sextet. From left to right: Raw data and corresponding background fits (red dashed lines), scaled form factor in time-domain, form factors in frequency domain; resulting distance distributions with $P_2 = 0.5, P_3 = 0.1$. *echo-crossing artefacts.

F.6.3. TAHA-ruler

Figure F.32 shows RIDME traces detected for different mixing times and detection positions for the Gd-TAHA ruler **4**. The form factors seem to be stable with increasing mixing time. Within the very low SNR also no changes can be observed for different detection positions.

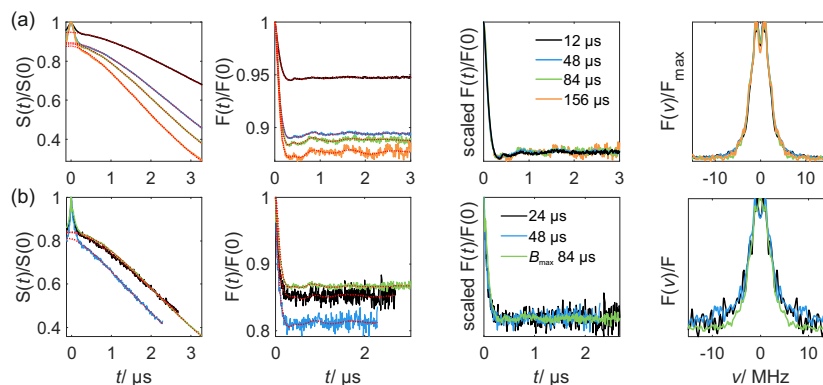


Figure F.32. W-band RIDME measurements on the Gd-ruler **4** at 10 K ($T_1 \sim 43 \mu\text{s}$). Detected at (a) maximum field B_{max} and (b) $B_{\text{max}} - 150$ G. From left to right: Raw data and corresponding background fits (red dashed lines), form factors in time domain and corresponding fits (red dashed lines), scaled form factors in time-domain, form factors in frequency domain.

Figure F.33 shows resulting distance distributions and form factor fits for four different sets of overtone coefficients. For $P_2 = P_3 = 0$ multiple-peak distance distribution with contributions from higher harmonic frequency overtones can be identified in comparison to the DEER distance distribution. Note that it is difficult to identify the ground truth from the DEER distance measurement due to a high level of artefacts in the standard version of the DEER experiments and regularization-induced broadening of the distributions due to low SNR in a UWB version with chirp pumped pulses (detected in a loop-gap resonator²⁵⁷) as shown in Figure F.34. For the set of overtone coefficients used in data analysis of the other model compounds ($P_2 = 0.4, P_3 = 0.09$), contributions from overtone frequencies are reduced, but some remain. They are strongly suppressed for the set of coefficients $P_2 = 0.45, P_3 = 0.12$, while for yet higher contributions ($P_2 = 0.5, P_3 = 0.15$) 'over-correction' is observed, i.e. increase in the long-distance artefact around $\frac{1}{2}\omega_{\text{dd}}$ and a slight shift towards larger mean distance.

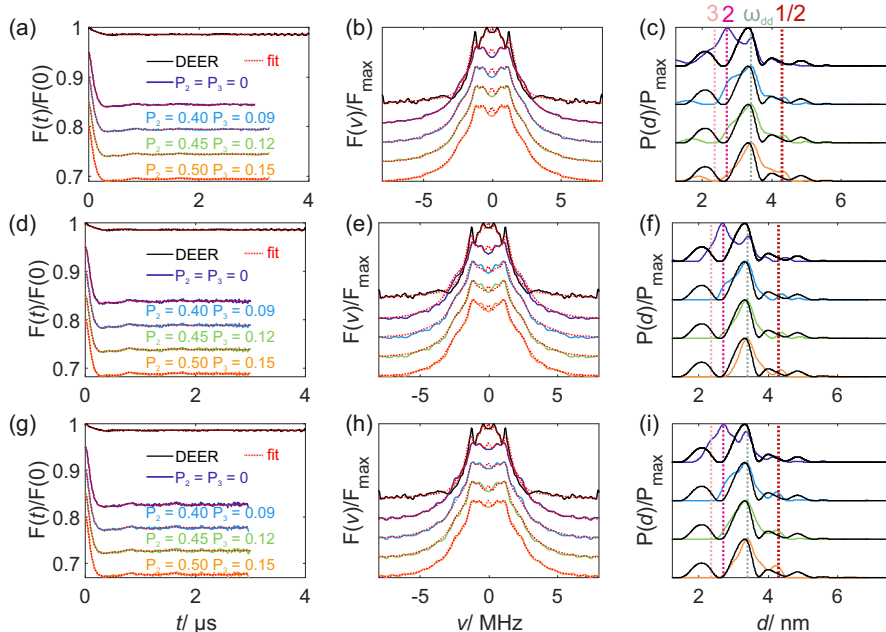


Figure F.33. Estimation of overtone coefficients for the Gd-ruler 4 for W-band RIDME measurements at 10 K. (a-c) $T_{\text{mix}} = 48 \mu\text{s}$, (d-f) $T_{\text{mix}} = 84 \mu\text{s}$, (g-h) $T_{\text{mix}} = 120 \mu\text{s}$. (a, d, g) Background-corrected form factors and (b, e, h) frequency-domain form factors. Fits, for each set of overtone coefficients (colour coded) are given by red dashed lines. (c, f, i) Resulting distance distributions for each set of overtone coefficients. The vertical dashed lines give the distance corresponding to triple (rose), double (magenta), single (grey) and half (dark red) of the dipolar frequency for a distance of 3.4 nm. The black curve corresponds to the DEER distance distribution.

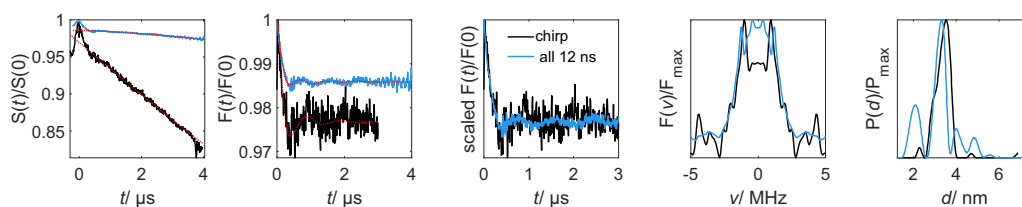


Figure F.34. Conventional (all pulses 12 ns) and UWB (linear chirp pump pulses) DEER experiments for the Gd-ruler 4 in Q band at 10 K. Linear chirps had a bandwidth of 1 GHz and were applied left and right to the central line with an offset of ± 200 MHz. From left to right: Raw data and corresponding background fits (red dashed lines), form factors in time domain and corresponding fits (red dashed lines), scaled form factors in time-domain, form factors in frequency domain; resulting distance distributions.

Figure F.35 shows the analysis of RIDME traces for the Gd-ruler 1_3 detected on the satellite transitions as well as for the Gd-ruler 1_7 detected at the central transition, for which in Chapter 8 slightly larger contributions of harmonic overtones were found. In these time traces the artefact peaks appear to be well suppressed by the set of overtone coefficients $P_2 = 0.45, P_3 = 0.12$.

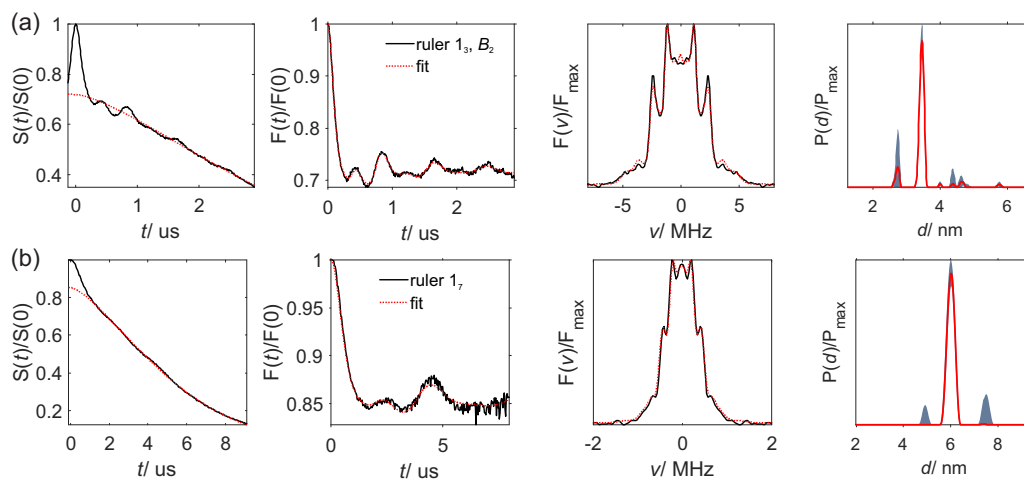


Figure F.35. W-band RIDME measurements on Gd-rulers 1_n at 10 K. (a) $n = 3$, detected at $B_2 = B_{\max} - 1400$ G and (b) $n = 7$, detected at B_{\max} . From left to right: Raw data and corresponding background fit (red dashed line), form factor in time domain and corresponding fit (red dashed lines), scaled form factor in time-domain (red dashed line), form factor in frequency domain; resulting distance distribution with $P_2 = 0.45, P_3 = 0.12$. The grey error bands mark the uncertainty resulting from 20% variation of overtone coefficients from the selected values.

F.7. RIDME on proteins

Figure F.36 shows some additional analysis to estimate the presence and strength of harmonic overtone contributions in the spin-labelled protein mutants. Clearly, in all three protein preparations, additional short distance peaks (violet distance distributions) appear with respect to DEER reference measurements (black lines) in the absence of harmonic overtones ($P_2 = P_3 = 0$). Data analysis with the coefficients calibrated on PyMTA-rulers with Gd(III) as central ion - $P_2 = 0.4, P_3 = 0.09$, do already rather well reproduce the DEER reference distance. Data analysis with $P_2 = 0.6, P_3 = 0.2$ introduces new peaks at longer distances, most probably artefacts from 'over-correction' of harmonic overtones (see Chapter 8.4.1), and the fit quality of the form factors decreases.

For the double-mutant Q388C/S475C in RBD 3/4, data analysis with $P_2 = 0.5, P_3 = 0.12$ leads to a further reduction of the short distance shoulder and long-distance peaks just start to appear. The fit quality is still similar and does not show significant characteristics of 'over-correction' as compared to data analysis with $P_2 = 0.6, P_3 = 0.2$. Therefore higher overtone coefficients lead to a bit narrower distributions, yet their shape still deviates from the one found with DEER measurements. For the other two mutant, no clear improvement in the shape of the distance distribution with respect to the shape of the DEER distance distribution can be observed for $P_2 = 0.5, P_3 = 0.12$. Using the validation tool available in OvertoneAnalysis and variation of the overtone coefficients in the order of 20% does allow to assess such changes in distance distributions.

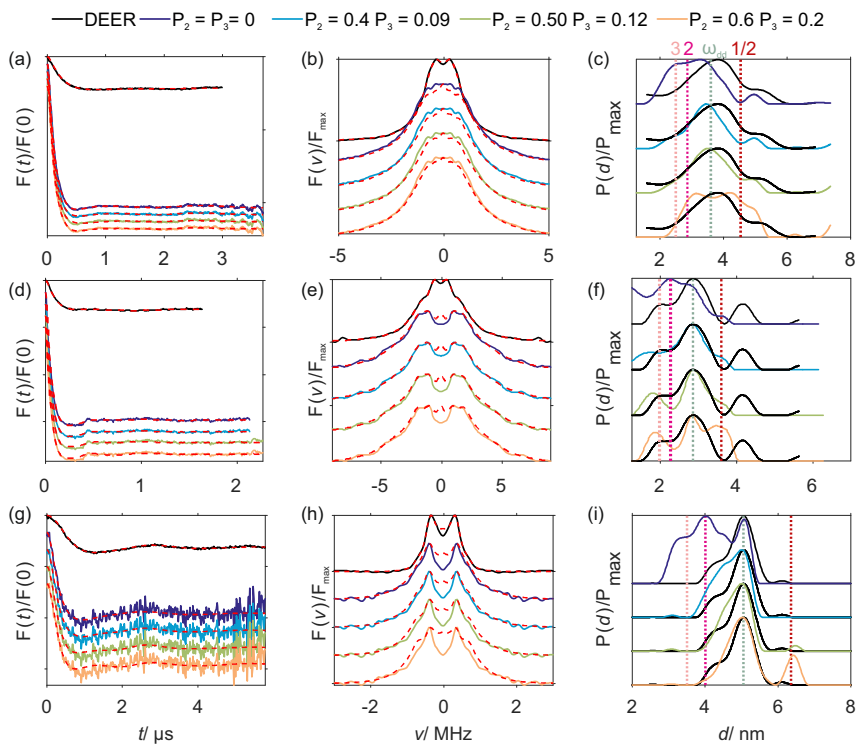


Figure F.36. Estimation of overtone coefficients. (a-c) Double-mutant T71C/T109C, RBD 1 at 20 K, $T_{\text{mix}} = 25 \mu\text{s}$; (d-f) double-mutant S204C/S240C in RBD 2 at 20 K, $T_{\text{mix}} = 45 \mu\text{s}$; (g-i) double-mutant Q388C/S475C in RBD 3/4 at 20 K, $T_{\text{mix}} = 20 \mu\text{s}$. (a, d, g) Background-corrected form factors and (b, e, h) frequency-domain form factors. Fits, for each set of overtone coefficients are given by red dashed lines. (c, f, i) Resulting distance distributions with colour coded set of overtone coefficients. The dashed lines give the distance corresponding to triple (rose), double (magenta), single (grey) and half (dark red) of the dipolar frequency. The black curve corresponds to the DEER distance distributions.

Figures F.37 - F.39 show the influence of mixing time, measurement temperature and detection position for the different protein mutants. Similar to molecular rulers, no significant deviations are observed for changing mixing time and measurement temperature, while shifting the detection position away from the central line appears to induce somewhat larger overtone coefficients. Figure F.39 reveals that background correction can be difficult and can contribute significant uncertainties in the measurement of long spin-spin distances.

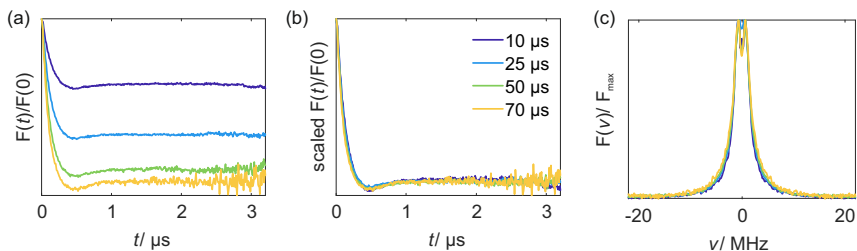


Figure F.37. Q-band RIDME data for the protein double-mutant T71C/T109C in RBD1 at 20 K. Different mixing times are colour coded. (a) Background-corrected form factors, (b) scaled form factors as in (a); (c) form factors in frequency domain.

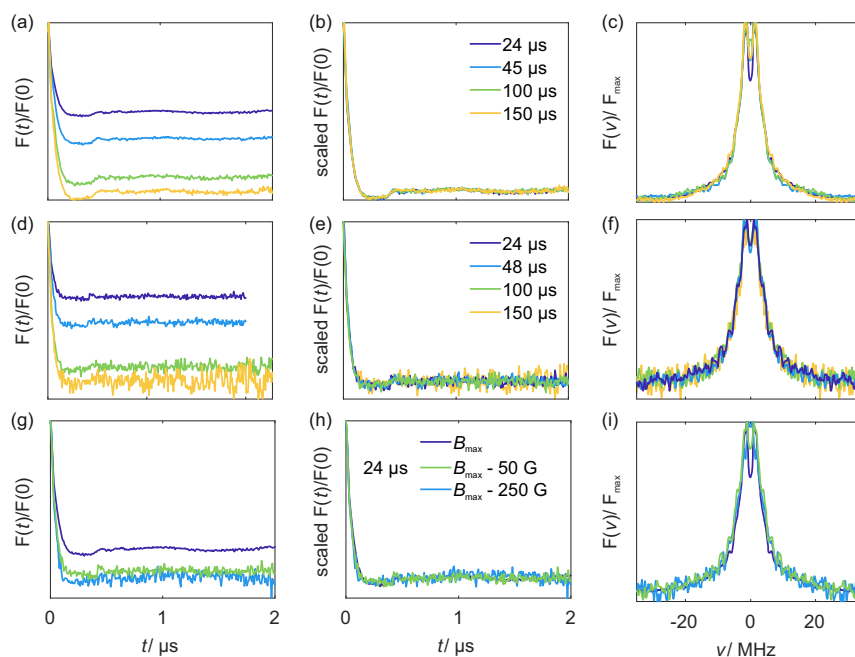


Figure F.38. W-band RIDME data for the protein double-mutant S204C/S240C in RBD2 at 10 K. Different mixing times are colour coded. (a-c) Detected at the field maximum B_{\max} , (d-f) detected at $B_{\max} - 50$ G, (g-h) comparison of different detection fields as colour encoded. (a, d, g) Background-corrected form factors, (b, e, h) scaled form factors; (c, f, i) form factors in frequency domain.

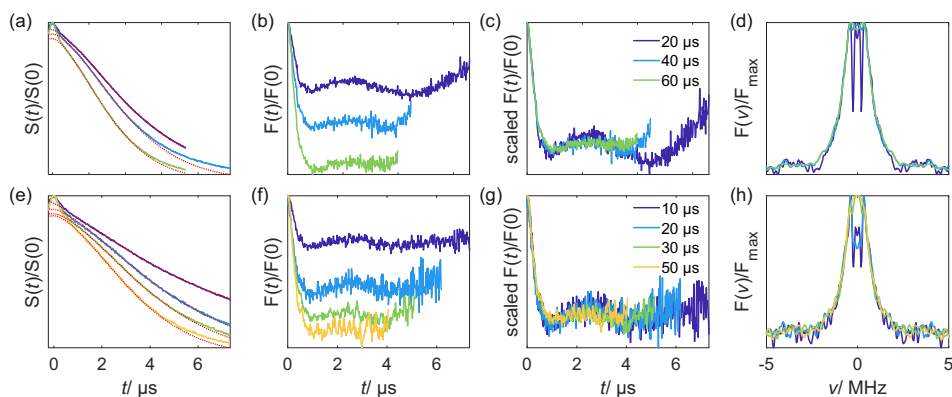


Figure F.39. W-band RIDME data for the protein double-mutant Q388C/S475C in RBD34. (a-d) 10 K, (e-h) at 20 K. Different mixing times are colour coded. (a, e) RIDME raw data and corresponding background fit (red dashed lines); (b, f) Background-corrected form factors, (c, g) scaled form factors; (d, h) form factors in frequency domain.

F.8. Two-point optimization curves

Figures F.41 - F.50 show two-point optimization curves for T_{mix} for Mn(II) (F.41 - F.42) and Gd(III) (F.43 - F.47) ruler compounds as well as Gd-DOTA spin labelled protein mutants (F.48 - F.50). The approach determines echo amplitude S_0 at the maximum of the traces and a measure λ_{2P} for the modulation depth. The product $S_0 \cdot \lambda_{2P}$ is a measure η_{2P} for sensitivity.

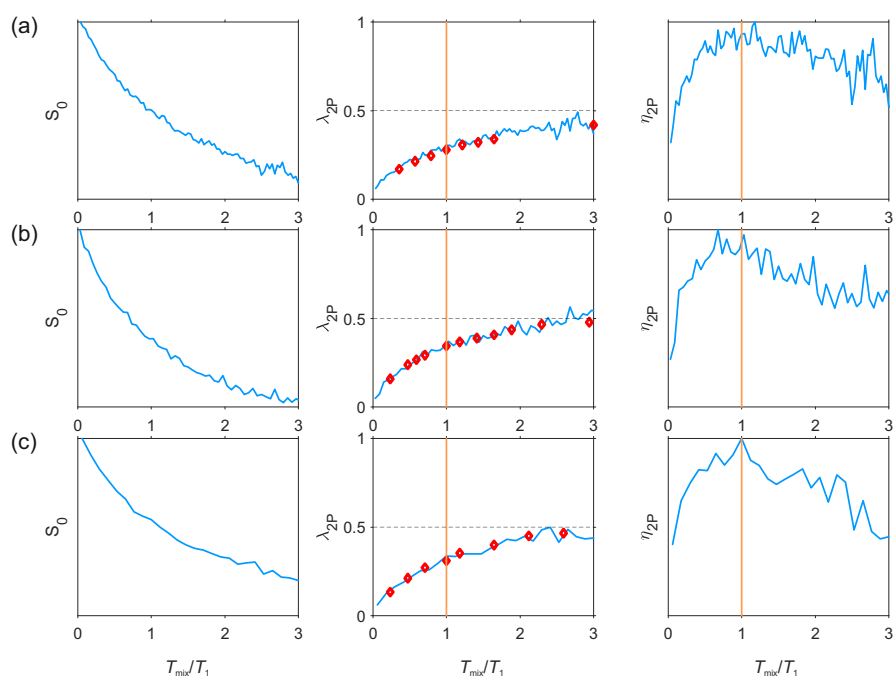


Figure F.40. W-band two-point optimization curves for the Mn-ruler $\mathbf{3}_3$. (a) 10 K, (b) 20 K, (c) 30 K. Detected at 3rd hyperfine line. The red markers give the reference modulation depth extracted from full RIDME time traces. The vertical orange line markers $T_{\text{mix}} = T_1$.

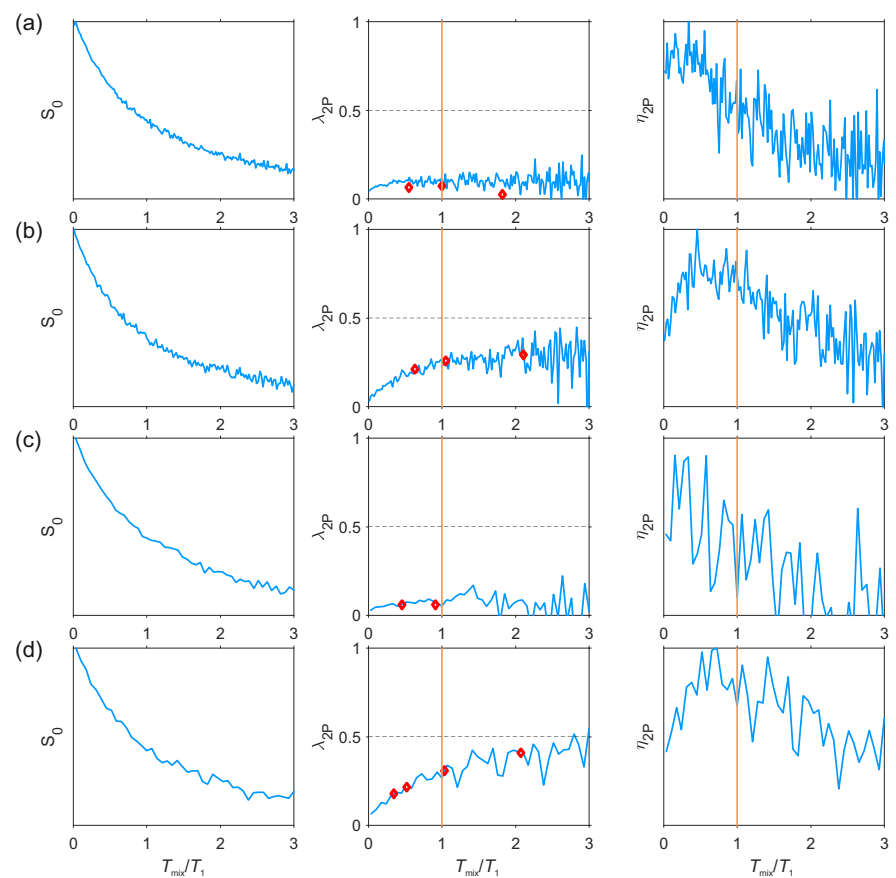


Figure F.41. W-band two-point optimization curves for Mn-ruler $\mathbf{2}$. (a, b) 10 K and (c, d) 20 K. (a, c) Detected at 3rd hyperfine line; (b, d) detected at 3rd valley of hyperfine sextet. The red markers give the reference modulation depth extracted from full RIDME time traces. The vertical orange line marks $T_{\text{mix}} = T_1$.

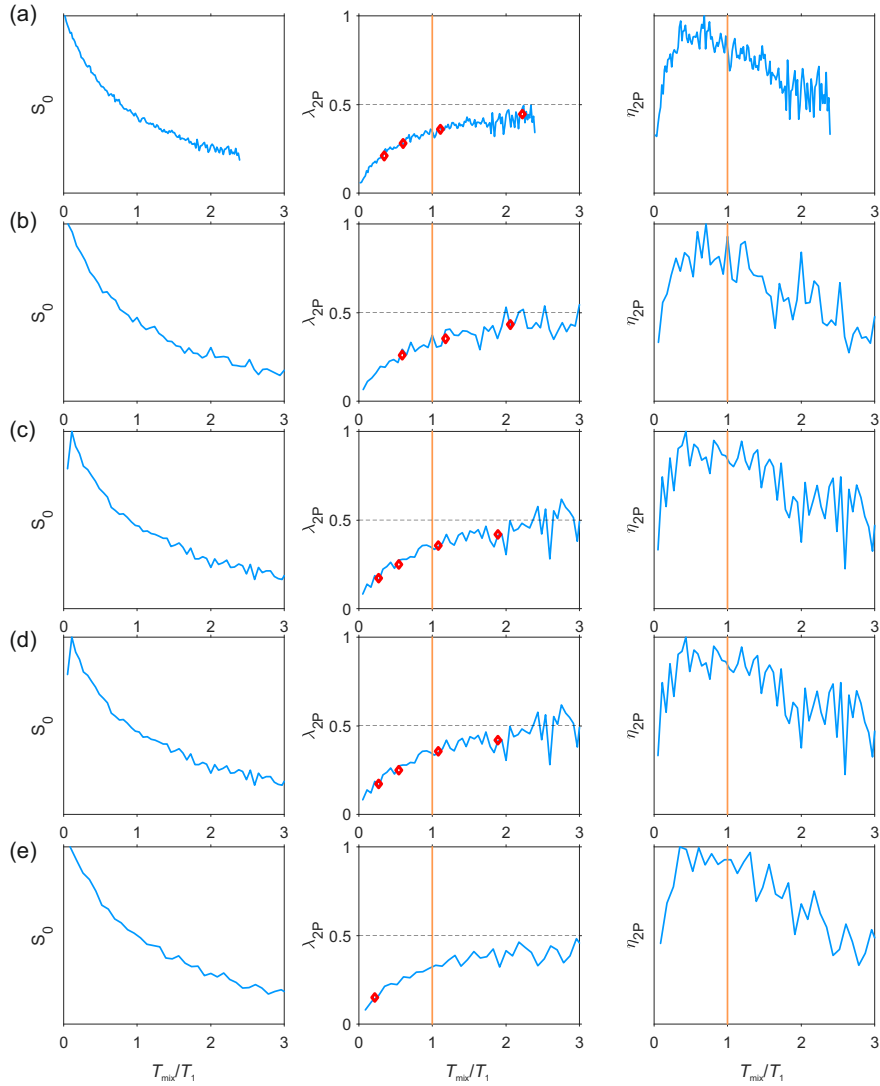


Figure F.42. W-band two-point optimization curves for Mn-ruler $\mathbf{3}_1$. (a) 10 K, (b - d) 20 K, (e) 30 K. (a, b, e) Detected at 3rd hyperfine line, (c) detected in 3rd valley, (d) detected at high field side of hyperfine sextet. The red markers give the reference modulation depth extracted from full RIDME time traces. The vertical orange line marks $T_{\text{mix}} = T_1$.

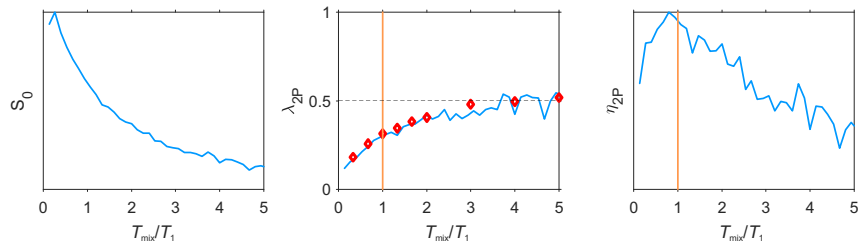


Figure F.43. W-band two-point optimization curves for the Gd-ruler $\mathbf{3}_3$. 20 K, detected at maximum field. The red markers give the reference modulation depth extracted from full RIDME time traces. The vertical orange line marks $T_{\text{mix}} = T_1$.

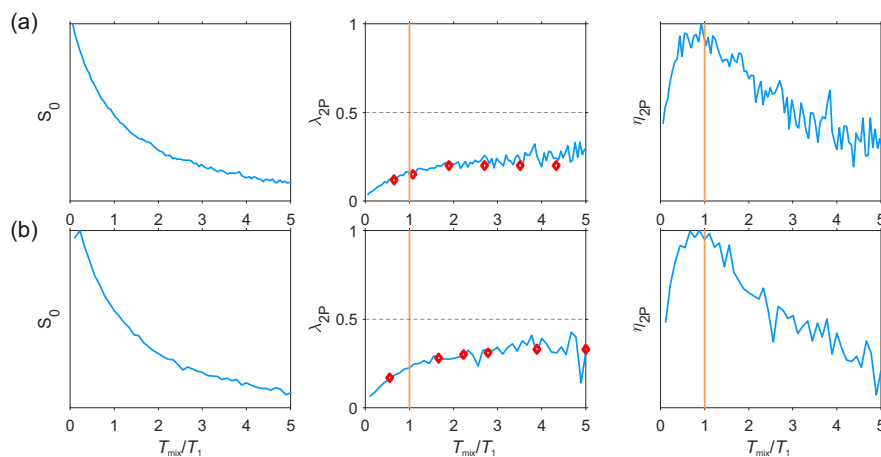


Figure F.44. W-band two-point optimization curves for the Gd-ruler $\mathbf{3}_1$. (a) 10 K, (b) 20 K. Detected at maximum field. The red markers give the reference modulation depth extracted from full RIDME time traces. The vertical orange line marks $T_{\text{mix}} = T_1$.

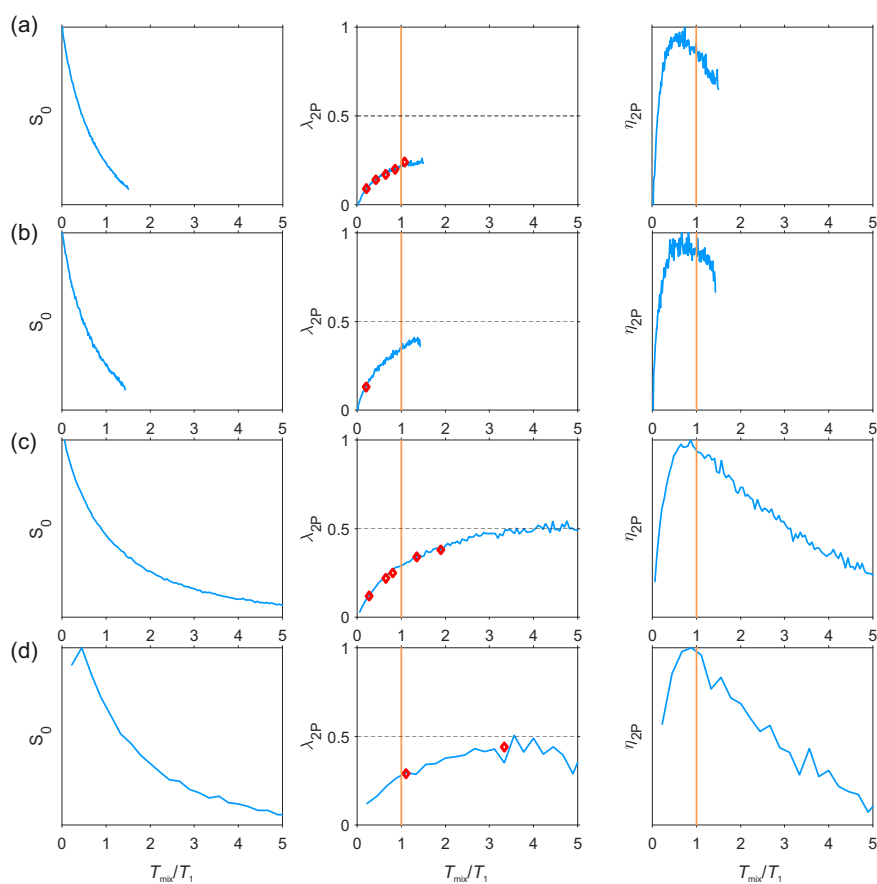


Figure F.45. Q-band two-point optimization curves for the Gd-ruler $\mathbf{3}_1$. (a) 10 K, (b, c) 20 K, (d) 30 K. (a, b, d) Detected at maximum field, (c) $B_{\text{max}} - 100$ G. The red markers give the reference modulation depth extracted from full RIDME time traces. The vertical orange line marks $T_{\text{mix}} = T_1$.

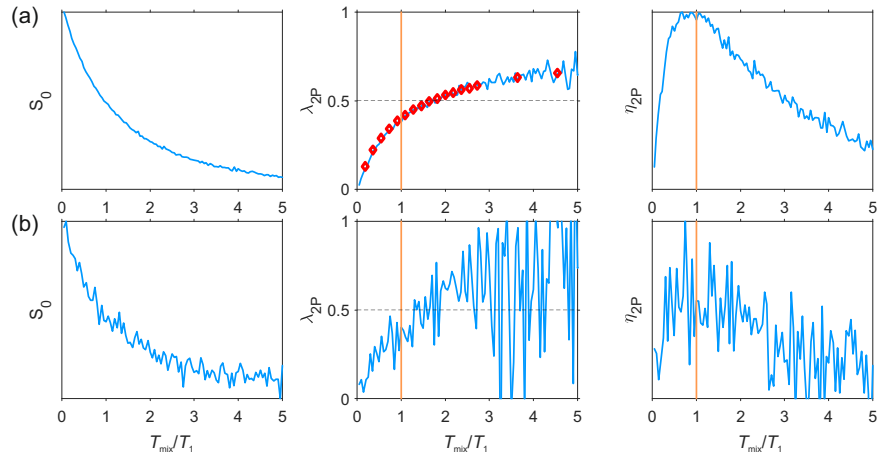


Figure F.46. Q-band two-point optimization curves for the Gd-ruler **1₃**. 20 K. (a) Detected at maximum field, (b) $B_{\max} - 100$ G. The red markers give the reference modulation depth extracted from full RIDME time traces. The vertical orange line marks $T_{\text{mix}} = T_1$.

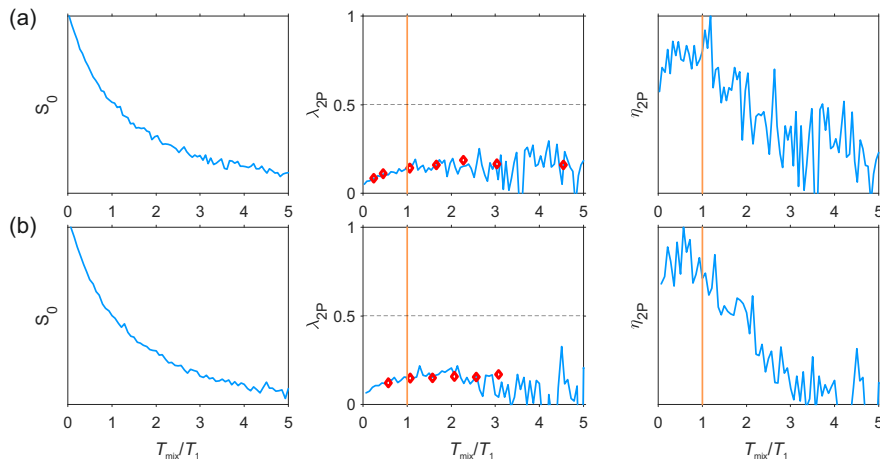


Figure F.47. W-band two-point optimization curves for the Gd-ruler **2**. (a) 10 K, (b) 20 K. Detected at maximum field. The red markers give the reference modulation depth extracted from full RIDME time traces. The vertical orange line marks $T_{\text{mix}} = T_1$.

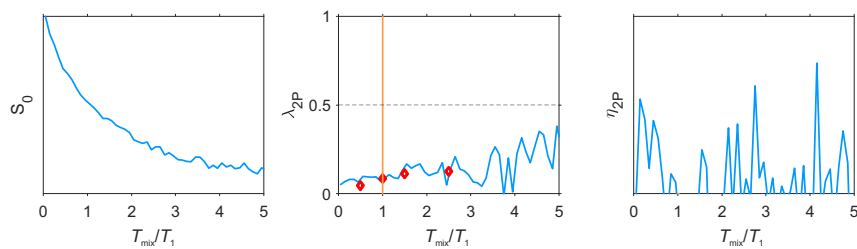


Figure F.48. Q-band two-point optimization curves for the protein double-mutant T71C/T109C in RBD1 at 20 K. Detected at maximum field. The red markers give the reference modulation depth extracted from full RIDME time traces. The vertical orange line marks $T_{\text{mix}} = T_1$.

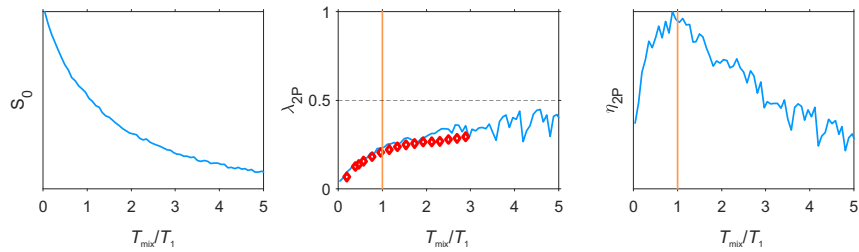


Figure F.49. W-band two-point optimization curves for the protein double-mutant S204C/S240C in RBD2 at 10K. (a) Detected at maximum field. (b) $B_{\max} - 50$ G. The red markers give the reference modulation depth extracted from full RIDME time traces. The vertical orange line marks $T_{\text{mix}} = T_1$.

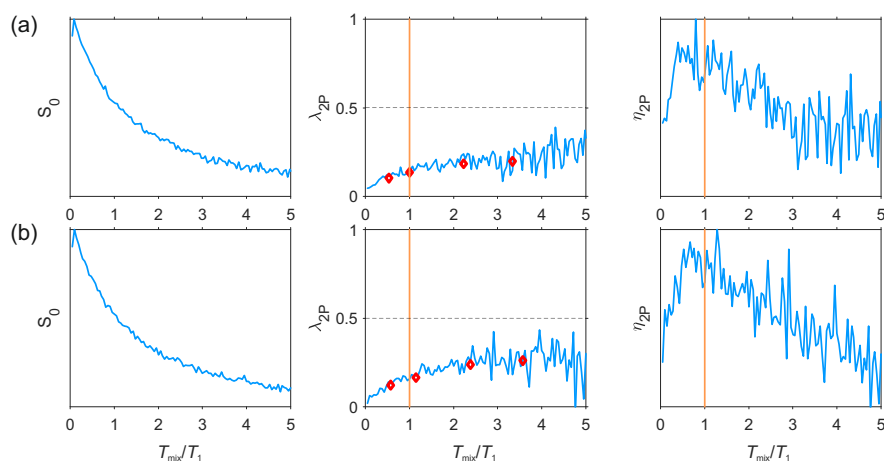


Figure F.50. W-band two-point optimization curves for the protein double-mutant Q388C/S475C in RBD34. 20 K. Detected at maximum field. The red markers give the reference modulation depth extracted from full RIDME time traces. The vertical orange line marks $T_{\text{mix}} = T_1$.

Supplementary Information to Chapter 10

G.1. Materials and Methods

G.1.1. Samples for CW-EPR

***HpDnaB* samples**

HpDnaB:AMP-PNP:Mn²⁺ complex

3.6 mM *HpDnaB* in buffer A (2.5 mM sodium phosphate, pH 7.5, 130 mM NaCl) was mixed with 0.3 mM $\text{MnCl}_2 \cdot 4\text{H}_2\text{O}$ and consecutively 5 mM AMP-PNP (18-fold molar excess of AMP-PNP compared to an *HpDnaB* monomer) and incubated for 2 h at 4°C.

MnCl₂:AMP-PNP reference solution

A solution of 0.3 mM $\text{MnCl}_2 \cdot 4\text{H}_2\text{O}$ and 5mM AMP-PNP in buffer A was prepared.

CW EPR spectra were measured for a sample with 12-fold excess of the *HpDnaB* monomers with respect to the Mn^{2+} ions, in order to ensure predominant presence of the metal ions in the form of *HpDnaB:AMP-PNP:Mn²⁺* complexes. In this case, most of protein oligomers should have only one Mn^{2+} ion bound. Note that the CW EPR spectrum of Mn^{2+} ions is dominated by the metal ion ligands and magnetic nuclei in the close vicinity. Unless the distances to the next neighbour Mn^{2+} species are below 2 nm, the interaction with other metal centres can be neglected. As the Mn^{2+} EPR spectrum is not dominated by the paramagnetic metal ions in close vicinity, it should not differ between this sample and the sample with all NBDs loaded with Mn^{2+} . CW experiments performed on a sample with *HpDnaB:Mn²⁺* ratio of 1:1 are shown in Figure G.1(a).

BmrA samples

BmrA:ATP:Mn²⁺:VO₄³⁻ complex

2 mL of BmrA 0.25 mg/mL (3.8 μM) in buffer solution (50 mM Tris, 100 mM NaCl, 5% glycerol) was incubated with ATP:Mn^{2+} in a ratio of 300:1 (1.140 mM ATP:Mn^{2+}) and 5 mM vanadate solution. The sample was sedimented and washed three times with the buffer solution. The final protein concentration was $\sim 200 \mu\text{M}$. Note typical ATP concentrations in bacteria range from about 1 to 10 mM,^{325;326} and may exceed the NBD concentration by an even larger ratio.

ATP:Mn²⁺:VO₄³⁻ reference solution

A solution of 1 mM ATP, 1 mM $\text{MnCl}_2 \cdot 4\text{H}_2\text{O}$ and 5mM Na_3VO_4 in 50 mM Tris, 100 mM NaCl, 5% Glycerol buffer was prepared.

For BmrA CW EPR measurements, the sample preparation was based on the slow kinetics of the Mn^{2+} dissociation from the binding sites in the NBDs. A 300-fold excess of Mn^{2+} was used to load Mn^{2+} ions into the binding site of BrmA. Then, the protein was sedimented and washed three times with the buffer solution without Mn^{2+} ions to remove unbound excess of Mn^{2+} ions as much as possible. The washing procedure took about three times five min. Immediately after washing the sample was placed in the CW spectrometer. The spectrum is shown in Figure 10.1(c) in comparison to the reference solution of Mn^{2+} ions in the buffer at room temperature. Single scans - detected before and after 1 hour of measurements - did not show significant spectral changes, indicating that the formed complex is stable for at least one hour.

G.1.2. Samples for pulsed EPR experiments

***HpDnaB* samples**

HpDnaB:AMP-PNP:Mn²⁺ complex

Buffer A was exchanged with the corresponding D_2O buffer (buffer B). For relaxation measurements, 0.6 mM *HpDnaB* in buffer B was mixed with 0.6 mM $\text{MnCl}_2 \cdot 6\text{H}_2\text{O}$ and consecutively 10 mM AMP-PNP (18-fold molar excess of AMP-PNP compared to an *HpDnaB* monomer) and incubated for 2 h at 4°C. The solution was mixed with glycerol- d_8 leading to a final protein concentration of 0.3 mM. For the DEER and RIDME experiments, a deuterated sample of *HpDnaB* was used with a 1.5-fold excess of Mn^{2+} compared to an *HpDnaB* monomer. The samples were filled into 3 mm outer diameter quartz sample tubes and subsequently shock-frozen by immersion into liquid nitrogen.

MnCl₂:AMP-PNP reference solution

A solution of 0.6 mM $\text{MnCl}_2 \cdot 4\text{H}_2\text{O}$ and 10 mM AMP-PNP in buffer B was prepared. The solution was diluted with glycerol- d_8 until concentrations of 0.3 mM $\text{MnCl}_2 \cdot 4\text{H}_2\text{O}$ and 5 mM AMP-PNP were reached.

MnCl₂ reference solution

A solution of 0.6 mM $\text{MnCl}_2 \cdot 4\text{H}_2\text{O}$ in buffer B was prepared. The solution was diluted with glycerol- d_8 (final $\text{MnCl}_2 \cdot 4\text{H}_2\text{O}$ concentration of 0.3 mM).

The protein-containing and reference samples were dissolved in buffer B:glycerol- d_8 (1:1, v:v). Samples were filled into 3 mm outer diameter quartz sample tubes for Q-band measurement and 0.5 mm inner diameter quartz tubes for W-band measurements. Samples were subsequently shock-frozen by immersion into liquid nitrogen. Pulsed EPR measurements were performed on a sample with 1:1 ratio between Mn^{2+} ions and *HpDnaB* monomers for echo-detected (ED) field-swept and relaxation measurements, and with 1.5:1 ratio between Mn^{2+} ions and *HpDnaB* monomers for distance measurements in order to obtain a sufficiently large fraction of multiply metal-loaded *HpDnaB* oligomers. For significantly lower relative amounts of *HpDnaB*, the fraction of Mn^{2+} ions not bound to the NBDs would be too high, resulting in a too low dipolar modulation depth in the DEER measurements. For significantly higher *HpDnaB* amounts the fraction of protein oligomers with only one Mn^{2+} ion bound would increase, again reducing the dipolar modulation depth in the distance experiment. Despite the presence of, on average, six Mn^{2+} ions per protein complex, multi-spin effects are negligible due to the modulation depth of only about

1.5% even when using ultra-wideband pump pulses.

BmrA samples

BmrA:ATP:Mn²⁺:VO₄³⁻ complex

1 mL of BmrA 0.25 mg/mL (3.8 μ M) in 50 mM Tris, 100 mM NaCl, 5% Glycerol was incubated with ATP-Mn²⁺ ratio 300:1 (1.140 mM ATP-Mn²⁺) and 5 mM vanadate solution. The sample was sedimented and resuspended with 40 μ L of buffer containing 50% glycerol (50 mM Tris, 100 mM NaCl, 50% Glycerol incubated).

MnCl₂:ATP reference solution

A solution of 100 μ M ATP and 100 μ M MnCl₂·4H₂O in 50 mM Tris, 100 mM NaCl, 50% Glycerol buffer was prepared.

For BmrA, the sample preparation was based on the slow kinetics of the Mn²⁺ dissociation from the binding sites in the NBDs (vide supra). Compared to the samples for CW EPR, the protein was centrifuged and the buffer was exchanged by the pure buffer/glycerol mixture without Mn²⁺ ions, and without the washing steps. Samples were then transferred to 3 mm outer diameter quartz tubes and immediately frozen by immersion into liquid nitrogen. Samples were kept frozen during handling and DEER measurements to avoid any kinetic effects occurring in between sample preparation and measurement.

G.1.3. Experimental details

CW-EPR experiments

CW X-band EPR spectra were detected using a Bruker EMX spectrometer equipped with a Bruker Eleksys Super High Sensitive probehead. Measurements were performed at room temperature, 100 kHz field modulation, 250 to 450 mT field sweep, 4 G modulation amplitude, and 1 mW microwave power (10 dB attenuation). The time constant was 10.24 ms and the conversion time 40.96 ms. The samples were filled into 0.9 mm inner diameter glass capillaries (10-20 μ l sample volume).

Pulsed EPR experiments

Pulsed experiments were performed on a customized Bruker Elexsys E580 Q-band spectrometer,⁹⁸ which is extended with an incoherent ultra-wide band (UWB) pulse channel based on a 12 GS/s arbitrary waveform generator (AWG, Agilent M8190A).¹¹⁷ The temperature was adjusted, using a helium flow cryostat, to 10 K for distance measurements. ED field-swept and relaxation measurements were performed at 20 K for samples related to *HpDnaB* and at 10 K for BmrA. ED field-swept spectra were acquired with a Hahn-echo pulse sequence $\pi/2 - \tau - \pi - \tau - \text{echo}$ using a $\pi/2$ pulse length of $t_p = 12$ ns, a π pulse length of $t_p = 24$ ns and $\tau = 400$ ns. The same sequence was used to record the phase memory decay by incrementing the initial interpulse delay τ in steps of 240 ns and 40 ns for samples related to DnaB and BmrA, respectively. Relaxation traces were detected in the valley between the 2nd and 3rd hyperfine line of Mn^{2+} . This position is indicated in the EDEPR spectra by an arrow in Figure G.1(b) for *HpDnaB*. The reason for this choice is the larger difference in linewidths of the central $|+1/2\rangle \leftrightarrow |-1/2\rangle$ transitions of different species as compared to the difference in widths for any other transition of the high-spin Mn^{2+} ions. The six sharp lines of the Mn^{2+} EPR spectrum correspond to the central $|+1/2, m_I\rangle \leftrightarrow |-1/2, m_I\rangle$ transition and are split by the ^{55}Mn hyperfine coupling (natural abundance 100%, nuclear spin $I = 5/2$). Considering the zero-field splitting (ZFS) term in the spin Hamiltonian as a small perturbation to the electron Zeeman interaction, in first (linear) order of a perturbation series this transition is not affected by the ZFS term, while all other transitions of Mn^{2+} are broadened by the orientation dependent ZFS interaction. In second order of the perturbation series the central transition of Mn^{2+} gets moderately broadened by the ZFS term. Thus, the dependence of the width of this transition on ZFS is steeper than for all other transitions. As a result, the intensity of the spin echo signal per fixed amount of molecules, measured at this transition, would differ to the largest extent for different Mn^{2+} species detected in our experiments. In the valley between any two hyperfine components of the central transition, the relative contributions of different species to the spin echo signal correspond more closely to their concentrations in the sample. Among all possible positions of the satellite transitions, the selected one corresponded to the maximum spin-echo intensity.

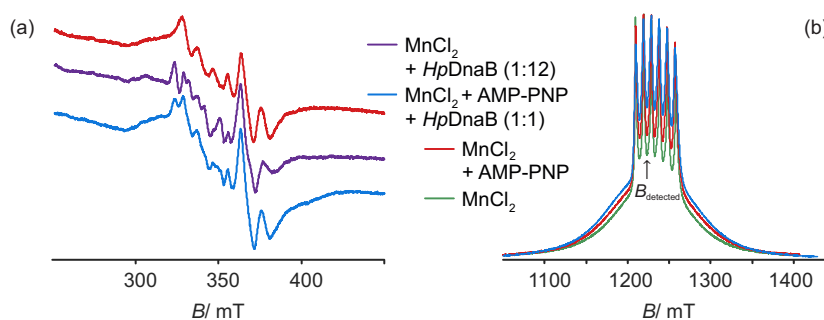


Figure G.1. (a) Comparison of EPR CW lineshapes for AMP-PNP: Mn^{2+} (red), 12:1 *HpDnaB*:AMP-PNP: Mn^{2+} (purple) and 1:1 *HpDnaB*:AMP-PNP: Mn^{2+} (blue) at room temperature. The spectrum of the sample with a 1:1 protein: Mn^{2+} ratio is a superposition of the spectrum of the AMP-PNP: Mn^{2+} sample and the sample with a 12:1 protein: Mn^{2+} ratio, thus indicating incomplete binding of Mn^{2+} to the NBDs in the case of a 1:1 protein: Mn^{2+} ratio. (b) Anisotropic broadening of EDEPR spectra at 20 K and 34.5 GHz indicating the binding of Mn^{2+} to *HpDnaB*: EDEPR spectra of a 0.3 mM MnCl_2 reference solution (green), AMP-PNP: Mn^{2+} (red) and 1:1 *HpDnaB*:AMP-PNP: Mn^{2+} (blue). In contrast to the room-temperature CW-EPR spectra, EDEPR experiments are performed in a frozen glassy matrix at 20 K and thus the spectral differences are dominated by changes in the zero-field splitting parameters, since molecular tumbling processes are frozen at these conditions. The observer field B_{detected} for relaxation and distance measurements is marked by an arrow.

The four-pulse DEER data were obtained using the sequence $\pm(\pi/2)_{\text{obs}} - \tau_1 - (\pi)_{\text{obs}} - \tau_1 + t - (\pi)_{\text{chirp}} - (\tau_2 - t) - (\pi)_{\text{obs}} - \tau_2$ -detection. For DnaB, a $\tau_1 = 400$ ns and $\tau_2 = 5000$ ns was used. For BmrA τ_1 was set to 600 ns and τ_2 to 1400 ns. The time t was incremented in steps of 8 ns. The observation pulses had a length of 12 ns and the observation frequency was placed in the valley between the 2nd and 3rd hyperfine line of the Mn^{2+} at about 34.5 GHz. The (π) linear frequency-swept (chirp) pulse settings were optimized analogous to the previously reported ones for Gd^{3+} - Gd^{3+} DEER measurements.¹¹⁵ To describe the chirp pulses used in this work, we refer to the start and end frequencies of the frequency sweep as f_1 and f_2 , respectively. Thus, the sweep width Δf is the absolute difference between f_1 and f_2 . Two chirp pump pulses were applied with lengths of 50 ns on both sides of the observer frequency and the pulse edges were smoothed with a quarter sine wave during 10 ns. DEER experiments were performed on the deuterated *HpDnaB* sample to prolong the accessible distance range.

For *HpDnaB*, two different sweep ranges were tested. First a sweep range from $f_1 = -0.6$ GHz to $f_2 = -0.2$ GHz and $f_1 = 0.6$ GHz to $f_2 = 0.2$ GHz with respect to the observer frequency, corresponding to a total pump bandwidth of 0.8 GHz (data shown in the top three subplots of Figure G.3) and a second sweep range from $f_1 = -0.8$ GHz to $f_2 = -0.2$ GHz and $f_1 = 0.8$ GHz to $f_2 = 0.2$ GHz with respect to the observer frequency, corresponding to a total pump bandwidth of 1.2 GHz (data shown in the middle three subplots of the Figure G.3). The pump pulses with a total bandwidth of 0.8 GHz resulted in a modulation depth of about 1.5%, while with the latter pulse settings a modulation depth of approximately 1.5% could be achieved (see Figure G.3). The data in the main text (Figure 10.3(a-f)) and in the bottom three subplots in the Figure G.3 show the average of both data sets.

For BmrA, three different pulse settings were tested (see Figure G.4). First a sweep range from $f_1 = -0.8$ GHz to $f_2 = -0.2$ GHz and $f_1 = 0.8$ GHz to $f_2 = 0.2$ GHz with respect to the observer frequency, corresponding to a total pump bandwidth of 1.2 GHz (data shown in the top three subplots of Figure G.4), a second sweep range from $f_1 = -0.9$ GHz to $f_2 = -0.3$ GHz and $f_1 = 0.9$ GHz to $f_2 = 0.3$ GHz with respect to the observer frequency, corresponding to a total pump bandwidth of 1.2 GHz (data shown in the middle three subplots of the Figure G.4) and a third sweep range from $f_1 = -0.7$ GHz to $f_2 = -0.3$ GHz and $f_1 = 0.7$ GHz to $f_2 = 0.3$ GHz with respect to the observer frequency, corresponding to a total pump bandwidth of 0.8 GHz (data shown in the bottom three subplots of the Figure G.4).

The five-pulse RIDME data were obtained using the sequence $(\pi/2) - \tau_1 - (\pi) - \tau_1 + t - (\pi/2) - T_{\text{mix}} - (\pi/2) - \tau_2 - t - (\pi) - \tau_2$ -detection. An eight-step phase cycle as described in Ref.⁶⁷ was applied. $(\pi/2) - (\pi)$ pulses were set to 16 - 32 ns. τ_1 was set to 600 ns. τ_2 was set to 1.4 μs . Longer time traces were also tested, but suffered from strong spectrometer instabilities and unbalanced detection channels of the W-band spectrometer at the time of these measurements. The mixing time was set to 24 μs , which is with $\sim 0.8T_1$ in the optimum sensitivity range according to Chapter 9. Slightly larger modulation may be reached for longer mixing times. RIDME experiments were performed on the deuterated *HpDnaB* sample to prolong the accessible distance range. RIDME data were analysed with the program OvertoneAnalysis,¹¹⁴ which allows for higher frequency overtones of the dipolar frequency ω_{dd} in the kernel function: $K_{\text{mod}}(r, t) = \int [P_1 \cos(\omega(r, \theta) \cdot t) + P_2 \cos(2\omega(r, \theta) \cdot t) + P_3 \cos(3\omega(r, \theta) \cdot t)] \sin(\theta) d\theta$. Data presented in Figure 10.3(e, f) show analysis with an overtone-free kernel ($P_2 = P_3 = 0$) as well as overtone coefficients $P_2 = 0.5$ and $P_3 = 0.1$ that were found to describe Mn^{2+} - Mn^{2+} RIDME measurements in Chapter 9.

G.2. Detailed description of determination of the fraction of bound Mn^{2+} by EPR relaxation measurements

Transverse relaxation of Mn^{2+} ions is strongly affected by the interaction with other paramagnetic centres, as well as with surrounding nuclear spins, via the spin diffusion mechanism. Among all nuclear spins, matrix protons contribute by far most strongly, if they are present. For the *HpDnaB* system this allows for a relaxation-based separation of the Mn^{2+} centres in the form of AMP-PNP: Mn^{2+} from the ones bound to the protein. By measuring the *HpDnaB*:AMP-PNP: Mn^{2+} sample in deuterated buffer/deuterated glycerol mixture a very low number of solvent protons in the vicinity of free AMP-PNP: Mn^{2+} species was ensured. For these species the protons in the vicinity of Mn^{2+} originated only from the very limited number of the AMP-PNP protons, whereas other nearby magnetic nuclei had much smaller gyromagnetic ratios and, accordingly, their flips contributed much less to the electron spin transverse relaxation. Binding of the AMP-PNP: Mn^{2+} complex to the protein brings the Mn^{2+} ions in close vicinity of a large pool of protons. This and the presence of several Mn^{2+} ions close to each other in the *HpDnaB*:AMP-PNP: Mn^{2+} species leads to a faster relaxation of the bound species as compared to unbound AMP-PNP: Mn^{2+} species. Since in the protein containing sample both types of species were present, the actual transverse relaxation decay trace shows a complex behaviour with quick initial decay, due to the bound species, and a significantly slower decaying tail due to the unbound species. This phenomenon allows, in the case of *HpDnaB*, to rather accurately estimate the fraction of Mn^{2+} ions attached to the protein NBDs. We can assume, in the same way as in an analogous longitudinal relaxation data analysis for lanthanide-radical pairs that the additional relaxation channel for the protein-bound species is independent from all other channels, and the total relaxation rate is a sum of the rates for all relevant relaxation channels.^{104;313} Under this assumption, division of the transverse relaxation time trace of the protein-containing sample by the corresponding trace for the sample with only AMP-PNP: Mn^{2+} species present, results in a ratio trace that contains a contribution from *HpDnaB*:AMP-PNP: Mn^{2+} , which decays with the rate corresponding only to the additional relaxation channel, while the unbound AMP-PNP: Mn^{2+} species contributes constant intensity. In reality, due to intermolecular interactions, and, perhaps, due to imperfect additivity of different relaxation rates, this latter signal is not constant, but rather decays very slowly, as it is seen in the Figure 10.2(b) of the Chapter 10. Still, we can rather accurately estimate the fraction of *HpDnaB*:AMP-PNP: Mn^{2+} species to be between the vertical coordinate of the kink of the division trace and the point where the prolongation of the slowly relaxing part of the division trace crosses the y -axis. One can see from Figure 10.2(b) that the relative intensity of the AMP-PNP: Mn^{2+} species is thus about 0.4, which corresponds to about 60% of the *HpDnaB*:AMP-PNP: Mn^{2+} species in the stoichiometric mixture. For BmrA, a detailed analysis is hampered by the unknown Mn^{2+} excess resulting from sedimentation and buffer replacement. Still, one can estimate the fraction of Mn^{2+} bound to the protein in the sample to 8% of the Mn^{2+} ions within the sample (see Figure 10.2(c)).

G.3. Additional discussion of the DEER distance measurements

Experiments were performed on the deuterated *HpDnaB* sample to prolong the accessible distance range. A comparison of phase memory times of deuterated and protonated *HpDnaB* samples is shown in Figure G.2(a). Due to the difference in the phase memory time between NBD bound

and free Mn^{2+} species, the dipolar modulation depth was decreasing with the increase of the transverse evolution time in the DEER experiment (Figure G.2(b)). Furthermore, it is possible that, due to the faster transverse relaxation times of the oligomers with higher number of bound Mn^{2+} ions, the longer distance peaks are also partially reduced in intensity, similar to the earlier results of Schiemann and coauthors.^{327;328}

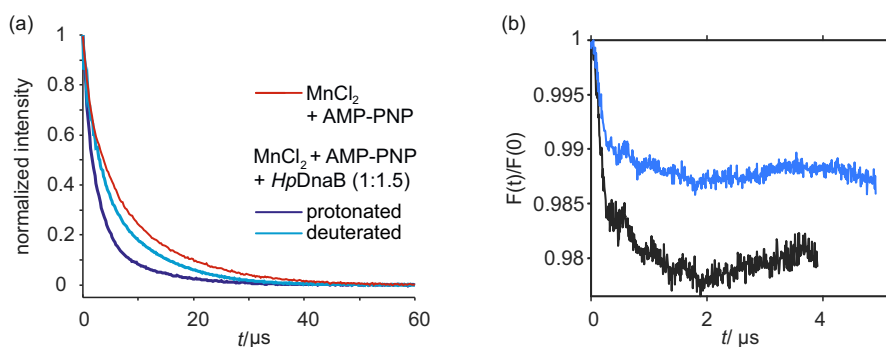


Figure G.2. (a) Hahn-echo decay at 20 K in Q band. Comparison of 0.3 mM *HpDnaB* phosphate/D₂O/glycerol-d₈ buffer expressed in protonated (purple) or deuterated (cyan) media. The MnCl_2 -AMP:PNP measurement (red) is shown for comparison. Expression in deuterated media allows for longer DEER time traces, and, accordingly, longer detectable Mn^{2+} - Mn^{2+} distances. However, relaxation is still faster for NBD-bound to solvent exposed Mn^{2+} . (b) Reduction of modulation depth for UWB-DEER time traces (pulse offset ± 0.3 GHz and bandwidth of 600 MHz) with increased trace length τ_2 of 5 μs (blue) compared to $\tau_2 = 4 \mu\text{s}$ (black).

Despite the use of broadband pump pulses and the presence of multiple Mn^{2+} ions in each protein oligomer, the observed depth of dipolar modulation of approximately 1.5% (Figure 10.3(b)) is comparable to earlier reports on doubly Mn^{2+} labelled molecules, where modulation depths of 0.4% and 1-2% were found for the DEER setups with narrower-band rectangular pump pulse.^{268;314} Here, apparently, the factors that increase the dipolar modulation depth are compensated by the rather large ZFS of the *HpDnaB*:AMP-PNP: Mn^{2+} complex, and the incomplete binding of the AMP-PNP: Mn^{2+} species to the NBDs. The paramagnetic Mn^{2+} ions in the buffer solution are on average quite remote from each other at the studied ion concentrations. Thus, the DEER signal from these Mn^{2+} ions would only contribute to the slowly changing intermolecular background decay and will not add to the dipolar modulation depth. Mn^{2+} - Mn^{2+} distances within the DEER distance range stem mainly from Mn^{2+} ions loaded into NBDs. Thus, the dipolar modulation depth is limited to the fraction of the spin-echo signal originating from only NBD-bound Mn^{2+} ions. If these ions have faster transverse relaxation than the Mn^{2+} ions in buffer, they contribute the less to the DEER time trace the longer this trace is. The dipolar modulation depth, which stems from these NBD-bound ions, scales according to their relative contribution to the signal, and is thus expected to decrease with increasing trace length. A longer transverse relaxation time of the AMP-PNP: Mn^{2+} species would thus further reduce the DEER modulation depth, especially for experiments with long dipolar evolution times. While a low dipolar modulation depth is more difficult to detect, the sample composition assured that in every oligomer no more than two Mn^{2+} spins were excited by the DEER pulse sequence. We can thus argue that no multi-spin effects, which would be potentially possible in such oligomer systems,³¹⁷ should be present in the reported DEER data.

Experimental data were processed using the DeerAnalysis software.⁷⁸ Distance distributions were obtained by Tikhonov-regularization using a regularization parameter of 1. In the distance distribution shown in the Figure G.3 (*HpDnaB* sample), the peak at about 3 nm (right panel)

is responsible for the clearly visible fast oscillations of the DEER form factor signal (central panel). Multiple full oscillations were detected for this peak and, thus, its shape is determined with good accuracy. The other peak in the distance range 5-6.5 nm corresponds to the shallow oscillation with the minimum at about 2 μ s (central panel). Only about one full period of oscillation could be detected for this peak, even with use of deuterated *HpDnaB*. Furthermore, part of this oscillation could be incorporated into the background model, and variation of this model with the validation tool in DeerAnalysis resulted in changes of the amplitude and mean distance of this peak indicated by the grey error band in Figure 10.3(c). More precisely, in the validation procedure the beginning of the background correction range was varied between 1000 and 2500 ns in 11 steps. Furthermore, 11 different artificial noise traces of the same average magnitude as the intrinsic noise in the DEER trace were added to this trace to verify the stability of the distance distribution to the level and realization of noise. Grey coloured bands in the Figures 10.3(c) and G.3 (right three panels) indicate the variation of the Mn^{2+} - Mn^{2+} distance distribution in the described validation procedure. These variations affected the peak at 3 nm much less than the peak at 5-6.5 nm. Still, for any background model tested, a peak in the range 5-6.5 nm was present although it varied in width, amplitude, and mean distance. The distance range between 5 and 6.5 nm is consistent with the homology model based Mn^{2+} - Mn^{2+} distances for the non-nearest neighbours as shown in Chapter 10 Figure 10.3(b). Thus, only the peaks at 3 and 5-6 nm are highly significant after validation and the remaining peaks could stem from the uncertainty of background validation due to short trace length and possibly from unspecifically bound Mn^{2+} and/or some flexibility of the structure.

For BmrA, three different pulse settings were tested (see Figure G.4). The pump pulse with a total bandwidth of 0.8 GHz resulted in a modulation depth of about 0.16%, while with the pulse settings with 1.2 GHz total bandwidth resulted in a modulation depth of approximately 0.14% for a 200 MHz offset and 0.12% for 300 MHz offset between pump and observed frequency. It is important to note that the distance distribution is not altered by the pump pulse settings. The data in Chapter 10 (Figure 10.3(g-i)) show the average of both 1.2 GHz total bandwidth measurements. Primary data including the *L*-curve for this averaged data set are shown in Figure G.5. In this case, the low dipolar modulation depth most likely results from the large fraction of unbound Mn^{2+} ions within the sample. This modulation depth still suffices to confirm the presence of the expected Mn^{2+} - Mn^{2+} distances in the sample. For the BmrA sample, the same analysis procedure as for the DnaB measurements was performed. For the validation procedure the background range was adjusted to 200 to 350 ns in 11 steps. It confirms a mean distance of about 1.9 nm in all cases. Note that these DEER data are obtained at the limit of sensitivity and stability of the EPR spectrometer. While the additional smaller peaks in the distance distribution might indicate some non-specific binding of the Mn^{2+} ions to the protein or lipid bilayers, they might as well originate from low-frequency noise or electronic instabilities of the spectrometer. An additional uncertainty arises in the zero time of the modulation for very short distances. Variation of the zero time shifts the maximum of the distance distribution slightly (see Figure G.6). This uncertainty of the mean distance, however, does not affect the conclusion of this work.

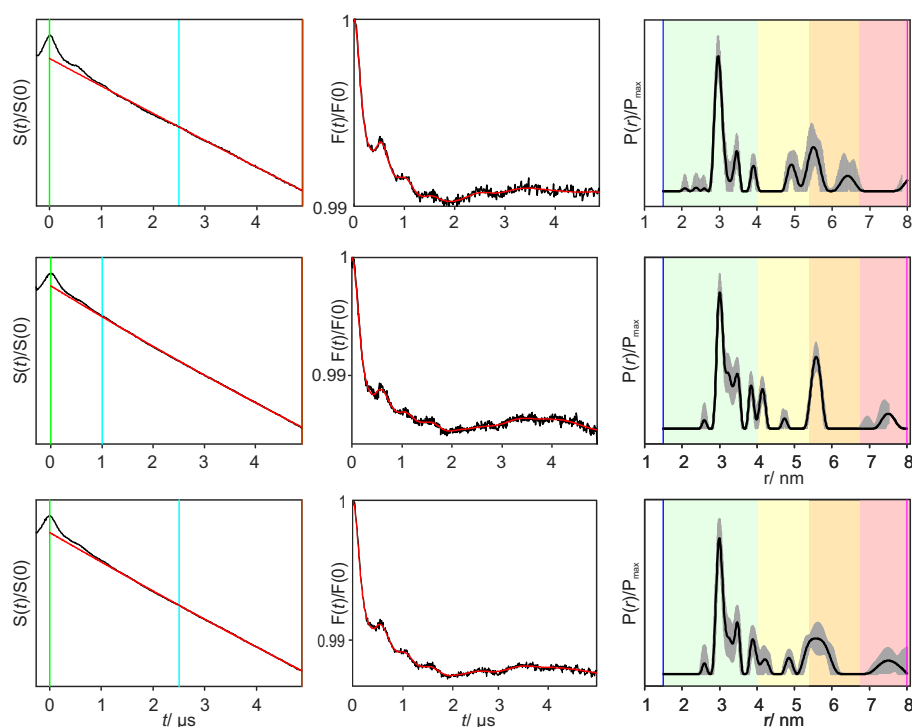


Figure G.3. Overview of the Mn^{2+} - Mn^{2+} Q-band DEER data of $Hp\text{DnaB}:\text{AMP-PNP}:\text{Mn}^{2+}$ expressed in deuterated media at 10 K. Data sets from top to bottom: 800 MHz chirp pump pulse, 1200 MHz chirp pump pulse, average of both primary data sets. Left three panels: Normalized primary DEER data (black line) and background fit (red line). The zero time is marked by the green vertical line, the cyan line marks the beginning of the background range fit, and the orange line labels the cut-off position. Middle three panels: Background-corrected form factor in the time domain (black line) and corresponding fit (red line). Right three panels: distance distribution. The shaded areas give an error estimate if the start of the background fit range is varied from 1000 to 2500 ns and different artificial noise traces are added. The colour-coding indicates reliability ranges resulting from the limited length of the dipolar evolution trace. Pale green: Shape of distance distribution is reliable. Pale yellow: Mean distance and width are reliable. Pale orange: Mean distance is reliable. Pale red: Long-range distance contributions may be detectable, but cannot be quantified (see DeerAnalysis manual).

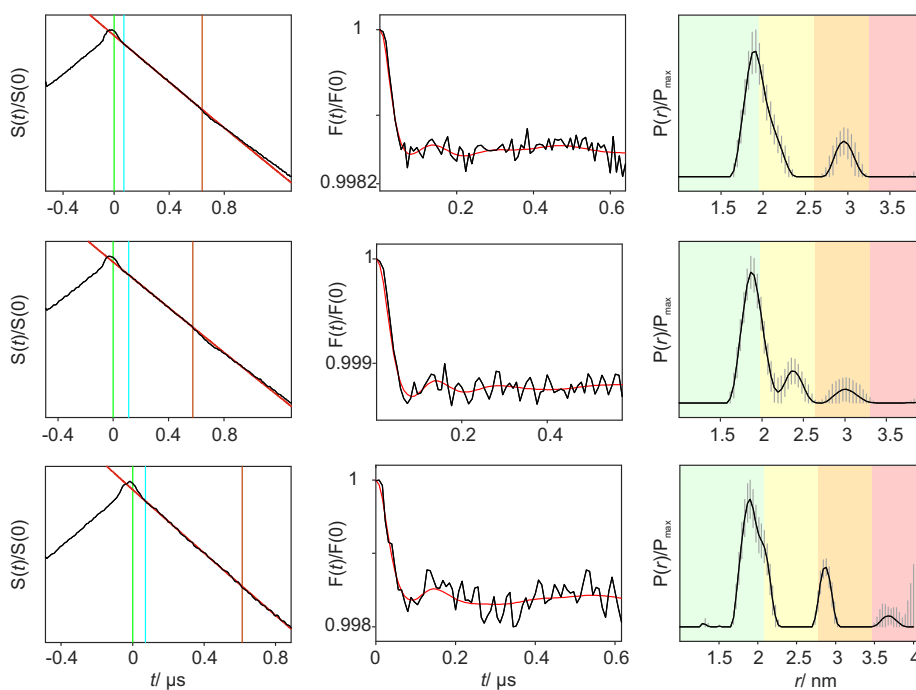


Figure G.4. Overview of the Mn^{2+} - Mn^{2+} Q-band DEER data recorded on $\text{BmrA:ATP:Mn}^{2+}:\text{VO}_4^{3-}$ at 10 K. Data sets from top to bottom: 1.2 GHz wide chimp pump pulse with 200 MHz offset between pump and observer frequency, 1.2 GHz wide chimp pump pulse with 300 MHz offset between pump and observer frequency and 0.8 GHz wide chimp pump pulse with 300 MHz offset between pump and observer frequency. Left three panels: Normalized primary DEER data (black line) and background fit (red line). The zero time is marked by the green vertical line, the cyan line marks the beginning of the background range fit, and the orange line labels the cut-off position. Middle three panels: Background-corrected form factor in the time domain (black line) and corresponding fit (red line). Right three panels: distance distribution. The shaded areas give an error estimate if the start of the background fit range is varied from 200 to 350 ns and different artificial noise traces are added. The colour-coding indicates reliability ranges resulting from the limited length of the dipolar evolution trace as described in Figure G.3.

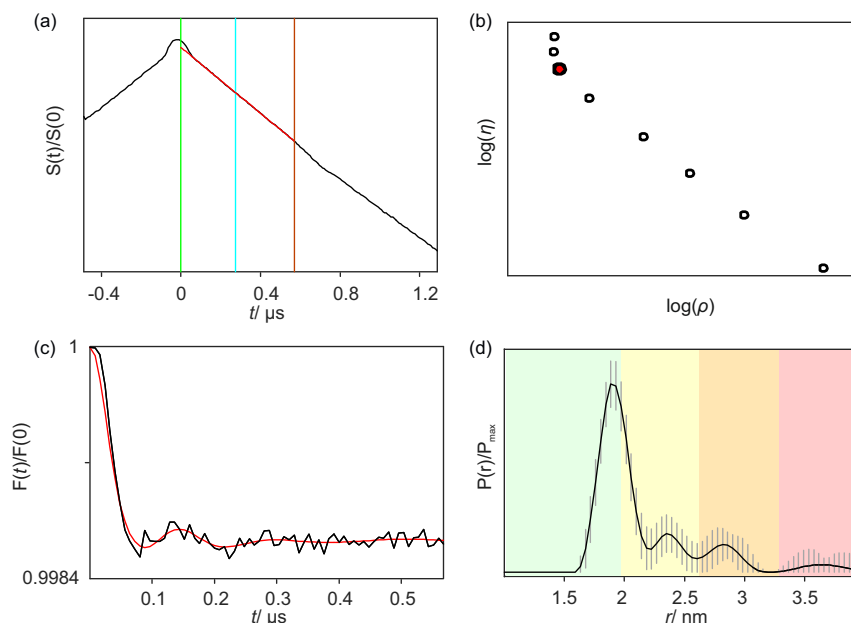


Figure G.5. Overview of averaged Mn^{2+} - Mn^{2+} Q-band DEER data in $\text{BmrA:ATP:Mn}^{2+}:\text{VO}_4^{3-}$ at 10 K. (a) Primary data, the green vertical line marks the zero time, the cyan line the start of the background correction and the orange line the cut-off frequency, which is chosen based on artefacts occurring in the primary data (black line). The red line shows the background fit, (b) L-curve resulting from Tikhonov regularization. The red dot marks the selected regularization parameter of 10.3, (c) background corrected form factor (black line) and corresponding fit (red line), (d) resulting distance distribution. The grey bands give an error estimate if the start of the background fit range is varied from 200 to 350 ns and different artificial noise traces are added. The colour-coding indicates reliability ranges resulting from the limited length of the dipolar evolution trace as described in Figure G.3.

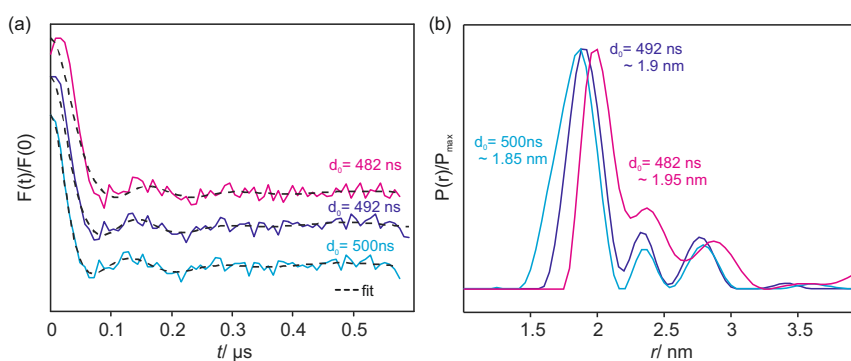


Figure G.6. Variation of form factor (a) and distance distribution (b) upon change in zero time for the averaged data set shown in Figure G.5. The broader shape of the maximum in the primary data (see Figure G.5) induces an uncertainty in the zero time. For very short distances this shifts the maximum of the distance distribution slightly. Setting the zero time to the theoretical value of 500 ns ($\tau_1 - t_{\text{init}}$, light blue line) gives a mean distance of about 1.85 nm, while placing the zero time rather symmetric around the maximum (~ 482 ns, magenta line) gives a mean distance of about 1.95 nm. This choice leads to a significant deviation between the measured (solid lines) and simulated DEER (black dashed lines) form factor. Placing the zero time to the start of the decay (~ 492 ns, violet line) results in a mean distance of about 1.9 nm, which we consider as the best estimate.

Publications and Conference contributions

Publications

- 2019 | K. Keller, M. Qi, C. Gmeiner, I. Ritsch, A. Godt, G. Jeschke, A. Savitsky, M. Yulikov, 'Intermolecular Background Decay in RIDME Experiments', *Phys. Chem. Chem. Phys.*, **221**, 8228-8245
- G. Stevanato, D Kubicki, A.-S. Chauvin, K. Keller, M. Yulikov, G. Jeschke, M. Mazzanti, L. Emsley, 'A factor two improvement in high-field dynamic nuclear polarization from Gd(III) complexes by design', *J. Am. Chem. Soc.*, **141**, 8746-8751
- 2018 | K. Keller, T. Wiegand, R. Cadalbert, B. H. Meier, A. Böckmann, G. Jeschke, M. Yulikov. 'High-Spin Metal Centres in Dipolar EPR Spectroscopy', *Chimia*, **72**, 216-220
- J. A. Clayton*, K. Keller*, M. Qi, J. Wegner, V. Koch, H. Hintz, A. Godt, S. Han, G. Jeschke, M. S. Sherwin, M. Yulikov. 'Quantitative analysis of zero-field splitting parameter distributions in Gd(III) complexes', *Phys. Chem. Chem. Phys.*, **20**, 10470-10492
- 2017 | K. Keller, V. Mertens, M. Qi, A. I. Nalepa, A. Godt, A. Savitsky, G. Jeschke and M. Yulikov. 'Computing distance distributions from dipolar evolution data with overtones: RIDME spectroscopy with Gd (III)-based spin labels', *Phys. Chem. Chem. Phys.*, **19**, 17856-17876
- T. Wiegand*, D. Lacabanne*, K. Keller*, R. Cadalbert, L. Lecoq, M. Yulikov, L. Terradot, G. Jeschke, B. H. Meier and A. Böckmann. 'Solid-state NMR and EPR Spectroscopy of Mn²⁺-Substituted ATP-Fueled Protein Engines', *Angew. Chem. Int. Ed.*, **56**, 3369-3373
- 2016 | K. Keller, A. Doll, M. Qi, A. Godt, G. Jeschke and M. Yulikov. 'Averaging of nuclear modulation artefacts in RIDME experiments', *J. Magn. Reson.*, **272**, 108-113
- K. Keller*, M. Zalibera*, M. Qi, V. Koch, J. Wegner, H. Hintz, A. Godt, G. Jeschke, A. Savitsky and M. Yulikov. 'EPR characterization of Mn (II) complexes for distance determination with pulsed dipolar spectroscopy', *Phys. Chem. Chem. Phys.*, **18**, 25120-25135
- 2015 | O. A. Blackburn, N. F. Chilton, K. Keller, C. E. Tait, W. K. Myers, E. J.L. McInnes, A. M. Kenwright, P. D. Beer, C. R. Timmel, S. Faulkner. 'Spectroscopic and crystal field consequences of fluoride binding by [Yb.DTMA]³⁺ in aqueous solution', *Angew. Chem. Int. Ed.*, **54**, 10783-10786

*equal contributions

Manuscripts in preparation

- 2019 | F. D. Breitgoff*, K. Keller*, M. Qi, D. Klose, M. Yulikov, A. Godt, G. Jeschke: 'Distance measurements in Cu(II)–Cu(II) spin pairs', *manuscript in preparation*
- K. Keller, M. Qi, M. Hülsman, X. Yao, H. Hintz, C. Gmeiner, G. Jeschke, A. Godt, M. Yulikov, 'Towards high-spin RIDME in structural biology', *manuscript in preparation*
- K. Keller, I. Ritsch, H. Hintz, M. Qi, F. Breitgoff, D. Klose, Y. Polyhach, M. Yulikov, A. Godt, G. Jeschke, 'Accessing Distributions of Exchange and Dipolar Couplings in Stiff Molecular Rulers with Cu(II) centres', *manuscript in preparation*

Conference contributions

- 2018 | Poster at the In Vivo Magnetic Resonance Gordon Research Conference, 'Spectroscopic Parameters and Electronic Relaxation of Paramagnetic Gadolinium Complexes', Andover, United States, Chemistry Travel Award
- Invited talk at the In Vivo Magnetic Resonance Gordon Research Seminar, 'Spectroscopic Parameters and Electronic Relaxation of Paramagnetic Gadolinium Complexes', Andover, United States.
- JOEL prize talk at the Royal Society of Chemistry ESR Conference, 'Metal centres in RIDME spectroscopy: methodology and application', London, United Kingdom, Runner-up
- 2017 | Contributed talk at the Swiss Chemical Society Fall Meeting, 'Metal centres in EPR Spectroscopy', Bern, Switzerland, Best Oral Presentation Award.
- Contributed talk at the Royal Society of Chemistry ESR Conference, 'EPR and solid-state NMR of Mn²⁺ substituted ATP-fueled protein engines', Oxford, United Kingdom.
- 2016 | Poster at the European federation of EPR meeting, 'Multi-Frequency EPR line shape analysis of Gd(III) complexes', Torino, Italy.
- Contributed talk at the RSC ESR Conference, 'Towards analysis of RIDME-based distance measurements in Mn(II) and Gd(III) spin pairs', Essex, United Kingdom.
- 2015 | Poster at the EFEPR SummerSchool, 'Analysis of RIDME-based distance measurements in Gd(III) and Mn(II) spin pairs', Berlin, Germany.
- Poster at the Euromar Conference, 'Characterization of metal chelate complexes for pulsed dipolar spectroscopy', Prague, Czech Republic.

Curriculum Vitae

Katharina Keller

Born on October 3rd 1989

Citizen of Germany

Education

- 03/2015 **PhD Candidate in the group of Prof. Jeschke, ETH Zurich, Switzerland**
- 03/2019 Focus on method development of pulse sequences and data analysis routines.
Application to chemical and biological systems. For details see publication list.
- 09/2012 **Master's in Interdisciplinary Science, ETH Zurich, Switzerland**
- 12/2014 Focus on physical chemistry and biomedical engineering.
- 09/2014 **University of Oxford, United Kingdom**
- 12/2014 External Master's thesis in the group of Prof. Timmel.
- 07/2013 **University of New South Wales, Australia**
- 11/2013 Research project in the group of Prof. Bilston at Neuroscience Research Australia.
- 09/2009 **Bachelor's in Interdisciplinary Science, ETH Zurich, Switzerland**
- 08/2012 Focus on physical chemistry and biophysics.

Work Experience

- 03/2015 **ETH Zurich, Switzerland**
- present Supervision of semester students, teaching assistant for molecular quantum mechanics and magnetic resonance, lab courses in physical chemistry.
- 04/2014 **Philips Technology GmbH, Germany**
- 07/2014 Intern at Innovative Technologies: Optimization of a MRI pulse sequence.
- 10/2010 **ETH Zurich, Switzerland**
- 06/2013 Public relations assistant: Organization and assistance in public events.
- 02/2012 **ETH Zurich, Switzerland**
- 06/2013 Teaching assistant for various physical chemistry lectures